ECCOMAS Thematic Conference
hosted by the Czech Technical University
Prague, Czech Republic, 25–27 June 2007

MHM 2007:
Modelling of Heterogeneous Materials

with Applications in Construction and Biomedical Engineering

Proceedings

edited by

Milan Jirásek
Zdeněk Bittnar
Herbert Mang

ISBN: 978-80-01-03762-1
Modelling of Heterogeneous Materials
Edited by M. Jirásek, Z. Bittnar and H. Mang
Prague, 2007

Contents

Preface

Virtually all natural and man-made materials exhibit a heterogeneous internal structure if observed on a sufficiently fine scale of resolution, and many of them contain pores filled by one or more pore fluids. Realistic description of deformation and failure mechanisms in such materials, as well as of their transport properties, still remains a major challenge of contemporary mechanics and physics. Moreover, in some cases the internal microstructure evolves in time due to chemical reactions or biological processes that often involve interaction with the environment.

The aim of the conference on *Modelling of Heterogeneous Materials with Applications in Construction and Biomedical Engineering* (MHM 2007) is to gather specialists in modelling of heterogeneous materials that work in different domains of application but face similar general problems. Attention focuses on theoretical modelling and numerical simulation on multiple scales, but advanced experimental techniques and characterization methods, e.g. on the nano- and micro-levels, are also represented. The central theme of the conference is closely related to sustainable development, in which new materials play a key role. Computational modelling, based on sound theory and supported by experiments, is an essential tool for the design and optimization of innovative materials, tailored for specific purposes. In the area of construction materials, a very important aspect is their multifunctionality. In biomedical engineering, an ever increasing attention is paid to novel materials to be used in advanced implants for critical organs such as the heart, liver and pancreas, and also to biomimetic gels and polymers for tissue repair as a treatment of arthritis and osteoporosis. We hope that this conference will not only display recent achievements but also contribute to cross-fertilization of different scientific communities and to formation of new international research teams.

The Faculty of Civil Engineering of the Czech Technical University in Prague already hosted two international workshops on modelling of a particular class of materials with important applications in the construction industry: the *US–Europe Workshop on Fracture and Damage in Quasibrittle Structures* (1994), and the *Workshop on Mechanics of Quasibrittle Materials and Structures* (1998). Both workshops were attended by leading experts in the field and, due to their relatively limited size and well-defined central theme, created a favorable climate for stimulating discussions. This year, we would like to build on the success of the workshops and prepare optimal conditions for the participants of a scientific gathering of a larger size and scope.

MHM 2007 is organized as one of the Thematic Conferences of ECCOMAS, the *European Community on Computational Methods in Applied Sciences*. In three days, 19 plenary lectures, 97 lectures in parallel sessions and 28 posters will be presented. The opening lecture will be delivered by a distinguished alumnus of the Czech Technical University, Professor Zdeněk P. Bažant, whose approaching 70th anniversary will be commemorated by a special workshop preceding the conference. Not only Zdeněk but also his alma mater celebrates an important anniversary. The Czech Technical University in Prague is a direct successor of one of the oldest engineering schools in Europe, established by an imperial decree in January 1707. We hope that the participants will enjoy the days spent on the campus of the CTU and in the city of Prague.

The Proceedings of MHM 2007 contain extended two-page abstracts grouped into thematic areas that correspond to sessions of the conference. The presenting author of each paper with multiple authors is marked by an asterisk. Searching for the work of a specific author is facilitated by the author index on the last pages of the Proceedings. Many contributions contain color figures, and we sincerely apologize that due to budget limitations it was possible to print in color only some of them. However, the book of proceedings is accompanied by a CD with a PDF file, in which all the color illustrations can be admired in their full beauty.

We would like to thank all coworkers who provided technical assistance with the editorial work, in particular M. Brouček, M. Horák, M. Posch, V. Šmilauer and J. Zeman. We also express our gratitude to all members of the Scientific Committee, which was composed of the following international experts: Z. P. Bažant, T. Belytschko, I. Carol, S. C. Cowin, F. Darve, W. Dienemann, M. Doblaré, L. Dormieux, W. Ehlers, D. Gawin, F. Glasser, Ch. Hellmich, G. A. Holzapfel, J. M. Huyghe, H. Jennings, E. Kuhl, K. Maekawa, R. W. Ogden, E. Oñate, G. Pijaudier-Cabot, G. W. Scherer, B. Schrefler, K. Scrivener, P. Steinmann, F.-J. Ulm and K. Willam. Last but not least, we would like to thank F. Caner, D. Ciancio, B. Markert, L. Sanavia, M. Šejnoha and J. Zeman who, in addition to several members of the Scientific Committee, organize minisymposia or sessions at MHM 2007. Let us hope that the conference will be enriching and stimulating for all of us.

Zdeněk Bittnar and Herbert Mang, conference chairmen

Milan Jirásek, chairman of the local organizing committee

Part I

Plenary Lectures

Microplane Modeling of Damage or Fracture and Multiscale Concepts

Z. P. Bažant

Northwestern University, 2145 Sheridan Road, CEE
Evanston, IL 60208, USA; z-bazant@northwestern.edu

Summary: The concepts of microplane model in representing the physical reality for materials with softening damage and fracturing are discussed, the basic features of microplane model M4 are outlined, and the relation to multiscale modeling approaches is critically examined.

Motivation, concepts and advantages

The classical constitutive models expressed in terms of stress and strain tensors and their invariants are attractive by their simplicity but cannot capture the intricate response of quasibrittle materials such as concrete, rock and polymer-fiber composites. For example, a relation between I_1 and J_2 characterizes internal friction only in a vague non-specific way. It cannot capture frictional slip or microcrack growth occurring solely on a few distinct planes of particular orientations. Neither can these classical models capture the vertex effect. To capture it, many simultaneous yield or damage surfaces (or loading potentials) intersecting at each current state point would have to be used. Ignoring the existence of many such surfaces is what leads to the expedience of non-associated flow rules. Although, in theory, Koiter's multisurface plasticity could be used, the difficulties appear unsurmountable if these surfaces are restricted to be functions of the stress invariants. Yet each yield or damage surface does not have to be invariant. Only their aggregate, the constitutive model as a whole, must be properly invariant. The microplane model overcomes all of the aforementioned problems. It can be regarded as non-classical multisurface plasticity or damage in which a yield or damage surface is associated with a generic plane of any orientation within the material, called the 'microplane', and is defined not in terms of tensors but in terms of stress and strain vectors. The tensorial invariance is ensured by integration or summation over the microplanes of all the spatial orientations. The advantages of the microplane modeling approach include: slip and crack openings of any orientations, automatic representation of the vertex effect, apparent deviations from normality, cross effects such as pressure sensitivity and dilatancy, Bauschinger effect and hysteresis. Realistic generalization for anisotropic material properties are possible and do not involve great increase of complexity.

Basic modeling features

In microplane models, the relation to continuum tensors is obtained by assuming the strain (or stress) vector on the microplane to be a projection of the strain (or stress) tensor, and using a variational principle to obtain the response stress (or strain) tensor, which leads to integration (or summation) over planes of all orientation. More fundamentally, the microplane model automatically ensues by assuming the free energy density to be a sum of the free energy densities associated with microplanes of all possible orientations. In numerical practice, only a finite number of discrete microplanes is used, based on an optimal Gaussian integration formula for the surface of a unit hemisphere. To avoid significant infringements on invariance, at least 21 discrete microplanes have proved to be necessary. The lecture reviews the characteristic uni-, bi-, and triaxial tests, proportional, nonproportional and cyclic, that must be correctly reproduced, and then outlines microplane model M4 for concretes which can describe these tests, along with extensions to capture distinct widely opened fractures. In contrast to Taylor models for non-softening plasticity, softening damage requires that the strain (rather than stress) vectors be the projections of the strain (rather than stress) tensors, which is called a kinematic (in contrast to static) constraint. Arbitrarily large finite strains are considered. The rate effects are included according to the activation energy of fracture growth and viscoelasticity of matrix. Generalizations to porous rocks, fiber reinforced concrete and orthotropic laminates are also described. One aspect, which is much less important for high deformation rates than for static loading, is the spurious localization of softening damage. Implementation of a nonlocal approach with a characteristic material length, needed for preventing spurious localization with mesh sensitivity and for capturing the energetic (non-statistical) size effect, is briefly addressed. It may be pointed out that an analog of microplane constitutive relations can be successfully applied in a random three-dimensional lattice model, which has the further advantage of automatically representing the nonlocality of softening damage. A crucial feature of the lattice model is that the lattice connections between the adjacent particles must transmit not only normal but also shear forces. The geometric randomness of the lattice serves to avoid bias in the direction of propagation, but is insufficient to produce realistic statistical scatter of structural resistance. For that purpose, the strength of lattice connections must be generated according to an autocorrelated random field. The capabilities of microplane model M4 are demonstrated by large-scale simulations (with up to 15 million finite elements) of explosions within a reinforced concrete structure, and of missile penetration and groundshock. An extension of microplane model to simulation of failure envelopes, fracture and size effect in highly orthotropic fiber-polymer laminates has also proven effective.

Do current multiscale concepts promise to be more powerful than microplane?

It is interesting to clarify the relationship of the microplane model to multiscale modeling. Its purpose is to capture microstructural phenomena with

(a) interactions among orientations, and
(b) interactions at distance.

The microplane model does not capture (a) but it does (a), though in a simplified way. Recognizing this, and scanning the palette of current multiscale formulations, one may distinguish 4 types of multiscale models:

Type 1. Embedment of subscale region discretization into a point of macro-scale continuum (e.g., into an integration point of a finite element).

Type 2. Overlapping of a finite region of a coarse mesh by a fine mesh that models the subscale (meso-scale).

Type 4. Microplane model, in which interactions among orientation are lumped into one macro-continuum point.

Type 4. Replacement of a finite region of a coarse mesh on the macro-scale with a refined discrete (lattice-particle) model of the meso-structure.

Normally only Types 1 and 2 are perceived as really multiscale, and this is indeed the case for hardening elasto-plastic behavior. However, in the case of softening damage or fracturing, subscale simulation of interactions at distance must primarily deliver to macro-continuum scale the characteristic material length l_0 (or the effective width of fracture process zone, or damage band), which is the salient property of the nonlocal or gradient formulations. It appears that the existing Types 1 and 2 do not achieve it, and it seems inconceivable that they could without simulating size effect. In some Type 1 and 2 variants, the simulated (embedded or overlapping) region is also a continuum, with an *assumed*, rather than physically determined, characteristic length, which is indispensable as the localization limiter on the macro-continuum scale (of nonlocal, second gradient or micropolar type). In others, a coarse (embedded or overlapping) subscale region is physically simulated and, if this region is $> l_0$, a damage localization band may be obtained; but this band cannot have a realistic size and orientation unless the subscale zone were supported, at all its boundary nodes, by springs representing the tangential stiffness of the entire surrounding structure, with correct loading-unloading combinations at all points (which would be required to capture the effect of the rate of energy release from the structure). Using the embedded or overlapping subscale region to calculate, from imposed strain or deformation increments, the stress increments to be delivered to the macro-continuum mesh is an approach that cannot capture the damage localization aspects. These stress increments, in general, represent strain-softening, yet no localization limiter appears to be used to handle it in Type 1 and 2 models. Such multiscale models cannot be objective. They exhibit spurious mesh sensitivity and converge to failure with zero energy dissipation as the mesh size is refined to zero. They run into the same classical trap of strain-softening, repeatedly encountered since 1976. So it appears that, for softening damage and fracturing, there currently exists no multiscale model that realistically captures the interactions at distance. Since such interactions also play some role in the interaction among orientations, none of the existing multiscale (or multiphysics) models promises to surpass the microplane model (Type 3). Types 1, 2 and 3 are, therefore only semi-multiscale models, conceivably having approximately the same modeling capability. Among them, the microplane model is the simplest. The only really multiscale model is Type 4, although it is not normally seen as such.

References

[1] Z. P. Bažant, F. C. Caner, I. Carol, M. D. Adley and S. A. Akers (2000): Microplane model M4 for concrete: I. Formulation with work-conjugate deviatoric stress. *J. of Engrg. Mechanics ASCE*, **126**, 944–953.

[2] Z. P. Bažant (1976): Instability, ductility, and size effect in strain-softening concrete. *J. Engrg. Mech. Div., Am. Soc. Civil Engrs.*, **102**, EM2, 331–344. More: www.civil.northwestern.edu/people/bazant.html

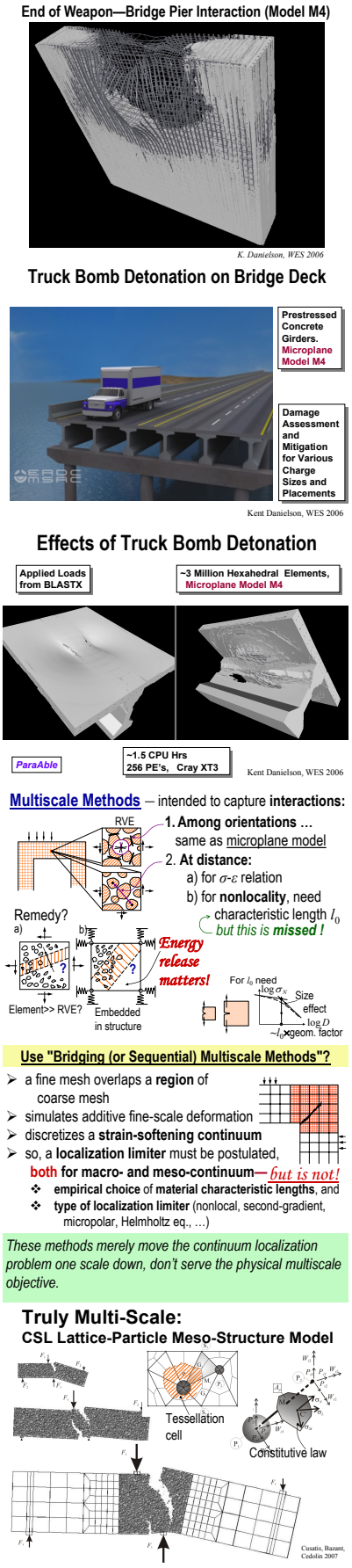

Figure 1: a,b,c) Explosions within a bridge pier and on bridge deck; e,f,g) problems of existing multiscale approaches. Reliability indices in FORM and SORM need to be modified.

Current Issues in Interface Mechanics

K. Willam*, C. Citto, B. Blackard

CEAE Department, University of Colorado-Boulder
Engineering Center ECOT 441, Boulder, CO 80309, USA
Willam@colorado.edu, Carlo.Citto@colorado.edu, blackard2@hotmail.com

Summary: This paper examines failure mechanics issues in composites at the example of brick masonry when the interaction of fired clay units and mortar layers leads to intriguing failure mechanisms [1]. The presentation highlights the difference of "finite thickness interface formulations" versus "zero-thickness interface models" which exhibit adhesive as well as frictional resistance.

Introduction

Due to the composite construction of masonry, progressive failure is a intriguing process. Masonry consists of two components, brick units and mortar joints, which exhibit very different stiffness and strength proprieties. Starting from the laboratory identification of the mechanical proprieties of brick and mortar, the failure processes in compression, tension and shear reveal the importance of mismatch among the elastic and inelastic proprieties of brittle brick units and bounding mortar layers. The studies reveal the critical role of the interface transition zone which exhibits a life of its own besides the brick units and the mortar binder.

Experimental results

Bricks, mortar, and masonry prisms were tested at the University of Colorado structural materials laboratory. The axial response behavior of the prism experiments is shown in Fig. 1 together with test data of mortar and brick.

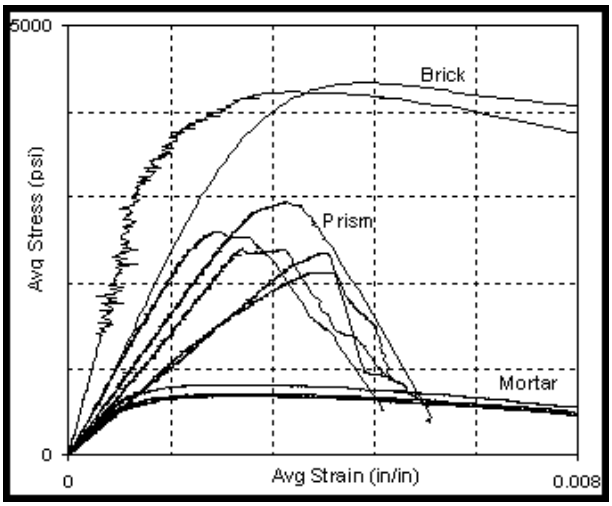

Figure 1: Experimental results for prism, brick and mortar tests.

Note the mortar strength in compression is less than a quarter of the brick strength, whereby both constituents have a much lower tension capacity when compared to their compressive counterparts. Probably the most interesting observation is the composite prism strength, which falls between the mortar and brick response in axial compression. Consequently, a masonry wall subjected to compression does not necessarily fail in compression of its weakest component, but it fails in tension due to mismatch conditions in the composite.

Numerical simulation

Several three dimensional finite element studies were performed on the masonry prism using the commercial software ABAQUS Version 6.5. Fig. 2 illustrates the 3D geometry whereby the ABAQUS damage-plasticity concrete model was used to characterize the elastic and inelastic behavior of mortar and solid brick units. The 3D simulation of the prism compression test was analyzed with and without lateral restraints at the top and bottom faces of the specimen. The results are shown in Fig. 3 together with the input data of the underlying calibration curves for the response behavior of mortar and brick units in axial compression. As expected from the experimental observations, the prism response falls between the mortar and brick behavior in axial compression.

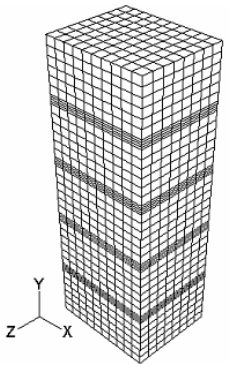

Figure 2: 3D finite element mesh.

For a better understanding of the progressive failure mechanism of the masonry composite, shear stress contours are shown in Fig. 4 at the mortar joint at mid-height at the last elastic load stage before plastic behavior develops in the prism. Due to the frictional restraint in the mortar-brick interfaces, the weaker mortar is confined and restrained from lateral expansion by the stiffer brick units. Consequently, the brick is in a state of biaxial tension-compression, while the mortar layer is subjected to a state of triaxial-compression.

A key point in the failure mechanism of a masonry prism is the initial mismatch of the elastic properties of brick and mortar. This leads to a failure mode which is governed by the tensile capacity of the brick units rather than the compression capacity of the mortar. For this reason, a generalized plane strain model was used to perform a number of sensitivity studies to

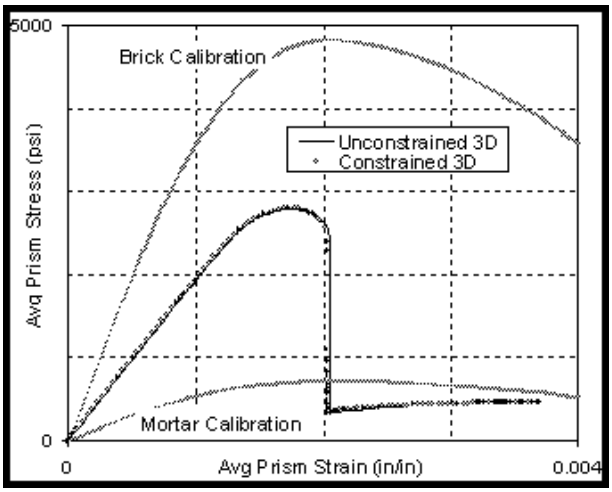

Figure 3: 3D numerical results.

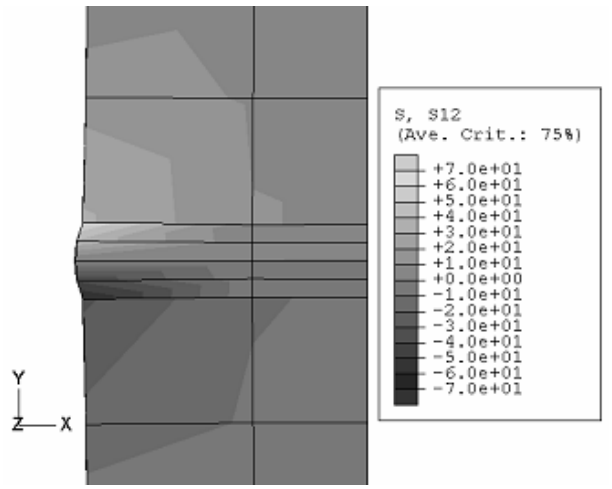

Figure 4: Shear stress at mortar joint.

examine the effect of different constitutive assumptions and to study the thickness effect of the mortar bed-joints [1]. The most important investigation was a study of the brick strength in tension on the overall prism capacity in compression. The results of this parametric study (Fig. 5) show that the increase of tensile brick strength significantly increases the capacity of the prism in compression. Moreover, the results indicate that the prism strength gradually approaches the high axial compression strength of brick unit when the tensile capacity of the brick increases. In concert with the results of the other sensitivity studies this observation supports the notion that prism failure is governed by the limited strength of the brick in biaxial tension-compression.

One of the mesh sensitivity studies was performed to investigate the critical role of the mortar in the overall failure mechanism. In addition to the standard 3D mesh shown in Fig. 2, three coarser meshes were considered to model the mortar bed joints. Using the same mesh layout for the bricks (3 elements high, 6 elements wide and 4 elements deep), the mortar joints were modeled by the "coarse mesh 2" using two layers of solid elements for the mortar thickness, while "coarse mesh 1" used only one layer. In contrast to the finite thickness representation of the mortar joints with continuum elements, "coarse mesh 0" inserted a single layer of zero-thickness cohesive interface elements between the bricks elements. The results of this mesh

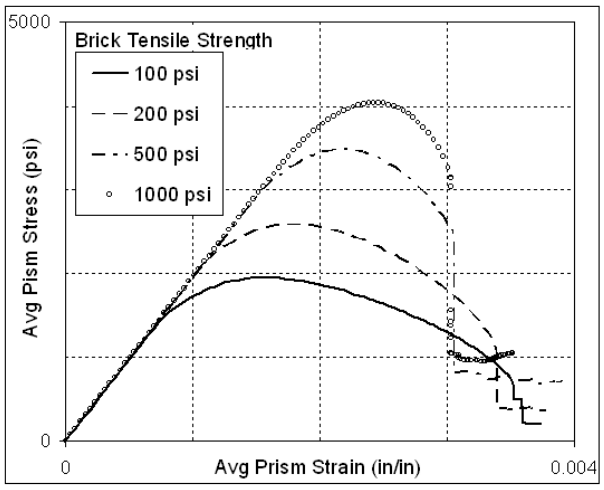

Figure 5: The effect of brick tensile strength.

sensitivity study are shown in Fig. 6. All continuum models

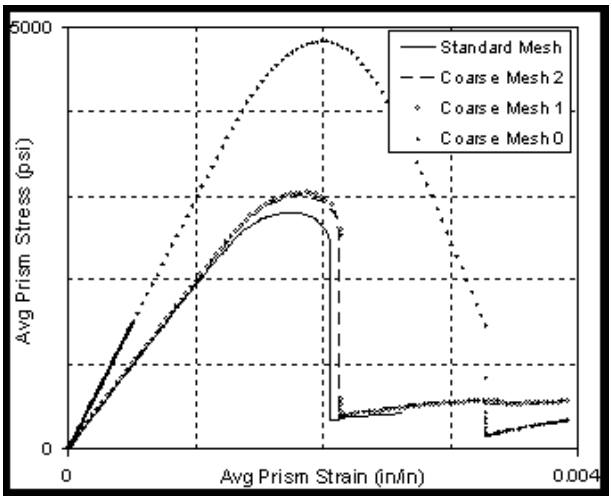

Figure 6: Mesh sensitivity study.

show close agreement with respect to the axial compression response of the masonry prism. This is primarily due to the mismatch in Poissons ratio which induces biaxial tension in the brick unit subjected to axial compression. The most interesting result of this parametric study is the failure mechanism predicted by the single layer of zero-thickness interface elements for the mortar joints, which results in an entirely different failure mechanism of the prism in compression [1]. This mode conversion stems from the inability of the zero-thickness cohesive interface elements to capture the lateral tension in the brick unit due to the mismatch of the two materials with regard to the Poissons ratio and their elastic stiffness. Consequently prism failure simply reproduces the brick calibration curve in compression except for a slight reduction of the overall ductility.

References

[1] B. Blackard, B. Kim, C. Citto, K. Willam and S. Mettupalayam (2007): Failure issues of brick masonry. *FraMCoS-6 Paper*, Catania (Sicily), June 17-22, 2007.

The Nanogranular Nature of Hydrated Nanocomposites: Concrete, Clay and Bone

F.-J. Ulm*, M. Vandamme, C. Bobko, J. A. Ortega

Massachusetts Institute of Technology
Cambridge, MA 02139, USA
ulm@mit.edu, vandamme@mit.edu, cbobko@mit.edu, ortega@mit.edu

Summary: Hydrated nanocomposites are a class of complex chemomechanical materials that possess a high degree of heterogeneity from atomistic to macroscopic scales. This includes the Calcium-Silicate-Hydrates (C-S-H), the binding phase in all cementitious materials; the load bearing clay fabric in shales, the sealing formations in most hydrocarbon reservoirs; and hydroxyapatite, the mineral binding phase of bone's ultrastructure. All these materials have in common the presence of structural water incorporated into an often plate or sheet like arrangement of atoms at nanoscales, which justifies their name as hydrated nanocomposites. These hydrated nanoparticles form the fundamental building block whose behavior is expected to delimitate macroscopic material diversity. The focus of this presentation is to advance emerging techniques that make it possible to assess in-situ the nanoproperties of such highly heterogeneous hydrated nanocomposites, and to identify common features of such materials at nano- and microscales.

Statistical indentation techniques

The method we introduced for measuring hardness and elastic properties of highly heterogeneous materials by a statistical analysis of instrumented indentation techniques, has widely been adopted and used in the characterization of nanomechanical behavior of C-S-H [1, 2, 3, 4], shales [5, 6] and bones [7]. Its attractiveness stems largely from the fact that properties of mechanically meaningful phases can be identified in-situ by performing large grids of indentations on highly heterogeneous samples, with a proper choice of the indentation depth to ensure the self-similar properties of classical continuum indentation analysis [8]. For this reason, the method is most suited for hydrated nanocomposites, whose multi-scale material phases cannot be recapitulated in bulk form, and for which it is difficult to indent on a specific material phase with sufficient repeatability.

Briefly, we recall that nanoindentation consists of making contact between a sample and an indenter tip of known geometry and mechanical properties, followed by a continuously applied and recorded change in load, P, and depth, h. Typical tests consist of a constantly increasing load, followed by a short hold and then a constant unloading; a $P-h$ curve is reported. The analysis of the $P-h$ curve proceeds by applying a continuum scale model to condense the indentation response into two indentation properties; indentation modulus, M

$$M = \frac{\sqrt{\pi}}{2}\frac{S}{\sqrt{A_c}} \tag{1}$$

and indentation hardness, H:

$$H = \frac{P}{A_c} \tag{2}$$

where $S = \frac{dP}{dh}$ is the (measured) initial slope of the unloading branch of the $P-h$ curve, P is the (measured) maximum indentation load, and A_c is the projected contact area of the indenter on the sample surface. The projected contact area, A_c, is typically determined as a function of the (measured) maximum indentation depth, $h_{\max}$ [8].

Recognizing the high heterogeneity of hydrated nanocomposites at the nano- and micro-scale, application of the indentation technique is a challenge, as it is difficult to choose to indent on a specific material phase with sufficient repeatability. To address this challenge, it is advantageous to perform large grids of indentations on heterogeneous samples, and subsequently perform a statistical deconvolution of the indentation results.

Microporomechanics analysis of indentation results

Hydrated nanocomposites, namely C-S-H, hydroxyapatite in bones, and clays, possess a very distinct disordered morphology of the solid phase, similar to a polycrystal [9, 5, 7, 3, 6]. For such highly disordered materials, linear and nonlinear microporomechanics [10] provides a link between the composite indentation properties (M, H) and the solid stiffness (m_s, ν_s) and strength properties (solid cohesion c_s, friction angle α_s) as a function of the packing density η of the porous material; in a dimensionless form [3, 11]:

$$\frac{M}{m_s} = \Pi_M\left(\nu_s, \eta, \eta_0\right) \tag{3}$$

$$\frac{H}{c_s} = \Pi_H\left(\alpha_s, \eta, \eta_0\right) \tag{4}$$

where $\eta_0 = 1/2$ for a polycrystal material. The previous equations allow one to determine from each indentation test the packing density of the solid phase. Carrying out a large array of tests then allows one to obtain, from a statistical analysis, mineral properties and packing density distributions [12]. By way of example, Fig. 1 shows the packing density scaling relations for (M, H) obtained from fitting 300 nanoindentation on a white cement paste. A statistical analysis then shows that the main hydration products present in cement-based materials have a packing density distribution that settles –on average– around two limit packing densities: the random packing limit of spheres of 64% and the ordered packing limit of spheres of 74%. These packing density distributions are consistent with

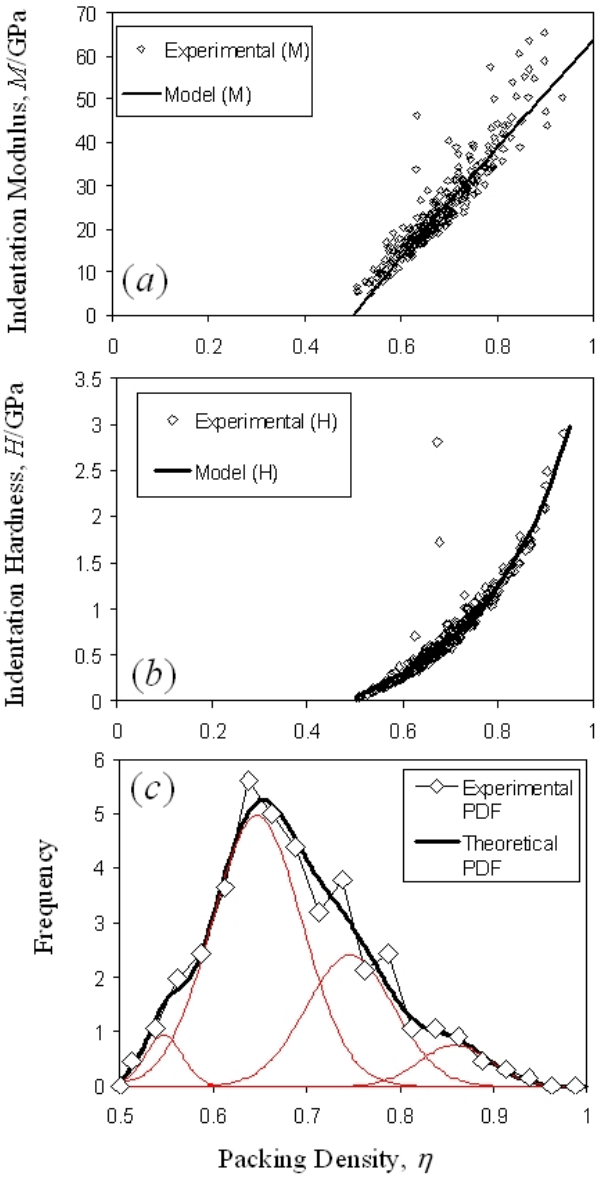

Figure 1: Packing density scaling of (a) indentation modulus M and (b) indentation hardness H of 300 nanoindentation tests on a $w/c = 0.5$ white cement paste. (c) Packing density distribution.

measurements of the packing density by mass density measurements [13].

Conclusion (from [12])

The overall picture which emerges from a comparative investigation is that hydrated nanocomposites are nanogranular materials, whose nanomechanical behavior is driven by the packing of their elementary particles: The elementary particles present in C-S-H, bone and shale all possess an isotropic strength behavior. We attribute this strength to cohesive bonds that are activated at particle-to-particle contact surfaces, which are expected to be sufficiently smaller than the mineral cohesion itself. The isotropy of the strength behavior hints towards a random orientation of the contact surfaces. Particles transmit forces over randomly oriented contact surfaces, activating the intrinsic elasticity of the nanoparticle. In the case of C-S-H and apatite, this intrinsic elasticity is found to be isotropic; while it turned out to be anisotropic in the case of the load bearing clay phase in shale. The elementary particles present in cement paste, bone and shale all possess an isotropic mechanical morphology. By isotropic morphology, we mean one in which the particle shape and aspect ratio do not affect significantly the nanomechanical response. This isotropic morphology is reminiscent of a random orientation of the particle-to-particle contact surfaces over which forces are transmitted. This randomness prevails even in the case of particles having a visible shape as it is the case of clay particles in shales. Such an isotropic morphology is indicative of a percolation threshold of $\eta_0 = 1/2$ as recognized by the polycrystal, or selfconsistent model of micromechanics, which turns out to be most suitable for hydrated nanocomposites.

Acknowledgment: Lafarge Corporation, MIT-OU Geo-Genome Industry Consortium, Ecole Nationale des Ponts et Chaussees (France), enabling M. Vandamme's doctoral studies at MIT.

References

[1] Constantinides G., Ulm F.-J., Van Vliet K. (2003). *Materials and Structures*, **36**, 191–196.

[2] Constantinides G., Ulm F.-J. (2004). *Cement and Concrete Research*, **34**, 67–80.

[3] Constantinides G., Ulm F.-J. (2007). *J. of the Mechanics and Physics of Solids*, **55**, 64–90.

[4] DeJong M. J., Ulm F.-J. (2007). *Cement and Concrete Research*, **37**, 1–12.

[5] Ulm F.-J., Abousleiman, Y. (2006). *Acta Geotechnica*, **1**, 77–88.

[6] Bobko C., Ulm F.-J. (2007): The nanomechanical morphology of shale, in review.

[7] Tai K., Ulm F.-J., Ortiz C. (2006). *Nano Letters*, **6**, 2520–2525.

[8] Oliver W. C., Pharr G. M. (2004). *J. of Materials Research*, **19**, 3–20.

[9] Hellmich C., Ulm F.-J. (2002). *J. of Biomechanics*, **35**, 1199–1212.

[10] Dormieux L., Kondo D., Ulm F.-J. (2006): *Microporomechanics*. J. Wiley & Sons, Chichester, UK.

[11] Cariou S., Ulm F.-J., Dormieux L. (2007). Hardness-packing density scaling relationships for cohesive-frictional porous materials, in review.

[12] Ulm F.-J., Vandamme M., Bobko C., Ortega J. A., Tai K., Ortiz C. (2007). Statistical indentation techniques for hydrated nanocomposites: concrete, bone and shale, in review.

[13] Jennings H. M. (2004). *Materials and Structures*, **37**, 59–70.

Stress and Growth in Soft Biological Tissues

D. Ambrosi*

Dipartimento di Matematica, Politecnico di Torino
corso Duca degli Abruzzi, 24, I-10129 Torino, Italia
davide.ambrosi@polito.it

Summary: Many soft tissues, and arteries *in primis*, exhibit residual stress after unloading, a characteristic related to the ability to self-organize their own constituents (cells and extracellular matrix proteins). This behavior can be theoretically predicted in a continuum mechanics framework assuming that the body self-remodels toward a *homeostatic* stress state. Open questions concern the characteristics of a stationary grown state, as dictated by the mechanical properties of the material and by the specific external load. Introducing a suitable mathematical framework, we perform numerical simulations for the remodelling of a two dimensional (axisymmetric) nonlinear elastic cylinder. In particular, the stress-modulated remodeling of the cylinder wall is addressed when local variations in the mechanical properties of the material occur. The main result is that, as in one spatial dimension, the tendency of the system to homeostasis generates, thanks to the remodeling process, a residual stress that homogenizes the tension in the body under load. Possible physiological implications of this result are discussed.

When observed on a sufficiently long time scale, biological systems are always open systems: they exchange mass and energy with the external environment. This characteristic makes the mathematical analysis of the biological systems inherently more complex than the purely mechanical ones, for which an assumption of closed system is possible. The mechanics of soft tissues is a specific example of problems that must include external actions (e.g. nutrients and mass inflow) when considered on a time scale longer than a few days. The arterial wall mechanics among this class of problems is particularly interesting for two reasons. On one hand its clinical interest is self-evident. On the other hand, in spite of numerous experimental works on the topic, the inner mechanisms of residual stress creation is not yet well understood.

A related specific aspect of the complexity of biological systems is that their relationship with the surrounding environment forces them into a continuous evolutionary process to attain a steady state, generally known as homeostasis. Derived from the Greek “similar” + “to stand”, homeostasis denotes the natural tendency of a living organism to maintain equilibrium. In order to maintain homeostasis, biological tissues undergo changes in mass as well as structural and functional adaptation to their environments. The present work focuses specifically on how the mechanical environment influences living tissues and, in particular, the category of biological tissues called soft tissues, which are characterized by large elastic deformation under physiologic loads. The basic hypothesis is that the gradual remodeling of soft biological tissues, through growth or resorption of cells and extracellular component is directly linked to the stress within the tissue and that remodeling proceeds toward stress homeostasis.

A key theoretical point is the statement of the growth law for the soft tissue, the *growth dynamics*. In general this will depend on many chemo-mechanical factors, including the availability of nutrients. To date, few heuristic laws for understanding growth based on experimental observations have been devised, and they are in essence based on the theory of homeostatic stress. The most relevant contribution is due to Taber and Eggers [2], who assume that the growth of an artery, schematically represented by a homogeneous elastic annulus of fung-like material, is ruled by the achievement of a radially constant equilibrium circumferential stress (the Cauchy one) and that this drives the system toward the associated residual tensional state.

Under suitable assumptions on the general framework mentioned above, it is possibile to recover the model proposed by Taber and Eggers as a small strain limit of a non-linear theory [1]. Numerical simulation elucidate the role of the remodeling process in a non-homogeneous aortic vessel under some geometrical simplifications. The body is considered to be axis-symmetric and made of non-linear orthotropic hyperelastic material. The wall is supposed to be stiffer in some part, an assumption mimicking the typical aneurysmatic conditions. The system evolves to a homeostatic state, assumed to be independent of possible local variations in the elastic properties. According to the numerical results, a stress-modulated remodeling of the wall of the vessel reduces the bending and, in this sense, can have a stabilizing effect with regards to possible local variations in the mechanical properties of the material. In fact both the radial and circumferential stresses after remodelling are homogeneized around a medium value, damping the peaks created by the inhomogeneity in the not-grown state.

References

[1] D. Ambrosi, F. Guana: Stress-modulated growth. *Math. Mech. Solids*, to appear.

[2] L. Taber, D. W. Eggers (1996): Theoretical study of stress modulated growth in the aorta, *J. Theor. Biol.*, **180**, 343–357.

[3] D. Ambrosi, A. Guillou, E. S. Di Martino: Stress-modulated remodelling of a non-homogeneous body, *Biomechanics and Modeling in Mechanobiology*, to appear.

Modeling and Simulation of Spheroidal Tumor Growth

B. Markert*, W. Ehlers

Institute of Applied Mechanics (CE), Universität Stuttgart
Pfaffenwaldring 7, 70569 Stuttgart, Germany
markert@mechbau.uni-stuttgart.de, ehlers@mechbau.uni-stuttgart.de

Summary: The theoretical description and numerical analysis of the avascular growth of neoplasms poses a very difficult challenge due to the complicated biological scenario on hand. In regard to the complex metabolic processes governed by nutrient, angiogenic, and growth factors, it is convenient to proceed from a macroscopic modeling approach instead of getting lost in the description of the physiochemical mechanisms on the cellular level. Following this, a thermodynamically consistent model for volumetric tumor growth is developed by recourse to mixture and porous media theories. In particular, the hydrated organic tissue is treated as a biphasic mixture constituted by a porous solid (tumor cells and extracellular matrix) which is permeated by an organic fluid. Since the imbalances of production and degradation of the individual constituents associated with growth and necrosis of the tumor tissue are strongly influenced by several chemical factors (nutrients, enzymes, etc.), the model incorporates two additional caloric state variables. Essentially, they can be thought of as locally available "growth energies" which are determined by the constituent energy balances.

Introduction

The application of continuum mechanics to material modeling of hard and soft biological tissues, such as bone, cartilage, or muscle, has been extensive in the last decades, where the nonlinear, inelastic, and anisotropic behaviors have been addressed. In that sense, a complete review of some achievements in the biomechanics of biological tissues including growth and remodeling is given by Taber [11] and Humphrey [6]. Here, particularly focusing on the biological process of growth, it is apparent that growing tissues not only undergo changes in size and shape but also in their inner structure and inherent properties. In fact, real biological tissues are composed of many constituents, like various cell types, abundant water, extracellular matrix (ECM), etc., cf. Cowin [5] for details, so that it is furthermore clear that changes in the relative amount and the properties of these components during growth affect the macroscopic behavior of the tissue. Following this, it seems to be natural to describe growing biological materials by use of multiphasic continuum theories, such as the theory of porous media (TPM), which enables the macroscopic (volume averaged) modeling of interacting components by recourse to the theory of mixtures (TM) but also accounts for the local composition through the concept of volume fractions. In this context, Preziosi and Farina [12] and Steeb and Diebels [13] formally employed the porous media approach to account for the separate contributions of each constituent during growth. In the same sense, Klisch and Hoger [15] additionally used the multiplicative geometric concept of Rodriguez et al. [17] by introducing a growth deformation gradient in combination with the TM, and Humphrey and Rajagopal [7] developed a theory that considers the continual production and removal of constituents in potentially different stressed configurations. In this context, the applications of porous media theories to growing tissues are, for instance, devoted to cartilage (Klisch et al. [14]) and bone (Kühn and Hauger [16]).

It is the goal of this contribution to present a consistent TPM model that enables the multi-dimensional analysis of the early stages of solid tumor growth. In particular, we consider the growth of a cluster of tumor (neoplastic) cells towards an avascular tumor which receives nutrients from the surrounding tissue only by diffusion as it is not yet supplied by blood vessels. The structure of an avascular tumor distinguishes an outer rim of proliferating tumor cells, an intermediate region where tumor cells are alive but do not proliferate (quiescent state), and a central core of nutrient-starved necrotic tumor cells. The mechanisms affecting the growth of cells are the diffusion and the consumption of nutrients and oxygen, the resistance or stress exerted by the surroundings on the cells, and the frequency of mechanical load on the cells, see, e. g., Sutherland [10] and Kunz-Schughart et al. [8]. The model concept and the constitutive relations are inspired by and partially adopted from the already existing continuum mechanical models for avascular tumor growth, such as the singlephasic formulation of Ambrosi and Mollica [1, 2] which is extended by a reaction-diffusion equation for the nutrients whose concentration is treated like a measure of a metabolistic energy, or the works of Byrne and Preziosi [4], Ambrosi and Preziosi [3], and Roose et al. [9] where tumor tissue is described as a multi-component material.

Biphasic porous media growth model

Based on the theory of porous media (TPM) [18], we consider a solid tumor as a saturated biphasic mixture consisting of two de facto immiscible contstituents, namely a solid skeleton φ^S representing the living tumor cells embedded into extracellular matrix and a single pore-fluid phase φ^F consisting of interstial liquid, necrotic debris, and cell precursers, cf. Fig. 1.

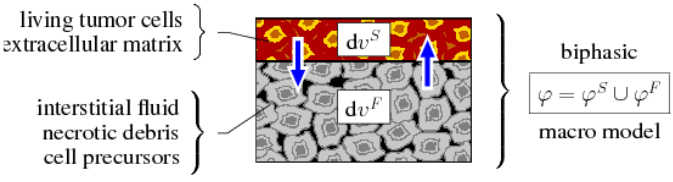

Figure 1: Biphasic porous media growth model.

In this regard, the growth process is described by a distinct mass exchange between both constituents, where the complex metabolic mechnisms are governed by a non-mechanical extension of the biphasic model. More precisely, temperature-equivalent "growth energies" $\mathcal{C}^{\alpha}_{\Theta} > 0$ $(\alpha \in \{S, F\})$ are introduced as measures of the average amount of chemical energy available for cell metabolism which can be regarded in full analogy to the thermodynamic temperature as a measure of the average kinetic energy of atoms. To be in line with continuum thermodynamics, this further entails the introduction of associated (conjugate) "configurational entropies" η^{α}_{c} as measures for the randomness in the distribution of matter analogously to the thermal entropy. In addition to the constituent growth energies $\mathcal{C}^{S}_{\Theta}$ and $\mathcal{C}^{F}_{\Theta}$, the further primary variables of the model are the solid displacements $\mathbf{u}_S$, the effective pore-fluid pressure p^{FR}, and the solid volume fraction n^S all governed by a corresponding partial or mixture balance relation in the context of the TPM approach, see Ehlers [18]. To close the set of equations, suitable constitutive laws, e. g., for the solid extra stress and the caloric interaction, have to be defined satisfying the entropy principle for mixtures.

Finite element analysis

The numerical treatment of such coupled multi-field problems can efficiently be performed by the mixed finite element method (FEM). Therefore, the weak forms of the governing balance relations, namely the momentum and volume balance of the mixture, the solid volume balance, and the solid and fluid energy balances are needed for the determination of the unknowns $\mathbf{u}_S, p^{FR}, n^S, \mathcal{C}^{S}_{\Theta}$, and $\mathcal{C}^{F}_{\Theta}$. It remains to implement a convergent algorithm for the solution of this nonlinear five-field variational problem. The general capabilities of the model can be seen from a first qualitative simulation of the finite 2-d growth of a tumor spheroid (Fig. 2).

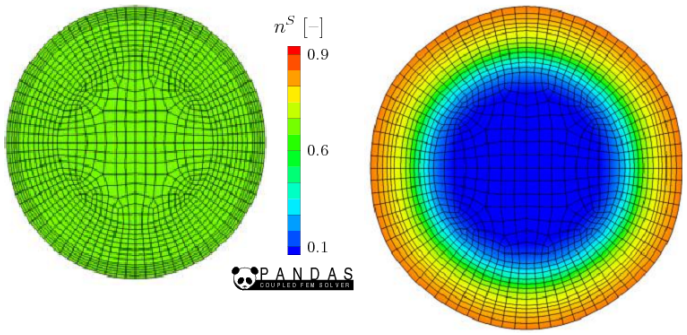

Figure 2: Qualitative 2-d simulation of a growing tumor spheroid. Depicted is the distribution of the solidity n^S (fraction of living tumor cells) in the initial and the final stage.

References

[1] D. Ambrosi, F. Mollica (2002): On the mechanics of a growing tumor. *International Journal of Engineering Science*, **40**, 1297–1316.

[2] D. Ambrosi, F. Mollica (2003): The role of stress in the growth of a multicell spheroid. *Journal of Mathematical Biology*, preprint.

[3] D. Ambrosi, L. Preziosi (2002): On the closure of mass balance models for tumor growth. *Mathematical Models and Methods in Applied Sciences*, **12**, 737–754.

[4] H. Byrne, L. Preziosi (2003): Modelling solid tumor growth using the theory of mixtures. *IMA Journal of Mathematical Medicine and Biology*, **20**, 341–366.

[5] S. C. Cowin (2000): How is a tissue built. *Journal of Biomechanical Engineering*, **122**, 553–569.

[6] J. D. Humphrey (2002): Continuum biomechanics of soft biological tissues. *Proc. R. Soc. Lond. A*, **1**, 1–44.

[7] J. D. Humphrey, K. R. Rajagopal (2002): A constrained mixture model for growth and remodeling of soft tissues. *Mathematical Models and Methods in Applied Sciences*, **12**, 407–430.

[8] L. A. Kunz-Schughart, M. Kreutz, R. Knuechel (1998): Multicellular spheroids: a three-dimensional in vitro culture system to study tumor biology. *International Journal of Experimental Pathology*, **79**, 1–23.

[9] T. Roose, P. A. Netti, L. L. Munn; Y. Boucher, R. K. Jain (2003): Solid stress generated by spheroid growth estimated using a poroelasticity model. *Microvascular Research*, **66**, 204–212.

[10] R. M. Sutherland (1988): Cell and environment interactions in tumor microregions: the multicell spheroid model. *Science*, **240**, 177–184.

[11] L. A. Taber (1995): Biomechanics of growth, remodeling and morphogenesis. *Applied Mechanics Review*, **48**, 487–545.

[12] L. Preziosi, A. Farina (2002): On Darcy's law for growing porous media. *International Journal of Non-Linear Mechanics*, **37**, 485–491.

[13] H. Steeb, S. Diebels (2003): A thermodynamic-consistent model describing growth and remodeling phenomena. *Computational Materials Science*, **28**, 597–607.

[14] S. M. Klisch, S. S. Chen, R. L. Sah, A. Hoger (2003): A growth mixture theory for cartilage with application to growth-related experiments on cartilage explants. *Journal of Biomechanical Engineering*, **125**, 169–179.

[15] S. M. Klisch, A. Hoger (2003): Volumetric growth of thermoelastic materials and mixtures. *Mathematics and Mechanics of Solids*, **8**, 377–402.

[16] S. Kühn, W. Hauger (2000): A theory of the adaptive growth of biological materials. *Archive of Applied Mechanics*, **70**, 183–192.

[17] E. K. Rodriguez, A. Hoger, A. D. McCulloch (1994): Stress-dependent finite growth in soft elastic tissues. *Journal of Biomechanics*, **27**, 455–467.

[18] W. Ehlers (2002): Foundations of multiphasic and porous materials, In W. Ehlers and J. Bluhm (eds.), *Porous Media: Theory, Experiments and Numerical Applications*, Springer-Verlag, Berlin, 3–86.

Hyperelastic Modeling of the Arterial Wall with Application to Abdominal Aortic Aneurysms

T. Ch. Gasser[1*], M. Auer[1], J. Swedenborg[2]

[1]Royal Institute of Technology (KTH), Department of Solid Mechanics
Osquars backe 1, SE–100 44 Stockholm, Sweden
tg@hallf.kth.se, ma@hallf.kth.se

[2]Department of Vascular Surgery, Karolinska University Hospital and Institute
Surgery N1:06, Karolinska University Hospital, 17176, Stockholm, Sweden
jesper.swedenborg@ki.se

Summary: An Abdominal Aortic Aneurysm is a frequently observed pathological enlargement of the infrarenal aorta, and if kept untreated, it might enlarge until rupture. Indication of clinical treatments is linked to a rupture risk assessment of these formations, which however, is under ongoing and controversial scientific discussion. Recently, strong evidence has been provided that a biomechanical analysis leads to reliable data for clinical decisions. Within this paper a recently proposed hyperelastic formulation for arterial layers is applied to predict the stress field in the aneurysm wall. The constitutive model accounts for dispersed collagen fiber orientations and has been integrated into Finite Element models with patient specific geometries. To this end the 3D geometries of aneurysms are reconstructed from standard clinical images using a segmentation technique, which is based on deformable models.

Motivation and background

Abdominal Aortic Aneurysms (AAAs) are pathological enlargements of the infrarenal aorta, frequently observed in the elder male population. Untreated (AAAs) eventually enlarge until they rupture; an event with mostly mortal consequences [3]. Up to date no effective therapeutic strategies either to limit the growth of these lesions or to prevent their eventual risk of rupture are available.

A surgical or minimal invasive method called (AAA) repair is the most common treatment, and according to the current clinical view, it is indicated when the aneurysm exceeds a certain dimension or expansion rate. However, this kind of rupture risk assessment is under ongoing and controversial scientific discussion and there is scientific evidence (for example [1]) that a detailed biomechanical analysis could provide much more reliable data for clinical decisions. Moreover, it allows deep insights in the mechanical loading condition of the aneurysm, which is of basic scientific requirement to understand this type of disease, and which might be useful to improve the human conditions of patients suffering from it.

Continued advances in computer technology and computational methods are increasing our ability to handle large amount of data and allows us to model patient specific problems nowadays. The Finite Element Method (FEM) provides a powerful numerical tool to solve the arising 3D (coupled) mechanical problems, it can handle the nonlinear character of the related problems and combines synergetically with medical imaging.

A hyperelastic model for arterial layers

Collagen fibres are key ingredients in the structure of arteries and in the adventitial and intimal layers, the orientation of the collagen fibres is dispersed, as shown by, e.g., polarized light microscopy of stained arterial tissue. As a result, continuum models that do not account for the dispersion are not able to capture the stress-strain response of these layers. Within this paper we apply the recently proposed structural continuum framework [2], which is able to capture the dispersion of the collagen fibre orientations. The approach allows the development of a new hyperelastic free-energy function that is particularly suited for representing the anisotropic elastic properties of arterial layers. In particular, the mechanical contributions derived from elastin and collagen are treated separately, and hence, the model allows an investigation of the biomechanical consequences of proteolytic degeneration of these structural proteins.

Description of the collagen fiber distribution

As a starting point of describing the collagen fiber distribution within a particular arterial layer, we introduce a density function $\rho(\mathbf{M})$. It characterizes the distribution of fibers in the reference configuration of the continuum with respect to the referential orientation $\mathbf{M}$; an arbitrary unit direction vector in the 3D Eulerian space, i.e. $|\mathbf{M}| = 1$. In addition, we assume that the collagen distribution can be seen as a superposition of transversely isotropic distributions within two families of collagen fibers. As shown recently [2], a transversely isotropic distribution can always be represented by the generalized structural tensor $\mathbf{H}$ of the comprehensive form

$$\mathbf{H}(\mathbf{a}_0, \kappa) = \kappa\mathbf{I} + (1 - 3\kappa)\mathbf{a}_0 \otimes \mathbf{a}_0, \qquad (1)$$

where $\mathbf{I}$ and $\mathbf{a}_0$ denotes the identity tensor and the mean orientation of the distribution. Remarkable, $\mathbf{H}$ depends on a single dispersion (structural) parameter κ, which represents the fiber distribution in an integral sense and describes its 'degree of anisotropy'. This structural parameter is linked to the density

function $\rho(\mathbf{M})$ according to

$$\kappa = \frac{1}{4}\int_0^\pi \rho(\mathbf{M}(\Theta))\sin^3\Theta \mathrm{d}\Theta, \tag{2}$$

where $\Theta \in [0,\pi]$ denotes the Eulerian angle between a particular collagen fiber and the mean orientation $\mathbf{a}_0$ of the distribution.

Constitutive model for the aneurysm wall

Clinical relevant AAA lesions are usually comprised by the aneurysm wall and the Intra-Luminal Thrombus (ILT). While the ILT can be modeled as an isotropic neoHookean material, the aneurysm wall is nonlinear and anisotropic [4]. In order to derive the deviatoric part $\overline{\Psi}$ of hyperelastic potential for the aneurysm wall, it is assumed that it can be represented by superposition of the isotropic potential $\overline{\Psi}_{\mathrm{g}}$ for the non-collageneous groundmatrix and the two transversely isotropic potentials $\overline{\Psi}_{\mathrm{f}\,i}, i = 1,2$ for the embedded families of collagen fibers. Hence, the free-energy function reads

$$\overline{\Psi}(\overline{\mathbf{C}}, \mathbf{H}_i) = \overline{\Psi}_{\mathrm{g}}(\overline{\mathbf{C}}) + \sum_{i=1,2} \overline{\Psi}_{\mathrm{f}\,i}(\overline{\mathbf{C}}, \mathbf{H}_i(\mathbf{a}_{0\,i}, \kappa)), \tag{3}$$

where $\overline{\mathbf{C}} = J^{-2/3}\mathbf{F}^{\mathrm{T}}\mathbf{F}$ and $\mathbf{H}_i = \kappa\mathbf{I} + (1-3\kappa)(\mathbf{a}_{0\,i} \otimes \mathbf{a}_{0\,i})$ are the modified right Cauchy-Green tensor and the generalized structural tensor, respectively. Here $\mathbf{F}$ denotes the deformation gradient with the volume ratio $J = \det\mathbf{F} > 0$.

The non-collageneous groundmatrix is captured by an incompressible isotropic neo-Hookean model and for the transversely isotropic free-energy function of the $i-$th family of collagen fibers the following form

$$\begin{aligned} \Psi_{\mathrm{f}\,i}(\overline{\mathbf{C}}, \mathbf{H}_i) &= \frac{k_1}{2k_2}\{\exp[k_2 \overline{E}_i{}^2] - 1\}, \qquad i = 1,2, \\ \text{with } \overline{E}_i &= \mathbf{H}_i : \overline{\mathbf{C}} - \mathbf{H}_i : \mathbf{I} \end{aligned} \tag{4}$$

is proposed, where $\mathbf{H}_i : \overline{\mathbf{C}}$ denotes an invariant of the symmetric generalized structural tensor $\mathbf{H}_i$ and the symmetric modified right Cauchy-Green strain tensor $\overline{\mathbf{C}}$. Moreover, we introduced the Green-Lagrange strain-like quantity $\overline{E}_i$, which characterizes the strain in the direction of the mean orientation $\mathbf{a}_{0\,i}$ of the $i-$th family of fibers. In eq. (4) k_1 and k_2 are material parameters to be determined from mechanical tests of the tissue, while $\mathbf{a}_{0\,i}$ and κ are structural parameters to be determined from histological data of the tissue.

Predicted stress fields in AAAs

The geometry of the aneurysm plays one major role in its biomechanical analysis, and hence, accurate 3D reconstruction from clinical data is a critical issue. In particular, image segmentation is a difficult task, and herein deformable models, which are thought to be the most promising approach to the problem, have been applied. To this end an active contour moves according to internal (defined by the elasticity of the image model) and external (defined by the properties of the image) forces until the image is successfully segmented. Within this work Computer Tomography (CT) images, which have been provided by the clinical cooperator, are automatically segmented and based on that 3D grids for the FE computations are generated. Principal material axes are defined and according to this frame the proposed anisotropic material model (3) is utilized. The incorporated structural and material parameters are defined from independent experimental investigations, where data from polarized light microscopy and planar biaxial testing [4] of AAA tissue is used. A quasi-static (blood) pressure loading of 13.33 kPa is assumed to act on the luminal site of the aneurysm, and the solutions of the arising non-linear problems lead to maximum principal Cauchy stress field typically shown in Figure 1.

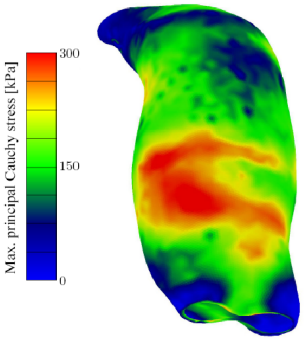

Figure 1: Distribution of the maximum principal Cauchy stress in the AAA wall loaded with 13.33 kPa blood pressure.

Conclusions

A detailed biomechanical analysis is thought to provide reliable data for a rupture risk assessment of AAAs. The developed model uses a new anisotropic hyperelastic model for the aneurysm wall and patient specific geometries are reconstructed from routinely taken clinical images. The proposed hyperelastic model reflects arterial wall histology and incorporates the distribution of the collagen orientation. At least for the adventitial and intimal layers, where the collagen orientations exhibit high dispersion, this is a crucial requirement to capture their mechanical properties.

References

[1] M. F. Fillinger, S. P. Marra, M. L. Raghavan, and F. E. Kennedy (2003): Prediction of rupture risk in abdominal aortic aneurysm during observation: wall stress versus diameter. *J. Vasc. Surg.*, **37**, 724–732.

[2] T. C. Gasser, R. W. Ogden, and G. A. Holzapfel (2006): Hyperelastic modelling of arterial layers with distributed collagen fibre orientations. *J. R. Soc. Interface*, **3**, 15–35.

[3] G. Johansson and J. Swedenborg (1994): Little impact of elective surgery on the incidence and mortality of ruptured aortic aneurysms.*Eur. J. Vasc. Endovasc. Surg.*, **8**, 489–93.

[4] J. P. Vande Geest, M. S. Sacks, and D. A. Vorp (2005): The effects of aneurysm on the biaxial mechanical behavior of human abdominal aorta. *J. Biomech.*, **39**, 1324–34.

Poromechanics of Compressible Charged Porous Media

J. M. Huyghe[1*], **M. M. Molenaar**[2], **F. P. T. Baaijens**[1]

[1]Department of Biomedical Engineering, Eindhoven University of Technology
P.O. Box 513, 5600MB Eindhoven, Netherlands, j.m.r.huyghe@tue.nl

[2]Shell International Exploration and production B.V.
Kessler Park 1, 2288GS, Rijswijk, The Netherlands

Summary: Osmotic, electro-static and/or hydrational swelling are essential mechanisms in the deformation behaviour of porous media, such as biological tissues, synthetic hydrogels and clay-rich rocks. Present theories are restricted to incompressible constituents. This assumption typically fails for bone, in which electrokinetic effects are closely coupled to deformation. An electro-chemo-mechanical formulation of quasi-static finite deformation of compressible charged porous media is derived from the theory of mixtures. The model consists of a compressible charged porous solid saturated with a compressible ionic solution. Four constituents following different kinematic paths are identified: a charged solid and three streaming constituents carrying either a positive, negative or no electrical charge, which are the cations, anions and fluid, respectively. The finite deformation model is reduced to infinitesimal theory. In the limiting case without ionic effects, the presented model is consistent with Biot's theory. Viscous drag compression is computed under closed circuit and open circuit conditions. Viscous drag compression is shown to be independent from the storage modulus.

Introduction

This paper focuses on the mechanics of ionised biological, mineral and synthetic porous media. As a consequence of the fixed charges a variety of physical phenomena are observed in these materials, such as streaming potentials, diffusion potentials, electro-osmosis, electro-phoresis. Biological materials consist mainly of water. A number of models for soft biological tissues have been developed in the past [4, 2]. They all assume incompressibility of their constituents, because this assumption is valid for soft tissue applications. Bone typically does not comply with the assumption of incompressible constituents. While soft tissues allow for volume change through squeezing and soaking of fluid, volume change in bone is associated with compression of the solid phase, compression of the fluid phase and squeezing and soaking of fluid from the environment. Soft tissues exhibit apparent compressibility, while hard tissues have intrinsic compressibility as well. Indeed, the bulk modulus of water is in the order of 2 GPa while the typical compressive stiffness of bone is one order of magnitude higher. In addition, bone is well known to exhibit streaming potentials under deformation [5]. Micromechanical models have been developed to predict the streaming potentials in a single canaliculus [1]. It is suspected that streaming potentials and streaming currents are a key element in the understanding of bone mechanosensing and remodelling [3]. On the other hand, poromechanical models are capable of handling a full osteon, but neglect the ionic component of the flow. The present paper aims at filling this gap and provide a poromechanical theory that does account for streaming potentials and currents. Minerals of the phyllosilicate class have a crystal structure consisting of silicate layers stacked upon each other, which becomes charged when exposed to water. Shale is a rock type containing a large amount of phyllosilicate type clay minerals. Swelling of shales is a major technical problem in petroleum engineering, which can severely threaten the stability of boreholes. As down hole pressures are typically in the order of tens of MPa, compressibility of constituents is vital in these applications. In the limiting case of incompressible constituents, the theory reduces to the quadriphasic theory presented earlier [2].

Theory

We consider a ionised porous medium saturated with a monovalent homoionic solution (e.g. NaCl) subjected to infinitesimal deformation. Conservation of mass of the streaming constituents (cations $\beta = +$, anions $\beta = -$ and water $\beta = f$) require:

$$\frac{\partial \zeta_\beta}{\partial t} - \nabla \cdot \boldsymbol{q}_\beta = 0 \tag{1}$$

in which ζ_β is the unstrained content of constituent β, $\frac{\partial}{\partial t}$ is the time derivative for an observer moving with the solid and $\boldsymbol{q}_\beta$ is the unstrained content flux of constituent β relative to the solid. The fluxes are related to the electro-chemical potentials μ_γ through a coupled Darcy/Fick/Ohm law:

$$\boldsymbol{q}_\beta = -\boldsymbol{k}_{\beta\gamma} \cdot \nabla \mu_\gamma \tag{2}$$

The electrochemical potentials are the derivative of the energy function W of the mixture with respect to the unstrained fluid volumes, while the stress is the derivative of the same energy with respect to strain. The energy function combines linear isotropic poroelasticity with classical Donnan osmosis:

$$\begin{aligned} W = & G\epsilon : \epsilon + \\ & + \tfrac{1}{2}(\lambda + \alpha^2 M) tr^2 \epsilon + \\ & + \sum_{\beta=f,+,-} [-\alpha M(\zeta_\beta - \zeta_{\beta 0}) tr\epsilon + \tfrac{1}{2} M(\zeta_\beta - \zeta_{\beta 0})^2] + \\ & + \sum_{i=+,-} [RT \frac{\zeta_i}{\overline{V}_i}(ln\zeta_i - ln\zeta_f - 1) + \frac{F z_\beta}{\overline{V}_i} \xi \zeta_i] \end{aligned} \tag{3}$$

in which G and λ are the Lamé constants, α the Biot coefficient, M the storage modulus, R the universal gas constant, T the absolute temperature, F Faraday's constant, $\overline{V}_\beta$ the molar volumes, ζ_β the valences and ξ the electrical potentials.

Viscous drag compression simulation

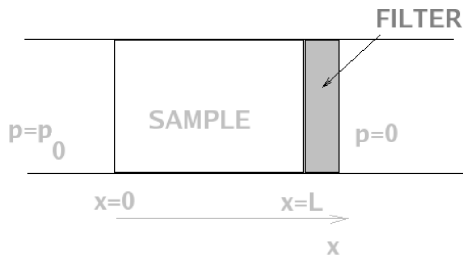

Figure 1: An ionised porous sample is subjected to a pressure gradient. The flow through the sample causes viscous drag compression.

A porous sample is subjected to a pressure gradient (Fig. 1) under (1) short-circuit conditions (no voltage difference between both sides of the sample) and (2) open circuit conditions (no electrical current across the sample). The material parameters are $G = 6\,\mathrm{GPa}$, $\lambda = 11.2\,\mathrm{GPa}$, $\alpha = 0.15$, $M = 36.4$ or $100\,\mathrm{GPa}$, hydraulic permeability $K = 2.210^{-7}\,\mathrm{mm}^4/\mathrm{Ns}$, diffusion coefficients are $1.9 \cdot 10^{-3}\,\mathrm{mm}^2/\mathrm{s}$ and $2.6 \cdot 10^{-3}\mathrm{mm}^2/\mathrm{s}$ for cations and anions. The fluid content is shown to depend on the storage modulus while the strain is not (Fig. 2 and 3) The voltage is different for the open citcuit versus closed circuit case (Fig. 4)

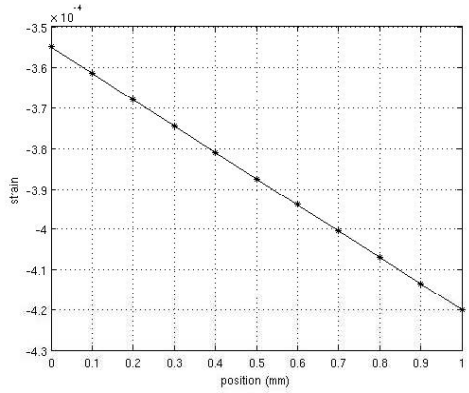

Figure 2: Strain as a function of depth for two values of the storage modulus. Continuous line: $M = 36.4\,\mathrm{GPa}$, typical value for the canalicular porosity.

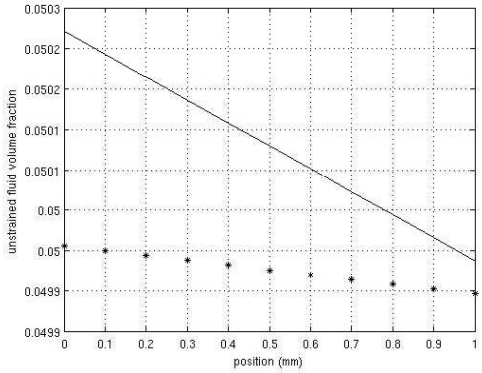

Figure 3: Unstrained fluid content as a function of depth for two values of the storage modulus. Continuous line: $M = 36.4\,\mathrm{GPa}$, typical value for the canalicular porosity.

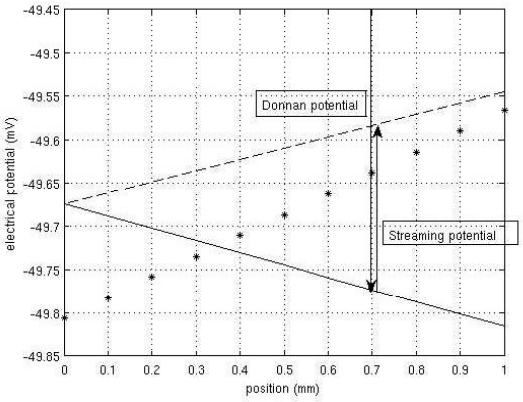

Figure 4: Computed electrical potential ξ as a function of depth x for a viscous drag experiment. Continuous line: closed circuit $M = 36.4\,\mathrm{GPa}$. Dashed line: open circuit $M = 36.4\,\mathrm{GPa}$. In closed circuit condition, the electrical potential is set to zero in the upstream and downstream reservoir. The potentials calculated are Donnan potentials. In the open circuit condition, the voltage of the upstream reservoir is set to zero. The resulting electrical potential profile is the sum of a Donnan potential and a streaming potential.

References

[1] S. C. Cowin, S. Weinbaum, Y. Zeng (1995): A case for bone canaliculi as the anatomical site of strain generated potential. *J. Biomechanics*, **28**, 1281–1297.

[2] J. M. Huyghe, J. D. Janssen (1997): Quadriphasic mechanics of swelling incompressible porous media. *Int. J. Eng. Sci.*, **35**, 793–802.

[3] J. M. Huyghe, T. Smit (2004): Comment les cellules de l'os ressentent-elles une contrainte mécanique? *Arch. Physiol. Bioch.*, **112**, 48–50.

[4] W. M. Lai, J. S. Hou, V. C. Mow (1991): A triphasic theory for the swelling and deformation behaviors of articular cartilage. *J Biomech Eng*, **113**, 245–258.

[5] W. M. Otter, V. R. Palmieri, D. D. Wu, K. G. Seiz, L. A. McGinitie, G. V. B. Cochran (1992): A comparative analysis of streaming potentials in vivo and in vitro. *Journal of Orthopedic Research*, **10**, 710–719.

Multiscale Methods for the Failure of Heterogeneous Materials

T. Belytschko*, S. Loehnert

Department of Mechanical Engineering, Northwestern University
2145 Sheridan Rd., Evanston, Illinois, USA
tedbelytschko@northwestern.edu, s-loehnert@northwestern.edu

Summary: In this contribution we explore two multiscale strategies for the prediction of failure processes in heterogeneous materials. The first method is based on a unit cell approach. Here the behavior of the discontinuity and the bulk material is transfered from the unit cell to the macroscale. The second method is based on a projection of the fine scale behavior onto the coarse scale model by using coarse scale test functions. The properties of the two methods are explored and illustrated with some examples.

The treatment of unit cells which lose positive definiteness of the tangent stiffness, i.e. are associated with a material that loses strong ellipticity, are a focus of this work. These methods can also be used when the material response predicted by the unit cell loses rank one stability. The adherence of this method to the energetic theorems of Hill are explored.

The use of subscale models such as unit cells, for the computation of failure still poses major difficulties. When failure progresses beyond a critical point at the macroscale, the tangent stiffness of the unit cell loses positive definiteness. As a consequence, the corresponding material models at the macroscale lose either strong ellipticity or rank one stability, and unless some modifications are made to the classical continuum formulation, the problem, broadly speaking, is no longer well-posed.

We describe two methods wherein failure at the microscale is modeled by an injected discontinuity at the macroscale. For the first method, the behavior of the discontinuity and bulk material is obtained from a unit cell and communicated to the coarser scale via a virtual unit cell that provides an intermediate step between the unit cell and the coarser scale continuum. The method is in the spirit of FE^2 [1].

We consider unit cells with sides of length $l = \alpha h$, where h is the element size and α is a parameter close to unity. A unit cell here is not a representative volume element for the boundary conditions are not periodic. Furthermore, it is not assumed that the fluctuations are periodic because the localization that accompanies microcrack growth, shear band formation and other damage modes is not periodic.

The schema for the method is shown in Fig. 1. At each point in the macromodel (usually only the critical points), a linkage is established with a virtual unit cell which in turn interrogates the actual unit cell. The procedure is strain driven: The strain experienced at a particular point in the macroelement is applied to the unit cell, which is displacement driven by this strain field.

The method is implemented via the extended finite element method, XFEM [2, 3]. As a consequence, arbitrary growth of the discontinuities can be treated. The discontinuity behavior predicted by the unit cell at the micro scale is used to drive the macroscale discontinuity.

A second method which is described employs a multiscale projection to obtain the fine scale behavior [4]. This approach is based on a two scale decomposition of the displacements and a projection to the coarse scale by using coarse scale test functions. On the coarse scale, we solve the weak form

$$\int_{\Omega^0} \operatorname{div}\left(\boldsymbol{\sigma}(\boldsymbol{u}^0 + \bar{\boldsymbol{u}}^1)\right) \cdot \boldsymbol{\eta}^0 \, \mathrm{d}\Omega = \int_{\Omega^0} \boldsymbol{f} \cdot \boldsymbol{\eta}^0 \, \mathrm{d}\Omega + \int_{\partial\Omega_t^0} \boldsymbol{t} \cdot \boldsymbol{\eta}^0 \, \mathrm{d}\partial\Omega \qquad (1)$$

for the coarse scale displacements $\boldsymbol{u}^0$ by incorporating the stress field $\boldsymbol{\sigma}(\boldsymbol{u}^0 + \bar{\boldsymbol{u}}^1)$ obtained from the fine scale computation, where we solve

$$\int_{\Omega^1} \operatorname{div}\left(\boldsymbol{\sigma}(\boldsymbol{u}^0 + \bar{\boldsymbol{u}}^1)\right) \cdot \boldsymbol{\eta}^1 \, \mathrm{d}\Omega = \int_{\Omega^1} \boldsymbol{f} \cdot \boldsymbol{\eta}^1 \, \mathrm{d}\Omega \qquad (2)$$

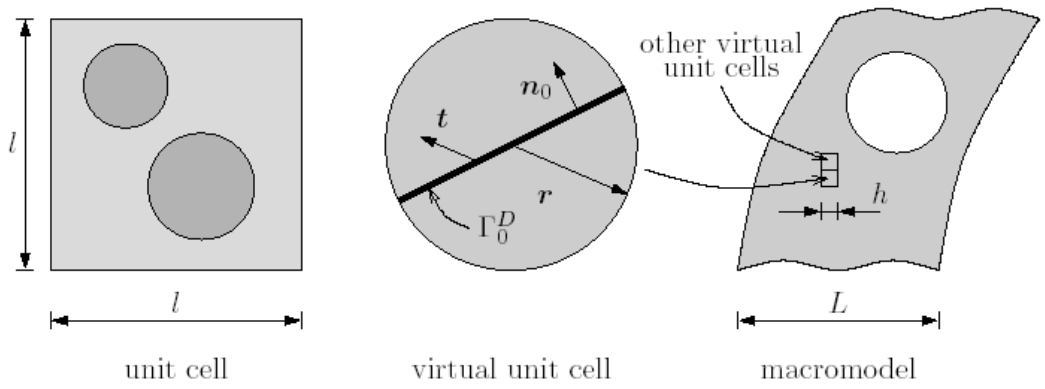

Figure 1: Schema of the multiscale method.

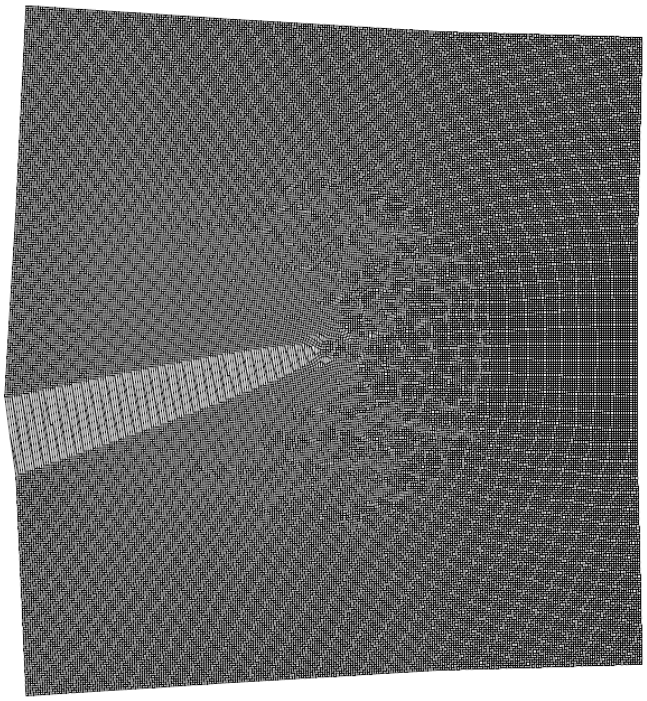

Figure 2: Deformed configuration of the fine scale domain.

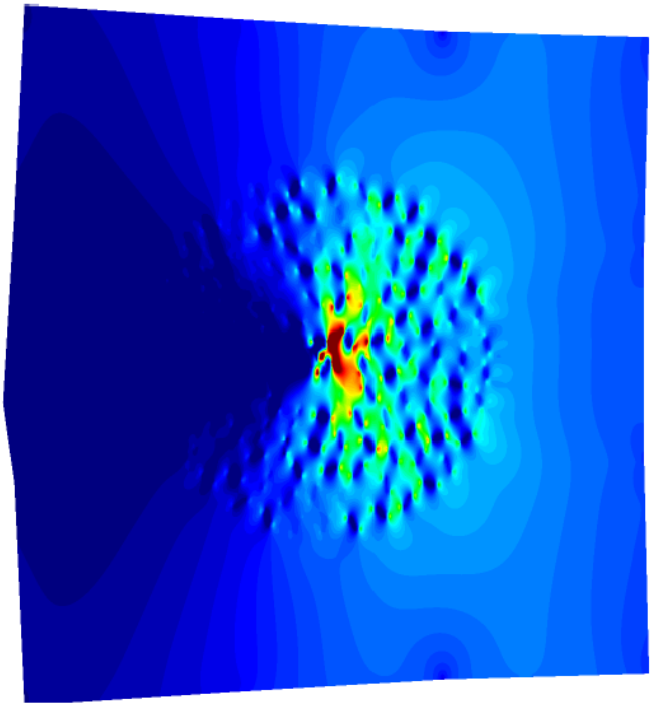

Figure 3: σ_{yy} stress component of the fine scale domain.

for the fine scale displacements $\boldsymbol{u}^1 = \boldsymbol{u}^0 + \bar{\boldsymbol{u}}^1$. For the fine scale computation we use the pure displacement boundary conditions $\bar{\boldsymbol{u}}^1 \equiv 0$ which guarantee compatibility between the coarse scale displacement field and the fine scale displacement field along the boundary of the fine scale domain. In the context of XFEM which is used on both scales to efficiently calculate cracks, these displacement boundary conditions require a special projection technique to avoid non-uniqunesses of the computed boundary conditions.

On the coarse scale only macrocracks, i.e. cracks that are larger than a typical element size are modeled wheras on the fine scale both, macrocracks and microcracks are considered. Thus, the effect of the microcracks on the macrocracks and the coarse scale response is captured only implicitly.

For this method, the right choice of the fine scale domain is of great importance. Since microcracks around the crack tip of a macrocrack strongly influence the propagation of the macrocrack, the fine scale domains are chosen to be located around the tips of the macrocracks. Since the influence of the microcracks decays rapidly with the distance to the macrocrack tip, it is sufficient if the fine scale domain has a diameter of a few times the length of a typical microcrack. This leads to a very efficient computation.

As an example, Fig. 4 shows a mixed mode multiple crack problem calculated with the multiscale method. The darkly shaded area is the fine scale domain containing 114 microcracks located around the crack tip of a macrocrack. For this example, the deformed configuration and the stress field of the fine scale domain are shown in Figs. 2 and 3.

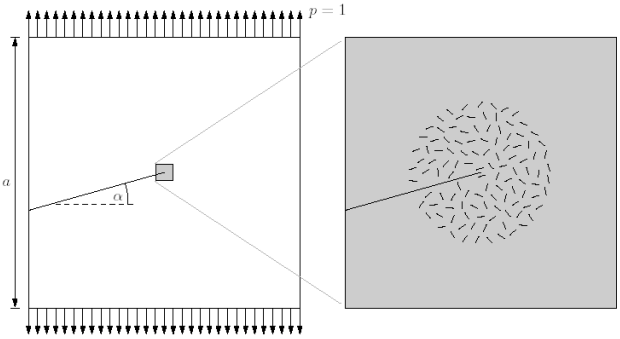

Figure 4: Mixed mode multiple crack problem.

References

[1] F. Feyel and J. L. Chaboche (2000): FE^2 multiscale approach for modelling the elastoviscoplastic behaviour of long fibre SiC/Ti composite materials. *Computer Methods in Applied Mechanics and Engineering*, **183**, 309–330.

[2] N. Moës, J. Dolbow, and T. Belytschko (1999): A finite element method for crack growth without remeshing. *International Journal for Numerical Methods in Engineering*, **46**, 131–150.

[3] T. Belytschko, N. Moës, S. Usui, and C. Parimi (2001): Arbitrary discontinuities in finite elements. *International Journal for Numerical Methods in Engineering*, **66**, 1378–1410.

[4] S. Loehnert, and T. Belytschko (2007): A multiscale projection method for macro / microcrack simulations. *International Journal for Numerical Methods in Engineering*, DOI:10.1002/nme.2001.

Modeling Fluids of Heterogeneous Materials Including Fluid-Structure Interactions Using the Particle Finite Element Method

S. R. Idelsohn[1,2*], E. Oñate[1], J. Marti[2], M. De Mier[1]

[1]International Centre for Numerical Methods in Engineering (CIMNE)
Gran Capitan s/n, Edif. C1 Campus Nord UPC, 08034 Barcelona, Spain
sergio@cimne.upc.edu, onate@cimne.upc.edu, dmier@cimne.upc.edu

[2]International Centre for Computational Methods in Engineering (CIMEC)
Guemes 3450, 3000 Santa Fe, Argentina
jmarti@ceride.gov.ar

Summary: We present a general Lagrangian formulation for treating problems in a unified form from fluid flows of heterogeneous materials to fluid-structure interactions between elastic solids and incompressible fluids. In our work the problem is solved via the Particle Finite Element Method (PFEM). The PFEM is an effective technique for modeling complex interactions between heterogeneous fluid materials with floating and submerged bodies including free-surface flows and internal interfaces, accounting for splashing of waves, large motions of the bodies and frictional contact conditions.
Examples of the unified Lagrangian formulation to a number of heterogeneous materials situations are given such as mixing of heterogeneous fluids, bed erosion and sediment transport in channels and fluid-structure interactions problems.

Introduction

Typical difficulties of modeling fluids and solids with heterogeneous materials using the FEM with both the Eulerian and ALE formulations include the treatment of the convective terms and the incompressibility constraint in the fluid equations, the modeling and tracking of the interfaces between the heterogeneous materials, free surface in the fluid, the transfer of information between the fluid and solid domains via the contact interfaces, the modeling of wave splashing as well on the free surface as in the internal interfaces, the possibility to deal with large rigid body motions of the structure within the fluid domain, the efficient updating of the finite element meshes for both the structure and the fluid, etc.

In our work we propose a different route for solving problems of heterogeneous fluids including fluid-structure interactions. Our goal is to solve the equations of fluid using a Lagrangian formulation. This allows following the different heterogeneous materials in a Lagrangian frame and, in case of FSI, allows the use for both, the fluid and solid domains, a unified formulation. This basically means that the analysis domain, containing both fluid and solid sub domains which interact with each other, is seen as a single continuum domain with different material properties assigned to each of the interacting sub domains (i.e. the fluid and solid regions). This allows making no distinction between fluids and solids for the numerical solution and a single computer code can be used for solving a FSI problem with heterogeneous fluids domains.

The key ingredients of the unified formulation presented are:

a) The use of a Lagrangian description to model the kinematics of both: heterogeneous fluid and solid domains.

b) The use of the Particle Finite Element Method (PFEM) for redefinition of the domain boundaries and treatment of frictional contact conditions.

c) The definition of a unified constitutive equation for the fluid and solid materials.

Most of these problems previously described in ALE and Euler formulations disappear if a Lagrangian description is used to formulate the governing equations of both the solid and the fluid domain. In the Lagrangian formulation the motion of the individual particles are followed and, consequently, nodes in a finite element mesh can be viewed as moving material points (here forth called “particles”. Hence, the motion of the mesh discretizing the total domain (including both the fluid and solid parts) is followed during the transient solution.

In this paper we present an overview of a particular class of Lagrangian formulation developed by the authors to solve problems involving heterogeneous fluids including the interaction between fluids and solids. The method, called the particle finite element method (PFEM), treats the mesh nodes in the fluid and solid domains as particles which can freely move and even separate from the main fluid domain representing, for instance, the effect of water drops. A finite element mesh connects the nodes defining the discretized domain where the governing equations are solved in the standard FEM fashion.

The PFEM is the natural evolution of recent work of the authors for the solution of fluid mechanics problems using Lagrangian finite element and meshless methods [1-3]. An obvious advantage of the Lagrangian formulation is that the convective terms disappear from the fluid equations. The difficulty is however transferred to the problem of adequately (and efficiently) moving the mesh nodes. Indeed for large mesh motions remeshing may be a frequent necessity along the time solution. We use an innovative mesh regeneration procedure blending elements of different shapes using an extended Delaunay tessellation [4]. Furthermore special polyhedral finite element needs special shape functions. In this paper, meshless finite element (MFEM) shape functions have been used [5].

Basic steps of the PFEM

Let us define the collection or cloud of nodes (C) pertaining to the fluid and solid domains, the volume (V) defining the analysis domain for the fluid and the solid and the mesh (M) discretizing both domains.
A typical solution with the PFEM involves the following steps.

1. The starting point at each time step is the cloud of points in the fluid and solid domains. For instance C_n denotes the cloud at time $t = t_n$.

2. Identify the boundaries for both the fluid and solid domains defining the analysis domain V_n in the fluid and the solid. This is an essential step as some boundaries (such as the free surface in fluids) may be severely distorted during the solution process including separation and re-entering of nodes. This allows modeling splashing of waves. The Alpha Shape method is used for the boundary definition.

3. Discretize the fluid and solid domains with a finite element mesh M_n. In our work we use an innovative mesh generation scheme based on the Extended Delaunay Tessellation [4].

4. Solve the Lagrangian equations of motion for the fluid and the solid domains using the unified formulation proposed in this work. Compute the relevant state variables in both domains at the next (updated) configuration for $t + \Delta t$: velocities, pressure and viscous stresses in the fluid and displacements, stresses and strains in the solid. Indeed this step requires an iterative scheme as large motion of both the fluid and solid domain may occur during the time step.

5. Move the mesh nodes to a new position C_{n+1} where $n+1$ denotes the time $t_n + \Delta t$, in terms of the time increment size. This step is typically a consequence of the solution process of step 4.

6. Go back to step 1 and repeat the solution process for the next time step.

Examples

A number of examples to show the powerful of the method are included in the extended paper. Fig. 1 shows, for instance, a time step during the mixing of two fluids of different densities. The representation of the free surface and the interface between the two flows represent a difficult task, easily solved using the technique presented in this paper.

Another interesting application of the PFEM is the solution of erosion and sediment transport in open channel flows. The phenomena of erosion and sediment transport may be treated as an interaction between two heterogeneous materials. Fig. 2 shows, for instance, a time step during the process of erosion of a sand channel under the action of an impacting water stream originated by a water jet. The domain includes an elastic body representing a bridge pile.

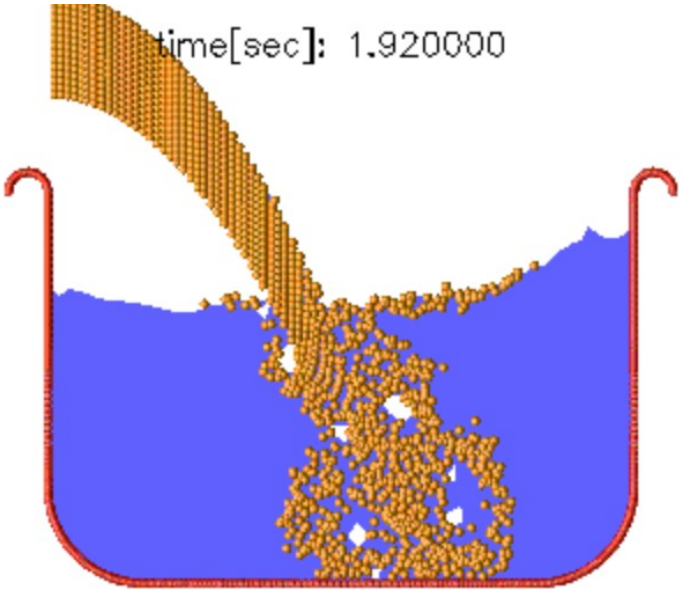

Figure 1: Mixing two fluids of different densities.

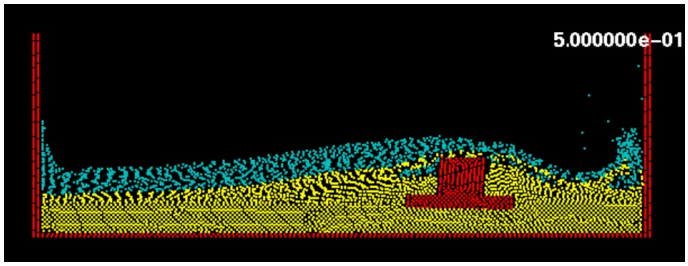

Figure 2: Erosion of a sand channel.

References

[1] S. R. Idelsohn, E. Onate, F. Del Pin, N. Calvo (2002): Lagrangian formulation: the only way to solve some free-surface fluid mechanics problems. *Fifth World Congress on Computational Mechanics*, Mang H. A., Rammerstorfer F. G., Eberhardsteiner J. (eds), July 7–12, Vienna, Austria.

[2] S. R. Idelsohn, E. Onate, F. Del Pin (2003): A Lagrangian meshless finite element method applied to fluid-structure interaction problems. *Computers and Structures*, **81**, 655–671.

[3] S. R. Idelsohn, E. Onate, F. Del Pin (2004): The particle finite element method: a powerful tool to solve incompressible flows with free-surfaces and breaking waves. *Int. J. Num. Meth. Engng.*, **61**, 964–989.

[4] S. R. Idelsohn, N. Calvo, E. Onate (2003): Polyhedrization of an arbitrary point set. *Comput. Method Appl. Mech. Engng.*, **192**, 2649–2668.

[5] S. R. Idelsohn, E. Onate, N. Calvo, F. Del Pin (2003): The meshless finite element method. *Int. J. Num. Meth. Engng.*, **58**, 893–912.

Enriched Finite Element Formulation for Coupled Cracking and Debonding Applied to Textile Reinforced Concrete

R. Chudoba[1*], **F. Peiffer**[1], **M. Mombartz**[2], **J. Hegger**[2]

[1]Chair of Structural Statics and Dynamics, RWTH Aachen
Mies-van-der-Rohe-Str. 1, 52074 Aachen, Germany
{rch,peiffer}@lbb.rwth-aachen.de

[2]Institute of Structural Concrete, RWTH Aachen
Mies-van-der-Rohe-Str. 1, 52074 Aachen, Germany
{mmombartz,heg}@imb.rwth-aachen.de

Summary: This paper describes the crack centered enrichment of the debonding between matrix and textile reinforcement. The basic fields are formulated with additional terms representing the discontinuity in matrix displacement as well as in the bond. The crack bridge parameters can be evaluated in a nonlinear computation embedded in the standard Newton-Raphson framework. We illustrate the method on the example of a 1D bar with two interacting cracks.

Introduction

A particularly important aspect of modeling cementitious composites reinforced with multi-filament yarns is an explicit representation of the crack edge geometry evolving during the failure process. It is the necessary condition for good reproduction of the strain fields at the hot spots of the damage both in the bond and in the yarn in the vicinity of the crack bridges. Only with the detailed crack geometry representation it is possible to consider the micro-scale effects occurring in cracks bridged by multi-filament yarns resulting from varying bond quality and bond-free length or lateral pressure.

Crack-centered debonding enrichments

This problem can be effectively tackled using adaptive enrichment techniques of the finite element method providing an efficient tool for introducing discontinuities and material interfaces into an originally smooth discretization [1]. Here we consider a one-dimensional two layered body occupying an interval Ω with boundary denoted by Γ. Debonded zones around discontinuities at points x_ξ are denoted by Ω_a. To present the approximation in a concise form, *effective values* of the basic fields (matrix m and fiber f) are defined by

for $x \in \Omega \setminus \Omega_a$

$$\begin{aligned} \bar{\sigma} &= \sigma_\mathrm{m} + \sigma_\mathrm{f} \\ \bar{\epsilon} &= \epsilon_\mathrm{m} = \epsilon_\mathrm{f} \\ \bar{u} &= u_\mathrm{m} = u_\mathrm{f} \end{aligned} \tag{1}$$

for $x \in \Omega_a$

$$\begin{aligned} \bar{\sigma} &= \sigma_\mathrm{m} + \sigma_\mathrm{f} \\ \bar{\epsilon} &= \frac{\bar{\sigma}}{E_\mathrm{m}+E_\mathrm{f}} = \frac{1}{E_\mathrm{m}+E_\mathrm{f}}(E_\mathrm{m}\epsilon_\mathrm{m} + E_\mathrm{f}\epsilon_\mathrm{f}) \\ \bar{u} &= \frac{1}{E_\mathrm{m}+E_\mathrm{f}}(E_\mathrm{m}u_\mathrm{m} + E_\mathrm{f}u_\mathrm{f}) \end{aligned} \tag{2}$$

The basic displacement functions u_m and u_f can be rewritten in terms of effective value $\bar{u}$

$$u_\mathrm{m} = \bar{u} + \bar{u}_\mathrm{m} \tag{3}$$
$$u_\mathrm{f} = \bar{u} + \bar{u}_\mathrm{f} \tag{4}$$

where $\bar{u}_\mathrm{m}$ and $\bar{u}_\mathrm{f}$ are the deviations of u_m and u_f, respectively, from the effective value $\bar{u}$. Using Eqs. (2) this can be rewritten as

$$u_\mathrm{m} = \bar{u} - \frac{E_\mathrm{f}}{E_\mathrm{m}}\bar{u}_\mathrm{f} \tag{5}$$
$$u_\mathrm{f} = \bar{u} + \bar{u}_\mathrm{f} \tag{6}$$

In order to introduce a discontinuity representing a single crack bridge at position $x = x_\xi$, the approximation of the effective displacement $\bar{u}$ can be enriched by the step function sign $(\cdot)$

$$\bar{u}^h = \boldsymbol{N}_s\hat{\boldsymbol{u}}_s + \mathrm{sign}\,(x - x_\xi)\,\hat{u}_e. \tag{7}$$

In the debonded domain Ω_a (slip between matrix and fiber) the enrichment must reflect the different displacement fields

$$\begin{aligned} u_\mathrm{m}^h &= \boldsymbol{N}_s\hat{\boldsymbol{u}}_s + \mathrm{sign}\,(\eta_a)\,\hat{u}_e + N_\mathrm{m}(\eta_a)\hat{u}_\mathrm{m} \\ u_\mathrm{f}^h &= \boldsymbol{N}_s\hat{\boldsymbol{u}}_s + \mathrm{sign}\,(\eta_a)\,\hat{u}_e + N_\mathrm{f}(\eta_a)\hat{u}_\mathrm{f} \end{aligned} \tag{8}$$

where

$$\eta_a = \frac{1}{a}(x - x_\xi) \tag{9}$$

is a unit coordinate system with the origin at the crack bridge ($x = x_\xi$) and $\eta_a = \pm 1$ marking the boundaries of the debonded zone. The extending functions $N_\mathrm{m}(\cdot)$ and $N_\mathrm{f}(\cdot)$ are constructed in such a way that the approximation (8) a-priori fulfills the kinematic conditions at points $x = a$ and $x = x_\xi$. Based on the analytical solutions of a symmetric pull-out problem with cohesive bond the functions N_m and N_f are defined as piecewise quadratic functions (Fig. 1) in the following way:

$$\begin{aligned} N_\mathrm{m}(\eta) &= \begin{cases} -(\eta+1)^2 & -1 < \eta < 0 \\ (\eta-1)^2 & 0 < \eta < 1 \end{cases} \\ N_\mathrm{f}(\eta) &= -N_\mathrm{m}(\eta) \end{aligned} \tag{10}$$

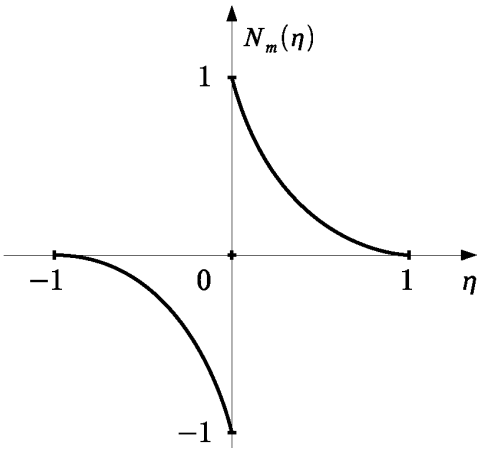

Figure 1: Enrichment function $N_{\mathrm{m}}(\eta)$.

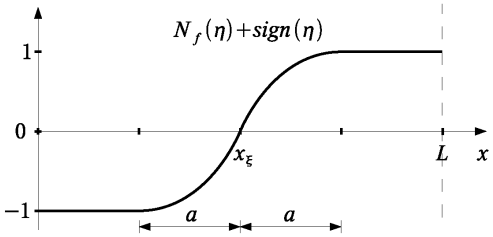

Figure 2: Enrichment functions for fiber.

The continuity of the fiber displacement fields imposes an additional constraint

$$\hat{u}_e = \hat{u}_{\mathrm{f}} \tag{11}$$

For the example of a single crack bridge the enrichment functions are depicted in Figs. 2 and 3.

Verification example

As an example we present a fiber reinforced tension bar with two interacting cracks. The crack bridge opening parameters are computed within the standard Newton-Raphson framework. Figs. 4–6 show the displacement fields, strains and stresses.

The described enrichment framework is constructed with the goal to couple the described meso-scopic enrichment with micro-scale crack bridges representation capturing the local damage and failure mechanisms [2].

References

[1] T. Belytschko, N. Moës, S. Usui, C. Parimi (2001): Arbitrary discontinuities in finite element. *International Journal for Numerical Methods in Engineering*, **50**, 993–1013.

[2] M. Konrad, R. Chudoba, K. Meskouris, A. Scholzen (2007): Effect of local imperfections in cracks bridged by multi-filament yarn on multi-cracking response. In *Modelling of Heterogeneous Materials*, Proc. MHM 2007, Prague.

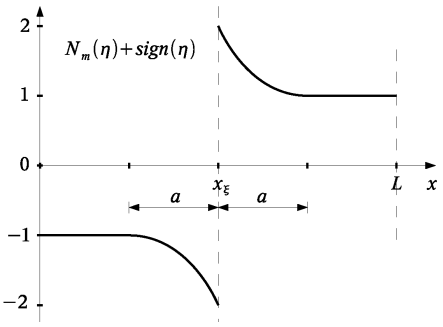

Figure 3: Enrichment functions for matrix.

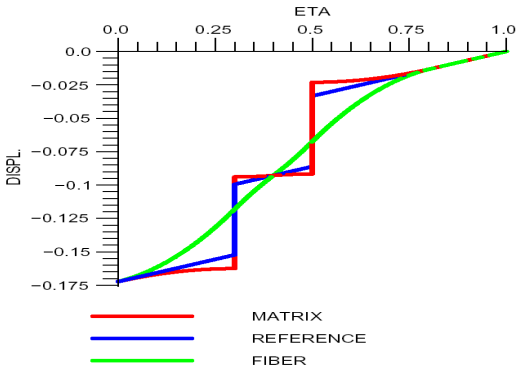

Figure 4: Displacement field of a tensioned 1D bar with two cracks: reference displacement field, matrix and fiber displacement.

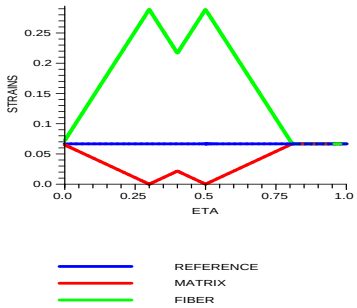

Figure 5: Strain field of a tensioned 1D bar with two cracks.

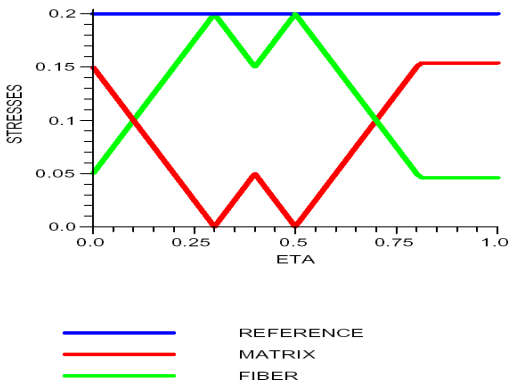

Figure 6: Stress field of a tensioned 1D bar with two cracks.

Multi-Physics Modelling of Partially Saturated Geomaterials

L. Sanavia[1]*, D. Gawin[2], B. A. Schrefler[1]

[1]Dipartimento di Costruzioni e Trasporti, Università degli Studi di Padova
via F. Marzolo 9, 35131 Padova, Italy
lorenzo.sanavia@unipd.it, bernhard.schrefler@unipd.it

[2]Department of Building Physics and Building Materials, Technical University of Lodz
Al. Politechniki 6, 90–924 Lodz, Poland
gawindar@p.lodz.pl

Summary: A mathematical model for non-isothermal multiphase geomaterials which considers the dissolution of air in water and air mass sources during its desorption at lower water pressure is presented. The solid skeleton is elasto-plastic, isothermal or non-isothermal; heat, water and air flows and water phase changes are taken into account. Numerical solution of the model equations by means of the Finite Element Method for coupled problems is presented and a numerical example is shown.

Porous materials are made of a solid phase and closed and open pores. The case where the open pores are filled with one or more fluids, i.e. multiphase media, is considered in this work. In recent years, increasing interest in thermo-hydro-mechanical analysis of saturated and partially saturated materials is observed, because of a wide spectrum of their engineering applications. Typical examples belong to environmental geomechanics, where, e.g., the pollutant transport problem within fractured zones due to shear bands development is of interest.

Strain localization in water saturated geomaterials has been modelled in recent years by several researchers (see e.g. the references in [1]). There are also experimental results available, e.g. [2]. The case of globally undrained dense (i.e. dilatant) sand samples are interesting because the experimental results show that the water pressure decreases continuously almost from the beginning on. At the onset of localization this pressure is decisively negative and is close to the cavitation pressure. This pressure is always reached at the onset of localization and cavitation was observed [2]. Usually these experiments are performed by saturating the specimens with de-aired water and making circulate fresh de-aired water in order to dissolve the rest of gas bubbles possibly trapped in the specimens and the circuits. In field conditions this is not the case. The question how the air dissolved in water can influence the evolution of water cavitation during the strain localization phenomenon and, more generally, how the dissolved air released can influence the rapid water saturation variation, is the main motivation for the development of the proposed model.

The low value of water pressure observed during strain localization in water saturated dense sands, causes a release of certain amount of air dissolved in water. This is so because the solubility of air in water, according to Henry's law, eq. (1), decreases proportionally to the pressure drop

$$p_i^g = K_{ca} \cdot c_{wa} \tag{1}$$

with c_{wa} the concentration of the air dissolved in water and $K_{ca}(p^w, T)$ the Henry law constant, dependent on the water pressure p^w and the temperature T. For example 1 dm^3 of water saturated sand and having porosity of 0.20, may contain at 20 C maximally about 3.98 ml of dissolved air at atmospheric pressure (p_{atm}= 101325 Pa) and only 0.09 ml of air at pressure of 2339 Pa (cavitation pressure value at 20^0 C). The excess amount of air is released in the form of small air bubbles, which play a role of nuclei for cavitation initiation. The process starts when the actual volume concentration of air dissolved in water is equal to the equilibrium one corresponding to the actual water pressure. Furthermore, this air can contribute to the gas pressure in the zone, accelerating water desaturation.

In this work, we extend the previous mathematical models of coupled heat and mass transport in fully and partially saturated soils [3], considering the air dissolved in pore water and air mass sources during its desorption at lower water pressure.

Mathematical model and a numerical simulation

The multiphase porous continuum is composed of a solid skeleton (s) and voids filled with water (w) and air (g). The latter is assumed to behave as an ideal mixture of dry air (ga) and water vapour (gw). Phase changes of water and heat transfer through conduction and convection, as well as latent heat transfer are considered in the model. The solid skeleton is modelled as an elasto-plastic deforming porous continuum in isothermal [3] or non-isothermal conditions. Small strains and quasi-static loading conditions are assumed. All fluids are in contact with the solid phase. The constituents are assumed to be isotropic, homogeneous, immiscible except for dry air and vapour, and chemically non reacting. Local thermal equilibrium is assumed. The primary variables are the solid displacements $\boldsymbol{u}$, the capillary p^c and the gas pressure p^g, the temperature T and the concentration of the air dissolved in water c_{wa}. Partial saturation is described at constitutive level. The interested reader can refers to [1] for the full mathematical model. The macroscopic balance equations are now summarized. The mass balance equation for the solid skeleton, water and vapour is:

$$\begin{aligned}
&n[\rho^w + \rho^{gw}]\frac{\partial S_w}{\partial t} + [\rho^w S_w + \rho^{gw} S_g]\,\mathrm{div}\left(\frac{\partial \boldsymbol{u}}{\partial t}\right) \\
&+nS_g\frac{\partial \rho^{gw}}{\partial t} - \mathrm{div}\left(\rho^g \frac{M_a M_w}{M_g^2}\boldsymbol{D}_g^{gw}\,\mathrm{grad}\left(\frac{p^{gw}}{p^c}\right)\right) \\
&-\mathrm{div}\left(\rho^w \frac{\boldsymbol{k}\,k^{rw}}{\mu^w}\left[\mathrm{grad}(p^g) - \mathrm{grad}(p^c) - \rho^w \boldsymbol{g}\right]\right) \\
&-\mathrm{div}\left(\rho^{gw} \frac{\boldsymbol{k}\,k^{rg}}{\mu^g}\left[\mathrm{grad}(p^g) - \rho^g \boldsymbol{g}\right]\right) - \beta_{swg}\frac{\partial T}{\partial t} = 0
\end{aligned} \tag{2}$$

The mass balance equation for dry air is:

$$\begin{aligned}&\mathrm{div}\left(\rho^{ga}\frac{\boldsymbol{k}\,k^{rg}}{\mu^{g}}[-\mathrm{grad}(p^{g})+\rho^{g}\boldsymbol{g}]\right)-n\rho^{ga}\frac{\partial S_{w}}{\partial t}\\&-\mathrm{div}\left(\rho^{g}\frac{M_{a}M_{w}}{M_{g}^{2}}\boldsymbol{D}_{g}^{ga}\mathrm{grad}\left(\frac{p^{ga}}{p^{g}}\right)\right)+nS_{g}\frac{\partial\rho^{ga}}{\partial t}\\&+\rho^{ga}S_{g}\mathrm{div}\left(\frac{\partial\boldsymbol{u}}{\partial t}\right)-\beta_{s}\rho^{ga}[1-n]S_{g}\frac{\partial T}{\partial t}=\dot{m}_{ga}\end{aligned}\tag{3}$$

with $\dot{m}_{ga}$ the rate of mass due to released dissolved air [1]:

$$\begin{aligned}&\dot{m}_{ga}=\mathrm{div}\left(c_{wa}\rho^{w}\frac{\boldsymbol{k}\,k^{rw}}{\mu^{w}}[\mathrm{grad}(p^{w})-\rho^{g}\boldsymbol{g}]\right)\\&+n\rho^{w}c_{wa}\frac{\partial S_{w}}{\partial t}+\mathrm{div}(\rho^{w}\boldsymbol{D}_{w}^{ga}\mathrm{grad}(c_{wa}))\\&-\rho^{w}c_{wa}S_{w}\mathrm{div}\left(\frac{\partial\boldsymbol{u}}{\partial t}\right)-n\rho^{w}S_{w}\frac{\partial c_{wa}}{\partial t}+c_{wa}\beta_{swg}\frac{\partial T}{\partial t}\end{aligned}\tag{4}$$

The energy balance equation is:

$$\begin{aligned}&\left(\rho^{w}C_{p}^{w}\boldsymbol{v}^{w}+\rho^{g}C_{p}^{g}\boldsymbol{v}^{g}\right)\cdot\mathrm{grad}(T)-\mathrm{div}(\chi_{eff}\mathrm{grad}(T))\\&+(\rho C_{p})_{eff}\frac{\partial T}{\partial t}=-\dot{m}_{vap}\Delta H_{vap}\end{aligned}\tag{5}$$

The linear momentum balance equation of the mixture in terms of effective Cauchy stress is written in (6), with $\rho=[1-n]\rho^{s}+nS_{w}\rho^{w}+nS_{g}\rho^{g}$ the mixture density. The form of the stress tensor in (6) is thermodynamically consistent, as derived in [4].

$$div(\boldsymbol{\sigma}'-[p^{g}-S_{w}p^{c}]\mathbf{1})+\rho\boldsymbol{g}=\mathbf{0}\tag{6}$$

A first simplified model can be derived assuming the gradient of c_{wa} small enough to neglect the effects of the diffusive fluxes of dissolved air. In this case, the source term in (3) can be reduced to $\dot{m}_{ga}=-n\rho^{w}S_{w}\partial c_{wa}/\partial t$ (see [1] for details).

The following numerical example deals with the simulation of the plane strain compression test described in [2] for a case of dense sand under globally undrained conditions, where strain localization and cavitation of the pore water was observed. The process is simulated with the numerical model considering these effects (case 2) and neglecting them (case 1 - see [3]). A rectangular sample of homogeneous soil of 34 cm height and 10 cm width has been discretized using quadrilateral elements. The material is initially water saturated and the boundaries of the sample are impervious and adiabatic. Imposed vertical displacements are applied on the top surface until strain localization is obtained. Vertical and horizontal displacements are constrained at the bottom surface. The initial temperature in the sample is fixed at the ambient value. Gravity forces are taken into account. The dilatant behaviour of the solid skeleton is simulated by using the elasto-plastic Drucker-Prager constitutive model, with isotropic linear softening and non associated plastic flow.

The numerical results indicate the pronounced accumulation of inelastic strains in narrow zones (Fig. 1) and a water pressure drop inside them up to the development of capillary pressures. At these conditions a vapour phase appears (i.e. water cavitation starts) only inside the dilatant plastic zones because the water pressure decreases below the saturation vapour pressure at ambient temperature of 2338.8 Pa (Fig. 2). A gradual water desaturation in the strain localization bands initiates. When the dissolved air is considered in the mathematical model (case 2), the decrease of water pressure inside the plastic zones causes a release of the dissolved air there, Fig. 1, what visibly accelerates, as compared to the case 1, the initiation of cavitation and desaturation process, about 12 s for the considered example, Fig. 2. Hence, it can be concluded that the dissolved air is of importance during simulation of cavitation in globally undrained initially water saturated dense sands. This is not the case when the water outflow due to gravity forces and accompanying water desaturation (Liakopoulos test) is modelled [5].

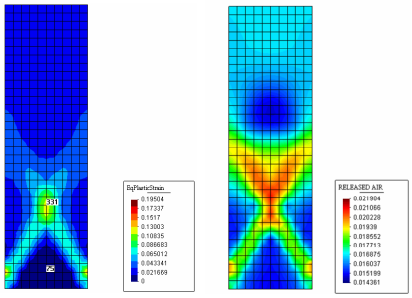

Figure 1: Equivalent plastic strain (left) and total amount of dissolved air released from the pore water (right) at t= 22 s.

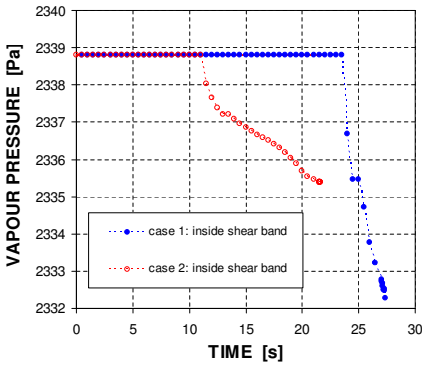

Figure 2: Vapour pressure vs. time.

References

[1] D. Gawin, L. Sanavia (submitted): Modelling of cavitation in water saturated porous media considering effects of dissolved air.

[2] M. Mokni, J. Desrues (1998): Strain localisation measurements in undrained plane-strain biaxial tests on Hostun RF Sand. *Mech. Cohes.-Frict. Mat.*, **4**, 419–441.

[3] L. Sanavia, F. Pesavento, B. A. Schrefler (2006): Finite element analysis of non-isothermal multiphase geomaterials with application to strain localisation simulation. *Computational Mechanics*, **37**, 331–347.

[4] W. Gray, B. A. Schrefler (2007): Analysis of the solid phase stress tensor in multiphase porous media. *Int. J. Numer. Anal. Meth. Geomech.*, **31**, 541–581.

[5] D. Gawin, L. Sanavia, B. A. Schrefler (in preparation): Numerical modelling of dissolved air effects on coupled hygro-thermal processes in saturated materials.

Modelling the Hydration of Portland Cement Using μic

S. Bishnoi, K. L. Scrivener*

Ecole Polytechnique Fédérale de Lausanne
EPFL-STI-IMX-LMC, Station 12, 1015 Lausanne, Switzerland
shashank.bishnoi@epfl.ch, karen.scrivener@epfl.ch

Summary: This paper presents "μic", a new model that simulates microstructural development of hydrating cement paste. The model uses the vector approach to preserve the multi-scale aspect of cement and can be used for microstructural characterization and micro-mechanical computations. The emphasis of this model is towards providing a flexible simulation platform to aid experimenters with interpreting experimental results.

Introduction

Our current knowledge of cement is limited to, often contradictory, experimental results on specimens that vary depending on different conditions. With many concurrent factors it becomes difficult to decouple their effects based on observations. Still, with most numerical models focussing on prediction, the availability of numerical tools aiding the interpretation of results is limited. This paper presents a model that aims at aiding, rather than replacing experimentation.

μic the model

This model is based on the vector approach, where all elements are represented as three-dimensional vector shapes rather than a collection of discrete pixels. The basics of this model are derived from work by Navi and Pignat [1, 2]. In the pixel approach, the size of the smallest possible object represented is restricted by the maximum resolution, that in turn is restricted by memory limitations [3]. So, the pixel approach can be argued not to be appropriate for multi-scale materials like cement. The vector approach provides a solution for such materials as it is not restricted by a maximum resolution. However, due to performance issues, the vector approach is largely limited to spheres. Reactions in μic are modelled as creation and expansion of spheres containing multiple concentric layers as discussed in the following section.

Purely object-oriented code in Java was developed with the objective of providing the user with the flexibility to include his ideas in simulation. The cement hydration tool-kit was developed to provide a customisable framework for the model. The tool-kit provides generic implementations for reactions, materials, particles, etc. that can be plugged in with customisations to implement particulate reactions. Reactions can, for example, be plugged in with user-defined reaction kinetics.

Spherical particles are packed into a numerical volume to represent different phases of cement. While different phases may be interspersed in varying proportions in the particles and be present as concentric layers, they can also be present as separate particles. Reactions can be defined as the consumption of defined proportions of user-defined materials and the production of other materials. The products can then either be deposited over the grains already present or be deposited in new clusters in the pores. Plugins can be used to define the amounts of materials being used up from different particles and the distribution of products in the available space. The general steps in defining a problem are listed in the following section.

Steps in modelling

Since μic has been designed to provide maximum customisability to the user, a large number of inputs are required for the definition of the problem. Although this might initially slow down or even make difficult the definition of the problem, all definitions can be reused and extended. The model also provides libraries for many common applications. The main steps in the definition of the problem as listed below.

- Definition of materials
- Definition of powder properties: water/solid ratio, particle size distribution, phase distribution
- Phase distribution of materials in particles using plugins
- Definition of particle types
- Definition of reactions
- Definition of consumption and deposition laws using plugins
- Definition of other plugins

The importance of plugins in the design of the model is apparent in the above list. One of the most important of these plugins are reaction kinetics. Reaction kinetics are defined to control the rate of consumption of materials according to laws based on experimental observations. Many other laws can be plugged

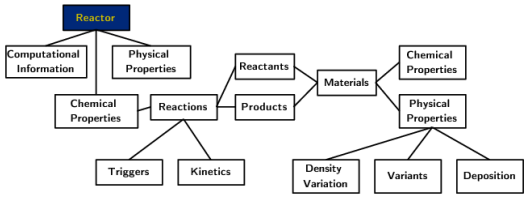

Figure 1: Structure of the model.

into the model. Using one of these plugins, the products can be deposited in varying proportion over different types of grains. For example, CSH can be allowed to deposit over Alite grains, filler particles or even as new clusters in pore space, all with different properties. This is achieved by defining the three types of CSH as different materials linked to each other. The proportion of CSH deposited in the three places can be controlled by managing the produced amounts of the three types of CSH. These

proportions are also not static and can be calculated at each moment using the plugin. Furthermore, another plugin can be attached to CSH to allow the production of CSH to increase the density of the particles already present, rather than just increasing the size of the particles.

Although most of the plugins are not obligatory to define and default and library implementations are provided for all of them, the full power of the model can be realised by using all its features.

An example plugin

The plugin below is a reaction trigger that can be used to limit the execution of a reaction to given start and end time.
boolean isActive(float time) {
if (time $<$ *startTime) return false;*
if (time $>$ *endTime) return false;*
return true;}
This code can be embedded in the standard plugin format, compiled independently and given as an input to the model. Future versions of the model would be able to dynamically compile plugins given as simple text input by the user reducing complexity for the user.

Execution of the reactions

Once the inputs listed above have been provided, the simulation can be started. The model first assembles the problem by creating instances of all materials, reactions, etc. plugged in with all user customisations. A numerical specimen, called the reactor, is first created and packed with the particles. The initial particles are generated based on the provided particle size gradation and the different phases are distributed in these particles. The packing is done using a random parking algorithm.

The reactor then takes over and simulates the reactions individually. The reactions in which the rate of reaction depends on the individual particles, the amount of each material reacting from each particle is calculated. The products that need to be deposited on the same particle are handled immediately while the others are collected in a buffer. Once all particles are handled for each reaction, the buffers are distributed in the system. If possible, some materials are handled together once all reactions have been calculated to improve performance. So, in effect, the reactions are simulated as change in radii of different layers in the particles.

Results

The evolving microstructure of cement is generated as the output of the program at each time step. At the same time the global quantities are also recorded. While the global quantities can be used for comparison with experimental data, the microstructural results can be used for comparison with micrographs. Values such as heat evolution and degree of hydration can are available at each step in simulation. Furthermore, the microstructure can be analysed for physical (e.g. permeability) and mechanical (e.g. Young's modulus) properties. Parallel projects are looking at extracting such information from the vector results. A new microstructural model called μic has been developed. This model focusses on providing the user with the flexibility to add his own ideas in simulations, allowing him to test his hypotheses by comparison with experimental results. Object oriented architecture also eases extensibility of the

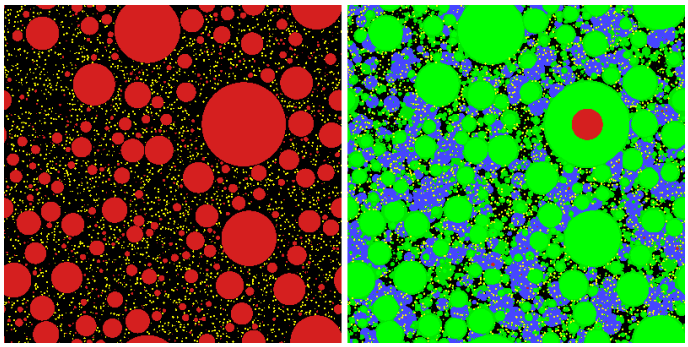

Figure 2: A typical 2D section of calculated microstructure.

model. The model is designed to be dynamic and evolutionary, and not limited to our current knowledge.

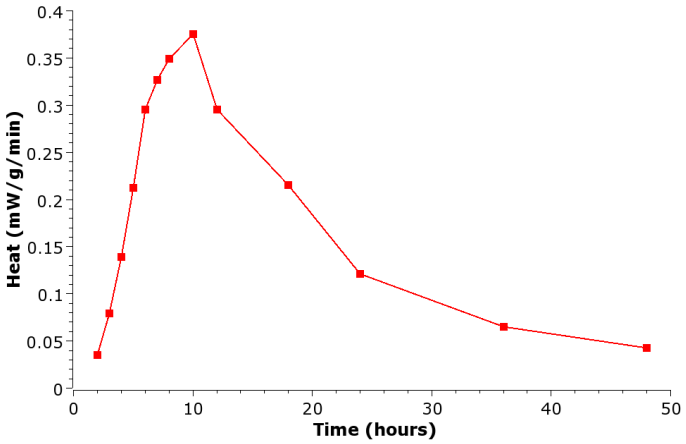

Figure 3: Normalised rate of heat evolution calculated.

Conclusion

Pore analysis of the microstructure is an integral part of this project. Currently under development, the vector approach and other multi-scale methods are being looked at to analyse the microstructure. Since the porosity of cement paste is hard to access and only indirect measurements are available for its characterisation, analysis of the numerical microstructure can prove to be the crucial link between experimental measurements and the actual properties.

References

[1] P. Navi, and C. Pignat (1996): Simulation of cement hydration and the connectivity of the capillary pore space, *Advances in Cement Based Materials*, **4**, 58–67.

[2] C. Pignat, P. Navi, and K. Scrivener (2005): Simulation of cement paste microstructure hydration, pore space characterization and permeability determination, *Materials and Structures*, **38**, 459–466.

[3] D. Bentz (2000): *CEMHYD3D: A three-dimensional cement hydration and microstructural development modelling package*, NISTIR 6485, U.S. Department of Commerce.

Bifurcations in Granular Materials: Continuous and Discrete Approaches

F. Darve[1*], L. Sibille[1], F. Prunier[1], F. Nicot[3], F. Donze[2], B. Chareyre[1]

[1]INPG, Laboratory Soils Solids Structures-Risks, Grenoble, France
[2]UJF, Laboratory Soils Solids Structures-Risks, Grenoble, France
[3]CEMAGREF-ETNA, UJF, Grenoble, France
Felix.Darve@hmg.inpg.fr

Summary: In a first part, the equations of the boundary of the bifurcation domain and of the cones of unstable stress directions are established for an incrementally piece-wise linear constitutive relation while, in a second part, these results are also obtained through discrete element computations. Diffuse failure is simulated numerically by perturbations of the bifurcation states.

Granular media are strongly non-associated elasto-plastic materials. Thus their elasto-plastic tensor does not satisfy the so-called "major symmetry". Essentially because of that, these media give rise to various classes of bifurcations strictly inside the Mohr-Coulomb plastic limit condition. These bifurcations are leading to various kinds of instabilities (geometrical instabilities, material instabilities, ...). Material or constitutive instabilities are related themselves to different failure modes (localized failure in shear bands, in compaction bands, in dilation bands, diffuse failure, ...); see [4].

Localised failure was extensively studied in the past from experimental, theoretical and numerical points of views. On the contrary, while diffuse failure was detected experimentally by various authors along "undrained" triaxial loading on loose sands or along "q constant" drained triaxial loading, theoretical studies have been devoted to this question only recently, even if this failure mode is important in practice in the case of landslides under small slope angles [5]. In this perspective this lecture is devoted to the analysis of diffuse failure as a bifurcation phenomenon detected by Hill's sufficient condition of stability (sign of second order work).

In a first part we consider a phenomenological approach by using incrementally piece-wise linear and non-linear elasto-plastic constitutive relations. Generalised stress-strain variables (basically linear combinations of stresses and strains) allow to introduce new limit states strictly inside Mohr-Coulomb plastic limit condition, where the second order work is vanishing. Since at these limit points the loading path is no more controllable [8] and the loading state is no more sustainable [2, 3], these points can be considered as bifurcation states. If we consider the incrementally piece-wise linear relation, the bifurcation criterion is given analytically by the vanishing generalised constitutive determinant and the boundary of the bifurcation domain can be obtained explicitly. According to the equations, inside the bifurcation domain, cones of unstable stress directions can be also determined, because the second order work is essentially a directional quantity. These cones are opening gradually when the stress state is approaching to the Mohr-Coulomb criterion. Having established the equations of the bifurcation domain and of the unstable cones, these results are verified numerically by considering direct integrations of the incrementally piece-wise linear relation. Finally a numerical comparison is performed with the incrementally non-linear relation, as in this case not any analytical proof can be exhibited [6, 7].

The bifurcation points (associated to generalised limit states) are related to vanishing eigenvalues of generalised constitutive matrices relating generalized stresses and strains. To these nil eigenvalues correspond eigenvectors which characterise the infinite number of solutions and the failure mechanism at these failure states through a "failure rule".

In a second part a discrete approach is considered by using a discrete element method [4]. This method allows to simulate by direct numerical computations the behaviour of a cubical specimen of 10000 spheres [9] interacting by a coulombian friction. First the sign of second order work (determined at the boundary of the cubical specimen) is computed along various loading paths and, at some stress-strain points, for various stress directions. It is remarkable that a bifurcation domain and cones of unstable stress directions were exhibited by these direct simulations. Having calibrated the incrementally non-linear constitutive relation on the numerical cubical specimen, it was possible to compare quantitatively the bifurcation domain and the unstable cones obtained with both these essentially different models. A convincing agreement is found [9]. Then it is tried to obtain a numerical diffuse failure at these presumed bifurcation states. Taking into account exactly the conditions given by the previous theory (i.e. stress states inside the bifurcation domain, incremental loading in unstable directions, proper control parameters), small perturbations of the loading parameters trying to trespass the limit states give rise to exponentially growing strains and to a burst of kinetic energy. The loading path is no more controllable in Nova's sense [8]. It was also verified that for the same perturbation applied "slightly" before the limit states nothing particular happens. Finally the numerical input of a small quantity of kinetic energy inside the specimen at the limit states gives rise also to the same kind of sudden diffuse failure. These states are not sustainable in Nicot's sense [2, 3].

References

[1] F. Darve, I. Vardoulakis (2004): Degradations and Instabilities in Geomaterials, Springer.

[2] F. Nicot, F. Darve (2006): Micro-mechanical investigation of material instability in granular assemblies, Int. J. Solids and Struct., 43, 3569–3595.

[3] F. Nicot, F. Darve (2007): A micro-mechanical investigation of bifurcation in granular materials, Int. J. Solids and Struct., in press.

[4] S. Magnier, F. Donze (1998): Numerical simulations of impacts using a discrete element method, Mech. of Cohes. Frict. Mater., 3, 257–276.

[5] F. Darve, F. Laouafa (2000): Instabilities in granular materials and application to landslides, Mech. of Cohes. Frict. Mater., 5, 627–652.

[6] H. D. V. Khoa, I. O. Georgopoulos, F. Darve, F. Laouafa (2006): Diffuse failure in geomaterials, experiments and modelling, Comp. and Geotech., 33, 1–14.

[7] F. Darve, G. Servant, F. Laouafa, H. D. V. Khoa (2004): Failure in geomaterials.Continuous and discrete analyses, Comp. Meth. in Appl. Mech. and Eng., 193, 3057–3085.

[8] R. Nova (1994): Controllability in the incremental response of soil specimens subjected to arbitrary loading programmes, J. Mech. Behav. Mater., 5, 193–201.

[9] L. Sibille, F. Nicot, F. Donze, F. Darve (2007): Material instability in granular assemblies from fundamentally different models, Int. J. Numer. and Anal. Meth. in Geomech., in press.

Coupled Deformation Diffusion Effects on Fault Zone Localization and Dynamic Slip Propagation

J. W. Rudnicki

Northwestern University
Evanston, Illinois, USA
jwrudn@northwestern.edu

Summary: This abstract describes recent work on the effect of induced pore fluid pressure on the mechanics of fault zones during rapid slip or shearing as occurs during earthquake faulting. One result suggests that thermal pressurization due to shear heating and fluid diffusion can cause localization of shearing into a very narrow zone, of order a few mm, even in a material having a strength that increases with shear strain rate. A second result shows that heterogeneity of poroelastic parameters in a narrow boundary layer near the slip plane can induce changes in pore fluid pressure. These changes cause alterations of effective normal stress that, for plausible parameters, are comparable to the changes in total normal stress induced by slip on a bimaterial interface.

Introduction

Recent field observations of mature faults [1, 2, 3, 4, 5, 6], that is, faults that have experienced large amounts of relative displacement, have revealed the following representative structure: A damage zone of the order of tens of meters wide separates relatively intact rock which may be of different types on the two sides of fault. Within the damage zone is a gouge zone of more highly damaged and permeable material having a width of the order of several meters. The principal slip occurs within a very narrow, ultracataclastic zone of the order of 10 to 100 mm and may be localized to an even narrower zone of only 1 to 5 mm thickness. This very narrow zone is relatively impermeable to flow across it with permeabilities around 10^{-19} to 10^{-20} m^2.

Shear localization

The observation of the occurrence of the principal shear in a very narrow zone is consistent with the calculation of the stability of homogeneous, undrained adiabatic shearing in a fluid-saturated gouge zone material. The shear strain rate of the material is assumed to be proportional to the effective normal stress (compressive stress minus the pore pressure) but with a friction coefficient that increases with the rate-of-shearing (if rate-weakening, deformation would localize at the onset of shear). This type of behavior applies to stable regions in which rupture cannot nucleate and to initially unstable regions that have been driven into a stable temperature regime by shear heating. A linearized perturbation analysis [7] shows that spatial nonuniformities with wavelengths greater than a critical value grow exponentially in time. The critical wavelenth is given by $\lambda_{cr} = 2\pi\sqrt{(c_{th}+c_{hy})/(z+2)H\dot{\gamma}_0}$ where c_{th} and c_{hy} are the thermal and hydraulic diffusivities, $\dot{\gamma}_0$ is the rate of uniform shearing, H is a characteristic weakening strain of the homogeneous solution, and z is a measure of the rate-strengthening. For $H \approx 0.1$, $z \approx 40$, based on laboratory friction experiments, $\dot{\gamma}_0 \approx 100$/s, consistent with a slip rate of 1 m/s over a 10 mm thick layer, $c_{th} = 1$ mm^2/s and two values of c_{hy}, 1.8 and 4.8 mm^2/s, $\lambda_{cr} = 0.38$ mm and 0.87 mm. A more detailed numerical analysis that takes into account nonlinearities and pressure and temperature dependencies of the shear zone poromechanical properties supports the approximate validity of the linear stability analysis in predicting the localized zone thickness [8].

Effective normal stress changes

Because slip causes compression on one side of the fault (idealized as a plane) and extension on the other, a mismatch of local poroelastic properties, in particular, permeability or storage coefficient, in the gouge zone causes an alteration in pore pressure. More specifically, the pore pressure increases at the interface if the compressive side is more permeable and decreases if the extensile side is more permeable. In addition, mismatch of the relatively intact material further from the slip surface also induces a change of pore pressure because of the change of normal stress and magnitudes of the discontinuous along-fault extensile strains induced by slip on a bimaterial interface. These changes in effective normal stress, due to changes in both total normal stress and pore pressure, can alter the resistance to slip.

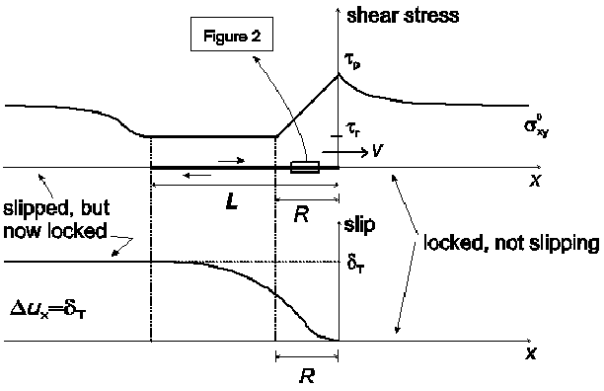

Figure 1: The Rice et al. [10] model for steady state propagation of a slip-weakening slip pulse. Model for near-fault behavior shown in Fig. 2.

Rudnicki and Rice [9] have analyzed the effects of near fault heterogeneity within the framework of the steady state, slip-weakening pulse model of [10] shown in Fig. 1. The slipping zone moves steadily to the right at a constant speed v. Slip δ

begins at $x = 0$ and increases to δ_T at $x = -L$. The frictional strength is of the form

$$\tau = c(\delta) - f_r(\sigma_{yy} + p) \quad (1)$$

where the first term is the cohesive part, assumed to weaken with slip and, for convenience, taken so that $c(\delta)$ decreases linearly with x from $x = 0$ to $x = -R$. In the second term, the friction coefficient f_r (assumed to be constant) multiplies the effective normal stress, the sum of the total normal stress σ_{yy} (positive in tension) and the pore fluid pressure p. Slip on plane in a homogeneous elastic solid causes no change in normal stress.The pore pressure on the fault plane is obtained by examining a narrow boundary layer (typically less than a few 10's of mm) where fluid diffusion occurs over the time scale of passage of the slip pulse (Fig. 2). This region is assumed to be so narrow that it experiences uniform along-fault strains. These will be equal in magnitude and opposite in sign if the material on the two sides of the slip zone is the same. The solution of this poroelastic problem reveals that the pore pressure on the fault has the same form as that for undrained conditions (no fluid flow) but with a modified coefficient that depends on the poroelastic properties in the near-fault boundary layer. Because the pore pressure change is proportional to the along-fault slip gradient, the solution can be extended to include the case where the elastic material on the two sides of the fault differs. In this case slip does cause a change in the total normal stress σ_{yy} on the slip plane and there is an additional contribution to the change in pore pressure because the along-fault strains differ in magnitude on the two sides.

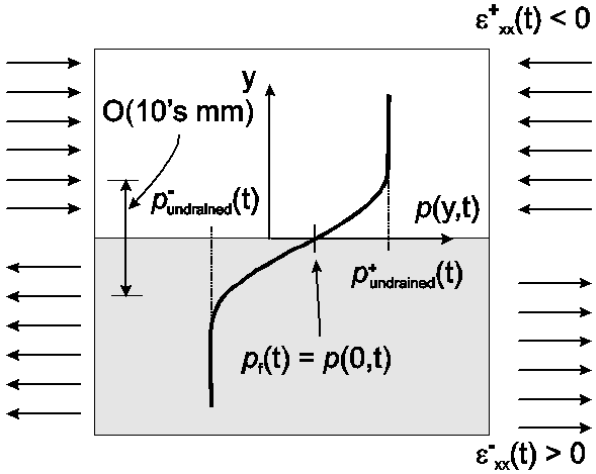

Figure 2: Schematic variation of pore in the near slip plane boundary layer region.

The effects due to heterogeneity of near-fault poroelastic properties and to mismatch of the elastic material outside the fault boundary layer are compared for representative values of material and transport properties and for mismatch of elastic properties suggested by seismic observations. The comparision indicates that the magnitude of the two effects may be similar although that due to mismatch of elastic material increases rapidly as the rupture velocity nears the generalized Rayleigh wave speed. Because the sign of both effects may be positive or negative depending on the arrangement of material properties, the sense of slip and the direction of rupture propagation, they may offset or reinforce each other.

References

[1] F. M. Chester, J. P. Evans, R. L. Biegel (1993): Internal structure and weakenng mechanisms of the San Andreas fault, *Journal of Geophysical Research*, **98**, 771–786.

[2] F. M. Chester, J. S. Chester (1998): Ultracataclasite structure and friction processes of the Punchbowl Fault, San Andreas System, California, *Tectonophysics*, **295**, 199–221.

[3] D. Lockner, H. Naka, H. Tanaka, H. Ito, R. Ikeda (2000): Permeability and strength of core samples from the Nojima fault of the 1995 Kobe earthquae, in *Proceedings of the International Workshop on the Nojima Fault Core and Borehole Data Analysis, Tsukuba, Japan*, Nov. 22-23, 1999, ed. H. Ito et al., U. S. Geopl. surv. Open File Repl, 00-129, 147–152.

[4] C. A. J. Wibberley and T. Shimamoto (2003): Internal structure and permeability of major stricke-slip fault zones: The Median Tectonic Line in Mie Prefecture, southwest Japan, *Journal of Structural Geology*, **25**, 59–78.

[5] J. Sulem, I. Vardoulakis, H. Ouffroukh, M. Boulon, J. Hans (2004): Experimental characterization of the thermo-poro-mechanical properties of the Aegion Fault gouge, *C. R. Geosci.*, **336**, 455–466.

[6] H. Noda and T. Shimamoto (2005): Thermal pressurization and slip-weakening distance of a fault: An example of the Hanaore fault, southwest Japan, *Bulletin of the Seismological Society of America*, **95**, 1224–1233.

[7] J. R. Rice, J. W. Rudnicki (2005): Unpublished work.

[8] J. R. Rice, J. W. Rudnicki, V. C. Tsai (2005): Shear localization in fluid-saturated fault gouge by instability of spatially uniform, adiabatic undrained shear, Abstract, *EOS, Trans. American Geophysical Union*, Fall Meeting Supplement.

[9] J. W. Rudnicki, J. R. Rice (2006): Effective normal stress alteration due to pore pressure changes induced by dynamic slip propagation on a plane between dissimilar materials, *Journal of Geophysical Research*, **111**, B10308,, doi:10.1029/2006JB004396.

[10] J. R. Rice, C. G. Sammis, R. Parsons (2005): Off-fault secondary failure induced by a dynamic slip-pulse, *Bulletin of the Seismological Society of America*, **95**, 109–134, doi10.1785/0120030166.

Microstrains, Macrostresses and the Role of Subsurface Fields in the Identification of Constitutive Laws

A. Roos[1*], E. Héripré[3], J. Crépin[2], J.-L. Chaboche[1]

[1]ONERA DMSE/LCME
29, avenue de la Division Leclerc, BP72, 92322 Châtillon CEDEX
arjen.roos@onera.fr, jean-louis.chaboche@onera.fr

[2]Laboratoire de Mécanique des Solides (LMS), Ecole Polytechnique
CNRS UMR 7649, 91128 Palaiseau CEDEX
crepin@lms.polytechnique.fr

[3]Centre des Matériaux, Ecole Nationale Supérieure des Mines de Paris
CNRS UMR 7633, BP87, 91003 Evry CEDEX
eva.heripre@mat.ensmp.fr

Summary: This paper presents a methodology for identifying the parameters of a constitutive law. Conventionally, identifications are based on macroscopic data only. However, this does not yield any information on the correctness of the microscopic fields, which control (for instance) crack initiation and propagation. It is for this reason that a coupled approach is proposed between macroscopic and microscopic measurements on the one hand, and finite element simulations on the other hand. The paper focuses on one particular aspect, which is the influence of the subsurfacic fields on the final parameter values.

Introduction

Local strain incompatabilities and stress concentrations can cause industrial structures to fracture prematurely. In some materials, these local fluctuations are very sensitive to small variations in microstructure. Up until very recently, they were not at all taken into account in the identification of constitutive laws (which are then used in life-time analyses).

This present paper elaborates and validates a methodology that fills this gap. It was originally motivated by the low ductility at room temperature of Titanium Aluminides, which is the major factor blocking their widespread use in aerospace industry, but in itself the methodology is completely general and can be applied to many materials.

Methodology

The coupled approach consists of a dialogue between experiments and numerical simulations, both at the macroscopic and at the microstructural length scale. The main idea is to measure the microscopic strain fields and the macroscopic stress-strain curve simultaneously, at several instants during the experiment, and then to carry out a simulation on the same microstructure with the same loading history. By comparing both macroscopic and microscopic results with their experimental counterparts, the parameters of the constitutive law can be adjusted in order to minimise the difference.

The experimental part is illustrated in Fig. 1 for a uniaxial compression test on a Ti-48Al-2Cr-2Nb microstructure, provided by ONERA DMMP. It shows the different steps of marker deposition (a), needed for superposition of the microscopic strain field with the morphology (and grain orientations) as determined by EBSD (b), the deposition of the microgrid, here with a step size of the order of a micrometer (c), which is used to measure the microscopic in-plane displacement field, and by derivation, the microscopic strain fields (d). Full details of the methodology can be found in [1, 2, 3]. Here it is only noted that the finite element mesh is based directly on the EBSD image (with the associated grain orientations), and that simulations use the *experimentally determined* displacement history as boundary conditions at the mesh edges.

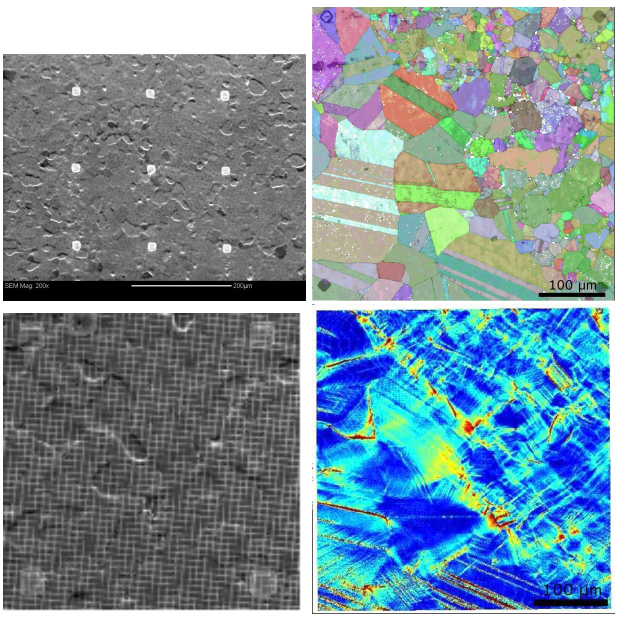

Figure 1: Experimental procedure. Top left (a): markers. Top right (b): EBSD analysis. Bottom left (c): microgrid. Bottom right (d): measured strain field (analysis with CorrelManuV).

Virtual experiments

The main drawback of the coupled approach is that it attempts to determine properties of the bulk material by using volume averaged information at the macroscale (the stress-strain curve), but only surface fields at the microscale. The question remains whether not knowing the exact grain morphology below the surface leads to significantly different parameters in the constitutive law. On the one hand, having different subsurface morphologies affects the surfacic fields [5]. On the other hand, the finite element simulations use the experimentally determined boundary displacements, and they already integrate the actual subsurface morphology, as well as the influence of the neighbouring grains. It may very well be that this is sufficient to yield robust parameters for the constitutive law.

In order to address this question, several virtual (numerical) experiments have been carried out. The idea is to construct a representative virtual volume of the sample, of which the three-dimensional grain morphology is known completely (Fig. 2). This grain morphology is generated by using a technique similar to [4]. One can now carry out the virtual test, for instance a uniaxial tension test, in which the parameters of the constitutive law are given certain reasonable values. This test gives a macroscopic (i.e. volume average) stress-strain curve, and a surface strain field. From now on, these results are considered as the reference results, i.e. they can be considered as the equivalent of a real, non-virtual experiment.

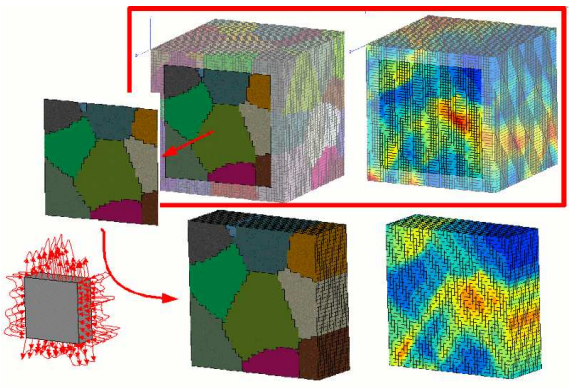

Figure 2: The virtual experiment. Top: representative virtual reference volume with (bottom) cut-out.

The methodology, as presented previously, can now be applied to a surface area which is cut out of this virtual specimen (Bottom Fig. 2). Instead of the field as measured by the microgrid, here the surface strain field of the virtual reference field is used. Obviously, the selected surface area should be sufficiently far away from the edges of the representative virtual volume. The methodology is then applied as follows:

1. The selected surface area is cut out from the virtual volume, with its associated strain field, and the displacements of its edges.
2. Another subsurface grain morphology is generated *with the same surface morphology*. This can be a simple extrusion in the thickness direction, or by the same procedure as before. In the latter case, the statistical properties of the surface area should be conserved in the volume.
3. The edge displacements, as measured on the selected surface area, are now applied as boundary conditions to this freshly generated volume. Care has to be taken in how the time evolution of these displacements is taken into account, because these are not always known experimentally [3].
4. The parameters of the constitutive law, that were fixed up until now, are reinitialised to random values, and re-optimised in the same manner as they would in a real experiment (as described in the introduction).
5. The optimised values of the parameters of the constitutive law can now be compared to their corresponding values in the virtual reference test. The advantage of having a virtual reference test is that these values are known exactly, which is not the case in the real experiment.

By repeating this procedure several times with different subsurface grain morphologies, some quantitative insight can be gained into how much this affects the final parameter values.

The first calculations have been carried out on a virtual representative volume element of about 30 grains (the one in Fig. 2), and compared to calculations on an extruded subsurface morphology. They show that with the extruded morphology, the initial critical shear stresses can be identified unambiguously. For other parameters, this is less clear, for instance the ones associated with the hardening. However, in the latter case this can be explained by the fact that for the purpose of testing the method, the calculations are not carried far beyond the initial macroscopic yield limit. These matters are currently under investigation.

References

[1] A. Allais, M. Bornert, T. Bretheau, D. Caldemaison (1994): Experimental characterization of the local strain field in a heterogeneous elastoplastic material. *Acta Metal. et Mater.*, **42**, 3865–3880.

[2] T. Hoc, J. Crépin, L. Gélébart, A. Zaoui (2004): A procedure for identifying the plastic behavior of single crystals from the local response of polycrystals. *Acta Mater.* **51**, 5477–5488.

[3] E. Héripré, M. Dexet, J. Crépin, L. Gélébart, A. Roos, M. Bornert, D. Caldemaison (2007): Coupling between experimental measurements and polycrystal finite element calculations for micromechanical study of metallic materials. *Int. J. Plasticity* (in press).

[4] D.M. Saylor, J. Fridy, B.S. El-Dasher, K.Y. Jung, A.D. Rollett (2004): Statistically representative three-dimensional microstructures based on orthogonal observation sections. *Met. Mat. Trans.*, **35A**, 1969-1979.

[5] A. Zeghadi (2005): Effet de la morphologie tridimensionnelle et de la taille de grain sur le comportement mécanique d'agrégats polycristallins. *Ph. D. Thesis*, Ecole des Mines de Paris.

On Dispersion and Band Gaps in Heterogeneous Media

E. Rohan[1*], **F. Seifrt**[1], **B. Miara**[2]

[1]Dept. of Mechanics, University of West Bohemia, Pilsen
Univerzitní 22, 306 14 Plzeň, Czech Republic
rohan@kme.zcu.cz, seifrt@kme.zcu.cz

[2]Laboratoire de Modélisation et Simulation Numérique
ESIEE 2, boulevard Blaise Pascal, 93160 Noisy-le-Grand, France
miarab@esiee.fr

Summary: Dispersion and existence of the band gaps belong to well known features of periodically arranged structures with finite scale of the heterogeneities. Assuming long waves propagation, these phenomena can be studied using the limit homogenized model of elastic, or piezo-elastic composites. For this a strong heterogeneity in the elastic coefficients is considered. To justify such artificial modelling assumption, we discuss a numerical convergence of the scale-dependent solution to the limit one. The influence of the microstructural topology and geometry on the homogenization result is discussed; in particular, two cases are considered: soft inclusions in stiff matrix and rigid inclusions in compliant matrix. The sensitivity analysis of the band gap distribution w.r.t. shape of the inclusions is presented, numerical examples are included.

Motivation – phononic crystals

Modelling of acoustic wave propagation in heterogeneous media gains growing interest as an attractive problem from both theoretical and practical points of view due to numerous applications in designing devices related to sound propagation. The *phononic crystals* – bi-phasic elastic media with periodic structure and with large contrasts in elasticity of the phases – are called often the *phononic band-gap materials* due to their essential property to suppress propagation of elastic waves in certain frequency ranges, as confirmed by measured transmission. Similar phenomena in the propagation of the electromagnetic field were studied even before in the context of the *photonic crystals*.

For elastic composites an existence of band gaps for certain wavelengths was shown in [2,3] as the consequence of the non positivity of the limit "homogenized mass density"; the same approach based on the two-scale homogenization was pursued in the problem of acoustic wave propagation in a *piezoelectric strongly heterogeneous composite*, [4].

Strongly heterogeneous microstructure

The periodic structure of the heterogeneous medium is generated by the reference periodic cell (RPC) $Y =]0,1[^3$ with inclusion $\overline{Y_2} \subset Y$, whereby the matrix part is $Y_1 = Y \setminus \overline{Y_2}$. According to the RPC decomposition, the composite occupying domain Ω is constituted by *matrix* Ω_1^ε perforated by disconnected *inclusions* Ω_2^ε, $\Omega_1^\varepsilon = \Omega \setminus \Omega_2^\varepsilon$, where ε is the usual scale parameter. While the material density ρ^ε is comparable in both the compartments, as an important feature of the modelling, all other constitutive parameters (elasticity c_{ijkl}^ε, dielectricity d_{kl}^ε and piezoelectric coupling g_{kij}^ε) are related to the geometrical scale of the underlying microstructure by coefficient ε^2, which represents the *strong heterogeneity*:

$$\rho^\varepsilon(x) = \begin{cases} \rho^1 & \text{in } \Omega_1^\varepsilon, \\ \rho^2 & \text{in } \Omega_2^\varepsilon, \end{cases} \tag{1}$$

however,

$$c_{ijkl}^\varepsilon(x) = \begin{cases} c_{ijkl}^1 & \text{in } \Omega_1^\varepsilon, \\ \varepsilon^2 c_{ijkl}^2 & \text{in } \Omega_2^\varepsilon, \end{cases} \tag{2}$$

$$g_{kij}^\varepsilon(x) = \begin{cases} g_{kij}^1 & \text{in } \Omega_1^\varepsilon, \\ \varepsilon^2 g_{kij}^2 & \text{in } \Omega_2^\varepsilon, \end{cases} \tag{3}$$

$$d_{ij}^\varepsilon(x) = \begin{cases} d_{ij}^1 & \text{in } \Omega_1^\varepsilon, \\ \varepsilon^2 d_{ij}^2 & \text{in } \Omega_2^\varepsilon. \end{cases} \tag{4}$$

Limit homogenized model

Propagation of incident waves with single frequency ω was treated by the two-scale homogenization in [3]. The limit model involves the homogenized stiffness tensor C_{ijkl} corresponding to the perforated medium with elasticity c_{ijkl}^1 (no influence of the material in Y_2) and the *homogenized mass tensor* M_{ij} which depends on frequency ω:

$$M_{ij}(\omega^2) = \frac{1}{|Y|}\int_Y \rho\delta_{ij} - \frac{1}{|Y|}\sum_{r\geq 1}\frac{\omega^2}{\omega^2-\lambda^r} m_i^r m_j^r \,, \tag{5}$$

where λ^r and $\boldsymbol{m}^r$ are the r-th eigenvalues and the r-th *eigenmomentum*, respectively, obtained by solving the eigenvalue problem in Y_2 with clamped boundary, c_{ijkl}^2 and ρ^2 define the material; the eigenmomentum is the integral over Y_2 of the eigenfunction.

If the piezoelectric material is considered, the homogenized dielectricity and piezo-coupling depend exclusively on the perforated matrix properties, as in the case of elasticity C_{ijkl}. The homogenized mass tensor is computed according to [5], however, the associated eigenvalue problem reflects the *piezoelectric coupling phenomenon*, involving eigenfunctions for the displacement and the electric potential.

Dispersion and band gaps

The dispersion properties depend on mass $M_{ij}(\omega^2)$. The band gaps are identified by analyzing the eigenvalues of $M_{ij}(\omega^2)$ for

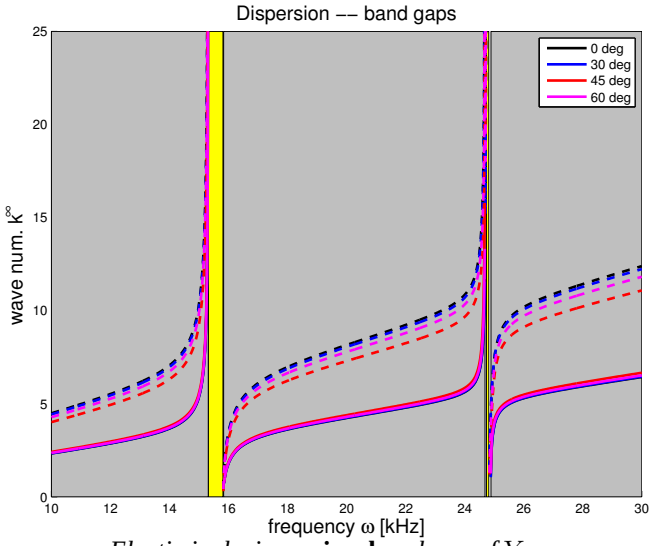

Elastic inclusions, **circular** *shape of* Y_2.

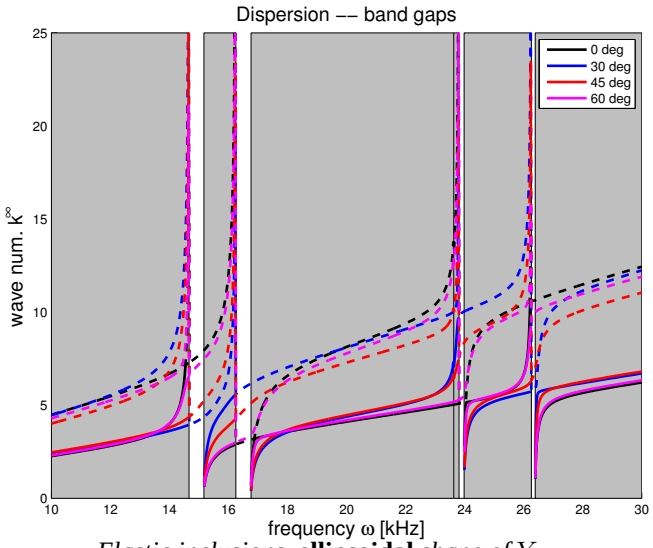

Elastic inclusions, **ellipsoidal** *shape of* Y_2.

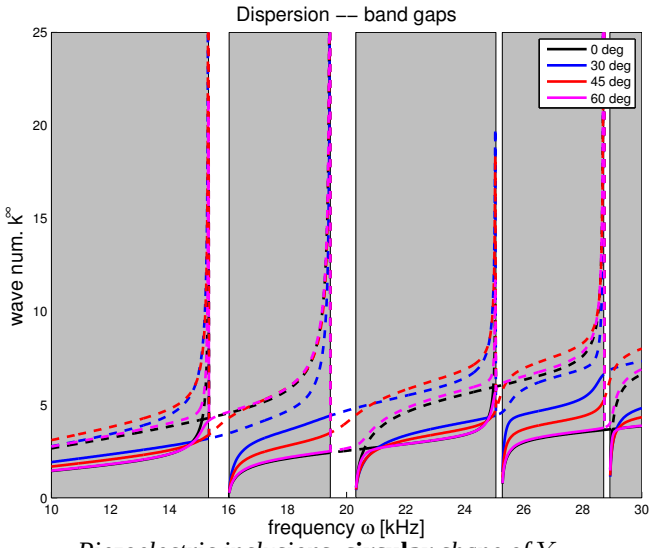

Piezoelectric inclusions, **circular** *shape of* Y_2.

Figure 1: Dispersion curves of guided long waves in 2D structures computed for different directions of propagation. The wave number is relevant to the homogenized model. Band gaps indicated by yellow (full stop gaps), or white (weak gaps).

a given ω, see Fig.2; if all these eigenvalues are negative, then ω falls into the full stop gap (no waves can propagate on this frequency), if some of them are positive (the weak band gap), then waves of this frequency can propagate in a specific direction (a manifold exists). The stability of the weak band gaps w.r.t. wave polarization depends on symmetry of the inclusions (geometrical features). In general, the distribution of the band gaps in the frequency spectrum is sensitive to the shape of the inclusions. This motivated development of the *shape sensitivity analysis* of the band gap width. Some preliminary studies of the composite *microstructure optimization* were performed, where the objective criterion was expressed in terms of the gap bounds.

Rigid inclusions in compliant elastic matrix

In this case the elastic coefficients in inclusions are $\approx 1/\varepsilon^2$ and high frequencies are assumed, so that $\omega^\varepsilon \approx 1/\varepsilon$. This leads to localized macroscopic behaviour with *vanishing* macroscopic elasticity; the homogenized mass tensor defined by an expression similar to [5], however the associated eigenvalue problem defined in Y_1 is characterized by periodic boundary conditions on ∂Y with displacement on ∂Y_2 restricted to the rigid body rotations of Y_2 about its barycenter.

Limit model vs. finite scale $\varepsilon > 0$

The aim of this study is to validate the modelling of standard heterogeneous materials (e.g. Epoxy resin and Duralumin) using the reported strong heterogeneity approach. Therefore, we consider a sequence of ε dependent models and analyze the wave propagation for structures with finite scale of inclusions and magnitudes of heterogeneities. For some one-dimensional structures it can be shown that the ε^2 "artificial scaling" allows to estimate the distribution of the band gaps for $\varepsilon > 0$ using the limit model (i.e. $\varepsilon \to 0$) with less computational effort.

Acknowledgment: The research is supported by the project GACR 101/07/1471 of Grant Agency of the Czech Republic.

References

[1] J. L. Auriault and G. Bonnet (1985): Dynamique des composites elastiques periodiques, *Arch. Mech.*, **37**, 269–284.

[2] A. Ávila, G. Griso, B. Miara (2005): Bandes phononiques interdites en élasticité linéarisée, *C. R. Acad. Sci. Paris*, Ser. I 340, 933-938.

[3] A. Ávila, G. Griso, B. Miara, E. Rohan (2006): *Multi-scale modelling of elastic waves, Theoretical justification and numerical simulation of band gaps*. Multiscale Modeling & Simulation", SIAM journal, submitted.

[4] E. Rohan, B. Miara (2006): Sensitivity analysis of acoustic wave propagation in strongly heterogeneous piezoelectric composite. To appear in *Topics on Mathematics for Smart Systems*, World Sci. Publ.

Continuum Models for Heterogeneous Solids under Dynamic Loading

C. T. Sun[1*], **G. L. Huang**[2]

[1]Purdue University
West Lafayette, Indiana, USA
sun@purdue.edu

[2]University of Arkansas at Little Rock
Little Rock, Arkansas, USA
glhuang@ualr.edu

Summary: In this paper an approach for developing continuum models that are capable of accounting for effects of micro/nano-structures in heterogeneous materials is presented. The unique feature of the present approach is that all material constants of the continuum model are derived explicitly from the constituents of the original system. Layered media and lattice systems are used for illustration. Harmonic wave transmission/reflection at the interface between the original system and the representative continuum is used to evaluate the accuracy of the continuum model.

Introduction

The conventional approach in treating heterogeneous solids with micro/nano structures has been to replace the original solid with an equivalent continuum in which the micro/nano structure is no longer present. Such an approach yields great simplifications and has been widely adopted for modeling and analyzing heterogeneous materials such as many forms of composite materials. However, classical continuum models become inadequate in describing the response of solids with micro/nano structures when the characteristic length (or wave length) of deformation becomes comparable to or smaller than the dimensions of the representative cell of the micro/nano structure. An example is the wavelength-dependent wave velocity in composite materials. If a composite is modeled as a homogeneous elastic solid, then the bulk plane wave (longitudinal or shear) would propagate at a constant speed. In contrast, the exact solution based on the model that retains the identity of the microstructure (fiber, particle) indicates that the wave is dispersive meaning that the wave speed is not a constant but is affected by wavelength (or strain gradient). Another example concerning the inadequacy of the classical continuum theory is cracks in materials with micro/nano structures. It is well known that, in a classical elastic solid, the stress and strain fields exhibit an inverse square root singularity near the crack tip. That is, the strain gradient near the crack is exceedingly large, making the representation of the solid with micro/nano structures by a homogeneous solid inadequate.

The main reason for the aforementioned deficiency of the classical continuum model can be attributed to its inability to account for the local motion of the micro/nano structure. A common way to solve this problem is to employ additional kinematic variables to describe the non-homogeneous local deformation in the microstructure of the solid. This approach leads to Cosserat continuum models [1]. There are variations among these models which are often referred to as microstructure, micropolar, or micromorphic models [2–6]. Some authors have even attempted to use these extended continuum models to bridge continuum theory and molecular dynamics down to the atomic scale [7]. Common to all the above models is that, in addition to the usual translational displacement vector to describe the average displacement, additional deformation kinematic variables or even multiple displacement vectors are introduced to describe the nonhomogeneous local deformation.

Among the existing Cosserat continuum type models, most of them only present a general form of the governing equations; extensive experiments are required to determine numerous material constants associated with the models. On the other hand the micro/nano-structure continuum models developed by the present autor and co-authors [5–10] are based on the unit cell of the original material and all the material constants of the continuum models can be derived analytically from the micro/nano structure. The governing equations are directly derived from the geometry and the mechanical properties of the micro or nano structure in the unit cell.

In this presentation, the general procedure for developing continuum models with microstructural effects for heterogeneous materials is reviewed. It is shown that different degrees of microdeformation can be described depending on the number of kinematic variables introduced. The lowest order of the continuum model developed in this manner only accounts for the microinertia effect and the governing equations resemble those of the classical continuum mechanics.

Continuum model with micro-inertia

As an example, the continuum model with micro-inertia is briefly reviewed. The macro-strain and stress are defined as the volume averages of the strain and stress in the representative volume element (RVE). The macro equation of motion is derived by Hamilton variational principle in which the strain energy density and kinetic energy density involve the micro-inertia terms. The macro equations of motion have the following form

$$\frac{\partial \Sigma_{ij}}{\partial X_j} + F_i = \bar{\rho}\ddot{U}_i \tag{1}$$

where Σ_{ij} is the macro stress, X_j is the macro coordinate, $\bar{\rho}$ is the average density, U_i is the macro displacement, and F_i is an effective body force that represents micro inertia. Without

considering the micro-inertia, this model appears to be the same as the classical continuum model except that the stresses and strains must be properly interpreted as the macromechanical quantities. The effective body force is determined by assuming an approximate local displacement field in the RVE and usually can be explicitly expressed in a rather simple form.

The effectiveness of the micro-inertia model to represent a heterogeneous system can be evaluated by studying transmission of harmonic waves through the heterogeneous system/micro-inertia continuum system interface. If there is little wave reflection, then the representation is good. If the micro inertia term F_i in Eq. (1) is set equal to zero then the micro-inertia model reduces to a classical elastic solid or the so-called effective modulus theory.

Wave transmission/reflection in layered media

Wave reflection and transmission are considered for layered media connected to a homogeneous continuum with micro-inertia as shown in Fig. 1. The micro-inertia continuum model developed by Wang and Sun [8] is adopted here. The thicknesses for layer 1 and layer 2 are denoted as L_1 and L_2, respectively, and the total length for each cell is $L = L_1 + L_2$. In the study, layer 1 is assumed to be connected to the homogeneous medium.

We consider the system of a layered medium connected to the micro-inertia continuum that represents the layered medium. The numerical results are shown in Fig. 2 for

$L_1/L_2 = 4, \mu_1/\mu_2 = 10, \rho_1/\rho_2 = 3, v_1 = 0.3$ and $v_2 = 0.35$

For comparison, the result obtained by dropping the micro-inertia (i.e., the effective modulus theory) is also presented in the figure. It is easy to see that the micro-inertia model allows almost perfect transmission of waves across the interface for wave lengths up to six times the size of the unit cell. This implies that, in this range of wave length, the micro-inertia model can accurately describe the dynamic characteristics of the layered medium.

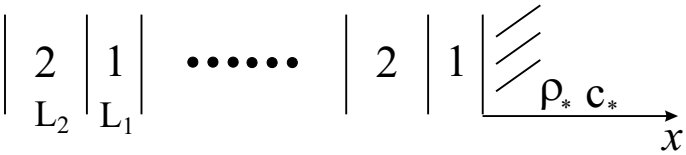

Figure 1: A layered medium connected to a representative homogeneous elastic medium.

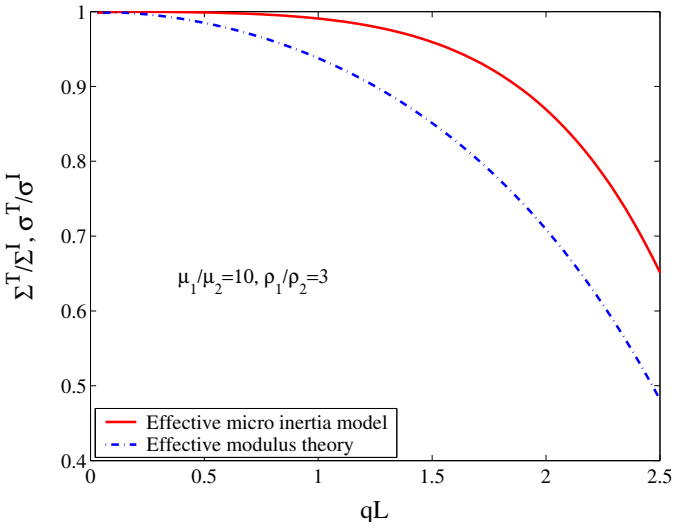

Figure 2: Effectiveness of wave transmission from a layered medium to a representative continuum system.The vertical axis is the ratio between the transmitted stress and the incident stress.

References

[1] E. Cosserat, F. Cosserat (1909): *Theorie des corps deformables.* A. Hermann Fils, Paris.

[2] R. A. Toupin (1962): Elastic materials with couple-stresses. *Archive Rational Mechanics and Analysis*, **11**, 385–414.

[3] R. D. Mindlin (1964): Micro-structure in linear elasticity. *Archive for Rational Mechanics and Analysis*, **16**, 51–78.

[4] A. C. Eringen and E. S. Suhubi (1964): Nonlinear theory of micro-elastic solids, II. *Int. J. Engng. Sci.*, **2**, 189–203.

[5] C. T. Sun, J. D. Achenbach, and G. Herrmann (1968): Continuum theory for a laminated medium. *J. Appl. Mech.*, **35**, 467–475.

[6] J. D. Achenbach, C. T. Sun and G. Herrmann (1968): On the vibrations of a laminated body. *J. Appl.Mech.*, **35**, 689–696.

[7] Y.-P. Chen and J. D. Lee (2003): Connecting molecular dynamics to micromorphic theory (I). Instantaneous and averaged mechanical variables. *Physics A*, **322**, 359–376.

[8] Z.-P. Wang, C. T. Sun (2002): Modeling micro-inertia in heterogeneous materials under dynamic loading. *Wave Motion*, **36**, 473–485.

[9] C. T. Sun, G. L. Huang (in press): Modeling heterogeneous media with microstructures of different scales. *J. Appl. Mechanics.*

[10] G. L. Huang, C. T. Sun (2006): A continuum model with microstructures for wave propagation in ultra thin films. *Int. J. Solids and Structures*, **43**, 7014–7027.

Formation of Dynamic Defect Structures in Metals at Extreme Loading Rates

A. Zubelewicz*, A. K. Zurek

Los Alamos National Laboratory
Los Alamos, NM 87545, USA
alek@lanl.gov, zurek@lanl.gov

Summary: Traditional thermodynamics tells us that all closed systems exhibit a tendency to maximize entropy. So it is a struggle to understand why so many systems are able to survive with their organizational and functional integrity intact. Progogine [1] concluded that the secret to survivability is in an exchange of energy. A stable complex system receives low-entropy energy from the environment while giving away energy that is entropy rich. A sustained exchange of the energies is in fact the condition for survivability. Since these phenomena are rarely observed in solids, mean-field theories of nonlinear continuum dynamics often provide sufficient representation of the solid behavior. These theories describe the deformation and damage processes with the use of constitutive models. Difficulties arise when a metal is subjected to extreme loading rates and becomes a thermodynamically open system characterized by an exchange of energy caused by dislocations travelling long distances with a nearly sonic velocity.

Formation of dynamic defect structures (DDS)

In standard continuum mechanics approach, there are total of 16 variables (six components of stress, six components of strain, three displacements, and mass density). There are also 16 governing equations (three equations of motion, six equations of kinematical compatibility, six constitutive relations, and mass conservation relation). Furthermore, it is assumed that any subvolume of a material can be isolated from its surroundings by imposing proper (static and kinematic) boundary conditions. Since the subvolume can be reduced to a material point, this suggests that all internal variables such as stress, strain, displacement, and/or energy are defined in a "local" manner. In what follows, we question validity of the assumption.

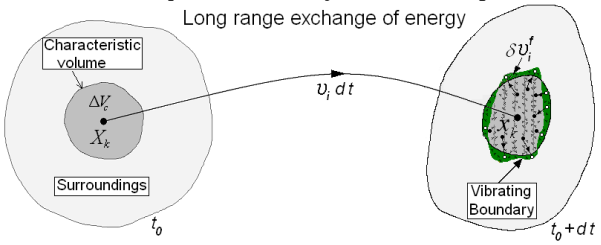

Figure 1: Exchange of energy in metals at extreme loading rates.

As shown in Fig. 1, a material point,$\{X_k\}$, and its well-defined surroundings (known volume, ΔV_c, and its enclosure,∂V_c) are placed in space at the initial time, t_0. Under deformation, both the point and the adjacent material move into a new location$\{x_k\}$ such that the total displacement is equal to $u_k = x_k - X_k$. The surroundings of $\{x_k\}$ and $\{X_k\}$ do not have the same constituents [3] because defects migrate into and out of ΔV_c. For instance, dislocations travelling through the material establish a higher-order cross interaction between distant material points. We may not be able to track the movement of each dislocation, but we can estimate an average frequency of these events as $t_d^{-1} = (2v_d/l_n)$.The term $2v_d/l_n$ represents the know dislocation frequency at the nanoscale of the material. The dislocations are moving with an average velocity v_d transporting energy and, in this manner, make the material a thermodynamically open system. Eventually, the mobile dislocations come to rest and form structures that consist of coarse slip bands, dislocation cell walls, etc. There is a continuous

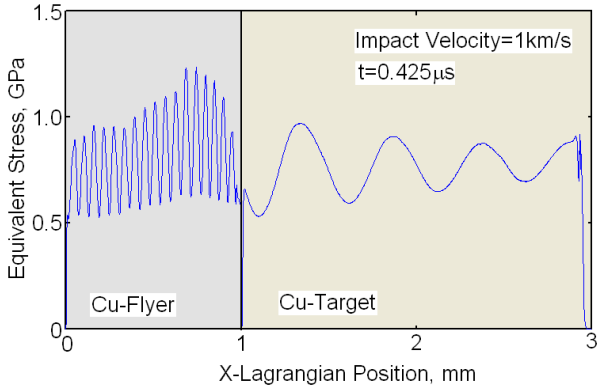

Figure 2: Fluctuating equivalent stress versus Lagrangian position in Cu-Cu impact problem, (impact velocity 1 km/s).

competition between the storage, annihilation, and nucleation of dislocations. In our dynamic defect structure (DDS) theory [2, 3], we recognize the fact that the mobile dislocations exchange energy between distant material points within a characteristic volume$\Delta V_c$and with its surroundings, Fig. 1. These events cause kinematical incompatibility. Under compressive loading conditions, the compatibility is restored at a macroscopic scale and that leads to the formation of energetically strong but not quite stable dislocation structures. At low deformation rates and high temperatures, dislocation travel slowly and short distances, and the material has enough time and ability to adapt itself to the changing environment. However, a material subjected to extreme conditions has no opportunity for such a gentle readjustment. In these circumstances an abrupt restructuring of the defect structures is the only option available. We characterize the rate of the incompatibility and call it an additional material variable. The rate of the incompatibility, $\dot{\psi}_{inc}$, vanishes when the plastic strain rate is homogenized within the characteristic volume, ΔV_c. Similarly as in [4], the plastic strain rate is expanded using Taylor series and truncated after the third term. In this manner, we find an approximate differential form of the macro-homogenization criterion.

The DDS theory predicts that various metals (alloys) subjected to extreme loading rates experience a strong mesoscale excitation leading to an entrapment of kinetic energy. While a significant portion of the energy is converted into heat, the remaining part supports a rearrangement of the material's internal struc-

ture and causes fluctuations in the field of velocity, strains, and stresses. The DDS theory explains the remarkable increase in the plastic hardening rate [3] observed in all metals tested at strain rates greater than 10^3 s^{-1}. In 1-D numerical simulations, we are able to reproduce conditions, at which two copper plates impacted with each other at the velocity of 1km/s, experience a noticeable excitation, Fig. 2.

Void nucleation as an alternative mechanism to DDS formation

Our objective is to identify a dilatational deformation in ductile metals, which may impede the formation of the DDS structures. A constitutive equation for ductile material is assumed to obey a power-law relation

$$\dot{e}^p_{eq} = \Lambda\, \sigma^3_{eq}, \tag{1}$$

where Λ is a constant and the equivalent plastic strain rate $\dot{e}^p_{eq}$is coupled with the equivalent stress σ_{eq}. Components of the plastic strain rates are defined through the use of a symmetric micro-mechanism tensor$N_{ij} = n_i s_j + s_i n_j$, in which unit vectors (n_i, s_i) represent the normal and slip directions. In this analysis we expressed N_{ij} in terms of stresses, that is $N^*_{ij} = N_{ij}\,(\sigma_{kl})$, such that the new tensor satisfies all the invariants of the original tensorN_{ij}. Following the derivations in [5], we find that the new tensor is

$$N^*_{ij} = \frac{2\sin\varphi/3}{\sqrt{3}\,\cos\varphi}\left(\delta_{ij} - \frac{3}{2J_2}S_{ik}S_{kj}\right) + \frac{\cos 2\varphi/3}{\sqrt{J_2}\,\cos\varphi}S_{ij} \tag{2}$$

where $S_{ij} = \sigma_{ij} - \delta_{ij}\,\sigma_{kk}/3$, $J_2 = \frac{1}{2}S_{ij}S_{ij}$, $J_3 = S_{ik}S_{kl}S_{li}/3$, and $\varphi = \sin^{-1}\left[3J_3\sqrt{3/J_2^3}/2\right]$. Components of the plastic strain rate are

$$\dot{\varepsilon}^p_{ij} = \frac{1}{2}N^*_{ij}e^p_{eq} \tag{3}$$

and the equivalent stress, defined as $\sigma_{eq} = \frac{1}{2}N^*_{ij}\sigma_{ij}$, is the Tresca stress. The material's dilatancy is allowed to exist. However, instead of imposing a predetermined relation for void nucleation a different approach is pursued here. We assume [6] that the rate of void nucleation and growth together with the rate of energy dissipation due to the volumetric change and shear are nonnegative quantities at any point of the material. The missing constitutive equation for void nucleation is replaced by a criterion of minimum rate of energy dissipation. In this manner, the volumetric deformation brings the material as close to its thermodynamic equilibrium as possible. As shown in Fig. 3, three distinct mechanisms of void nucleation and growth are possible near in a ductile surroundings of the mode I crack tip. In this plot, values of the minimum energy triaxiality ratio χ are defined as

$$\chi = \int_{\Delta V_c} \sigma_{kk}\dot{\varepsilon}^p_{kk}dV \;/\; \int_{\Delta V_c} \sigma_{eq}\dot{e}^p_{eq}dV, \tag{4}$$

where σ_{kk} is the hydrostatic stress, $\dot{\varepsilon}^p_{kk}$is the rate of void nucleation and growth and $\dot{e}^p_{eq}$is the maximum shear strain rate. The energy ratio χ (vertical axis) is plotted as a function of the stress singularity factor λ(horizontal axis); where the stresses near the crack $\sigma_{ij} = R^\lambda\,\sigma^\theta_{ij}(\theta)$ are defined in the polar coordinate system $\{R, \theta\}$ attached to the crack tip. A change in the stress singularity factor λ indicates the extent of damage done to the material. The first mechanism (red line) describes the well-known Gurson's (stress triaxiality,σ_{kk}/σ_{eq}) criterion, where voids are uniformly distributed near the crack tip. At more advanced stage of deformation (brown line) voids nucleate predominantly along a narrow process zone extending ahead of the crack. This mechanism is governed by the maximum tensile stress. There is also a third dilatational mechanism (blue line), in which voids are distributed along two branches at 50 degrees with respect to the crack direction.

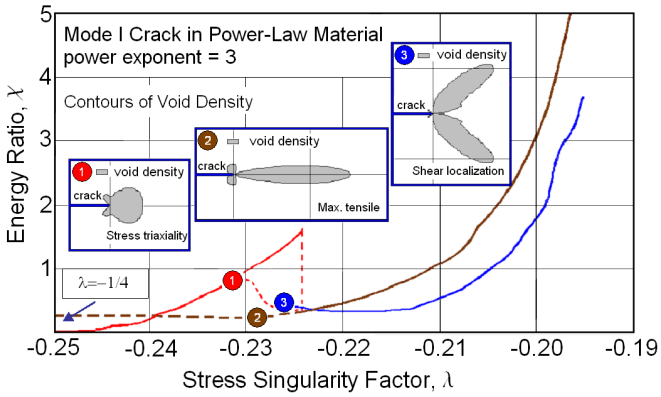

Figure 3: Three dilatational deformation mechanisms in ductile surroundings of mode I crack tip. Plot presented in terms of the ratio of the rates of energy dissipation due to cavitation and slip versus the stress singularity factor.

Summary and findings

1. Metals subjected to extreme loading rates exhibit behavior that is characteristic of a thermodynamically open system. The phenomenon is linked to the motion of mobile dislocations, which exchange energy between distant material points.
2. We accept the fact that the mesoscale plastic strain does not satisfy the conditions of kinematical compatibility. Consequently, the kinematical incompatibility,ψ_{inc}, becomes the 16-th variable added to the stresses, strains, and displacements. The incompatibility triggers strong perturbations in displacements, strains, stresses, and energy.

It is possible to recover kinematical compatibility at the length scale at which the incompatibility occurs. The above analysis suggests that void nucleation is such a mechanism. Often the dilatational deformation is not a thermodynamically favorable mechanism. Then, the formation of orderly dislocation structures is the only mechanism available.

References

[1] I. Progogine (1977): Time, Structure, and Fluctuations. *Nobel Lecture*. Nobel Prize in Chemistry, Royal Academy of Sweden.

[2] A. Zubelewicz, P. J. Maudlin, G. T. Gray III, and A. K. Zurek (2005):, *Phys. Rev. B* **71**, 104107.

[3] A. Zubelewicz (2007): *Mechanics of Materials*, accepted.

[4] Z.P. Bažant and A. Zubelewicz (1988): *Int. J. Solids Structures*, **24**, 659.

[5] A. Zubelewicz (1993): *J. Mech. Phys. Solids* **41**, 1711.

[6] A. Zubelewicz (2005): *Int. J. Solids Struct.* **42**, 2755.

Static Analysis of Soil Reinforcement

D. Kolymbas

University Innsbruck, Institute of Infrastructure, Unit of Geotechnical and Tunnel Engineering
Technikerstr. 13, A 6020 Innsbruck,
dimitrios.kolymbas@uibk.ac.at

Summary: Static analysis of reinforced soil constructions is usually based on failure mechanisms consisting of rigid blocks. The applicability of this approach is questionable, since it does not take into account deformations apt to mobilize the pull-out resistance of nails. In this paper an alternative approach is presented which is based on homogenisation and consideration of reinforced soil as a two-phase material.

Introduction

In this paper we call "reinforcement" any stiff inlet placed into soil, be it steel nail or geotextile. It is generally expected that such inlets increase the stiffness and strength of soil. However, their action is not yet completely understood. Collapses of nailed walls could indicate that nailing does little or nothing to stabilize slopes. Admittedly, small scale model test showed that nailing stabilizes slopes in cohesionless soil [2], but these results cannot be directly assigned to full scale situations. On the other hand, the stability of many nailed slopes could, perhaps, be attributed to the fact that, in reality, cohesion of undisturbed soil is often larger than assumed. In reinforced concrete the situation is simpler because there is a clear sharing of tasks: concrete sustains compression and reinforcement sustains extension forces. In contrast, in soil there are no considerable tensile stresses, the bearing performance is mainly achieved by shear stresses. What is then the role of reinforcement in soil? The existing design rules for nailed soil slopes are based on the consideration of rigid block collapse mechanisms such as slip circles. The underlying idea is that the appearance of shear bands, i.e. strain localization, characterizes limit states of soil structures and limit analysis has ever been the backbone of static proofs in civil engineering. However, the considered rigid block collapse mechanisms do not take into account the fact that the reinforcement needs an appropriate deformation to mobilize tensile forces. This has been taken into account in the case of steel fibre reinforced shotcrete, where tensile forces in the steel fibres are only mobilized when cracks appear in the shotcrete. Cracked shotcrete is generally considered as an acceptable service state, if there are still some bearing capacity reserves. This is, however, not the case in geotechnical engineering, where strain localisation means that the structure is already beyond the state of serviceability. Thus, nails expected to improve soil

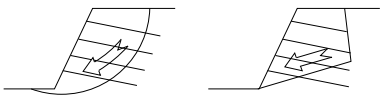

Figure 1: Failure mechanisms for design of nailed cuts.

strength should become active *before* tha appearance of localisation. Existing design rules are based on the concept that the reinforcement is loaded according to some rigid block collapse mechanisms, i.e. after the appearance of localization (Fig. 1). The related shear bands are more or less perpendicular to the reinforcement, which implies that the latter is loaded only by transverse forces but *not* by tensile loads. Despite this, the reinforcement is considered to resist pull-out. This contradiction is recognised by the design rules, see e.g. CLOUTERRE [1] stating that *"At this stage calculations can also be made based on pure tensions, i.e., by assuming that, whatever the angle of incidence on the potential failure surface, the nails are only working in tension and their bending stiffness can be neglected . . . "* This, however, remains questionable and constitutes an important assumption, as recognised by CLOUTERRE (p. 97): *"One basic assumption to any limit equilibrium method is the simultaneous mobilization of all the resistances . . . This assumption . . . is only approximated in actual conditions . . . Even though the question of the simultaneous mobilization of the various resistances has not been fully answered, it would nevertheless seem . . . further studies on failed structures clearly need to be conducted."*

Proposed method of analysis

A method to treat reinforced structures is homogenisation. This means that reinforcement is assumed as smeared, i.e. homogeneously distibuted within the body, which is considered as a two-phase material. Its points are simultaneously occupied by soil *and* reinforcement. The nails are assumed as inextensible, and it is further assumed that they render the entire structure inextensible in their direction. In other words, nails are considered as internal constraint. Such constraints are related with stresses that cannot be inferred from the constitutive relation of the matrix material, because they result from deformations that do not occur. Such stresses can be determined as follows (cf. [4]): The internal constraint is expressed by the equation $f(\mathbf{D}) = 0$ with $\mathbf{D}$ being the stretching tensor. The corresponding stress results from $\mathbf{Z} = \lambda \mathbf{n} \otimes \mathbf{n} = \lambda n_i n_j$. With the degree of reinforcement μ_s, i.e. the surface or volume fraction of the nails, the tensile stress within the nails reads: $\sigma_s = Z/\mu_s$, with $Z = |\mathbf{Z}|$. If a retaining wall reinforced with nails (Fig. 2) inclined by the angle β is loaded by the earth pressure E, then the nails receive a stress and counteract the deformation of the nailed retaining wall. ¿From Fig. 3 it can be seen that the maximum elongation of nails within a sheared soil body is obtained if the nails are inclined by the angle $\beta = 45°$. To calculate the stress in the nails we first consider the stiffness of the un-reinforced soil wall. Following an important theorem

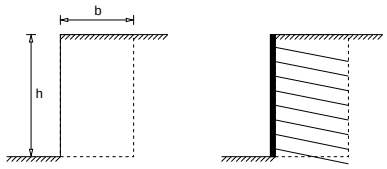

Figure 2: Reinforced retaining earth wall.

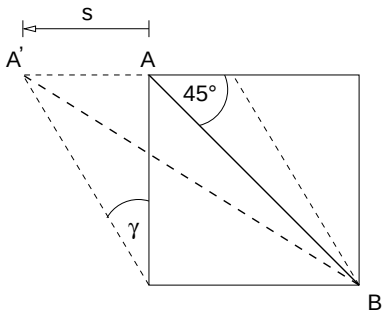

Figure 3: Elongation of a $45°$-inclined nail at shear.

from elasticity theory, according to which all static deformations (i.e. deformations that don't take place) are elastic ([4], Sect. 43), we obtain with the shear modulus G of the soil the shear stress $\sigma_s = \sqrt{2}G\gamma/\mu_s$. We obtain the necesary degree of reinforcement if we take for σ_s the allowable stress for the considered nails. The constraint of inextesibility is somehow contradictional: If soil is inextensible in the direction of the nails, then there are no relative displacements between soil and nails, thus no shear can be transmitted into the nails. To circumvent this contradiction we assume rigid-idealplastic force transmission between nail and soil. As with every homogenisation problem, the following question hast still to be answered: How fine has the distribution of nails to be in order to consider it as homogeneous? In other words, would a single thick nail be enough or should we install many thin ones? This question can be answered if we consider the shear stress acting between reinforcement and soil. Owing to the assumed rigid-idealplastic behaviour, this stress equals its maximum value, $\tau = \tau_0$. With l being the length of the nails, $A = \pi r^2$ their cross section and $U = 2\pi r$ their circumference, we have: $U\tau l/2 = \sigma_s A$. Herein, $l/2$ is the length, where the maximum shear stress prevails. Thus, we obtain the condition $r \leq l\tau/\sigma_s$ for the maximum radius of the nails. The equations stated above can be used to verify the internal stability of a retaining wall made of reinforced soil. Its bright can be obtained form the usual requirement of sufficient safety against tilting.

The model described so far assumes that force transmission occurs entirely along the nail shafts. Alternatively, we can assume endplates mounted at the outer end of the nails. Similar problems referring to rockbolting of tunnels are analysed by the author [3].

References

[1] (1993): *Recommendations* CLOUTERRE *1991*. Presses de l'ENPC, Paris.

[2] G. Gäßler (1987): Vernagelte Geländesprünge – Tragverhalten und Standsicherheit. *Veröffentlichungen des Instituts für Bodenmechanik und Felsmechanik der Universität Karlsruhe*, **108**.

[3] D. Kolymbas (2005): Tunnelling and Tunnel Mechanics. *Springer*.

[4] C. A. Truesdell, W. Noll, (1965): The Non-Linear Field Theories of Mechanics. *Encyclopedia of Physics*, Springer, Vol. IIIc.

Part II

Multiscale Modelling of Heterogeneous Materials

Multiscale Analysis of Heterogeneous Materials for Second Order Continuum

Ł. Kaczmarczyk*, C. Pearce, N. Bićanić

Department of Civil Engineering, University of Glasgow
Rankine Building, Glasgow G12 8LT, U.K.
lukasz@civil.gla.ac.uk, c.pearce@civil.gla.ac.uk

Summary: Formulation of the scale transition equations coupling the microscopic and macroscopic variables in the second order computational homogenisation of heterogeneous materials and the enforcement of generalised boundary conditions for the representative volume element are considered. Differences in response predictions between the first and the second order homogenisation are examined and a comparative study comprising benchmark problems highlights the effects of different ways of enforcing RVE boundary conditions.

Introduction

A wide range of materials produced by industry, as well natural materials, are heterogeneous at a certain scale of observation. In terms of modelling, the macroscopic (equivalent) properties of heterogeneous material are required to represent the essence of the microstructural response and they must be independent of its macrostructural loads and geometry. Furthermore, the transitions of properties and variables between the micro and macro levels must be consistent with basic principles of continuum mechanics, i.e. they are subjected to the principles of conservation of mass, momentum, energy, and second law of thermodynamics.

A comprehensive review of the overall properties of heterogeneous materials is provided in [7]. Traditionally, equivalent material properties have been obtained as a result of analytical or semi-analytical homogenization techniques. In recent years, a promising alternative approach has been developed, i.e. computational homogenization [6]. This micro-macro modelling procedure does not lead to closed-form constitutive relations but determines the stress-strain relationship at a selected macro level point to which a detailed microstructure is attributed and represented by a representative volume element (RVE) - see Figure 1. This approach does not require the constitutive response on the macro level to be known a priori and enables the incorporation of nonlinear geometric and material behaviour [1, 6]. Moreover, computational homogenization is possible for any discretization technique in space and time, although the Finite Element Method has traditionally been adopted for quasi-static problems. Kouznetsova [6] presented a second-order computational homogenization framework whereby all microstructural constituents are treated as classical continua and described by classical equilibrium and constitutive equations. In this paper, the averaging method for this second-order scheme is extended to encompass not only periodic type boundary conditions for the Representative Volume Element (RVE) but also traction and displacement boundary conditions in a generalized manner.

Multi-scale models are constructed using three main ingredients (Figure 1) [2]:

1. Modelling of mechanical behaviour at microscale (RVE)
2. A downscaling rule which determines the local solution inside the RVE, for given macroscopic deformation measures
3. An upscaling rule for the macroscopic stress measures, given the micromechanical stress state.

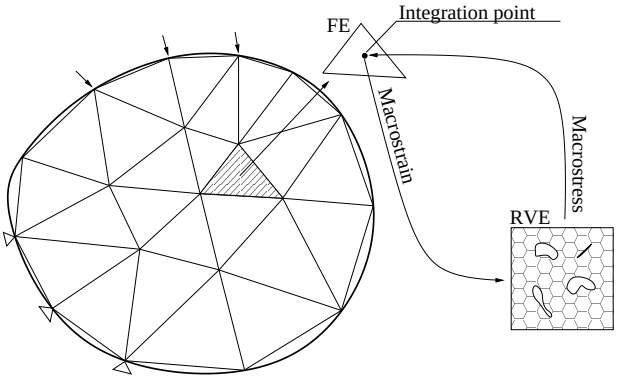

Figure 1: Illustration of computational homogenization scheme.

Scale Transition

This paper focuses on the strategy for the transition of strains and strain gradients from the macro-scale to the discretised microstructure. The boundary conditions enforce, in an average sense, the deformation of the representative volume element (RVE) according to a given macroscopically determined strain and strain gradient. Here a novel approach is proposed which can handle any type of boundary conditions (e.g. displacement, periodic and traction). It is worth noting that the proposed method is used to couple two different continua: a classical (first-order) one at the microscale, and a higher (second-order) continuum at the macro-scale.

The displacement field in the RVE is obtained from a truncated Taylor's series expansion of the macroscopic displacement field about the geometric centre of the RVE:

$$\mathbf{u}(\mathbf{X},\mathbf{x}) = \mathbf{u}^0(\mathbf{X}) + \mathbf{x}\cdot\bar{\boldsymbol{\varepsilon}}(\mathbf{X}) + \frac{1}{2}\mathbf{x}\otimes\mathbf{x} : \bar{\boldsymbol{\eta}}(\mathbf{X}) + \mathbf{r}(\mathbf{X},\mathbf{x}), \quad (1)$$

where $\bar{\boldsymbol{\varepsilon}} = \mathrm{sym}[\mathrm{grad}[\mathbf{u}]]$ is the macrostrain tensor, $\bar{\boldsymbol{\eta}} = \mathrm{grad}[\mathrm{grad}[\mathbf{u}]]$ is the second-order macrostrain tensor. The additional term $\mathbf{r}$ represents the microstructural fluctuation of displacement and has been added to account for the microscale

contribution to the displacement field and is necessary to fulfil equilibrium in the RVE.

The boundary conditions of the RVE can be expressed in an integral form as

$$\int_\Gamma \delta\mathbf{t}\cdot\mathbf{r}\,\mathrm{d}\Gamma = 0,\ \int_\Gamma \mathbf{n}\otimes\mathbf{r}\,\mathrm{d}\Gamma = \mathbf{0},\ \int_\Gamma \mathbf{n}\otimes\mathbf{x}\otimes\mathbf{r}\,\mathrm{d}\Gamma = \mathbf{0}, \quad (2)$$

where $\mathbf{n}$ is the normal vector field and $\delta\mathbf{t}$ is statically admissible variation of tractions on the boundary. The first integral satisfies the Hill-Mandel theorem and the second and third integral enforce the deformation of RVE according to a given macrostrain tensor and a given gradient of the macroscopic strain tensor respectively, in an average sense. For Finite Element discretisation of the RVE, the boundary conditions can be expressed in terms of the microscopic displacement field and the macrostrain tensor (1) as

$$\int_\Gamma \delta\mathbf{t}\cdot(\mathbf{u} - \mathbf{x}\cdot\overline{\boldsymbol{\varepsilon}} - \frac{1}{2}\mathbf{x}\otimes\mathbf{x} : \overline{\boldsymbol{\eta}})\,\mathrm{d}\Gamma = 0, \quad (3)$$

$$\int_\Gamma \mathbf{n}\otimes(\mathbf{u} - \mathbf{x}\cdot\overline{\boldsymbol{\varepsilon}} - \frac{1}{2}\mathbf{x}\otimes\mathbf{x} : \overline{\boldsymbol{\eta}})\,\mathrm{d}\Gamma = \mathbf{0}, \quad (4)$$

$$\int_\Gamma \mathbf{n}\otimes\mathbf{x}\otimes(\mathbf{u} - \mathbf{x}\cdot\overline{\boldsymbol{\varepsilon}} - \frac{1}{2}\mathbf{x}\otimes\mathbf{x} : \overline{\boldsymbol{\eta}})\,\mathrm{d}\Gamma = \mathbf{0}. \quad (5)$$

To complete the formulation it is necessary to identify the upscaling of the microstructural response to define the macroscopic stress and strain measures in terms of the microscopic quantities. For a statistically homogeneous body, the macroscopic quantities can be defined as the average of the microscopic quantities over the volume of the RVE [7]. For simplicity, assuming geometric linearity and a quadrilateral RVE in 2D, this leads to

$$\overline{\boldsymbol{\varepsilon}} = \frac{1}{V}\int_\Gamma \mathbf{n}\otimes\mathbf{u}\,\mathrm{d}\Gamma, \quad \overline{\boldsymbol{\sigma}} = \frac{1}{V}\int_\Gamma \mathbf{x}\otimes\mathbf{t}\,\mathrm{d}\Gamma, \quad (6)$$

$$\frac{1}{2}\int_V (\mathbf{x}\otimes\mathbf{x}\otimes\mathbf{1} + \mathbf{x}\otimes\mathbf{1}\otimes\mathbf{x} + \mathbf{1}\otimes\mathbf{x}\otimes\mathbf{x})\,\mathrm{d}V : \overline{\boldsymbol{\eta}} = \int_\Gamma \mathbf{n}\otimes\mathbf{x}\otimes\mathbf{u}\,\mathrm{d}\Gamma, \quad (7)$$

$$\overline{\boldsymbol{\tau}} = \frac{1}{2V}\int_\Gamma \mathbf{x}\otimes\mathbf{x}\otimes\mathbf{t}\,\mathrm{d}\Gamma, \quad (8)$$

where $\overline{\boldsymbol{\sigma}}$ is the second-order macrostress tensor that is work-conjugate to $\overline{\boldsymbol{\varepsilon}}$, $\overline{\boldsymbol{\tau}}$ is third-order macrostress tensor work-conjugate to $\overline{\boldsymbol{\eta}}$. It can be noted that macroscopic quantities are expressed exclusively by displacements and traction forces on the boundary of RVE. According to Hill-Mandel theorem it can be shown that the work of macrostrains on macrostresses is equal to the volume average of the work of the microstrains on microstresses in the RVE associated with a macroscopic point.

Summary

This work has concentrated on the formulation of the equations coupling the microscopic and macroscopic variables in second order computational homogenization and on the definition and enforcement of boundary conditions for the representative volume element. The proposed formulation means that any type of RVE boundary conditions can be applied (e.g. displacement, traction, periodic). A comprehensive description of presented approach and numerical examples can be found in [4, 5, 3].

A number of benchmark problems (not concluded here) have been studied in order to highlight the effects of enforcing the RVE boundary conditions in different ways for higher order continuum.

Acknowledgements The authors gratefully acknowledge the support of the UK Engineering and Physical Sciences Research Council (Grant Ref: EP/D500273). The first author also acknowledges the support of the Polish Ministry of Scientific Research and Information Technology Society (Grant Ref: 4 T07E060 29) and guidance received from Professor Zenon Waszczyszyn of Cracow University of Technology.

References

[1] F. Feyel (1999): Multiscale FE2 elastoviscoplastic analysis of composite structures. *Computational Materials Science*, **16**, 344–354.

[2] F. Feyel (2003): multilevel finite element method (FE2) to describe the response of highly non-linear structures using generalized continua. *Comput. Methods Appl. Mech. Engrg*, **192**, 3233–3244.

[3] Ł. Kaczmarczyk Ł. (2006): Enforcing Boundary Conditions in Micro-Macro Transition for Second Order Continuum. *Computers, Materials & Continua*, **12**, 55–62.

[4] Ł. Kaczmarczyk (2006): *Numerical analysis of multiscale problems in mechanics of heterogenous media*. Cracow University of Technology (PhD thesis).

[5] Ł. Kaczmarczyk (2006): Thin layer shear and second order homogenization method. *Computer Assisted Mechanics and Engeneering Science*, **13**, 537–546.

[6] V. G. Kouznetsova V.G (2002): *Computational homogenization for the multi-scale analysis of multi-phase materials*,Technishe Universitiet Eindhoven (PhD thesis).

[7] S. Nemat-Nasser, M. Hori (1999): *Micromechanics: overall properties of heterogeneous materials*. Elsevier.

Boundary Conditions for Multiscale Simulations of Heterogeneous Microstructures: Continua and Granular Materials

S. Mesarovic, J. Padbidri*

School of Mechanical and Materials Engineering
Washington State University, Pullman, WA 99164-9290, USA
mesarovic@mme.wsu.edu

Summary: We consider two-scale problems: the fine-scale model and the coarse-scale continuum. The key question in this class of problems is related to the simulation of the fine-scale cell: How are the coarse-scale fields to be passed onto the fine scale? The mathematical conditions that answer this question are called *minimal boundary conditions* (MBC). They are minimal in the sense that nothing but the desired constraint is imposed in contrast to periodic boundary conditions. Owing to their integral nature, the MBC can be applied to any shape of the fine-scale computational cell. We summarize the application to fine-scale continuum models to fine-scale discrete models with local interactions granular materials. The key to this application is the equivalent representation of kinematics of granular flow using the Delaunay network.

Introduction

Rapid growth in microelectronics, thin films and MEMS industries, as well as recent advances in nanotechnology have brought to light the problems on scale that is too small to be modeled by traditional continua, yet too large to be economically treated by more accurate fine scale models. As a result, multiscale modeling and simulations have been one of the fastest growing research areas during the last decade.

We consider two-scale problems: the fine-scale model and the coarse-scale continuum. When the models are invoked sequentially and information is passed from one scale to another, the key question is related to the simulation of the fine-scale cell: *How are the coarse-scale fields to be passed onto the fine scale?* The mathematical conditions that answer this question will be called **minimal boundary conditions** (MBC) [1]. The attribute *minimal* signifies that such conditions impose no additional restrictions on the fine-scale computational cell (other then the desired coarse-scale field).

The drawbacks of popular periodic boundary conditions are well-known. They (i) introduce superficial cell-size wavelengths in the solution fields, (ii) allow localization only on specific planes (Fig. 1 left), and, (iii) prevent response with higher order gradients (Fig. 1 right) – a feature that is regularly expected in functionally graded materials. Recently, kinematic MBC for fine scale continua have been discussed [1] and implemented into the finite element framework. The conditions

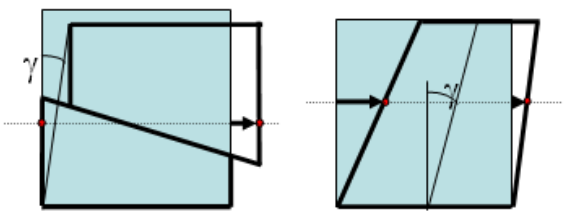

Figure 1: Impossible solutions under periodic boundary conditions: shear localization on an inclined plane (left), and, strain gradient, e.g., in functionally graded material (right).

are based on the definition of the coarse strain, as the volume average of the microscopic strain field, $\boldsymbol{\varepsilon}(\mathbf{x})$:

$$\mathbf{E} = \frac{1}{V}\int_V \boldsymbol{\varepsilon}(\mathbf{x})\, dV = \frac{1}{2V}\int_S (\mathbf{un} + \mathbf{un}) dS \qquad (1)$$

where **u(x)** is the displacement vector, and **n** is the unit normal to the surface. The FE implementation is very simple [1]; the integral in (1) is evaluated using the FE interpolation functions. Remarkably, the problem with the weak, integral boundary conditions (1) has the same sufficient condition for uniqueness as the standard boundary value problem with pointwise boundary conditions: pointwise positive definiteness of the fine-scale material stiffness.

Compared to periodic boundary conditions, the MBC show superior accuracy and computational economy [1].

Granular materials as networks

The governing equations are of the fine-scale model are similar to atomistic models. The differences are twofold: models for granular materials must include the rotational degrees of freedom of particles, and, atoms have nonlocal (albeit short-range) interactions.

The main vehicle for studying the topological evolution of the granular material will be the geometric description in terms of *Delaunay graph*, illustrated in Fig. 2, which is the complementary graph to the Dirichlet (or Voronoi) tessellation graph [2]. To create an equivalent fine-scale continuum for granular statics, we use the cell-based description of strain in granular materials [2, 3, 4], which defines an effective C^0 continuum, formally equivalent to a set of constant strain finite elements.

Thus, the implementation for quasistatic problems is identical to the one used in the fine-scale continuum model. The main challenge is the development of efficient Delaunay construction and boundary detection algorithms.

For dynamic, explicit integration models, such as those used for granular materials and atoms, the additional challenge is efficient implementation. The main feature is time-integration of Newton equations with updated forces. This structure enables

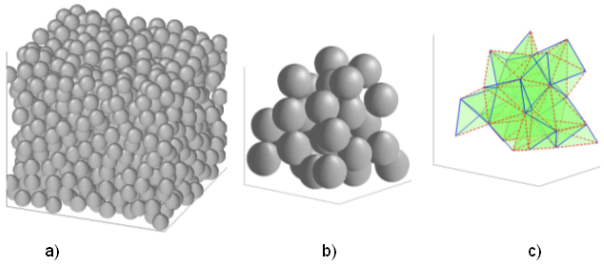

Figure 2: (a) Packing of 1,000 spheres with volume density of about 0.5. (b) A small sample from the packing (a). (c) Delaunay graph of the sample in (b): true contact (blue, solid lines), no contact (red, dashed lines).

efficient parallelization and should be preserved. A direct implementation of integral MBC [1, 4] would introduce coupling between all boundary degrees of freedom and would result in inefficient computations. We implement these boundary conditions by means of penalty method [5]. The penalty is imposed on the violation of the prescribed strain rate rather then strain, since the computation of strain requires re-tessellation in each increment.

Results and discussion

To illustrate the applicability of kinematic MBC to discrete models we consider a 2D assembly of discs with uniform size distribution between $\frac{1}{2}$ and 1 (Fig. 3a). First, we apply hydrostatic pressure using the interpretation of Delaunay cells as CSFE. Then, axial strain in vertical direction is applied (Fig. 3b). Using MBC, any component of strain, or any combination of strains can be prescribed. Shear strain application is illustrated in Fig. 3c. MBC are applicable to any shape of computational cell. A circular computational cell, subjected to shear is shown in Fig. 4. In summary:

- Equivalent network kinematics enables implementation of kinematic MBC for discrete particle models such as the discrete element model used here. The implementation is direct extension of the earlier application to fine-scale FE continua.
- Efficient explicit integration of particle dynamics is preserved by using the penalty method to implement MBC. Future challenges include applications to:
- Atomistic simulations. The assemblies of atoms are also subject to Dirichlet tessellation with complementary Delaunay graph. The difficulty lies in the nonlocal (short-range) nature of interatomic forces, particularly near the boundary.
- Fine-scale models with long-range interactions, such as dislocation dynamics.
- Eulerian fine-scale models, such as molecular dynamics of fluid flow, which require matter transport in and out of computational cell.

This work is supported by USDOE/MICS, grant # DE-FG02-05ER25709.

References

[1] S. Dj. Mesarovic, J. Padbidri (2005): Minimal kinematic boundary conditions for simulations of disordered microstructures, *Phil. Mag.* 85, 65–78.

[2] K. Bagi (1996): Stress and strain in granular materials, *Mech. Materials* 22, 165–177.

[3] K. Bagi (1999): Microstructural stress tensor of granular assemblies with volume forces, *J. Appl. Mech.*, 66, 934–6.

[4] M. Satake (2004): Tensorial form definitions of discrete-mechanical quantities for granular assemblies, *Int. J. Solids Structures*, 41, p. 5775.

[5] S. D. Mesarovic, J. Padbidri (2006): Transition between the models in multiscale simulations: Continua and granular materials, *Proc. Multiscale & Functionally Graded Materials*, Oahu Island, Hawaii. In press.

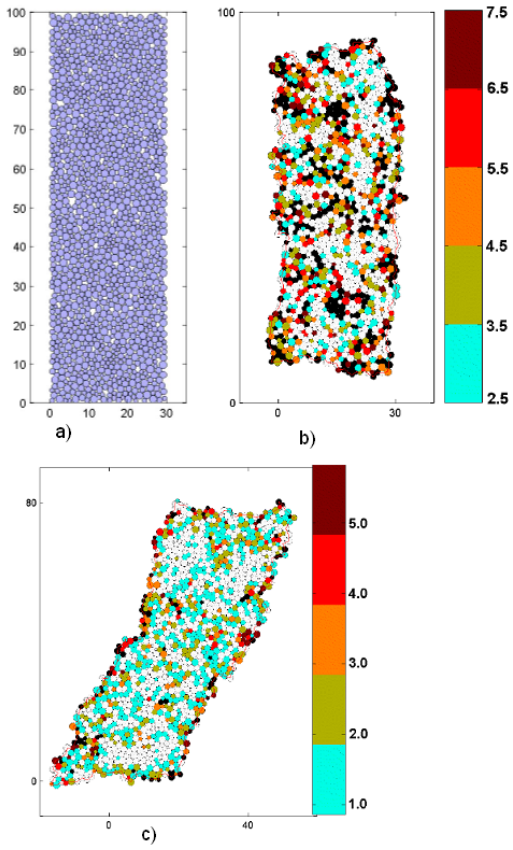

Figure 3: MBC applied to a 2D granular assembly. Hydrostatic pressure is applied first. (a) Initial configuration. Rotation contour plot (radians) (b) for axial strain 0.2, and (c) for shear strain 0.225.

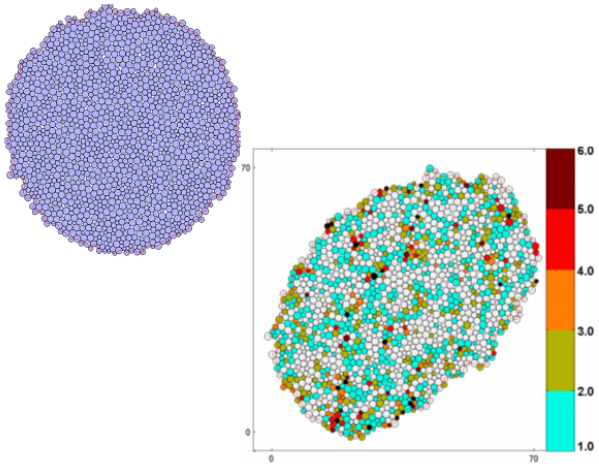

Figure 4: MBC shear applied to a circular sample.

On Application of Adaptive FEM to Multiscale Modeling

W. Cecot

Institute for Computational Civil Engineering
Faculty of Civil Engineering, Cracow University of Technology, Krakow, Poland
plcecot@cyf-kr.edu.pl

Summary: The paper tackles the problem of an adaptive finite element approximation of solutions evaluated by multiscale models. In particular, we propose a novel approach to the mesh adaptation at the macroscale. The key point in taking advantage of the adaptive mesh refinement at this scale is an independent approximation of the solution and the effective quantities.

Introduction

We consider structural components that are constructed of a heterogenous material which globally possesses either elastic or inelastic properties. We assume that a periodic microstructure of the material is known a'priori and modeling by the homogenization technique, with at least two scale computation, may be used.

Therefore, despite the homogenization error the discretizations at both scales result in approximation errors. We consider here the methods of error assessment and its reduction by the adaptive mesh refinement [4] in order to obtain reliable results with possibly small number of degrees of freedom. While adaptation at the fine scale may be done in a standard way, the coarse scale mesh refinement is more challenging since mapping of the solution between old and new representative volume elements (RVE) would be cumbersome.

The paper is organized in the following way. First we formulate mathematically the problem considered. Then, the adaptive FEM discretization is presented with special attention paid to error estimation. Next, the strategy of the mesh adaptation at the macroscale is proposed. An example of adaptive discretization of the representative volume element (RVE) is presented and concluding remarks are formulated.

Formulation of the problem

We consider here the solid mechanics model at both scales. The micro-scale problem (defined over an RVE) consist of finding the displacement field ($\boldsymbol{u}$) as well as the resulting strains ($\boldsymbol{\epsilon}$) and stresses ($\boldsymbol{\sigma}$) that satisfy the following equations.

$$\begin{cases} \operatorname{div}(\dot{\boldsymbol{\sigma}}) = 0 & \forall \boldsymbol{x} \in \Omega,\ \forall \tau \in [0,T] \\ \dot{\boldsymbol{\epsilon}} = \frac{1}{2}[\nabla \dot{\boldsymbol{u}} + (\nabla \dot{\boldsymbol{u}})^T] & \forall \boldsymbol{x} \in \Omega,\ \forall \tau \in [0,T] \\ \dot{\boldsymbol{\sigma}} = \boldsymbol{C}(\dot{\boldsymbol{\epsilon}} - \dot{\boldsymbol{\epsilon}}^*) & \forall \boldsymbol{x} \in \Omega,\ \forall \tau \in [0,T] \\ \dot{\boldsymbol{\epsilon}}^* = \boldsymbol{f}(\sigma, \boldsymbol{\epsilon}^*, ...) & \forall \boldsymbol{x} \in \Omega,\ \forall \tau \in [0,T] \\ \dot{\boldsymbol{u}} = \hat{\dot{u}} & \forall \boldsymbol{x} \in \partial\Omega_D,\ \forall \tau \in [0,T] \\ \dot{\boldsymbol{\sigma}}\boldsymbol{n} = \hat{\dot{\boldsymbol{t}}} & \forall \boldsymbol{x} \in \partial\Omega_N,\ \forall \tau \in [0,T] \\ \boldsymbol{\epsilon}^* = \boldsymbol{\epsilon}_0^* & \forall \boldsymbol{x} \in \overline{\Omega},\ \tau = 0 \end{cases} \quad (1)$$

where the superimposed dot stands for the time derivative. The Lipschitz boundary $\partial\Omega = \overline{\partial\Omega}_D \cup \overline{\partial\Omega}_N$, $\partial\,\Omega_D \cap \partial\,\Omega_N = \emptyset$ and if $n > 1$ then measure of the Dirichlet boundary is greater than zero ($\text{meas}(\partial\Omega_D) > 0$). Functions $\hat{\boldsymbol{u}}, \hat{\dot{\boldsymbol{t}}}, \boldsymbol{\epsilon}_0^*$ as well as the continuously (or piecewise continuously) varying constitutive tensor $\boldsymbol{C}$ are known. We also assume that the initial conditions are compatible with the loading. Function $\boldsymbol{f}$ that defines the rate of inelastic strains is given by the Bodner-Partom constitutive law [2]. If the material constants of the RVE are piecewise continuous appropriate subdomains have to be considered and the well known continuity conditions included.

At the coarse scale we assume a similar formulation as (1). This time however, the constitutive tensor and the inelastic strains are evaluated by the micro-scale analysis in RVEs attributed to selected points. We propose to select a grid of such points independently of the FEM mesh and approximate the effective data over the macroscale domain using the moving least square (MLS) approximation [6]. Due to the continuous approximation of the macroscale effective quantities the well posedness of the macroscale problem is assured.

Error estimation

Each mesh adaptation requires an a'posteriori error estimation. Let us briefly review the basic methods of the error estimation.

1. Hierarchical - based on two solution approximations
2. Interpolation type - takes advantage of the interpolation theory
3. Residual - makes use of the residuum of the differential equation considered
   - in either explicit
   - or implicit way
4. Recovery (Zienkiewicz-Zhu) - based on the flux postprocessing

We prefer the residual type error estimates since they are mathematically proved [1] and the equilibrated version is now accepted as the best error estimate.

Distribution of the grid points that are attributed to RVEs is controlled by the interpolation type error estimate. Furthermore we also control the homogenization error in the sense proposed in [7].

Fine scale adaptation

Mesh adaptation of the micro-scale problem is assumed to be performed in a well established way. Since the problem is often nonlinear, a special attention has to be paid to both the error

estimation and strategy of mesh adaptation. For the details concerning inelastic problems we refer to [3]. An example of a discretization obtained by h-adaptive FEM for a quarter of an RVE constructed as an inelastic metallic material with a hole at the center and subject to uniform tension in vertical direction is presented in Fig. 1.

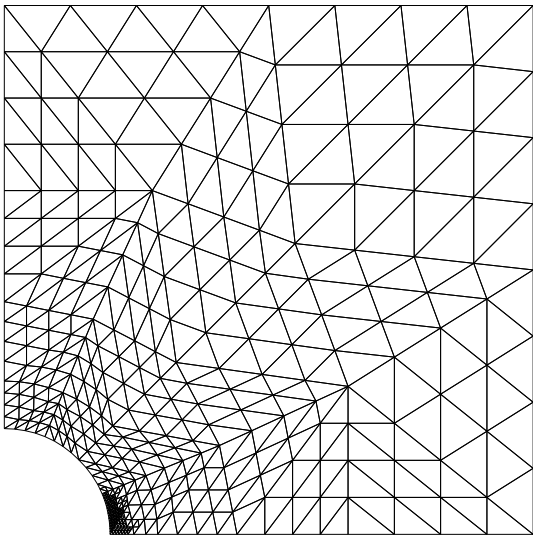

Figure 1: Fine scale analysis; example of an h-adaptively refined, 1-irregular FEM mesh in a quarter of an RVE

Coarse scale adaptation

Mesh adaptation at the macroscale is much more challenging task since after mesh refinement the solution has to be mapped onto the new mesh. Naturally, the whole numerical analysis may be repeated on the newly obtained mesh. However, in the case of time dependent or nonlinear problems we would like to avoid such a time consuming procedure.

Three factors contributing to adaptation at the macroscale are discussed here. They are: solution mapping after mesh refinement or unrefinement, adaptive distribution of RVE and localized multiscale approach [5].

The solution mapping is generally not an easy task [8]. We assume that only the internal variables and inelastic strains are mapped from the old mesh to the new one. They are used to evaluate all necessary rates and together with the current loading value uniquely define actual displacements, strains and stresses. As it was already mentioned, we propose to make use of a fixed distribution of points that are attributed to RVEs. Thus, the macroscale (effective) quantities like tensor of material parameters are approximated by a continuous or piecewise continuous functions on the basis of these point-wise values. This way despite having well posedness of the macroscale problem we avoid the necessity of ambiguous transfer of the problems from the old RVE grid to the new one.

In order to provide an optimal distribution of the RVEs they should be positioned in such a way that the approximation error of the macroscale quantities is as small as possible. Naturally, this optimal distribution of RVEs may vary during the loading process. Therefore, a rough (e.q. one scale) initial analysis of the whole loading history may be considered in order to predict the required positions of the RVEs.

Finally, we assume that the multiscale analysis may be performed only in selected subregions resulting in a hybrid approach. Therefore, one should asses where in the considered domain the multiscale approach is necessary. It may be done on the basis an a'priori knowledge. E.g. the area surrounding the tip of a propagating crack is suitable for multiscale modeling.

Concluding remarks

We have focused in this work on adaptive mesh refinement at the macroscale level. Continuous approximation of effective quantities, that is independent of FEM discretization, results in both the well posedness of the macroscale problem and a straightforward mapping of the solution after each mesh refinement or unrefinement. The strategy proposed above is now being tested on selected benchmark problems. The adaptive approach not only enables effective numerical analysis but also delivers reliable, error controlled results.

References

[1] M. Ainsworth and J. T. Oden (2000): *A Posteriori Error Estimation in Finite Element Analysis*, J. Wiley & Sons.

[2] S. R. Bodner and Y. Partom (1975): Constitutive equations elastic viscoplastic strain-hardening materials, *J. Appl.Mech.*, **42**, 385–389.

[3] W. Cecot (2006): Adaptive analysis of inelastic problems with Bodner-Partom constitutive model, *Comp. Assist. Mech. Engng Scs*, **13**, 513–521.

[4] L. Demkowicz, Ph. Devloo, and J. T. Oden (1985): On an h type mesh refinement strategy based on a minimization of interpolation error, *Comp. Meth. Appl. Mech. Engng*, **3**,67–89.

[5] W. E and B. Engquist (2003), The heterogeneous multiscale methods, *Comp. Math. Sci.*, 1:87–133.

[6] P. Lancaster and K. Salkauskas (1981): Surface generated by moving least squares methods, *Mathematics of Computation*, **155**, 141–158.

[7] J. T. Oden and K. S. Vemaganti (1999): Adaptive hierarchical modeling of heterogenous structures, *Physica D*, **133**, 404–415.

[8] W. Wunderlich, H. Cramer, and G. Steinl (1998): An adaptive finite element approach in associated and non-associated plasticity considering localization phenomena, In P. Ladeveze and J. T. Oden, editors, *Adaptive Computational Methods in Mechanics*, pages 293–332, Elsevier

Nanoholes and Nanoshapes: The Influence of Nanotube Geometry on Polymer Composite Properties

I. Schmidt[1]*, **L. C. Brinson**[2]

[1]University of the Federal Armed Forces Hamburg, Institute of Mechanics
Holstenhofweg 85, D-22043 Hamburg, Germany
ina.schmidt@hsu-hh.de

[2]Northwestern University, Department of Mechanical Engineering, Department of Materials Science and Engineering
2145 Sheridan Road, Evanston IL 60208, USA
cbrinson@northwestern.edu

Summary: This paper describes micromechanical and numerical simulations of nanotube polymer composites. In particular, the work focuses on the impact of the hollow nature of the nanotubes on composite response. While this geometrical detail of nanotubes is typically ignored in existing simulations which use solid cylinders to represent nanotubes, recent results demonstrating the importance of nanotube curvature and interphase effects indicate the key significance of these structural details in nanocomposites. Finite element simulations, traditional Mori-Tanaka predictions and a new micromechanics homogenization method [9] for coated inclusions are employed in the study.

Introduction

Due to the intrinsic mechanical properties of carbon nanotubes, including tensile moduli on the order of 1 TPa, strength in excess of 50 MPa and seemingly contradictory large strains to failure, these materials have recently been heavily investigated as fillers in polymeric matrices. The differences between nanotube fillers and traditional micron sized fiber fillers are vast. Of central importance are the orders of magnitude larger surface area per unit volume, the extremely high aspect ratio, the in situ curvature of the nanoinclusions and the tubular nature of the hollow, rolled graphene sheet. For these reasons, modeling strategies to elucidate the deformation mechanisms of such nanotube-reinforced polymers are needed.

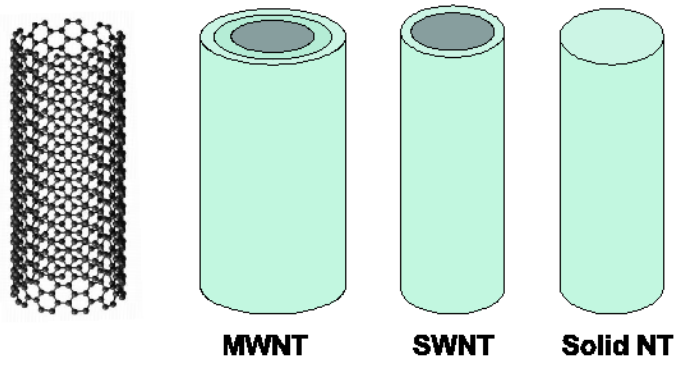

Figure 1: Atomistic and various continuum models for carbon nanotubes.

Common micromechanical methods require an ellipsoidal geometry of inclusions. Consequently the vast majority of nanocomposite simulations to date have modeled the nanotube inclusions as solid, straight cylinders. Similarly, most finite element simulations have also represented nanotubes as solid cylinders. However, it is certain that the hollow nature of the nanotubes (Fig. 1) significantly impacts their deformation mechanics, load transfer and reinforcing mechanisms in the composite. As an indication of the importance of such geometric features, recently it has been shown that the waviness or inherent in situ curvature of nanotubes, remarkably lowers the stiffness of nanotube-reinforced polymers [1].

In this work, we first examine the influence of the hollow nanotube geometry in the context of composites with well dispersed single wall nanotubes (SWNT). Furthermore the added stiffness contributions of additional shells on multiwall nanotubes (MWNT) are investigated, effects which have to date not been quantified. Finally, the influence of an interphase between nanotube and matrix can also be captured by the same modeling strategy. Recent experimental results have led to the conclusion that the dramatic property changes of polymer nanocomposites beyond the pure matrix polymer result significantly from the formation of an interphase region in the vicinity of the nanoscale fillers [3-6]. A schematic of the underlying physics of this effect is shown in Fig. 2.

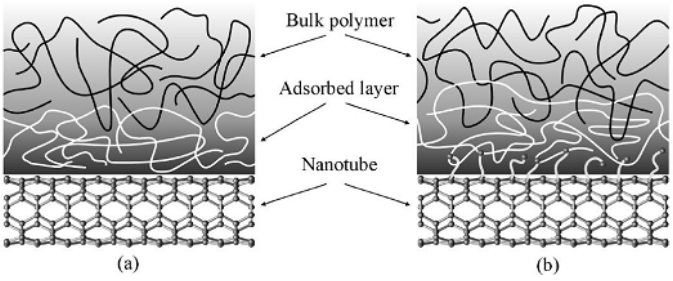

Figure 2: Schematic of formation of an interphase region in the vicinity of a nanotube a) without, b) with functionalization [7].

The aim of the presented work is to clarify the influence of the shell-structure of nanotubes or inclusions containing nanotubes (e.g. nanotube with strong interphase) on the stiffness of nanotube-reinforced polymers. In this study, numerical and micromechanical methods are used.

Initial results

A hybrid finite element-micromechanical modeling technique similar to that presented in [1-3] has been used to determine the dilute strain concentration tensor for a solid cylindrical and a tubular nanoinclusion (see Fig. 3) directly by a sequence of finite element calculations. Subsequently for the cylindrical inclusion case the effective stiffness of the polymer matrix containing randomly oriented nanotube-inclusions has been calculated using the Mori-Tanaka method.

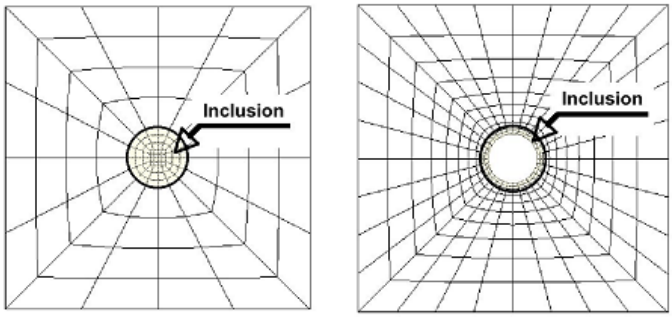

Figure 3: Cross-section of the 3-D finite element mesh for a solid cylindrical (left) and a tubular (right) nanoinclusion.

For comparison, results by Frankland et. al. [8] have been used. In [8], a micromechanical analysis based on the Mori-Tanaka method was carried out using the Eshelby tensor for spheroidal inclusions. The example uses inclusions with transversely isotropic material properties as the nanotubes in an isotropic polyimid-matrix. The predicted moduli from our hybrid analysis match the results given in [8] very well.

The finite element-micromechanical modeling techniques used in the presented work avoid the calculation of the Eshelby tensor and therefore they can also be applied to microstructures containing non-ellipsoidal inclusions. However, difficulties are encountered with application of the Mori-Tanaka method directly from the results of the tubular inclusion. Thus, additional micromechanical investigations are carried out.

Further micromechanical and numerical calculations and outlook

As mentioned before, common micromechanical approaches require ellipsoidal inclusions. Recently Shen and Li developed a new method for homogenization of fibers with an inhomogeneous interphase [9]. These models convert fibers with interphases into effective fibers which can be used directly in existing micromechanics methods, such as the Mori-Tanaka method. The models presented by Shen and Li have some difficulties in calculation of extremely weak fibers with stiff coatings. Therefore in this work, the applicability of this analytical method to hollow nanotube-reinforced polymers is examined. Calculations are carried out for hollow SWNTs, multiple shell MWNTs and the impact of these geometries on composite properties compared to the usual solid cylinder model are presented. Additionally, the model will be extended to incorporate the effects of the interphase by adding additional tubular shells of altered matrix polymer. These simlulations quantitatively demonstrate the importance of the interphase in nanocomposite properties. Qualitative comparison of the modeling results to experimental data on nanocomposites will be presented.

References

[1] F. T. Fisher, R. D. Bradshaw, L. C. Brinson (2003): Fiber waviness in nanotube-reinforced polymer composites–I: Modulus predictions using effective nanotube properties. *C*omposites Science and Technology, **63**, 1689-1703.

[2] R. D. Bradshaw, F. T. Fisher, L. C. Brinson (2003): Fiber waviness in nanotube-reinforced polymer composites–II: modeling via numerical approximation of the dilute strain concentration tensor. *C*omposites Science and Technology, **63**, 1705-1722.

[3] H. Liu, L. C. Brinson (2006): A Hybrid Numerical-Analytical Method for Modeling the Viscoelastic Properties of the Polymeric Nanocomposites *Journal of Applied Mechanics, **73**,* 758-768.

[4] T. Ramanathan, L. C. Brinson (2005): Functionalized SWNT/Polymer Nanocomposites for Dramatic Property Improvement. *Journal of Polymer Science B, **43**,* 2269-2279.

[5] A. Bansal et. al. (2005): Quantitative equivalence between polymer nanocomposites and thin polymer films. *Nature materials, **4**,* 693-698.

[6] K. W. Putz et. al. (2004): Elastic modulus of single-walled carbon nanotube-poly(methyl methacrylate) nanocomposites. *Journal of polymer science B, **42**,* 2286-2293

[7] A. Eitan, F. T. Fisher, R. Andrews, L. C. Brinson, L. S. Schadler (2006): Reinforcement Mechanisms in MWCNT-Filled Polycarbonate *Composites Science and Technology, **66**,* 1162-1173.

[8] S. J. V. Frankland, G. M. Odegard, M. N. Herzog, T.S. Gates, C.C. Fay (2004): Cross-Linked Nanotube Materials with Variable Stiffness Theters. NASA Langley Research Center *ASC/ASTM-D30 Joint 19th Annual Technical Conference*, Atlanta, GA, October 17-20, 2004.

[9] L. Shen, J. Li (2005): Homogenization of a fibre/sphere with an inhomogeneous interphase for the effective elastic moduli of composites. *Proceedings of the Royal Society A, Published online doi:10.1098/rspa.2005*, 1447.

Creasing Behavior of Corrugated Paper Board

B. K. Thakkar*, L. G. J. Gooren, R. H. J. Peerlings, M. G. D. Geers

Department of Mechanical Engineering
Eindhoven University of Technology, Eindhoven, The Netherlands
{B.Thakkar;R.H.J.Peerlings;M.G.D.Geers}@tue.nl

Summary: This paper presents an experimental and numerical study on creasing behavior of corrugated paper boards. Experiments have been carried out on corrugated paper board and its constituent papers. Finite element simulations have been carried out on a plane-strain model, incorporating Hill's plasticity criterion. The finite element simulations are found to be in good agreement with experimental observations up to initial buckling. The study presented here is intended to help in determining the optimum creasing depth to prevent cracking of paper boards during creasing and folding operations while manufacturing packaging boxes.

Introduction

Packaging boxes are usually made from corrugated paper board. The corrugated architecture imparts bending stiffness to the board. Corrugated paper boards are folded to make the boxes of required shape and size. To obtain neat folds, it is required to make fold lines (creases) on the board. These creases reduce the stiffness of the board along the fold lines, thus facilitating neat folds in the board.

Creasing is performed by indenting a creaser knife on the corrugated board. If the crease is too deep, excessive strain develops in the inner liner. If the strain is higher than the rupture strain of the constituent paper, it results in cracking of the inner liner. Whereas, if the crease is too shallow, the outer liner may crack during folding due to excessive tensile strain. Thus, it becomes extremely important to clearly understand the behavior of corrugated paper board during the creasing process in order to arrive at an optimum crease depth.

Barbier [1] presents a detailed review of various processes in paper and highlights some work, mainly experimental, in the area. Gilchrist et al. [2] performed nonlinear finite element analyses of corrugated boards. Uni-axial, biaxial and in-plane shear tests were done to obtain the model constants. An elastic-plastic material model was applied to the model constituting of shell elements. For the failure prediction, isotropic hardening and Hill's yield locus was adopted.

Not much experimental and analytical work have been reported on creasing of corrugated boards. In our study, creasing experiments have been conducted on corrugated board samples to observe their behavior during creasing. Experiments have also been conducted on sample constituent paper in order to obtain the mechanical properties of paper. Using these measured properties, finite element simulations have been performed to compare and correlate with experimental observations.

Experiments

In-plane tensile and compressive tests have been conducted on the liner and flute materials. During creasing, the top and bottom liners are under tension, while the flute is predominantly under compression. Hence, in-plane tension properties of the liners and in-plane compressive properties of the flute material are of most relevance during creasing. A representative tensile stress-strain curve for liner material is shown in Fig. 1. Experiments have been conducted on creasing of corrugated

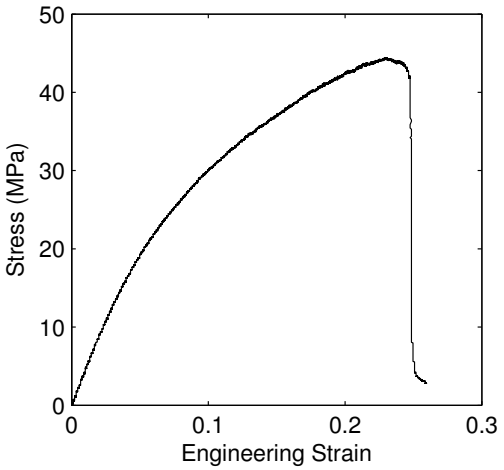

Figure 1: Tensile stress strain curve of liner material

board with the creaser parallel to peak and valley lines. The extreme cases for the creaser position are peak position and valley position as shown in figure 2. During creasing at the valley position, the inner liner is more prone to cracking and during folding, the outer liner is prone to cracking. The experimental setup consists of a corrugated paper board sample held between an anvil and a creaser in a tensile stage. The creaser displacement and load applied are measured and recorded. A schematic of the creasing test setup, and important creaser positions are shown in figure 2.

Numerical analysis

Numerical simulations, considering orthotropic behavior of paper have been performed using MSC Marc Mentat. Corrugated board has been modeled using 2D plane strain elements. The experimentally obtained mechanical properties have been incorporated in the model. The elastic modulus in tension and compression in machine direction is taken as E_{MD} = 3950 MPa. Poisson's ratios ν_{12} = 0.65, ν_{31} = 0.0035 and ν_{32} = 0.0055 have been adopted. The elasticity modulus in cross direction

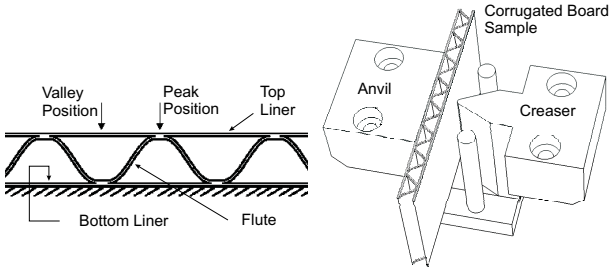

Figure 2: Creaser schematic with important creaser positions

and thickness direction is taken as 1650 MPa. Since the creaser is parallel to peak and valley lines and corrugations are in machine direction, the board can be safely considered to be in plane-strain condition. The mechanisms of inelastic strain in paper are not similar to mechanisms of plasticity of metals. However, the inelastic strain can be modeled with reasonable accuracy by using Hill's plasticity criterion [2] and hence, it has been adopted to incorporate the inelastic behavior. The final simulated deformed shape after creasing through the corrugated board and the degradation in upper liner near creaser are shown in Fig. 3.

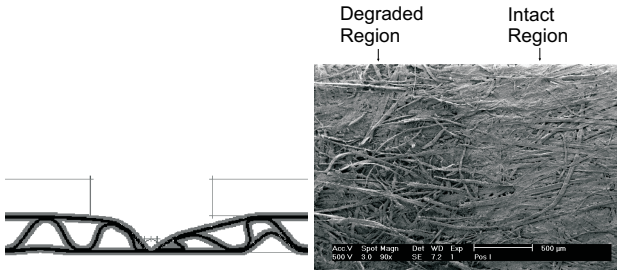

Figure 3: Final deformed shape and degradation near creaser

Discussion

The experimental load displacement curve during creasing of a 5mm wide sample at peak position and corresponding numerical simulation are shown in Fig. 4.

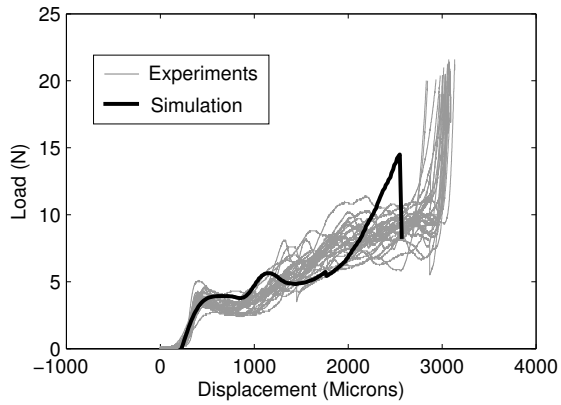

Figure 4: Load displacement curve during creasing of corrugated board

The load-displacement curve of creasing behavior shows that initially, the top liner is under bending action. With increase in creasing depth, the top liner is no more under bending behavior and contributes to the strength by direct tension; hence the board exhibits an increase in stiffness. The first peak, which is seen near 400 micron creaser displacement, indicates buckling of the flute. This matches well with the experimental observation. The board experiences an almost sudden loss in stiffness. The corrugated board gains stiffness then after due to more flute waves contributing to the load. Post first peak, the numerical simulation describes a different behavior from the experimental observation. This could be attributed to the incompressible Hill's plasticity model adopted in the model. It clearly indicates a requirement of failure description considering the mechanisms in paper at micro-scale. Each peak in the load-displacement curve indicates a buckling of the flute or liner. Cracking of the board sample was not observed in the experiments. However, considerable degradation was seen in upper liner near the creaser, when observed under a microscope. The absence of visible crack could also be attributed to the boundary condition resulting from the small sample size, which is not as realistic as the actual conditions in the factories.

Conclusion

Mechanical characterization of constituent paper for corrugated paper board has been done by experiments. Corrugated paper board has been modeled numerically using the finite element method. The finite element simulations compare well with the experimental observations up to the first peak and a little beyond; however, the post peak behavior needs refinement. This may be achieved by incorporating appropriate failure models driven by micro-mechanical studies.

References

[1] C. Barbier (2004): Folding of paper: A literature survey, *38th International Wood Composites Symposium Proceedings*, USA.

[2] A. C. Gilchrist, J. C. Suhling, T. J. Urbanik (1999): Nonlinear finite element modeling of corrugated board, *Mechanics of Cellulosic Materials*, ASME.

Modeling Fibrillar Structures in Bones: A Multiscale Approach

V. Sansalone*, T. Lemaire, S. Naïli

Laboratoire de Biomécanique et Biomatériaux Ostéo-Articulaires
CNRS UMR 7052, Université Paris 12 61, Av. Du Général de Gaulle, 94010 Créteil Cedex, France
vittorio.sansalone@univ-paris12.fr, lemaire@univ-paris12.fr, naili@univ-paris12.fr

Summary: In this paper we describe a first step towards a multiscale modeling of bone, focusing on its basic structural unit: the mineralized collagen fibril. We studied the elastic axial response of the fibril as a function of the mineral volume fraction. The computationally oriented framework leads to a paradigmatic uncoupling of models at the different scales and is well suited to further extension.

Introduction

Exceptional mechanical properties of bones are mainly due to its specific hierarchical structure [1]. From the visible down to the nano-scale, it is possible to distinguish: osteons, collagen fibres, collagen fibrils, elementary constituents. For an effective modeling of bones at the macro-scale it is essential to take into account all these structures and the way they work in concert to produce the overall mechanical and chemical properties [2].

Here we describe the first step towards such a throughout multiscale modeling, focusing on the bone basic unit: the mineralized collagen fibril. We follow the multiscale approach described in [3]: at the fibrillar scale, we recover an equivalent continuum on the basis of a detailed description of the sub-fibrillar structure. The latter is modeled as a composite material where the hydroxyapatite platelets act as a reinforcement of the elastic collagenous matrix [4,5].

In the present work, we restrict our attention to the elastic properties of the fibril. More precisely, we focus on the dependency of the apparent axial elastic modulus on the mineral volume fraction, a factor which strongly influences the elastic properties of bone [6]. Nevertheless, the setting is quite general and is well suited for dealing with a large class of nonlinear problems.

Multiscale model of mineralized collagen fibrils

We look at the mineralized collagen fibril as a collagenous matrix reinforced by hydroxyapatite platelets. We assume perfect adhesion between mineral platelets and collagen molecules, and we restrict our attention to a linearized kinematics.

The goal of this study is to identify, at the fibrillar scale, a continuum model able to effectively take into account the main features of the sub-fibrillar structure. To this aim, we follow the multiscale procedure outlined in [3]: (*i*) we characterize a *periodic module* at the sub-fibrillar scale; (*ii*) we identify an *equivalent continuum* at the fibrillar scale. The identification procedure is based on a variational homogenization procedure. The basic hypothesis of this approach are: **(a)** the admissible deformations for the module are considered homogeneous; **(b)** the average strain energy of the module is equal to the strain energy density of the equivalent continuum. Then, it is possible to identify the macroscopic stress measures in terms of the actions at the micro-scale. The equivalent continuum turns out to be, in general, a Cosserat continuum.

However, here we study the dependency of the axial modulus of the fibril on the mineral volume fraction. In this case, the fibres do not undergo any rotation and the homogenized response corresponds to that of an anisotropic Cauchy continuum [3].

Collagen molecules are organized inside the fibrils according to the *Hodge-Petruska* staggered pattern. Molecules are connected with each other by non collagenous proteins to form a crosslinked network embedding the mineral platelets, which we assume to be arranged according to a quarter-staggered scheme [4,5]. Then, we can consider at the sub-fibrillar level a periodic module as depicted in Fig. 1. Mineral platelets (the dark shaded bars in the figure) are described as rigid bodies, while the collagenous matrix is represented by a set of elastic springs (the thick segments in the figure) connecting the fibres in pairs. The springs are located at the middle of the edges of the module (light shaded area in Fig. 1).

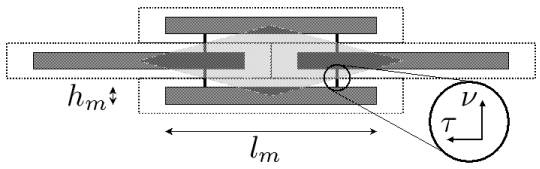

Figure 1: Sketch of the sub-fibrillar discrete model. Light shaded area represents the periodic module.

The effectiveness of the equivalent continuum strongly depends on the accuracy of the lower-scale model. In particular, it is of main importance to characterize as precisely as possible the sub-fibrillar structure, and namely the mechanical response of the springs representing the collagenous matrix. The required constitutive ingredients should be provided by a detailed numerical or experimental analysis at the sub-fibrillar scale. At the present, there is not a model able to describe the complex molecular interactions between all the constituents at this scale. Therefore, as a first step, we decided to oversimplify the problem and to consider a linearly elastic response for the springs.

Since only the axial response is considered, we can drop from the analysis the issues related to the rotation of the fibres. Then, only the springs acting on relative displacements of fibres can be retained. Their stiffness is assumed to be:

$$\mathsf{K}_{\vec{t}} = \mathsf{K}_{\vec{t}}^{\nu\nu}\, \boldsymbol{\nu} \otimes \boldsymbol{\nu} + \mathsf{K}_{\vec{t}}^{\tau\tau}\, \boldsymbol{\tau} \otimes \boldsymbol{\tau}\,, \tag{1}$$

where $\boldsymbol{\nu}$ and $\boldsymbol{\tau}$ are unit vectors parallel and orthogonal to the spring axis, respectively.

Identification of the sub-fibrillar module

The elastic coefficients $\mathsf{K}_{\vec{t}}^{\nu\nu}$ and $\mathsf{K}_{\vec{t}}^{\tau\tau}$ are identified performing a detailed finite element (FE) analysis of the staggered collagen-mineral structure and using the same energy equivalence argument used before for identifying the equivalent continuum.

The sub-fibrillar structure has been studied by the software COMSOL Multiphysics. A sketch of the simulated system is shown in Fig. 2.

Figure 2: Geometry of the sub-fibrillar FE model. Volume fraction of the mineral phase: $V_m = 0.40$*; aspect ratio of the platelets:* $l_m/h_m = 40$.

FE simulations have been performed applying Dirichlet boundary conditions corresponding to uniaxial deformation in two orthogonal directions. We considered as a parameter the mineral volume fraction: $V_m = 0.05, \ldots, 0.60$, while keeping constant the aspect ratio of the mineral platelets, $l_m/h_m = 40$.

The strain energy of system obtained by FE simulations, Φ_{FE}, is equated to that stored in the springs of the module:

$$\Phi_{FE} \equiv 4 \times \tfrac{1}{2} \left[\mathsf{K}_{\vec{t}}^{\nu\nu} \, (\vec{u}^{\nu})^2 + \mathsf{K}_{\vec{t}}^{\tau\tau} \, (\vec{u}^{\tau})^2 \right] . \qquad (2)$$

Here, $\vec{u}^{\nu}$ and $\vec{u}^{\tau}$ are the components of the relative displacement between a pair of fibres, computed applying to the module the same deformation state as the FE model.

The values of $\mathsf{K}_{\vec{t}}^{\nu\nu}$ and $\mathsf{K}_{\vec{t}}^{\tau\tau}$ so obtained, together with the morphological information, completely characterize the module.

Numerical simulation at the fibrillar scale

The morphological and constitutive information of the module are parameterized by the mineral volume fraction. In turn, the module is used as a lower-scale model for the equivalent continuum. In Fig. 3 we show the dependency of the axial modulus of the fibril on the mineral volume fraction.

Numerical simulations have been performed by a computer code which has been designed in order to reflect the multiscale procedure outlined above. An important feature of the proposed approach is the *uncoupling of the models* at the different scales. In fact, it is possible to show [3] that the operators which handle the transition between the two scales do not depend on the specific constitutive assumptions at the lower scale. Moreover, they can be given a general expression which does not depend on the specific arrangement of the lower scale components (position, form, orientation of the fibres and springs). Then, a very few effort must be done to study the "macroscopic" effects of different "microscopic" ingredients.

Final remarks

In this work, we studied the elastic axial response of a mineralized collagen fibril as a function of the mineral content by a multiscale approach. At the macroscopic level, the body is

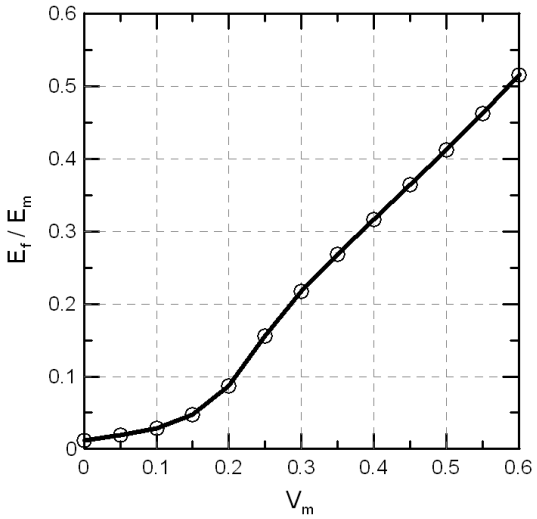

Figure 3: Axial modulus of the fibril as a function of the mineral volume fraction. Elastic modulus of the mineral phase: $E_m = 120$ *GPa; aspect ratio of the platelets:* $l_m/h_m = 40$.

described by an anisotropic Cauchy continuum, while at the micro-scale a staggered periodic module is adopted. The model is well suited for describing the effect of the microstructural features on the macroscopic response.

The variational multiscale approach provides a mechanically funded basis for establishing a bridge between the two scales. The formalism is quite general and suitable for further extensions. The numerical homogenization leads to a strong uncoupling of the models, which eases the taking into account of different morphological and constitutive ingredients at the sub-fibrillar level.

References

[1] S. C. Cowin ed. (2001): *Bone Mechanics Handbook*. CRC Press, Boca Raton, FL-USA.

[2] C. Hellmich, F.-J. Ulm, L. Dormieux (2004): Can the diverse elastic properties of trabecular and cortical bone be attributed to only a few tissue-independent phase properties and their interactions? *Biomechan. Model. Mechanobiol.*, 2, 219–238.

[3] V. Sansalone, P. Trovalusci, F. Cleri (2006): Multiscale modelling of materials by a multifield approach: Microscopic stress and strain distribution in fibre-matrix composites. *Acta Materialia*, 54, 3485–3492.

[4] I. Jäger, P. Fratzl (2000): Mineralized collagen fibrils: A mechanical model with a staggered arrangement of mineral particles. *Biophysical Journal*, 79, 1737–1746.

[5] S. P. Kotha, N. Guzelsu (2007): Tensile behavior of cortical bone: Dependence of organic matrix material properties on bone mineral content. *J. Biomech.*, 40, 36-45.

[6] J. D. Currey (1988): The effect of porosity and mineral content on the Youngs modulus of elasticity of compact bone. *J. Biomech.*, 21, 131–139.

Effect of Local Imperfections in Cracks Bridged by Multi-Filament Yarn on Multi-Cracking Response

M. Konrad[1*], **R. Chudoba**[1], **K. Meskouris**[1], **A. Scholzen**[2]

[1]Chair of Structural Statics and Dynamics, RWTH Aachen University
Mies-van-der-Rohe-Str. 1, 52074 Aachen, Germany
konrad@lbb.rwth-aachen.de, rch@lbb.rwth-aachen.de, kmeskou@lbb.rwth-aachen.de

[2]Institute of Concrete Structures, RWTH Aachen University
Mies-van-der-Rohe-Str. 1, 52074 Aachen, Germany
scholzen@imb.rwth-aachen.de

Summary: This paper introduces a numerical framework for the evaluation the influence of local imperfections in the material structure on the multi-cracking performance of brittle matrix composites with multifilament reinforcement. The micromechanical model of the bond between the multifilament yarn and the cementitious matrix is presented. The chaining of the crack bridges utilizing the stochastic cracking theory proposed by Cuypers [2] is described.

Introduction

In comparison with other composite materials, brittle matrix composites like textile reinforced concrete exhibit a high degree of heterogeneity and imperfection that requires special treatment in the development of numerical models. The micromechanical model with the fine resolution of filaments (bond-layer model) used for studying the crack bridge performance has been thoroughly described in [3].

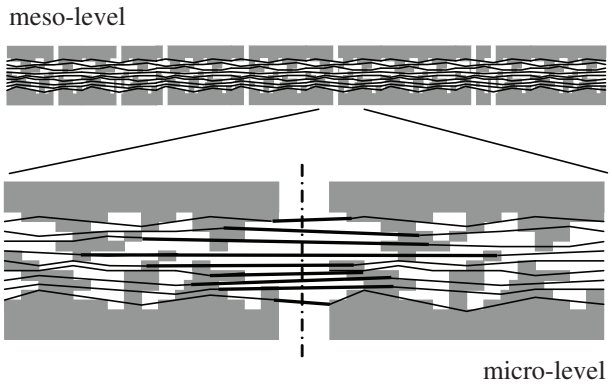

Figure 1: Idealization of the material structure at micro- and meso-level.

Previous studies using the bond layer model have shown the significant influence of local imperfections on the performance of the crack bridge. These imperfections are exemplified by non-parallel orientation of filaments within the bundle or by varying bond quality between filaments and matrix across the bundle. As a result, the damage localization process of textile reinforced concrete exhibits interactions between elementary failure mechanism in the matrix, in the reinforcement and in the bond.

The hot spots of the microscopic damage occur in the vicinity of the crack bridges. In addition, the damage evolves simultaneously in multiple interacting cracks distributed along the tensile specimen. In order to establish the link between the microscopic effects and the overall response of the specimen we combine the micro-crack-bridge model with the mesoscopic representation of the chain of crack bridges.

Micro-crack-bridge model

The single crack bridge can be idealized as an extremely short tensile test on yarn extended with a shear-lag-like clamping of filaments. Due to the varying penetration profile along the yarn, the quality of the shear lag clamping exhibits high scatter. The effect of variations in the material structure of the crack bridge can be included using a deterministic model with predefined profiles of material parameters across the bundle (see Fig. 2).

It should be emphasized, that this class of models can only describe a qualitative correspondence between the material parameters and response of the crack bridge. The combined use of statistical and deterministic models of a crack bridge has been provided in [4].

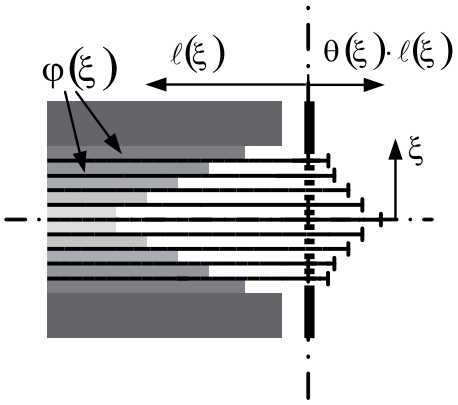

Figure 2: Micro-crack-bridge-model.

The present model for studying the behavior of the crack bridge falls into the category of deterministic models with explicitly defined profiles of material parameters. The effect of higher statistical moments is not included. The interface layer between the yarn and the matrix is regarded as a set of parallel laminas interacting with the matrix through the given bond law. The

laminas represent groups of filaments with the same characteristics and are coupled with the matrix using zero thickness interface elements.

The characteristics are assigned to the individual laminas based on the prescribed profiles of filament properties. In particular, (1) the profile of the bond quality φ, diminishing from the outside to the inside of the yarn, (2) the profile of the bond free length ℓ increasing from the outside to the inside of the yarn and (3) the profile delayed activation θ of filaments (slack) within the bond free length. These profiles do not represent the disorder in the filament bundle directly. The mentioned profiles induce an inhomogeneous stress transfer throughout the bond layer that is assumed to occur in a similar way in the heterogeneous material structure.

The model is able to capture the influence of the variations in the bond performance on the macroscopically observable failure process so that these variations may be quantified in a calibration procedure. The calibration of the model is performed both using the load-displacement curve and the curve representing the instantaneous fraction of broken filaments during the loading process. By calibrating the model to reproduce the experimental data it is possible to derive the effective bond law of the bond layer between the whole yarn (filament bundle) and the matrix that can be used at the higher modeling levels.

Multi-cracking

At the meso-scale the chaining of crack bridges follows the concept of the Aveston-Cooper-Kelly Model [1]. The behavior of a fiber reinforced brittle matrix composite under uniaxial loading is divided into into three stages: (1) the pre-cracking stage, (2) the multi-cracking stage and (3) the post-cracking stage (Fig. 3).

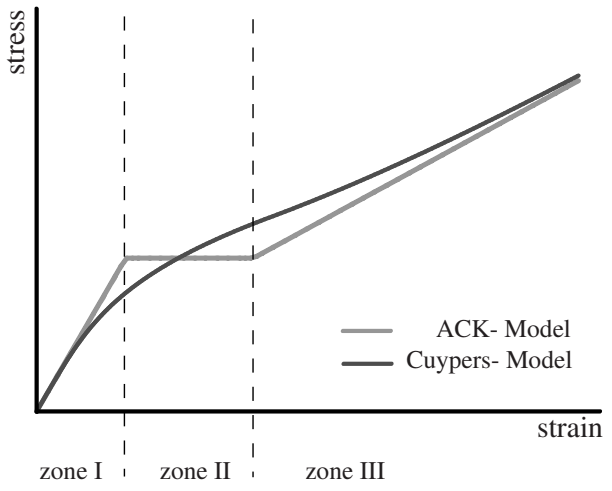

Figure 3: Multi-cracking.

Based on the ACK-Model which assumes a constant matrix cracking stress Cuypers has developed [2] a stochastic cracking theory by describing the failure properties of the matrix using two parameter Weibull model:

$$P(\sigma) = 1 - \exp\left[-\left(\frac{\sigma}{\sigma_R}\right)^m\right] \qquad (1)$$

with σ standing for the uniform tensile stress in the material, σ_R for the reference failure stress and m for the Weibull modulus.

By dividing the final crack spacing $\langle \mathrm{cs} \rangle_f$ by the percentage of matrix cracks that already propagated, the average crack spacing $\langle \mathrm{cs} \rangle$ for a certain composite stress can be derived:

$$\langle \mathrm{cs} \rangle = \langle \mathrm{cs} \rangle_f \left(1 - exp\left[-\left(\frac{\sigma}{\sigma_R}\right)^m\right]\right)^{-1} \qquad (2)$$

The multifilament yarn is represented by a monofil with effective properties. Assuming a constant frictional interface shear stress τ_0 along the debonded interface, the debonding length δ_0 can be evaluated analytically. Then average composite strain has to be evaluated separately for the two cases $\langle \mathrm{cs} \rangle > 2\delta_0$ and $\langle \mathrm{cs} \rangle < 2\delta_0$.

In the present paper the micro-crack-bridge model is used to evaluate the average composite strain $\langle \mathrm{cs} \rangle$ and the maximum stress transfer length $\delta_{\max}$ for a given intermediate crack spacing based on the stochastic cracking theory. The coupling of the micro-crack-bridge model with the stochastic cracking theory establishes a link between the heterogeneity in the micro structure and the performance of the composite during the micro cracking.

References

[1] J. Aveston, G. A. Cooper, A. Kelly (1971): Single and multiple fracture, the properties of fibre composites. *Proc. Conf. National Physical Laboratories, IPC Science and Technology Press Ltd. London*, 15–24.

[2] H. Cuypers (2001): *Analysis and Design of Sandwich Panels with Brittle Matrix Composite Faces for Building Applications*. Vrije Universiteit Brussel (PhD thesis).

[3] M. Konrad, R. Chudoba (2004): The influence of disorder in multifilament yarns on the bond performance in textile reinforced concrete. *Acta Polytechnica*, **44**, 186–193.

[4] M. Konrad, J. Jerabek, M. Vorechovsky, R. Chudoba (2006): Evaluation of mean performance of cracks bridged by multifilament yarns. *Proc. EURO-C 2006 – Computational Modelling of Concrete Structures*, 873–880.

Numerical Modeling of Mixed-Mode Crack Propagation in Reinforced Concrete

J. R. Carmona*, R. C. Yu, G. Ruiz

ETSI de Caminos, C. y P., Universidad de Castilla-La Mancha
Avda. Camilo José Cela, s/n; 13071 Ciudad Real, Spain
jacinto.ruiz@uclm.es

Summary: We propose a methodology to model mixed-mode crack propagation and diagonal tension failure in reinforced concrete beams subjected to static loading. The discrete cohesive approach, accompanied by an insertion algorithm, is adopted and a modified dynamic relaxation method is chosen as an alternative solver. The concrete matrix and steel re-bars are modeled explicitly; the connection in between is represented by means of interface elements. The methodology is validated against three-point bending beams with notches shifted from the middle span.

Introduction

In this paper we investigate the evolution of 3D complex fracture processes in reinforced concrete specimens subjected to static loading. We endeavor to model explicitly the diagonal tension failure in concrete bulk and debonding of the re-bar. We simulate the concrete matrix, the steel re-bars and the interface between the two materials explicitly. The cracks in the concrete matrix are described by using cohesive theories of fracture combined with the direct simulation of fracture and fragmentation. In reinforced concrete, the crack advancing through the concrete matrix is hindered by the presence of reinforcing bars. The development of the cracking process from then on implies the deterioration of the interface, which is modeled by inserting interface elements endowed with an effective adherent law along the steel-concrete contact. As the external loads increase the cracks in the matrix are finally able to propagate through the steel bar. Thus, the *sewing effect* of the steel bars is modeled explicitly. The difficulty of looking for a stable solution is avoided by means of the dynamic relaxation method, which always succeeds in finding a solution if such a solution exists. The slow convergence of the method is compensated for by means of a modified technique [1, 2]. The feasibility of the proposed methodology is validated against fracture tests on reinforced beams in flexure [3].

Finite element methodology

The cohesive theory of fracture

For completeness and subsequent reference, we will now outline the main features of the cohesive law and the interface constitutive law used in our calculations. A more detailed account of the theory and its finite-element implementation can be found elsewhere [4]. A variety of mixed-mode cohesive laws accounting for tension-shear coupling are established by the introduction of an effective opening displacement w,

$$w = \sqrt{\beta^2 w_s^2 + w_n^2}, \tag{1}$$

which assigns different weights to the normal w_n and sliding w_s opening displacements. Supposing that the cohesive free-energy density depends on the opening displacements only through the effective opening displacement w, a reduced cohesive law, which relates w to an effective cohesive traction

$$t = \sqrt{\beta^{-2} t_s^2 + t_n^2}, \tag{2}$$

where t_s and t_n are the shear and the normal tractions respectively, can be obtained. The weighting coefficient β is considered a material parameter that measures the relationship between the shear and tensile resistance of the material.

A modified dynamic relaxation method as an alternative solver

The crack propagation was led by a fragmentation algorithm that was able to modify the topology of the mesh at each loading step. This inevitably induces high geometric roughness upon the existing material non-linearity, hence a challenge for most implicit solvers when searching for static solutions. To avoid this problem we consider the explicit dynamic relaxation (DR) method as a feasible alternative solver. One of the common difficulties with the DR method is its slow convergence rate when non-monotonic spectral response is involved. We adopt a modified technique illustrated in [1] in order to sidestep this difficulty. Instead of critically damping the system of equations from the beginning, as suggested by all the standard DR procedures, the motion is kept as *strong* as possible. Through *under-damping* the system, the local movement provoked at the loading area or the crack tip can spread to the rest of the system; in this way the convergence rate is significantly improved.

Experimental setup

In order to validate the numerical methodology, we choose an experimental program reported in [3]. The program was designed to study mixed-mode crack propagation in reinforced concrete. In addition, an exhaustive material characterization to allow a complete interpretation of the test results was provided. The tests were carried out on beams with off-notched from the mid-span. A single, mixed-mode, macro crack carried on to the entire loading process, see Fig. 1. The load, P, and the displacement under the load point, δ, were continually monitored and recorded. A resistive extensometer centered on the tensioned face of the beam at the mouth of the notch was used to measure

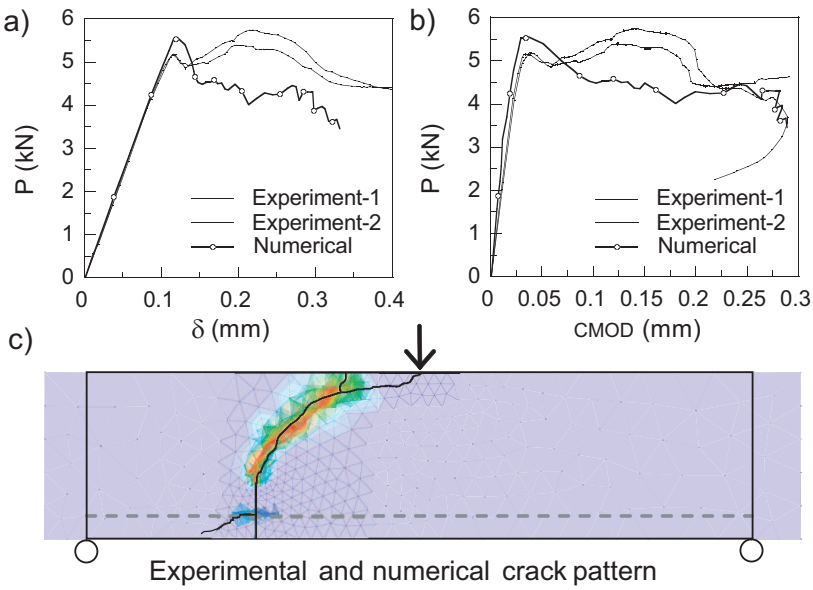

Figure 1: Numerical and experimental comparison: (a) P-δ curve, (b) P-CMOD curve, and (c) crack patterns.

the crack opening displacement, CMOD. The mechanical properties of concrete and its characteristic length are shown in in Table 1; the parameters for steel and the bond-slip strength of the steel-concrete interface are are given in Table 2.

Numerical results

We compare the numerical simulations against the experimental data for a three point bend tests on a 150×50×600 mm notch beam. The beam is reinforced with 2 longitudinal ribbed bars of 2.5 mm of diameter, this gives a reinforcement ratio of 0.13%. The comparison of P-δ, P-CMOD and crack patterns are shown in Figures 1a, b and c respectively. The numerical model captures the peak load, the crack trajectory, the debonding and micro cracking around the bars at the notch position. The overall performance is remarkable, taking into consideration that all the material parameters fed to the numerical model were directly measured in the experiments.

Conclusions

We have proposed a methodology to model mixed-mode crack propagation and consequently the diagonal tension failure in reinforced concrete beams subjected to static loading. The discrete cohesive approach accompanied by an insertion algorithm is adopted, and a modified dynamic relaxation method is chosen as an alternative solver. The concrete matrix and steel re-bars are modeled explicitly. The methodology is validated against three-point bending tests on notched, reinforced beams. A wealth of information can be extracted from this *explicit* simulation, including the complete loading-displacement curves, detailed crack patterns at the loading plane and around the re-bars, the stress distribution within the bars.

Table 1: Concrete mechanical properties.

f_c	f_{ts}	E_c	G_F	ℓ_{ch}
MPa	MPa	GPa	N/m	mm
36.3	3.8	28.3	43.4	86.8

Table 2: Steel mechanical properties and the interface bond strength.

E_s	$f_{y,0.2}$	f_u	ε_u	τ_c
GPa	MPa	MPa	%	MPa
174	563	632	4.6	6–8

References

[1] R. C. Yu and G. Ruiz (2004): Static multi-crack modeling in concrete solved by a modified DR method. *Computers and Concrete*, **1**, 371–388.

[2] R. C. Yu and G. Ruiz (2006): Explicit finite element modeling of static crack propagation in reinforced concrete. *International Journal of Fracture*, **141**, 357–372.

[3] J. R. Carmona, G. Ruiz and J. R. del Viso (2007): Mixed mode crack propagation through reinforced concrete. *Engineering Fracture Mechanics*, In Press.

[4] M. Ortiz and A. Pandolfi (1999): Finite-deformation irreversible cohesive elements for three-dimensional crack propagation analyses. *International Journal of Numerical Methods*, **44**, 1267–1282.

Multiscale Modelling of Anisotropic Clay

L. Kong[1], **P.-Y. Hicher**[1*], **C. Chang**[2]

[1]Research Institute in Civil and Mechanical Engineering UMR CNRS 6183
Ecole Centrale de Nantes, 44321 Nantes Cedex, France
kong_ lingrong@hotmail.com, pierre-yves.hicher@ec-nantes.fr

[2]Department of Civil and Environmental Engineering
University of Massachusetts, 30 Marston Hall, Amherst, MA 01002, USA
chang@ecs.umass.edu

Summary: This paper presents an extension of the elasto-plastic model for granular materials with microstructural consideration [1], to model the stress-strain relationship of clay considering its inherent anisotropy. The micro elasto-plastic model includes a Hertz-Mindlin's elastic law for the elastic part and a double yield surface for the plastic behavior on each contact plane of neighboring clay aggregates. Drained triaxial tests with loading in vertical and horizontal directions were performed on Shanghai clay. The comparison between numerical and experimental data demonstrates that the new version of the model is capable of taking into account the inherent anisotropy influence on the mechanical behavior of soft clay.

Introduction

Microstructural models for elastic stress-strain behavior of granular material can be derived from properties of inter-particle contacts, considering inter particle forces and displacements. This apprach has been successfully applied to reproduce the mechanical behavior of granular materials such as sands [1]. In this paper we extend it to clay by considering a clayey material as a collection of aggregates made of several particles.
The deformation of a representative volume of the material is generated by the mobilization of contact aggregates in all orientations. Thus, the stress-strain relationship can be derived as an average of the mobilization behavior of local contact planes in all orientations. The forces and movements from the contact planes of all orientations are suitably superimposed to obtain the macroscopic stress strain tensors.

Inter-particle behavior

Elastic part: The contact stiffness of an orientation includes normal stiffness, k_n^α, and shear stiffness, k_r^α, of the contact plane. The value of the stiffness can be estimated from Hertz-Mindlin's formulation.

Plastic part: The sliding direction may be upward or downward, and the shear dilation/contraction takes place simultaneously. The dilatancy effect can be described by

$$\frac{d\delta_n^p}{d\Delta^p} = \frac{T}{f_n} - \tan\phi_0 \tag{1}$$

where ϕ_0 is a material constant which, in most cases, can be considered equal to the internal friction angle ϕ_μ. T is the generalized shear force and $d\Delta^p$ is the rate of plastic sliding.

The yield function is assumed to be of Mohr-Coulomb type,

$$F(f_i, \kappa) = T - f_n \kappa\left(\Delta^p\right) = 0 \tag{2}$$

where $\kappa(\Delta^P)$ is an isotropic hardening/softening parameter.

$$\kappa = \frac{k_{p0}\tan\phi_p\,\Delta^p}{|f_n|\tan\phi_p + k_{p0}\Delta^p} \tag{3}$$

Interlocking influence: One of the important elements to consider in granular modeling is the critical state concept. Under critical state, the granular material will remain at constant volume while it is subjected to a continuous distortion. The void ratio corresponding to this state is e_c.

The critical void ratio e_c is a function of the mean stress. The relationship has traditionally be written as follows:

$$e_c = \Gamma - \lambda\log\left(p'\right) \text{ or } e_c = e_{ref} - \lambda\log\left(\frac{p'}{p_{ref}}\right) \tag{4}$$

Γ and λ are two material constants and p' is the mean stress of the packing, and (e_{ref}, p_{ref}) is a reference point on the critical state line.

The internal friction angle ϕ_μ is a constant for the material. However, the peak friction angle, ϕ_p, on a contact plane is dependent on the degree of interlocking by neighboring particles, which can be related to the state of packing void ratio e by:

$$\tan\phi_p = \left(\frac{e_c}{e}\right)^m \tan\phi_\mu \tag{5}$$

where m is a material constant [2].

Stress-strain relationship

Using the static hypotheses proposed by Liao et. al [3], we obtain the relation between the global strain and inter-particle displacement (we do not consider the finite strain condition)

$$\dot{u}_{j,i} = A_{ik}^{-1}\sum_{\alpha=1}^{N}\dot{\delta}_j^\alpha l_k^\alpha \tag{6}$$

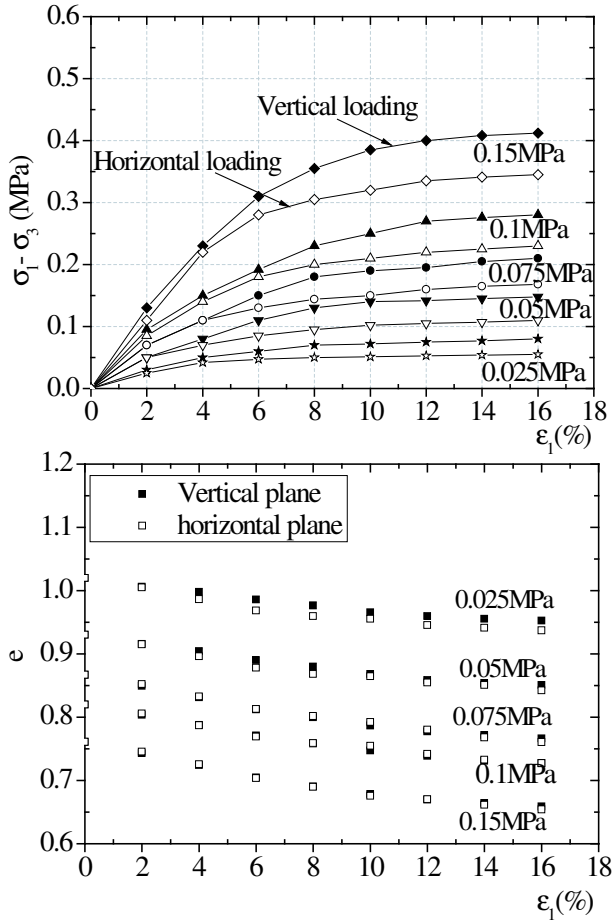

Figure 1: Drained triaxial tests on Shanghai clay.

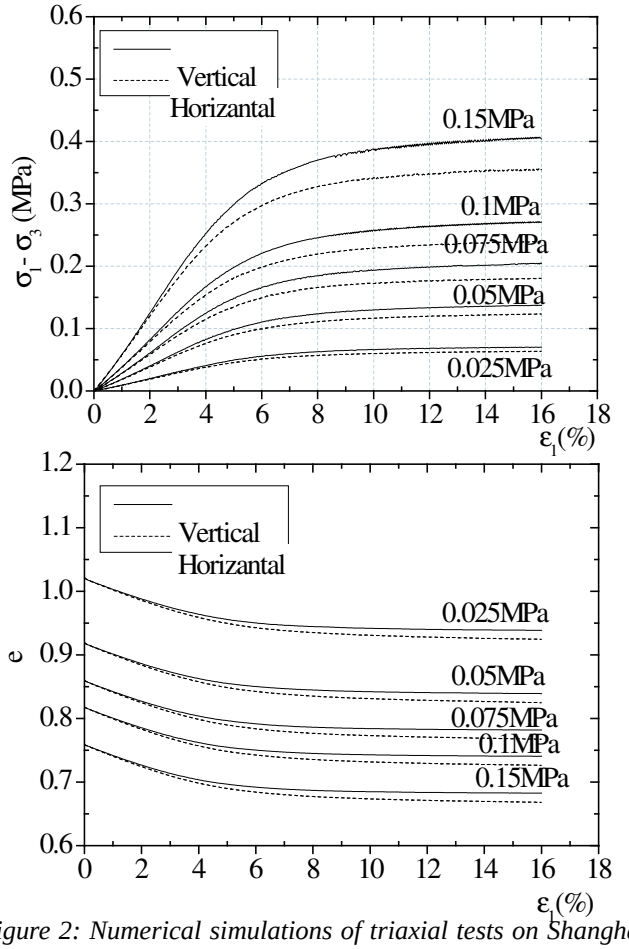

Figure 2: Numerical simulations of triaxial tests on Shanghai clay.

where the branch vector l_k^α is defined as the vector joining the centers of two particles, and the fabric tensor is defined as

$$A_{ik} = \sum_{\alpha=1}^{N} l_i^\alpha l_k^\alpha \tag{7}$$

The mean force and moment on the contact plane of each orientation are

$$\dot{f}_j^\alpha = \dot{\sigma}_{ij} A_{ik}^{-1} l_k^\alpha V \tag{8}$$

and one can obtaine the following relationships:

$$\dot{\sigma}_{ij} = \frac{1}{V} \sum_{\alpha=1}^{N} \dot{f}_j^\alpha l_i^\alpha \tag{9}$$

Triaxial testing on Shanghai clay

Experimental results: The specimens correspond to typical Shanghai marine clay and were taken at the depth of about 5 m. The tests results are presented in Fig. 1 for various confining pressures [4]. When loaded in vertical (depositional) direction, the specimen appear stiffer and the maximum strength is higher, which corresponds to a higher friction angle.

Numerical simulations: In order to reproduce the anisotropic behavior of Shanghai clay, mean values and degree of anisotropy of the parameters were determined by curve fitting, using the experimental results obtained from the triaxial tests at $\sigma_3 = 0.075$ MPa for vertical and horizontal loading. The results of the numerical simulations are presented in Fig. 2.

Conclusion

A microstructural elasto-plastic constitutive model for clay was successfully developed to capture the inherent anisotropy of Shanghai clay. It was able to reproduce the stiffer behavior of the specimens when loaded in the direction of deposition.

References

[1] Chang, C.-S., Hicher, P.-Y. (2005): An elastoplastic model for granular materials with microstructural consideration, *Int. J. of Solids and Structures*, **42**, 4258-4277.

[2] Biarez J., Hicher, P.-Y. (1994): *Elementary Mechanics of Soil Behaviour*, Balkema, p. 208.

[3] Liao, C.-L., Chang T.-P., Young D. and Chang C.-S. (1997): Stress-strain relationship for granular materials bases on hypothesis of best fit, *International Journal of Solids and Structures*, **34**, 4087–4100.

[4] Yuan, J.-Y., Yang X.-Z., Zhao X.-H., Dong J.-G. (1996): Experimental study on anisotropic characteristics of Shanghai soft clay. *Chinese Journal of Dam Observation and Geomechanical Test.*, **20**, 10–14

Numerical Solution of Two-Phase Steady and Unsteady Flow with Condensation

J. Fořt, J. Halama*

Department of Technical Mathematics, Faculty of Mechanical Engineering, Czech Technical University Prague
Karlovo nám. 13, Praha 2, Czech Rep.
fort@marian.fsik.cvut.cz, halama@marian.fsik.cvut.cz

Summary: The compressible flow of wet steam, i.e. of mixture containing water vapor and droplets, is an important issue in many practical applications, e.g in modelling of flow in steam turbines, modelling of gas drying etc. This work is aimed at the modelling of steady and unsteady flow in steam turbine cascades and stages. The condensation of vapor, i.e. the creation of droplets, influences the flow field structure, especially for transonic flow, decreases the work output and may cause turbine vibrations. We present numerical solution of cases (the flow in nozzles, turbine cascades and turbine stages), where the working fluid at the inlet is pure vapor and starts to condensate during an expansion inside the given geometry.

Mathematical model

To model such flow of condensing steam we consider inviscid compressible flow models (1D, 2D and 3D Euler equations) or viscous laminar compressible flow model (2D Navier-Stokes equations) for the flow of mixture and transport equations for integral parameters of droplets. Further we consider homogenous nucleation, zero slip velocity between vapor and droplets and the same pressure for mixture and vapor. The example of system of equations for 2D inviscid case is given by the Euler's equations for the mixture of vapor and droplets complemented by the transport equations for the parameter's of Hill's approximation Q_0, Q_1, Q_2, [2]:

$$\frac{\partial}{\partial t}\mathbf{W} = -\frac{\partial}{\partial x}\mathbf{F} - \frac{\partial}{\partial y}\mathbf{G} + \mathbf{Q}, \tag{1}$$

where

$$\begin{aligned}
\mathbf{W} &= [\rho, \rho u, \rho v, e, \rho\chi, \rho\chi Q_2, \rho\chi Q_1, \rho\chi Q_0]^T, \\
\mathbf{F} &= \left[\rho u, \rho u^2 + p, \rho uv, (e+p)u, \rho\chi u, \rho\chi Q_2 u, \rho\chi Q_1 u, \rho\chi Q_0 u\right]^T, \\
\mathbf{G} &= \left[\rho u, \rho vu, \rho v^2 + p, (e+p)v, \rho\chi v \rho\chi Q_2 v, \rho\chi Q_1 v, \rho\chi Q_0 v\right]^T, \\
\mathbf{Q} &= \left[0, 0, 0, 0, \rho\left(\tfrac{4}{3}\pi r_c^3 \rho_l \tfrac{J}{\rho} + \tfrac{4}{3}\pi 3 Q_2 \dot{r}\rho_l\right), \rho\left(r_c \tfrac{J}{\rho} + Q_0 \dot{r}\right), \rho\tfrac{J}{\rho}\right]^T,
\end{aligned}$$

symbol ρ denotes mixture density, u and v mixture velocity components, p mixture pressure, e mixture total energy per unit volume, χ wetness (i.e. the mass fraction of liquid phase), t time and x and y space coordinates. System of equations is closed by the equation for pressure [5]:

$$p = (\gamma - 1)\frac{(1-\chi)}{1 + \chi(\gamma - 1)}\left[e - \frac{1}{2}\rho(u^2 + v^2) + \rho\chi L\right], \tag{2}$$

where γ is specific heat ratio and L is latent heat of condensation. The nucleation rate J is computed according to classical theory of Becker and Döring [1] with correlation of Petr and Kolovratník [6]. The droplet growth $\dot{r}$ is computed according to heat exchange between droplet and surrounding vapor.

Due to our applications in internal aerodynamics a solution domain is always bounded. We recognize different types of domain boundaries: inlet boundary where the flow enters the domain, outlet boundary where the flow leaves the domain, periodical boundary if some periodicity of solution can be expected and wall boundary where the flow is going along this boundary. Since the governing equations represents hyperbolic system (in case of inviscid flow), the boundary conditions are specified according to theory of characteristics.

Numerical scheme

To discretize the computational domain we use structured quadrilateral grid. Numerical method is based on the Strang splitting [3], i.e. instead of solving the above system of equations (1) we successively solve following three equations:

$$\begin{aligned}
\frac{\partial}{\partial t}\mathbf{W} &= \mathbf{P} && (i) \\
\frac{\partial}{\partial t}\mathbf{W} &= -\frac{\partial}{\partial x}\mathbf{F} - \frac{\partial}{\partial y}\mathbf{G} && (ii) \\
\frac{\partial}{\partial t}\mathbf{W} &= \mathbf{P} && (iii)
\end{aligned} \tag{3}$$

and the complete numerical method can be expressed like

$$\begin{aligned}
\mathbf{W}_{i,j}^{(0)} &= \mathbf{W}_{i,j}^{n} \\
\mathbf{W}_{i,j}^{(k+1)} &= \mathcal{RK}(\mathbf{W}_{i,j}^{(k)}, \frac{\Delta t}{2\mathcal{N}}),\ k = 0, \ldots, \mathcal{N}-1 \\
\mathbf{W}_{i,j}^{(\mathcal{N}+1)} &= \mathcal{CV}(\mathbf{W}_{i,j}^{(\mathcal{N})}, \Delta t) \\
\mathbf{W}_{i,j}^{(k+1)} &= \mathcal{RK}(\mathbf{W}_{i,j}^{(k)}, \frac{\Delta t}{2\mathcal{N}}),\ k = \mathcal{N}+1, \ldots, 2\mathcal{N} \\
\mathbf{W}_{i,j}^{n+1} &= \mathbf{W}_{i,j}^{(2\mathcal{N}+1)}
\end{aligned} \tag{4}$$

where $\mathcal{RK}(\mathbf{W}, \frac{\Delta t}{2\mathcal{N}})$ denotes one step of two-stage Runge-Kutta method for equation (i) and (iii) with initial condition $\mathbf{W}$ and time step $\frac{\Delta t}{2\mathcal{N}}$. The symbol $\mathcal{CV}(\mathbf{W}, \Delta t)$ denotes one step of numerical method based on Lax-Wendroff scheme for cell-vertex finite volumes and with artificial dissipation of Jameson's type for the equation (ii) with initial data $\mathbf{W}$ and time step Δt. The time step Δt comes from stability condition of method for the Eq. (ii), the number of sub-iterations $\mathcal{N} = \Delta t/\tau$, where τ corresponds to the time scale of condensation. Instead of two-stage Runge-Kutta method for equations (i) and (iii) we use also implicit Euler method, which has better stability properties. The nonlinear equation is then solved by iterative method.

Example of numerical solution

One of the examples is the flow of condensing steam in axial turbine stage, see the figures 1 and 2, where the flow is going from the left to the right, the first blade row from the left

(called stator) is fixed and the second row of blades (called rotor) moves upwards. The computational domain is splitted into two parts. The structured quadrilateral grid in each part is fixed to the blade row. Both grids are connected directly by the grid lines using the technique of 'interface cells' of Giles [4], see also [7]. The figure 1 show the instantaneous pressure field and the figure 2 the instantaneous wetness field in the turbine stage. The condensation zone is concentrated to the rear part of stator cascade.

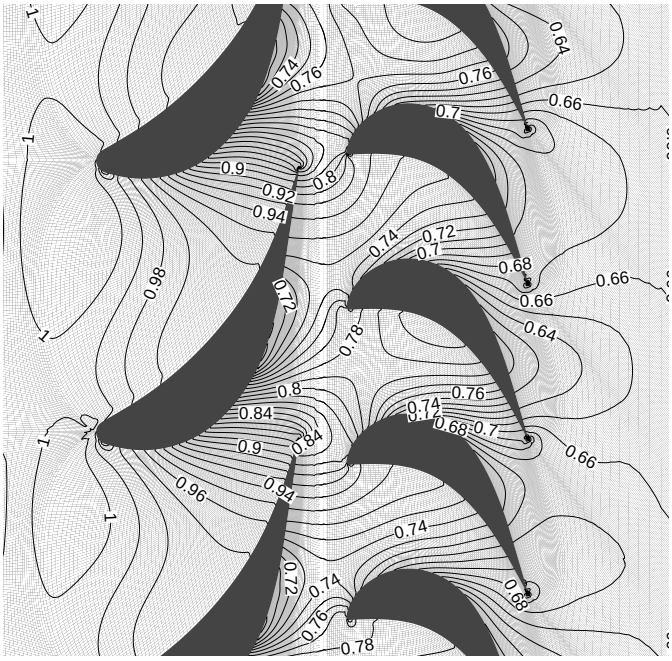

Figure 1: Instantaneous pressure isolines in turbine stage.

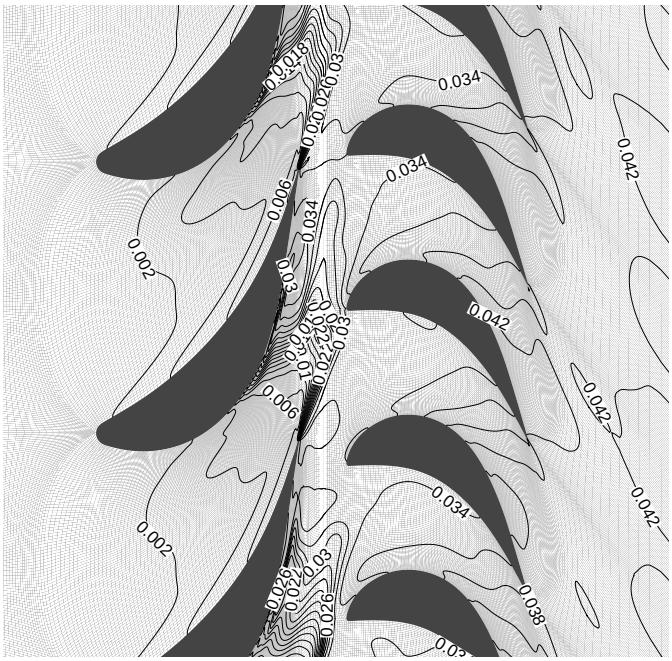

Figure 2: Instantaneous isolines of wetness in turbine stage.

Acknowledgements

This work is supported by the grant No. 101/05/2536 of GACR and the Research plan of MSM CR No. 6840770003.

References

[1] R. Becker, W. Döring (1935): Kinetische Behandlung der Keimbildung in übersättingten Dämpfen. *Ann. d. Physik*, **24**.

[2] P. G. Hill (1966): Condensation of water vapor during supersonic expansion in nozzles, part 3. *Journal of Fluid Mechanics*, **3**, 593–620.

[3] G. Strang (1968): On the construction and comparison of difference schemes. *SIAM Journal of Numerical Analysis*, **5**, 506–517.

[4] M. B. Giles (1990): Stator/rotor interaction in a transonic turbine. *Journal of Propulsion*, **6**, 621–627.

[5] M. Šejna (1995): *Numerical modelling of two–phase flow of steam with homogenous condensation*. PhD thesis, Prague (in czech).

[6] V. Petr, M. Kolovratník (2001): Heterogeneous Effects in the Droplet Nucleation Process in LP Steam Turbines. *4th European Conference on Turbomachinery*, Firenze, Italy.

[7] J. Halama, T. Arts, J. Fořt (2004): Numerical solution of steady and unsteady transonic flow in turbine cascades and stages. AMIF 2002 conference, *Journal Computers and fluids*, **33**, 729–740.

[8] J. Dobeš, J. Fořt, J. Halama (2005): Numerical solution of single and multi-phase internal transonic flow problems. *International Journal for Numerical Methods in Fluids*, **48**, 91–97.

Part III

Discrete Cracking, Fracture and Interface Elements

Geometrically Nonlinear Interface Elements for De-Cohesion Analysis of Adhesively Bonded Joints

N. Valoroso[1*], **L. Champaney**[2]

[1]Istituto per le Tecnologie della Costruzione, Consiglio Nazionale delle Ricerche
viale Palmiro Togliatti 1473 - 00155 Roma, Italy
nunziante.valoroso@itc.cnr.it

[2]Laboratoire de Mécanique et Technologie, ENS de Cachan / CNRS UMR 8535 / Université Paris VI
61, Avenue du Président Wilson - 94235 Cachan Cedex, France
laurent.champaney@lmt.ens-cachan.fr

Summary: Cohesive elements are developed for the analysis of adhesive joints configurations failing in the fully nonlinear regime. The core of the adopted approach is that of using a corotational formulation to mimic the behavoiur of the adhesive layer during deformation and fracture. The performances are demonstrated by means of a representative numerical example.

Introduction

Adhesive bonding is a technique of interest in a variety of industrial applications as it can offer improved performances with respect to mechanical fastening methods, basically originating from the fact that adhesive connections can transmit stresses with more uniform distributions compared to bolts and rivets. Typically, the adhesive is likely to be the weakest link in a structural joint and the bond region possesses a thickness that can be considered small compared to both that of the joined bodies and to its in-plane dimensions; hence, the adhesive layer can be conveniently schematized as a damaging interface where a cohesive process zone is lumped. The many advantages of the cohesive-zone approach over the more classical methods of Fracture Mechanics are well-known; in particular, one of its most appealing features is that it can be easily combined with arbitrary non-linearities of the bulk material.

In this work the adherends are allowed to experience large elastoplastic deformations while the progressive interface decohesion is modelled via the damage mechanics approach developed by the authors in [1], that is here extended to include large rotations effects; to this end use is made of a corotational formulation to develop interface cohesive elements compatible with nonlinear kinematics. A numerical example and a comparison with experimental results is provided that shows the ability to tracking the highly nonlinear response obtained in the asymmetric T-peeling test, where fracture of the adhesive layer is accompanied by large rotations and extensive plastic deformations of the joint arms.

Nonlinear kinematics and cohesive law

The basic geometry considered is a body Ω consisting of the assembly of two adherends denoted as Ω^+ and Ω^- that are initially in contact through a planar adhesive layer S. At each instant $t \in [0,T]$ the current configuration of the structure is defined by the sets $\Omega^{\pm}(t) \subseteq \Re^3$ described by the displacements $\boldsymbol{u}^{\pm}$ from the reference configuration:

$$\boldsymbol{u}^{\pm}(\boldsymbol{X},t) = \chi^{\pm}(\boldsymbol{X},t) - \boldsymbol{X} \tag{1}$$

relating the placements $\boldsymbol{X}$ in the reference configuration to the deformed ones $\boldsymbol{x}^{\pm} = \chi^{\pm}(\boldsymbol{X},t)$ occupied at time t in the current configuration via the deformation $\chi^{\pm}$. In this context, the virtual power identity in the spatial description of motion reads:

$$\int_{\Omega} \boldsymbol{\sigma} \cdot \operatorname{sym} \operatorname{grad}(\delta\mathbf{v}) \, \mathrm{d}\Omega + \int_{S} \mathbf{t} \cdot [\![\delta\mathbf{v}]\!] \, \mathrm{d}S = P_{ext} \quad \forall \delta\mathbf{v} \tag{2}$$

where $\boldsymbol{\sigma}$ and $\mathbf{t}$ are the Cauchy stress and the surface traction, respectively, P_{ext} is the power of external forces, $\delta\mathbf{v}$ the virtual spatial velocity and the symbol $[\![\cdot]\!]$ denotes the jump $(\cdot)^+ - (\cdot)^-$.

In order to formulate the interface cohesive law, two main issues have to be addressed, namely, the transformation rule of the spatial velocity jump under a superimposed rigid-body motion and the transformation of the area elements of S [2]. Actually, spatial fields are generally affected by a change in observer, and so is for $[\![\delta\mathbf{v}]\!]$; moreover, when contact is lost and a fracture propagates through the adhesive layer, unicity of the the normal to the cohesive surface is lost as well. However, both frame-invariance for $[\![\delta\mathbf{v}]\!]$ and elimination of possible ambiguities in the definition of the unit normal $\mathbf{n}$ are guaranteed if one admits that the discontinuity in displacements across the cohesive surface is small, i.e. $[\![\chi(X,t)]\!] \simeq 0$ before complete separation, as basic continuum mechanics arguments show [3].

The cohesive constitutive relationship stems from the following stored energy function [1]:

$$\psi([\![\boldsymbol{u}]\!], \mathbf{n}, D) = \frac{1}{2}(1-D)\left[k_n [\![u_n]\!]^2 + k_s [\![u_s]\!]^2\right] \tag{3}$$

where $D \in [0,1]$ is the scalar damage variable, k_n, k_s are undamaged interface stiffnesses and $[\![u_n]\!]$ and $[\![u_s]\!]$ denote the normal and tangential components of the displacement jump vector in the rotating frame attached to the interface, whose orientation is defined by the unit normal $\mathbf{n}$. The constitutive relationships follow from the classical thermodynamics argument; in particular, the mixed-mode damage energy release rate reads:

$$Y_m = \frac{1}{2} k_n \delta^2 \tag{4}$$

where δ is the equivalent opening displacement:

$$\delta = \left(\langle [\![u_n]\!] \rangle_+^2 + \frac{k_s}{k_n} [\![u_s]\!]^2 \right)^{1/2} \tag{5}$$

and the cohesive law in the rotating frame is obtained as:

$$t_\delta = (1 - D)k_n\delta \tag{6}$$

t_δ being the equivalent scalar traction:

$$t_\delta = \left(\langle t_n \rangle_+^2 + \frac{k_n}{k_s} t_s^2 \right)^{1/2} \tag{7}$$

It is worth emphasizing that the above expressions directly emanate from the potential (3), no a priori assumption is required on the shape of the fracture locus and that mode partition is made only based on the mode-mixity ratio defined as:

$$\boldsymbol{\beta} = \sqrt{\frac{k_s}{k_n}} \frac{[\![u_s]\!]}{\langle [\![u_n]\!] \rangle_+} \tag{8}$$

Basically, the model requires as input parameters the undamaged interface stiffnesses k_n and k_s, that can be estimated via acoustic measurements, the pure-mode critical fracture energies G_{cI}, G_{cII} and two interaction criteria for damage onset and decohesion propagation, see [1] for a detailed discussion.

Numerical simulation of a T-peel test

In this section we consider the application of the model briefly discussed in the previous section to predict the response of an adhesively-bonded assembly.

The geometry of the test is shown in Figure 1 (all dimensions are in mm). The material data set for the adherends, made from the 5754 aluminum alloy, and the bonded interface, made from XD 4600 Ciba-Geigy epoxy adhesive, is derived from [4].

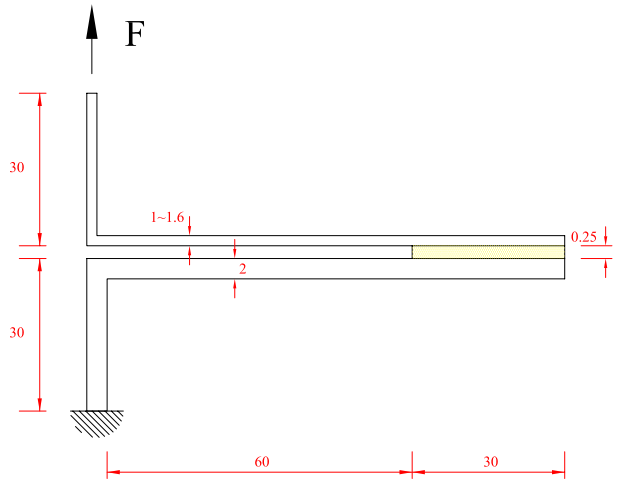

Figure 1: T-peel joint. Model problem

The cohesive model has been implemented within a user-defined interface element as a part of general-purpose FE code FEAP rel. 7.4 [5]. In the numerical simulation the material parameters for the interface are taken as k_n = 8500, k_s = 750 (N/mm^3) G_{cI} = 1.00, G_{cII} = 5.40 (N/mm). The aluminum alloy is modeled using the finite deformation logarithmic stretch-based Mises model with saturation-type isotropic hardening [6] under plane strain conditions.

The elastic constants for the adherends are taken as E=70 (GPa) and $\nu = 0.33$, while the yield stresses and strain-hardening characteristics are extracted from an experimentally measured stress-strain curve as σ_y^0=100, σ_y^∞=240, H_{iso}=100 (MPa), β = 20.

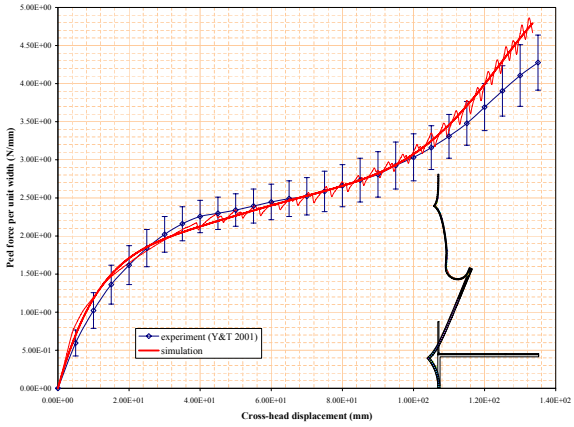

Figure 2: T-peel joint. Numerical vs experimental results

Figure 2 compares, for the specimen with adherend ticknesses of 1.0/2.0 mm, the numerically predicted load-deflection curve and the experimentally observed one documented in [4]. The numerical simulation is recognized to capture all the major features of the macroscopic response of the structure, that includes large rotations, asymmetry of bending and extensive plastic deformations of the adherends, as it can be appreciated from the deformed shape of the sample that is also reported in Figure 2.

References

[1] N. Valoroso, L. Champaney (2006): A damage-mechanics-based approach for modelling decohesion in adhesively bonded assemblies. *Engineering Fracture Mechanics*, **73**, 2774–2801.

[2] O. Allix, A. Corigliano (1999): Geometrical and interfacial non-linearities in the analysis of delamination in composites. *International Journal of Solids and Structures*, **36**, 2189–2216.

[3] M. Ortiz, A. Pandolfi (1999): Finite-deformation irreversible cohesive elements for three-dimensional crack-propagation analysis. *International Journal for Numerical Methods in Engineering*, **44**, 1267–1282.

[4] Q. D. Yang, M. Thouless (2001): Mixed-mode fracture analyses of plastically-deforming adhesive joints. *International Journal of Fracture*, **110**, 175–187.

[5] R. L. Taylor (2002): FEAP - User Manual. University of California at Berkekey, *http://www.ce.berkeley.edu/∼rlt*.

[6] J. C. Simo (1992): Algorithms for static and dynamic multiplicative plasticity that preserve the classical return mapping schemes of the infinitesimal theory. *Computer Methods in Applied Mechanics and Engineering*, **99**, 61–112.

A Damage Interface Model with Cohesive-Frictional Transition

G. Borino*, B. Failla, F. Parrinello

Università di Palermo, Dipartimento di Ingegneria Strutturale e Geotecnica
Viale delle Scienze, I-90128 Palermo (Italy)
borino@unipa.it, bfailla@diseg.unipa.it, parrinel@diseg.unipa.it

Summary: This paper presents a mechanical interface model able to describe the continuous transition from cohesive to frictional behaviour. The interface constitutive laws are derived in a thermodynamically consistent framework and are potentially capable do describe decohesion initiation, fracture propagation, closure with friction, either in the process zone, or in the fully fractured zone. Monotonic or cyclic loading conditions can be successfully reproduced.

Introduction

The study of the adhesion between bodies, and/or the fracture propagation along surfaces, have been successfully approached by interface models. Combination of cohesive fracture and damage mechanics are the main ingredients for the constitutive modelling of interfaces. Another aspect of relevance is the frictional behaviour between rough surfaces in sliding contact, which usually is approached independently of the previous decohesion problem. In this contribution a unified approach to the decohesion and frictional sliding, including the transition between the two phenomena, is presented. Beside some contributions, [1, 2], there are few studies on that matter, and here a quite general framework, based on thermodynamics and internal state variables, is presented. The proposed interface model is based on the concept that the damage variable ω, not only describes the stiffness degradation, but it is also a geometrical measure of the fraction of the sound area around a point. Namely, the part $(1-\omega)ds$ is the cohesive fraction, whereas the complementary part $\omega\, ds$ is the decohesed fraction, where friction sliding may develop.

Interface formulation

The interface considered is a zero thickness layer interposed between two linear elastic solids. It is assumed that the interface is the only locus where nonlinear dissipative phenomena may occur (opening, decohesion and frictional sliding deformation modes). Small strain hypothesis is assumed. The state of integrity of the interface is measured by a damage variable ω, a scalar internal variable ranging between 0 and 1. With reference to the value of the damage, three states can be observed. Namely: i) sound, $\omega = 1$; ii) damaged, $0 < \omega < 1$; iii) fractured, $\omega = 1$, (see Fig. 1a). The kinematics of the interface is given by the displacement discontinuity vector $[\![\boldsymbol{u}]\!] = \boldsymbol{u}^+ - \boldsymbol{u}^-$ which can be decomposed in two components $[\![u_N]\!]$ and $[\![u_T]\!]$, normal and tangential components, respectively. Further kinematic variables are the frictional displacement $\boldsymbol{\delta}$ and the gap displacement vector $\boldsymbol{g}$ in case of opening and fully damaged state (see Fig. 1b). These two variables are not independent with respect to the configurational variable $[\![\boldsymbol{u}]\!]$. The relevant conjugate forces describing the statics of the interface is a traction vector $\boldsymbol{t}$ (see Fig. 1c) and two further traction-like variables: $\boldsymbol{t}^c$ traction related to the cohesive (reversible) component and $\boldsymbol{t}^f$ traction related to the frictional component (see Fig. 1c).

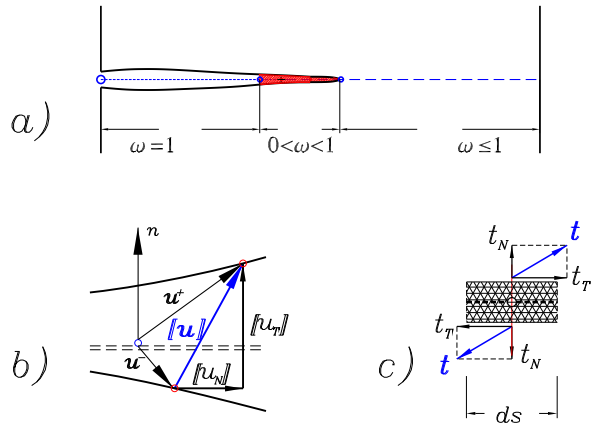

Figure 1: a) Interface with the fractured, partially fractured (process zone), and integer zones; b) kinematics of the interface; c) statics of the interfaces.

The constitutive relations link static variables to the kinematic ones. The model proposed here has some similarities with the one presented in [2] where a multi-scale approach were invoked for describing the state of the process zone. Namely, in the process zone, where $0 < \omega < 1$ it is assumed (see Fig. 2a) that $(1-\omega)ds$ is the sound fraction, whereas the complementary part $\omega\, ds$, is the decohesed fraction, where frictional modes may develop. Under this assumption internal congruence gives, $[\![\dot{\boldsymbol{u}}]\!] = \dot{\boldsymbol{\delta}} = \dot{\boldsymbol{u}}^c$, where $\boldsymbol{u}^c$ is a strain measure in the cohesive fraction $(1-\omega)dS$, whereas $\boldsymbol{\delta}$ is the strain measure in the frictional fraction $\omega\, dS$. Moreover, by applying the virtual power principle the internal equilibrium equation is given in the form $\boldsymbol{t} = \boldsymbol{t}^f + \boldsymbol{t}^c$. The decomposition principle, typical of small strain plasticity, for the frictional strain component is assumed $\boldsymbol{\delta} = \boldsymbol{\delta}^e + \boldsymbol{\delta}^f$ where $\boldsymbol{\delta}^e$ is the elastic (reversible) strain component, and $\boldsymbol{\delta}^f$ is the pure frictional (irreversible) strain components. The physical meaning of $\boldsymbol{\delta}^e$ can be associated to the reversible deformation of the microasperities formed in the damaged portion of the interface (see Fig. 2b). In order to develop a thermodynamic consistent setting, let us assume the following form for the Helmoltz free energy density (for unit interface length)

$$\begin{aligned}\psi &= \frac{1}{2}(1-\omega)\left[K_N^+\langle u_N^c\rangle_+^2 + K_N^-\langle u_N^c\rangle_-^2 + K_T u_T^{c2}\right] \\ &+ \frac{1}{2}\omega\left[k_N^a\delta_N^{e2} + k_T^a\delta_T^{e2}\right] + \psi_{in}(\xi), \end{aligned} \tag{1}$$

where ψ_{in} is the internal free energy component, ξ is an inter-

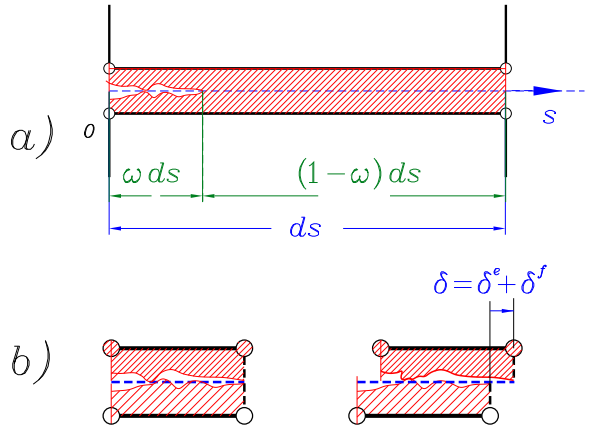

Figure 2: a) Interface infinitesimal element with the two surface fractions; b) sliding deformation mode with the decomposition of the sliding displacement.

nal variable describing damage hardening state; K_N^+, K_N^- and K_T are the interface stiffness coefficients, k_N^a and k_T^a are the stiffness coefficients related to the micro-asperities. The second thermodynamic principle in the form of Clausius-Duhem inequality reads

$$D = \boldsymbol{t}^T \dot{\boldsymbol{u}} - \dot{\psi} \geq 0. \tag{2}$$

Developing the rate of the Helmoltz free energy of eqs. (1), and substituting in eq. (2), considering also the internal compatibility conditions

$$\begin{aligned} D &= \left(t_N - \frac{\partial \psi}{\partial u_N^c} - \frac{\partial \psi}{\partial \delta_N^e}\right) \dot{u}_N^c + \left(t_T - \frac{\partial \psi}{\partial u_T^c} - \frac{\partial \psi}{\partial \delta_T^e}\right) \dot{u}_T^c \\ &- \frac{\partial \psi}{\partial \omega} \dot{\omega} - \frac{\partial \psi}{\partial \xi} \dot{\xi} \geq 0, \end{aligned} \tag{3}$$

which, following well established thermodynamic procedures, gives the following state equations

$$t_N^c = \frac{\partial \psi}{\partial u_N^c} = [(1-\omega)\, H(u_N)\, K_N^+ + H(-u_N)\, K_N^-] u_N^c; \tag{4}$$

$$t_T^c = \frac{\partial \psi}{\partial u_T^c} = (1-\omega)\, K_T\, u_T^c; \tag{5}$$

$$t_N^f = \frac{\partial \psi}{\partial \delta_N^e} = \omega\, k_N^a\, \delta_N^e; \tag{6}$$

$$t_T^f = \frac{\partial \psi}{\partial \delta_T^e} = \omega\, k_T^a\, \delta_T^e; \tag{7}$$

$$\chi := \frac{\partial \psi}{\partial \xi}, \tag{8}$$

$$\begin{aligned} Y := -\frac{\partial \psi}{\partial \omega} &= \frac{1}{2}[K_N^+ \langle u_N^c \rangle_+^2 + K_N^- \langle u_N^c \rangle_-^2 + K_T u_T^{c2}] \\ &- \frac{1}{2}[k_N^a \delta_N^{e2} + k_T^a \delta_T^{e2}]; \end{aligned} \tag{9}$$

It should be observed that the last term in eq. (9) is a micro-strain energy component to be subtracted to standard energy release rate, since this energy is stored at the micro-structure level as reversible deformation of the micro-asperities and is not available to drive damage increments. Two dissipative mechanisms are observable; namely, damage and friction. Two criteria for the activation of damage and the friction are assumed

$$\phi_d(Y, \chi) = Y - \chi - Y_0 \leq 0; \tag{10}$$

$$\phi_f(\boldsymbol{t}^f) = |t_T^f| - a\, t_N^f \leq 0. \tag{11}$$

where Y_0 is the initial damage treshold. Equation (11) is a Coulomb law and a is a coefficient related to the internal friction angle. Moreover, in order to have a dilatancy effect an frictional potential function is defined as

$$\Omega_f(\boldsymbol{t}^f) = |t_T^f| - b\, t_N^f; \qquad b < a. \tag{12}$$

Assuming generalized associativity, for the damage, and nonassociativity for the friction, the flow rules read:

$$\dot{\omega} = \frac{\partial \phi_d}{\partial Y} \dot{\lambda}_d \qquad \dot{\xi} = -\frac{\partial \phi_d}{\partial \chi} \dot{\lambda}_d \qquad \dot{\lambda}_d \geq 0. \tag{13}$$

$$\dot{\delta}_N^f = \frac{\partial \Omega_f}{\partial t_N^f} \dot{\lambda}_f \qquad \dot{\delta}_T^f = \frac{\partial \Omega_f}{\partial t_T^f} \dot{\lambda}_f \qquad \dot{\lambda}_f \geq 0. \tag{14}$$

The constitutive framework is completed by the loading/unloading conditions in the form $\phi_d \dot{\lambda}_d = \dot{\phi}_d \dot{\lambda}_d = 0$ and $\phi_f \dot{\lambda}_f = \dot{\phi}_f \dot{\lambda}_f = 0$.

Figure 3. shows a typical cyclic and monotonic response of an interface under a fixed compressive load and a monotonic or cyclic variable horizontal load.

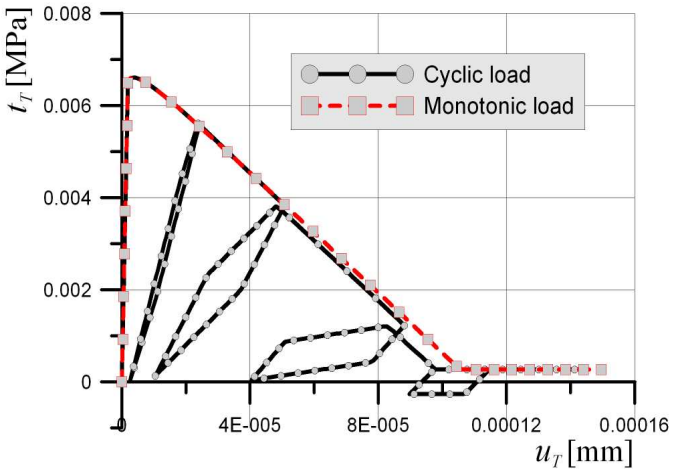

Figure 3: Tangential load-displacement responses for monotonic or cyclic variable tangential load with fixed compressive load.

References

[1] J. L. Chaboche, F. Feyel, Y. Monerie (2001): Interface debonding models: a viscous regularization with a limited rate dependency. *International Journal of Solids and Structures*, **38**, 3127–3160.

[2] G. Alfano, S. Marfia, E. Sacco (2006): A cohesive damage-frictional interface model accounting for water pressure on crack propagation. *Computer Methods in Applied Mechanics and Engineering*, **196**, 192–206.

A Stress Recovery Method for Nodes along Planar Bi-Material Interfaces

D. Ciancio[1*], **I. Carol**[1], **M. Cuomo**[2]

[1]School of Civil Engineering (ETSECCPB), Technical University of Catalonia
Barcelona, Spain
daniela.ciancio@upc.edu, ignacio.carol@upc.edu

[2]Department of Civil and Environmental Engineering, University of Catania
Catania, Italy
massimo.cuomo@dica.unict.it

Summary: A stress recovery method for planar bi-material interfaces is based on the double minimization of an objective function, representing the error between the inter-element stress tractions along the mesh-lines converging at an element node and the projection along the same planes of the best-fit stress tensor T. An application is presented, showing significant improvement in terms of computational efforts and accuracy of the results, in comparison with other *standard* stress recovery methods.

Introduction

The stress state along planar bi-material interfaces is required in the analysis of heterogenous materials or of multi-body structures. For example, in the meso-mechanical fracture analysis of concrete, the stress state along mortar-aggregate interfaces is needed to verify the failure conditions, and thus if a crack can start opening or not.

Several nodal stress recovery "smoothing" procedures have been proposed in the literature. Evaluating directly stresses at the nodes of each element, or using the stress at the Gauss points, in any case requires then some kind of averaging since stresses are in general different for elements sharing the same node. These averages may incorporate weights based on distances, contributing areas or angles, etc. Other more complicated methods such as "generalized inversion" [1, 2] work better at interior and exterior nodes, but, due to their computational requirements, can only be performed with regard to part of the mesh. The calculation of the stress state at all the mesh points, for large meshes, may require a computational effort higher than the one needed for the FE analysis itself.

The stress scenario becomes more complicated at a bi-material interface, in which, following intuitive understanding, two different stress tensors must exist, one for each material. The stress situation at both sides of the bi-material interface is the one presented in Fig. 1, in which two elementary cubes of different materials are presented. Across the interface, equilibrium conditions ensure the identity of the traction vectors on both surfaces in contact. Along the other directions, stress tractions may differ, as shown in the figure. The inhomogeneity, therefore, implies the existence of two different Mohr circles, one for each material.

In the literature, the stress state along bi-material interfaces is also obtained through the *ad-hoc* insertion of zero-thickness interface elements within the FE mesh. These elastic elements are extremely stiff, in order not to affect the response of the overall structure, and their easy implementation in the context of the FEM makes it possible to obtain the stress state along the interface without any additional post-processing. However, the insertion of an interface element implies node-duplication, that leads to an increase in the number of d.o.f. and, consequentially, to additional computational costs.

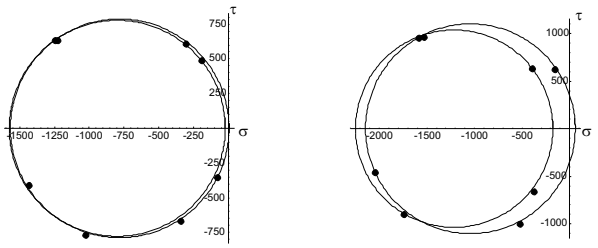

Figure 1: Stress state along a planar bi-material interface.

The main objective of the work described in this paper is to show the advantages in terms of accuracy and efficiency of a recently developed stress recovery method [3].

Formulation

Element nodal forces (instead of the traditionally used stress tractions at Gauss points) around the node (from now on, node A) at which the stress state has to be computed represent the input data for the proposed procedure. Denoting with $\mathbf{T}_1$ the stress tensor at node A relative to material 1, with $\mathbf{T}_2$ the stress tensor relative to material 2 and with $\mathbf{t}^{(k)} = (\sigma^{(k)}, \tau^{(k)})$ the stress traction along each mesh line concurrent to node A, an objective function Φ, inspired on microplane model [4], can be written as sum of two contributions, $\Phi = \Phi_1 + \Phi_2$, with:

$$\begin{array}{l} \Phi_1 = \sum_{k=1}^{N_1} [(\sigma_1^{(k)} - \boldsymbol{n}^{(k)} \mathbf{T}_1 \boldsymbol{n}^{(k)})^2 + (\tau_1^{(k)} - \boldsymbol{t}^{(k)} \mathbf{T}_1 \boldsymbol{n}^{(k)})^2] \\ \Phi_2 = \sum_{k=1}^{N_2} [(\sigma_2^{(k)} - \boldsymbol{n}^{(k)} \mathbf{T}_2 \boldsymbol{n}^{(k)})^2 + (\tau_2^{(k)} - \boldsymbol{t}^{(k)} \mathbf{T}_2 \boldsymbol{n}^{(k)})^2] \end{array} . \quad (1)$$

being N_1 and N_2 the number of mesh-lines respectively on the side of material 1 and material 2, and $(\mathbf{n}^{(k)}, \mathbf{t}^{(k)})$ the normal and tangential direction vectors on each mesh line. The function Φ represents the error between the projection of the stress tensors $\mathbf{T}_1$ and $\mathbf{T}_2$ along each mesh-line and the unknown stress tractions along the same planes. Note that in equation 1 the unknowns are the components of the stress tensors $\mathbf{T}_1$ and $\mathbf{T}_2$ and the stress tractions along $N_1 + N_2$ planes. With the use of equilibrium equations at each element node between the nodal

forces and the nodal inter-element forces (assumed to be equal to the stress tractions multiplied times a contributive area), the numbers of the unknown in equation 1 reduced to 2. A double minimization procedure allows to compute the remaining unknowns, leading to a linear 2x2 system. Further details on the formulation can be found in [3].

Example

The example reported in this section represents a concrete structure on a rock foundation. The stress state at node A of the bi-material interface is studied (see Fig. 2). This example is purely academic and it is meant to show only qualitatively the results of the proposed method. The mesh is made of 6-node quadratic triangular elements. The applied boundary conditions are illustrated in (Fig. 2) (also the weight of the structure and of the foundation are taken into account). Both materials are linear elastic. Two applications have been carried out: the first a) in which the rock Young modulus E_r is set equal to twice the modulus E_c of the concrete, and a second in which E_r is 200 times E_c.

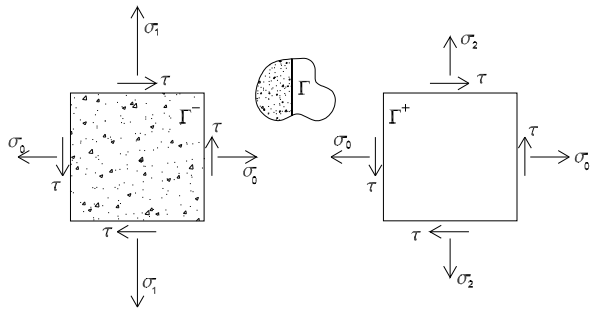

Figure 2: On the left, stress tensors for case a: $E_r \simeq E_c$; on the right, stress tensors for case b: $E_r \gg E_c$.

The Mohr's circles and the stress tractions (the black dots) for each case are reported in (Fig. 3). For $E_r \simeq E_c$ the two stress tensor T_1 and T_2 are similar. For $E_r \gg E_c$ one can appreciate two different stress tensors.

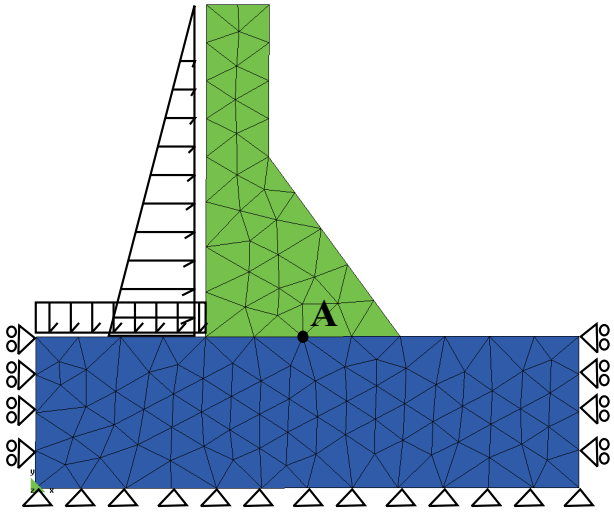

Figure 3: FE mesh and boundary conditions of the proposed example.

Comparison with other procedures

Due to the low computational costs of this method (it only requires the solution of a linear 2-equation system), the obtained solution for case b) has been compared with another computationally simple procedure, i.e. the average of the stresses at the Gauss point surrounding the node at the bi-material interface. Table 1 shows the ratio between the average-stresses and the stresses obtained by using the proposed method. The continuity along the vertical direction of the stress field is not ensured by the Gauss average method, i.e. $\sigma_{y\_c} \neq \sigma_{y\_r}$ and $\tau_{xy\_c} \neq \tau_{xy\_r}$.

Table 1: Comparison between the proposed procedure and the Gauss stress average method

	$\frac{\sigma_{xGauss}}{\sigma_x}$	$\frac{\sigma_{yGauss}}{\sigma_y}$	$\frac{\tau_{xyGauss}}{\tau_{xy}}$
concrete	0.7755	1.0240	1.1620
rock	0.8211	1.0078	0.8022

The results obtained by inserting zero-thickness very stiff interface elements along the bi-material interface coincide with those obtained by using the proposed formulation. However, the insertion of the interface implies the duplication of nodes where the interfaces are inserted, and this represents a further computational effort.

Acknowledgments

The first author wishes to thank the support received by programme *Juan de la Cierva* from MEC, Spain. The second author acknowledges research Grants MAT2003-02481 and BIA2006-12717 also from MEC. Research project 2004/33 from MFOM (Madrid) is also gratefully acknowledged.

References

[1] T. J. R. Hughes (1987): *Finite element method - Linear static and dynamic finite element analysis.* Prentice-Hall.

[2] B. Boroomand, O. C. Zienkiewicz (1997): Recovery by equilibrium patches. *International Journal for Numerical Methods in Engineering* **40**, 137–164.

[3] D. Ciancio, I. Carol, M. Cuomo (2006): On inter-element forces in the FEM-displacement formulation, and implications for stress recovery. *Int. J. for Numerical Methods in Engineering* **66**, 502–528.

[4] I. Carol, P. Prat, Z. Bazant (1992): New explicit microplane model for concrete: theoretical aspects and numerical implementation. *International Journal of Solids and Structures* **29**, 1173–1191.

Modeling of Cohesive Fracture Processes by Intra-Element Interfaces

M. Cuomo*, L. Contrafatto, M. Micciché

Department of Civil and Environmental Engineering
University of Catania, Italy
mcuomo@dica.unict.it, lcontra@dica.unict.it

Summary: A formulation of the SDA method is given that allows its application with damage interface elements. The extension is useful for generalising the method to more complex cracking phenomena and to heterogeneous materials.

Introduction

The occurrence of discontinuities in the displacement field within the framework of quasi brittle materials (cohesive fracture) can be effectively modeled by means of interface elements, equipped with a suitable constitutive behaviour. Interface elements, however, suffer of several drawbacks: the impossibility of having continuous stress fields; the need to introduce conventional elastic relative displacements, unless special damage models are used; furthermore, it is questionable whether the solution converges upon refinement of the mesh, that usually modifies the measure of the surface where relative displacements occur.

Interelement discontinuities are very useful for modeling physical interfaces between two materials, in this case, moreover, elastic displacements are often observed, like occurs when the surfaces are glued together. Discontinuities within a single phase can be more effectively described by means of models that incorporate the kinematics of strong discontinuities, like the so-called Elements with Embedded Discontinuities [1],[2] or the eXtended Finite Element Method.

Main goal of this paper is to develop a FE formulation of Strong Discontinuities that allows a consistent introduction of an interface constitutive model completely analogous to the one used in interface elements, so that the two formulations can be used simultaneously for modeling different physical situations. For obtaining this result, we had to extend a recently proposed algorithmic framework [3] based on the formal analogy with the theory of classical plasticity to the case of damaging materials. This was done through a different interpretation of the L_2 orthogonality condition for the enhanced strains.

The model proposed can be extended to handle the case of bimaterial interfaces and multiple cracks by means of a suitable choice of the kinematic fields.

Kinematics and constitutive laws

In this section a short summary of the kinematics associated with the Strong Discontinuity Approach (SDA) is given. For further details, refer to [2]. Let $\Omega \subset \Re^3$ be a domain and S a surface dividing the domain Ω into two parts Ω^+ and Ω^- along which the displacement field can be discontinuous, according to the format

$$\mathbf{u}(\mathbf{x},t) = \bar{\mathbf{u}} + H_S[\![\mathbf{u}]\!](\mathbf{x},t) \tag{1}$$

where H_S is the Heaviside function related to the surface S and $\bar{\mathbf{u}}, [\![\mathbf{u}]\!]$ are two continuous and regular functions. The linearized strain tensor is obtained as

$$\varepsilon(\mathbf{x},t) = \nabla^S \mathbf{u}(\mathbf{x},t) = \nabla^S \bar{\mathbf{u}} + \nabla^S [\![\mathbf{u}]\!] H_S + ([\![\mathbf{u}]\!] \otimes \mathbf{n})^S \delta_S \tag{2}$$

where it has been applied the generalized derivative to the Heaviside function and δ_S represents the Dirac delta distribution with respect to the surface S.

An alternative form more useful for the finite element approximation of the SDA [2] is obtained introducing a regular function $\phi(\mathbf{x}) \in [0,1]$ fulfilling the conditions

$$\phi(\mathbf{x}) = \begin{cases} 1, & \mathbf{x} \in (\Omega \backslash \Omega_\phi) \cap \Omega^+ \\ 0, & \mathbf{x} \in (\Omega \backslash \Omega_\phi) \cap \Omega^- \end{cases} \tag{3}$$

so that the displacement field becomes

$$\mathbf{u}(\mathbf{x},t) = \hat{\mathbf{u}}(\mathbf{x},t) + [\![\mathbf{u}]\!](\mathbf{x},t)\,(H_S - \phi(\mathbf{x})) \tag{4}$$

with $\hat{\mathbf{u}} = \bar{\mathbf{u}} + [\![\mathbf{u}]\!]\phi(\mathbf{x})$. The deformation field can then be written

$$\begin{aligned} \varepsilon(\mathbf{x},t) = \quad & \nabla^S \hat{\mathbf{u}}(\mathbf{x},t) + \nabla^S [\![\mathbf{u}]\!](H_S - \phi(\mathbf{x})) \\ & \underbrace{- ([\![\mathbf{u}]\!] \otimes \nabla\phi(\mathbf{x}))^S + ([\![\mathbf{u}]\!] \otimes \mathbf{n})^S \delta_S}_{\gamma} \end{aligned} \tag{5}$$

In the applications we shall take a constant jump field $[\![\mathbf{u}]\!](\mathbf{x})$, so that the second term in (5) will be dropped from now on. The deformation field in the continuum is thus given by the sum

$$\varepsilon(\mathbf{x},t) = \nabla^S \hat{\mathbf{u}}(\mathbf{x},t) - ([\![\mathbf{u}]\!] \otimes \nabla\phi(\mathbf{x}))^S = \hat{\varepsilon}(\mathbf{x},t) - \bar{\varepsilon}(\mathbf{x},t) \tag{6}$$

The previous relation can be interpreted in the sense that the total compatible deformation $\hat{\varepsilon}$ is obtained as sum of two contributions, the deformation of the bulk of the body, ε, and the anelastic deformation related to the displacement discontinuity, that can be interpreted as a plastic distortion of the continuum. Therefore separate constitutive laws have to be assigned for the continuum and for the occurrence of the jump.

In order to account for a non linear material evolution, a generalised damage model is adopted according to [4], introducing the internal damage variable ω, conjugated to the damage energy ζ. The constitutive equations are thus obtained from internal energy and dissipation functionals, $\phi(\varepsilon_e, \omega_e), d(\varepsilon_p, \bar{\omega}_p)$ for the continuum, and $\phi_S([\![\mathbf{u}]\!]_e), d_S([\![\mathbf{u}]\!]_p, \alpha_p, \omega_p)$ for the interface. In this work it is assumed that the continuum is elastic, and that the the discontinuity derives from energy dissipation

on the interface. The constitutive equations in the continuum are thus

$$\begin{aligned} \sigma = &\quad \partial_\varepsilon \phi(\varepsilon_e, \omega_e) \\ \zeta = &\quad \partial_\varepsilon \phi(\varepsilon_e, \omega_e) \end{aligned} \tag{7}$$

where $\omega_e = 0$ throughout the whole deformation process.

The anelastic displacement jump is obtained from the activation condition of the interface, for which it is adopted the one proposed in [5], of the form

$$f(\mathbf{t}_n, \zeta_S) = \tau^2 + 4\mu^2(\sigma_k - \sigma - \zeta_S)(\zeta_S - \zeta_{S_0}) = 0 \tag{8}$$

The condition (8) represents an activation condition in the space of the surface stress acting on the surface S, and ζ_S rule the evolution of the limit surface. The condition has been used for modeling fibre reinforced concrete.

Weak formulation

The original implementation of the SDA according to Simo et al., is based on the EAS concept. Following this methodology, the starting point of the formulation can be taken as the mixed multi-fields functional Π. In the classical form it is written as (the generalisation to internal variables can be found in [6]

$$\begin{aligned} \Pi(\hat{\mathbf{u}}, \sigma, \gamma, \varepsilon) = &\int_\Omega \sigma \cdot \nabla^S \hat{\mathbf{u}} d\Omega + \int_\Omega \sigma \cdot \gamma d\Omega - \int_\Omega \sigma \cdot \varepsilon d\Omega \\ &- \int_\Omega \rho b \cdot \hat{\mathbf{u}} d\Omega - \int_\Gamma t^* \cdot \hat{\mathbf{u}} d\Gamma + \Phi(\eta_e) + d_S^c(\mathbf{t}_S^n)\delta_S \end{aligned} \tag{9}$$

The classical equations of SDA are obtained under the hypotheses (not necessary, however) that the jump field $[\![\mathbf{u}]\!]$ be constant. After some algebra, they are:

$$\begin{aligned} &\int_\Omega \sigma \cdot \nabla^S \delta\hat{\mathbf{u}} d\Omega = \int_\Omega \rho b \cdot \delta\hat{\mathbf{u}} d\Omega + \int_\Gamma t^* \cdot \delta\hat{\mathbf{u}} d\Gamma \\ &\partial\phi^c(\sigma) = \nabla^S \hat{\mathbf{u}} - ([\![\mathbf{u}]\!] \otimes \nabla\phi)^S \\ &[\![\mathbf{u}]\!] \in \partial d_S^c(\sigma\mathbf{n}) \\ &\frac{1}{V_e}\int_{\Omega_e} \sigma\mathbf{n} d\Omega = \frac{1}{A_S}\int_S \mathbf{t}_S dS \end{aligned} \tag{10}$$

The last equation is obtained taking a Petrov-Galerkin approximation of the incompatible strain in the orthogonality condition between stresses and enhanced strain.

From (9) using a self-equilibrated stress field (that is, one such that $\int_\Omega \tau_0 \cdot \nabla^S \hat{u} d\Omega = 0$), it is clearly seen that the enhanced deformation field γ is non compatible. Equations (10) can be solved at element level by means of a return algorithm (see [6] for details)

Numerical results

The model can be applied to a broad range of different material failures such as mode I, mode II and mixed mode. The model has been implemented in a 4-node bilinear plane stress element using FEAP.

The results of a three point bending test on a notched concrete beam are presented in Fig.1. The test is performed prescribing the vertical displacement. The analysis has been repeated for two different specimens whose dimensions are 2900×600 mm and 1450×300 mm with thickness $t = 150$ mm. The results obtained with the implemented SDA model are compared with those given by a continuum damage model with element regularisation. Fig. 2 shows the distribution of the internal variable representing the crack width for the 2900×600 mm specimen.

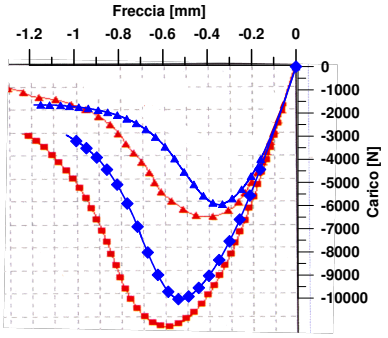

Figure 1: 3-point bending test - displacement of center beam

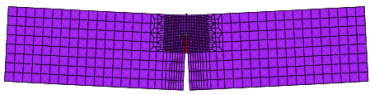

Figure 2: 3-point bending test - opening displacements

References

[1] J. Simo, J. Oliver, F. Armero (1993): An analysis of strong discontinuities induced by strain softening in rate independent inelastic solids. *Computational Mechanics*, **12**, 277–296.

[2] J. Oliver (1996): Modelling of strong discontinuities in solid mechanics via strain softening constitutive equations. Part 2: Numerical simulation. *International Journal for Numerical Methods in Engineering*, **39**, 3601–3623.

[3] J. Mosler (2004): On the modeling of highly localized deformations induced by material failure: The strong discontinuity approach. *Archives of Computational methods in Engineering*, **11**, 389–446.

[4] L. Contrafatto, M. Cuomo (2002): A new thermodinamically consistent continuum model for hardening plasticity coupled with damage. *International Journal of Solids and Structures*, **39**, 6241–6271.

[5] M. Cuomo (2002): An interface model for fibre reinforced concrete. In *Analytical and Computational Fracture Mechanics of Non-homogeneous Materials*, ed. B. Karihaloo, Kluwer, 395–400.

[6] M. Micciché (2006): *Modeling of cohesive fracture processes through embedded discontinuities.* PhD Thesis, University of Catania.

Sequentially Linear Analysis of Discrete Cracking in Masonry Panels

J. G. Rots[1], **S. Invernizzi**[2*]

[1]Faculty of Civil Engineering & Geosciences and Faculty of Architecture, Delft University of Technology
PO Box 5043, 2600 GA Delft, The Netherlands
j.g.rots@tudelft.nl

[2]Dipartimento di Ingegneria Strutturale e Geotecnica, Politecnico di Torino
Corso Duca degli Abruzzi 24, 10129, Torino, Italy
stefano.invernizzi@polito.it

Summary: In the present paper, the sequentially linear approach is extended and implemented for a particular class of finite elements useful in describing discrete rather than smeared fracture, namely the so called interface elements. Some details are given about the general formulation and the required regularization. Applications to plane concrete cracking and masonry panels are briefly outlined.

Introduction

The sequentially linear approach in modeling strain softening materials and structures has recently been demonstrated to be effective especially when the ratio between the elastic energy stored and the energy that can be dissipated by fracture is large, i.e. in the case of real-scale structures [1,2]. The model simulates the resulting peaks and local snap-backs effectively. The model replaces the downward stress-strain curve by a saw-tooth curve, either saw-tooth tension- softening for unreinforced material or saw-tooth tension stiffening for reinforced material. A linear analysis is performed, the most critical element is traced, the stiffness and strength of that element are reduced according to the saw-tooth curve, and the process is repeated. The sequence of scaled critical steps provides the global load displacement response.

Basic interface formulation

The general approach is almost identical to the one followed to implement the smeared cracking [1]. This time, the structure is discretized using both standard elastic continuum elements and interface elements where potential cracks can arise. Young's modulus and Poisson's ratio are assigned to the continuum elements, while the initial stiffness and strength are given to interface elements. Subsequently, the following steps are sequentially carried out:

- Add the external load as a unit load.
- Perform a linear elastic analysis.
- Extract the 'critical element' from the results. The 'critical element' is the interface element for which the stress level divided by its current strength is the highest in the whole structure.
- Calculate the ratio between the strength and the stress level in the critical element: this ratio provides the 'global load factor'. The present solution step is obtained rescaling the 'unit load elastic solution' times the 'global load factor'.
- Increase the damage in the critical element by reducing its stiffness and strength, i.e. the interface stiffness k_n and tensile strength f_t, according to a saw-tooth constitutive law as described in the next section.
- Repeat the previous steps for the new configuration, i.e. rerun a linear analysis for the structure in which k_n and f_t of the previous critical element have been reduced. Trace the next critical saw-tooth in some element; repeat this process until the damage has spread into the structure to the desired level.

The way in which the stiffness and strength of the critical elements are progressively reduced constitutes the essence of the model. In other words, it is necessary to provide a saw-tooth approximation of the cohesive stress-displacement relation.

The modeling of geometrical discontinuities, like discrete cracks in concrete or joints in rock and masonry, can be conveniently done with multipurpose structural interface elements. These elements relate the tractions acting on the interface to the relative displacements of the two sides of the interface.

The adopted constitutive law for discrete cracking is based on a *total deformation* theory, which expresses the tractions as a function of the total relative displacements, the crack width Δu_n and the crack slip Δu_t (Fig. 1).

The generic intersection between the secant starting from the origin and the softening curve is obtained solving:

$$k_{n.i}\Delta u^+_{n.i} = D\left(\Delta u^+_{n.ult} - \Delta u^+_{n.i}\right) \tag{1}$$

where, the superscript + refers to the uplifted softening curve. This uplift is necessary to guarantee the mesh size objectivity. The amount of the uplift is determined further in order to keep the area underneath the softening curve equal to the fracture energy regardless the number of teeth. D is the so-called softening modulus. In the present case, for linear softening:

$$D = \frac{f_t}{\Delta u_{n.ult} - f_t/k_n} \tag{2}$$

Equation (1) provides the generic crack opening:

$$\Delta u^+_{n.i} = \Delta u^+_{n.ult}\frac{D}{k_{n.i} + D} \tag{3}$$

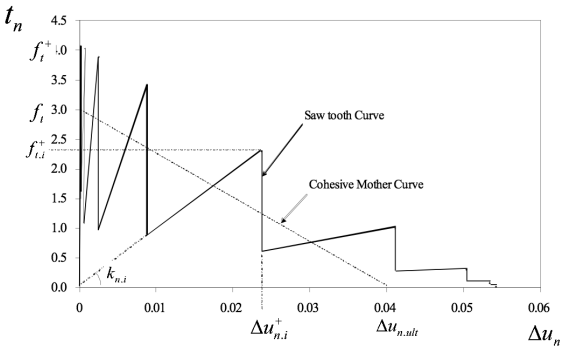

Figure 1: Saw-tooth softening curve with stepwise reduction of the interface stiffness. Ten teeth approximation with a = 4, and p = 36%.

Consequently, the generic uplifted strength becomes:

$$f_{t,i}^+ = \left(\Delta u_{n.ult} + p\frac{f_t}{D}\right) k_{n.i}\frac{D}{k_{n.i}+D} \tag{4}$$

where p is the percentage of the softening curve uplift. If we adopt a stepwise reduction of the interface stiffness, the rule to update k_n becomes:

$$k_{n.i+1} = \frac{k_{n.i}}{a} \tag{5}$$

where a is a constant factor. The choice of the magnitude of a is an important issue for the method, and is performed depending of the ultimate crack opening. For instance, if a is chosen to be too small, then all the teeth concentrate in the upper part of the softening mother curve. The adequate choice depends on the values of initial dummy stiffness, the strength and the fracture energy.

The area beneath the saw-tooth softening can be expressed as:

$$A^+ = \sum_{i=0}^{N-1} A_i^+ = \sum_{i=0}^{N-1} \frac{1}{2}\Delta u_{n.i}^+ f_{t.i}^+ b_i \tag{6}$$

In order to achieve the mesh size objectivity it is sufficient to prescribe that:

$$A^+ = G_f^I \tag{7}$$

which, after some algebraic manipulations, provides the optimal amount of the softening curve uplift.

Applications

A symmetric notched beam of total length 500 mm; span 450 mm; height 100 mm; thickness 50 mm and notch depth 10 mm was selected for analysis. The distance between the loading points in the symmetric four-point loading scheme is 150 mm. Interface elements are placed in the central section, where experimentally the crack takes place. Five different meshes were used, referred to as very coarse, coarse, medium, fine and very fine. Results are shown in Fig. 2.

The behaviour of a masonry wall (Fig. 3) subjected to non-proportional normal and shear load can also be analyzed. In this case, the issue of non-proportional loading must be considered, which implies some differences compared to the standard sequentially linear approach. The masonry texture is represented using interface elements for the mortar joints and the potential cracks in the blocks. The scaling algorithm traces the most critical interface elements and discrete cracks open up consecutively. The system is always positive definite due to the saw-tooth ascending diagrams, providing a solution at each step without difficulties. Contrarily, in the nonlinear analysis the negative tangent stiffness requires a cumbersome choice of increments and steering parameters, and optimal convergence could not be achieved throughout the process, even though arc-length techniques are used.

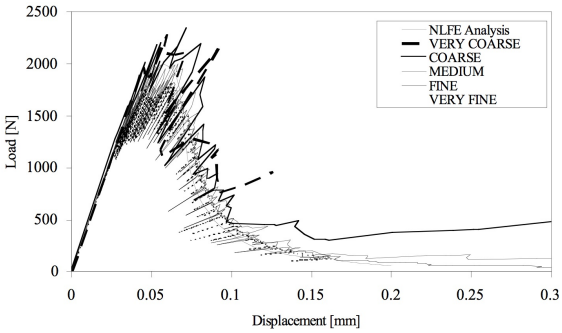

Figure 2: Linear softening with stepwise reduction of the interface stiffness, N =10, all the meshes.

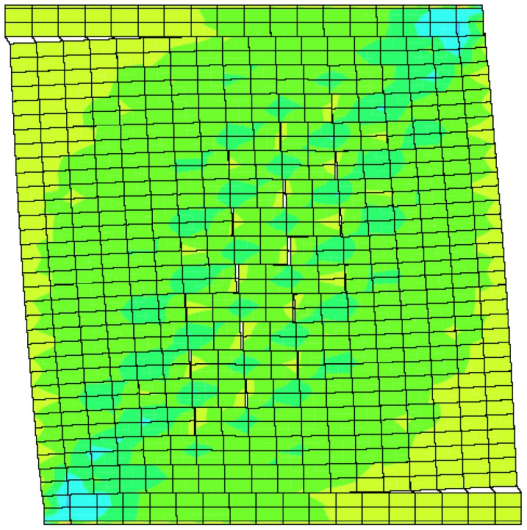

Figure 3: Shear stresses in the masonry wall subjected to compression and shear.

References

[1] J. G. Rots (2001): Sequentially linear continuum model for concrete fracture. In *Fracture Mechanics of Concrete Structures*, R. de Borst, J. Mazars, G. Pijaudier-Cabot, J.G.M. van Mier (Eds). Balkema, Lisse, 831–839.

[2] J. G. Rots, S. Invernizzi (2004): Regularized sequentially linear saw-tooth softening model. *Int. J. Numer. Analytical Methods Geomech.*, **28**, 821–856.

Part IV

Parameter Identification and Inverse Analysis

Probabilistic Aspects for Heterogeneous Materials Failure

M. Hautefeuille, J. B. Colliat*, S. Melnyk, A. Ibrahimbegović

Ecole Normale Supérieure de Cachan, LMT
61, avenue de président Wilson, 94235 Cachan, France
e-mail: {colliat,hautefeuille}@lmt.ens-cachan.fr

Summary: In order to describe accurately the behavior of heterogeneous building material, an identification of stochastic parameters of material properties is here proposed in order to both take into account the heterogeneity and the intrinsic randomness of such materials. Using a stochastic description of the meso structure and simple Monte Carlo method, we propose a framework to compute statistics of material properties governing the failure of cement based media.

The domain of numerical analysis for ultimate load behavior Civil Engineering structures leads to many important issues, among them the modeling of heterogenous materials. Cement-based materials, such as concrete or mortar, can be modelled at different scales, depending on the objectives and the physical mechanisms to be accounted for. Namely, for engineering applications and computations at the structure scale (macro-scale), such materials might be considered as homogeneous, and their properties obtained by using the key concept of RVE (see [1, 2]) to obtain phenomenological models of inelastic behavior (e.g. see [3, 4, 5]) The main advantage of those models is their robustness and small computational cost, hence this approach is widely spread. On the other hand, such phenomenological models are based on a set of ”material” parameters which ought to be identified, mainly from experiments performed with prescribed load paths. This methodology leads to a set of parameters which is linked to the chosen load-path, which will not be adapted to another path, thus leading to a non-predictive macro-model.

In order to overcome this major drawback many authors tried to furnish micro-mechanical basis to the macroscopic model set of parameters (see [6, 7])and provide a more predictive model. One way to achieve this goal is to employ homogenization methods leading to accurate results for linear problems. In case of non-linearities such methods are not providing good estimates for the effective (macroscopic) properties (see [8]). Moreover such approach do not take into account the inherent uncertainties attached to heterogeneous materials.

Considering a small scale, this variability might be viewed from the geometrical point of view through the stochastic description of the meso-structure. In this work we propose to compute the macroscopic parameters for a porous media as well as their statistics by taking into account the variability of the meso-structure. The key point is that the material parameters at this level are assumed to be deterministic, so that the variability is only related to the size and the positions of the voids.

Moreover, meshing is one of the major issue in modeling heterogeneous two-phase materials and frequently leads to undesirably high number of degrees-of-freedom and distorted meshes. For that reason, the meshing process might require a complex and time-consuming algorithm and, more importantly, produce the set of discrete equations which is poorly conditioned. In this section, we present another approach by using structured (regular) meshes which are not constrained by the physical interfaces between different phases. The key ingredient for providing such models are field discontinuities introduced inside the elements in which the physical interfaces are present. The latter can be developed as the kinematics enhancements which belong within the framework of the Incompatible Modes Method (see [9, 10]). This model relies on classical CST elements, whose kinematics description is enriched by the use of strain and displacements discontinuities in order to represent two phases.

In order to solve this stochastic problem and compute the statistical moments for the response quantities, we employ the Monte-Carlo method within a distributed software environment. This stochastic integration method is based on many evaluations of the meso-structures responses thus leading to a time-consuming process. Moreover, as the error can directly be evaluated in terms of the number of realizations, it is necessary to choose a relatively small discrete problem, even in the case of complex meso-structures. Using the Components Template Library (CTL) and the Finite Elements code FEAP we produced 9999 realizations. The statistics of the outcome properties exhibit quite narrow confidence intervals. These numerical results can then be viewed as macroscopic properties for this porous media within the context of a classical phenomenological model.

References

[1] M. Bornert, T. Bretheau and P. Gilormini (2001): *Homogéneisation en mécanique des matériaux*, volume I, II, Hermes-Science, Paris.

[2] T. Kanit, S. Forest, I. Galliet, V. Mounoury and D. Jeulin (2003): *Determination of the size of the representative volume element for random composites: Statistical and numerical approach*, International Journal of Solids and Structures, **40**, 3647–3679.

[3] O. C. Zienkiewicz and R. L. Taylor (2005): *The Finite Element Method, 6th edition, Volumes 1 and 2*, Elsevier, Oxford.

[4] K.J. Bathe (1996): *Finite Element Procedures*, Prentice Hall.

[5] A. Ibrahimbegovic (2006): *Nonlinear Computational Solid Mechanics*, Hermes-Science Publication, Paris, in French.

[6] D. Markovic, A. Ibrahimbegovic (2004): *On micro-macro interface conditions for micro-scale based fem for inelastic behavior of heterogeneous material*, Computer Methods in Applied Mechanics and Engineering.

[7] P. Ladevéze, O. Loiseau and D. Dureisseix (2001): *A micro-macro and parallel computational strategy for highly heterogeneous structures*, International Journal for Numerical Methods in Engineering.

[8] P. Gilormini (1995): *A shortcoming of the classical nonlinear extension of the self-consistent model*, C.R. Acad. Sci. Paris, **320**, 115–122.

[9] E.L. Wilson, R.L. Taylor, W.P. Doherty, J. Ghaboussi (1973): *Incompatible displacement models*, Numerical and Computer Methods in Structural Mechanics, 43–57, Academic Press, New York.

[10] A. Ibrahimbegovic, E.L. Wilson (1991): *A modified method of incompatible modes*, Communications in Applied Numerical Methods, **7**, 187–194.

Multiple Cracking in Cementitious-Matrix Composites: Parameter Identification via Inverse Methods and Optical Full-Field Measurements

S. Bossuyt*, H. Cuypers

Vrije Universiteit Brussel, Department of Mechanics of Materials and Constructions
Pleinlaan 2, B-1050 Brussels, Belgium
sven.bossuyt@vub.ac.be. heidi.cuypers@vub.ac.be

Summary: Fibre-reinforced cement matrix composites typically exhibit non-linear constitutive behaviour in tension, due to multiple cracking in the matrix and load redistribution to the fibres. Parameter identification for multi-scale physics-based models, to fully describe important aspects of the multiple cracking behaviour, is hampered by the variability in effective local properties that results from the heterogeneous microstructure. To distinguish the effects of this variability from the behaviour of individual cracks, we augment collective load-displacement curves with data on separate cracks obtained using optical full-field techniques.

Multiple cracking model

In brittle matrix composites under tensile loading, fibres that bridge the cracks continue to carry increasing load after the maximum tensile strain of the matrix is reached. Thus, the matrix progressively cracks in multiple places, until the crack spacing is such that, at every crack, the gradual stress transfer at the fibre matrix interface is interrupted by the stress relief from the next crack before the strength of the matrix is exceeded [1,2]. This implies that the fiber-matrix interface is strong enough to prevent complete ”pull-out” of the fibers, but not so strong that the stress concentrations at the cracks in the matrix immediately break the fibers.

By impregnating textile reinforcements with a cementitious matrix—as opposed to mixing loose fibres into the cement—composites with high fiber volume fractions can be produced, providing significantly higher tensile load carrying capacity than the unreinforced cement. To design lightweight structures, efficiently using such composites, it becomes necessary to quantitatively predict the material behaviour in the multiple cracking and post-cracking regions, including cyclic loading and environmental effects [3,4].

One aspect of multiple cracking behaviour in cementitious-matrix composites, that quickly becomes apparent when comparing theory with experiment, is the variability in the effective local strength of the matrix material. This variability may be attributed to variations in material chemistry, residual stresses, or defect densities. Experiments and specimens may be designed to avoid the variability, and enable studies of specific phenomena one at a time. These are very useful to determine the functional form that a model of the phenomena should take. However, the material parameters determined on a model system may differ significantly from those of the corresponding material incorporated in the composite [5]. Therefore, in practical applications the parameters must be determined for the actual composite material that will be used.

Parameter identification

In the collective response of a heterogeneous material, the intrinsic behaviour is convoluted with the statistical distribution of local properties. Thus, a ‘blurred’ average of the intrinsic behaviour is observed in the stress-strain curve of textile-reinforced cement-matrix composites. As a result, it is no longer possible to simply read each model parameter from a clearly identifiable section of the curve. Instead, the parameters in the model are identified by an inverse method, optimizing the agreement between theory and experiment. Explicitly taking a statistical distribution of properties into account in the model requires additional parameters to characterize the distribution, but improves the agreement.

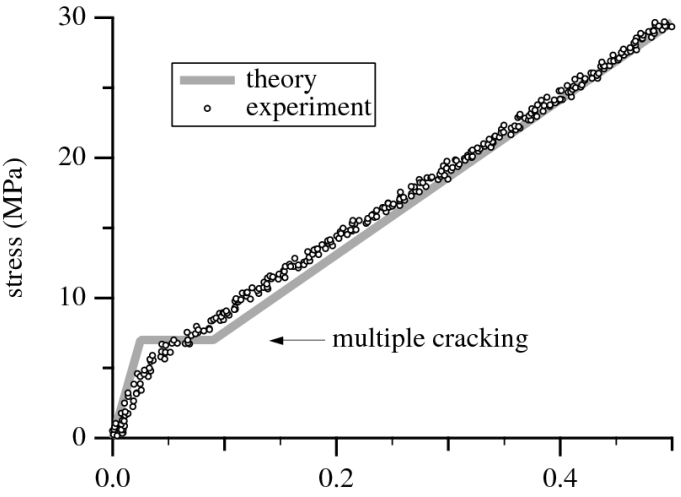

Figure 1: ACK model of multiple cracking in brittle matrix composites [2] with data for a glass-fibre reinforced inorganic phosphate cement.

Poorly conditioned sensitivity matrices indicate that different adjustments in the model parameters can give rise to very similar changes in the predicted collective behaviour. Those different adjustments may give very different results, however, when the model is used to extrapolate beyond the available experimental data. Durability of cement matrix composites in lightweight constructions provides a good example; accurate predictions will require multi-scale models of interacting mechanical and chemical degradation mechanisms. These mechanisms are more sensitive to details of the multiple cracking behaviour at the micro-scale, than the multiple cracking behaviour itself is to those details, especially when only the averaged collective

behaviour is considered. Experiments that distinguish the averaging effect of local parameter variations from the behaviour of individual cracks provide data that may be extrapolated with more confidence.

Optical full-field measurements

Optical methods that record displacements at a large number of discrete locations on the surface of a specimen under loading are enabling new developments in experimental mechanics. Full-field measurement results are very attractive for comparison with finite element calculations. When the deformation behaviour is relatively smooth and deterministic, quantitative comparison is possible, including full-fledged inverse methods for parameter identification [6]. Full-field data is even more useful when investigating localized deformation events, such as cracks, whose location is not known in advance. E.g., Electronic Speckle Pattern Interferometry [7] and Digital Image Correlation [8] have been used to characterize crack formation and propagation in stone and concrete.

In combination with conventional measurement of the collective load-displacement curve, these techniques —now applied on a much smaller length scale— can be used to characterize multiple cracking behaviour on multiple levels. Direct observations of the local displacement field surrounding the cracks can then be used to validate and augment the parameter identification methods based on the collective multiple cracking behaviour. By including a number of separate cracks in the optical field of view, statistical information on the variability of parameters is obtained even from a single experiment. In addition, the measurements provide boundary conditions and local information for models at the level of individual cracks. Thus, a multiscale mixed numerical-experimental characterization technique is envisioned, based on physical models of the relevant phenomena in a heterogeneous microstructure.

Acknowledgements

This work was funded by the Research Foundation – Flanders (FWO–Vlaanderen).

References

[1] J.Aveston, G.A.Cooper, A.Kelly (1971): Single and multiple fracture, The Properties of Fibre Composites. In *Proc. Conf. National Physical Laboratories*, IPC Science & Technology Press Ltd., London, 15–24.

[2] J. Aveston, A. Kelly (1973): Theory of multiple fracture of fibrous composites. *Journal of Materials Science*, **8**, 411–461.

[3] H. Cuypers (2001): Analysis and Design of Sandwich Panels with Brittle Matrix Composite Faces for Building Applications. *Doctoral thesis*, Vrije Universiteit Brussel, Brussels, Belgium.
`wwwir.vub.ac.be/memc/pdf/heidi_phd.pdf`

[4] H. Cuypers, J. Wastiels (2006): The effect of durability on the design of self-bearing sandwich panels with cementitious composite faces. In *Proc. 8th Int. Symp. On Brittle Matrix Composites*, Warsaw.

[5] H. Huypers, J. Wastiels (2006): Stochastic matrix-cracking model for textile reinforced cementitious composites under tensile loading. *Journal of Materials and Structures*, **39**, 777–786.

[6] D. Lecompte, A. Smits, H. Sol, J. Vantomme, D. Van Hemelrijck (2007): Mixed numerical-experimental technique for orthotropic parameter identification using biaxial tensile tests on cruciform specimens. *International Journal of Solids and Structures*, **44**(5), 1643–1656.

[7] K. De Proft, L. J. Sluys, W. P. De Wilde (2003): Combined experimental-numerical study to monotonic and cyclic behaviour of limestone. In *Damage and Fracture Mechanics*, Wessex Institute of Technology, UK.

[8] D.Lecompte, J.Vantomme, H. Sol (2006): Crack Detection in a Concrete Beam using Two Different Camera Techniques. *Structural Health Monitoring*, **5**, 59–68.

Identification of Quasibrittle Material Parameters Based on Stochastic Nonlinear Simulation and Artificial Neural Networks

D. Novák*, D. Lehký

Institute of Structural Mechanics, Faculty of Civil Engineering, Brno University of Technology
Veveří 95, 66237 Brno, Czech Republic
novak.d@fce.vutbr.cz, lehky.d@fce.vutbr.cz

Summary: A new approach of inverse analysis is proposed to obtain material parameters of a constitutive law for quasibrittle material in order to achieve the best agreement with experimental data. The inverse analysis is based on the coupling of a stochastic simulation and an artificial neural network (ANN). The identification parameters play the role of basic random variables with a scatter reflecting the physical range of potential values. A novelty of the approach is the utilization of the efficient small-sample simulation method Latin Hypercube Sampling (LHS) used for the stochastic preparation of the training set utilized in training the neural network. Once the network has been trained, it represents an approximation consequently utilized to provide the best possible set of model parameters for the given experimental data.

Introduction

The nonlinear numerical analysis requires the use of an appropriate and realistic material model. Generally, the more sophisticated model the more model parameters are needed. Basic parameters as compressive strength, modulus of elasticity, etc. are usually known. Typically, some other parameters, e.g. fracture energy, can be estimated using the recommended formulas from literature, but in most cases these formulas can be used only as a first approximation of the parameters. The objective is very often to find such a set of material parameters, which gives the best agreement between the simulated and experimental load-deflection curves.

A strong interest has been developed for formulating inverse analysis methods to determine the quasi-brittle fracture behaviour of concrete. There are basically two groups of inverse analysis techniques: (1) those that use the complete load-deflection curve of one specimen size and shape; (2) those that use the peak loads of specimens of different sizes and shapes capturing the size effect phenomenon.

The aim of this work is to describe a new methodology of inverse analysis based on the coupling of the stratified simulation of Monte Carlo type and artificial neural networks (ANN). The emphasis is mainly on: (1) the efficiency of the training set preparation for the neural network training using small numbers of simulations based on Latin Hypercube Sampling (LHS); (2) the multipurpose character of the methodology relatively easy to apply. Details can be found in papers, e.g. [1–3].

Methodology of the proposed inverse analysis

The proposed inverse analysis technique is based on the combination of the statistical simulation method of the Monte Carlo type and ANN. Fundamental scheme of the approach is shown in Fig. 1; ANN is trained by values of load-deflection curve and values of identified parameters (considered to be random variables) in repeated stochastic way—the preparation of training set for neural network uses stratified simulation.

The whole procedure is itemized as follows:

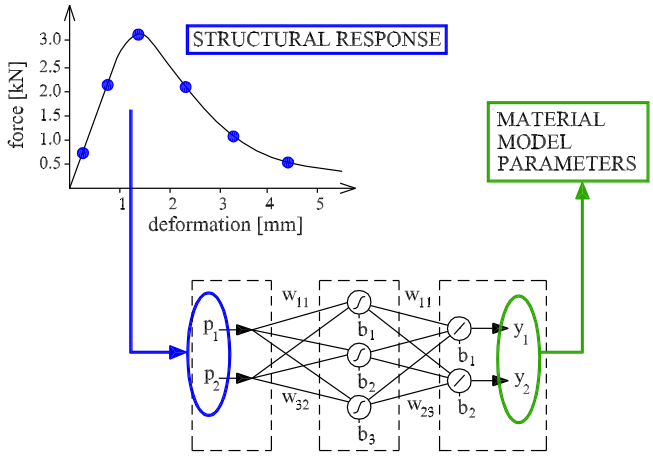

Figure 1: Scheme of inverse analysis.

1. Computational model has to be first developed using the appropriate FEM software (e.g. ATENA [4]) which enables modeling of both pre-peak and post-peak behavior. An initial calculation uses a set of initial material model parameters.

2. The parameters of a material model for identification are considered as random variables described by a probability distributions—rectangular distribution represents the bounded range of physical existence. These parameters are simulated randomly using LHS [5].

3. A multiple calculation of deterministic computational model using random realizations of material model parameters is performed resulting in a bundle of load-deflection curves (usually overlapping the experimental curve), Fig. 2.

4. Realizations of the load-deflection curves serve as a basis for training of an appropriate ANN. After the training procedure, ANN is ready for key task: to select the material model parameters which can capture the experimental load-deflection curve as close as possible.

5. Final calculation using the identified material parameters should verify how well the parameters were identified, Fig. 3.

Numerical examples

A traditional experiment of three-point bending of a notched plane concrete beam was performed in order to determine fracture parameters of concrete for the mass production of railway sleepers (specimens 80×80×480 mm). Parameters for identification were modulus of elasticity, tensile strength, compressive strength, fracture energy and compressive strain in the uniaxial compressive test. For stochastic training, randomness was introduced using the same coefficient of variation 0.15 and the rectangular probability distribution for all random variables. 20 simulations of LHS resulted in load-deflection curves presented in Fig. 2. This input-output information serves for the training of ANN: network with 20 inputs, one hidden layer consisting of 15 nonlinear neurons and one output layer of 5 linear neurons. Also the second alternative with only 3 output neurons (3 dominant material parameters) was used. Final calculation results using identified parameters are shown in Fig. 3. More details can be found in [1].

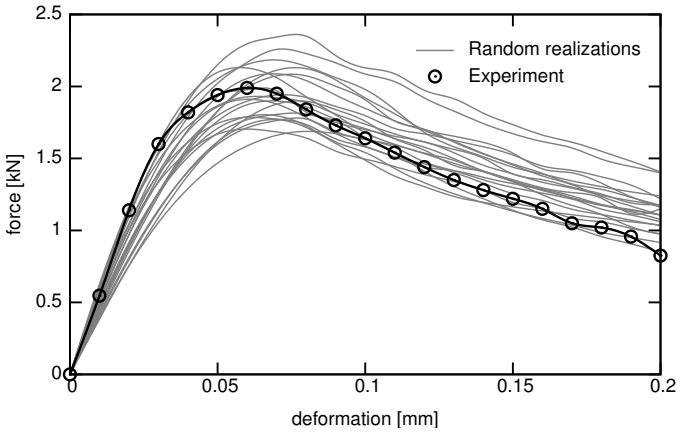

Figure 2: Random load-deflection curve realizations.

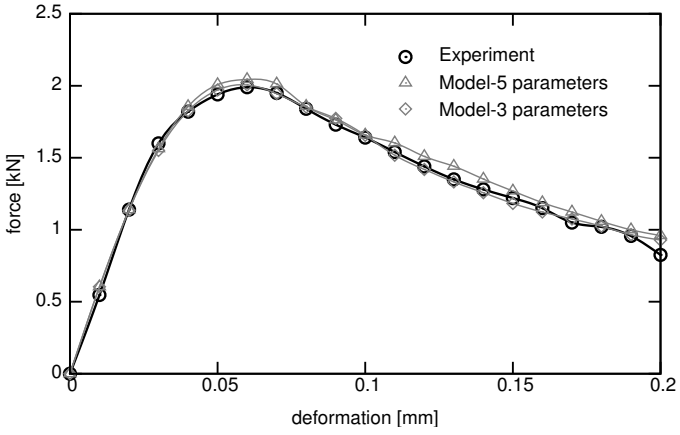

Figure 3: Load-deflection curves—experiment and numerical simulation using identified parameters.

Another example is the shear wall shown in Fig. 4 [6]. Loading by the vertical force was applied first to represent a dead load. Then a horizontal force was applied and increased to failure. The behavior during the experiment reported extensive diagonal cracking prior to failure followed by an explosive crushing of concrete. The experimental and simulated failure and a bundle of load-deflection curves used to train ANN in order to provide best estimates of 10 material parameters are shown in Fig. 4.

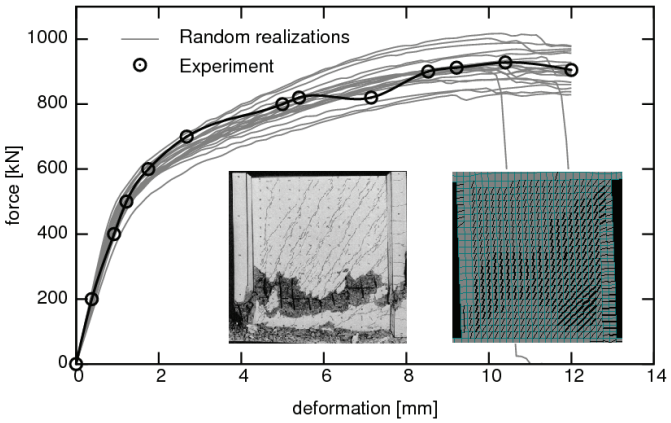

Figure 4: Random load-deflection curve realizations—20 simulations of LHS, experimental and virtual failure.

Acknowledgements

This research was conducted with the financial support of the Ministry of Education of the Czech Republic, project No. 1M680470001, within activities of the CIDEAS research centre. Authors acknowledge also the grants No.103/07/0760 and No.103/07/P380 from the Grant Agency of Czech Republic.

References

[1] D. Novák, D. Lehký (2006): ANN Inverse Analysis Based on Stochastic Small-Sample Training Set Simulation. *Journal of Engineering Application of Artificial Inteligence*, **19**, 731–740.

[2] D. Novák, D. Lehký (2004): Neural network based identification of material model parameters to capture experimental load-deflection curve. *Acta Polytechnica*, **44**, Prague, Czech Republic, 110–116.

[3] D. Lehký, D. Novák (2004): Probabilistic inverse analysis: Random material parameters of reinforced concrete frame. In 9^{th} *International Conference on Engineering Applications of Neural Networks (EAAN2005)*, Lille, France, 147–154.

[4] V. Červenka, R. Pukl (2005): *ATENA Program documentation*. Cervenka Consulting, Czech Republic.

[5] D. Novák, M. Vořechovský, R. Rusina (2007): *FReET—Feasible Reliability Engineering Tool, Users and Theory guides*. Brno/Cervenka Consulting, Czech Republic, http://www.freet.cz.

[6] V. Červenka, D. Novák, D. Lehký, R. Pukl (2005): Identification of shear wall failure mode. In *CD-ROM Proc. of* 11^{th} *Int. Conf. on Fracture*, Turin, Italy.

Parameter Identification of Continuum-Discrete Damage Model Capable of Representing Heterogeneous Strain Field in Localized Failure

A. Kučerová[1,3*], D. Brancherie[2], A. Ibrahimbegović[3], J. Zeman[1], Z. Bittnar[1]

[1]Czech Technical University in Prague, Faculty of Civil Engineering, Department of Mechanics
Thákurova 7, 166 29 Prague 6, Czech Republic
{anicka,zemanj}@cml.fsv.cvut.cz, bittnar@fsv.cvut.cz

[2]Université de Technologie de Compiègne, Laboratoire Roberval
BP 20529, 60205 Compiègne Cedex, France
delphine.brancherie@utc.fr

[3]École Normale Supérieure de Cachan, Laboratoire de Mécanique et Technologie
61, av. du président Wilson, 94235 Cachan, France
ai@lmt.ens-cachan.fr

Summary: The present paper deals with the parameter identification of the constitutive model introduced in [1] from the results of a three-point bending test. The model itself is capable of describing behavior of massive structures taking into account both the diffuse damage mechanisms as well as localized failure phenomena. As all parameters of the model have a clear physical meaning, the identification procedure can be split into a sequence of three problems, each related to a specific mode of the material behavior. The numerical optimization strategy is based on an adaptive approximation of the objective function by the Radial Basis Function Network dynamically evolved by minima located by a real-encoded genetic algorithm.

Introduction

Concrete is perhaps the most widely used construction material in Civil Engineering. It can be considered as a quasi-brittle material with very complex mechanical behavior. A model proposed in [1] is a typical example of relatively simple constitutive laws aimed at concrete-like materials. Despite its simplicity (only seven parameters are needed for a particular material), the model itself is capable of describing response of a massive quasi-brittle structure until the point of localized failure. Perhaps the most important advantage of the proposed model is the fact that all its parameters have a clear physical interpretation and can be straightforwardly visualized in terms of the shape of a stress-strain diagram. In addition, influence of each parameter is dominant only for specific, easily recognizable, stages of material behavior.

Identification procedure

In this paper, we discuss the identification of the model parameters from experimental measurements made on a structural level. Generally speaking, the complexity of the identification procedure is determined by the choice of the experimental setup. Solely from the identification point of view, the simplest experiment to execute is the uniaxial tensile test. In this case, the strain field stays mostly homogeneous during the whole procedure and the global response, represented by the load-displacement diagram, is very similar to the stress-strain curve for one material point. The model parameters can be then directly determined from the shape of the load-displacement curve. Such a uniform loading is, however, difficult and expensive to perform in a laboratory, especially for quasi-brittle materials. Therefore, other tests are often used in experimental practice.

The three-point bending test, in particular, is considered to be much simpler to perform and its results are well-reproducible. Therefore, we focus on the identification procedure for the proposed model parameters directly from the output of three-point bending test. The main difficulty is in this case imposed by heterogeneity of the stress and the strain fields, which is present since the very start of the experiment. The macro-scale measurements provide the load-deflection curve that integrates data from different parts of the specimen experiencing different regimes of (in)elastic behavior. For that reason, the possibility of a simple determination of model parameters from load-deflection curve is lost and an advanced calibration procedure needs to be applied.

To exploit the specific structure of the model, the identification procedure should be divided into three sequential stages. From the algorithmic point of view, the material calibration can be then understood as a sequential optimization problem. Such approach has two main advantages: first, solving three simpler identification steps in a batch form is typically much more efficient then the full-scale problem; second, it allows to use only a subset of simulations for initial stages of the identification process and also for latter stages, where new simulations can be started from the end points of diagrams identified in previous stages.

The gradient-based methods are usually considered to be the most computationally efficient optimization algorithms available. The accuracy of numerical approximation to the 'exact' sensitivities is driven by the choice of a pseudo-time step used in numerical simulations. Clearly, to reduce the computational time, the pseudo-time step should be used as large as possible. Therefore, the response-based objective function will not be smooth and gradient-based methods are unlikely to be very successful.

As an alternative, techniques of soft-computing can be employed for optimization of complex objective functions. For the current case, complexity of the optimization can be attributed rather to its non-smooth character than to the appearance of multiple optima; the family of problems where evolutionary algorithms are the most successful methods. This opens the way to more specialized tools, which deliver higher efficiency when compared to usually time-consuming evolutionary algorithms. The approach adopted in the present work is based on an adaptive smoothing of the objective function by the Radial Basis Function Network [3], dynamically evolved by minima located by a real-encoded genetic algorithm GRADE [2]. In the actual implementation, the identification process is decomposed into three stages: elastic stage, where Young's modulus E and Poisson's ration ν are determined; hardening stage, influenced by the limit stress $\bar{\sigma}_f$ and the hardening parameter K and the softening stage, which is governed also by the limit normal traction $\bar{\bar{\sigma}}_f$ and the softening parameter $\bar{\bar{\beta}}$. Once the parameters are determined from one stage, their values remain fixed during the remaining stages of the identification procedure. Of course, the sequential procedure inevitably leads to the accumulation of errors, which in turn requires setting the stopping precision to rather small values. This fact in documented by Table 1, storing the maximal and average errors calculated relatively to the size of the addmissible interval obtained from 100 independent optimization runs.

Table 1: Influence of stopping precision on accuracy of identified parameters.

Parameter	Stopping precision on F	Average error [%]	Maximal error [%]
E	10^{-5}	0.41	1.23
ν	10^{-5}	0.16	2.20
$\bar{\sigma}_f$	10^{-2}	0.87	2.58
K	10^{-2}	0.78	2.49
$\bar{\sigma}_f$	10^{-3}	0.30	0.59
K	10^{-3}	0.49	1.54
$\bar{\bar{\sigma}}_f$	10^{-2}	0.47	1.32
$\bar{\bar{\beta}}$	10^{-2}	2.34	12.21
$\bar{\bar{\sigma}}_f$	3×10^{-3}	0.33	0.67
$\bar{\bar{\beta}}$	3×10^{-3}	0.26	2.68

The effect of the increased accuracy is further documented by deviation of the "identified" curves from the reference one displayed in Fig. 1.

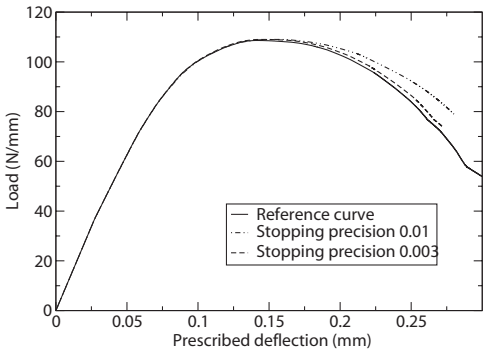

Figure 1: Comparison of load-deflection diagrams.

Conclusion

We have proposed a very straightforward identification procedure for the parameters of a constitutive model representing the localized failure of massive structures. The sequential identification approach has a clear link with the structure of the constitutive model. Due to the physical insight into the model, it was possible: first, to construct simple objective functions with a high sensitivity to the relevant parameters; second, to use only a part of the test simulation for each of three stages, which leads to substantial computational time savings. The non-smooth and non-convex objective functions were optimized by robust soft-computing methods. The proposed identification procedure was verified on 100 independent optimization processes executed for each objective function. In the worst case, the reliability of the algorithm is 76% due to very small number of objective functions calls set in the termination condition to 150 and high accuracy of searched values (smaller than 5%). The average number of function evaluations was smaller then 50 for all three stages of identification. The major difficulty of the proposed methods is to properly identify the three stages of structural behavior. From the point of view of method verification, where the reference load-deflection diagram is not noisy, the problem was successfully resolved. To fully accept the procedure, however, the experimental validation of the method appears to be necessary. For more details about proposed methodology we refer an interested reader to [4].

Acknowledgments: The financial supports for this work by the Czech Ministry of Education (research project MSM 6840770003) and the French Ministry of Research are gratefully acknowledged.

References

[1] A. Ibrahimbegović, D. Brancherie (2003): Combined hardening and softening constitutive model of plasticity: precursor to shear slip line failure. *Comp. Mech.*, **31**, 88–100.

[2] A. Ibrahimbegović, C. Knopf-Lenoir, A. Kučerová, P. Villon (2004): Optimal design and optimal control of elastic structures undergoing finite rotations. *Int. J. Num. Meth. Eng.*, **61**, 2428–2460.

[3] M. K. Karakasis, K. C. Giannakoglou: On the use of surrogate evaluation models in multi-objective evolutionary algorithms, in *ECCOMAS 2004, Proc. of the European Congress on Computational Methods in Applied Sciences and Engineering*, P. Neittaanmaki, T. Rossi, K. Majava and O. Pironneau (editors), Jÿvaskÿla, Finland, July 2004.

[4] A. Kučerová, D. Brancherie, A. Ibrahimbegovic, J. Zeman, Z. Bittnar (2007): Novel anisotropic continuum-discrete damage model capable of representing localized failure of massive structures. Part II: Identification from tests under heterogeneous stress field. *Computers & Structures*, submitted.

Part V

Modelling of Biological Tissues

A Finite Element Analysis of the End-to-Side Anastomosis and Posterior Re-Stenosis Process

M. A. Martínez*, J. F. Rodríguez, V. Alastrué, M. Doblaré

Group of Structural Mechanics and Materials Modelling, Aragón Research Institute (I3A), University of Zaragoza
Maria de Luna 7, Campus Rio Ebro, "Agustín de Betancourt" Building, 50018 Zaragoza, Spain
miguelam@unizar.es, jfrodrig@unizar.es, victorav@unizar.es, mdoblare@unizar.es

Summary: From clinical observations, it is known that intimal hyperplasia occurs at the outflow anastomosis of prosthetic bypass grafts, preferentially around the suture-line and on the host artery bed. Investigators have suggested that hemodynamic factors promote hyperplasia growth, however around the junction, compliance mismatch may play an important role on its development. A fully three-dimensional finite element model of a prosthetic end-to-side anastomosis surgery operation is here developed in order to study arterial response to the anastomosis. Both residual stresses and the evolving response of the arterial wall were modelled by means of a multiplicative decomposition of the deformation gradient tensor.

Introduction

Atherosclerosis is a disease of arteries in which atheromas (masses of plaques of degenerated thickened arterial intima) are formed within the intima (inner wall layer) and media (middle wall layer) of large and medium sized arteries [2]. Atherosclerosis can result in decreases in the lumen cross-section of the artery, leading to reduced blood flow to parts of the body. After those lumen reduction or blockage process in the artery, which may promote a stroke or other cardiovascular diseases, surgery or specialized treatments are required. A common surgical treatment in use is to by-pass the affected region with an end-to-side anastomosis surgery, using a venous autologous or synthetic graft. This surgical procedure is a way to treat blocked arteries by creating new passages for blood. Vein segments from different parts of the body or prosthetic implants, are taken as grafts to reroute the blood around the blocked artery. The graft is sewn into place in the artery, above and below the atherosclerotic blockage.

Unfortunately, after end-to-side anastomosis surgery, hyperplasia an re-stenosis might occur leading to serious clinical problems. Surgical imperfection and geometry or mechanical properties mismatches between the graft and the artery are pointed out as factors which promote intimal hyperplasia. From clinical observations, it is known that intimal hyperplasia occurs at the outflow anastomosis of prosthetic bypass grafts, preferentially around the suture-line and on the host artery's bed [1]. Investigators have suggested that hemodynamic factors promote hyperplasia [4], however around the junction, compliance mismatch and surgical techniques may play an important role on its development [1]. Local mechanical stress, caused by these hemodynamic an mechanical factors influence the remodelling and growth of blood vessels leading to re-stenosis.

The aim of this work is to study the role of geometry and mechanical properties in the stress distribution generated by the anastomosis, as well as the intimal hyperplasia generated by the stress concentrations in the arterial wall. A fully three-dimensional finite element model of a prosthetic end-to-side anastomosis surgery is developed (see Fig. 1). Some aspects have to be accounted for in order to make the model as realistic as possible. The existence of residual stresses in the arterial wall [2], the multilayer nature of the artery, and the marked anisotropic character of each layer [3], strongly affect the global response of the artery, and were therefore accounted for the simulations.

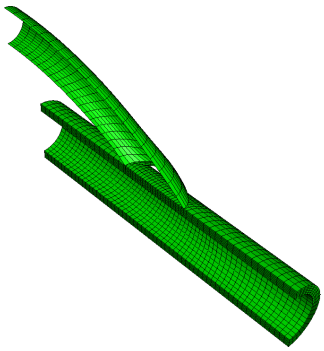

Figure 1: Finite element mesh of the anastomosis model.

Finite element modelling

Finite element model geometrical parameters were taken from the literature for human iliac artery [7], and are collected in Table 1.

The anastomosis is performed with a Dacron prosthetic graft implanted into the host artery as a bypass, with an end-to-side configuration. The angle between the graft and the artery was

Table 1: Geometrical data.

Geometrical parameter	Value
Internal artery radius	$r_i = 3.66$ mm
External artery radius	$r_0 = 4.96$ mm
Internal artery opening radius	$R_i = 5.2$ mm
Arterial longitudinal pre-stretch	$\lambda_z = 1.07$ (-)
Arterial opening angle	$\Theta = 94^\circ$
Arterial length	$L_A = 48$ mm
Graft radius	$R_g = 2.9$ mm
Graft thickness	$t_g = 0.6$ mm
Anastomosis angle	$\alpha = 30^\circ$

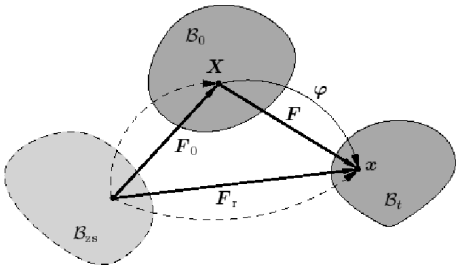

Figure 2: Deformation gradient tensor decomposition diagram for residual stress imposition [6].

set to 30°, which is commonly used in experimental studies [9]. Graft diameter and thickness are set initially as 5 mm and 0.6 mm respectively.

Four load steps are considered in the simulations: *(i)* Imposition of initial strain, *ii)* Incision, *(iii)* Graft anastomosis, *(iv)* Blood flow reestablishment.

Residual stress modelling

Residual stress has been modelled by means of the imposition of a non-compatible deformation gradient tensor. For these purposes, the initial configuration of the artery was assumed as corresponding to the open sector of a tube. The tensor $\mathbf{F}_0$ was computed as the solution to the closing of a pure bending problem. In Fig. 2 it is depicted the diagram of the appearing configurations in the residual stress process [6].

Volumetric growth modelling

Volumetric growth was modelled by means of the decomposition of the deformation gradient tensor as $\mathbf{F} = \mathbf{F}_e\mathbf{F}_g$, where $\mathbf{F}_g$ represents a non-compatible strain field responsible for the volume change and $\mathbf{F}_e$ is an elastic tensor causing the stress field in the equilibrium configuration [5]. Homeostatic stress values were assumed as proposed in [8] so that the principal stretches of $\mathbf{F}_g$ are computed as defined in equation 1,

$$\frac{\partial \lambda_r}{\partial t} = \frac{\sigma_r - \sigma_r^h}{T_r \sigma_r^h}, \quad \frac{\partial \lambda_\theta}{\partial t} = \frac{\sigma_\theta - \sigma_\theta^h}{T_\theta \sigma_\theta^h}, \quad \frac{\partial \lambda_z}{\partial t} = \frac{\sigma_z - \sigma_z^h}{T_z \sigma_z^h}, \tag{1}$$

where λ_i are the principal stretches, the $(\bullet)^h$ superscript denotes an homeostatic value and T_r, T_θ and T_z are time valued constants.

Results

Obtained results show the presence of elevated stresses in the anastomotic area for a prosthetic end-to-side graft due to compliance mismatch (see Fig. 3). Maximal stress values appear near the arterial incision edges, toe and heel. This observation is in agreement with experimental results [1, 9], where they observed cellular hyperplasia near the suture lines in the end-to-side graft anastomosis and are the main reason for the increase in tissue volume.

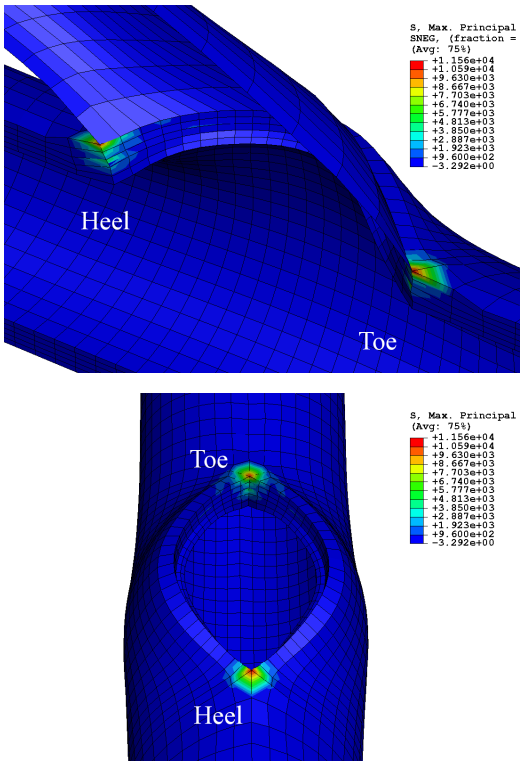

Figure 3: Maximal principal stress concentration (MPa): (top) graft insertion, (bottom) final artery configuration.

References

[1] P. D. Ballyk, C. Walsh, J. Butany, and M. Ojha (1997): Compliance mismatch may promote graft-artery intimal hyperplasia by altering suture-line stresses. *J. Biomech.*, **31**, 229–237.

[2] Y. C. Fung (1990): *Biomechanics: Mechanical Properties of Living Tissues*. Springer.

[3] G. A. Holzapfel, T. C. Gasser, and R. W. Ogden (2000): A new constitutive framework for arterial wall mechanics and a comparative study of material models. *J. Elasticity*, **61**, 1–48.

[4] S. Q. Liu (1998): Prevention of focal intimal hyperplasia in rat vein grafts by using a tissue engineering approach. *Atherosclerosis*, **140**, 365–377.

[5] E. K. Rodriguez, A. Hoger, and A. D. McCulloch (1994): Stress-dependent finite growth in soft elastic tissues. *J. Biomech*, **27**, 455–467.

[6] J. Rodriguez, J. M. Goicolea, and F. Gabaldon (2006): A volumetric model for growth of arterial walls with arbitrary geometry and loads. *J. Biomech*, in Press, Corrected Proof, DOI:10.1016/j.jbiomech.2006.05.002.

[7] C. A. J. Schulze-Bauer, C. Morth, and G. A. Holzapfel (2003): Passive biaxial mechanical response of aged human iliac arteries. *J. Biomech. Eng.*, **125**, 395–406.

[8] L. A. Taber (1998): A model for aortic growth based on fluid shear and fiber stresses. *J. Biomech. Eng.-T. ASME*, **120**, 348–354.

[9] W. Trubel, H. Schima, M. Czerny, K. Perktold, M. G. Schimek, and P. Polterauer (2004): Experimental comparison of four methods of end-to-side anastomosis with expanded polytetrafluoroethylene. *Brit. J. Surg.*, **91**, 159–167.

Mechanical and Numerical Models for the Deformation of the Arterial Wall

M. de Luca*, **A. Veneziani, T. Passerini**

MOX-Modeling and Scientific Computing, Department of Mathematics, Politecnico di Milano
Via Bonardi 9, Milan, Italy
mariarita.deluca@polimi.it, alessandro.veneziani@polimi.it, tiziano.passerini@polimi.it

Summary: The objective of this work is to realize numerical simulations in order to comprehend how the arterial walls can yeld and cause the aneurysms formation. The model we consider makes use of a constitutive equation that is able to represent at the same time the nonlinearity and the inelasticity of the arterial wall. This constitutive equation, unlike the classical single mechanism iperelastic constitutive relation, employs two mechanisms. They represent the mechanical response of elastin and collagen, which are the most important elements of the arterial wall.

Introduction

Saccular Aneurysms are abnormal dilations of cerebral arteries, primarily found at apices of arterial bifurcations and in correspondence to curved arterial segments or near the Circle of Willis. These pathologies are highly outstanding since the rupture of the aneurysm wall causes a subarachnoid hemorrhage, which as often as not lead to death or to a severe disability. Pathological evidences suggest that, at first stage of aneurism growth, the arterial wall dilation has no identifiable edges, afterwards it evolves in a saccular aneurism with a clear neck region [1], but the time course of this development is unpredictable. The biggest problem is that 90% of cerebral aneurysms remains asymptomatic until rupture. Only the wide ones may show some disease symptoms since they compress other cerebral structures.
The most important elements of the arterial wall are collagen and elastin. Their behavior represent the mechanical response of the arterial wall and the model considered in this work involve a dual mechanism related to these components of the tissue. The first mechanism is based on the work of collagen and elastin at the same time, the collagen recruitement is modelled by introducing the second mechanism at a particular deformated configuration, while the elastin breackage is modelled by deactivating the first mechanism at a later deformed state. In the literature the growth of the aneurysms is related with the damage of the elastin, probably caused by an excessive mechanical loading [2]. Thus, in order to model the development of an aneurysm from a segment of arterial wall, it is necessary to include the failure of the elastin as a load bearing mechanism separately from the bulk failure of the entire wall. Classic continuum models of arteries treat all structural components in the wall as a single mechanism and therefore do not suite this purpose [3]. The dual mechanism model can be viewed as a structurally motivated phenomenological model since we obtain information about the mechanical behavior of the collagen and elastin, but it isn't a "strictly sayng" structural model, because it does not include the material properties of independent components.
In this work, we start from this mechanical model (proposed by Wulandana [4]), by extending his work with 3D numerical simulations and by comparing his results with other models.

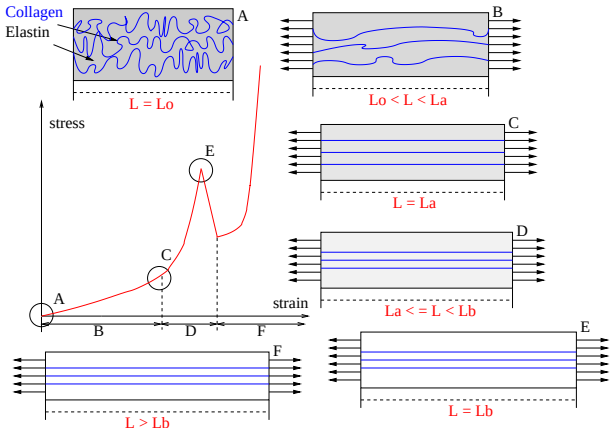

Figure 1: Proposed mechanisms of an idealized arterial wall tissue under uniaxial loading (draw by [4]).

Mechanical model

The role of elastin and collagen is at the basis of the theoretical model, since the nonlinearity and inelasticity of the arterial tissue can be represented with the dual mechanisms. The first one describes the role of elastin and collagen which work at the same time and the second one starts after the breackage of elastin and only involves the collagen.
To better understand how the model works, the contribution of these components may be illustrated by considering an idealized uniaxial model of an arterial wall strip with undeformed length L_0. The oversimplified diagram of this idealization is depicted in Figure 1, where the strain is the ratio between deformed lenght L and L_0. At the beginning, the strip is unloaded (position A), the collagen fibers are the black ones and the elastin is the grey background. When the loading starts, the collagen fibers will be stretched out until they are as long as the arterial strip. During this range strain (gap B), the mechanical response of the arterial wall is due only to elastin. When the strain gets to the first critical level $L = La$, the collagen work starts (position C). Then the D gap represent the functional range in which the mechanical response of the tissue is brought by both collagen and elastin. This represent the working of the first mechanism. In correspondance to the second critical level of strain $L = Lb$ (stage E) the damage of the elastin fibers occurs (white background). In this model it is hy-

pothesized that the birth of the aneurysm happens at this stage. Upon further loading, only collagen fibers resist stretch. The strain range where only the collagen works represents the second mechanism. The main feature of this model is to have two reference configurations, one for the first mechanism and the other for the second.
By unloading the arterial strip from the stage E, the tissue goes back to the initial configuration (stage A). In this strain range the arterial wall has an elastic behavior, and its components are both able to carry the stress. After the elastin breackage only the collagen fibers work: in this case by unloading the strip it goes back to another reference configuration.

Kinematics for the dual mechanism model

Some kinematics definitions are necessary to understand how the dual mechanism works. The physical segment of artery is represented by body $\mathcal{B}$. The initial configuration is k_1 and $\boldsymbol{X}_1$ is the vector position in the reference configuration. The deformated configuration is k and $\boldsymbol{x}$ is the corrisponding vector position, like in the Figure 2. Using this notation, the motion of an arbitrary particle can be described with the relationship:

$$\boldsymbol{x} = \boldsymbol{\chi}_{k_1}(\boldsymbol{X}_1, t), \tag{1}$$

and the deformation gradient at time t is given by:

$$\boldsymbol{F}_1(t) = \boldsymbol{F}_{k_1}(\boldsymbol{X}_1, t) = \frac{\partial \boldsymbol{\chi}_{k_1}(\boldsymbol{X}_1, t)}{\partial \boldsymbol{X}_1}. \tag{2}$$

After the body $\mathcal{B}$ is put through the critical strain level, which causes the damage of the elastin fibers, it has to consider configuration k_2 as new reference configuration. The relation between the position vector $\boldsymbol{X}_2$ in the new reference configuration and the vector position $\boldsymbol{x}$ in the deformed configuration is:

$$\boldsymbol{x} = \boldsymbol{\chi}_{k_2}(\boldsymbol{X}_2, t), \tag{3}$$

while the relation between the two reference configurations is:

$$\boldsymbol{X}_2 = \boldsymbol{\chi}_{k_1}(\boldsymbol{X}_1, \widetilde{t}), \tag{4}$$

where $\widetilde{t}$ is the time which the second mechanism stars.
The deformation gradient for the second mechanism is:

$$\boldsymbol{F}_2(t) = \boldsymbol{F}_{k_2}(\boldsymbol{X}_2, t) = \frac{\partial \boldsymbol{\chi}_{k_2}(\boldsymbol{X}_2, t)}{\partial \boldsymbol{X}_2}. \tag{5}$$

The collagen and elastin are both considered iperelastic materials. As a consequence the constitutive law can be written by using a strain energy function. For this dual mechanism model the strain energy function W depends on the deformation gradients $\boldsymbol{F}_1$ e $\boldsymbol{F}_2$. In the functional range of the first mechanism:

$$W(t) = W(\boldsymbol{F}_1(t), \boldsymbol{F}_2(t)), \tag{6}$$

and when elastin no longer contributes to load bearing, the strain energy function depends only on $\boldsymbol{F}_2$:

$$W(t) = W(\boldsymbol{F}_2(t)) \tag{7}$$

To define the constitutive law, it is practical to use the left

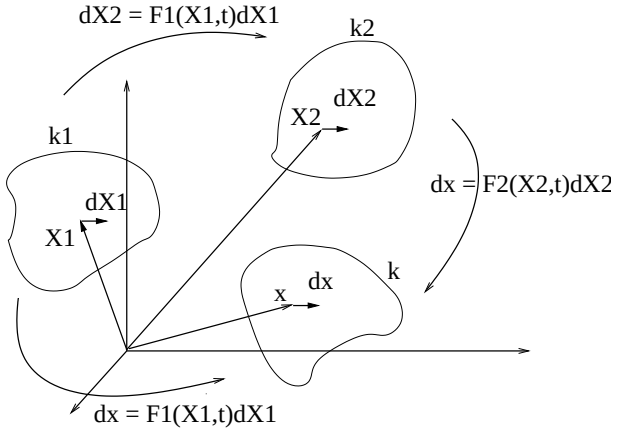

Figure 2: Schematic of relevant reference configuration for the dual mechanism constitutive model, (draw by [3]).

Cauchy-Green stretch tensor $\boldsymbol{B}_1$ and $\boldsymbol{B}_2$:

$$\boldsymbol{B}_1 = \boldsymbol{F}_1 \cdot \boldsymbol{F}_1^T, \quad \boldsymbol{B}_2 = \boldsymbol{F}_2 \cdot \boldsymbol{F}_2^T. \tag{8}$$

By using $\boldsymbol{B}_1$, $\boldsymbol{B}_2$ and their principal invariants I_1, II_1, I_2 and II_2 the corresponding Cauchy stress tensor $\boldsymbol{T}$ is:

$$\boldsymbol{T} = -p\boldsymbol{I} + 2\frac{\partial W}{\partial I_1}\boldsymbol{B}_1 - 2\frac{\partial W}{\partial II_1}\boldsymbol{B}_1^{-1} + 2\frac{\partial W}{\partial I_2}\boldsymbol{B}_2 - 2\frac{\partial W}{\partial II_2}\boldsymbol{B}_2^{-1}, \tag{9}$$

which depends on the dual mechanisms. Further details are shown in [3].

Numerical solutions

The 3D numerical simulation according to this model will be carried out by means of LifeV. This is a finite element (FE) library providing implementations of state of the art mathematical and numerical methods. LifeV is the joint collaboration between three institutions: Ecole Polytechnique Fédérale de Lausanne (CMCS) in Switzerland, Politecnico di Milano (MOX) in Italy and INRIA (BANG) in France.
Simplified geometries as well as real geometrical models obtained by CT scans will be used and some comparison with more simple models, like the Kirchhoff Saint-Venant one, will be performed.

References

[1] W. D. Forbus (1930): On the origin of miliary aneurysms of the superficial cerebral arteries. *Bulletin of the Johns Hopkins Hospital*, **47**, 239–284.

[2] S. Scott, G. Ferguson, M. R. Roach (1972): Comparison of the elastic properties of human intracranial arteries and Aneurysms. *Canadian Journal of Physiology and Pharmacology*, **50**, 328–332.

[3] R. Wulandana, A. Robertson (2005): An inelastic multi-mechanism constitutive equation for cerebral arterial tissue. *Biomech. Model. Mechanbiol.*

[4] R. Wulandana (2003): *A Nonlinear and Inelastic Constitutive Equation for Human Cerebral Arterial ans Aneurisms Walls*. PhD Thesis, University of Pittsburg.

Simulation of Arterial Walls using FETI Domain Decomposition Methods

D. Balzani[1]*, A. Klawonn[2], O. Rheinbach[2], J. Schröder[1], D. Brands[1]

[1]Institute of Mechanics, University of Duisburg-Essen, Department of Engineering Science, Division Civil Engineering
Universitätsstr. 15, 45117 Essen, Germany
{daniel.balzani, j.schroeder, dominik.brands}@uni-due.de

[2]Department of Mathematics, University of Duisburg-Essen
Universitätsstr. 3, 45177 Essen, Germany
{axel.klawonn, oliver.rheinbach}@uni-due.de

Summary: Biological soft tissues in arterial walls are characterized by a nearly incompressible, anisotropic, hyperelastic material behavior in the physiological range of deformations. For the representation of such materials we apply a polyconvex strain energy function in order to ensure the existence of minimizers and in order to satisfy a priori the Legendre-Hadamard condition. The 3D discretization results in a large system of equations, thus, a parallel algorithm is applied to solve the equilibrium problem. We are using a dual-primal FETI (Dual-Primal Finite Element Tearing and Interconnecting) method to solve elasticity problems for three dimensional models of arterial walls and present numerical results.

Introduction

The understanding of the anatomy and composition of arterial walls is an essential topic for the modeling of their mechanical behavior. Because of the interest in large deformations we focus on the modeling of elastic arteries. An example of a healthy elastic artery is shown in Fig. 1. The classification into three layers is a common abstraction of an arterial wall. These layers are named intima (tunica intima), media (tunica media), and adventitia (tunica externa).

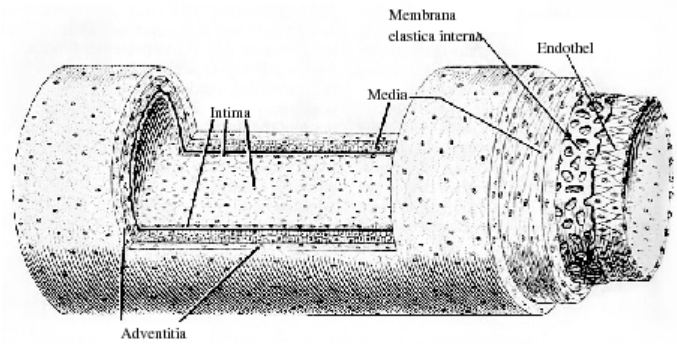

Figure 1: Composition of a healthy artery [6].

The FE-simulation of an arterial wall, especially of a diseased one, represents a challenging task with view to the large number of degrees of freedom. Robust, parallel solvers are essential for the solution of the resulting large linear systems of equations. FETI-DP domain decomposition methods have been shown to be numerically and parallely scalable and robust for a huge class of problems in structural mechanics, see also [4, 7, 8, 9].

Modeling of arterial tissues

We consider hyperelastic materials, which postulate the existence of a so-called strain energy function ψ, assumed to be defined per unit reference volume. Due to the fact that arterial tissues consist of an isotropic matrix and two embedded fiber families wounding helically around the longitudinal axis, we consider the additively decoupled structure of the strain energy

$$\psi = \psi^{iso} + \sum_{a=1}^{2} \psi^{ti}_{(a)} \,, \tag{1}$$

cf. [5]. In order to account for the principle of material frame indifference we focus on reduced representations where the energy depends on the right Cauchy-Green deformation tensor defined by

$$\mathbf{C} = \mathbf{F}^T\mathbf{F} \quad \text{with} \quad \mathbf{F} = \text{Grad}[\varphi] \,. \tag{2}$$

The nonlinear transformation φ maps points of an undeformed reference state to points of a deformed actual configuration. In order to reflect the material symmetries we introduce an additional argument tensor, the so-called structural tensor

$$\mathbf{M} := \mathbf{a} \otimes \mathbf{a} \quad \text{with} \quad ||\mathbf{M}|| = 1 \,, \tag{3}$$

wherein $\mathbf{a}$ denotes the direction vector of the fiber orientation. Herewith, we obtain a strain energy function of the type $\psi = \hat{\psi}(\mathbf{C}, \mathbf{M})$. For the construction of specific functions in a coordinate invariant setting we need the principle invariants

$$I_1 := \text{tr}[\mathbf{C}], \quad I_2 := \text{tr}[\text{cof}\mathbf{C}], \quad I_3 := \det[\mathbf{C}] \,, \tag{4}$$

and the mixed invariants

$$J_4 := \text{tr}[\mathbf{CM}], \quad J_5 := \text{tr}[\mathbf{C}^2\mathbf{M}] \,. \tag{5}$$

With view to the existence of minimizers the polyconvexity condition of Ball [1] represents an important concept. A variety of polyconvex transversely isotropic energy functions for the mechanical description of biological soft tissues occurring in arterial walls is derived in [3, 2]. Here, we consider the isotropic strain energy

$$\psi^{iso} = c_1 \left(\frac{I_1}{I_3^{1/3}} - 3 \right) + \varepsilon_1 \left(I_3^{\varepsilon_2} + \frac{1}{I_3^{\varepsilon_2}} - 2 \right) \,, \tag{6}$$

with $c_1 > 0$, $\varepsilon_1 > 0$, $\varepsilon_2 > 1$, and the transversely isotropic energy

$$\psi^{ti}_{(a)} = \begin{cases} \alpha_1 \left(K_3^{(a)} - 2 \right)^{\alpha_2} & \text{for } K_3^{(a)} \geq 2 \\ 0 & \text{for } K_3^{(a)} < 2 \end{cases} \,, \tag{7}$$

with $\alpha_1 > 0$ and $\alpha_2 > 2$ in order to ensure polyconvexity and smooth tangent moduli. $K_3^{(a)} = I_1 J_4^{(a)} - J_5^{(a)}$ is a fundamental polyconvex function for transverse isotropy introduced in [10].

FETI domain decomposition

Linearization and discretization of our mechanical problem results in large linear equation systems that need to be solved efficiently on parallel computers. For this, we apply the paradigm of domain decomposition. Domain decomposition methods are iterative algorithms that create concurrency by a geometrical partitioning of the problem and achieve numerical (quasi-) optimality by introduction of a small global coarse problem. In FETI-DP domain decomposition methods [7, 8, 9, 4] the computational domain Ω is partitioned into N nonoverlapping subdomains $\Omega_i, i = 1, \ldots, N$, i.e.

$$\overline{\Omega} = \bigcup_{i=1}^{N} \overline{\Omega}_i \,, \qquad \Omega_i \cap \Omega_j = \emptyset \quad \text{if} \quad i \neq j \,. \tag{8}$$

Each subdomain is the union of shape-regular finite elements with matching finite element nodes across the interface,

$$\Gamma := \bigcup_{i \neq j} \partial\Omega_i \cap \partial\Omega_j, \tag{9}$$

where $\partial\Omega_i, \partial\Omega_j$ are the boundaries of Ω_i, Ω_j, respectively. These nonoverlapping subdomains are also often referred to as substructures. We then have certain conditions on the interface Γ that will be forced to hold throughout the iteration. We introduce Lagrange multipiers to enforce continuity of the global solution at convergence. This results in a mixed system of the form

$$\begin{bmatrix} \tilde{\mathbf{K}} & \mathbf{B^T} \\ \mathbf{B} & \mathbf{0} \end{bmatrix} \begin{bmatrix} \mathbf{u} \\ \lambda \end{bmatrix} = \begin{bmatrix} \tilde{\mathbf{f}} \\ \mathbf{0} \end{bmatrix}. \tag{10}$$

Elimination of $\mathbf{u}$ then results in a system

$$\mathbf{F}\lambda = \mathbf{d} \tag{11}$$

which is solved using a suitable Krylov subspace method and the FETI-DP Dirichlet preconditioner.

Parallel simulation of arteries

For the analysis of an arterial wall simulation we consider a slightly diseased artery with a moderate atherosclerotic plaque. We use the material parameters for the media and adventitia found in [2] and take into account an extracellular lipid pool, calcification and degenerated intima as the plaque. We use our parallel FETI-DP implementation [8, 9] to solve the linearized equation systems. The domain decomposition is performed as shown in Fig. 2 (left), where different colors indicate the particular domains. We apply an internal pressure of approximately 95 mmHg, which can be interpreted as an average blood pressure. As an example a deformed configuration of an artery is shown in Fig. 2 (right), where the distribution of von Mises stresses is depicted.

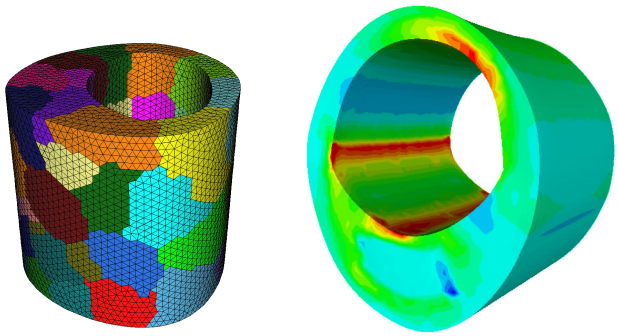

Figure 2: Decomposition of an arterial segment in the FETI-DP algorithm (left) and distribution of von Mises stresses in an inflated artery (right).

References

[1] J. M. Ball (1977): Convexity conditions and existence theorems in non-linear elasticity, *Arch. Ration. Mech. Anal.* **63**, 337–403.

[2] D. Balzani (2006): *Polyconvex Anisotropic Energies and Modeling of Damage Applied to Arterial Walls*, PhD-Thesis, Scientific Report of the Institute of Mechanics, Universität Duisburg-Essen, Verlag Glückauf, Essen.

[3] D. Balzani, P. Neff, J. Schröder, G. A. Holzapfel (2006): A Polyconvex Framework for Soft Biological Tissues. Adjustment to Experimental Data, *Int. J. Solids Struct.* **43**, 6052–6070.

[4] C. Farhat, M. Lesoinne, P. LeTallec, K. H. Pierson, D. Rixen (2001): FETI-DP: A dual-primal unified FETI method - Part I: A faster alternative to the two-level FETI method. *Internat. J. Numer. Methods Engrg.* **50**, 1523–1544.

[5] G. A. Holzapfel, T. C. Gasser, R. W. Ogden (2000): A new constitutive framework for arterial wall mechanics and a comparative study of material models, *Journal of Elasticity* **61**, 1–48.

[6] L. C. Junqueira, J. Carneiro (1991): *Histologie*, Springer.

[7] A. Klawonn, O. B. Widlund (2006): Dual-Primal FETI Methods for Linear Elasticity, *Comm. Pure Appl. Math.* **59**, 1523–1572.

[8] A. Klawonn, O. Rheinbach (2006): A parallel implementation of Dual-Primal FETI methods for three dimensional linear elasticity using a transformation of basis, *SIAM J. Sci. Comput.* **28**, 1886–1906.

[9] O. Rheinbach (2006): Parallel Scalable Iterative Substructuring: Robust Exact and Inexact FETI-DP Methods with Applications to Elasticity, PhD-Thesis, Department of Mathematics, Universität Duisburg-Essen.

[10] J. Schröder, P. Neff (2003): Invariant Formulation of Hyperelastic Transverse Isotropy Based on Polyconvex Free Energy Functions, *Int. J. Solids Struct.*, **40**, 401–445.

Effects of Connective Tissue Pathologies on Mitral Valve Response

V. Prot[1*], **B. Skallerud**[1], **G. A. Holzapfel**[2]

[1]Department of Structural Engineering Norwegian University of Science and Technology, Trondheim, Norway
victorien.prot@ntnu.no, bjorn.skallerud@ntnu.no

[2]Department of Solid Mechanics, Royal Institute of Technology, Stockholm, Sweden
gh@biomech.tu-graz.ac.at

Summary: This study presents a three-dimensional finite element model of the mitral apparatus using a transversely isotropic hyperelastic material model for the leaflets. The mitral valve is an important valve of the heart between the left atrium and the left ventricle. During systole, the valve prevents blood from flowing back into the left atrium. The purpose of this study is to illustrate the influence of the loss of stiffness in the chordae on the mitral valve response.

Introduction

This study presents a three-dimensional finite element model of the porcine mitral valve. This model uses a saddle shaped annulus and a hyperelastic transversely isotropic material model for the leaflets. We simulate a part of the cardiac cycle starting from the beginning of systole and ending at the peak pressure in the left ventricle. Several finite element analyses were performed in order to investigate the influence of the reduction in chordae stiffness on the mitral valve response. This loss of stiffness in the chordae corresponds to the Marfan syndrome. In the Marfan syndrome the connective tissue is defective and does not act as it should. Because connective tissue is present in many parts of the body, it can affect many body parts such as heart valves and blood vessels.

Methods

Geometry and boundary conditions

The mitral geometry is based on anatomical measurements made on a pig post mortem. The annulus of the valve was assumed saddle shaped. We assumed the free edge of the posterior leaflet to be divided in three scallops, a large middle one and two smaller ones representing the commissural parts of the valve. The dimensions of the mitral apparatus are reported in Figure 1. The leaflets were allowed to rotate at the annular attachment. The translations were constrained at the attachment between the chordae and the papillary muscles. We assumed fixed boundary conditions for the papillary muscles. In order to prevent the leaflets from interpenetrating each other upon closure, a contact condition was set between the two surfaces. The measured blood pressure in the left ventricle of the pig during the isovolumetric contraction phase up to the maximum pressure in the left ventricle in the ejection phase was applied as load history.

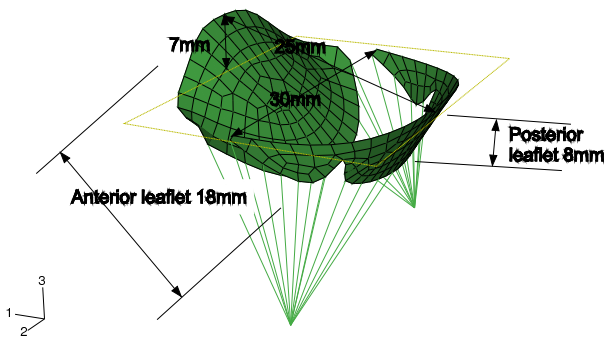

Figure 1: Initial geometry of the valve.

Material models

The leaflets were modelled with an incompressible hyperelastic transversely isotropic material model. The strain energy function employed to derive the constitutive model is the one proposed in [1],

$$\Psi(I_1, I_4) = c_0[\exp^{c_1(I_1-3)^2+c_2(I_4-1)^2} - 1] + p(J-1), \quad (1)$$

where c_i, $i = 0, 1, 2$, are material parameters, $\sqrt{I_4}$ represents the stretch of the collagen fibers, the scalar p serves as an indeterminate Lagrange multiplier and $J = \det \mathbf{F}$ is the Jacobian of the deformation. The material parameters c_i, $i = 0, 1, 2$ were fitted to biaxial *in vitro* tests on porcine mitral valve tissue carried out by May-Newman and Yin [2], using a nonlinear least square technique.
The expression of the spatial elasticity tensor $\mathbb{c}$ is given as,

$$\begin{aligned} \mathbb{c} \;=\; & 4\psi_{11}\mathbf{B}\otimes\mathbf{B} \\ & +4\psi_{14}(\mathbf{B}\otimes\mathbf{a}\otimes\mathbf{a}+\mathbf{a}\otimes\mathbf{a}\otimes\mathbf{B}) \\ & +4\psi_{44}\mathbf{a}\otimes\mathbf{a}\otimes\mathbf{a}\otimes\mathbf{a} \\ & +2\,\mathbf{1}\otimes\left(\mathbf{F}\frac{\partial p}{\partial \mathbf{C}}\mathbf{F}^T\right) - 2p\mathbb{I}, \qquad (2) \\ & \text{where} \quad \psi_{ij} = \frac{\partial^2\Psi}{\partial I_i \partial I_j} \quad (i,j=1,4), \end{aligned}$$

where Ψ_{ij} may be derived from 1.
The material model was implemented into ABAQUS/standard by using the user-defined subroutine UMAT. The derivation, implementation and validation of this material model are fully described in [3].
The chordae were modeled with an incompressible isotropic hyperelastic material. The material model was derived from the following strain-energy function U, i.e.

$$U(I_1) = a_1(I_1 - 3) + a_2[\exp^{a_3(I_1-3)} - 1], \qquad (3)$$

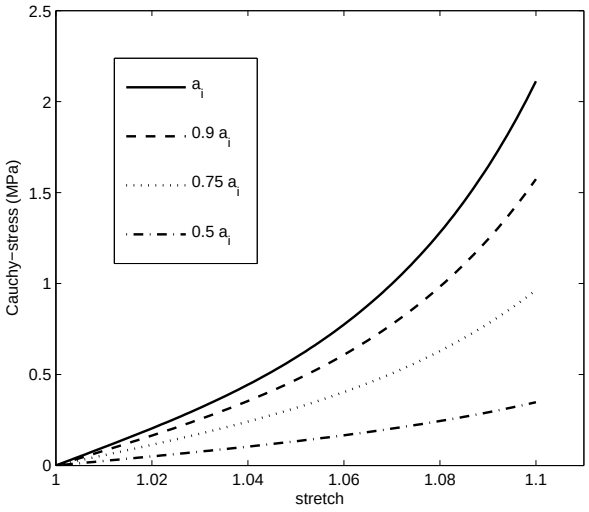

Figure 2: Stress-stretch behaviour in uniaxial tension of the strut chordae with the four sets of material parameters.

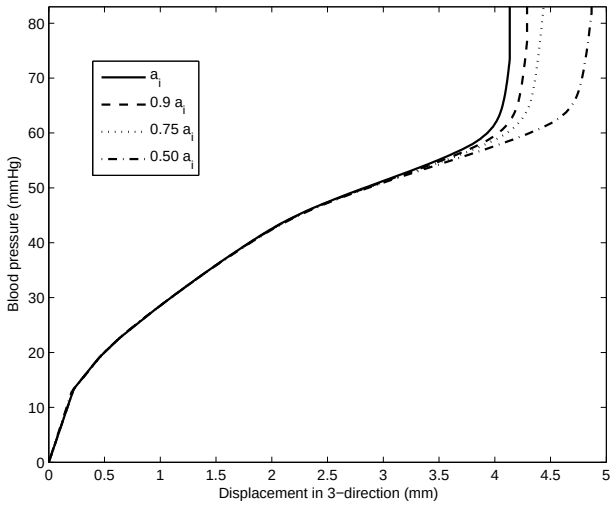

Figure 3: Apical displacement (3-direction, see Figure 1) of one node positioned in the middle of the anterior leaflet with different material parameters for the chordae.

where a_1, a_2 and a_3 are the material parameters determined from the experimental data published by Kunzelman and Cochran [4] and Ritchie et al. [5]. These values are considered to correspond to the healthy case. In the present study, four analyses were conducted with decreasing values for the material parameters $a_i, i = 1, 2, 3$. The values determined from the experiments were multiplied by 0.9, 0.75 and 0.5. The uniaxial behaviour of the strut chordae with respect to the different sets of material parameters are shown in Figure 2.

Results

The apical displacement of one node located in the middle of the anterior leaflet is plotted in figure 3 for the different sets of material parameters used for the chordae. Until the ventricular blood pressure reaches 50 mmHg, the displacement of the node is identical in all cases. The apical displacement of the node is the largest when the stiffness of chordae is the lowest. When the material parameters are divided by two, the apical displacement is 1.17 times higher than in the healthy case.

Conclusion

This study shows the importance of the chordae properties to maintain the mitral valve in the right position. These simulations were conducted with realistic material models in the healthy case for both the leaflets and the chordae. However, this study is numerical and qualitative, no tests data on diseased tissue have been used.

References

[1] G. A. Holzapfel, G. Sommer, C. T. Gasser, and P. Regitnig (2005): Determination of the layer-specific mechanical properties of human coronary arteries with nonatherosclerotic intimal thickening, and related constitutive modelling. *Am. J. Physiol. Heart Circ. Physiol.*, **289**, 2048–2058.

[2] K. May-Newman and F. C. P. Yin (1998): A constitutive law for mitral valve tissue. *J. Biomech. Eng.*, **120**, 38–47.

[3] V. Prot, B. Skallerud, G. A. Holzapfel (2007): Transversely isotropic membrane shells with application to mitral valve mechanics. Constitutive modeling and finite element implementation. *International Journal for Numerical Methods in Engineering* (in press).

[4] K. S. Kunzelman and R. P. Cochran (1990): Mechanical properties of basal and marginal mitral valve chordae tendineae. *ASAIO Trans.*, **36**, 405–408.

[5] J. Ritchie, J. Jimenez, Z. He, M. S. Sacks, A. P. Yoganathan (2006): The material properties of the native porcine mitral valve chordae tendineae: an in vitro investigation. *J. Biomech.*, **39**, 1129–35.

Application of a Strain Damage Model to Viscoelastic Anisotropic Biological Soft Tissues

E. Peña*, B. Calvo, M.A. Martínez, M. Doblaré

Group of Structural Mechanics and Materials Modeling, Aragón Institute of Engineering Research, University of Zaragoza
María de Luna, 3. E-50018 Zaragoza, Spain
fany@unizar.es

Summary: Many fibred soft tissues exhibit elastic and viscous material behavior. Furthermore, non-physiological loads drive soft tissue to damage that may induce a strong reduction of the stiffness. The aim of this paper is to present a three dimensional finite-strain damage model for visco-hyperelastic fibrous soft tissue. Continuum damage mechanics is used to describe the softening behavior under large deformation. We present a 3D simulation of the behavior of the human medial collateral ligament. Results show that the model is able to capture the typical stress-strain behavior observed in fibrous soft tissues.

Introduction

Biological soft tissues are subjected to large deformations with negligible volume changes and show an anisotropic mechanical response due to their internal structure. Usually, the description of the constitutive behaviour of this type of materials relies on the identification of an appropriate strain energy density function from which stress-strain relations are derived. Their use is limited, in most cases, to a given range of physiological loads. In order to obtain a more realistic and complete material model, damage may be coupled with viscoelasticity to account for both inelastic features. Some computational models of viscoelastic materials with damage have previously been developed in the literature. All these models are isotropic and were mainly applied to model rubber-like materials.

Phenomenological viscoelastic damage model

The free energy density can be written as the augmented free energy:

$$\Psi(\mathbf{C},\mathbf{M},\mathbf{N},D_k,\mathbf{Q}_{ij}) = \Psi^0_{vol}(J) + \sum_{k=m,f_1,f_2}(1-D_k)\bar{\Psi}^k_0 - \frac{1}{2}\sum_{i=1}^{n}\sum_{k=m,f_1,f_2}(\bar{\mathbf{C}}:\mathbf{Q}_{ik}) + \Xi(\sum_{i=1}^{n}\sum_{k=m,f_1,f_2}\mathbf{Q}_{ik}) \quad (1)$$

where $\mathbf{Q}_{ik}$ may be interpreted as non-equilibrium stresses, in the sense of non-equilibrium thermodynamics, and remain unaltered under superposed spatial rigid body motions [3]. $\mathbf{Q}_{im}$ are the isotropic contribution due to the matrix material associated to I_1 and I_2 invariants and $\mathbf{Q}_{if_1},\dots,\mathbf{Q}_{if_2}$ are the anisotropic contribution due to the two families of fibres associated to $I_4,\dots,I_9$ invariants [1]. Finally $(1-D_k)$ are known as the reduction factors [3], where the internal variables $D_k \in [0,1]$ are normalized scalars referred to as the damage variables for the matrix D_m and the two families of fibres D_{f1} and D_{f2} respectively [2].

Standard arguments based on the Clausius-Duhem inequality $\mathcal{D}_{int} = -\dot{\Psi} + \frac{1}{2}\mathbf{S}:\dot{\mathbf{C}} \geq 0$, lead to the following representation

$$\mathbf{S} = 2\frac{\partial\Psi(\mathbf{C},\mathbf{M},\mathbf{N},D_k,\mathbf{Q}_{ij})}{\partial\mathbf{C}} = \mathbf{S}_{vol} + \sum_{k=m,f_1,f_2}\left\{(1-D_k)\bar{\mathbf{S}}^0_k - J^{-\frac{2}{3}}\sum_{i=1}^{n}DEV\mathbf{Q}_{ik}\right\} \quad (2)$$

The nonequilibrium second Piola Kirchhof stresses in (2), $\mathbf{Q}_{ik}$, are assumed to be governed by a set of linear rate equations [1]

$$\dot{\mathbf{Q}}_{ik} + \frac{1}{\tau_{ik}}\mathbf{Q}_{ik} = \frac{\gamma_{ik}}{\tau_{ik}}(1-D_k)DEV[2\frac{\partial\bar{\Psi}^0_k(\bar{\mathbf{C}},\mathbf{M},\mathbf{N})}{\partial\bar{\mathbf{C}}}] \qquad \lim_{t\to-\infty}\mathbf{Q}_{ik} = \mathbf{0} \quad (3)$$

where $\gamma_{ik} \in [0,1]$ are free energy factors associated with relaxation times $\tau_{ik} > 0$.

We define a damage criterion in the strain space by the condition that, at any time t of the loading process, the following expression is fulfilled [3]

$$\phi_k(\mathbf{C}(t),\Xi_{k_t}) = \sqrt{2\bar{\Psi}^0_k(\bar{\mathbf{C}}(t))} - \Xi_{k_t} = \Xi_k - \Xi_{k_t} \leq 0 \quad (4)$$

where $\bar{\mathbf{C}}(s)$ is the modified right Cauchy-Green tensor at time s and Ξ_{k_t} are defined as follow

$$\Xi_{k_t} = \max_{s\in(-\infty,t)}\sqrt{2\bar{\Psi}^0_k(\bar{\mathbf{C}}(s))} \quad (5)$$

The equation $\phi_k(\mathbf{C}(t),\Xi_{k_t}) = 0$ defines a damage surface in the strain space [2]. The damage functions proposed correspond to the expressions

$$D_k = \begin{cases} 0 & \text{if} \quad \Xi_{k_t} < \Xi^0_{min_k} \\ \xi^2[1-\beta_k(\xi^2-1)] & \text{if} \quad \Xi^0_{min_k} \leq \Xi_{k_t} \leq \Xi^0_{max_k} \\ 1 & \text{if} \quad \Xi_{k_t} > \Xi^0_{max_k} \end{cases} \quad (6)$$

with $\xi = \frac{\Xi_{k_t}-\Xi^0_{min_k}}{\Xi^0_{max_k}-\Xi^0_{min_k}}$ a dimensionless variable, $\Xi^0_{min_k}$ are the variables (4) associated to the strain energies at initial damage for matrix and fibres respectively, $\Xi^0_{max_k}$ the variables (4) associated to the strain energy at total damage for matrix and fibres, and β_k exponential parameters, see [2].

Numerical example

The model presented has been linearized and implemented into the finite element program ABAQUS. We reproduce in a human medial collateral ligament (MCL) the experiment developed by Woo et al. [4] in a rabbit MCL. That study was performed to determine the viscoelastic behavior of ligaments at different loading rates, such as those associated with sports-related trauma. The particular form of the deviatoric functions $\bar{\Psi}_0^m$ and $\bar{\Psi}_0^f$ are defined in (7) [5] and the volumetric part of the strain energy function is always stated as $\Psi_{vol} = \frac{1}{D}\ln J^2$ [6]. The damage functions for the matrix and fibres were those established in (6).

$$\bar{\Psi}_m^0 = C_1(\bar{I}_1 - 3)$$
$$\bar{\Psi}_{f1}^0 = \frac{C_3}{C_4}(\exp^{C_4(\bar{I}_4-1)} - C_4(I_4 - 1) - 1) \qquad (7)$$

The human model of the MCL was constructed to test quasi-static, physiological and impact conditions at displacement rates of 0.01 mm/s and 113 mm/s corresponding to strain rates of approximately 0.0025%/s and 28%/s, respectively.The elastic, viscoelastic and damage parameters for the human MCL were fitted and are shown in Table 1.

Table 1: Material, viscoelastic and damage parameters for the human MCL (MPa)

C_1	C_2	C_3	C_4	D	
0.1539	0.0	0.1507	34.7929	3.986e-4	
γ_m	τ_m	γ_{f1}	τ_{f1}		
0.4352	0.15	0.1500	2		
ψ_{min}^m	ψ_{max}^m	β^m	ψ_{min}^f	ψ_{max}^f	β^f
0.0750	0.0932	0.120	0.3389	1.6652	0.1538

Damage distributions in matrix and fibres at 0.01 mm/s and 113 mm/s of displacement rates are presented in Figures 1 and 2. We consider failure of the MCL when damage reached a value of 0.6. At 113 mm/s of displacement rate, damage in matrix and fibres was much lower than that at 0.01 mm/s. This effect is especially evident in the fibres where damage decreased from 0.36 during the quasi-static test (0.01 mm/s) to 0.24 (113 mm/s) in the impact test. The peak values appeared in the ligament substance also has been reported in previous experimental studies [4]. Damage during distraction usually appears in that region.

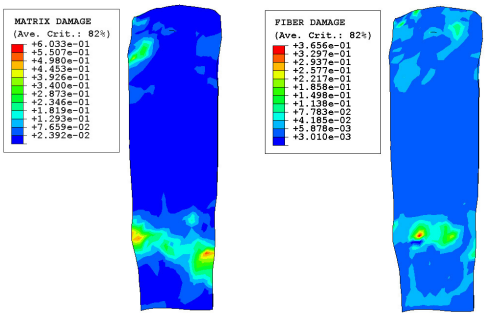

Matrix damage Fibre damage

Figure 1: Damage in a human MCL at 0.01 mm/s

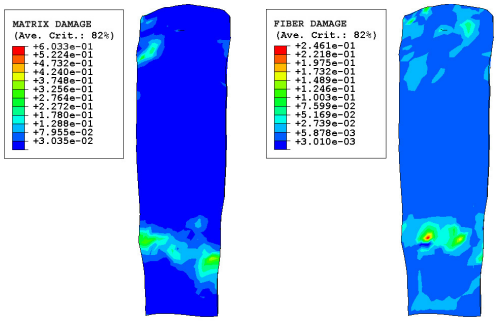

Matrix damage Fibre damage

Figure 2: Damage in a human MCL at 113 mm/s

Conclusions

A good qualitative agreement was found between numerical and some experimental results in the literature, indicating that the constitutive viscoelastic damage model can capture the typical stress-strain behavior observed in fibrous soft tissue. Some possible applications may be mentioned such as sports (skiing, basketball, soccer) and traffic accidents that are the most important causes of ligament injury. In fact, the strain-rate during injury is very important regarding the magnitude of the lesion. Vascular surgery simulations (balloon angioplasty, arterial clamping or stenting), corneal laser interventions or plastic surgery are other interesting applications to be considered in the near future.

References

[1] E. Pea, B. Calvo, M. A. Martnez, and M. Doblar (2007): An anisotropic visco-hyperelastic model for ligaments at finite strains: Formulation and computational aspects. *Int J Solids Struct*, **44**, 760–778.

[2] B. Calvo, E. Pea, M.A. Martnez, and M. Doblar (2007): An uncoupled directional damage model for fibered biological soft tissues. Formulation and computational aspects. *Int J Numer Meth Engng*, **69**, 2036–2057.

[3] J.C. Simo (1987): On a fully three-dimensional finite-strain viscoelastic damage model: Formulation and computational aspects. *Comput Methods Appl Mech Engrg*, **60**, 153–173.

[4] S. L-Y Woo, R.H. Peterson, K.J. Ohland, T.J. Sites, and M.I. Danto (1990): The effects of strain rate on the properties of the medial collateral ligament in skeletally inmatura and mature rabbits: A biomechanical and histological study. *J Orthopaed Res*, **8**, 712–721.

[5] A.N. Natali, P.G. Pavan, E.L. Carniel, M.E. Luisiano, and G. Taglialavoro (2005): Anisotropic elasto-damage constitutive model for the biomechanical analysis of tendons. *Med Eng Phys*, **27**, 209–214.

[6] G. A. Holzapfel (2000): *Nonlinear Solid Mechanics*. Wiley, New York.

On a Mesomechanical Modelling of Skeletal Muscles

M. Böl*, S. Reese

Institute of Solid Mechanics
Braunschweig University of Technology, D-38106 Braunschweig, Germany
m.boel@tu-bs.de, s.reese@tu-bs.de

Summary: The structure of a skeletal muscle is dominated by its hierarchical architecture in which thousands of muscle fibres are arranged within a connective tissue network. The single muscle fibres consist of many force-producing cells, known as sarcomeres. These microbiological engines are part of a motor unit and contribute to the contraction of the whole muscle. From the mechanical point of view the material behaviour of muscles is highly non-linear. They undergo large deformations in space, thereby changing their shape significantly, so that geometrical nonlinearity has to be considered. The present approach is based on the use of the finite element method. The material behaviour of the muscle is split into a so-called active and a passive part. To describe the passive part special unit cells consisting of one tetrahedral element and six truss elements have been derived. Embedded into these unit cells are further truss elements which represent bundles of muscle fibres. In summary, the present concept has the advantage that a three-dimensional model is developed which allows us take into account many physiological processes at the micro level.

Introduction

Skeletal muscles can be considered to be a complex organisation of thousands of force-producing muscle fibres arranged within a connective tissue. The muscular system holds about 40% of the total body weight. Muscles are responsible for the movement of the human body, they provide strength, serve as shock absorber and protect the skeleton system against external loads.

One of the first mathematical models was developed by Hill [1, 2]. This phenomenological model is derived from force-velocity measurements on an entire muscle. As an early representative of the group of microstructural approaches the concept of Huxley [3] is crucially based on investigations of the behaviour of the cross bridges which are assumed to have only two possible states: coupled or uncoupled. Both, the phenomenological as well as the micro mechanically-based models are applied to describe the contraction of the whole muscle. These types of models are used in movement analysis and muscle performance studies as known from multibody dynamics systems.

To incorporate further, more complex geometrical aspects of skeletal muscles, planimetric and three-dimensional models were designed, see e.g. [4, 5]. Most of these continuum-based models use a macroscopic description of the passive muscle behaviour (soft tissue) combined with a one-dimensional, possibly micromechanically-motivated, modelling of the active muscle fibres.

The present contribution differs from earlier approaches insofar as it is formulated at the mesomechanical level, as previously introduced in the framework of rubber-like polymers, cf. [6]. In this way the actual geometry of the muscle, i.e. the directional distribution of the muscle fibres, can be easily taken into account. The mechanical behaviour of muscles is, as earlier mentioned by Van Leeuwen [7], split into a passive and an active part. The here proposed concept is based on the idea of representing the passive part by means of an assembly of non-linear truss elements. In each truss element the force-stretch behaviour of a certain group of collagen fibres is implemented. The truss elements are arranged in such a way that one of them lies on each edge of one finite tetrahedral element. In this way a so-called tetrahedral unit cell is formed. The tetrahedral element of the unit cell serves to model the (near-)incompressible behaviour of skeletal muscles. By using a random assembling procedure we are able to model arbitrary geometries. An ensemble of these unit cells lets us simulate the behaviour of the soft tissue alone. To incorporate muscle activation, bundles of muscle fibres in form of non-linear truss elements are embedded in the before mentioned assembly of unit cells. These trusses contain a mathematical description of the activation at the fibre level. In this way we are able to simulate complex muscle structures with arbitrary muscle fibre distributions.

Material modelling of skeletal muscles

According to the aforementioned split of the material behaviour into active and passive parts also the Helmholtz free energy

$$W = W_{\text{active}} + W_{\text{passive}} \tag{1}$$

is additively decomposed into active (W_{active}) and passive (W_{passive}) contributions.

The active muscle behaviour

One fundamental property of a skeletal muscle fibre is its ability to contract without any mechanical influence from outside. In the present contribution this behaviour is implemented into three-dimensional truss elements. The force in one truss element is given by

$$F_{\text{active}} = f_{\text{fibre}}\, \bar{P}_t\, f_t\,(t)\, f_\lambda\,(\lambda_{\text{fibre}})\, f_v\,(\dot{\lambda}_{\text{fibre}}) \tag{2}$$

where $\bar{P}_t$ denotes the largest applied force inside the fibre. This force is correlated with the activation function $f_t\,(t)$.

Due to the high number of fibres inside a muscle it is impossible to discretise *each* muscle fibre by *one* truss element. To

compensate this, in Equation (2) the ratio

$$f_{\text{fibre}} = \frac{N_{\text{fibre}}}{N_{\text{truss f}}} \tag{3}$$

has been introduced. This parameter denotes the relation between the number of N_{fibre} in a reference cross section divided by the number of truss elements $N_{\text{truss f}}$ in the same reference cross section.

Furthermore $f_\lambda\,(\lambda_{\text{fibre}})$ is a function of the fibre stretch λ_{fibre} and $f_v\,(\dot{\lambda}_{\text{fibre}})$ denotes a function depending on the stretch rate $\dot{\lambda}_{\text{fibre}}$ of the muscle fibre. For more details of these functions see [8].

The passive muscle behaviour

One characteristic of soft tissues is their incompressible material behaviour. It is common to simulate this behaviour by means of rubber-like material laws. In the present work we use an approach by Böl & Reese [6] to simulate the passive muscle behaviour (W_{passive}). As aforementioned this approach bases on a so-called unit cell represented by an ensemble consisting of one tetrahedral element and six truss elements. Here again the passive part of the Helmholtz free energy is split into two contributions, the first one which is represented by the truss element includes the behaviour of bundles of collagen fibres. The second part takes care for the (near-)incompressibility of the material.

Numerical simulations

Beside the study of muscle behaviour one main object of this work is to apply the material model to realistic muscle geometries to be responsive to patients-specific questions. Therefore simulations of realistic muscle geometries are shown. Here the

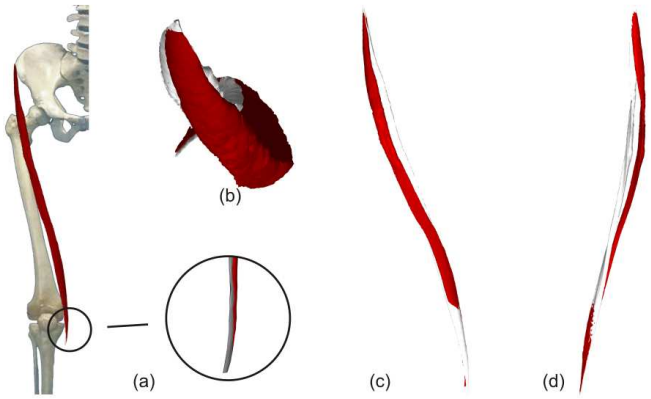

Figure 1: Geometry and simulation results (only tetrahedral elements are shown) of the sartorius muscle: (a) Muscle geometry (red = muscle tissue, grey = tendon), (b) axial, (c) coronal and (d) sagittal view (light-grey = undeformed muscle, red = deformed muscle).

longest muscle of the human body, the sartorius muscle, is studied which arises by tendinous fibres from the anterior superior iliac spine, running obliquely across the upper and anterior part of the thigh in an inferomedial direction, see Fig. 1. It descends as far as the medial side of the knee, passing behind the medial condyle of the femur to end in a tendon. This tendon curves anteriorly to join the tendons of the gracilis and semitendinous muscles which together form the pes anserinus, finally inserting into the proximal part of the tibia on the medial surface of its body. The action of sartorius is to cross the legs, by flexion of the knee, and flexion and lateral rotation the hip. Fig. 1 (a) shows the whole sartorius muscle including the tendon (coloured grey).

The sartorius muscle belongs to the group of fusiform muscles. That means that the global load direction of the muscle and the muscle fibres are aligned in parallel. Due to the spiral geometry of the muscle also the deformation behaviour is characterised by a torsion-like deformation in combination with a contraction, cf. Fig. 1 (b)-(d). This is conform to the physiological "function" of the muscle, because it bends the joints of the hip and the knee in combination with a movement of the thigh to the middle while the lower thigh is rotated to the inner site of the thigh.

References

[1] A. V. Hill (1922): The maximum work and mechanical efficiency of human muscles, and their most economical speed. *The Journal of Physiology*, **56**, 19–41.

[2] A. V. Hill (1938): The heat of shortening and the dynamic constants of muscle. *Proceedings of Royal Society of London*, **B126**, 136–195.

[3] A. F. Huxley (1957): Muscle structure and theories of contraction. *Progress in biophysics and biophysical chemistry*, **7**, 255–318.

[4] C. P. Tsui, C. Y. Tang, C. P. Leung, K. W. Cheng, Y. F. Ng, D. H. K. Chow, C. K. Li (2004): Active finite element analysis of skeletal muscle-tendon complex during isometric, shortening and lengthening contraction. *Bio-Medical Materials and Engineering*, **14**, 271–279.

[5] S. S. Blemker, P.-M. Pinsky, S. L. Delp (2005): A 3D model of muscle reveals the causes of nonuniform strains in the biceps brachii. *Journal of Biomechanics*, **38**, 657–665.

[6] M. Böl, S. Reese (2006): Finite element modelling of rubber-like polymers based on chain statistics. *International Journal of Solids and Structures*, **43**, 2–26.

[7] J. L. van Leeuwen (1992): Muscle Function in Locomotion. *Mechanics of Animal Locomotion*, Spriner-Verlag, Heidelberg.

[8] M. Böl, S. Reese, P. Meier, R. Blickhan (2005): Skeletal muscle modeling by means of an innovative finite element technology. *Proceedings of the 1st GAMM Seminar on Continuum Biomechanics*, **II-14**, 13–23.

An Approximate Formula Estimating Young's Modulus of Smooth Muscle Tissues in Dependence on Their Microstructural Parameters

M. Holeček*, P. Kochová, F. Moravec, Z. Tonar

Department of Mechanics
University of West Bohemia in Pilsen, Czech Republic
holecek@kme.zcu.cz, kochovap@centrum.cz, fanny@kme.zcu.cz, tonar@ntc.zcu.cz

Summary: We estimate the deformation energy of living tissue sample to obtain an approximate formula for its Young's modulus. It includes a nontrivial term that cannot be obtained by a simple homogenization of elastic properties. We show its importance in explaining the effective stiffness control during the smooth muscle stimulation and present some experimental data.

Introduction

Living tissues are an excellent example of highly heterogeneous materials. Their realistic modeling by continuum is an ambitious task of biomechanics. The crucial step of such a modeling is the way in which the heterogenous structure is "homogenized". In this contribution, we target the mechanical behavior of smooth muscle tissues. From mechanical point of view, they appear as perfectly organized "machines" being able to change very effectively their mechanical parameters in a wide range. In our study, we try to show that this ability is given by a *special arrangement* of tissues structure. Namely, the sophisticated combination of fibers, fluids and membranes leads to an additional term when averaging elasticity of the whole structure. This term describes a nontrivial *structural effect* resulting from impermeability of cell membranes and high anisotropy of the cellular arrangement. It cannot be found by a naive homogenization that gives simply an averaged stiffness of individual components. The magnitude of this term plays important role in tissue elasticity and is very sensitive on small changes in proportions of cellular lengths in individual directions. It explains an extreme ability of smooth muscle tissues to change its stiffness very effectively.

Deformation of the tissue

Let us split mentally the tissue sample into N volume elements of nearly identically structured parts – *representative volume elements* (RVE). Each RVE includes one cell and a corresponding part of intercellular space surrounding the cell. At any state, the energy of j-th RVE, $E^{(j)}$, is defined so that the energy of the whole sample equals $\sum_{j=1}^{N} E^{(j)}$. The energy $E^{(j)}$ depends on many physical parameters of the cell and of its near surrounding (local stress-strain characterization at the place where the cell is located, the actual structure of fibers, their physical parameters, electro-chemical parameters, the structure of cell membrane, chemical compositions of various liquids, temperature, etc.). We can combine and arrange these parameters in such a way that $E^{(j)}(c_1, c_2, c_3, \delta_1, \delta_2, \delta_3, \ldots)$ where c_i and δ_i $(i = 1, 2, 3,)$ characterize dimensions of the cell and mean distances between cells (Fig. 1), respectively; whereas $\Delta x_i \equiv c_i + \delta_i$ corresponds to the actual size of RVE in the i-th spatial direction. The smooth muscle cells are usually very closely side-by-side, i.e. $\delta_i \ll c_i$.

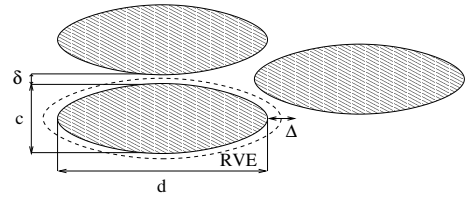

Figure 1: The choice of RVE and a schematic explanation of the defined length parameters.

Let us choose an arbitrary RVE, say the j-th, and consider a sample of tissue being in natural state, i.e. without an external load. Stability of the natural state implies that $E^{(j)}$ has the local minimum at this state. We suppose cylindrical geometry, i.e. $c_1 = c_2 \equiv c_0$, $c_3 \equiv d_0$, $\delta_1 = \delta_2 \equiv \delta_0$, $\delta_3 \equiv \Delta_0$. Now, let us study a *small deformation* of the sample that preserves the cylindrical geometry, i.e. the deformations in which $c_1 = c_2 = c$, $c_3 = d$, $\delta_1 = \delta_2 = \delta$, $\delta_3 = \Delta$. Choosing the coordinate axis x_1, x_2, x_3 so that the lengths d and Δ are defined along the coordinate x_3, we can define the local stretches at the "point" where the RVE is located, namely

$$\beta_i = \frac{\Delta x_i}{\Delta x_i^0} = 1 + \epsilon_i, \tag{1}$$

where $\Delta x_1^0 = \Delta x_2^0 = c_0 + \delta_0$, $\Delta x_3^0 = d_0 + \Delta_0$. Let us suppose that the increase of the energy of the RVE, $\delta E^{(j)}$, is approximately the same for each RVE. Supposing that $\epsilon \equiv \epsilon_3$ characterizes the deformation of a macroscopic sample, we obtain the Young's modulus of the tissue as

$$Y \approx \frac{\delta E^{(j)}(\epsilon)}{\epsilon^2 V_{RVE}}. \tag{2}$$

Energy of deformation

During the small deformation, the free energy of the RVE increases since we leave the local minimum. The energetic "landscape" around the local minimum may be described by a nonnegative function f_E reaching the zero value at the local minimum, namely

$$f_E = f_{RVE} + f_{cell} + f_{qv}, \tag{3}$$

where the functions f_{RVE} and f_{cell} represent the energy connected with change of volumes of the RVE (V_{RVE}) and of the

cell (V_{cell}), respectively. They have local minimum at 0, where $f_{RVE}(0) = f_{mem}(0) = 0$. The term f_{qv} corresponds to a change of values of all other physical quantities, like the length of various fibers, the shape of the cell membrane, and so on. We expand f_{qv} into the Taylor series around the point of local minimum and neglect terms of the third and higher orders and all mixed derivatives, namely

$$f_{qv} \approx 2K_c(c-c_0)^2 + K_d(d-d_0)^2 + 2K_\delta(\delta-\delta_0)^2 + \dots . \quad (4)$$

When performing the small deformation defined by the value of ϵ, we reach another point on the energy "landscape". We suppose that this state (defined by the constraint $d + \Delta = (d_0 + \Delta_0)(1 + \epsilon) \equiv C(\epsilon)$) will be stable too. It means that all free parameters of the problem relax into such values that minimizes the value of the free energy f_E. The relaxation is thus an additional "movement" on the energy "landscape" defining the free energy corresponding to the small deformation as

$$\delta E^{(j)}(\epsilon) = \min_{d+\Delta=C(\epsilon)} f_E. \quad (5)$$

The study of the minimum (5) is the crucial point of our work. We notice first that the energy corresponding to the change of volumes is considerable larger than the energy connected with the change of other parameters. It means that the minimum (5) can be reached only if V_{RVE} and V_{cell} remain constant, i.e. $\beta_1\beta_2\beta_3 = 1$ and $c^2 d = c_0^2 d_0$.

By using perturbation techniques (defined in [1]) we obtain

$$\delta E^{(j)}(\epsilon) = E_{spring}(\epsilon) + E_{membrane}(\epsilon), \quad (6)$$

where the first term,

$$E_{spring}(\epsilon) \approx \left(\frac{1}{2}\frac{K_c K_\delta}{K_c + K_\delta} c_0^2 + \frac{K_d K_\Delta}{K_d + K_\Delta} d_0^2\right)\epsilon^2, \quad (7)$$

corresponds to elasticity of a regular heterogeneous system consisting of parts with different stiffness. If there were no impermeable membranes in the structure, the deformation energy would equal to this term only. The presence of second term,

$$E_{membrane}(\epsilon) \approx \left(2A_c^{-1}c_0^{-2} + A_d^{-1}d_0^{-2}\right)^{-1} G^2\epsilon^2, \quad (8)$$

($A_c = K_c + K_\delta$, $A_d = K_d + K_\Delta$) is nontrivial and corresponds to a *structural effect* caused by the presence of the impermeable cell membrane. The parameter G,

$$G = \left(1 + \frac{\delta_0}{c_0}\right)\left(1 + \frac{K_c}{K_\delta}\right)^{-1} - \left(1 + \frac{\Delta_0}{d_0}\right)\left(1 + \frac{K_d}{K_\Delta}\right)^{-1}, \quad (9)$$

vanishes if the structure is *isotropic*.

Young's modulus and experimental data

The Young's modulus can be determined by putting (6) into (2). The stiffness of extracellular junction is much bigger than the stiffness of the internal cell structures (cytoskeleton and membrane) [2, 3]. That is, $K_c \ll K_\delta$ and $K_\Delta \ll K_d$. It implies that the Young's modulus corresponding to the energy E_{spring} equals approximately to the Young's modulus of the cell alone, Y_{cell}. Moreover, the term G may be approximated too and we obtain the approximate formula,

$$Y \approx Y_{cell} + \frac{1}{2}\frac{c_0}{\delta_0}\left(\frac{V_{RVE} - V_{cell}}{V_{cell}} - 3\frac{\delta_0}{c_0}\right)^2 Y_{connect}, \quad (10)$$

where $Y_{connect}$ is the Young's modulus of extracellular junction and $\eta \equiv (V_{RVE} - V_{cell})/V_{cell}$ is a mean proportion of the extracellular and cellular volume. The formula shows an eminent importance of the second term in the muscle cell activation when the shape of the cell changes by increasing the diameter c_0. It means the increasing size of the second term because η ($> 3\delta_0/c_0$) remains constant.

The parameters Y_{cell}, $Y_{connect}$ may be estimated from literature: $Y_{cell} \sim 0,25$ kPa, $Y_{connect} \sim 12,7$ kPa [2, 3] (though their variability for different tissues may be expected). The ration η, as well as the parameters c_0 and d_0 may be measured by microscopic methods. It differs considerable for various tissue (see Fig. 2 with our results). We have measured the Young's modulus of the smooth muscle tissue of gastropods, and obtain $Y \approx 28 \pm 5$ kPa. The formula (10) leads to an approximate value of 20 kPa.

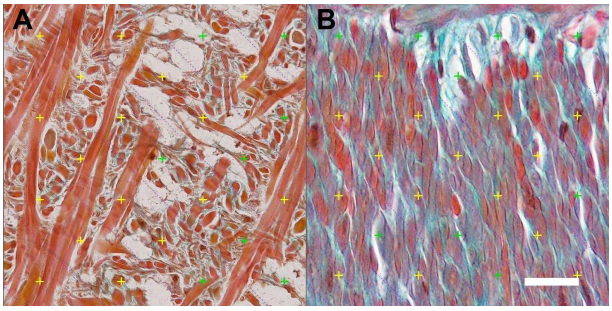

Figure 2: Estimating the volume fraction of smooth muscle by counting intersections of the isotropic point grid with profiles of smooth muscle cells in histological section through integument of a gastropod Arion sp., $\eta \approx 0.45$ (A), and intestine of a frog Xenopus sp. Trichrome stain, $\eta \approx 0.68$ (B), scale bar 30 micrometers.

Acknowledgement This work has been supported by the Czech Grant Agency, the grant number 106/05/0219.

References

[1] M. Holeček, F. Moravec (2006): Hyperelastic model of a material which structure is formed by "balls and springs". *Int. Journal of Solids and Structures*, **43**, 7393–7406.

[2] H. J. Ra, C. Picart, H. Feng., H. L. Sweeney, D. E. Discher (1999): Muscle cell peeling from micropatterned collagen: direct probing of focal and molecular properties of matrix adhesion. *Journal of Cell Science*, **112**, 1425–1436.

[3] D. M. Broday (2000): Diffusion of Clusters of Transmembrane Proteins as a Model of Focal Adhesion Remodeling. *Bulletin of Mathematical Biology*, **62**, 891-924.

Conception of the Multicompartment Model for Cerebral Perfusion Estimation, Homogenization of Hierarchical Branching Structures

E. Rohan[1*], R. Cimrman[1], V. Lukeš[1], V. Rohan[2]

[1]Dept. of Mechanics, University of West Bohemia, Pilsen
Univerzitní 22, 306 14 Plzeň, Czech Republic
rohan@kme.zcu.cz, cimrman3@ntc.zcu.cz, lukes@kme.zcu.cz

[2]Dept. of Neurology, University Hospital Pilsen
Alej Svobody 80, 323 00, Plzeň, Czech Republic
rohan@fnplzen.cz

Summary: The paper deals with modelling the cerebral perfusion (CP) using an advanced microstructure based model. The presented approach is based on a layered representation of the vascular tree hierarchies; in each-one the strongly heterogeneous medium described by the Biot model is upscaled using the two-scale homogenization of a periodic structure. The model involves macroscopic pressures associated with different compartments of the perfusion system. Convected diffusion of the contrast medium is considered; the spatial macroscopic distribution of its concentration is the measure of the perfusion.

Motivation – cerebral perfusion monitoring

Existing studies [5, 4] have shown that analysis of the cerebral perfusion (CP) is potentially useful in the diagnosis and understanding pathologies in brain. One of the frequently used procedures of the CP experimental assessment is based on the CT or MRI monitoring of the injected contrast medium, so that differences between the measured concentration image (in time) and its modeling based prediction indicate local zones of non-physiological perfusion. The measured quantity is the residual concentration $c(t)$, defined at any location; according to the literature, nowadays its time response is assumed to obey a simple convolution rule

$$c(t) = F_{\rm eff} \int_0^t c_a(\tau) R(t-\tau)\, d\tau, \qquad (1)$$

where $c_a(t)$ is the arterial concentration input, $F_{\rm eff}$ is the effective cerebral blood flow (related to the local porosity) and $R(t)$ is the *residual function*. The key point of such a modelling is a convenient estimation of $R(t)$; the existing methods are based purely on experimental observations supplemented by data-fitting methods (typically *ill-conditioned*), or on some more advanced approaches which consider few physiological parameters and a statistic distribution (e.g. the Bayesian estimation).

In this paper we suggest a more complex approach to the residual concentration modelling which takes into account the hierarchical structure of the cerebral blood flow. Namely, we attempt to approximate the branching vascular tree at several levels comprising arteries, arterioles, precapilaries, capilaries, venulae and veins. Concentration $c(t)$ is computed using the model of convected diffusion in heterogeneous porous medium.

Two-scale model of parallel flows

Recently a homogenized model of blood perfusion in deforming tissue was developed which assists in understanding some diffusion-deformation phenomena inherited by the upscaled model. In particular, one can see how the microstructural geometry and topology influence the form of the homogenized constitutive laws and how the individual homogenized coefficients reflect specific modes of interactions at the microscopic level. The micromodel considered in the homogenization procedure is based on the Biot model for the incompressible medium (σ_{ij} is the Cauchy stress, $e_{ij}(u)$ is the small strain of displacement field u, p is the bulk pressure and w is the perfusion velocity)

$$-\operatorname{div}\sigma^\varepsilon = f\ , \qquad \operatorname{div}\frac{\mathrm{d}}{\mathrm{d}t}u^\varepsilon + \operatorname{div} w^\varepsilon\ = 0\ , \qquad (2)$$

where

$$\begin{aligned} \sigma^\varepsilon_{ij} &= -p^\varepsilon \delta_{ij} + D^\varepsilon_{ijkl} e_{kl}(u^\varepsilon)\ , \\ w^\varepsilon_i &= -K^\varepsilon_{ij}\partial_j p^\varepsilon\ . \end{aligned} \qquad (3)$$

Above, the dependence on the scale of the heterogeneities ε, is indicated by superscript $^\varepsilon$.

Strong heterogeneity in the permeability coefficients w. r. t. reference volume decomposition is considered; in particular, the ε^2-scaling of permeability K^ε_{ij} accounts for the "microscopic" fluid flow through the *interface compartment* corresponding to the network of capilaries.

The limit homogenized equations obtained for infinitely small scale of the microstructure involve the stress-equilibrium equation and other two equations governing the mass redistribution, describing the parallel diffusion in two high-conducting compartments (arterial and venous sectors) separated by the low conducting matrix. The homogenized coefficients are defined in terms of the characteristic response of the reference volume element. It is possible to identify the instantaneous and fading memory viscoelastic coefficients; other effective parameters, controlling the fluid redistribution between the compartments, are involved also in time convolutions. Rigorous treatment of the homogenization procedure for similar model was published in [2].

Although the deformation and fluid flow are almost uncoupled in normal conditions of the cerebral perfusion, potentially this model enables us to treat non-physiological situations, when blood pulsation occurs.

Hierarchically arranged compartments

The existing model is convenient to approximate the lowest hierarchy of the vasculature where the flow between the high-conductive compartments (the arterial and the venous ones) is enabled through the interface (matrix) compartment corresponding to the capilaries and venulae; at this level the very tiny vessels are blurred, being taken as a non-distinguishable constituent of the surrounding tissue. Therefore, we treat the convected diffusion of the contrast medium through this interface, although it cannot penetrate into the extravascular space in real tissue.

To account for higher levels we suggest the *layered hierarchical structure*, where the conductive channels associated with the arterial tree split into several downstream branches in each layer (for the venous tree, analogical arrangement is considered). Let $\varepsilon\gamma_n$ be the characteristic distance of the parallel channels arranged transversally w. r. t. the layer at the n-th hierarchy, $n = 1, 2, \ldots, \bar{n}$ (locally periodic structure assumed at each layer) and ν_n be the branching, see Fig. 1. Then

$$\gamma_n = \gamma_{n-1}/\nu_{n-1} \ , \quad \gamma_0 = L_0 \ , \ \nu_0 = 1 \ , \tag{4}$$

where L_0 is the reference length. This is a simple layout of the branching, in a more realistic structure some branching would also shunt the flow backwards form hierarchy n to $n-1$.

This layout of the hierarchical structure leads to homogenization of (2)–(3) with following modifications of the present model:

- in each layer the "in-plane periodicity" is considered, whereas the transversal dimension is fixed;
- at each hierarchy (layer) the *matrix* M separating the highly conductive channels C_α, $\alpha = 1, 2$ is permeable, however the permeability κ_α of the surface Γ_α between M and C_α is introduced, as proposed in [6, 7], such that the non-physiological "short circuit" effects at the upper hierarchies (usually for $n = 1, \ldots, \bar{n}-1$) are disabled by setting the surface permeability zero;
- in addition to (2)-(3), the convection diffusion problem [3] is considered to define the spatial distribution of the residual concentration in time:

$$\frac{\mathrm{d}}{\mathrm{d}\,t}(\phi c^\varepsilon) = \partial_i \left(d^\varepsilon_{ij} \partial_j c^\varepsilon - w^\varepsilon_i c^\varepsilon \right) \ , \tag{5}$$

  where d^ε_{ij} is the diffusivity of the Fick law and ϕ is the microstructural porosity. It is worth noting that concentration c^ε is uncoupled with other fields involved in (2)–(3), therefore (5) is homogenized once w^ε_i is known for $\varepsilon \to 0$.

The limit homogenized residual concentrations computed by the upscaled macromodel can be interpreted at the microscopic level at each hierarchy; for a finite scale $\varepsilon > 0$, thus, we have an alternative expression for concentration c, replacing the convolution in (1) by a more refined transition scheme reflecting the geometrical and topological features of the cerebral vasculature.

Preliminary studies. Viability of the proposed modelling approach is demonstrated on numerical examples computed by the in-house developed software for the multiscale analysis of the porous media. Since full implementation of the refined model of the CP is a long period task, we focus on simulation of the contrast medium flux at the lower level hierarchies, showing the dispersive response to a concentration increase input at the highest considered hierarchy.

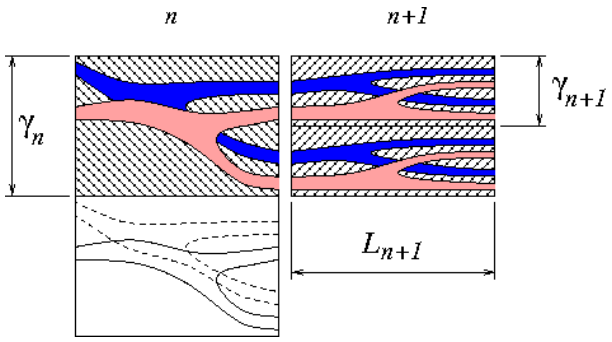

Figure 1: Vascular tree: arteries and veins at two hierarchies $n, n+1$ for binary splitting, $\nu = 2$. The hatched regions (the matrix) separating the two vascular trees represent the mixture of capilaries, venulae and the extravascular tissue; except of the lowest hierarchy $\bar{n}$, the segments of the vascular trees are impermeable.

Acknowledgment The research is supported by the project MSM 4977751303 of the Czech Republic.

References

[1] R. Cimrman, E. Rohan (2007): On modelling the parallel diffusion flow in deforming porous media. *Mathematics and Computers in Simulation*, special volume: Proc. of the conference Modelling 2005, Plzeň (to appear).

[2] G. Griso, E. Rohan (2006): On homogenization of diffusion-deformation problem in strongly heterogeneous media. *Ricerche di Matematica* (accepted for publication).

[3] U. Hornung (1997): *Homogenization and Porous Media*. Springer-Verlag, Berlin.

[4] K. Mouridsen, K. Friston, N. Hjort, L. Gyldensted, L. Ostergaard, S. Kiebel (2006): Bayesian estimation of cerebral perfusion using a physiological model of microvasculature. *NeuroImage* (to appear).

[5] T. S. Koh, C. K. M. Tan, L. H. D. Cheong, C. C. T. Lim (2006): Cerebral perfusion mapping using a robust and efficient method for deconvolution analysis of dynamic contrast-enhanced images. *NeuroImage*, **32**, 643–653.

[6] E. Rohan (2006): Modelling large deformation induced microflow in soft biological tissues. *Theor. Comput. Fluid Dynamics*, **20**, 251–276.

[7] E. Rohan, R. Cimrman, V. Lukeš (2006): Numerical modelling and homogenized constitutive law of large deforming fluid saturated heterogeneous solids. *Int. J. of Computers & Structures*, **84**, 1095–1114.

A Multiphase Model for Biological Tissue including Growth and Remodelling

T. Ricken[1], **J. Bluhm**[2*]

[1]Computational Mechanics, [2]Institute of Mechanics, University of Duisburg-Essen, D-45117 Essen, Germany
tim.ricken@uni-due.de, joachim.bluhm@uni-due.de

Summary: A triphasic model (solid, interstices filled with water containing nutrients) based on the Theory of Porous Media (TPM) is proposed for the phenomenological description of transversely isotropic saturated biological tissues including the phenomena of growth and remodelling. Finally, we gain a coupled set of equations determining the solid motion, mixture temperature, inner pressure as well as solid and nutrient volume fractions. After presenting the developed framework of the calculation concept, a representative numerical example is examined.

Basic model

The investigated porous body consists of φ^{S} (solid) which is saturated by φ^{F} (fluid). The fluid itself is composed of φ^{L} (liquid) and φ^{N} (nutrients), see Fig.1. The volume fraction n^{α} refer

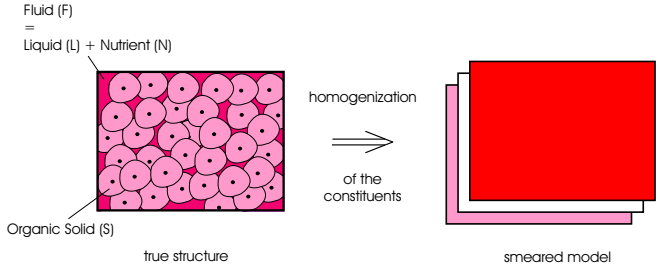

Figure 1: Homogenization

the volume elements dv^{α} of the constituents φ^{α} to the bulk volume element dv, viz.

$$\mathrm{n}^{\alpha}(\mathbf{x},\mathrm{t}) = \frac{\mathrm{dv}^{\alpha}}{\mathrm{dv}}\,, \qquad \sum_{\alpha=1}^{\kappa} \mathrm{n}^{\alpha}(\mathbf{x},\mathrm{t}) = \sum_{\alpha=1}^{\kappa} \frac{\rho^{\alpha}}{\rho^{\alpha\mathrm{R}}} = 1, \quad (1)$$

where $\mathbf{x}$ is the position vector of the spatial point x in the actual placement and t is the time. The partial density $\rho^{\alpha} = \mathrm{n}^{\alpha}\,\rho^{\alpha\mathrm{R}}$ is related to the real density of the materials $\rho^{\alpha\mathrm{R}}$ involved via the volume fractions n^{α}, see $(1)_2$. Moreover, we define the Jacobian $\mathrm{J}_{\alpha} = \det \mathbf{F}_{\alpha}$, where $\mathbf{F}_{\alpha} = (\partial \mathbf{x}_{\alpha})/(\partial \mathbf{X}_{\alpha}) = \mathrm{Grad}_{\alpha}\, \boldsymbol{\chi}_{\alpha}$ is the deformation gradient. The differential operator "Grad_{α}" denotes a partial differentiation with respect to the reference position $\mathbf{X}_{\alpha}$. The local statements of the balance equations of mass and momentum are given for the constituents φ^{α} by

$$\begin{aligned} &(\rho^{\alpha})'_{\alpha} + \rho^{\alpha}\,\mathrm{div}\,\mathbf{x}'_{\alpha} = \hat{\rho}^{\alpha}\,, \\ &\mathrm{div}\,\mathbf{T}^{\alpha} + \rho^{\alpha}\,(\mathbf{b} - \mathbf{x}''_{\alpha}) + \hat{\mathbf{p}}^{\alpha} - \hat{\rho}^{\alpha}\,\mathbf{x}'_{\alpha} = \mathbf{o}\,. \end{aligned} \quad (2)$$

Therein,"div" denotes the spatial divergence operator, $\mathbf{x}'_{\alpha}$ is the velocity of the constituent φ^{α}, $\hat{\rho}^{\alpha}$ represents the mass supply between the phases which has to conform to $\hat{\rho}^{\mathrm{S}} + \hat{\rho}^{\mathrm{L}} + \hat{\rho}^{\mathrm{N}} = 0$, $\mathbf{T}^{\alpha}$ is the partial symmetric Cauchy stress tensor, $\rho^{\alpha}\,\mathbf{b}$ specifies the volume force and $\hat{\mathbf{p}}^{\alpha}$ describes the interactions of the constituents φ^{α} which are restricted to $\hat{\mathbf{p}}^{\mathrm{S}} + \hat{\mathbf{p}}^{\mathrm{L}} + \hat{\mathbf{p}}^{\mathrm{N}} = \mathbf{o}$.

The system is investigated under the condition of a material incompressible components. The nutrient phase is assumed to be contained in the liquid phase, so that both phases are assigned the same velocity $\mathbf{x}'_{\mathrm{F}}$ and to the same pore pressure λ. Moreover, we assume that the liquid phase is not involved in the mass transition and we exclude accelerations.

Constitutive modeling

The entropy inequality for the mixture yields the following constitutive relations for the partial Cauchy stress tensors

$$\begin{aligned} \mathbf{T}^{\mathrm{S}} &= -\,\mathrm{n}^{\mathrm{S}}\,\lambda\,\mathbf{I} + 2\,\rho^{\mathrm{S}}\,\mathbf{F}_{\mathrm{S}}\frac{\partial \psi^{\mathrm{S}}}{\partial \mathbf{C}_{\mathrm{S}}}\,\mathbf{F}_{\mathrm{S}}^{\mathrm{T}} = -\,\mathrm{n}^{\mathrm{S}}\,\lambda\,\mathbf{I} + \mathbf{T}_{\mathrm{E}}^{\mathrm{S}}, \\ \mathbf{T}^{\mathrm{F}} &= -(\mathrm{n}^{\mathrm{L}} + \mathrm{n}^{\mathrm{N}})\,\lambda\,\mathbf{I} = -\,\mathrm{n}^{\mathrm{F}}\,\lambda\,\mathbf{I}\,, \quad \mathrm{n}^{\mathrm{F}} = \mathrm{n}^{\mathrm{L}} + \mathrm{n}^{\mathrm{N}} \end{aligned} \quad (3)$$

of the constituents solid and fluid ($\varphi^{\mathrm{F}} = \varphi^{\mathrm{L}} + \varphi^{\mathrm{N}}$) with the realistic fluid pressure λ, the tensor of identity $\mathbf{I}$ and the right Cauchy-Green tensor $\mathbf{C}_{\mathrm{S}} = \mathbf{F}_{\mathrm{S}}^{\mathrm{T}}\,\mathbf{F}_{\mathrm{S}}$ related to the solid.

In many living tissues, an anisotropic strain response can be observed, which is caused by the inner structure of the tissue. Therefore, we introduce the so-called structural tensor $\mathbf{M} = \mathbf{A} \otimes \mathbf{A}$ where $\mathbf{A}$ denotes the vector of the preferred direction. In [1] a functional dependency of the stored energy is suggested with the usage of the principle invariants $\mathrm{I}_{1,2,3}$ of $\mathbf{C}_{\mathrm{S}}$ and the basic invariant $\mathrm{J}_4 := \mathrm{tr}[\mathbf{C}_{\mathrm{S}}\,\mathbf{M}]$ of the argument tensors $(\mathbf{C}_{\mathrm{S}}, \mathbf{M})$. The stored energy function can be written now as $\psi^{\mathrm{S}} = [\mathrm{n}^{\mathrm{S}}/(\mathrm{n}^{\mathrm{S}}_{0\mathrm{S}})]^{\mathrm{n}}\,\psi^{\mathrm{S}}_{\mathrm{iso,\,neo}}(\mathrm{I}_1, \mathrm{I}_2, \mathrm{I}_3) + \psi^{\mathrm{S}}_{\mathrm{ti}}(\mathrm{J}_4)$. Therein, the term connected with the solid volume fraction n^{S} describes the change of solid rigidity relating to the reference solid volume fraction $\mathrm{n}^{\mathrm{S}}_{0\mathrm{S}}$ at $\mathrm{t} = \mathrm{t}_0$. The isotropic part of $\psi^{\mathrm{S}}_{\mathrm{iso,\,neo}}$ is of Neo-Hookean type, viz.

$$\begin{aligned} &\psi^{\mathrm{S}}_{\mathrm{iso,\,neo}} = \psi^{\mathrm{S}}_{\mathrm{iso,\,neo}}(\mathrm{I}_1,\, \mathrm{J}_{\mathrm{S}} = \sqrt{\mathrm{I}_3}) \\ &= \frac{1}{\rho^{\mathrm{S}}_{0\mathrm{S}}}\{\lambda^{\mathrm{S}}\,\frac{1}{2}\,(\log \mathrm{J}_{\mathrm{S}})^2 - \mu^{\mathrm{S}}\,\log\,\mathrm{J}_{\mathrm{S}} + \frac{1}{2}\,\mu^{\mathrm{S}}(\mathrm{I}_1 - 3)\}, \end{aligned} \quad (4)$$

where μ^{S} and λ^{S} are the macoscopic Lamé constants. For the transversely isotropic part of the Helmholtz free energy function we choose for this first try a lightly modified function with

$$\psi^{\mathrm{S}}_{\mathrm{ti}} = \psi^{\mathrm{S}}_{\mathrm{ti}}(\mathrm{J}_4) = \begin{cases} \dfrac{1}{2\,\rho^{\mathrm{S}}_{0\mathrm{S}}}\;\alpha_1\,(\mathrm{J}_4 - 1)^{\alpha_2} & \text{for } \mathrm{J}_4 \geq 1 \\ 0 & \text{for } \mathrm{J}_4 < 1, \end{cases} \quad (5)$$

where $\alpha_{1,2} \geq 1$ are parameters due to the stiffness of the preferred direction $\mathbf{A}$. With this, the solid effective Cauchy stress tensor reads

$$\mathbf{T}^{\mathrm{S}}_{\mathrm{E}} = \left(\frac{\mathrm{n}^{\mathrm{S}}}{\mathrm{n}^{\mathrm{S}}_{0\mathrm{S}}}\right)^{\mathrm{n}} \mathrm{J}_{\mathrm{S}} \frac{\rho^{\mathrm{S}}}{\rho^{\mathrm{S}}_{0\mathrm{S}}} \mathbf{T}^{\mathrm{S}}_{\mathrm{E,\,iso,\,neo}} + \mathrm{J}_{\mathrm{S}} \frac{\rho^{\mathrm{S}}}{\rho^{\mathrm{S}}_{0\mathrm{S}}} \mathbf{T}^{\mathrm{S}}_{\mathrm{E,\,ti}}\,,$$
$$\mathbf{T}^{\mathrm{S}}_{\mathrm{E,\,iso,\,neo}} = \frac{1}{\mathrm{J}_{\mathrm{S}}}\left[2\,\mu^{\mathrm{S}}\,\mathbf{K}_{\mathrm{S}} + \lambda^{\mathrm{S}}\,(\log \mathrm{J}_{\mathrm{S}})\,\mathbf{I}\right], \qquad (6)$$
$$\mathbf{T}^{\mathrm{S}}_{\mathrm{E,\,ti}} = \frac{1}{\mathrm{J}_{\mathrm{S}}}\,\alpha_1\,\alpha_2\,[\mathrm{tr}(\mathbf{C}_{\mathrm{S}}\,\mathbf{M}) - 1]^{\alpha_2 - 1}\,\mathbf{F}_{\mathrm{S}}\,\mathbf{M}\,\mathbf{F}^{\mathrm{T}}_{\mathrm{S}}.$$

Herein, the Karni-Reiner strain $\mathbf{K}_{\mathrm{S}} = 1/2\,(\mathbf{B}_{\mathrm{S}} - \mathbf{I})$ with the left Cauchy-Green tensor $\mathbf{B}_{\mathrm{S}} = \mathbf{F}_{\mathrm{S}}\,\mathbf{F}^{\mathrm{T}}_{\mathrm{S}}$ and $\mathbf{m} = \mathbf{F}_{\mathrm{S}}\mathbf{A} \otimes \mathbf{F}_{\mathrm{S}}\mathbf{A} = \mathbf{a} \otimes \mathbf{a}$ as the structural tensor has been used.

The motions of both the solid and the fluid are connected by the interaction forces $\hat{\mathbf{p}}^{\mathrm{F}} = -\hat{\mathbf{p}}^{\mathrm{S}}$ with $\hat{\mathbf{p}}^{\mathrm{F}} = \lambda\ \mathrm{grad}\ \mathrm{n}^{\mathrm{F}} - \mathbf{S}_{\mathrm{F}}\ \mathbf{w}_{\mathrm{FS}}$, where $\mathbf{S}_{\mathrm{F}}$ is obtained with $\mathbf{S}_{\mathrm{F}} = 1/(\mathrm{S}_{\mathrm{F}} - \hat{\rho}^{\mathrm{F}})\,[\,\alpha_1\,\mathbf{I} + \alpha_2\,\mathbf{M}\,]^{-1}$. Herein, $\mathbf{S}_{\mathrm{F}}$ describes the permeability tensor between the fluid and solid phase in connection to the seepage velocity $\mathbf{w}_{\mathrm{FS}} = \mathbf{x}'_{\mathrm{F}} - \mathbf{x}'_{\mathrm{S}}$ and $\alpha_{1,2}$ are the parameters for the isotropic and transversely isotropic ratio of porosity respectively. The material parameter function S_{F} is postulated with $\mathrm{S}_{\mathrm{F}} = \mathrm{k}^{\mathrm{S}}_0/\mu^{\mathrm{FR}}\,[\mathrm{n}^{\mathrm{F}}_{0\mathrm{S}}/\mathrm{n}^{\mathrm{F}}]^{\mathrm{m}} + \hat{\rho}^{\mathrm{F}}$, where m denotes a dimensionless material parameter, $\mathrm{k}^{\mathrm{S}}_0$ is the initial intrinsic permeability and μ^{FR} denotes the shear viscosity of the fluid, see e.g. [2] or [3].

We assume a mass exchange which acts between the solid and nutrient phase only ($\hat{\rho}^{\mathrm{F}} = \hat{\rho}^{\mathrm{L}} + \hat{\rho}^{\mathrm{N}} = -\hat{\rho}^{\mathrm{S}},\ \hat{\rho}^{\mathrm{L}} = 0$). In view of the mass transfer, the inequality is fulfilled if the dissipation part $\mathrm{D}_{\hat{\rho}^{\mathrm{S}}} = -\hat{\rho}^{\mathrm{S}}\,(\Psi^{\mathrm{S}} - \Psi^{\mathrm{N}}) \geq 0$ holds where $\Psi^{\alpha} = \psi^{\alpha} + \mathrm{n}^{\alpha}\,(\lambda/\rho^{\alpha} + \partial\psi^{\alpha}/\partial\mathrm{n}^{\alpha})$ denotes the chemical potential if the influence of the velocity square is neglected. Using the ansatz $\hat{\rho}^{\mathrm{S}} = -\delta^{\mathrm{L}}_{\hat{\rho}}\,(\Psi^{\mathrm{S}} - \Psi^{\mathrm{N}})$, the aforementioned dissipation part is fulfilled if $\delta^{\mathrm{L}}_{\hat{\rho}} \geq 0$. Under consideration of this restriction it will be postulated that $\hat{\rho}^{\mathrm{S}}$ is a function of the norm of the total Kirchhoff stresses τ_{vMi} and of the solid and the nutrient content, i.e.,

$$\hat{\rho}^{\mathrm{S}} = \hat{\rho}^{\mathrm{S}}_{\mathrm{max}}\ \ \hat{\rho}^{\mathrm{S}}_{\mathrm{n^N}}\ \ \hat{\rho}^{\mathrm{S}}_{\tau_{\mathrm{vMi}}}\,, \quad \hat{\rho}^{\mathrm{S}}_{\mathrm{n^N}} = -\exp\left[-\kappa_{\mathrm{n^N}}\,(\mathrm{n}^{\mathrm{N}})^2\right] + 1\,,$$
$$\hat{\rho}^{\mathrm{S}}_{\tau_{\mathrm{vMi}}} = -2\exp\left[-\log(2)\,\tau_{\mathrm{vMi}}/\tau_{\mathrm{vMi0}}\right] + 1\,. \qquad (7)$$

Under consideration of the above given constitutive relations a closed calculation concept has been developed by use of the finite element approximation, see [4], which enables the calculation of the following example.

Example: femur

In the example, we consider the remodelling of bone with respect to a given load case. In the following we discuss changes belonging to the internal architecture namely the density, the nutrients as well as the inner trabecular structure. Fig.2$_{\mathrm{c,e}}$ illustrate a x-ray and a photograph of a femur. The bone compensates the loads from the body as a change in density and structure. The material is assumed to be orthotopic where the preferred directions follow the eigenvectors of $\mathbf{T}^{\mathrm{S}}$, see Fig. 2$_{\mathrm{f}}$. In the initial configuration the values of density and nutrients belong to $\mathrm{n}^{\mathrm{S}} = 0.1$ and $\mathrm{n}^{\mathrm{N}} = 0.7$ concerning the total domain. Due to the stress and nutrient indicated growth, we expect a bone density remodeling to an optimized state. Comparing the calculated density distribution as well as the trabecular bone structure given in Fig.2$_{\mathrm{d,f}}$ with the photographs in Fig.2$_{\mathrm{c,e}}$ a good approximation can be considered.

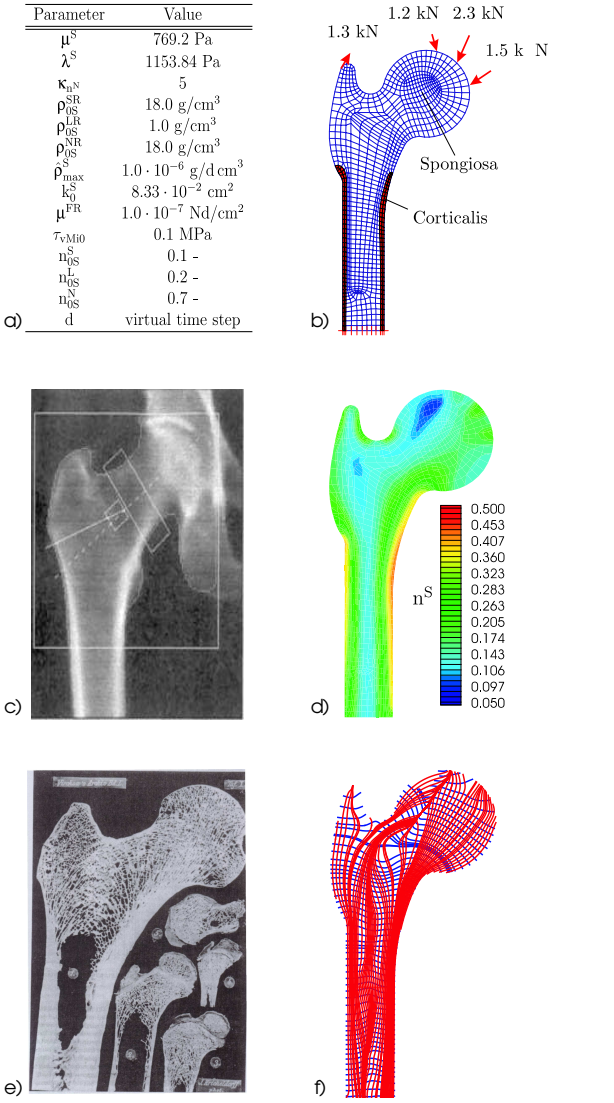

Figure 2: a) Material parameters, b) load case [5] and discretization, c) X-ray of a femur [6], d) calculated density, e) photograph of bone structure [7], f) calculated trabecular directions.

References

[1] Schröder, J., Neff, P., Balzani, D. (2005), *International Journal of Solids and Structures* **42**, 4352-4371.

[2] Eipper, G. (1998), Dissertation, Bericht Nr. II-1 aus dem Institut für Mechanik (Bauwesen), Universität Stuttgart.

[3] Ricken, T., de Boer, R. (2003), *Computational Materials Science* **28**, Issues 3-4, 704-713.

[4] Ricken, T., Schwarz, A., Bluhm, J. (2007), *Computational Materials Science*, in press.

[5] Carter, D.R., Beaupré, G.S (2001), Cambridge University Press.

[6] Lernbass, I., Grampp, S., Krestan, C. (2002), Journal für Mineralstoffwechsel **9** (1), 34–35.

[7] Fung, Y.C. (1990), Springer-Verlag.

A Computational Approach on Stress Adaptive Bone Remodeling with Applications to Implant Design Optimization

U. Nackenhorst*, A. Lutz

Institute for Mechanics and Computational Mechanics, Leibniz Universität Hannover
Appelstr. 9A, 30167 Hannover, Germany.
nackenhorst@ibnm.uni-hannover.de, lutz@ibnm.uni-hannover.de

Summary: In this contribution a modeling approach for stress adaptive bone remodeling caused from stress shielding due to hip-joint endoprosthes is presented. The constitutive model is place in a thermodynamic consistent framework. Special emphasis is laid on the description of statically equivalent load sets for joint loads and muscle forces, which is obtained from an inverse approach based on measured CT-data. The computational method is applied for studies on the biomechanical compatibility of different hip-joint prostheses by fully 3D finite element analysis.

Introduction

Stress shielding and related bone remodeling has been recognized as one major reason for aseptic loosening of orthopedic implants, and in addition because the bone stock quality is decreased the success of revision is often less promising. Computational mechanics techniques can assist in optimizing this medical treatment.

Computational methods for the analysis of stress adaptive bone remodeling are under development since more that 15 years, see e.g. [1, 2]. After solving some basic numerical problems, cf. [3] for example, nowadays numerically stable and efficient algorithms are available, e.g. [4, 5], which incorporate a consistent constitutive framework. In parallel multi-scale approaches are currently under development for a better description of the mechanotransduction process by related bone cells [5, 6].

In summary, nowadays powerful computational methods are available to predict bone remodeling caused from changed loading conditions qualitatively in a reliable manner. These techniques enable for studies on the optimization of bone implants, which will be shown illustratively in this presentation, while special emphasis is laid on the overall modeling approach. Starting with a consistent constitutive modeling of stress adaptive bone remodeling within the continuum mechanics framework, which also ensures numerical reliability and efficiency, and ending up with an approach for the computation of statically equivalent load sets from CT-data. Based on this carefully developed first order approach predictions on the bone remodeling caused from different hip-joint endoprostheses system obtained from detailed 3–dimensional finite element models will be presented. The reliability of the methods will be underlined by observations from clinical studies.

Modeling Approach

The internal architecture of bones with distinguished cortical and spongious sections is described by an continuum approach with an averaged bone mass density ϱ. For the constitutive model the bone mass density serves as internal variable, such that a free energy density function is stated as

$$\psi = \tilde{\psi}(\boldsymbol{\varepsilon}, \varrho) \; . \tag{1}$$

Within a linear elastic first order approach a constitutive relationship between Youngs modulus E and the bone mass density is concluded from the entropy principle as follows

$$E = E_0 \left(\frac{\varrho}{\varrho_0} \right)^2 \; , \tag{2}$$

where E_0 and ϱ_0 are reference values, e.g. for cortical bone. A further ingredient is the formulation of a growth function in analogy to damage mechanics, which in its simplest kind reads,

$$f = \psi - \psi_{\text{bio}} = 0 \; , \tag{3}$$

and which describes that the bone aspires to organize itself such that each volume element is stressed in a biologically comfortable manner, expressed by ψ_{bio}. From the assumption that the biological dissipation potential tends to extreme values, an evolution equation for the bone mass density is derived

$$\dot{\varrho} = \dot{\lambda} \frac{\partial f}{\partial \varrho} \tag{4}$$

which is solved in the classical numerical concepts of damage mechanics.

Besides the constitutive description an important issue is the modeling of the boundary conditions. A statically equivalent load distribution due to muscle forces and related joint loads is computed by an inverse approach. For that measured bone mass density distributions are mapped onto the 3–dimensional finite element mesh of the bone. The points of applications for resulting muscle forces and joint loads are defined and by genetic algorithms the magnitude and spatial orientation of the loads are computed such that the remodeling approach tends to results that fit best with the measured density distribution. In a second step the joint loads are distributed onto the finite element mesh by a least squares technique.

As an example, on the left of fig. 1 the computed joint load distribution is depicted, the corresponding bone mass density distribution is shown on the right in an gray-scale coding to be interpreted as inverse radiograph representation. The obtained structural topology is in good agreement with the original CT-data.

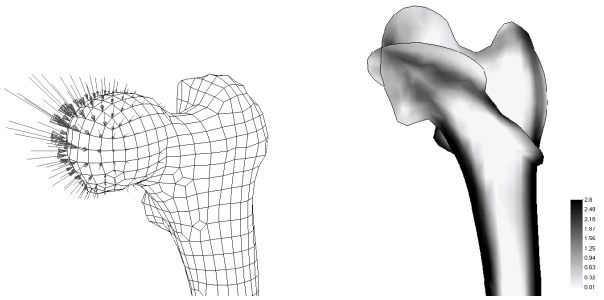

Figure 1: Distributed joint force (left) and mass density distribution computed as the bio-mechanical equilibrium state.

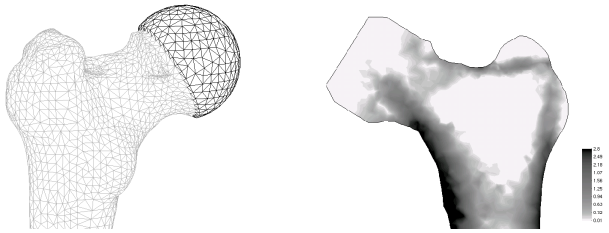

Figure 2: Finite element femur model with a resurfacing prosthesis (left) and computed long term bone mass distribution in a frontal plane cut.

Studies on Hip–Joint Endoprostheses

In computational studies, the bio-mechanical compatibility of different endoprostheses systems has been studied. Each computation starts with a bio-mechanical equilibrated bone model as depicted in Fig. 1. Into this bone mass distribution an implant is integrated and under the same loading conditions the bone reaction caused from the changed stress transfer is computed as described before. The quality is judged by the amount of bone loss due to remodeling.

It is well known from systematical follow ups that classical steem-endoprostheses lead to a loss of bone quality surrounding the steem, cf. [7] for example. This effect is clearly reflected from the finite element simulations. In contrast to radiographic follow up investigations, which deliver only 2–dimensional information, the computation results 3–dimensional visualizations which provide additional insight. It is obvious that due to the loss of bone mineralization density in the surrounding of a prosthesis steem, a poor bone stock is released for revisions. Thus, especially for younger patients, great effort is spent in finding more compatible implant designs in the bio-mechanical sense.

A couple of metaphyseal anchored prostheses have been analyzed which are designed for less arthrophy especially in distal regions of the femur to remain a good basis for revision. In one case a complete failure of such a development has been argued from these studies, which is underlined by clinical experience too.

A relatively new study is performed on the renaissance of the hip-resurfacing technique. The finite element model and the computed bone mass density distribution is depicted in Fig. 2. Regarding the femoral part of the hip, the advantage is obvious because of minimal arthrophy.

Conclusions

A numerically efficient model for the analysis of bone remodeling phenomena has been presented. Besides the constitutive modeling within a thermodynamic consistent continuum framework, special emphasis has been laid onto the description of statically equivalent load sets.

These computational techniques enable for qualitative studies on bone reactions due to artificial hip-joint replacement for example. The results computed for traditional steem-prostheses are in good agreement with clinical studies. Additionally these computations allow for a more detailed 3–dimensional analysis of the effects, while radiographic techniques provide only a thickness averaged image.

Computer simulations have been performed for some recent developments, designed for younger patients with a high risk of revision surgery. A qualitative rating of different implant designs is possible, by which misdevelopments can be excluded at an early stage. Thus computational mechanics techniques provide powerful tools for the development of implants with optimized bio-mechanical compatibility.

References

[1] G. S. Beaupre, T. E. Orr, D. R. Carter (1990): An Approach for Time–Dependent Bone Modeling and Remodeling — Theoretical Development. *J. of Orthopaedic Research*, **8**, 651–661.

[2] H. Weinans, R. Huiskes, H. J. Grootenboer (1992): The Behavior of Adaptive Bone Remodeling Simulation Models. *J. of Biomechanics*, **25**, 1425–1441.

[3] C. R. Jacobs, M. E. Levenston, G. S. Beaupre, J. C. Simo, D. R. Carter (1995): Numerical instabilities in bone-remodeling simulations: the advantage of a node-based finite element approach. *J. of Biomechanics*, **28**, 449–459.

[4] M. Doblare, J. M. Garcia (2002): Anisotropic bone remodelling model based on a continuum damage-repair theory. *J. of Biomechanics*, **35**, 1–17.

[5] U. Nackenhorst (2006): Computational Methods for Studies on the Biomechanics of Bones. *Foundations of Civil and Environmental Engineering*, **7**, 251–271.

[6] R. Ruimerman, P. Hilbers, B. van Rietbergen, R. Huiskes (2005): A theoretical framework for strain-related trabekular bone maintenance and adaption. *J. of Biomechanics*, **38**, 931–941.

[7] J. Hanebeck (2001): *Postoperative Knochendichteänderungen am Femur nach Implantation der zementfreien Zweymüller-Hüftendoprothese unter Berücksichtigung klinischer und röntgenologischer Parameter*. Humboldt Universität Berlin (PhD thesis).

Finite Swelling of Cartilaginous Tissues

W. Ehlers, B. Markert*, A. Acartürk

Universität Stuttgart
Institute of Applied Mechanics
Pfaffenwaldring 7, 70569 Stuttgart, Germany
{ehlers, markert, acar}@mechbau.uni-stuttgart.de

Summary: The modelling of non-linear swelling of biological tissues is presented in this contribution. The model under consideration is based on the Theory of Porous Media (TPM) and incorporates electro-static effects as well as chemical effects like osmosis and diffusion. Moreover, the solid matrix is modelled by a finite neo-Hookean material law accounting for the compression point of the porous solid matrix. The challenge of the materials under study is the numerics, since the boundary depend on the current deformation state of the boundary. A numerical example will show the capabilities of the model.

Introduction

The material under consideration exhibits finite swelling behaviour and is composed of multiple constituents. Porous media like this could be, e. g., the inner part of the intervertebral disc, articular cartilage, hydrogel or clay, cf. [4] and [7]. In particular, these materials consist of a charged solid matrix and an ionized fluid, wherein the ions of a salt are dissolved. Generally, the Theory of Porous Media (TPM) is used to model such multiphasic materials with an unknown microstructure by a thermodynamically consistent way, cf. [1] and [3]. The continuum mechanical approach of the TPM is based on the Theory of Mixtures, cf. [2], enriched by the concept of volume fractions.

Multiphase formulation

Describing a swelling solid, the TPM model of a binary aggregate with the immiscible constituents solid matrix (φ^S) and fluid phase (φ^F) is extended by incorporating volume free fixed charges to the solid matrix and, furthermore, by modelling the fluid phase as a mixture of miscible components, namely, the liquid solvent (φ^L), the cations (φ^+) and the anions (φ^-) of a dissolved salt. Following this, and introducing the volume fractions $n^\alpha = \mathrm{d}v^\alpha/\mathrm{d}v$, the saturation condition is given by

$$\begin{aligned} &\sum_\alpha n^\alpha = n^S + n^F = 1\,, \\ \text{where}\quad &n^F = \sum_\beta n^\beta = n^L + n^+ + n^-\,. \end{aligned} \tag{1}$$

To introduce the balance relations, the model is restricted to materially incompressible constituents, mass exchanges among the constituents like chemical reactions and phase transitions are excluded and quasi-static processes are assumed. Therefore, the volume balances for the phases φ^α, the concentration balances of the fluid components φ^β and the overall momentum balance read:

$$(n^\alpha)'_\alpha + n^\alpha \operatorname{div} \overset{\prime}{\mathbf{x}}_\alpha = 0\,, \tag{2}$$

$$(n^F c^\beta_m)'_\beta + n^F c^\beta_m \operatorname{div} \overset{\prime}{\mathbf{x}}_\beta = 0\,, \tag{3}$$

$$\mathbf{0} = \operatorname{div}(\,\mathbf{T}^S_{E\,\text{mech.}} - p\,\mathbf{I}\,) + \rho\,\mathbf{b}\,. \tag{4}$$

Therein, $(\,\cdot\,)'_\alpha$ represents the material time derivative with respect to φ^α. Furthermore, c^β_m denotes the molar concentration of φ^β in the fluid, $\mathbf{T}^S_{E\,\text{mech.}}$ the purely mechanical solid extra stress and $\rho\,\mathbf{b}$ the volume force acting on the mixture as a whole. Note that p is the overall pore pressure consisting of two parts, the Lagrangean multiplier $\mathcal{P}$ denoting the purely hydraulic part given by the boundary conditions and the osmotic pressure π developing from concentration differences:

$$p := \mathcal{P} + \pi\,. \tag{5}$$

The solid volume balance is solved analytically by integration such that $n^S = n^S_{0S}\,(\det\,\mathbf{F}_S)^{-1}$. Additionally, a volume balance for the fixed charges is introduced, which is also integrated analytically to yield $c^{fc}_m = c^{fc}_{m0S} n^F_{0S} (\det\,\mathbf{F}_S - n^S_{0S})^{-1}$, thus relating the initial values denoted by $(\,\cdot\,)_{0S}$ to the current ones via the determinant of the solid deformation gradient. Making use of the electroneutrality condition, it is evident that the anion concentration depends on the concentration of φ^+ and φ^{fc}, cf. [5, 8]. Finally, with the assumption c^L =const. and $\overset{\prime}{\mathbf{x}}_L \approx \overset{\prime}{\mathbf{x}}_F$, only the volume balance of the overall fluid, the cation concentration balance and the overall momentum balance are left to be solved numerically.

Constitutive equations

The solid skeleton is described by the extended neo-Hookean material law proposed by [6], which accounts for the compaction point, a specific feature of porous materials in the large deformation range:

$$\begin{aligned} \boldsymbol{\tau}^S_{E\,\text{mech.}} := {}& \mu^S(\,\mathbf{B}_S - \mathbf{I}\,) + \\ &+\lambda^S (1 - n^S_{0S})^2 \Big(\frac{\det\mathbf{F}_S}{1 - n^S_{0S}} - \frac{\det\mathbf{F}_S}{\det\mathbf{F}_S - n^S_{0S}} \Big)\,\mathbf{I}\,. \end{aligned} \tag{6}$$

Therein, the Kirchhoff stress tensor $\boldsymbol{\tau}^S_{E\,\text{mech.}}$ is related to the Cauchy stress $\mathbf{T}^S_{E\,\text{mech.}}$ via $\boldsymbol{\tau}^S_{E\,\text{mech.}} = \det\mathbf{F}_S\,\mathbf{T}^S_{E\,\text{mech.}}$. Furthermore, μ^S and λ^S are the Lamé constants, and $\mathbf{B}_S$ is the left Cauchy-Green deformation tensor ($\mathbf{B}_S = \mathbf{F}_S\,\mathbf{F}_S^T$). The fluid flow is described by an extended Darcy's law, which includes the gradients of the ion concentrations and the electrical potential. Furthermore, the ion diffusion is described by an extended Nernst-Planck equation, cf. [5]. Given the fluid and ion motion, the gradient of the electrical potential can be calculated from $c^+_m \mathbf{w}_+ - c^-_m \mathbf{w}_- = \mathbf{0}$.

Numerical treatment and example

In the numerical computations, it is assumed that the boundary layer is immediately in equilibrium with the external solution. Therefore, the Donnan equation together with the electroneutrality condition can be used to calculate the boundary concentration and the boundary osmotic pressure as well as the corresponding initial values:

$$c_m(\mathbf{u}_S,t) = \sqrt{\bar{c}_m{}^2(t) + \left(\frac{c_m^{fc}(\mathbf{u}_S)}{2}\right)^2} + \frac{c_m^{fc}(\mathbf{u}_S)}{2}\,,$$
$$\pi(\mathbf{u}_S,t) = R\theta\left[2c_m(\mathbf{u}_S,t) - c_m^{fc}(\mathbf{u}_S) - 2\bar{c}_m(t)\right].$$

Therein, the values of the external solution are marked by a bar. From the above equations, it is obvious that the boundary conditions depend on the internal variable $c_m^{fc}(\mathbf{u}_S)$. Therefore, the boundary conditions have to be considered implicitly by incorporation into the weak formulations of the governing equations in order to obtain physically sound solutions (cf. Fluid Structure Interaction). To obtain the weak formulations, the balance relations are weighted by their corresponding independent test functions δp, δc_m and $\delta\mathbf{u}_S$, respectively. After integration over the spatial domain Ω with the surface Γ, one obtains the following setting in the primary variables p, c_m and $\mathbf{u}_S$:

$$\begin{aligned}
\int_{\Gamma_q} \bar{q}\,\delta p\,\mathrm{d}a &= \int_\Omega n^F \mathbf{w}_F\cdot\operatorname{grad}\delta p\,\mathrm{d}v - \int_\Omega \operatorname{div}(\mathbf{u}_S)'_S\,\delta p\,\mathrm{d}v \\
&\quad + \int_{\Gamma_p}\left[p - \bar{\mathcal{P}} - R\theta\,(2c_m - c_m^{fc} - 2\bar{c}_m)\right]\delta p\,\mathrm{d}a\,, \\
\int_{\Gamma_j} \bar{j}\,\delta c_m\,\mathrm{d}a &= \int_\Omega n^F c_m \mathbf{w}_+\cdot\operatorname{grad}\delta c_m\,\mathrm{d}v \\
&\quad - \int_\Omega\left[\,n^F(c_m)'_S + c_m\operatorname{div}(\mathbf{u}_S)'_S\,\right]\delta c_m\,\mathrm{d}v \\
&\quad + \int_{\Gamma_{c_m}}\left[c_m - \sqrt{\bar{c}_m^2 + \left(\frac{c_m^{fc}}{2}\right)^2} - \frac{c_m^{fc}}{2}\,\right]\delta c_m\,\mathrm{d}a, \\
\int_{\Gamma_t} \bar{\mathbf{t}}\cdot\delta\mathbf{u}_S\,\mathrm{d}a &= \int_\Omega (\mathbf{T}^S_{E\,\text{mech.}} - p\,\mathbf{I})\cdot\operatorname{grad}\delta\mathbf{u}_S\,\mathrm{d}v \\
&\quad - \int_\Omega (\rho^S + \rho^F)\,\mathbf{b}\cdot\delta\mathbf{u}_S\,\mathrm{d}v\,.
\end{aligned} \tag{7}$$

Note in passing that the boundary conditions (7) are incorporated into the weak forms of the overall volume balance and the cation concentration balance. The terms on the left hand side marked by a bar denote the boundary terms. In particular, $\bar{q} = n^F\,\mathbf{w}_F\cdot\mathbf{n}$ is the fluid volume efflux, $\bar{j} = n^F c_m \mathbf{w}_+\cdot\mathbf{n}$ is the outward-oriented cation diffusion, and $\bar{\mathbf{t}} = (\mathbf{T}^S_{E\,\text{mech.}} - p\,\mathbf{I})\,\mathbf{n}$ is the traction force.

Finally, this model is implemented into the FE tool PANDAS[1] and, as an example, the swelling of an elliptic hydrogel disc is simulated. The disc is generated with diameters of 3.0 mm and 3.7 mm and a height of 2.0 mm meshed with hexahedral elements. Note that for numerical stability reasons use is made of mixed Taylor-Hood elements, where the solid displacement $\mathbf{u}_S$ is approximated by quadratic shape functions and the overall pore pressure p as well as the cation concentration c_m by linear shape functions.

[1] **P**orous media **A**daptive **N**onlinear finite element solver based on **D**ifferential **A**lgebraic **S**ystems (`www.get-pandas.com`)

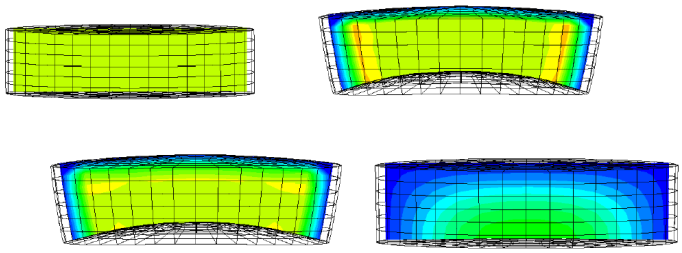

Figure 1: Numerical simulation by the FE tool PANDAS.

To initiate the swelling process, the cation concentration of the external solution is decreased on the upper and circumferential surface from 0.20 mol/l to 0.15 mol/l within 10 s. The contour plot in Figure V exhibits the decreasing cation concentration. As one can see, the specimen initially begins to swell in the upper and the circumferential boundary, thus yielding a bending of the specimen. At the end of the simulation, when equilibrium is reached, the bending vanishes.

References

[1] R. de Boer (2000): *Theory of Porous Media*. Springer-Verlag, Berlin.

[2] R. M. Bowen (1980): Incompressible porous media models by use of the theory of mixtures. *International Journal of Engineering Science*, **18**, 1129–1148.

[3] W. Ehlers (2002): Foundations of multiphasic and porous materials. In *Porous Media: Theory, Experiments and Numerical Applications*, Ehlers, W. & Bluhm, J., eds., Springer-Verlag, Berlin, 3–86.

[4] W. Ehlers, N. Karajan, B. Markert (2006): A porous media model describing the inhomogeneous behaviour of the human intervertebral disc. *Materialwissenschaften und Werkstofftechnik* **37**, 546–551.

[5] W. Ehlers, B. Markert, A. Acartürk (2005): Swelling phenomena of hydrated porous materials. In *Poromechanics III, Proceedings of the 3rd Biot Conference on Poromechanics*, Abousleiman, Y. N., Cheng, A. H.-D. & Ulm, F. J., eds., Balkema Publishers, 781–786.

[6] G. Eipper (1998): *Theorie und Numerik finiter elastische Deformationen in fluidgesättigten porösen Festkörpern*. Dissertation, Bericht Nr. II-1 aus dem Institut für Mechanik (Bauwesen), Universität Stuttgart.

[7] B. Loret, T. Hueckel, A. Gajo (2002): Chemo-mechanical coupling in saturated porous media: elastic-plastic behaviour of homoionic expansive clays. *International Journal of Solids and Structures*, **39**, 2773–2806.

[8] D. N. Sun, W. Y. Gu, X. E. Guo, W. M. L. V. C. Mow (1999): A mixed finite element formulation of triphasic mechano-electrochemical theory for charged, hydrated biological soft tissues. *International Journal for Numerical Methods in Engineering*, **45**, 1375–1402.

Failure in Cartilaginous Tissues

J. M. Huyghe[1]*, C. Jongeneelen[1], Y. Schroeder[1], F. Kraaijeveld[1], R. de Borst[2], F. P. T. Baaijens[1]

[1]Department of Biomedical Engineering, Eindhoven University of Technology
P.O. Box 513, 5600MB Eindhoven, Netherlands
j.m.r.huyghe@tue.nl

[2]Koiter Institute, Faculty of Aerospace Engineering, Delft University of Technology
P.O. Box 5, 2600AA Delft, Netherlands

Summary: Cartilaginous tissues high load bearing capacity is explained by osmotic prestressing putting the collagen fiber reinforcement under tension and the proteoglycan gel under compression. The osmotic forces are boosted by a further 50 % by the affinity of the collagen with the aquous solution. The high osmolarity of the tissue provides a strong protection against crack propagation. Degeneration results in degradation of the prestressing and hence to internal damage. 3D visualisation of a discontinuity of the collagen struction of the disc is achieved by confocal laser scanning microscopy. The collagen and the cells are visualised by means of a two fluorescent probes. The discontinuity is shown to open and close depending on the osmotic loading of the tissue. The process of internal degradation is presently modelled using Partition of Unity method in a osmotically prestressed fluid-solid mixture.

Introduction

Unlike most biological tissues, cartilaginous tissues tissues has no blood perfusion. The cells of the tissue obtain nutrition and removal of waste materials through diffusion only. This fact implies that cartilaginous tissues renew themselves at a much lower rate than any other tissue in the human body. The capacity of cartilaginous tissues to withstand relatively high loads of several MPa during a lifetime of up to 100 years, is a noteworthy achievement, especially in view of its low stiffness, low renewal rate and high water content. Cartilaginous tissues consists of a fluid-filled extra-cellular matrix, in which living cells are sparsely dispersed. The mechanical function is highly dependent on the composition of the extra-cellular matrix, which primary consists of collagen fibrils and negatively charged proteoglycans. Due to the fixed charges of the proteoglycans (PGs), the cation concentration inside the tissue is higher than in the surrounding synovial fluid. This excess of ion particles leads to an osmotic pressure difference, which causes swelling of the tissue [4]. The fibrillar collagen network resists straining and swelling pressures. This combination makes cartilaginous tissue a unique, highly hydrated and pressurized tissue, enforced with a strained collagen network. It has been shown that the osmotic pressure inside cartilaginous tissues is much higher than would be expected based on its FCD [5, 2]. This is because part of the water in the tissue is absorbed by the collagen fibers. The proteoglycan molecules, because of their large size, are excluded from this intra-fibrillar space. This means that their effective concentrations are much higher in the extra-fibrillar space than if they were distributed uniformly throughout the entire matrix. Hence, the effective fixed charge density is higher than if computed from total tissue water content. Wilson et al. [6] predict the depth dependent stress-strain curve of articular cartilage solely from its composition and the inclusion of the intrafibrillar/extrafibrillar water compartments and their associated osmotic pressures. A corresponding analysis for intervertebral disc tissue (Fig. 1) demonstrates that intrafibrillar water affects pressure distribution, osmolarity and stress within the disc substantially [3]. Confined compression and swelling experiments on canine intervertebral disc samples were performed and fitted by Huyghe et al [1] using the concept of intrafibrillar water as well.

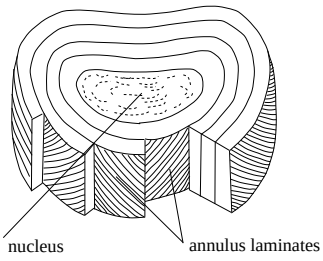

Figure 1: The intervertebral disc is a cartilaginous tissue connecting two vertebrae in the spine. It consists of a gelatinous nucleus surrounded by a fibrous annulus.

Fractures in the intervertebral disc

A peculiar observation in intervertebral disc degeneration is the finding that human intervertebral discs develop fractures with age virtually independently from load to which they are subjected (Fig. 2). Concommitantly, the osmotic prestressing is decreasing. Wognum et al. [7] studied the opening of a crack

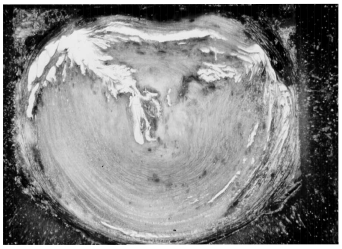

Figure 2: Patent fractures in a human intervertebral disc. Delamination is observed in the annulus. Courtesy of Tapio Videman, Calgary, Canada.

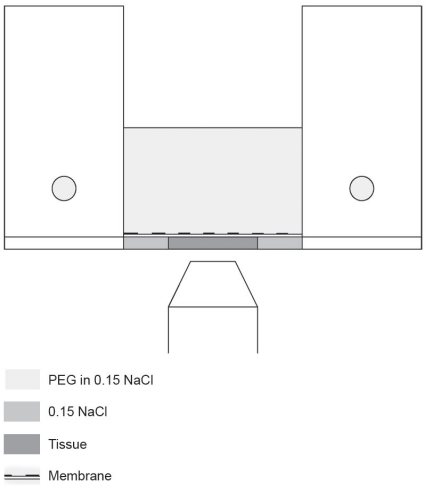

Figure 3: The bovine intervertebral disc samples are osmotically prestressed using a polyethylene glycol solution on top of a half-permeable membrane.

in a numerical and physical model of the degenerated intervertebral disc. Degeneration was modelled as a progressive decrease in osmotic presstressing. They demonstrate that, while the osmotic prestressing is decreasing, the overal fiber stress is decreasing as well, but the stress at the crack tip increases sharply, because the shrinking of the tissue induces opening of the crack. This phenomenon is intrinsically multiscale in nature and may explain the poor relationship between external loads and crack propagation. None of the models used by Wognum et al [7] considers the intrafibrillar water effect mentioned earlier, while experimental data suggest that 30 % of the water contained in the annulus is grabbed by the collagen and is not seen by the charges fixed to the proteoglycan chains. This suggests that the protective effect of osmorality against failure is further enhanced by intrafibrillar water.

In vitro observation of the tissue

To observe the genuine tissue in 3D, a new method is created to visualize micromechanical swelling in the intervertebral disc annulus fibrosus. The deformations of the collagen fibers and the cells under osmotic loading are observed by fluorescent labelling under the confocal microscope (Fig. 3). A digital image correlation technique calculates displacements and finite strains. The results show the heterogeneous character of the tissue as well as the non-affine nature of the deformation (Figs. 4–5). A Partition of Unity formulation of fluid-solid mixture is presently developed to describe the osmotic failure mechanism.

Acknowledgement

The authors acknowledge financial support from the Technology Foundation STW, the Technological Branch of the Netherlands Organisation of Scientific Research NWO and the Ministry of Economic Affairs (DLR5790, Multiscale Computational Mechanics, joint project with Deutsche Forschungsgemeinschaft)

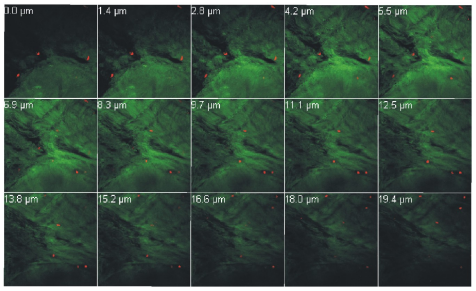

Figure 4: Z-stacks of a closed discontinuity in the collagen structure of the tissue under high osmotic loading.

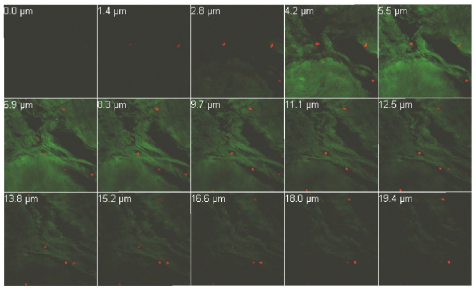

Figure 5: Z-stacks of a patent discontinuity in the collagen structure of the tissue under low osmotic loading.

References

[1] J. M. Huyghe, G. B. Houben, M. R. Drost, and C. C. van Donkelaar (2003): An ionised/non-ionised dual porosity model of intervertebral disc tissue: experimental quantification of parameters. *Biomechanics and modelling in mechanobiology*, **2**, 3–19.

[2] A. Maroudas and C. Bannon (1981): Measurement of swelling pressure in cartilage and comparison with the osmotic pressure of constituent proteoglycans. *Biorheology*, **18**, 619–632.

[3] Y. Schroeder, S. Sivan, W. Wilson, J. M. Huyghe, A. Maroudas, and F. P. T. Baaijens: Are disc pressure, stress and osmolarity affected by intra and extrafibrillar fluid exchange? *J. Orthop. Res.*, submitted.

[4] J. P. G. Urban and A. Maroudas (1979): The measurement of fixed charge density in the intervertebral disc. *Biochim Biophys Acta*, **586**, 166–178.

[5] J. P. G. Urban and J. F. McMullin (1988): Swelling pressures of the lumbar intervertebral discs: influence of age, spinal level, composition and degeneration. *Spine*, **13**, 179–187.

[6] W. Wilson, J.M. Huyghe, and C. C. van Donkelaar (2006): A composition-based cartilage model for the assessment of compositional changes during cartilage damage and adaptation. *Osteoarthritis and Cartilage*, **14**, 554–560.

[7] S. Wognum, J. M. Huyghe, and F. P. T. Baaijens (2006): Influence of osmotic pressure changes on the opening of existing cracks in 2 intervertebral disc models. *Spine*, **31**, 1783–1788.

A Porohyperelastic Fiber Rinforced Model for Human Cartilage Using the Natural Element Method

A. Pérez del Palomar*, B. Calvo, M. Doblaré

Group of Structural Mechanics and Materials Modelling
Aragón Institute of Engineering Research (I3A), University of Zaragoza, Spain
amaya@unizar.es

Summary: This paper exposes the capabilities of the Natural Element Method (NEM) in simulating large deformations of human cartilage. A fibre-reinforced porohyperelastic model is presented and used for the simulation of soft hydrated tissues, like cartilage. An Augmented Lagrangian formulation has been used to enforce the incompressibility condition in the whole tissue. Porohyperelasticity has been included in order to simulate the biphasic nature of the tissue associated to a porous solid matrix and interstitial fluid. Anisotropy in the hyperelastic behaviour has been formulated by means of a strain energy function that takes into account the influence of collagen fibres. The results using a natural element method are compared with the classical finite element approximation.

Introduction

Numerical simulation plays a fundamental role in many branches of science. Computational Biomechanics is one of these branches in which the numerical simulation of very complex processes takes place. Simulation of soft organs and bony structures deals with complex geometries, large deformations and involved models of constitutive behaviour. The appearance of the Finite Element Method (FEM) in the fifties allowed to perform such simulations in that field. However, the method relies on the proper discretization of the geometry, an aspect which might become cumbersome with actual geometries. In this regard, mesh generation in a general three dimensional model is far from being completely automatised and the development of a specific finite element model usually takes a large amount of user time, and indeed when the modelled organ suffers large deformations, a remeshing strategy is frequently required in order to avoid numerical errors that can break out the simulation.

Cartilage is a biological material that undergoes large deformations in order to absorb the loads within the joints. This tissue is mostly composed of two phases: a fiber reinforced solid matrix and a fluid phase that moves inside. The classical approach to simulate this material is under a finite element approximation. In this work, a porohyperelastic fiber reinforced model is proposed for human cartilage using the Natural Element Method, and the results are compared with a classical finite element approximation.

Materials and methods

The equilibrium equations for a biphasic solid can be written as,

$$\boldsymbol{\nabla} \cdot \boldsymbol{\sigma}_e^s - \phi^s \boldsymbol{\nabla} p - \boldsymbol{K} \cdot (\boldsymbol{v}^s - \boldsymbol{v}^f) = 0 \quad (1)$$

$$-\phi^f \boldsymbol{\nabla} p + \boldsymbol{K} \cdot (\boldsymbol{v}^s - \boldsymbol{v}^f) = 0 \quad (2)$$

where $\boldsymbol{\sigma}_e^s$ is usually known as effective stress. The fundamental variables of the problem are the solid displacements, the fluid velocities and the pressure. In this formulation, the incompressibility condition is imposed using an Augmented Lagrangian formulation [1].

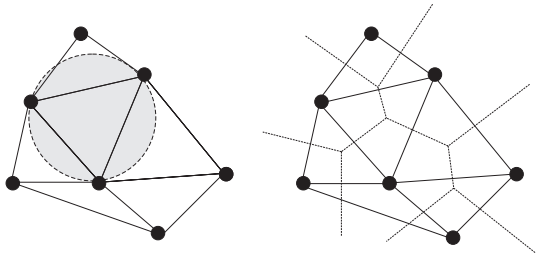

Figure 1: Delaunay triangulation and Voronoi diagram of a cloud of points.

The representation theorem for transversely isotropic scalar functions states that a scalar function W of the right Cauchy-Green tensor C is transversely isotropic if and only if it can be expressed as:

$$\overline{\psi}^s = W(I_1, I_2, I_3, I_4, I_5) \quad (3)$$

where $I_j, j = 1, ..., 3$ are the principal invariants of C associated with an isotropic behaviour and the other two, additional invariants proposed by Ericksen and Rivlin [4] that arise directly from anisotropy.

The NEM is based on the Natural Neighbour interpolation scheme [3, 2] that relies on the concepts of Delaunay triangulations and Dirichlet tesselations [6, 5] of a set of nodes (see Fig. 1).

The NE method has some important properties, such as the interpolatory character of the shape functions, the linear consistency of the interpolant and the partition of unity property. In other words, the natural neighbour interpolant can exactly reproduce a linear or constant displacement field [7]. Another important property of the interpolant described above is its ability to reproduce a linear interpolant along convex boundaries (Fig. 2).

Results

In this abstract the results for the articular disc of the Temporomandibular Joint (TMJ) are presented. This component is a biconcave, fibrocartilaginous structure, which provides the glid-

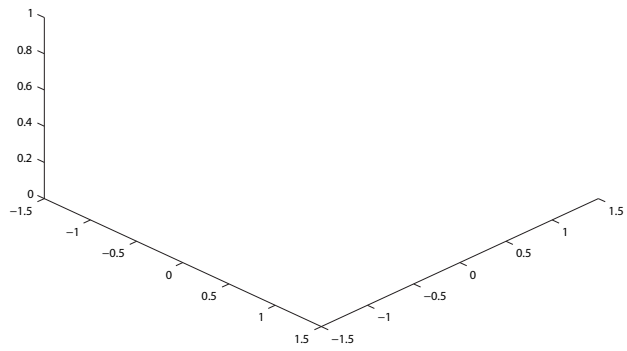

Figure 2: Linear interpolation along non-convex boundaries.

ing surface for the mandibular condyle, resulting in smooth joint movement.

The stress distribution can be seen in Figs. 3 and 4. One of the advantages of the natural element method is that the discontinuities that arise in the finite element method due to irregularities in the mesh can be avoided. It can be appreciated how the stress distributions are smooth along the top and bottom surfaces. As can be seen in Fig. 3, the maximum principal stresses were located at the posterior band of the disc where the disc tries to open as it is compressed. However, the maximum compressive stresses were located in the intermediate zone (both in the bottom and top surfaces) of the disc (Fig. 4).

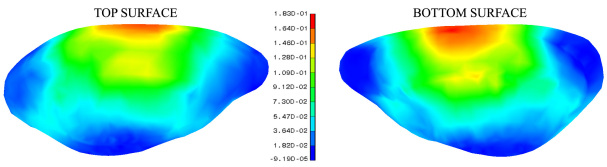

Figure 3: Maximum principal stresses in the articular disc.

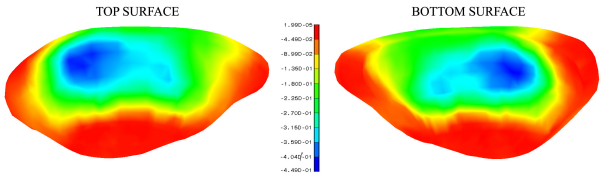

Figure 4: Minimum principal stresses in the articular disc.

Discussion

The main objective of this work is to present the possible advantages of using meshless methods in simulations of biomechanics problems, specifically in application to modelling human cartillage. This family of methods present some appealing characteristics comparing to the well-known Finite Element Method. They avoid the difficult task of mesh generation in very complex geometries, such as the case of living tissues. A finite element meshing process can be very costly depending on the complexity of the geometry, but a volume reconstruction approach and distribution of points inside this volume is relatively simple. Meshless methods appear to be an efficient alternative to FEM for this type of problems.

Biomechanics of living soft tissues usually involves several geometric non-linearities such us large displacements and strains, as well as material non-linearities. Hydrated soft tissues can be seeing as a network of fibre collagenous or muscular tissue embedded in a high compliant matrix with a fluid phase. In the NEM there is virtually no limitation to mesh distortions, showing that results are much less dependent on the regularity of the nodal distribution than FE methods. Compared to the finite element method, NEM is better at handling large deformation without any special numerical treatment because it is less dependent on the original mesh. From these results, NEM appears to be an efficient alternative to FEM for large deformation problems, especially when using a total Lagrangian description.

References

[1] A. Pérez-Palomar and M. Doblaré (2006): On the numerical simulation of the mechanical behaviour of articular cartilage. *International Journal for Numerical Methods in Engineering*, **67**, 1244–1271.

[2] R. Sibson (1981): Interpreting multivariate data. V. Barnett (Editor). A Brief Description of Natural Neighbour Interpolation. John Wiley, pp 21–36.

[3] R. Sibson (1980): A vector identity for the Dirichlet Tesselation. *Mathematical Proceedings of the Cambridge Philosophical Society*, **87**, 151–155.

[4] J. L. Ericksen and R. S. Rivlin (1954): Large elastic deformations of homogeneous anisotropic materials. *Journal of Rational Mechanics and Analysis*, **3**, 281–301.

[5] B. Delaunay (1934): Sur la Sphre Vide. A la memoire de Georges Voronoi. *Izvestia Akademii Nauk SSSR, Otdelenie Matematicheskii i Estestvennyka Nauk*, **7**, 793–800.

[6] G. M. Voronoi (1908): Nouvelles applications des paramtres continus la thorie des formes quadratiques. Deuxime Memoire: Recherches sur les parallllodres Primitifs. *J. Reine Angew. Math.*, **134**, 198–287.

[7] N. Sukumar (1998): *The Natural Element Method in Solid Mechanics.* Northwestern University. Evanston, Illinois.

Simulation of Curved Incisions for Astigmatism Correction

A. Pérez del Palomar*, E. Lanchares, B. Calvo, M. Doblaré

Group of Structural Mechanics and Material Modelling, Aragón Institute for Engineering Research (I3A)
University of Zaragoza, María de Luna 3, E-50018 Zaragoza, Spain
elanchar@unizar.es

Summary: A model of the ocular globe has been developed to simulate several curved incisions in clear cornea *(arcuates)* used to correct astigmatism. In order to provide a pre-operative planning tool for surgeons for a more accurate values for parameters of the corneal incisions according to each case, corneal incisional surgery was simulated in this work varying some of the parameters involved. The model provides results very close to the theoretical ones stated in Lindstrom's nomogram [1].

Introduction

The most frequent cause of vision default is the wrong refraction of the components of the eye. The cornea is responsible of 75% of the whole vision of the eye. Astigmatism is a refractive error due to the non-spherical shape of the cornea, that is, the refractive power is not uniform in all meridians. Refractive surgery techniques are used to modify the radius of curvature in order to repair the faulty refraction by making the cornea as spherical as possible. It is widely extended in cataract surgery to perform corneal incisions at the same time to achieve emetropy. According to the optical power to be corrected, different sort of incisions can be performed: radial, arcuates (> 3 diopters) or limbal relaxing ones (1-3 diopters).

The variety of parameters to be decided before arcuates surgery (number of incisions, angle, depth, shape, symmetry, optical zone) makes very complex to design an accurate nomogram to be used as a universal reference to achieve a spherical equivalent and astigmatism correction as expected. Moreover, the same surgical technic (same angle, optical zone, ...) usually leads to different results for different patients. It is therefore necessary to study the parameters involved in nomograms and others like the material properties of the cornea which can be quite different between patients with the same level of pathology, to plan a patient-specific surgery that minimizes the uncertainty in results. A biomechanical study before surgery is therefore very convenient to asses quantitatively the effect of each parameter on the optical outcome.

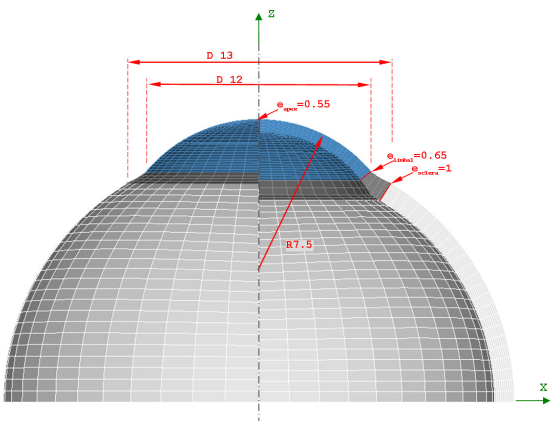

Figure 1: Model geometry [mm].

Materials and methods

A three-dimensional finite element model has been generated from the anterior half ocular globe geometry. A revolution symmetry of the model has been assumed to simplify the complexity of the real geometry, assumption widely used before by other authors [2, 3]. The model is composed of three different parts: cornea, limbus and sclera, as is shown in Fig. 1.

As other biological tissues, the cornea and limbus are composed by an extracellular matrix, highly moisturized, and collagen fibrils disposed in one (limbus) or two (cornea) preferential orientations (see Fig. 2). For this reason, these materials present an hyperelastic, incompressible and anisotropic constitutive behaviour, strongly dependent on the physiological collagen fibril distribution that therefore should be considered in any model. An isotropic behaviour has been assumed for the sclera.

It has been used a mechanical model of the human eye based on that proposed by Alastrué et al. [2]. The Holzapfel and Gasser [4] strain-energy density function for soft tissues has been considered and implemented into a finite element context to simulate the effects of curved corneal incisions.

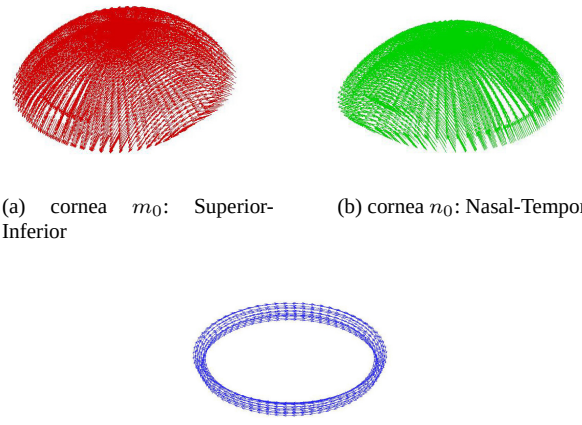

(a) cornea m_0: Superior-Inferior

(b) cornea n_0: Nasal-Temporal

(c) limbus n_0: Circumferencial

Figure 2: Direction of the collagen fibrils

The free energy is considered in a decoupled form:

$$\Psi = \Psi_{vol} + \Psi_{iso}^{matrix} + \Psi_{iso}^{fibers} \quad (1)$$

The material parameters which define the behaviour of the matrix and the collagen fibrils were taken from literature [5] or estimated in an iterative process.

Before carrying out the simulation the model has to be driven to a situation that represents the same conditions as the real eye. The stress free configuration of the cornea is not known a priori, only the one deformed by the intraocular pressure [3, 6]. The point is therefore to introduce in the model the initial stresses caused by the IOP.

The curved incisions are cuts performed in clear cornea, about 90% of the thickness deep and perpendicular to the surface. According to the diopters to be corrected, the parameters of the incisions are decided: radio, angle, number of incisions... After surgery the incised axis flattens, that is to say the curvature radius is larger, and its perpendicular one steepens so its curvature radius becomes smaller (Fig. 3). These changes achieve a compensation in the refractive difference between the two perpendicular intrinsic optical axis of the cornea.

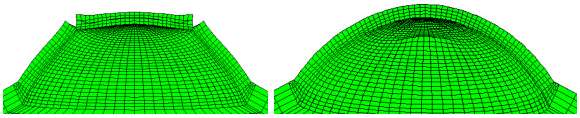

(a) Incised meridian. (b) Perpendicular meridian.

Figure 3: Flattening and steepening effect of incisional surgery. Amplified 10%.

Results

After surgery simulation the optical power measured in diopters is estimated. The incised astigmatic principal axis and the secondary one, defined by the final position of the nodes belonging to the corneal anterior surface and inside the optical zone, is fitted by means of least squares and two radius of curvature are obtained, one for each axis. Then the diopters can be calculated using the expression [7]:

$$D \simeq \frac{n-1}{R} \quad (2)$$

where n is the corneal refractive index whose value is 1.377 and R [m] is the curvature radius in each axis (incised and non-incised). The results for the incisions that have been simulated are shown in Table 1. In every performed simulation the incisions are 3 mm from the apex.

The same simulation was also carried out by varying the values for the constants to obtain more or less rigid corneas and correct results are only achieved with accurate values for the material parameters.

The model offers another point of view to analyze the surgery technic and its results. The after-surgical stresses show interesting values and distributions that deserve to be discussed, as it seems to be a relation between these distributions and the keratometric maps.

Table 1: Results of simulation vs. Lindstrom's nomogram [1]

N incisions	1	1	2	1	2	2
Angle *(deg)*	45	60	45	90	60	90
D Sim. result	1.47	2.13	3	2.72	4.5	5.95
D Lindstrom	1.5	2.25	3	3	4.5	6

Discussion

A tool has been developed to simulate incisions for astigmatism correction in order to provide the surgeon a technical evidence to make his decision while planning the surgery or designing new incisional techniques. The results obtained by simulation for optical power seem to be correct being very similar to those proposed by the Lindstrom's nomogram [1], which is nowadays a worldwide reference in corneal surgery.

It has also been discussed the influence of the material properties. As the same incisions achieve different optical outcomes for different patients, it would be necessary to check if the corneal material properties variation from patient to patient is so relevant to cause these results.

An interesting conclusion of this work is the probable relation between the distributions of strains and keratometry after surgery.

References

[1] Y. R. Chu, D. R. Hardten, T. D. Lindquist and R. L. Lindstrom (2005): Astigmatic Keratotomy. In *Duane's Ophthalmology*, Lippincott Williams & Wilkins.

[2] V. Alastrué, B. Calvo, E. Pena and M. Doblaré (2006): Biomechanical Modelling of Refractive Corneal surgery. *J. Biomech. Eng*, ASME, **128**, 150–160.

[3] P. M. Pinsky, D. Van Der Heide and D. Chernyak (2005): Computational modeling of mechanical anisotropy in the cornea and sclera. *J. Cataract. Refract. Surg.*, **31**, 136–145.

[4] G. A. Holzapfel and T. C. Gasser (2001): A viscoelastic model for fiber-reinforced composites at finite strains: Continuum basis, computational aspects and applications. *Comput. Methods Appl. Mech. Engrg.*, **190**, 4379–4403.

[5] D. A. Hoeltzel, P. Altman, D. Buzard and K. Choe (1992): Strip extensometry for comparison of the mechanical response of bovine, rabbit and human corneas. *Journal of Biomechanical Engineering*, **114**, 202–215 .

[6] A. Pandolfi and F. Maganiello (2006): A model for the human cornea: constitutive formulation and numerical analysis. *Biomech. Model. Mechanobiol.*, **5**, 237–246.

[7] C. R. Munnerlyn, S. J. Koons and J. Mearshall (1988): Photorefractive qeratectomy: A technique for laser refractive surgery. *J. Cataract. Refract. Surg.*, **14**, 46–52.

An Incompressible Finite Shell Element with Crimped Collagen Fibers for Numerical Analyses of the Human Eye

R. Grytz*, G. Meschke

Institute for Structural Mechanics, Ruhr-University Bochum
44801 Bochum, Germany
rafael@grytz.de, guenther.meschke@rub.de

Summary: The human eye has the macroscopic structure of a thick shell with incompressible and anisotropic material properties. A microstructural constitutive model is presented for the hyperelastic response of crimped collagen fibrils found in the eye tissues. The model is based on observations that collagen fibril embedded in a soft matrix crimp into a smooth 3D pattern when unloaded. Following ideas presented by Beskos and Jenkins [1], Freed and Doehring [2] the collagen fibril crimp is approximated by a cylindrical helix. The presented model is derived from the nonlinear axial force-stretch relationship of an extensible helical spring including the fully extension of the spring as a limit case. This helical spring model is introduced as a fiber-matrix constitutive formulation into an incompressible finite shell element [3], where the incompressibility constraint is enforced through elimination of displacement and strain variables. The ability of the present numerical model to reproduce the biomechanical response of individual human eye shells to different intraocular pressure levels opens a promising perspective to predict a certain risk for the development of glaucoma.

Crimped collagen fiber model

Organized collagen fibers form fibrous networks that introduce strong anisotropic and highly nonlinear attributes into the constitutive response of soft tissues. We approximate the constitutive response of one collagen fiber family by the geometrically exact solution of an extensible helical spring under tension (Fig. 1). The nonlinear relationship between the force $\mathbf{P}$

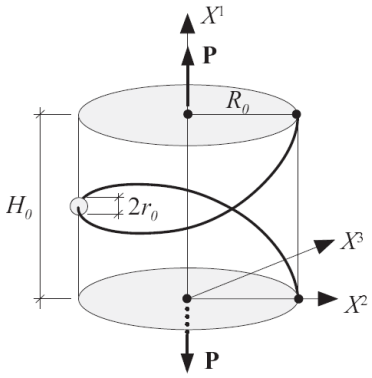

Figure 1: Geometrical variables and force $\mathbf{P}$ *acting along the centerline of the helical spring.*

and the axial stretch $\lambda_f = H/H_0$ can be derived by an iterative solution [5] and is used to formulate the axial 1. Piola-Kirchhoff stress response of one collagen fiber family as

$$P_f(\lambda_f) = \frac{|\mathbf{P}(\lambda_f)|}{\pi r_0^2 \sin\alpha_0} , \qquad (1)$$

where the helix angle α_0 can be calculated from $\tan(\alpha_0) = H_0/2\pi R_0$. The helical model can be expressed by three independent parameters, which are chosen in accordance to [2] as the geometrical values H_0/r_0, R_0/r_0 and the elastic modulus of the filament E. Fig. 2 contains a comparison between results from a strip extensiometry experiment on porcine corneas performed by Anderson et al. [4] and model results. The respective model parameters have been identified

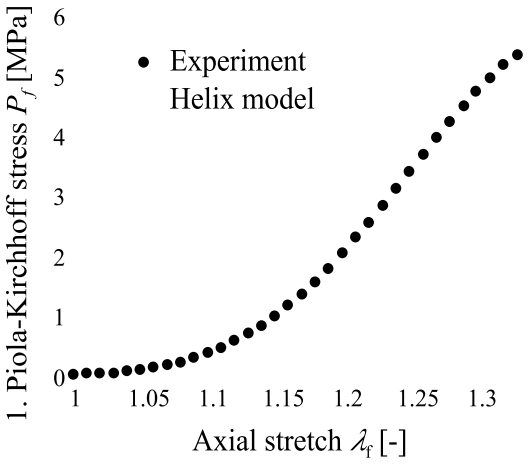

Figure 2: A fit of the helix model to data taken from strip extensiometry experiments on porcine corneas [4].

as $E = 30.0$ MPa, $R_0/r_0 = 1.94$ and $H_0/r_0 = 23.32$. The proposed model replicates the typical "J-type" shape of the stress-stretch curve in excellent agreement with the experimental observations. It should be noted, that the stress response of the helical spring model (1) represents a *strictly convex* function including compressive stress states and the almost linear region of fully extended fibers. However, the stress-stretch relationship can not be presented in closed form and needs to be solved by an iterative algorithm.

Incompressibility at large strains

Soft tissues such as those involved in the human eye are characterized by anisotropy introduced through collagen fibers and by incompressible (volume conserving) or almost incompressible deformation behavior. The present work extends the incompressible finite-rotation shell element [3] to an anisotropic formulation considering the previously described helical spring

model. In this work we postulate a curvilinear coordinate system Θ^i having the property

$$G_{\alpha 3} = G^{\alpha 3} = 0 \,, \quad G_{33} = G^{33} \,. \tag{2}$$

Furthermore, the coordinate system Θ^i is supposed to be subjected only to coordinate transformations of the form

$$\bar{\Theta}^\alpha = \bar{\Theta}^\alpha \left(\Theta^1, \Theta^2\right) \,, \quad \bar{\Theta}^3 = \Theta^3 \,, \tag{3}$$

where $(\bar{.})$ denotes a new set of coordinates. Accordingly, the position of the index $'3'$ is irrelevant in component relations and the base vector $\mathbf{G}_3 = \mathbf{G}^3$ is an invariant quantity. Note that such a coordinate system is useful for modelling shell structures. If the conditions (2) and (3) hold, the variables

$$\hat{\mathbf{C}} = C_{\alpha\beta}\, \mathbf{G}^\alpha \otimes \mathbf{G}^\beta \,, \quad \mathbf{c} = C_{\alpha 3}\, \mathbf{G}^\alpha \,, \quad C_3^3 \tag{4}$$

$$\hat{\mathbf{H}} = H_{\alpha\beta}\, \mathbf{G}^\alpha \otimes \mathbf{G}^\beta \,, \quad \mathbf{h} = H_{\alpha 3}\, \mathbf{G}^\alpha \,, \quad H_3^3 \tag{5}$$

which form *surface* tensors of second $(\hat{\mathbf{C}}, \hat{\mathbf{H}})$ and first order $(\mathbf{c}, \mathbf{h})$ while C_3^3, H_3^3 are invariant scalar-valued quantities of the right Cauchy-Green strain tensor $\mathbf{C} = \mathbf{F}^T \mathbf{F}$ and the generalized structure tensor [6]

$$\mathbf{H} = \kappa \mathbf{I} + (1 - 3\kappa) \mathbf{e}_0 \otimes \mathbf{e}_0 \,, \tag{6}$$

where $\mathbf{I}$ denotes the identity tensor and $\kappa \in [0; 1/3]$ represents the fiber distribution in an integral sense about the mean preferred direction $\mathbf{e}_0$. The first, third and fourth invariants of $\mathbf{C}$ required for the formulation of the strain energy function (11) can be expressed by means of (4), (5) as

$$I_{\mathbf{C}} = \mathrm{tr}\mathbf{C} = \mathrm{tr}\hat{\mathbf{C}} + C_3^3 \tag{7}$$

$$III_{\mathbf{C}} = \det\mathbf{C}$$

$$= \det\left(\hat{\mathbf{C}} + \mathbf{c} \otimes \mathbf{G}^3 + \mathbf{G}^3 \otimes \mathbf{c}\right) + C_3^3 \det\hat{\mathbf{C}} \tag{8}$$

$$IV_{\mathbf{C}} = \mathbf{C} : \mathbf{H} = \hat{\mathbf{C}} : \hat{\mathbf{H}} + 2(\mathbf{c} \cdot \mathbf{h}) + C_3^3 H_3^3 \,. \tag{9}$$

To assure pure *isochoric* deformations equation (8) is used to eliminate the transverse strain component C_3^3 in (7), (9) by means of the *incompressibility condition* $III_{\mathbf{C}} = 1$

$$C_3^3 = \frac{1 - \det\left(\hat{\mathbf{C}} + \mathbf{c} \otimes \mathbf{G}^3 + \mathbf{G}^3 \otimes \mathbf{c}\right)}{\det\hat{\mathbf{C}}} \,. \tag{10}$$

The strain energy of the fiber-matrix constitutive formulation is composed of an isotropic part related to the energy contribution of the ground substance (g) and an anisotropic part related to the energy contribution of n collagen fiber families (fi)

$$W(I_{\mathbf{C}}, IV_{\mathbf{C}i}) = W_{\mathrm{g}}(I_{\mathbf{C}}) + \sum_{i=1}^{n} W_{\mathrm{f}i}(IV_{\mathbf{C}i}) \tag{11}$$

$$= c_1(I_{\mathbf{C}} - 3) + \sum_{i}^{n} \int_1^{\lambda_{\mathrm{f}i}} P_{\mathrm{f}i}(\lambda_{\mathrm{f}i}) \mathrm{d}\lambda_{\mathrm{f}i} \,,$$

where the Neo-Hooke model is used to describe the isotropic part and the earlier introduced axial 1. Piola-Kirchhoff stress of an extensible helical spring (1) represents the anisotropic response of collagen fibers as a function of the mean fiber stretch $\lambda_{\mathrm{f}i} = \sqrt{IV_{\mathbf{C}i}}$.

Finite element model of the human eye

The presented fiber-matrix constitutive formulation is implemented into an incompressible bilinear finite shell element with a quadratic kinematic assumption in thickness direction [3]. To ensure an unique determination of the director and to consider shell intersections an updated rotation formulation is used. The eye model considers two spherical shells representing the cornea and the sclera tissues with an intersection at the limbus and the lamina cribrosa (LC) (Fig. 3). The LC is characterized

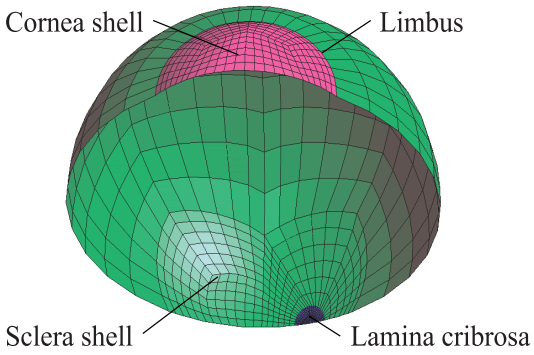

Figure 3: Finite shell element model of the human eye.

by a complex sieve-like network of collagen fibers, which allows the axons of the optic nerve to leave the eye ball. The response of the LC structure to different levels of intraocular pressure values is of special interest in the field of glaucoma research. The material parameters of the considered tissues have been fitted to different experiments, where the sclera and the LC tissue are assumed to consist of one randomly distributed collagen fiber family ($\kappa = 1/3$). The material behavior of the cornea tissue is considered to be anisotropic with two preferred fiber directions.

References

[1] D. E. Beskos, J. T. Jenkins (1975): A Mechanical Model for Mammalian Tendon. *ASME J. Appl. Mech.*, **42**, 755–758.

[2] A. D. Freed, T. C. Doehring (2005): Elastic Model for Crimped Collagen Fibrils. *J. Biom. Eng.*, **124**, 587–593.

[3] Y. Başar, R. Grytz (2004): Incompressibility at Large Strains and Finite-Element Implementation. *Acta Mechanica*, **168**, 75–101.

[4] K. Anderson, A. El-Sheik, T. Newson (2003): Modelling The Biomechanical Effect Of Increasing Intraocullar Pressure On The Porcine Cornea. *16th ASCE Engineering Mechanics Conference*, 1–11.

[5] W. Jiang, W. K. Jones, K. H. Wu, T. L. Wang (1989): Non-Linear and Linear, Static and Dynamic Analyses of Helical Springs. *Structures, Structural Dynamics and Materials Conference, 30th*, 386–395.

[6] T. C. Gasser, R. W. Ogden, G. A. Holzapfel (2006): Hyperelastic Modelling of Arterial Layers with Distributed Collagen Fiber Orientations. *J. R. Soc. Interf.*, **3**, 15–35.

Part VI

Multi-Phase, Multi-Physics Modelling of Porous Media

Interface Flow Simulations in Multi-phase Particulate Media

J. E. Bolander*, Z. Li

University of California, Davis
One Shields Ave., Davis, California 95616-5294, USA
jebolander@ucdavis.edu, zhnli@ucdavis.edu

Summary: Irregular lattice models are developed to simulate moisture transport in cement-based composites. Explicit modeling of the matrix-inclusion interface enables rudimentary simulations of percolation phenomena. Special procedures are used to calculate nodal flux and track particle flow across the computational domain. These determinations of moisture flow are being coupled to ongoing simulations of fracture at the concrete mesoscale.

Background

Most physio-chemical degradation mechanisms of structural concrete require a supply of moisture, and thus the transport properties of the material can greatly affect structural durability [1]. Differential shrinkage due to non-uniform drying, and shrinkage accompanied by other forms of restraint, can cause cracking that modifies the transport properties. The behavior of the matrix-inclusion interface is of particular interest in the coupling of moisture flow and potential cracking, as it is generally more porous and weaker compared to either the matrix or inclusion phases.

In this extended abstract, an irregular lattice model is used to simulate moisture flow local to aggregate inclusions. The model formulation is based on the theory of nonlinear moisture diffusion [2, 3]. The lattice elements can be viewed as one-dimensional conduits of the field quantity (e.g. moisture content) that interconnect at the lattice nodes. The topology of the lattice is determined by the Delaunay tessellation of the lattice nodes, whereas the element properties scale according to the dual Voronoi tessellation. One goal of this work is its eventual coupling to models of fracture in multi-phase particulate media, which are based on similar Delaunay/Voronoi definitions of the lattice topology and element properties [4]. Figure 1 shows the Voronoi discretization of a notched three-point bend specimen used for such fracture simulations.

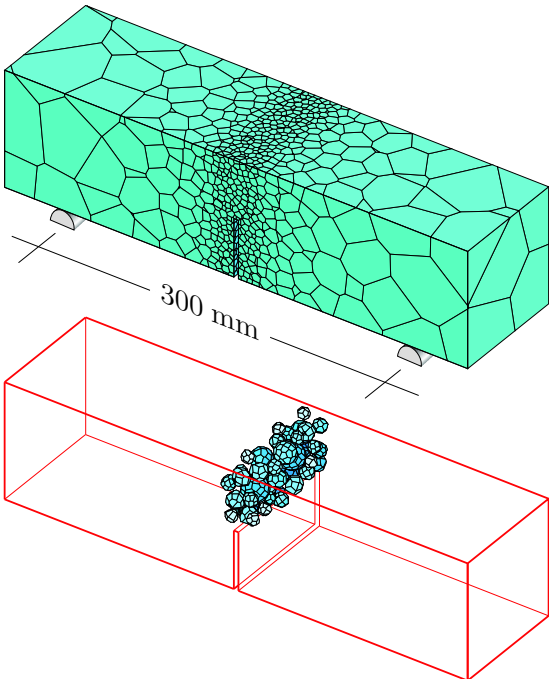

Figure 1: a) Voronoi discretization of concrete beam; and b) coarse aggregate distribution above prenotch

Nodal flux calculations

Nodal flux is calculated to determine the magnitude and direction of flow within the continuum. After solving for nodal potentials, the elemental flows Q_k are known. Based on conservation of mass of the transport substance the net flow into a node, or Voronoi cell, is zero (Fig. 2a). The Voronoi cell is sectioned through the corresponding node and perpendicular to the direction of interest (θ, ϕ), as shown in Fig. 2b. The flow $Q_{\theta\phi}$ through the newly established cut face (of area $A_{\theta\phi}$) is determined by summing the weighted flow contributions of all n elements framing into the node:

$$Q_{\theta\phi} = \sum_{k=1}^{n} R_k Q_k \qquad (1)$$

Weighting factor $R_k = A'_k/A_k$, where A_k is the area of facet k and A'_k is the area of facet k on the negative side of the cut plane, as defined by normal direction (θ, ϕ). Principal flow vectors are determined from flux $q_{\theta\phi} = Q_{\theta\phi}/A_{\theta\phi}$ computed for three mutually perpendicular orientations of the cut face.

Modeling the matrix-inclusion interface

The surface of a spherical inclusion, and the matrix-inclusion interface, are discretized by placing pairs of nodes on randomly directed rays from the sphere center; the nodes of each pair are at distances a and $a + t$ from the sphere center, where a is the sphere radius and t is the thickness of the interface. Each nodal pair defines a lattice element normal to and spanning the interface. Such elements, whose Voronoi facets are shown in Fig. 3a, are most relevant when modeling fracture of the interface [4]. For modeling moisture transport, however, the structure and properties of the lattice parallel to the interface are also important. As part of the Delaunay tessellation of the domain, the set of nodes at distance $a + t$ from the sphere center are triangulated, forming the structures shown in Fig. 3b.

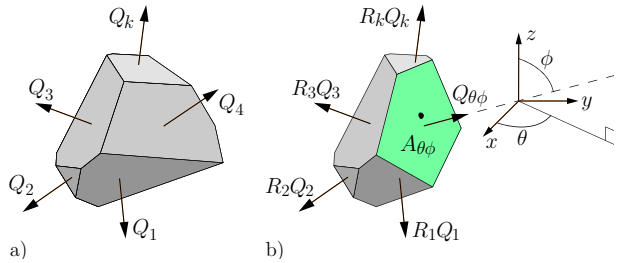

Figure 2: a) Elemental flow through a Voronoi cell; and b) sectioning of Voronoi cell for nodal flux calculation

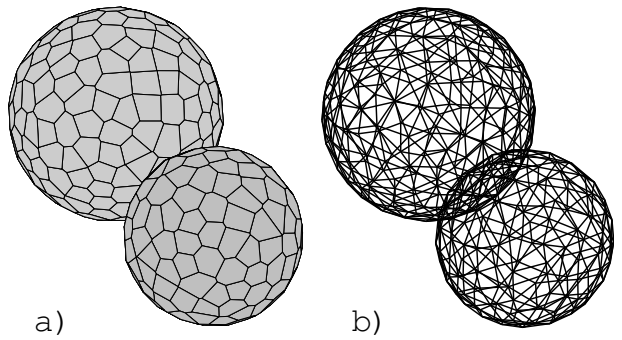

Figure 3: a) Voronoi discretization of spherical inclusions; and b) Delaunay triangulation of interface layer

As a starting point for the mesoscale modeling of moisture transport in concrete materials, consider steady-state inviscid flow about a single spherical inclusion in a semi-infinite domain. This situation is governed by the Laplace equation, subject to appropriate boundary conditions. Figure 4 shows moisture particle streamlines for two basic cases, where ρ is measured from the axis of radial symmetry. Particle movement is tracked using a conventional Euler explicit scheme. Flux vectors for an arbitrary point within the domain are interpolated from the nodal values of the enclosing Delaunay tetrahedron. The impermeable inclusion and void are modeled by assigning sufficiently small and large diffusivity values, respectively, to the lattice elements within the sphere. For the case of a spherical void, flow is drawn inward toward the void as shown in Fig. 4b and flow along the x-axis is magnified rather than impeded. The irregular geometry of the lattice does not bias the flow field, as evident from the linear flow trajectories away from the inclusion.

Flow past two neighboring inclusions is shown in Fig. 5, where the nodal flux vectors are determined by the mass conservation scheme depicted in Fig. 2 (in which angles θ and ϕ correspond to the principal flux direction for each node location.) Nearly all flow is through the connected interfaces, which have been assigned high diffusivity values relative to those of the matrix and inclusions. Flow occurs throughout the matrix phase of the domain, yet the associated flow vectors are small and well-below the plotting threshold. These and other simulations indicate a jump in effective permeability upon establishing interface percolation across the domain. In forthcoming work, the transport properties of the interface will be modified to reflect interfacial cracking, as determined from the fracture analyses.

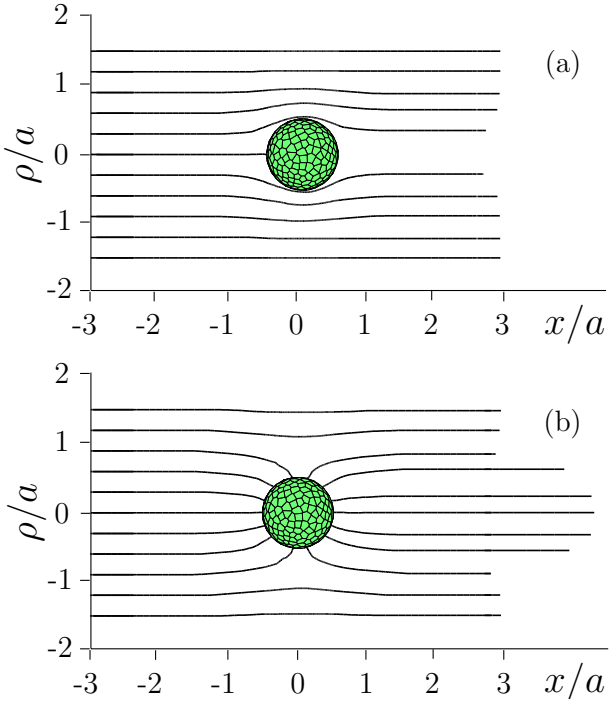

Figure 4: Tracking of moisture movement past: a) impermeable spherical inclusion; and b) spherical void.

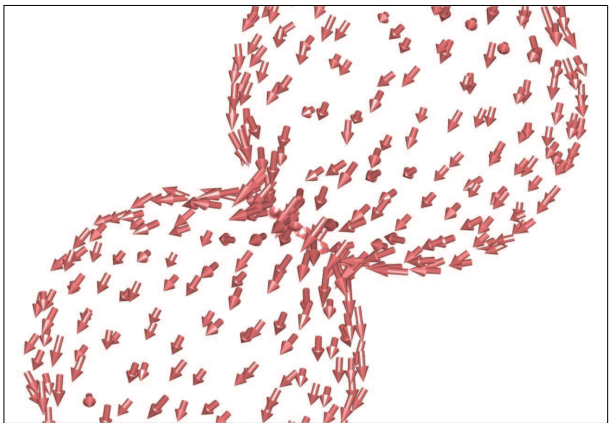

Figure 5: Nodal flux description of interface percolation.

References

[1] Comité Euro-international du Béton (1992): *Durable concrete structures—design guide, 2nd Ed.*. Thomas Telford, UK.

[2] Z. P. Bažant, L. J. Najjar (1971): Drying of concrete as a nonlinear diffusion problem. *Cement and Concrete Research*, **1**, 461–473.

[3] J. E. Bolander, S. Berton (2004): Simulation of shrinkage induced cracking in cement composite overlays. *Cement and Concrete Composites*, **26**, 861–871.

[4] M. Yip, Z. Li, B.-S. Liao, J. E. Bolander (2006): Irregular lattice models of fracture of multiphase particulate materials. *International Journal of Fracture*, **140**, 113–124.

Chemo-Poroplastic Model for Durability Analysis of Concrete

M. Cuomo*, **A. Nicolosi**

Department of Civil and Environmental Engineering
University of Catania, Italy
mcuomo@dica.unict.it, anicolo@dica.unict.it

Summary: The paper discusses a model for calcium leaching of the cement paste due to interaction with low calcium content water. The methodology is also applicable to other chemical interactions. Chemical damage and mechanical cracking are strongly coupled. The paper introduces a constitutive model able to capture the coupled nature of the problem.

Methodology and objectives

Degradation of concrete caused by dissolution of the cement paste due to the action of moving groundwater is a relevant phenomenon in structures designed for long life, like underground storage for aggressive waste. The phenomenon, first studied by Ulm [1], is commonly referred to as *calcium leaching*.

Due to the interaction with the mechanical crack pattern and with the presence of an interstitial fluid phase, the chemical leaching is strongly coupled with the mechanical and hydraulic processes taking place in the material. The strong coupling and the non-linear nature of the phenomenon cause severe troubles in the numerical simulations. The structural problem is ruled by the equations of conservation of momentum and of conservation of mass of the species, in addition to energy balance for non isothermal problems. All the equations are coupled and nonlinear.

In the paper it is proposed a multiphysic constitutive model, so that the problem can be solved by the main field equations coupled at the constitutive level, through the introduction of proper internal variables. A complete poro-plastic damaging model is used for the solid phase, and the constitutive equations are derived from a consistent thermodynamic model developed within the framework of the Generalized Standard Material Model. This allows to use robust numerical integrators, similar to those used in standard plasticity.

The model is limited to small deformations. Since in the problems of interest the temperature does not usually rise above 65^oC, isothermal conditions are assumed.

Damage model

Fully saturated concrete in isothermal conditions is considered, in order to simulate the situation of a structural element completely immersed in groundwater. In the context of the Theory of Active Porous Media, developed by Biot and Coussy [2, 3], the internal structure is thus fully defined by the porosity ϕ, representing the local average volume ratio occupied by connected voids, referred to the total RVE volume. The following partition holds

$$\phi = \phi_0 + \phi_m^e + \phi_m^p + \phi_c \tag{1}$$

The first term is the initial porosity of the material, the second and third term are related to the reversible and irreversible porosity variation due to the deformation of the solid matrix. The last term accounts for the increase of the void ratio due to the dissolution of the matrix, and is assumed as a measure of the chemical damage undergone by the material. It is proportional to the calcium concentration in solution in the solid phase, and is a measure of the chemical damage. The mechanical degradation of the solid matrix is modeled, in the context of the Continuum Damage Model, by means of two scalar variables ω_1 and ω_2 accounting for cracking in presence of tensile or compressive stress states, following the approach depicted in [4].

The coupled damage process affects, in addition to the mechanical characteristics of concrete, its transport properties. The hydraulic conduction is ruled by a Darcy-like law; the related permeability coefficient is assumed as dependent on the porosity ϕ and on the cracks, through ω_1 and ω_2. Because of the cement paste dissolution, a calcium ion flow arises inside the material; this can be thought as the sum of a *diffusive* term and a *convective* term, due to the motion of the fluid phase. The diffusive term is ruled by a Fick-like law, where the diffusivity depends on the porosity and on the liquid calcium concentration (see [5, 6] for further details). In the next section the chemo-mechanical constitutive model will be presented in some detail.

Mechanical constitutive model

The constitutive laws are ruled by the free energy, defined as a function of the *reversible* parts of the kinematic variables:

$$\psi = m_{Ca}\psi_{Ca}(c) + \bar{\psi}_s\left(\boldsymbol{\varepsilon}^e, \phi_m^e, \alpha^e, \omega_i^e, s^e\right) \tag{2}$$

where the kinematic variables are split in the sum of their reversible and irreversible components:

$$\begin{array}{ll} \boldsymbol{\varepsilon} = \boldsymbol{\varepsilon}^e + \boldsymbol{\varepsilon}^p & \text{strain} \\ \phi_m - \phi_0 = \phi_m^e + \phi_m^p & \text{porosity} \\ \alpha = \alpha^e + \alpha^p = 0 & \text{hardening} \\ \omega_i = \omega_i^e + \omega_i^p = 0 & \text{damage} \\ s = s^e + s^p = s_0 & \text{solid calcium concentration} \end{array} \tag{3}$$

The dual mechanical counterparts are:

$$\begin{array}{ll} \boldsymbol{\sigma} & \text{stress} \\ p & \text{fluid pressure} \\ \chi & \text{hardening static variable} \\ \zeta_i & \text{damage static variables} \\ \Gamma & \text{solid calcium potential} \end{array} \tag{4}$$

In (2) the free energy of the calcium ion species has been included, that allows to evaluate the electro-chemical potential μ_{Ca} of the ions. The free energy functional of the solid phase, depending on the elastic components of the state variables, is chosen in the form

$$\begin{aligned}\bar{\psi}_s =& \frac{1}{2}\boldsymbol{\varepsilon}^e : \mathbf{C}^u(\omega^e, s^e) : \boldsymbol{\varepsilon}^e + \frac{1}{2}N(\omega^e, s^e){\phi_m^e}^2 \\ & - b(\omega^e, s^e)N(\omega^e, s^e)\varepsilon_v^e\phi_m^e + \frac{1}{2}H(\omega^e, s^e){\alpha^e}^2 \\ & + \int_{s_0}^{s} \bar{\Gamma}(s^e)ds^e + \Gamma_0\, s^e\end{aligned} \tag{5}$$

where $\bar{\Gamma}(s^e)$ is the equilibrium solid calcium chemical potential. A multiplicative dependence on mechanical and chemical damage is assumed for the global bulk modulus K only. This assumption is based on the hypothesis that the global stiffness is damaged because of the erosion of the solid matrix, but the latter preserves its intrinsic elastic properties. As a consequence, it is assumed

$$\begin{aligned}K\left(\omega^e, s^e\right) &= \left(1+\omega^e\right)^n \left[1-\phi_c(s^e)\right] K_0 \\ G\left(\omega^e, s^e\right) &= \left(1+\omega^e\right)^n \left[1-\phi_c(s^e)\right] G_0 \\ K_s &= \text{const}\end{aligned} \tag{6}$$

The elastic moduli appearing in (5) are obtained from the above positions [6].

The static variables are obtained by differentiation of the functional (2) w.r.t. to their kinematic counterparts. Due to the energetic approach, the constitutive equations exhibit cross-effects between mechanical and chemical phenomena, as a consequence of the Maxwell symmetries of the energy functional (2).

The *irreversible* processes are described by defining suitable plastic domains in the enriched space of the static variables. In particular, a *mechanical* domain $g_m(\boldsymbol{\sigma}, p, \chi, \zeta_i)$ and a *chemical* domain $g_c(p, \Gamma)$, describing the driving force of the leaching process, are introduced. According to the expression of the dissipation, both functions depend on the pressure. Associated flow rules are postulated. The chemical dissipation is described by means of viscoplastic flow rules, since the leaching process is a slow time-dependent phenomenon. The chemo-mechanical coupling is then solved at the constitutive level in a classical return mapping scheme.

Applications

In this section some of the results obtained by the application of the proposed model are reported.

Fig. 1 shows the degradation of the mechanical properties of concrete, in terms of peak strength and Young modulus vs. fluid calcium concentration, in a softening test. The specimen is first loaded until a fixed strain is reached, kept constant while a chemical leaching process occurs. The abrupt steps in the diagrams are related to the onset of the dissolution of the several calcium phases contained in the cement paste.

Fig. 2 shows, on the contrary, the results of a compression creep test. The specimen is first loaded until a fixed elastic stress is reached. This stress level is kept constant while a leaching process is applied, and the strain is measured as the erosion takes

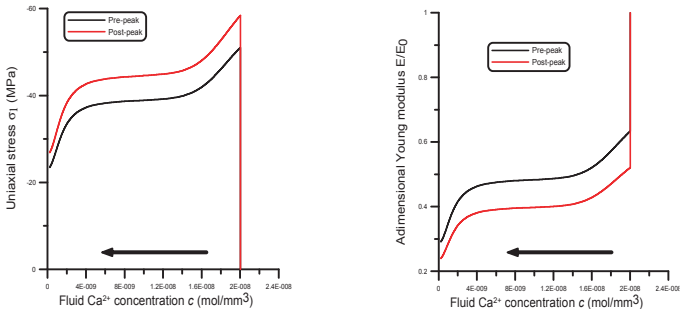

Figure 1: Softening test—compression, uniaxial loading.

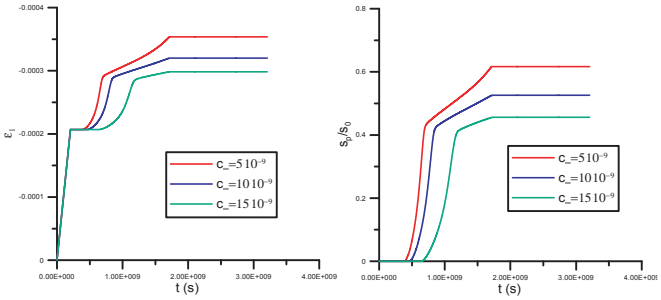

Figure 2: Creep test—compression, uniaxial loading.

place. In the figure the strain and the eroded calcium ratio are reported as a function of time for different values of the final level of calcium concentration in the solution.

The results show the ability of the model to capture the coupled nature of the chemical corrosion of concrete, so that it can be usefully employed for durability analyses.

References

[1] F. J. Ulm, J. M. Torrenti and F. Adenot (1999): Chemo-poroplasticity of calcium leaching in concrete. *ASCE Journal of Engineering Mechanics*, **125**, 1200–1211.

[2] M. A. Biot and D. Willis (1957): The elastic coefficients of theory of consolidation. *Journal of Applied Mechanics*, **24**, 594–601.

[3] O. Coussy (2004): *Poromechanics*, Wiley and Sons, Chichester.

[4] L. Contrafatto, M. Cuomo (2006): A framework for an elastic-plastic damaging model for concrete under multiaxial stress states. *International Journal of Plasticity*, **22**, 2272–2300.

[5] M. Cuomo, A. Nicolosi (2006): A poroplastic model for hygro-chemo-mechanical damage of concrete. *Proceedings of Euro-C 2006 Computational Modelling of Concrete Structures*.

[6] A. Nicolosi (2006): *A Poroplastic Model for the Analysis of Chemically Leached Concrete*, PhD thesis, University of Catania.

Thermo-Mechanical Modeling of Alkali-Silica Reaction Damage in Concrete

C. Comi, R. Fedele, U. Perego*

Department of Structural Engineering, Politecnico di Milano
Piazza L. da Vinci, 32 - 20133 Milano (Italy)
claudia.comi@polimi.it, roberto.fedele@polimi.it, umberto.perego@polimi.it

Summary: In this study a thermo-chemo-damage model is developed in order to simulate the swelling phenomena and the correlated deterioration of stiffness and strength in concrete due to the alkali-aggregate reaction. The model is validated on the basis of accelerated laboratory tests.

Thermo-chemo damage model

The chemical reaction between the alkali of the mortar, the silica of the aggregates and the water, i.e. the so-called alkali-silica reaction (ASR), produces a gel phase with an increase of volume causing swelling and progressive damage of concrete. The velocity of the reaction is strongly dependent on temperature and humidity of concrete. Many important concrete structures built some decades ago exhibit damage caused by ASR: a reliable evaluation of the actual safety margin of these structures is still a challenging task.
In this work we develop a model for concrete affected by the ASR in the framework of the poromechanics theory (see e.g. the comprehensive book [1]), in the line of what proposed in [2–4]. We consider concrete as a two-phase material: the concrete skeleton and the expanding gel. In our modelization we assume that a single variable ξ, called extent of the reaction, can be used to measure the degree of advancement of the reaction. This nondimensional variable grows from zero and reaches the unit value when the reaction is completed. The gel formation and the gel expansion are considered as simultaneous, so that the volumetric deformation of the gel due to the reaction is assumed linearly proportional to the reaction extent ξ. The microcracking dissipation phenomena of the concrete matrix are modeled by an internal variable $D = 1 - D(1 - D_t)(1 - D_c)$, where D_t and D_c, are isotropic damage variables, one for stress states of prevailing tension and the other for stress states of prevailing compression, as proposed in [5].
The overall macroscopic stress $\boldsymbol{\sigma}$ is expressed as the difference between the effective stress $\boldsymbol{\sigma}'$ in the concrete skeleton and the swelling pressure p in the gel as

$$\boldsymbol{\sigma} = \boldsymbol{\sigma}' - b\,p\,\mathbf{1} \tag{1}$$

where b is the Biot coefficient and $\mathbf{1}$ is the unit tensor. The effective stress and the pressure are related to deviatoric strains $\mathbf{e}$ and volumetric strain $\mathrm{tr}\,\varepsilon$ by

$$\boldsymbol{\sigma}' = (1-D)[2\mu\mathbf{e} + K(\mathrm{tr}\,\varepsilon - \alpha\vartheta)\mathbf{1}] \tag{2}$$

$$p = -(1-D)Mb(\mathrm{tr}\,\varepsilon - \alpha\vartheta - \kappa\xi) \tag{3}$$

where μ and G are the shear and bulk modulus of the skeleton, M is the Biot modulus, α is the volumetric thermal expansion coefficient, $\vartheta = T - T_0$ is the temperature variation from the reference temperature T_0 and κ is a parameter proportional to the volumetric deformation due to ASR under isothermal stress-free condition ε_∞,

$$\kappa = \frac{K + Mb^2}{Mb^2}\varepsilon_\infty \tag{4}$$

Under the hypothesis of full saturation, reasonable e.g. for gravity dams, the rate of ASR can be considered to depend only on the temperature history $T(t)$ through an internal characteristic time $t_c(T)$ as described in [2] and not on the relative humidity.

$$\dot{\xi}(t) = \frac{1}{t_c(T(t))}(1 - \xi(t)) \tag{5}$$

The activation of damage is governed by two loading functions f_t and f_c depending on both the macroscopic stress $\boldsymbol{\sigma}$ and the gel pressure p through an "inelastic effective stress" $\boldsymbol{\sigma''}$

$$\boldsymbol{\sigma}'' = \boldsymbol{\sigma} + \beta\,p\,\mathbf{1} \tag{6}$$

where the non-dimensional factor β, with $\beta \leq b$, governs the damage level achievable in a concrete specimen under free expansion due to ASR. For $\beta = 0$ the swelling pressure of the gel does not intervene in the damage activation, in this case the ASR only produces an imposed volumetric strain, additional to the thermal one. Activation functions are given the mathematical expressions proposed in [5]:

$$f_t(\boldsymbol{\sigma}'', D_t) = \frac{\mathbf{s}:\mathbf{s}}{2} - a_{0t}(\mathrm{tr}\,\boldsymbol{\sigma}'')^2 + a_{1t}\mathrm{tr}\,\boldsymbol{\sigma}''h_t(D_t) - a_{2t}h_t^2(D_t) \tag{7}$$

$$f_c(\boldsymbol{\sigma}'', D_c) = \frac{\mathbf{s}:\mathbf{s}}{2} - a_{0c}(\mathrm{tr}\,\boldsymbol{\sigma}'')^2 + a_{1c}\mathrm{tr}\,\boldsymbol{\sigma}''h_c(D_c) - a_{2c}h_c^2(D_t) \tag{8}$$

where $\mathbf{s}$ is the deviatoric stress, h_t and h_c are the hardening-softening functions and a_{it}, $a_{ic}, i = 0, 1, 2$, are non-negative material parameters governing the shape and the size of the elastic domain.

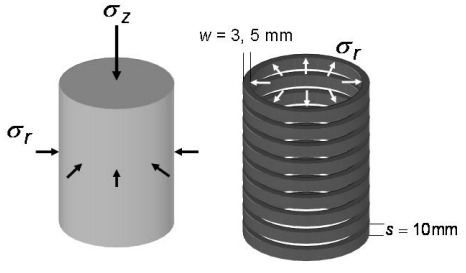

Figure 1: Multon's tests geometry and loading [6].

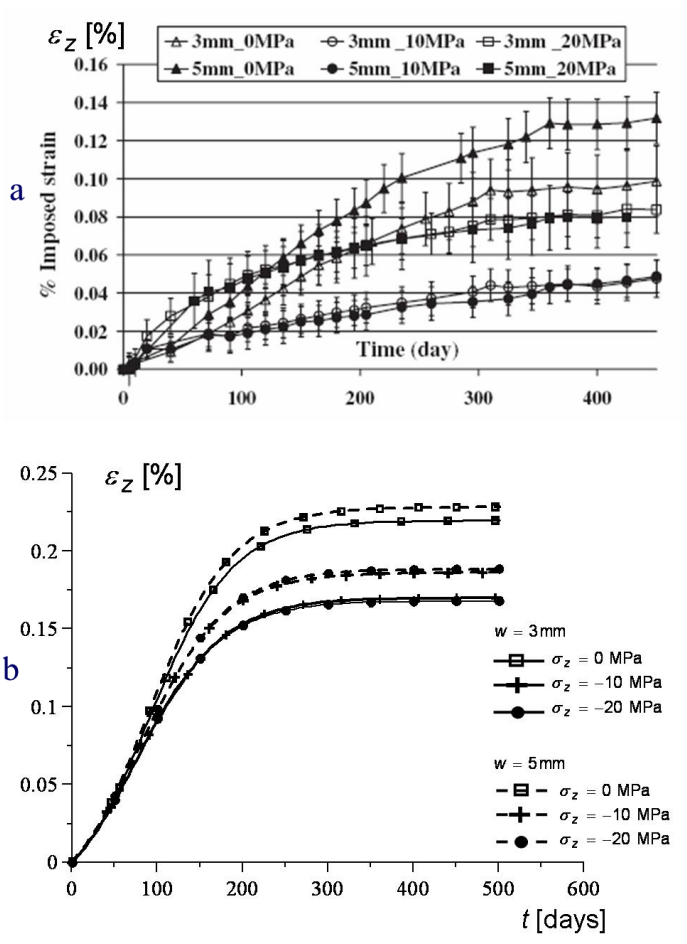

Figure 2: Longitudinal strain evolution: (a) experimental results from [6], (b) model prediction.

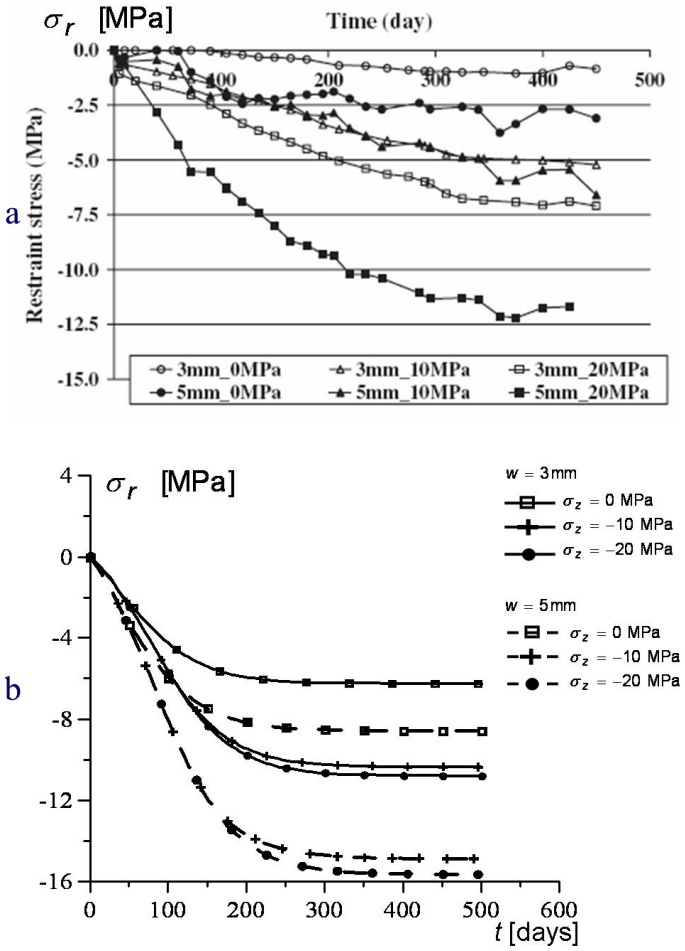

Figure 3: Radial stress evolution (a) experimental results from [6], (b) model prediction.

Model validation

The model has been used to simulate the experimental results reported in [6]. In these tests the expansion due to ASR under isothermal condition is monitored on small cylindrical specimen of reactive concrete transversally constrained by thin steel rings with and without an imposed axial stress, see Fig. 1. The experimental setting was intended to generate within the specimens multi-axial stress states, close to those expected within a large structure in service conditions. The experimental results in terms of longitudinal strain ε_z and radial stress σ_r are compared in Figs. 2 and 3 with the predictions of the proposed model.

Despite the simplicity of the proposed model and in particular the independence of the reaction extent of the stress state, eq. (5), the model is able to qualitatively reproduce the decrease of the longitudinal ASR expansion due to the presence of external compressive stress. Also the effect of the stress triaxiality is correctly reproduced: the thicker the steel rings, and hence the higher the radial stress, the higher the longitudinal expansion.

Conclusions

The comparisons with the experimental tests confirm that the model correctly reproduces the swelling phenomenon and its structural effects. The proposed model has been implemented in a finite element code. Simulation of the effects of ASR in a concrete dam are currently in progress.

References

[1] O. Coussy (2004): *Poromechanics*, John Wiley & Sons, New York.

[2] F. J. Ulm, O. Coussy, L. Kefei, C. Larive (2000): Thermo-chemo-mechanics of ASR expansion in concrete structures. *J. Eng. Mech*,**126**, 233–242.

[3] F. J. Ulm, M. Peterson, E. Lemarchand (2002): Is ASR-expansion caused by chemo-poroplastic dilatation?, *J. Concrete Sci. Eng.*, **4**, 47–59.

[4] C. Larive (1998): *Apports combins de l'expérimentation et de la modélisation a la compréhension de l'alcali réaction et de ses effets mécaniques*, PhD Thesis LCPC.

[5] C. Comi, U. Perego (2001): Fracture energy based bi-dissipative damage model for concrete, *Int. J. Solids and Structures*, **38**, 6427–6454.

[6] S. Multon, F. Toutlemonde (2006): Effect of applied stresses on alkali-silica reaction-induced expansions, *Cement and Concrete Research*, **36**, 912–920.

Discrete Modelling of Fracture and Moisture Transport in Heterogeneous Materials

P. Grassl*, C. Pearce

Department of Civil Engineering, University of Glasgow, Glasgow, UK
grassl@civil.gla.ac.uk, pearce@civil.gla.ac.uk

Summary: The present paper discusses the discrete modelling of fracture and moisture transport in quasibrittle heterogeneous materials. The rigid body spring method is used to describe the coupled mechanisms within one framework. The elastic response of the material is described by springs connecting the rigid bodies. Fracture is modelled by damaging those springs. Moisture transport is divided into two parts, i.e. Darcy flow in porous media and discrete flow along fractures. Darcy flow is modelled perpendicular to the interfaces of rigid bodies, whereas the discrete flow is described along the interfaces, which are interpreted as micro-cracks. Fracture and moisture transport are coupled and the modelling approach is validated by benchmark tests.

Introduction

The coupling of fracture and moisture transport is often the determining mechanism in many structural phenomena observed in construction materials, i.e. spalling of concrete covers due to corrosion of the reinforcement or excessive cracking due to delayed ettringite formation. The present work deals with modelling of fracture and flow in heterogeneous quasi-brittle materials, such as concrete, toughened ceramics, rocks and stiff soils. This research area is well developed and many continuum approaches have been proposed in the literature to describe the two mechanisms. However, these approaches are computationally very demanding and become almost prohibitive for the simulation of the evolution of the microstructure of these materials. Therefore, a discrete approach is presented here. In the following a short overview on the modelling approach is given.

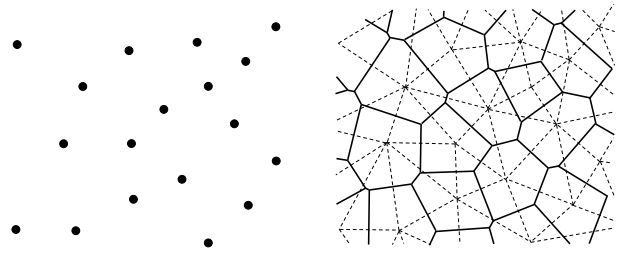

Figure 1: Random placement of vertices and Voronoi tesselation.

Modelling of fracture

The mechanical response is described by a two-dimensional Rigid-Body-Spring-Model (RBSM), which was originally proposed by Kawai [1] and in recent years further developed and applied to concrete, for instance, by Bolander [2].

The main idea of the RBSM is to decompose the domain into rigid bodies connected by springs, which describe both the elastic and inelastic mechanical response of the solid. Each rigid body has 3 degrees of freedom, namely two translations and one rotation. Fracture is modelled by an elasto-damage law for the springs.

The decomposition of the domain is based on the Voronoi tesselation. First, vertices are placed randomly in the domain. Then, the Voronoi tesselation is performed. The random placement of the vertices is constrained by a minimum distance between any two vertices and between vertex and the specimen boundary. The relation of the number of vertices for a chosen domain and the minimum distance determines the distribution of the sizes of rigid bodies. A saturated arrangement, i.e. maximum number of vertices for a specific domain and minimum distance, results in rigid bodies of similar size (Figure 1).

The degrees of freedom $\mathbf{u} = \{u_1, v_1, \phi_1, u_2, v_2, \phi_2\}^{\mathrm{T}}$ of two rigid bodies sharing an interface (see Figure 2) are related to the displacement discontinuities $\mathbf{u}_{\mathrm{c}} = \{u_{\mathrm{c}}, v_{\mathrm{c}}\}^{\mathrm{T}}$ at the mid point of the interface where the springs are located. The discontinuity

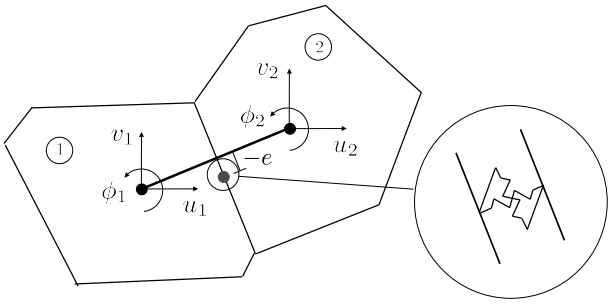

Figure 2: Rigid body spring model.

components u_{c} and v_{c} are the normal and shear components respectively. The constitutive response is expressed by a stress-strain law, where the strain is $\boldsymbol{\varepsilon} = \{\varepsilon_{\mathrm{u}}, \varepsilon_{\mathrm{s}}\}^{\mathrm{T}} = \dfrac{1}{L}\{u_{\mathrm{c}}, v_{\mathrm{c}}\}$ and L is the distance between the two vertices. The tensile failure is described by an elasto-damage model following [3].

Heterogeneous materials are characterised by spatially varying material properties. In the present work this is reflected in an two-folded approach. Aggregates larger than 5 mm are modelled discretely, whereas the heterogeneity due to finer particles is described by an autocorrelated random field, which is generated using the spectral representation according to [4] and [5]. This mixed approach is a compromise between model detail and computational time, which allows a realistic description of the tensile failure of concrete as it is shown in Figure 3.

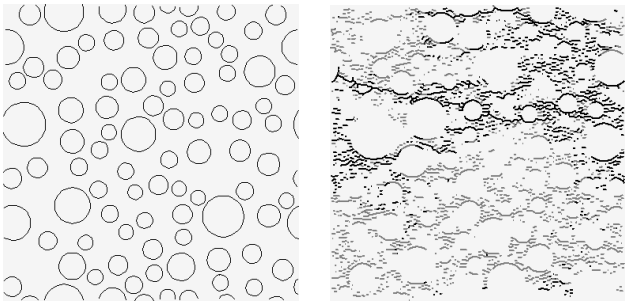

(a) (b)

Figure 3: Concrete subjected to uniaxial tension: (a) heterogeneous microstructure. (b) fracture pattern at peak load.

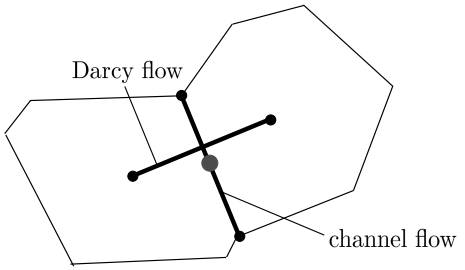

Figure 4: Discretisation of Darcy and channel flow within the RBSM framework.

Modelling of moisture transport

Moisture transport is decomposed into two parts: first, Darcy flow in porous media and second, moisture transport along fractures. The former is modelled via a discrete network of one-dimensional conduit elements [6]. This network is defined by the nodes of the rigid bodies (Figure 4) which already account for the translations and rotations of the mechanical problem. Thus, these nodes are enriched by an additional degree of freedom for the transport problem. In order to obtain equivalence between a continuum description and the proposed discrete system, the one-dimensional flow description is tuned accordingly.

In addition to this primary transport process, moisture transport along fractures is also defined via a channel flow using a Bingham flow description. Thus, the finite elements which connect the two vertices and describe the mechanical response and the porous flow are augmented by two additional nodes along the interfaces between the rigid bodies, which allow the description of all three physical features (mechanical, Darcy flow and channel flow) by means of a super element with one integration point located at the midpoint of the interfaces.

Modelling of the coupling of fracture and moisture transport

Both flow regimes are influenced by fracturing of the interface between rigid bodies. Crack opening will allow or enhance channel flow along this interface while flow perpendicular to the crack opening will also be influenced. This work investigates this mechanical-transport coupling and in particular the relationship between the flow parameters and crack opening.

Conclusions

The present work deals with a discrete approach to modelling of fracture and moisture transport in heterogeneous materials. The importance of the coupling of these two physical features is demonstrated by means of benchmark tests. It is shown that a discrete approach is computationally efficient and an attractive alternative to continuum descriptions of multiphysic phenomena in heterogeneous materials.

Acknowledgements

The simulations were performed with the object-oriented finite element package OOFEM [7] extended by the present authors.

References

[1] T. Kawai (1977): New element model in discrete structural analysis. *Journal of Society of Naval Architecture in Japan*, **141**, 187–193.

[2] J. E. Bolander, S. Saito (1998): Fracture analysis using spring networks with random geometry. *Engineering Fracture Mechanics*, **61**, 569-591.

[3] M. Ortiz, A. Pandolfi (1999): Finite-deformation irreversible cohesive elements for three-dimensional crack-propagation analysis. *International Journal for Numerical Methods in Engineering*, **44**, 1267-1282.

[4] M. Shinozuka and C.-M. Jan (1972): Digital simulation of random processes and its applications. *Journal of Sound and Vibration*, **25**, 111-128.

[5] M. Shinozuka and G. Deodatis (1972): Simulation of multi-dimensional gaussian stochastic fields by spectral representation. *Applied Mechanics Reviews*, **49**, 29-53.

[6] J. E. Bolander and S. Berton (2004): Simulation of shrinkage induced cracking in cement composite overlays. *Cement and Concrete Composites*, **26**, 861-871.

[7] B. Patzák (1999): Object oriented finite element modeling. *Acta Polytechnica*, **39**, 99-113.

New Computational Model for Fracturing Porous Media

R. Al-Khoury*, L. J. Sluys

Faculty of Civil Engineering and Geosciences, Delft University of Technology
P.O. Box 5048, 2600 GA Delft, The Netherlands
r.alkhoury@citg.tudelft.nl, L.J.Sluys@citg.tudelft.nl

Summary: This research work involves the development of a new computational model for simulating the fracturing process in a porous medium using the finite element method. Two independent numerical techniques are utilized for describing this process. The partition of unity method is used for describing the fracturing process, and the double porosity model is used for describing the resulting fluid flow. The basic mechanism of the proposed model is described here.

Mechanism of the model

The basic mechanism of a fracturing porous medium can be described such that, upon application of external loads and/or sudden changes in water levels or hydraulic pressures at the boundaries of the medium, fractures (fissures) might initiate and propagate in the medium, the degree of which depends on the material properties and the amount and type of the external forces. As a result of the fracturing process, a pressure gradient occurs between the fluid within the matrix pores and the fluid in the adjacent fractures. This gradient causes a fluid to flow from a high pressure zone to a low pressure zone. Fluid flow may alter the effective stress state and can cause a reduction of the material bearing capacity that may result into complete collapse of the system.

Fig. 1 illustrates the mechanism of the fracturing process in a porous medium and the resulting fluid flow, as well as the modeling approach adopted in this work. The figure shows that, due to the fracturing process, the solid phase is divided into two (or more) sub-domains defined as Ω^+ and Ω^-, and the fluid phase exhibits flow towards the fracturing zone (flow towards the porous matrix is also possible, depending on the pressure gradient).

The fracturing process is modeled using the partition of unity finite element method. In this method, a displacement discontinuity is introduced in the displacement field of the finite elements. This is done by decomposing the displacement field into a continuous part and a discontinuous part, where the latter is enhanced by use of the Heaviside function. One of the main advantages of the partition of unity method is that the discontinuity, once initiated, can propagate through a body independent of the finite element mesh size. As a result of the fracturing process, fluid starts to flow between the fractured zone and the surrounding porous matrix. This process is modeled using the double porosity model. In this model, the fluid flow is simulated as a superposition of the flow in two overlapping continuum domains; one representing a continuum porous matrix and the other representing a continuum fractured zone (fissured network). The overlap between the two domains is made via a leakage process. The pore pressure in the porous matrix is defined as P^{w1} and the pore pressure in the fractured zone is defined as P^{w2}. The fracturing zone, dependent on the properties of the medium, might have different configurations such as banded (weak) discontinuities or strong discontinuities. This is illustrated in the right hand side circle of Fig. 1, in which the fractured zone can be either a single crack (black line representing a strong discontinuity) or a combination of many fissures (black and gray lines representing a fissured network). In this paper, emphasis is placed on the presence of a strong discontinuity.

The coupling between the fracturing process and the fluid flow is made by the use of the Biot theory of consolidation. The model assumes that there is an explicit coupling between the solid deformation and the pore pressure in the porous matrix, and an implicit coupling with the pore pressure in the fractured zone. The latter coupling is satisfied by a leakage term between the pore pressure in the porous matrix and the fractured zone.

The capability of the model is illustrated in detail in [1]. The numerical results show that, using the proposed model, the very complicated physical and mechanical processes of the fracturing porous media can be simulated properly and efficiently.

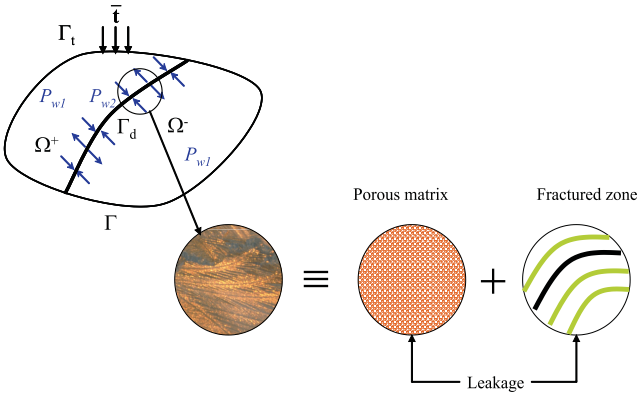

Figure 1: Fracturing mechanisms and modeling approach.

Governing Equations

Equilibrium equations: For a two-phase medium, i.e. solid and water, the static equilibrium equation in terms of total stress tensor, $\boldsymbol{\sigma}$, can be expressed as

$$\nabla \cdot \boldsymbol{\sigma} + \rho \mathbf{g} = 0 \tag{1}$$

in which **g** is the gravity force vector per unit mass, and $\rho$is the porous matrix density, defined as

$$\rho = (1 - n)\, \rho^s + n\, S_w\, \rho^w$$

Where $\rho^s$is the skeleton density, ρ^w is the water density, S_w is the degree of saturation and n is the porosity.

The total stress is defined as

$$\boldsymbol{\sigma} \;=\; \boldsymbol{\sigma}'' \;-\; \alpha\, S_w\, \mathbf{m}\, P^w \tag{2}$$

in which $\boldsymbol{\sigma}''$ is a general form of the effective stresses, P^w is the pore pressure in the porous matrix (in what follows this pore pressure will be presented as P^{w1}), $\mathbf{m}^T \;=\; [1,\, 1,\, 1,\, 0,\, 0,\, 0]^T$ and $\alpha \;=\; 1 \,-\, K_T/K_s$ is the Biot compressibility parameter with K_s the bulk modulus of the grain material and K_T the bulk modulus of the skeleton.

Continuity equations: Following the double porosity model, the continuity equation for water flow in a partially saturated porous matrix (subscript 1) and a fractured zone (subscript 2) can be expressed as follows.
Porous matrix:

$$\begin{aligned}
&\nabla^T \left\{ \frac{k^{r1}\,\mathbf{k}_1}{\mu_w\, B_{w1}} \left(-\nabla\, P^{w1} \;+\; \rho^w\, \mathbf{g}\right) \right\} \;+ \\
&\frac{\bar{\alpha}\, k^{r1}\, \mathbf{k}_1}{\mu_w\, B_{w1}} \left(P^{w1} \;-\; P^{w2}\right) \;+ \\
&\left(\frac{\alpha \;-\; n_1}{K_s\, B_{w1}}\, S_{w1}^2 \;+\; \frac{n_1\, S_{w1}}{K_w\, B_{w1}} \right) \frac{\partial\, P^{w1}}{\partial\, t} \;+ \\
&\left(\frac{\alpha \;-\; n_1}{K_s\, B_{w1}}\, P^{w1}\, S_{w1} \;+\; \frac{n_1}{B_{w1}} \right) \frac{\partial\, S_{w1}}{\partial\, t} \;+ \\
&\alpha\, S_{w1}\, \mathbf{m}^T\, \frac{\partial\, \boldsymbol{\varepsilon}}{\partial\, t} \;=\; 0
\end{aligned} \tag{3}$$

Fractured zone:

$$\begin{aligned}
&\nabla^T \left\{ \frac{-\,k^{r2}\, \mathbf{k}_2}{\mu_w\, B_{w2}}\, \nabla\, P^{w2} \right\} \;-\; \frac{\bar{\alpha}\, k^{r2}\, \mathbf{k}_2}{\mu_w\, B_{w2}} \left(P^{w1} \;-\; P^{w2}\right) \;+ \\
&\left(\frac{n_2\, S_{w2}}{K_w\, B_{w2}} \right) \frac{\partial\, P^{w2}}{\partial\, t} \;+\; \left(\frac{n_2}{B_{w2}} \right) \frac{\partial\, S_{w2}}{\partial\, t} \;=\; 0
\end{aligned} \tag{4}$$

Here, $\mathbf{k}_1$ and $\mathbf{k}_2$ are the permeability of the porous matrix and the fractured zone, respectively, k^{r1} and k^{r2} are dimensionless parameters varying from zero to one, representing the relative permeability of the porous matrix and the fractured zone, respectively, μ_w is the dynamic viscosity of water, K_w is the water bulk modulus, and ε is the strain vector. P^{w1} and P^{w2} are the excess pore pressures in the porous matrix and the fractured zone, respectively. The degree of saturation, S_w and the relative permeability, k^r, can be pore pressure dependent, such that $S_w \;=\; S_w\,(p^w)$, $k^{r1} \;=\; k^{r1}\,(p^w)$ and $k^{r2} \;=\; k^{r2}\,(p^w)$.

The second term in Eqs. 3 and 4 is the leakage term, which describes a leakage process between the porous matrix and the fractured zone. In this term, $\bar{\alpha}$ is a coefficient, which depends on the fracture width and geometry and describes the fluid flow due to the pressure gradient between the porous matrix and the fractured zone. B_w is the water formation volume factor defined as water and dissolved gas volume at reservoir conditions divided by water volume at standard conditions. This value can often be neglected, since it is always close to 1.

Casting Eqs. (1)–(4) in the partition of unity finite element method framework leads to

$$\begin{aligned}
\mathbf{K}_{11} &= \int_\Omega \mathbf{B}^T\, \mathbf{D}\, \mathbf{B}\, d\,\Omega \\
\mathbf{K}_{12} &= \int_{\Omega^+} \mathbf{B}^T\, \mathbf{D}\, \mathbf{B}\, d\,\Omega \\
\mathbf{K}_{13} &= \int_\Omega \mathbf{B}^T\, \alpha\, \mathbf{m}\, S_w\, \mathbf{N}_p\, d\,\Omega \\
\mathbf{K}_{21} &= \int_\Omega \mathbf{B}^T\, \mathbf{D}\, \mathbf{B}\, d\,\Omega \\
\mathbf{K}_{22} &= \int_{\Omega^+} \mathbf{B}^T\, \mathbf{D}\, \mathbf{B}\, d\,\Omega \;+\; \int_{\Gamma_d} \mathbf{N}_u^T\, \mathbf{T}\, \mathbf{N}_u\, d\,\Gamma \\
\mathbf{K}_{23} &= \int_{\Omega^+} \mathbf{B}^T\, \alpha\, \mathbf{m}\, S_w\, \mathbf{N}_p\, d\,\Omega^+ \\
\mathbf{K}_{33} &= \int_\Omega (\nabla\, \mathbf{N}_p)^T\, \frac{\mathbf{k}_1\, k_{rw1}}{\mu_{w1}\, B_{w1}}\, \nabla\, \mathbf{N}_p\, d\,\Omega \;+ \\
&+ \int_{\Omega d} \mathbf{N}_p^T\, \frac{\bar{\alpha}\, \mathbf{k}_1\, k^{r1}}{\mu_{w1}\, B_{w1}}\, \mathbf{N}_p\, d\,\Omega \\
\mathbf{K}_{34} &= -\int_{\Omega d} \mathbf{N}_p^T\, \frac{\bar{\alpha}\, \mathbf{k}_1\, k^{r1}}{\mu_{w1}\, B_{w1}}\, \mathbf{N}_p\, d\,\Omega \\
\mathbf{K}_{43} &= -\int_{\Omega d} \mathbf{N}_p^T\, \frac{\bar{\alpha}\, \mathbf{k}_2\, k^{r2}}{\mu_{w1} B_{w1}}\, \mathbf{N}_p\, d\,\Omega_d \\
\mathbf{K}_{44} &= \int_{\Omega d} (\nabla\, \mathbf{N}_p)^T\, \frac{\mathbf{k}_2\, k^{r2}}{\mu_{w2}\, B_{w2}}\, \nabla\, \mathbf{N}_p\, d\,\Omega_d \;+ \\
&+ \int_{\Omega d} \mathbf{N}_p^T\, \frac{\bar{\alpha}\, \mathbf{k}_2\, k^{r2}}{\mu_{w1} B_{w1}}\, \mathbf{N}_p\, d\,\Omega_d \\
\mathbf{C}_{31} &= \int_\Omega \mathbf{N}_p^T\, \frac{S_{w1}}{B_{w1}}\, \mathbf{m}^T\, \mathbf{B}\, d\,\Omega \\
\mathbf{C}_{32} &= \int_{\Omega^+} \mathbf{N}_p^T\, \frac{S_{w1}}{B_{w1}}\, \mathbf{m}^T\, \mathbf{B}\, d\,\Omega^+ \\
\mathbf{C}_{33} &= \int_\Omega \mathbf{N}_p^T\, \lambda_{w1}\, \mathbf{N}_p\, d\,\Omega \\
\mathbf{C}_{44} &= \int_{\Omega d} \mathbf{N}_p^T\, \lambda_{w2}\, \mathbf{N}_p\, d\,\Omega_d
\end{aligned}$$

where $\lambda_{w1} \;=\; \frac{\alpha - n_1}{K_s\, B_{w1}}\, S_{w1}^2 \;+\; \frac{n_1\, S_{w1}}{K_w\, B_{w1}}$ and $\lambda_{w2} \;=\; \frac{n_2\, S_{w2}}{K_w\, B_{w2}}$.

$$\begin{pmatrix} \mathbf{K}_{11} & \mathbf{K}_{12} & \mathbf{K}_{13} & 0 \\ \mathbf{K}_{21} & \mathbf{K}_{22} & \mathbf{K}_{23} & 0 \\ 0 & 0 & \mathbf{K}_{33} & \mathbf{K}_{34} \\ 0 & 0 & \mathbf{K}_{43} & \mathbf{K}_{44} \end{pmatrix} \begin{pmatrix} \bar{\mathbf{a}} \\ \bar{\mathbf{b}} \\ \bar{\mathbf{P}}^{w1} \\ \bar{\mathbf{P}}^{w2} \end{pmatrix} + \begin{pmatrix} 0 & 0 & 0 & 0 \\ 0 & 0 & 0 & 0 \\ \mathbf{C}_{31} & \mathbf{C}_{32} & \mathbf{C}_{33} & 0 \\ 0 & 0 & 0 & \mathbf{C}_{44} \end{pmatrix} \frac{\partial}{\partial\, t} \begin{pmatrix} \bar{\mathbf{a}} \\ \bar{\mathbf{b}} \\ \bar{\mathbf{P}}^{w1} \\ \bar{\mathbf{P}}^{w2} \end{pmatrix} = \begin{pmatrix} \mathbf{F}_1 \\ \mathbf{F}_2 \\ \mathbf{0} \\ \mathbf{F}_4 \end{pmatrix}$$

References

[1] R. Al-Khoury, L. J. Sluys (2007): A computational model for fracturing porous media. *International Journal for Numerical Methods in Engineering* 70, 423–444.

Effective Stress in Multi-phase Porous Media with Double Porosity

A. Koliji*, L. Laloui, L. Vulliet

Ecole Polytechnique Fédérale de Lausanne (EPFL)
Soil mechanics laboratory, CH-1015 Lausanne, Switzerland
azad.koliji@epfl.ch, lyesse.laloui@epfl.ch, laurent.vulliet@epfl.ch

Summary: Effective stress in multi-phase porous media with double porosity is evaluated. Derivation procedure using Biot's theory approach as well as the theory of multi-phase mixtures is briefly described. Comparative evaluation of the effective stress parameters in two methods and their quantification in terms of physically measurable parameters are presented.

Introduction

Mechanical constitutive study of multi-phase porous media requires, in the first step, determination of the effective stress in solid skeleton. Expressed as a function of the externally applied stresses and the internal fluid pressures, the effective stress converts a multiphase, multi-porous media into a mechanically equivalent, single-phase, single-stress state continuum. Indeed, the effective stress principle has been at the foundation of the advancements in the modern geomechanics. Over the years, significant contributions have been made to the understanding and evaluation of effective stress in single-phase [1, 2] and two-phase [3, 4] saturating fluids in single porosity media. Nevertheless, many natural geomaterials exhibit two scales of porosity: macro and micro porosity. Aggregated soils, fissured clays and fractured rocks are examples of geomaterials with double porosity. In addition to showing two scales of porosity, the void space in these materials is frequently filled with more than one fluid and requires multi-phase or unsaturated constitutive modelling.
A substantial amount of work has been undertaken in the area of double porous media following the concept of double porosity [5]. However, the use of the effective stress in unsaturated double porous media has rarely been investigated [6]. In this work, systematic approaches for the derivation of the effective stress equations for unsaturated double porous media are evaluated. The effective stress parameters of the system are identified and physically measurable entities are introduced for their determination.

Effective stress in double porous media

Significant differences of opinion exist in the literature concerning the definition of the effective stress in porous media with two or more fluid phases. Here, effective stress is simply defined as that emanating from the elastic (mechanical) straining of the solid skeleton,

$$\boldsymbol{\varepsilon}^e = \boldsymbol{C}^e \boldsymbol{\sigma}' \tag{1}$$

in which $\boldsymbol{\varepsilon}^e$ is the elastic strain of the solid skeleton, $\boldsymbol{C}^e$ is the drained compliance matrix, and $\boldsymbol{\sigma}'$ is the effective stress tensor. We place no further restriction on the definition of the effective stress. Any stress satisfying Equation (1) is regarded as the effective stress. The effective stress defined in this manner is applicable to elastic as well as elastic-plastic analysis of porous media. It is noted that even in the elastic-plastic region the effective stress is determined based on the elastic component of straining. In terms of pressure of fluid constituents, the effective stress in the total sense is expressed as,

$$\boldsymbol{\sigma}' = \boldsymbol{\sigma} - \sum_{\pi=1}^{N} \alpha_\pi \mathrm{p}_\pi \boldsymbol{I} \tag{2}$$

in which $\boldsymbol{\sigma}$ is the total stress tensor, α is the effective stress parameter, p is the fluid phase pressure, and $\pi = 1, \ldots N$ represents the number of fluid phases within the system. $\boldsymbol{I}$ is the second order identity tensor.

Parameters of effective stress

There are two main approaches to the mechanical study of continuum multiphase porous media. The first one, named Biot's approach, is a phenomenological approach associated with the early work of Biot [7] where the phases are not treated separately. The second family of approaches, including averaging and theory of multiphase mixtures, uses the concept of volume fraction in order to consider each single phase of the multiphase system. These methods are used here to determine the effective stress parameters in equation (2).

To derive the effective stress parameters for an unsaturated double porous medium using the first approach, an elementary volume of fissured porous medium subjected to an isotropic external mean stress is considered with internal fluid pressures p_w^1, p_a^1, p_w^2 and p_a^2 in the pore-water, pore-air, fissure-water and fissure-air, respectively (Fig. 1a). To obtain the volumetric strain of the element, the stresses acting on the element are decomposed into five loading cases. Case I corresponds to an external isotropic stress with internal fluid pressures maintained at a reference value of zero, Case II corresponds to an equal pore-water, pore-air, fissure-water, fissure-air and external isotropic pressure, Case III corresponds to an equal fissure-water, fissure-air and external isotropic pressure and zero pore-water and pore-air pressures, Case IV corresponds to an equal fissure-water, fissure-air, pore-air and external isotropic pressure and zero pore-water pressure, and finally Case V corresponds to an equal fissure-air, pore-air and external isotropic pressure and zero pore-water and fissure-water pressures. The crucial aspect in the above decomposition is that the compressibility coefficient, and thus the volumetric strain, of the various component cases can be readily measured

through a series of simple experiments. The volumetric elastic strain of the elementary volume, $\varepsilon_v^e = \text{tr}\,\boldsymbol{\varepsilon}$, can be obtained by summation of volumetric elastic strain in the five loading cases.

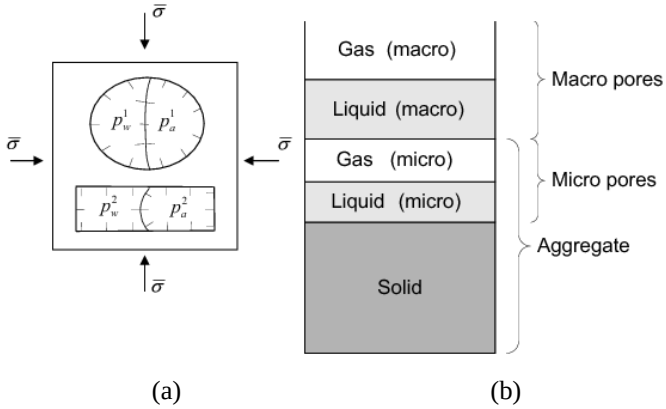

Figure 1: (a) Air and water pressure in unsaturated double porous media, and (b) schematic representation of phases in unsaturated double porous media (aggregated soil).

Volumetric elastic strain in each loading case is calculated by multiplying the applied stresses of each case by a relevant compressibility of the system. Starting from the smallest material scale, five compressibilities can be identified for quantification of the effective stress parameters. These are: compressibility of solid grains, compressibility of the porous blocks, overall compressibility coefficient of fissured porous medium, compressibility coefficient of porous blocks with respect to a change on pore matric suction, and compressibility coefficient of fissured porous medium with respect to a simultaneous change in matric suction of pores and fissures. The effective stress obtained hereby is compared to the one given through equation (1) and (2). This gives the effective stress as:

$$\boldsymbol{\sigma'} = \boldsymbol{\sigma} - (\alpha^1 p_a^1 + \alpha^2 p_a^2)\boldsymbol{I} + \alpha^1\chi^1 s^1 \boldsymbol{I} + \alpha^2\chi^2 s^2 \boldsymbol{I} \qquad (3)$$

Parameters of effective stress in this equation, α^m and χ^m ($m = 1, 2$) are defined in terms of measurable compressibilities of the system.

In the second approach, a multi-phase mixture is considered with immiscible fluids at two scales of porosity (Fig. 1b). Following the mixture theory analyses, the stress tensor is written for each constituent separately. The stress tensors of fluid constituents are given by their partial pressure. The stress tensor in solid constituents is written as:

$$\boldsymbol{\sigma}_s = -n_s\beta_s\boldsymbol{I} + \boldsymbol{\sigma'} \qquad (4)$$

In this equation n_s and β_s are volume fraction and configuration pressure of the solid constituent, respectively, and σ' is the extra part of solid stress tensor or effective stress. Configuration pressure of the solid constituent represents the forces exerted at the interface of solid particles with fluid. This force is exerted by the fluid constituents, namely liquid and gas in both mixtures and it should therefore be equal to a fluid pressure averaged over the mixtures. Herein, the total fluid pressure can be written in analogy to the Dalton's law [8]:

$$\beta_s = \frac{1}{n}\sum_{m=1,2}\sum_{\pi} n_\pi p_\pi \qquad (5)$$

where n_n and p_π are respectively volume fraction and intrinsic pressure of the fluid constituent π, and n denotes the total porosity. The first summation is made over the two levels of porosity. Therefore, equation (4) together with equation (5) determine the stress tensor in the solid constituent in terms of effective stress, fluid pressure and volume fraction of fluids. The total stress tensor of the mixture is obtained by summing the partial stress tensor of all constituents. The relation of effective stress with total stress is then established through the expression of total stress tensor. The total stress tensor obtained in this way can be rearranged as in equation (3). However, parameters of effective stress determined in this approach are given in terms of the volume fraction of constituents: α_1 and α_2 are respectively ratio of macro and micro porosity over the total porosity, and χ_1 and χ_2 are local values of degree of saturation at two levels of porosity.

Concluding remarks

The two approaches result in similar expression of effective stress in unsaturated double porous media. Parameters of effective stress are physically different in the two approaches. However, physical comparison of these parameters suggests the idea that compressibility of a double porous medium can be related to the two existing levels of porosity.

References

[1] K. Terzaghi (1936): *The shear resistance of unsaturated soil*. Proc. 1st Int. Conf. Soil Mech. and Foundation Engng., 1, 54–56.

[2] A. W. Skempton (1961): *Effective stress in soils, concrete and rocks.* Pore Pressure and Suction in Soil. Butterworths: London, 4–16.

[3] B. Loret and N. Khalili (2002): *An effective stress elasto-plastic model for unsaturated soils*. Mechanics of Materials, 44, 97–116.

[4] L. Laloui, G. Klubertanz and L. Vulliet (2003): *Solid-liquid-air coupling in multiphase porous media*. Int. J. Numer. Analy. Meth. Geomech, 27, 3, 183–206.

[5] G. I. Barenblatt, I. P. Zeltov and N. Kochina (1960): *Basic concepts in the theory of seepage of homogenous liquids in fissured rocks.* Piril. Mat. Mekh., 24, 852-864.

[6] N. Khalili, R. Witt, L. Laloui, L. Vulliet and A. Koliji (2005): *Effective stress in double porous media with two immiscible fluids.* Geophysical Research Letters, 32, L15309.

[7] M. A. Biot (1941): *General theory of three-dimensional consolidation.* J. Appl. Phys., 12, 155-164.

[8] W. Ehlers, T. Graf and S. Diebels (2003): *On the description of partially saturated soils by the theory of porous media*. PAMM, 2, 230–231.

A Constitutive Model for Partially Saturated Sands and Silts

R. Kohler, G. Hofstetter*

University of Innsbruck
Technikerstr. 13, A-6020 Innsbruck, Austria
Roman.Kohler@uibk.ac.at, Guenter.Hofstetter@uibk.ac.at

Summary: An elastic-plastic constitutive model for partially saturated sands and silts, formulated in terms of two stress state variables, is presented. It serves as a material model in the context of a three-phase formulation with the three phases consisting of the solid phase and the two fluid phases, water and air. The ability of the model to describe the material behavior of partially saturated sands and silts is demonstrated by the numerical simulation of an extensive series of suction controlled tests for a silty sand.

Introduction

Partially saturated soils are three-phase media consisting of a deformable soil skeleton and the two fluid phases, water and air. The difference between the pressures in the water and the air phase, called capillary pressure or matric suction, has a considerable impact on the mechanical behavior of partially saturated soils.

Several elastic-plastic material models for unsaturated soils have been proposed in the last fifteen years, see e.g. [1, 2, 3, 4, 5, 6, 7]. Most of these material models focus on clays and adopt some type of CAM CLAY formulation.

The present constitutive model has been developed for sands and silts in the context of the application of compressed air as a means for displacing the groundwater in soils. This method can be applied to soils with a certain range of permeability, i.e. to sands and silts. For these types of soils a cap model, in which a shear failure surface is available, seems to be an appropriate choice.

Stress state variables

It is generally accepted that two independent stress state variables are required for describing the material behavior of partially saturated soils. Possible definitions of stress state variables being work conjugate to the strains of the soil skeleton are derived, e.g. in [8, 9, 10]. From thermodynamic considerations it follows that a material model for the soil skeleton of a partially saturated soil can be formulated in terms of the effective stress tensor for partially saturated soils, $\boldsymbol{\sigma}'$, and matric suction p^c:

$$\boldsymbol{\sigma}' = \boldsymbol{\sigma} - [\, S^w\, p^w - (1 - S^w)\, p^a \,]\, \mathbf{I}\,, \quad p^c = p^a - p^w, \quad (1)$$

where $\boldsymbol{\sigma}$ denotes the total stress tensor, S^w represents the degree of water saturation and p^w and p^a are the pressures of the fluid phases water and air; $\mathbf{I}$ denotes the second order unit tensor. In the present model p^c plays the role of a stress-like plastic internal variable. The choice of $\boldsymbol{\sigma}'$ as stress state variable is advantageous, because for the limiting case of a water saturated soil, characterized by $S^w = 1$, $\boldsymbol{\sigma}'$ degenerates to the well known effective stress tensor for water saturated soils. Thus, material models for partially saturated soils, formulated in terms of $\boldsymbol{\sigma}'$ and p^c, allow a straightforward transition from partially saturated to saturated conditions.

Cap model for partially saturated soils

The constitutive relations are given as

$$\boldsymbol{\sigma}' = \mathbf{C} : (\boldsymbol{\varepsilon} - \boldsymbol{\varepsilon}^p) \quad (2)$$

with $\mathbf{C}$ denoting the elasticity tensor and $\boldsymbol{\varepsilon}$ and $\boldsymbol{\varepsilon}^p$ representing the total and the plastic strains, respectively.

The degree of water saturation S^w is expressed as a function of matric suction by the approximation proposed in [11]:

$$S^w = S_r^w + (S_s^w - S_r^w) \left[1 + \left(\frac{p^c}{p_b^c} \right)^n \right]^{-m}, \quad (3)$$

where S_s^w and S_r^w denote the maximum and residual degree of water saturation, respectively, and p_b^c is the air entry value; m and n are parameters to fit the empirical equation to experimental data.

The functional form of the shear failure surface is defined as

$$f_1\,(\boldsymbol{\sigma}', p^c) = L(\vartheta)\|\mathbf{s}\| - F_e\,(I_1') - F_s(p^c) \quad (4)$$

with

$$F_e\,(I_1') = \alpha + \theta I_1' \quad \text{and} \quad F_s(p^c) = k\, p^c\,, \quad (5)$$

where I_1' and $\|\mathbf{s}\|$ denote the first invariant and the norm of the deviatoric part of $\boldsymbol{\sigma}'$, $L(\vartheta)$ accounts for the dependence of the yield surface on the third invariant of the stress tensor according to [12] and α, θ and k are material parameters.

The functional form of the strain hardening cap is given as

$$f_2\,(\boldsymbol{\sigma}', \kappa(p^c), p^c) = \\ = F_c\,(\|\mathbf{s}\|, I_1', \vartheta, \kappa(p^c)) - F_e\,(\kappa(p^c)) - F_s(p^c) \quad (6)$$

with $\kappa(p^c) \le I_1' \le X\,(\kappa(p^c))$ and

$$F_c\,(\|\mathbf{s}\|, I_1', \vartheta, \kappa(p^c)) = \sqrt{L^2(\vartheta)\,\|\mathbf{s}\|^2 + \left(\frac{I_1' - \kappa(p^c)}{R} \right)^2}, \quad (7)$$

where R is a material parameter, defining the ratio of the major to the minor axis of the elliptic cap. The yield surface of the cap model is shown in Fig. 1.

The plastic potentials g_1 and g_2 for the non-associated flow rule are obtained from the yield functions (6) and (7) by setting $L(\vartheta) = 1$ and by replacing θ by ψ, which determines the amount of plastic dilation.

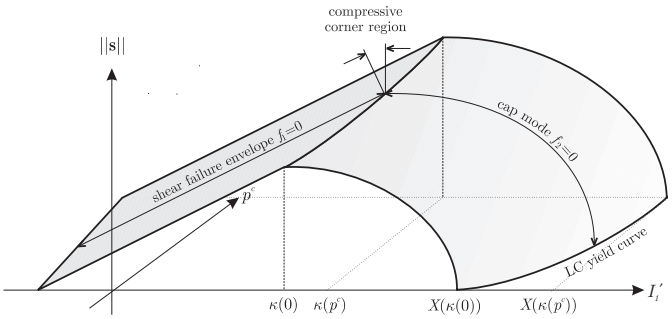

Figure 1: Yield surface of the cap model.

For the cap surface a logarithmic hardening law which relates the plastic volumetric strain rate $\dot{\varepsilon}_v^p$ to the hardening parameter $\kappa(p^c)$ is employed:

$$\dot{\varepsilon}_v^p = \lambda\left(p^c\right) \frac{\dot{X}\left(\kappa(p^c)\right)}{X\left(\kappa(p^c)\right)} \,. \tag{8}$$

$X(\kappa(p^c))$ denotes the apex of the elliptical cap, which is given as

$$X\left(\kappa(p^c)\right) = \kappa(p^c) + R\left[F_e\left(\kappa(p^c)\right) + F_s(p^c)\right] \tag{9}$$

and

$$\lambda\left(p^c\right) = \lambda(0)\left[(1-r)\exp(-\beta p^c) + r\right] \tag{10}$$

is a scaling factor for the plastic volumetric strain rate. It is assumed to decrease from $\lambda(0)$ at zero matric suction to $\lambda\left(p^c\right) \to r \cdot \lambda(0)$ for $p^c \to \infty$ with β and r ($r < 1$) as material parameters accounting for the increasing plastic stiffness under hydrostatic loading with matric suction [1].

(8) together with (10) is used to determine the intersection $X(\kappa(p^c))$ of the strain hardening cap with the $I_1' - p^c$ plane, which is essential for partially saturated soil models as it accounts for the increasing elastic domain with increasing matric suction in hydrostatic compression and for the irreversible decrease in volume on wetting at high values of effective stress. Hence, it is referred to as loading collapse (LC) yield curve (Fig. 1).

Numerical simulation of suction controlled tests

The material model is validated by the numerical simulation of an extensive series of suction controlled tests [13, 14], conducted on cubical specimens of a silty sand. The stress paths include (i) hydrostatic compression tests, consisting of loading and unloading at three different values of matric suction, (ii) triaxial compression tests and (iii) conventional triaxial compression tests, (iv) simple shear tests and (v) triaxial extension tests at different values of matric suction and different values of hydrostatic net stress. Comparisons of the numerical results with the experimental data can be found in [15].

References

[1] E. E. Alonso, A. Gens, A. Josa (1990): A constitutive model for partially saturated soils. *Géotechnique*, **40**, 405–430.

[2] S. J. Wheeler, V. Sivakumar (1995): An elasto-plastic critical state framework for unsaturated soils. *Géotechnique*, **45**, 35–53.

[3] G. Bolzon, B. A. Schrefler (1996): Elastoplastic soil constitutive laws generalized to partially saturated states. *Géotechnique*, **46**, 279–289.

[4] F. Geiser, L. Laloui, L. Vulliet (2000): Modelling the behaviour of unsaturated silt. *In:* A. Tarantino, C. Mancuso (eds.): *Experimental Evidence and Theoretical Approaches in Unsaturated Soils*, 155–176.

[5] D. Gallipoli, A. Gens, R. Sharma, J. Vaunat (2003): An elasto-plastic model for unsaturated soil incorporating the effects of suction and degree of saturation on mechanical behaviour. *Géotechnique*, **53**, 123–135.

[6] R. Tamagnini, (2004): An extended Cam-Clay model for unsaturated soils with hydraulic hysteresis. *Géotechnique*, **54**, 223–228.

[7] R. Santagiuliana, B. A. Schrefler (2006): Enhancing the Bolzon-Schrefler-Zienkiewicz Constitutive Model for Partially Saturated Soil. *Transport in Porous Media*, **65**, 1–30.

[8] G. T. Houlsby (1997): The work input to an unsaturated granular material. *Géotechnique*, **47**, 193–196.

[9] B. A. Schrefler (2002): Mechanics and thermodynamics of saturated/unsaturated porous materials and quantitative solutions. *Applied Mechanics Reviews*, **55**, 351–387.

[10] R. I. Borja (2004). Cam-clay plasticity, part V: A mathematical framework for three-phase deformation and strain localization analyses of partially saturated porous media. *Computer Methods in Applied Mechanics and Engineering*, **193**, 5301–5338.

[11] M. Th. Van Genuchten, D. R. Nielsen (1985): On describing and predicting the hydraulic properties of unsaturated soils. *Annales Geophysicae*, **3**, 615–628.

[12] R. de Borst, A. E. Groen (2000): Computational strategies for standard soil plasticity models. *In:* M. Zaman, J. Booker, G. Gioda (eds.): *Modeling in Geomechanics*. John Wiley & Sons, Ltd.

[13] E. J. Macari, L. R. Hoyos, P. Arduino (2003): Constitutive modeling of unsaturated soil behaviour under axisymmetric stress states using a stress/suction-controlled cubical test cell. *International Journal of Plasticity*, **19**, 1481–1515.

[14] E. J. Macari, L. R. Hoyos (2001): Mechanical behavior of an unsaturated soil under multi-axial stress states. *Geotechnical Testing Journal*, **24**, 14–22.

[15] R. Kohler (2006): Numerical modelling of partially saturated soils in the context of a three-phase-FE-formulation. University of Innsbruck, Austria. (PhD thesis)

Micromechanical Modelling of Unsaturated Granular Media

L. Scholtès*, B. Chareyre, F. Darve

Soils-Solids-Structures-Risks (3S-R) Laboratory
UMR-CNRS (INPG, UJF)
Domaine Universitaire, BP 5338 041 Grenoble cedex 9, France
luc.scholtes@hmg.inpg.fr, bruno.chareyre@hmg.inpg.fr, felix.darve@hmg.inpg.fr

Summary: A discrete three-dimensional (3-D) polydisperse model for unsaturated granular soils has been developped. The presence of interparticle water is taken into account by introducing specific interaction forces between grains that are quantified through capillary theory. In order to deal with water transfer mechanisms, the model is suction-controlled. At every suction level, capillary forces are directly linked to the water content and computed on the basis of the Laplace-Young equation.

Introduction

Macroscopic properties of granular materials such as soils depend on interparticle contact properties. For dry materials, interparticle forces are related to the applied external stresses as it has already been well investigated in the past, by means of the Discrete Element Method, [1]. In unsaturated soils new additional elements should be defined in order to understand properly their behaviour. When a soil is unsaturated, the presence of water between particles leads to the formation of liquid bridges (menisci), introducing new interparticle forces. Capillary theory, through the Laplace-Young equation, allows the force induced by a liquid bridge to be linked to the local geometry of the contact and to the volume of water found at a given contact. A multi-scale approach [2] seems, therefore, to provide a pertinent view of the phenomenon, and DEM appears completely suitable for analyzing capillary implications at the macroscopic level.

Along these lines, we present a 3-Dimensional micromechanical model for unsaturated granular media made of spherical particles. The model has the particularity of being suction controlled, which enables it to simulate some laboratory experiments on unsaturated soils. This model can be an acceptable approximation for granular soils such as medium to fine sands and silts, where suction mostly arises from capillarity (no osmotic suction like in clays).

Capillary phenomenon at the grain scale

Capillarity can be explained by superficial tension phenomena that develop at the interface between water and air, [3]. In a liquid bridge between two grains, superficial tension causes the liquid-gas interface to behave like a stretched membrane, which, as a consequence, maintains solid particles together. In addition, a discontinuity is created between the pressure of the gas and the liquid phases. Laplace theorem (1805), expresses this pressure difference $\Delta p = p_{gaz} - p_{liquide}$ as the product of the surface tension σ of the liquid and the mean curvature C of the liquid bridge surface:

$$\Delta\, p = \sigma\, C \tag{1}$$

Capillary phenomenon is considered at the scale of a "capillary doublet", made of a pair of grains, spherical in our case, linked by a liquid bridge whose shape and profile $y(x)$ are defined by the Laplace equation:

$$\Delta p\, y(x) + \sigma \frac{1 + y'^2(x) - y(x)y''(x)}{(1 + y'^2(x))^{3/2}} = 0 \tag{2}$$

A geometrical description of a capillary doublet is presented in Fig. 1. Grains of radii R_1 and R_2 are separated by a length called the intergranular distance D, angles δ_1 and δ_2 represent the wetting angles corresponding to the wetting part of the solid grain. The way the grains are wet by the liquid is obvious by the contact angle marks θ. The x-axis is defined as the line passing through the centers of the two spheres and constitutes a symmetric volume whose shape is described by the profile. The gorge radius y_0 is defined like the smaller value of this profile.

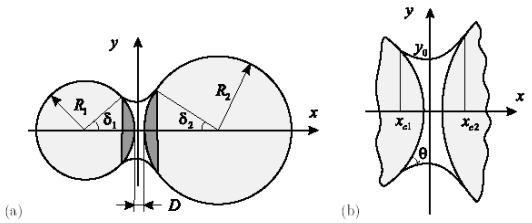

Figure 1: Capillary doublet (polydisperse case): (a) global view, (b) geometry of the liquid bridge.

Through these considerations, interaction geometry (water volume V, intergranular distance) and capillary interparticle force are given by:

$$V = \pi \int_{x_{c1}}^{x_{c2}} y^2(x) \cdot dx - V_1 - V_2 \tag{3}$$

where

$$V_i = \frac{1}{3}\pi R_i^3\, (1 - \cos\delta_i)^2\, (2 + \cos\delta_i) \tag{4}$$

$$D = x_{c2} - R_2(1 - \cos\delta_2) - x_{c1} - R_1(1 - \cos\delta_1) \tag{5}$$

$$F_{cap} = 2\pi y_o \sigma + \pi y_o^2 \Delta p \tag{6}$$

Obviously in a granular assembly, particularly one with a high water content, several particles can be included in the meniscus and capillary interactions are then more complex than this doublet configuration. The model is therefore not valid for high degree of saturation.

Hydro-micromechanical model

A 3D code called YADE (Yet Another Dynamic Engine) has been developed based upon the work of Donz and Magnier, [4]. Each particle of the material is a sphere that is identified independently by its own mass, m, and radius, R. Contact in-

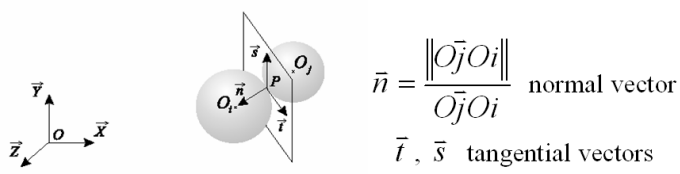

Figure 2: Interaction geometry.

teractions are described by a linear elastic law, which defines the normal force F_n in relation to the intergranular distance (see Fig. 2 for the definition of the local coordinate system):

$$F_n = \begin{cases} -K_n D & \text{if} \quad D \leq 0 \\ 0 & \text{if} \quad D > 0 \end{cases} \tag{7}$$

where K_n is the contact stiffness.

Friction between grains produces a shear force F_t in the tangential plane of contact, opposite to the incremental tangential displacement dU_t, and obeying the Coulomb friction law:

$$dF_t = -K_t\, dU_t \tag{8}$$

$$F_t \max = -\mu\, F_n \tag{9}$$

where K_t is the shear stiffness, and μ the friction coefficient.

To account for capillarity, a numerical resolution of the Laplace equation has been developed in order to link capillary pressure (or suction) to capillary forces and water volume. The result is a suction-controlled model where, at every time-step during the simulation, capillary forces and water volumes are computed based upon the microstructure and the imposed suction level, as described by equations (1)–(3).

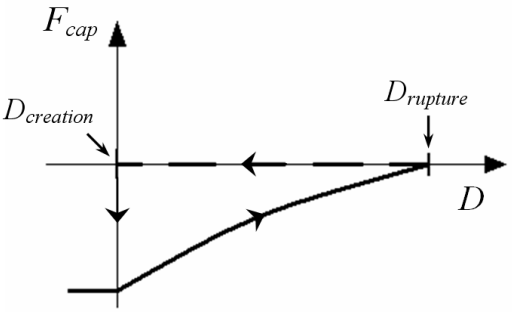

Figure 3: Evolution of the capillary force F_{cap} with D.

A schematic diagram of the capillary law implemented is shown in Fig. 3. The choice was made to define the appearance of a meniscus when grains are strictly in contact (no roughness effects). Furthermore, it is to be noted that the formulation introduced intrinsically defines the distance from which the meniscus breaks off as depending on the given pressure and interacting geometry.

Perspectives

The current aim of this work is to study the results of this capillary model when numerical samples are subjected to loading programs such as triaxial and suction variation tests. Fig. 4 shows the characteristic curve obtained for a sample made up of 10 000 grains, with radii ranging from 0.1 mm to 0.6 mm, submitted to a wetting-drying path. It is to be noted that results are quantitatively comparable to experimental curves, [7]. Currently, the model enables suction to be directly linked

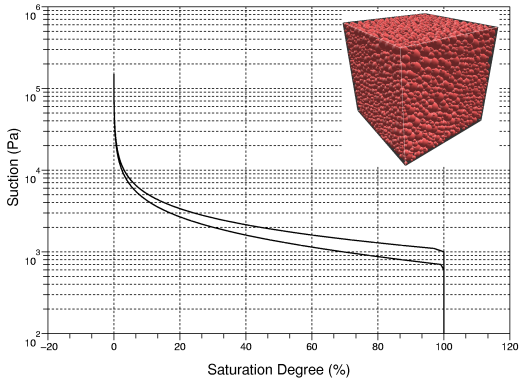

Figure 4: Characteristic suction-saturation degree curve for a 10,000 grain assembly.

to capillary forces and water content inside the material at the micro-level. Development of homogenization techniques, [2, 6, 7], will allow insights to be obtained regarding the capillary induced stresses and more generally unsaturated granular media behaviour.

References

[1] P. A. Cundall, O. D. L. Strack (1979): A discrete numerical model for granular assemblies. *Géotechnique*, **29**, 47–65.

[2] F. Nicot, F. Darve (2005): A multiscale approach to granular materials. *Mechanics of Materials*, **37**, 980–1006.

[3] P. G. de Gennes, F. Brochard-Wyart, D. Quéré (2002): *Gouttes, bulles, perles et ondes*. Collection Echelles, Belin, Paris.

[4] F. V. Donzé, S. A. Magnier (1997): Spherical Discrete Element Code. *Discrete element project report 2*, Laboratory GEOTOP, Université du Québec, Montréal.

[5] B. Cambou, M. Jean (2001): *Micromécanique des milieux granulaires*. Hermes Sciences.

[6] F. Nicot, F. Darve (2006): On the elastic and plastic strain decomposition in granular materials. *Granular Matter*, **8**, 221–237.

[7] S. L. Houston (1995): Foundations and pavements on unsaturated soils. *Proceedings of the First International Conference on Unsaturated Soils UNSAT'95*, 1421–1439. E. E. Alonso & P. Delage eds, Balkema, Paris.

Chemo-Physical Coupling of Porous Medium

W. Pao[1*], **R. W. Lewis**[2]

[1]School of MACE, The University of Manchester
PO Box 88, Sackville Street, Manchester M60 1QD, UK
William.Pao@manchester.ac.uk

[2]School of Civil and Computational Engineering, Swansea University
Singleton Park, Swansea SA2 8PP, UK
Roland.W.Lewis@Swansea.ac.uk

Summary: The objective is this paper is to report a coupled chemo-physical formulation within the framework of Biot´s poroelasticity to describe the phenomenon of hydration swelling and chemo-osmotic effects. The osmotic coefficient is responsible for the gradient of the chemical potential, and is inversely proportional to the dissipation of the pore pressure and directly proportional to the swelling. The Fickian diffusion coefficient controls the rate at which the solute diffuses through the sample, and in doing so, affects the rate at which the pore pressure and displacement evolution, indirectly.

Introduction

An oil reservoir is formed over millions of years. First, organic material on the bottom of a lake or the sea is buried under miles of sand and mud. Whilst this is happening, the heat and pressure from the earth "cooks" the organic material, forming shale. The oil then migrates from the shale where it is formed, to a more porous rock in which it is then stored, and it is finally trapped in the reservoir by an impermeable rock. Therefore, where there is an oil reservoir, there will be shale.

Shale, whose original constituents are mud, clay and organic material such as algae, can vary from a fissile, fine grained sedimentary rock, to a highly cemented shaley siltstone. It is a very low permeability rock, prone to fragmentation due to brittleness, and fracture due to its low tensile strength. It is also a water absorbing rock, which swells as it absorbs the water – this is known as hydration swelling.

Drilling can be carried out by either percussive or rotary action breaking up the ground at the drill tip, and the excavated material is then removed by circulating a pressurised mud solution, which also serves to cool the bit, lubricate the drill pipe, keep corrosion in check, and prevent caving. Borehole instability is extremely costly - both in time and labour, as drilling rig can be lost, the borehole may need to be re-drilled, or sidetracked, and the logging may be lost. The mud solution is one of the most important factors in the success of a well, helping the borehole to remain stable during drilling.

The vast majority of drilling muds are water-based [1], and consist primarily of three parts: water, the colloidal fraction, and the inert fraction. The colloidal fraction is the part of the mud which is reactive, giving the mud viscosity, and the inert fraction is the part which gives the mud weight. Drilling through shale poses particular problems of instability due to the interaction between the shale and the drilling fluid. Shale is a low permeability rock, in which hydraulic and chemical gradients induce changes in pore pressure, due to hydraulic and ionic diffusion and osmotic effects [2]. The drilling fluid must enable the confining stresses in the rock around the wellbore to remain high enough for the well to support itself, by controlling the pore pressure through utilising this osmotic membrane behaviour.

The objective is this paper is to report a coupled chemo-physical formulation within the framework of Biot's poroelasticity to describe the phenomenon of hydration swelling and chemo-osmotic effects.

Formulation

The mechanical behaviour of the porous medium is given in the incremental form by [3]

$$d\boldsymbol{\sigma} = d\boldsymbol{\sigma}' - \boldsymbol{\alpha}\mathbf{m}dp + \omega\mathbf{m}dC. \tag{1}$$

Using the principle of virtual work, the coupled equilibrium equation can be written as

$$\begin{aligned}&\int_{\Omega} \delta\boldsymbol{\varepsilon}^T \left[\mathbf{D}_T\left(\boldsymbol{\varepsilon} - \boldsymbol{\varepsilon}_o\right) + \boldsymbol{\sigma}_o - \boldsymbol{\alpha}\mathbf{m}p + \omega\mathbf{m}C\right] d\Omega \\ &- \int_{\Omega} \delta\mathbf{u}^T\mathbf{b}d\Omega - \int_{\Gamma} \delta\mathbf{u}^T\boldsymbol{\tau}d\Gamma = 0\end{aligned} \tag{2}$$

where $\boldsymbol{\sigma}$, $\boldsymbol{\sigma}'$, p, $\boldsymbol{\alpha}$, ω, C are total stress, effective stress, pore pressure, Biot coefficient, swelling coefficient, and solute concentration, respectively, and $\mathbf{m} = \left[\begin{array}{ccc} 1 & 1 & 0 \end{array}\right]^T$.

To take into account the presence of osmotic pressure due to solute, the Darcy's mass flux $\mathbf{M}$ is modified according to

$$\mathbf{M} = -\frac{\mathbf{k}}{\mu}\left(\nabla p - \Phi\Re\nabla C\right) \tag{3}$$

where k, μ, Φ are intrinsic permeability, dynamic viscosity, and the osmotic coefficient, respectively. The reflection coefficient accounts for the perfect and imperfect membrane effect such that $0 \leq \Re \leq 1$. We can now introduce the continuity equation in the form

$$\nabla \cdot \left(\rho\mathbf{M} + \rho\phi\mathbf{v}_s\right) + \frac{\partial}{\partial t}\left(\rho\phi\right) = 0 \tag{4}$$

while the rate of change of the porosity can be written as

$$\begin{aligned} d\phi \;\; = \;\; & \left(1-\phi\right)\mathbf{m}^T d\boldsymbol{\varepsilon} \\ & -\frac{\mathbf{m}^T}{3K_s}(d\boldsymbol{\sigma}' - \boldsymbol{\alpha}\mathbf{m}dp + \omega\mathbf{m}dC)dp + \frac{1-\phi}{K_s}dp \end{aligned} \tag{5}$$

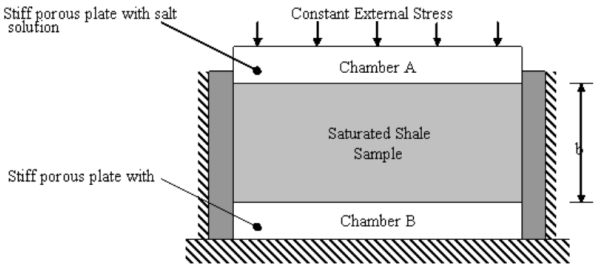

Figure 1: Schematic view of numerical experiment [4].

The transport of solute in porous medium can be described by the Fickian flux, taking into account the membrane effects in the solute transport [4]:

$$-\nabla\cdot(L\nabla p)-\nabla\cdot(\mathbf{D}\nabla\mathbf{c})+\phi\frac{\partial c}{\partial t}=0 \qquad (6)$$

Numerical example

The numerical experiment performed has the setup shown in Fig. 1. The thickness of the sample is 15 mm, with width 30 mm. The sample is encased in between two stiff porous plate, maintained at a constant pressure, p_o. The upper plate is subjected to a constant stress of $\boldsymbol{\sigma_c}$ and at time $t = 0$, a salt solution with concentration C_b is introduced. Table 1 shows the material properties used for the calculation.

Table 1: Material properties of shale sample.

Material property	value
Young's modulus E [MPa]	2000
Poisson's ratio ν	0.3
Hydraulic conductivity k/μ [m/s]	5×10^{-3}
Biot's constant α	1
Porosity ϕ	0.4
Fickian coefficient D [$\mathrm{m^2 s^{-1}}$]	1×10^{-4}
Osmotic coefficient Φ [$\mathrm{MPa\,m^3\,mol^{-1}}$]	-3.33×10^{-5}
Swelling ω [$\mathrm{MPa\,m^3\,mol^{-1}}$]	0

The main objective of this exercise is to investigate the membrane and the associated osmotic-enhanced effect on the swelling and hydraulic properties of the coupled formulation. Fig. 2 shows that an increase in Φ increases the swelling of the sample as expected and thus prolonged the consolidation process. This behaviour can be rightly understood by referring to equation (3), where the osmosis effect is interfering with the Darcy's flux causing a delay in the pressure dissipation. Notice that all this happened when the swelling coefficient is assigned a zero value. Fig. 3 illustrates a very rapid pore pressure dissipation, in proportional to the value of the osmotic coefficient, in the bottom porous plate even though the pressure has been maintained in the upper chamber. The pore pressures increases slowly after a while when there is sufficient solute concentration in the bottom chamber to establish a concentration gradient, thus equalising the pressure differential and restoring the pore pressure in the Chamber B to its original value. Fig. 4 shows the diffusion of the salt solution throughout the sample and since its variation remains the same for different osmotic coefficient, only one set of curve is shown here.

Conclusions

The osmotic coefficient is responsible for the gradient of the chemical potential, and thereby affects the dissipation of the pore pressure and swelling. The Fickian diffusion coefficient controls the rate at which the solute diffuses through the sample, and in doing so, affects the rate at which the initial pore pressure and displacement change, indirectly. The coupled model developed herein is in fact a weakly coupled model. This is because the rate of change of porosity in the solute equation is ignored and porosity change is assumed to be constant. Future research will relax this restriction and to investigate the effect of permeability change as the porous solid deforms.

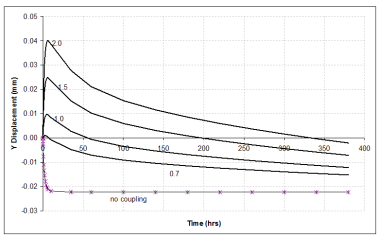

Figure 2: Effect of osmotic coefficient on displacement.

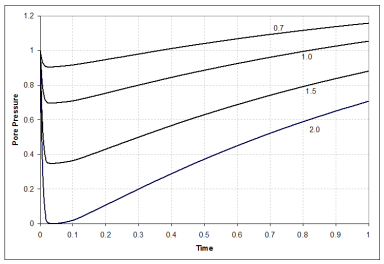

Figure 3: Effect of osmotic coefficient on normalised pore pressure in porous plate.

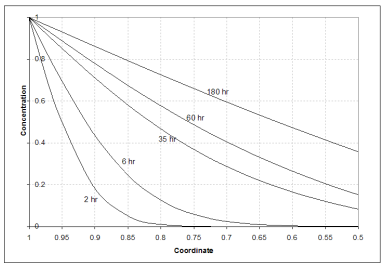

Figure 4: Diffusion of solute through sample.

References

[1] J. R. Mills (1979): Driller training and reference manual, *National Water Well Association of Australia*, St. Lyes, NSW, Australia

[2] E. S. Muniz et al. (2005): Rock-drilling fluid interaction studies on the diffusion cell. SPE 94768-MS.

[3] R. W. Lewis and B. A. Schrefler (1987): *The Finite Element Method in the Deformation and Consolidation of Porous Media*, 1st Ed., John Wiley & Son, 1987.

[4] W. K. Heidug, S. W. Wong (1996): Hydration swelling of water-absorbing rocks: a constitutive model. *Int. Jour. Numer. Analy. Meth. Geomech.*, **20**: 403–430.

An Enhanced Assumed Strain Four Node Quadrilateral Element for Coupled Problems in Soil Dynamics

P. Mira[1*], **M. Pastor**[2]

[1]Centro de Estudios y Experimentación de Obras Públicas
Alfonso XII no 3, 28014 Madrid, Spain
pmira@cedex.es

[2]E.T.S. de Ingenieros de Caminos, Canales y Puertos, Universidad Politécnica de Madrid
Avda Profesor Aranguren s/n, 28040 Madrid, Spain
mpastor@cedex.es

Summary: An Enhanced Assumed Strain four node quadrilateral element for coupled problems (displacement-pore pressure) in soil dynamics is presented and tested for numerical stability in the undrained incompressible limit, following a technique based on the well known inf-sup condition.

Introduction

It is a very frequent engineering situation to find soils saturated with a fluid, most typically water. It is important to include in the governing equations the effect of the pore fluid and its interaction with the soil skeleton.

It is precisely that what the well known Biot equations do, either in their original version [3, 4] or in the more developed ones due to Zienkiewicz and coworkers at Swansea University [9].

Unless certain requirements are met numerical models based on coupled formulations become ill conditioned when the water compressibility and the soil permeability are small, causing stability problems. A necessary condition for stability is given by the so called patch test for mixed formulations due to Zienkiewicz, Qu, Taylor and Nakazawa [12]. A mathematically more involved treatment of the problem is due to Babuska [2] and Brezzi [5] through the so called inf-sup condition. Its satisfaction is a sufficient condition for stability. The numerical evaluation of the inf-sup condition gives rise to the inf-sup test [7].

The extension of the standard four node displacement formulation to a coupled formulation by using a standard four node interpolation for both displacements and pressures produces an element type that satisfies neither the patch test for mixed formulations nor the inf-sup test. This problem is usually overcome by using a higher interpolation order in displacements than in pressures. However, it is possible through special techniques [6, 9, 13] to produce stable formulations with equal order interpolation in displacements and pressures. The goal of equal order interpolation is to provide a higher degree of approximation for pressures and to produce simpler and faster codes. One of these formulations [8] is based on the Simo-Rifai enhanced strain element [10, 1].

The objective of the present work is to extend this formulation to the range of soil dynamics, that is to include inertia effects of the soil-fluid mixture.

Governing equations

For the present work the solid skeleton-pore fluid interaction problem shall be modeled following Zienkiewicz and Shiomi [11]. The governing equations include a linear momentum balance equation for the mixture in the first place and secondly a mass balance equation for the fluid phase:

$$\mathbf{S}(\sigma' - \mathbf{m}p) + \rho_m \mathbf{b} - \rho_m \ddot{\mathbf{u}} = \mathbf{0} \tag{1}$$

$$\mathbf{m}^T \mathbf{S}\dot{\mathbf{u}} - \nabla^T \mathbf{k} \nabla p + \frac{\dot{p}}{Q^*} + \nabla^T \mathbf{k} \rho_w \mathbf{b} = \mathbf{0} \tag{2}$$

where $\mathbf{S}^T = \begin{bmatrix} \frac{\partial}{\partial x} & 0 & \frac{\partial}{\partial y} \\ 0 & \frac{\partial}{\partial y} & \frac{\partial}{\partial x} \end{bmatrix}$, $\mathbf{m}^t$=(1,1,0), $\mathbf{b}$= body forces, ρ_m= density of the mixture, $\mathbf{k}$= permeability matrix, ρ_w= water density, $\frac{1}{Q^*} = \frac{n}{K_w} + \frac{1-n}{K_s}$, n=porosity, K_w =water bulk modulus, K_s= solid grain bulk modulus.

Numerical formulation

The proposed formulation is based on the assumption that the strain is the sum of the standard component and an additional strain field $\tilde{\varepsilon}$ which is not subjected to interelement continuity as explained in [6]:

$$\boldsymbol{\varepsilon} = \nabla^s \mathbf{u} + \tilde{\boldsymbol{\varepsilon}} \tag{3}$$

The problem is initially formulated with standard the weighted residual technique and four fields $(\boldsymbol{u}, \boldsymbol{\sigma}, \tilde{\varepsilon}, p)$. In a second step the stress field $\boldsymbol{\sigma}$ is eliminated, and the remaining three fields $(\boldsymbol{u}, \tilde{\boldsymbol{\varepsilon}}, p)$ are approximated with the corresponding interpolation functions:

$$\mathbf{u} = \mathbf{N}_u \bar{\mathbf{u}} \tag{4}$$

$$\tilde{\boldsymbol{\varepsilon}} = \mathbf{G}\bar{\alpha} \tag{5}$$

$$p = \mathbf{N}_p \bar{\mathbf{p}} \tag{6}$$

where $\mathbf{N}_u$ and $\mathbf{N}_p$ are based on standard four node interpolation functions and $\mathbf{G}$ is the interpolation matrix for field $\tilde{\boldsymbol{\varepsilon}}$, based on seven internal modes [1]. Finally the following equations are obtained:

$$\mathbf{M}\ddot{\bar{\mathbf{u}}}_{n+1} + \int_\Omega \mathbf{B}^T \boldsymbol{\sigma}' d\Omega - \mathbf{Q}_u \bar{\mathbf{p}}_{n+1} = \mathbf{f}^u_{n+1} \tag{7}$$

$$\int_\Omega \mathbf{G}^T \boldsymbol{\sigma}' d\Omega - \mathbf{Q}_\alpha \bar{\mathbf{p}}_{n+1} = \mathbf{0} \quad (8)$$

$$\mathbf{Q}_u \ddot{\mathbf{u}}_{n+1} + \mathbf{Q}_u \ddot{\bar{\alpha}}_{n+1} + \mathbf{H}\bar{\mathbf{p}}_{n+1} + \mathbf{C}\dot{\bar{\mathbf{p}}}_{n+1} = \mathbf{f}^p_{n+1} \quad (9)$$

where

$\mathbf{M}$= mass matrix= $\int_\Omega \mathbf{N}_u^T \rho_m \mathbf{N}_u d\Omega$

$\mathbf{Q}_u$= coupling matrix displacement-pressures= $\int_\Omega \boldsymbol{B}^T \mathbf{N}_p d\Omega$

$\mathbf{Q}_\alpha$= coupling matrix enhanced strain-pressures= $\int_\Omega \boldsymbol{G}^T \mathbf{N}_p d\Omega$

$\mathbf{H}$= permeability matrix= $\int_\Omega (\nabla \mathbf{N}_p)^T k \nabla \mathbf{N}_p d\Omega$

$\mathbf{C}$= compressibility matrix = $\int_\Omega \mathbf{N}_p^T \frac{1}{Q^*} \mathbf{N}_p d\Omega$

$\mathbf{f}^u_{n+1}$ = loading vector associated to $\mathbf{u}$ field

$\mathbf{f}^p_{n+1}$ = loading vector associated to p field

Approximation in time is done with the same Generalized Newmark scheme GN22 for fields $\mathbf{u}$ and α**,** and with a GN11 scheme for pore pressure p. The different approximations are expressed in the following equations:

$$\ddot{\bar{\mathbf{u}}}_{n+1} = \ddot{\bar{\mathbf{u}}}_n + \Delta\ddot{\bar{\mathbf{u}}}_n \quad (10)$$

$$\dot{\bar{\mathbf{u}}}_{n+1} = \dot{\bar{\mathbf{u}}}_n + \Delta t \ddot{\bar{\mathbf{u}}}_n + \beta_1 \Delta t \Delta\ddot{\bar{\mathbf{u}}}_n \quad (11)$$

$$\bar{\mathbf{u}}_{n+1} = \bar{\mathbf{u}}_n + \Delta t \dot{\bar{\mathbf{u}}}_n + \frac{1}{2}\Delta t^2 \ddot{\bar{\mathbf{u}}}_n + \frac{1}{2}\beta_2 \Delta t^2 \Delta\ddot{\bar{\mathbf{u}}}_n \quad (12)$$

$$\dot{\bar{\mathbf{p}}}_{n+1} = \dot{\bar{\mathbf{p}}}_n + \Delta\dot{\bar{\mathbf{p}}}_n \quad (13)$$

$$\bar{\mathbf{p}}_{n+1} = \bar{\mathbf{p}}_n + \Delta t \dot{\bar{\mathbf{p}}}_n + \theta \Delta t \Delta\dot{\bar{\mathbf{p}}}_n \quad (14)$$

Substituting these expansions in equations (7)–(9) the following set of non linear equations is obtained:

$$\mathbf{G}^u_{n+1} = \mathbf{M}\Delta\ddot{\bar{\mathbf{u}}}_n + \int_\Omega \mathbf{B}^T \boldsymbol{\sigma}' d\Omega - \mathbf{Q}_u \bar{\mathbf{p}}_{n+1} - \mathbf{F}^u_{n+1} = \mathbf{0} \quad (15)$$

$$\mathbf{G}^\alpha_{n+1} = \int_\Omega \mathbf{G}^T \boldsymbol{\sigma}' d\Omega - \mathbf{Q}_\alpha \bar{\mathbf{p}}_{n+1} - \mathbf{F}^\alpha_{n+1} = \mathbf{0} \quad (16)$$

$$\mathbf{G}^p_{n+1} = \mathbf{Q}_u \beta_1 \Delta t \Delta\ddot{\bar{\mathbf{u}}}_n + \mathbf{Q}_u \beta_1 \Delta t \Delta\ddot{\bar{\alpha}}_n + \mathbf{H}\theta\Delta t \Delta\dot{\bar{\mathbf{p}}}_n + \mathbf{C}\Delta\dot{\bar{\mathbf{p}}}_{n+1} - \mathbf{F}^p_{n+1} = \mathbf{0} \quad (17)$$

These equations can be expressed in a more compact fashion through the following equation:

$$\mathbf{G}(\mathbf{x}) = \mathbf{0} \quad (18)$$

where

$$\mathbf{x} = \begin{Bmatrix} \Delta\ddot{\bar{\mathbf{u}}}_n \\ \Delta\ddot{\bar{\alpha}}_n \\ \Delta\dot{\bar{\mathbf{p}}}_n \end{Bmatrix}, \quad \mathbf{G} = \begin{Bmatrix} \mathbf{G}^u_{n+1} \\ \mathbf{G}^\alpha_{n+1} \\ \mathbf{G}^p_{n+1} \end{Bmatrix} \quad (19)$$

and solved through a standard Newton-Raphson algorithm expressed in the following equation:

$$\mathbf{G}(\mathbf{x}_i) + \frac{\partial \mathbf{G}}{\partial \mathbf{x}_{\mathbf{x}=\mathbf{x}_i}} d\mathbf{x}_i = \mathbf{0} \quad (20)$$

Following the standard Enhanced Assumed Strain technique [6], the additional strain field is eliminated through static condensation, resulting in a four node displacement-pore pressure formulation.

The element is tested for stability in the undrained incompressible limit following a technique based in the inf-sup condition [2, 5, 7, 8]. Numerical examples to illustrate the new formulation are included.

References

[1] U. Andelfinger and E. Ramm (1993): EAS-elements for two-dimensional, three dimensional, plate and shell structures and their equivalence to HR-elements, *International Journal for Numerical Methods in Engineering*, 36, 1311–1337.

[2] I. Babuska (1973): The finite element method with Lagrange multipiers, *Num. Math.*, 20, 179–192.

[3] M. A. Biot (1941): General theory of three-dimensional consolidation, *Journal of Applied Physics*, 12, 155–164.

[4] M. A. Biot (1955): Theory of elasticity and consolidation for a porous anisotropic solid, *Journal of Applied Physics*, 26, 182-185.

[5] F. Brezzi (1974): On the existence, uniqueness and approximation of saddle point problems arising from Lagrangian multipliers, *RAIRO*, 8, 129–151.

[6] F. Brezzi and J. Pitkaranta (1984): "On the stabilization of finite element approximations of the Stokes problem", *Efficient solutions of elliptic problems, Notes on Numerical Fluid Mechanics*, 10, W. Hackbusch (Eds.), 11–19, Vieweg, Wiesbaden.

[7] D.Chapelle, K. J. Bathe (1993): The inf-sup test, *Computers and Structures* 47, 537–545.

[8] P. Mira, M. Pastor, T. Li, X. Liu (2003): A new enhanced strain element with equal order interpolation for soil consolidation problems, *Comp.Methods Appl. Mech.Engrg.* 192, 4257-4277.

[9] M. Pastor, M. Quecedo and O. C. Zienkiewicz (1996): A mixed displacement-pressure formulation for numerical analysis of plastic failure, *Comp. and Structures*.

[10] J. C. Simo and M. S. Rifai (1990): A Class of Mixed Assumed Strain Methods and the Method of Incompatible Modes, *International Journal for Numerical Methods in Engineering*, 29, 1595–1638.

[11] O. C. Zienkiewicz, T. Shiomi (1984): Dynamic behaviour of saturated porous media: The generalised Biot formulation and its numerical solution, *Int. J. Num. Anal. Meth. Geomech.*, 8, 71–96.

[12] O. C. Zienkiewicz, S. Qu, R. L. Taylor and S. Nakazawa (1986): The patch test for mixed formulations, *Int. J. Numer. Meth. Eng.*, 23, 1873–1883.

[13] O. C. Zienkiewicz, M. Huang, J. Wu and S. Wu (1993): A New Algorithm for the Coupled Soil-Pore Fluid Problem, *Shock and Vibration*, 1, 3–14.

Experimental and Numerical Investigation on a Cellular Rubber

M. Johlitz*, S. Diebels, H. Steeb

Saarland University, Chair of Applied Mechanics
D-66 123 Saarbrücken, Germany
{m.johlitz, s.diebels, h.steeb}@mx.uni-saarland.de

Summary: In this contribution we experimentally investigate a compressible cellular rubber. In an appropriate model we apply the theory of porous media to describe the viscoelastic properties. The model parameters are identified by an algorithm based on evolution strategies.

Introduction

Cellular rubber is a material which is produced since a lot of decades. In particular, its variable application area is very important for the industry. In the majority of cases, cellular rubber is found in the automotive industry and its subcontractors, for example in every kind of gaskets or tubes which are used e. g. for doors and windscreens. Therefore, it becomes necessary to understand the material behaviour of cellular rubber and to develop appropriate models.

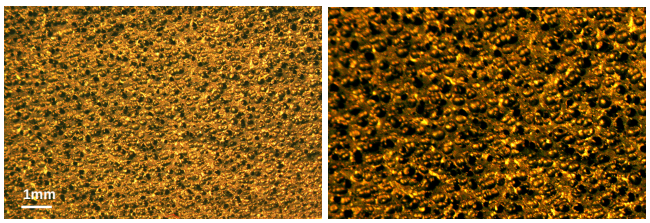

Figure 1: Pore structure of the investigated cellular rubber on different length scales (right: magnification of 2.5).

During the last decades a lot of research work has been performed on the manufacturing process of cellular rubber itself in order to establish a reproducible material with a homogeneous pore distribution and homogeneous properties, cf. Haberstroh [7, 8, 9]. For this purpose the interaction of the foaming process and the vulcanisation has to be understood. In current contributions the mechanical behaviour of cellular rubber is usually modelled on the basis of material laws developed for rubber, i. e. on the basis of an incompressible material law extended by a volumetrical modification. This kind of modelling becomes insufficient for large volumetrical strains, i. e. close to the point of compaction and, therefore, may cause unphysical results.

Experiments

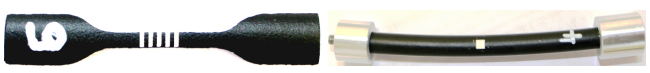

Figure 2: Dogbone specimen (left) and cylindrical tension specimen (right).

In the present contribution, we investigate the mechanical properties of an EPDM[2] cellular rubber. Based on some elementary mechanical tests the material behaviour is classified to be viscoelastic with a fastly decaying overstress as can be seen in Fig. 3. On the one hand, the material is found to be highly compressible according to its cellular structure. On the other hand, the material behaves nearly incompressible if the point of compaction is reached, i. e. if all pores are closed by a volumetric deformation.

On the experimental side we accomplish uniaxial tension tests on dogbone specimens and on cylindrical specimens (Fig. 2).

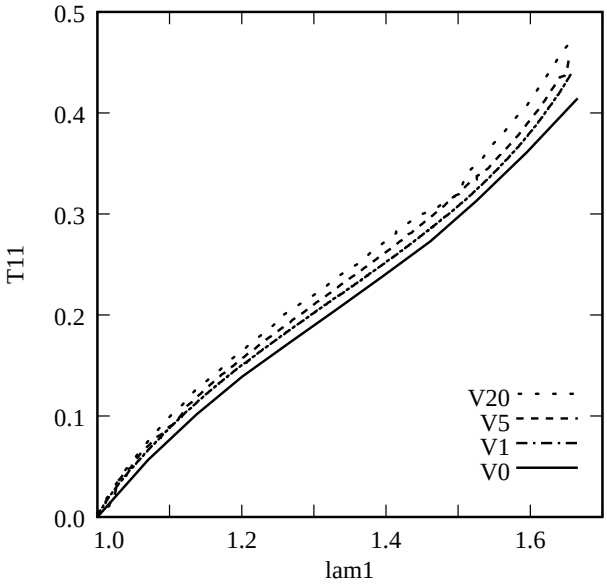

Figure 3: First Piola-Kirchhoff stress P_{11} versus stretch λ_1 for different rates.

In order to characterize the visco-elastic behaviour both quasi-static and time dependent experiments are carried out. The deformation is measured contactless by optical measurement of the stretch in longitudinal and in transversal direction, respectively. Furthermore, we perform uniaxial compression tests and hydrostatic pressure tests in order to get information of the material behaviour under pressure. All experiments are performed in high-precision custom-made devices.

Modelling and parameter identification

According to the micro-structure of cellular rubber we apply the well-known theory of porous media (TPM) (cf. Bowen

[2] Ethylen-Propylen-Dien-Kautschuk

[1], Mow [10], Ehlers [4]), i. e. the concept of superimposed continua extended by the concept of volume fractions. In the present case, a hybrid two-phase model is chosen consisting of a materially incompressible solid skeleton and a compressible pore gas, cf. Diebels [2, 3]. Assuming a closed pore structure both constituents are coupled kinematically. Therefore, it is assumed that no relative motion occurs between the porous matrix material and the pore gas. Following the lines of Eipper & Ehlers [5] and Eipper [6] a point of compaction is included into the model. Therefore, the stress response tends to $-\infty$ if the pores are closed by a volumetrical deformation. If the solid sekletton is assumed to be materially incompressible, the point of compaction is reached if the value of the Jacobian J_S reaches the value of the initial solidity n_0^S.

In a last part of the contribution the model parameters are identified with respect to the experimental results. Therefore, an algorithm based on multimembered evolution strategies is applied, as it was first introduced by Rechenberg [11] and Schwefel [12]. Based on the selection of different starting parameter vectors (*parents*) new vectors (*descendants*) are generated by random mutation. Besides the mutation procedure the mechanism of recombination, i. e. combining different parameters form different parent vectors, is used in order to generate additional descendant parameter vectors. Afterwards the boundary value problem corresponding to the experimental setup is evaluated for each of the descendants, where the vectors with the best objective functions are selected to become parents of the next generation. The evalulation of the boundary value problems can be done in parallel on a PC cluster. This algorithm was found to be robust, stable and reliable.

References

[1] R. M. Bowen (1980): Incompressible porous media models by use of the theory of mixtures. *Int. J. Engng. Sci.*, **18**, 1129–1148.

[2] S. Diebels (1999): Mikropolare Zweiphasenmodelle: Modellierung auf der Basis der Theorie Poröser Medien. *Transport Porous Med.*, **34**, 193–208.

[3] S. Diebels (2000): *Mikropolare Zweiphasenmodelle: Modellierung auf der Basis der Theorie Poröser Medien*. Habilitationsschrift, Institut für Mechanik (Bauwesen), Nr. II-4, Universität Stuttgart.

[4] W. Ehlers (1989): *Poröse Medien - Ein kontinuumsmechanisches Modell auf der Basis der Mischungstheorie*. Berichte aus dem Fachbereich Bauwesen, Universität GH-Essen.

[5] W. Ehlers, G. Eipper (1999): Finite elastic deformations in liquid-saturated and empty porous solids. *Transport Porous Med.*, **34**, 179–191.

[6] G. Eipper (1998): *Theorie und Numerik finiter elastischer Deformationen in fluidgesättigten porösen Festkörpern*. Dissertation, Bericht-Nr. II-1(1998) aus dem Institut für Mechanik (Bauwesen), Lehrstuhl II, Universität Stuttgart.

[7] E. Haberstroh, A. Kremers (2002): Modellierung der Vernetzung von EPDM-Moosgummiprofilen. *GAK*, **9**, 588–593.

[8] E. Haberstroh, A. Kremers (2004): Expansion chemisch geschäumten Kautschukmischungen. *Kaut. Gummi Kunstst.*, **3**, 105–108.

[9] E. Haberstroh, A. Kremers, K. Epping (2005): Extrusion von physikalisch geschäumten Kautschukprofilen. *Kaut. Gummi Kunstst.*,**9**, 449–454.

[10] V. C. Mow, S. C. Kuei, W. M. Lai, C. G. Armstrong (1980): Biphasic creep and stress relaxation of articular cartilage in compression: Theory and experiments. *J. Biomech. Eng.*, **102**, 73–84.

[11] I. Rechenberg (1973): Evolutionsstrategie: Optimierung technischer Systeme nach Prinzipien der biologischen Evolution. *Frommann-Holzboog, Stuttgart.*

[12] H. P. Schwefel (1995): Evolution and Optimum Seeking. *John Wiley & Sons, New York.*

Modelling of Curved Poroelastic Interphases: A General Coordinate-Free Asymptotic Approach

C. Bouby*, Q.-C. He, V. Pensée

Université de Marne la Vallée, Laboratoire de Mécanique
5 bd. Descartes 77454 Marne-la-Vallée Cedex 2, France
celine.bouby@univ-mlv.fr, qi-chang.he@univ-mlv.fr, vincent.pensee@univ-mlv.fr

Summary: The purpose of our study is to model a thin curved poroelastic interphase between two poroelastic media as a curved surface endowed with certain appropriate jump conditions. In contrast with most of the recent studies on curved thin interphases (see, e.g. [1, 2]), the present work deals with a coupled phenomenon and elaborates a coordinate-free asymptotic approach. The poroelastic interface model thus obtained is new and general. It can be implemented with reference to a Cartesian coordinate system. Particularized to some special situations, it allows us to rediscover the widely used empirical poroelastic interface models.

Consider a curved poroelastic interphase of small constant thickness h between two individually homogeneous poroelastic media referred to as medium 1 and medium 2 (Fig. 1). The sub-domain of $\mathbb{R}^3$ occupied by the interphase is denoted by $\Omega^{(0)}$ while the sub-domains occupied by media 1 and 2 are designated by $\Omega^{(1)}$ and $\Omega^{(2)}$, respectively. The interfaces S_1 and S_2 are both assumed to be perfect. Then, the main objective of the study is to replace the thin interphase by an appropriate zero-thickness imperfect interface S_0 between media 1 and 2, located at the middle surface parallel to S_1 and S_2 (Fig. 2).

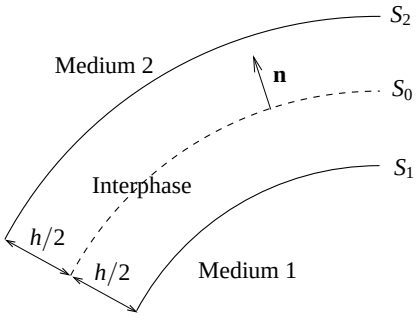

Figure 1: Media 1 and 2 connected by a poroelastic interphase.

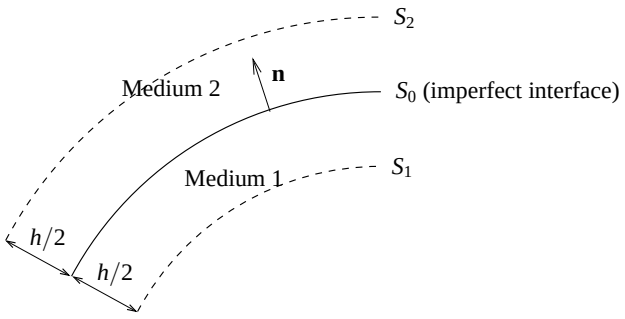

Figure 2: Media 1 and 2 connected by an equivalent imperfect poroelastic interface.

Assumed to be linearly poroelastic, the material constituting each medium is characterized by

$$\boldsymbol{\sigma} = \mathbb{C} : \boldsymbol{\varepsilon} - \mathbf{B}p, \quad p = -M_\phi \mathbf{B} : \boldsymbol{\varepsilon} + M_\phi \phi, \tag{1}$$

where $\boldsymbol{\varepsilon}$ is the infinitesimal strain tensor, $\boldsymbol{\sigma}$ denotes the Cauchy stress tensor, p and ϕ are the pressure and porosity increase from the initial state, $\mathbb{C}$ is the drained elastic tensor, M_ϕ designates Biot's modulus and $\mathbf{B}$ stands for Biot's tensor.

Assuming that fluid density variations are neglected, the classical transport law for porous media, namely Darcy's law, reads

$$\frac{\mathbf{w}}{\rho_0} = -\mathbf{k}.\nabla p, \tag{2}$$

where $\mathbf{k}$, ρ_0 and $\mathbf{w}$ are respectively the permeability tensor, the initial mass density of the fluid and the fluid flux. In addition to the foregoing constitutive laws, the strain tensor field $\boldsymbol{\varepsilon}$ must be derived from a displacement field $\mathbf{u}$ as

$$\boldsymbol{\varepsilon} = \frac{1}{2}\left[\nabla \mathbf{u} + (\nabla \mathbf{u})^{\intercal}\right], \tag{3}$$

the stress tensor field has to satisfy the equilibrium equations

$$\operatorname{div} \boldsymbol{\sigma} = 0 \tag{4}$$

in the absence of body forces, and the fluid flux vector must verify the conservation of the fluid mass m

$$\dot{m} + \operatorname{div} \mathbf{w} = 0. \tag{5}$$

Furthermore, the interfaces S_1 and S_2 are assumed to be perfect, so that the traction vector $\mathbf{t} = \boldsymbol{\sigma}.\mathbf{n}$, displacement vector $\mathbf{u}$, pressure change p and normal fluid flux $w_n = \mathbf{w}.\mathbf{n}$ are continuous across them:

$$\mathbf{t}^{(0)} \mid_{S_i} = \mathbf{t}^{(i)} \mid_{S_i}, \quad \mathbf{u}^{(0)} \mid_{S_i} = \mathbf{u}^{(i)} \mid_{S_i}, \tag{6}$$

$$p^{(0)} \mid_{S_i} = p^{(i)} \mid_{S_i}, \quad w_n^{(0)} \mid_{S_i} = w_n^{(i)} \mid_{S_i}, \tag{7}$$

where $i = 1$ or 2 according to whether the interface S_1 or S_2 is concerned. Above and hereafter, a quantity $(\cdot)$ belonging to $\Omega^{(j)}$ ($j = 0, 1, 2$) and evaluated on S_i is symbolized by $(\cdot)^{(j)} \mid_{S_i}$.

As in [2] and [3], the basic idea used in the present work to establish a poroelastic imperfect interface model consists in: (i) substituting the interphase of thickness h by a zero-thickness interface S_0 separating medium 1 directly from medium 2; (ii) endowing S_0 with certain jump relations to be satisfied by the diplacement vector $\mathbf{u}$, traction vector $\mathbf{t}$, pressure p, normal

fluid flux w_n. Thus, the main step towards obtaining the imperfect interface model is the derivation of appropriate poroelastic jump relations for S_0.

The first step consists in expressing the jump satisfied by the displacement vector in configuration of Fig. 1 across the interphase with the help of Taylor expansions, continuity conditions and constitutive laws:

$$\mathbf{u}^{(2)}|_{S_2} - \mathbf{u}^{(1)}|_{S_1} = \frac{h}{2}\Big[-\boldsymbol{W}^{(0)} : (\nabla_s \mathbf{u}^{(2)}|_{S_2} + \nabla_s \mathbf{u}^{(1)}|_{S_1}) + \mathbf{Q}^{(0)}.(\mathbf{t}^{(2)}|_{S_2} + \mathbf{t}^{(1)}|_{S_1}) + \mathbf{v}^{(0)}(p^{(2)}|_{S_2} + p^{(1)}|_{S_1})\Big] + \mathbf{0}(h^2) \tag{8}$$

where use has been made of surface derivative $\nabla_s \mathbf{u}$ (see e.g. [4]), the vector $\mathbf{v}^{(i)}$ and third-order tensor $\boldsymbol{W}^{(i)}$ are defined by

$$\mathbf{v}^{(i)} = \mathbf{Q}^{(i)}.\mathbf{B}^{(i)}.\mathbf{n}, \quad \boldsymbol{W}^{(i)} = \mathbf{Q}^{(i)}.\boldsymbol{H}^{(i)}, \tag{9}$$

with $\mathbf{Q}^{(i)} = (\mathbf{n}.\mathbb{C}.\mathbf{n})^{-1}$, $(\boldsymbol{H}^{(i)})_{pqr} = (\mathbb{C}^{(i)})_{psqr} n_s$.

We now consider the configuration of Fig. 2 where the interface S_0 separating media 1 and 2 is imperfect. Denote by $\mathbf{u}^{(\pm)}$, $\mathbf{t}^{(\pm)}$, $p^{(\pm)}$ and $w_n^{(\pm)}$ the displacement vector, traction vector, pressure change and normal fluid flux, respectively, evaluated at S_0 on the side of medium 1 for the superscript "$-$" and on the side of medium 2 for the superscript "$+$". The deduction of the jumps $[\![\mathbf{u}]\!] = \mathbf{u}^{(+)} - \mathbf{u}^{(-)}$, $[\![\mathbf{t}]\!] = \mathbf{t}^{(+)} - \mathbf{t}^{(-)}$, $[\![p]\!] = p^{(+)} - p^{(-)}$ and $[\![w_n]\!] = w_n^{(+)} - w_n^{(-)}$ across S_0 is based on the requirement that the jumps in displacement, traction, pressure change and normal fluid flux when moving from S_1 to S_2 in the configuration of Fig. 2 are (within the terms of order $0(h^2)$ and higher orders) the relevant jumps when passing from S_1 to S_2 in the configuration of Fig. 1.

To determine the jump $[\![\mathbf{u}]\!]$ across S_0, we develop $\mathbf{u}^{(i)}\ |_{S_i}$, $\mathbf{t}^{(i)}\ |_{S_i}$ and $p^{(i)}\ |_{S_i}$ about S_i in the configuration of Fig. 2 by means of Taylor's expansions. Then, introducing them in (8) and using constitutive laws yields

$$[\![\mathbf{u}]\!] = \frac{h}{2}\Big[\Big(\mathbf{Q}^{(0)} - \mathbf{Q}^{(2)}\Big)\cdot\mathbf{t}^{(+)} + \Big(\mathbf{Q}^{(0)} - \mathbf{Q}^{(1)}\Big)\cdot\mathbf{t}^{(-)} + \Big(\boldsymbol{W}^{(2)} - \boldsymbol{W}^{(0)}\Big) : \nabla_s\mathbf{u}^{(+)} + \Big(\boldsymbol{W}^{(1)} - \boldsymbol{W}^{(0)}\Big) : \nabla_s\mathbf{u}^{(-)} + \Big(\mathbf{v}^{(0)} - \mathbf{v}^{(2)}\Big)p^{(+)} + \Big(\mathbf{v}^{(0)} - \mathbf{v}^{(1)}\Big)p^{(-)}\Big] + \mathbf{0}(h^2). \tag{10}$$

It is worthwhile to notice that the displacement jump equation (3.16) of [2] in the case of elastic interphase, is rediscovered by setting $p^{(+)} = p^{(-)} = 0$. The expressions for the traction, pressure and normal fluid flux jumps, which have been derived by similar reasoning, are omitted due to the limitation of pages.

To know the different classes of interphases enclosed in this model, we take an interest in extremal cases for the isotropic behaviour. The components of drained elastic tensor $\mathbb{C}_{ijkl}$ are assumed to be bounded and of the same order of magnitude, verifying the Lamé's coefficient relations $\lambda^{(0)} \ll \lambda^{(1)}, \lambda^{(2)}$ and $\mu^{(0)} \ll \mu^{(1)}, \mu^{(2)}$. Under these assumptions, for a soft interphase, the displacement and traction jumps are reduced to

$$[\![\mathbf{t}]\!] = 0, \tag{11}$$

and

$$[\![\mathbf{u}]\!] = h\left[\frac{1}{\mu^{(0)}}\mathbf{t} - \frac{\lambda^{(0)} + \mu^{(0)}}{\mu^{(0)}(\lambda^{(0)} + 2\mu^{(0)})}(\mathbf{n}.\mathbf{t})\mathbf{n}\right] + \frac{h}{2}\left[\frac{b^{(0)}}{(\lambda^{(0)} + 2\mu^{(0)})}(p^{(+)}\mathbf{n} + p^{(-)}\mathbf{n})\right] \tag{12}$$

where $b^{(i)}$ designates the isotropic Biot's coefficient of medium i. For a stiff interphase, when $\lambda^{(0)} \gg \lambda^{(1)}, \lambda^{(2)}$ and $\mu^{(0)} \gg \mu^{(1)}, \mu^{(2)}$, the displacement and traction jumps are given by:

$$[\![\mathbf{u}]\!] = 0, \tag{13}$$

$$[\![\mathbf{t}]\!] = -2h\mu^{(0)}\frac{\lambda^{(0)}}{\lambda^{(0)} + 2\mu^{(0)}}\,\mathrm{div}_s\,[\mathtt{tr}(\nabla_s\mathbf{u})(\boldsymbol{\delta} - \mathbf{n}\otimes\mathbf{n})] - 2h\mu^{(0)}\,\mathrm{div}_s\,\boldsymbol{\varepsilon}_s - h\mu^{(0)}\,\mathrm{div}_s\,[\mathbf{n}\otimes(\mathbf{n}.\nabla_s\mathbf{u}) + (\mathbf{n}.\nabla_s\mathbf{u})\otimes\mathbf{n}] + h\mu^{(0)}b^{(0)}\,\mathrm{div}_s\left[(\boldsymbol{\delta} + \mathbf{n}\otimes\mathbf{n})\,(p^{(+)} + p^{(-)})\right], \tag{14}$$

where $\boldsymbol{\delta}$ is the second-order identity tensor, $\boldsymbol{\varepsilon}_s$ the interface strain tensor.

Finally, referring to isotropic permeability of medium i with $k^{(i)}$, the pressure and normal fluid flux jumps read

$$[\![p]\!] = 0, \quad [\![w_n]\!] = hk^{(0)}\Delta_s p, \tag{15}$$

in the case of a weakly permeability interphase ($k^{(0)} \ll k^{(1)}, k^{(2)}$) and

$$[\![w_n]\!] = 0, \quad [\![p]\!] = -h\frac{1}{\rho_0^f}\frac{1}{k^{(0)}}w_n, \tag{16}$$

for a highly permeability interphase ($k^{(0)} \gg k^{(1)}, k^{(2)}$). The foregoing equations explicitely show that the empirical open-pore condition is a particular case of the general interface model established here. The latter can be also particularized to rediscover other existing empirical imperfect interface models.

References

[1] Z. Hashin (2001): Thin Interphase/Imperfect Interface in Conduction. *J. Appl. Phys.*, **89**, 2261–2267.

[2] Y. Benveniste (2006): A general interface model for a three-dimensional curved thin anisotropic interphase between two anisotropic media. *J. Mech. Phys. Solids*, **54**, 708–734.

[3] P. Bövik (1994): On the modelling of thin interface layers in elastic and acoustic scattering problems. *Q. J. Mech. Appl. Math.*, **47**, 17–42.

[4] M. E. Gurtin, J. Weissmüller, F. Larché (1998): A general theory of curved deformable interfaces in solids at equilibrium. *Philosophical Magazine A*, **78**, 1093–1109.

Micromechanics Contribution to Permeability-Stress Couplings in Macro-Fractured Geomaterials

E. Lemarchand[1*], L. Dormieux[2], C. Davy[3], F. Skoczylas[1]

[1]Laboratoire de Mécanique de Lille, France
eric.lemarchand@univ-lille1.fr, frederic.skoczylas@ec-lille.fr

[2]Institut Navier, Ecole Nationale des Ponts et Chaussées, Champs-sur-Marne, France
dormieux@lmsgc.enpc.fr

[3]ERGI,Ecole Centrale de Lille, France
catherine.davy@ec-lille.fr

Summary: The crucial point of the mechanically-activated permeability evolution of macrocracked geomaterials undergoing increasing confining pressures is here adressed within the framework of micromechanics arguments. The proposed modelling allows one to clearly intercept the key role of the pore space connectedness within the macro-fracture.

This scientific contribution lies in the industrial context of fracture processes likely to develop on the walls of excavated tunnels. The geomaterial of interest is a shale-like material, but the theoretical reasoning may be easily adapted to cement-like materials. In real-life situations, fracture processes do dramatically change the permeability and reduce confinement capacity of host materials. This becomes a crucial point as soon as this fractured shale is used as a natural barrier for the underground storage of radioactive waste. Within this context, an important experimental campaign has been developed at the Laboratoire de Mcanique de Lille (France) on Callovo-Oxfordian (Bure site, Meuse, France) saturated clay-shales. Chemo-physical couplings related to clay-shales/water interactions deserve a special attention and are disregarded here in order to concentrate our analysis to the coupling existing between the mechanical response of tested samples (evolution of the confining pressure versus the fracture closure) and the evolution of their gaz-permeability coefficients ($\approx O(10^{-14}\mathrm{m}^2)$).

The theoretical analysis based on the experimental results takes advantage of micromechanics tools. Indeed, the irregularities of the surfaces associated to the two lips of the macroscopic fracture, physically intercepted by the conceptual rugosity, may be considered as the physical origin of the observed non linear mechanical and hydraulic responses. In order to reproduce the progressive reclosure of the macroscopic fracture under confinement, the idea consists in modelling this macroscopic fracture by a local parallel arrangement of crack-like pores. Thus, the applied confining loading progressively closes the cracks, beginning by the ones having the smallest initial aspect ratio. We first derive the reclosure law for the cracks as a function of the macroscopic loading. Then, this physical mechanism allows one to derive both the macroscopic fracture closure law and the evolution of the sample permeability coefficients.

Based on Eshelby's work [3], cracks are modelled as oblate spheroids that can undergo large transformations. They are defined by a unique orientation, uniform radii (a) but different initial aspect ratios (small-to-big axes ratio $X = c/a$). Thus, considering an isotropic compressive macroscopic stress ($\boldsymbol{\Sigma} = -\Sigma\mathbf{1}$ with $\Sigma > 0$ in compression), reclosure of a crack family occurs as soon as the stress reaches a threshold $\boldsymbol{\Sigma}^{c\ell}$ related to a given initial aspect ratio according to the following law:

$$X = X_o - \frac{T_n}{3k^s}\left(\boldsymbol{\Sigma} - \boldsymbol{\Sigma}_o\right) \quad \rightarrow \quad \rightarrow \quad \boldsymbol{\Sigma}^{c\ell} = \boldsymbol{\Sigma}(X=0) = \boldsymbol{\Sigma}_o + \frac{3k^s}{T_n} X_o \quad (1)$$

where $\boldsymbol{\Sigma}_o = \boldsymbol{\Sigma}(X = X_o)$ stands for the reference state of stress while T_n is a given parameter of the problem that may be analytically derived as a function of the un-fractured solid matrix Poisson ratio (bulk modulus k^s)

- At the macroscopic scale, the fracture ($\mathcal{F}$) closure is controlled by a closure variable denoted by c_c [1] and defined as :
$$c_c = -\frac{1}{2R}\int_{\mathcal{F}} [\boldsymbol{\xi}]\cdot\boldsymbol{n}\, d\Gamma \quad (2)$$
where R is the (cylindrical) tested samples [1], while $[\boldsymbol{\xi}]$ is the displacement jump through fracture lips. The micromechanics reasoning then allows to derive the evolution law $c_c = c_c(\boldsymbol{\Sigma})$, that accounts for the reclosure state of the fracture with respect to the macroscopic stress intensity applied on the samples.
- Concerning advective transport properties, classical micromechanics reasonings start from the morphological assumption that a crack may be considered as a system of two parallel planes [4, 5] with a characteristic value of the permeability given by the factor $c^2/3$. Theoretical developments show that the macroscopic permeability derived by the classical mixture law, specific for a 2D-configuration, clearly underestimates the experimentally measured permeability. Besides, resorting to a continuous distribution of initial aspect ratios allows one to exhibit a monotonic decreasing function of the macroscopic permeability evolution law $k^{hom} = k^{hom}(\boldsymbol{\Sigma})$. Improvements are finally obtained by using the Self-Consistent Scheme that naturally accounts for the concept of cracks percolation phenomenon responsible for dramatic permeability increase [2].

The last part of the study deals with the validation of the proposed micromechanics model with respect to the results obtained by the experimental tests [1]. We prove that application of the Self-Consistent Scheme for the local mechanism of cracks closure contains all the physics that permits to reproduce the experimental evolution laws $c_c(\mathbf{\Sigma})$ and $k^{hom}(\mathbf{\Sigma})$.

References

[1] C.A. Davy, F. Skoczylas, J.D. Barnichon, and P. Lebon (2006): Permeability of macro-cracked argilite under confinement: Gas and water testing. *Physics and Chemistry of the Earth* (in press).

[2] L. Dormieux and D. Kondo (2004): Approche micromécanique du couplage perméabilité-endommagement. *Comptes Rendus Mecanique*, **332**, 135–140.

[3] J.D. Eshelby (1957): The determination of the elastic field of an ellipsoidal inclusion, and related problems. *Proc. Roy. Soc. London*, **241**, 235–251.

[4] Y. Guegen and V.V. Palciauskas (1992): *Introduction la Physique des Roches*. ditions Hermann, Paris.

[5] E. Lemarchand (2001): *Contribution de la micromécanique à l'étude des phénomènes de transport et de couplage poromécanique dans les milieux poreux: Application aux phénomènes de gonflement dans les géomatériaux*. École nationale des ponts et chaussées, Paris (PhD thesis).

Multi-Scale–Multi-Physics Modeling of Flow and Transport in Heterogeneous Porous Media with Application to Subsurface Flow and Brain Cancer Treatment

J. Niessner*, H. Class, R. Helmig, M. Darcis,

Universität Stuttgart, Institute of Hydraulic Engineering, Chair of Hydromechanics and Hydrosystem Modeling
70550 Stuttgart, Germany
{holger.class, rainer.helmig, melanie.darcis, jennifer.niessner}@iws.uni-stuttgart.de

Summary: When modeling flow and transport in porous media, often different kinds of physical processes dominate in different parts of the model domain under consideration. Highly complex processes generally show a strong dependence on fine-scale properties. A multi-scale–multi-physics approach is presented in which complex processes are modeled on a finer scale then the less complex processes and in which the complex processes are restricted to regions where they are actually governing. Such a multi-scale multi-physics modeling approach is needed in many fields of engineering, like – among many others – the contamination of the unsaturated zone of the groundwater by a light non-aqueous phase liquid, the sequestration of carbon dioxide, or biomechanical applications. In this work, we will present results for the application of the multi-scale–multi-physics algorithm to the modeling of flow and transport in the subsurface, and also first results for the modeling of brain cancer treatment including possible future enhancements obtainable by application of the algorithm.

Introduction

Flow and transport phenomena in porous media are the governing processes in many natural and industrial systems. Considering the flow and transport processes on the one hand, they occur on different spatial and temporal scales and may also differ locally. Highly complex processes may take place in one part of the system necessitating an examination of the processes on a fine spatial and temporal scale, while in other parts of the system, physically simpler processes may take place allowing an examination on a coarser scale. Considering the porous medium on the other hand, its heterogeneous structure shows a high dependence on the spatial scale. The porous medium is generally heterogeneous on every spatial scale, but different kinds of heterogeneities predominate on different scales.

To study these issues, one might consider a variety of applications ranging from soil science over industrial applications to biomechanical systems. As an example, consider a domain with randomly distributed heterogeneities where complex multi-phase–multi-component processes are relevant only in a small (local) subdomain. This situation might well be an LNAPL contamination in the unsaturated zone of the groundwater (an LNAPL is a light non-aqueous phase liquid, i.e. a liquid that is not miscible with water and whose density is smaller than that of water), where complex three-phase–three-component processes take place in a subdomain in and around the contaminated zone, see Fig. 1. This subdomain needs fine resolution as the complex processes are governed by small-scale effects. For a comprehensive fine-scale model taking into account multi-phase–multi-component processes as well as heterogeneities in the whole (global) model domain, the data collection is often far too expensive and the computational effort is high.

Therefore, a general multi-scale concept has been developed, see [2].

The presentation is structured in two main parts. In the first part, the mathematics and numerics of the multi-scale–multi-physics algorithm with focus on its application to the case of an LNAPL contamination in the unsaturated zone of the subsurface is demonstrated. In the second part, contrarily, the modeling of the treatment of a brain tumor is shown as a possible future application of the multi-scale–multi-physics algorithm.

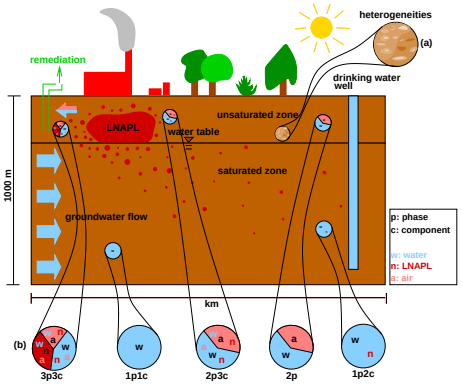

Figure 1: Multi-physics processes in the subsurface occuring on different scales.

Multi-scale–multi-physics concept for an LNAPL saturation in the unsaturated zone

For the *mathematical* description of the considered processes, a system of coupled partial differential equations is set up. It is possible to decouple this fully-coupled system of equations to a so-called fractional flow formulation where processes are partly separated, e.g. it is solved separately for pressure, saturation or concentration. Like this, it is possible to solve for different kinds of processes on different scales (we will solve for saturation on a coarer scale) and to treat mathematically different equation types in a numerically adequate fashion.

When modeling multi-phase–multi-component processes, concentration equations are solved from which total concentrations

are obtained. For the solution of the pressure equation, the saturation distribution is needed which can be calculated form the pressure and concentration field using so-called flash calculations. These flash calculations use equilibrium relationships for the mass transfer between fluid phases.

For the *numerical* solution of the partial differential equation system consisting of pressure, saturation, and concentration equations, a discretization in space and time is necessary. On the one hand, the space discretization scheme has to be flexible enough to treat elliptic as well as hyperbolic equations, on the other hand it has to ensure that numerical diffusion is low. The latter is an especially important aspect as due to the upscaling of the saturation equation to the coarse scale, a macro-dispersion term results. If the numerical diffusion is of a similar magnitude as the macro-dispersion, the results are not very valuable any more. For these reasons, a discontinuous Galerkin scheme [1] is used for which higher order discretization is easily possible.

For discretization in time, the elliptic pressure equation is solved using a time-implicit numerical scheme, while the hyperbolic saturation and concentration equations are solved using an explicit Runge-Kutta scheme with a modified minmod slope limiter.

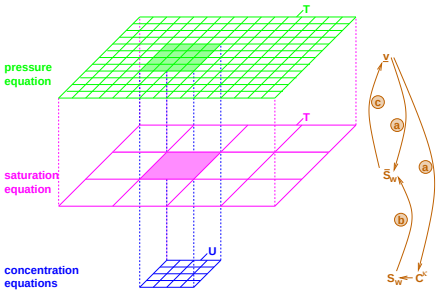

Figure 2: Principle of the multi-scale algorithm.

The principal idea of the developed multi-scale–multi-physics algorithm can be taken from Fig. 2. On the one hand, the global flow field influences the local multi-phase–multi-component processes on the fine-scale. On the other hand, the coarse-scale effects of the fine-scale multi-phase–multi-component processes in the subdomain are captured by source / sink terms and the coarse-scale effects of fine-scale heterogeneities by a macrodispersion term.

The main benefit of the multi-scale algorithm is that less data is required due to the local solution of the concentration equations and due to the upscaling of the saturation equation, and that computing time can be reduced.

Next steps to do. Having developed this multi-scale–multi-physics algorithm, further research still is to be done. Numerical performance can be improved by additionally upscaling the pressure equation. Next, the boundary conditions of the local domain need further fine-tuning and more flexible approaches like a moving mesh following the LNAPL plume are possible. Finally, as the algorithm is constructed in a flexible fashion, it can be adapted to more complex or other physical processes. As an example, the application to the modeling of brain cancer treatment is shown as a possible future research field.

Outlook: modeling of the treatment of brain tumors

Brain tumors are especially complicated to treat because a blood–brain barrier exists which does not allow for substances to leave the blood vessels in the brain, see Fig. 3. Therefore the

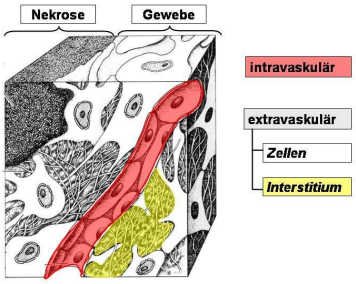

Figure 3: Composition of a human brain.

medicine has to be injected locally, that means directly into the brain tumor. Around the injection zone, high deformations may occur due to the injection needle and the injected flux. Currently, first numerical simulations of this injection process are going on which model all processes on the same scale and deformation processes in the whole model domain. Fig. 4 shows the concentration distribution of the medicine at a certain point in time after the injection.

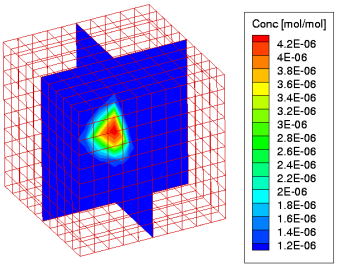

Figure 4: Concentration distribution of injected medicine in a brain.

As data, e.g. structural information, is available from MRT in high density for the brain, this data would need to be upscaled before being applicable in a numerical simulator. Furthermore, high deformations only occur in the vicinity of the injection. Therefore, computational time could be significantly reduced by solving the deformation equation only locally around the injection zone and to solve globally, in the whole brain section of interest, for flow and transport of the medicine.

References

[1] P. Bastian (2003): Higher Order Discontinuous Galerkin Methods for Flow and Transport in Porous Media.*Challenges in Scientific Computing – CISC 2002*, **35**.

[2] J. Niessner, R. Helmig (2006): Multi-scale modeling of two-phase – two-component processes in heterogeneous porous media. *Numerical Linear Algebra with Applications*, **13**, 699–715.

Multiscale Modelling of Transport in Porous Media with Structural Evolution

P. Charrier[1*], **B. Dubroca**[1], **C. Preux**[2,4], **G. Vignoles**[3]

[1]Université Bordeaux 1
IMB-Applied Mathematics, F-33405 Talence, France
Pierre.Charrier@math.u-bordeaux1.fr, Bruno.Dubroca@math.u-bordeaux1.fr

[2]CEA/CESTA
F-33114 LeBarp, France
christophe.preux@ifp.fr

[3]Université Bordeaux 1
Lab. for ThermoStructural Composites (LCTS), UMR 5801, CNRS-CEA-Snecma-Université Bordeaux 1, 3, Allée La Boëtie,
F-33600 Pessac, France
vinhola@lcts.u-bordeaux1.fr

Summary: This paper describes a multi-scale approach for modelling heat and mass transfer in porous media with evolutive microstructure. The application is focused on the chemical vapor infiltration process for the fabrication of ceramic-matrix composite materials. The approach is based on a hierarchy of models and associated computing tools. The basic physical assumptions as well as the mathematical framework leading to the various models are described and numerical results are presented.

Introduction

In several applications a key issue is the modelling of heat and mass transfer in a porous medium whose microstructure evolves during the process, *e.g.* under the action of heterogeneous chemical reactions. In some cases the problem is furthermore complicated by the fact that the gas transferred through the porous medium is rarefied. Example of such a situation are the chemical vapor infiltration process for fabrication of composite material, the pyrloysis of decomposable material of Thermal Protection Systems, or the smoldering, ... ([1], [2]). We present here a multi-scale approach for such problems, based on a hierarchy of models and associated computing tools in which larger scale models use informations such as microstructure evolution or constitutive laws given by more detailed, smaler-scale simulations. The macroscopic (*i.e.* engineering scale) model in this hierarchy is an extension of the Asymptotic Transport Model (ATM) introduced in ([3]) for porous media with fixed microstructure featuring structural evolution.

Mathematical modelling

To set-up a model for heat and mass transfer in porous media with structural evolution we start from a set of equations describing the flow and heat transfer at the smaller scale. The flow is described at a kinetic level by Boltzmann equation (or by a "model equation" such as BGK equation), which allows to consider flows in rarefied or transitional regime in the pores. The heat transfer in the solid phase is described by the heat equation and the system is closed by coupling conditions at the interface: a diffusive reflexion condition and a relation which ensures the continuity of the energy fluxes. These conditions take into account the fact that the interface is moving during the simulation.
Then, by an asymptotic analysis which combines an homogenization process (assuming a periodic structure of the material) and the hydrodynamic limit for the kinetic equation we derive a transport model at the larger scale. Moreover we take into account the heterogenous chemical reactions that are the cause of the structural evolution and we finally get :

$$\begin{aligned}
\epsilon(t,x)\partial_t(\rho_g) + \mathrm{div}_x J &= \omega_g && (1)\\
J + D\nabla_x\rho_g - \tilde{D}\nabla_x T &= 0 && (2)\\
\partial_t\rho_s &= \omega_s && (3)\\
\partial_t[\epsilon_s\rho_s e_s(T) + \epsilon\rho_g e_g(T)] - \mathrm{div}_x(K\nabla_x T) &= 0 && (4)\\
\epsilon_s(t,x) &= \frac{\rho_s(t,x)}{\rho_s^{\#}} &&\\
\epsilon(t,x) &= 1-\epsilon_s && (5)
\end{aligned}$$

where ρ_g and ρ_s are the apparent density of the gas and solid, $\rho_s^{\#}$ is the intrinsic density of the solid phase, T is the temperature, ϵ_s the volume fraction of the solid phase, ϵ the porosity, ω_g, e_g and ω_s, e_s the production terms and internal energy of gas and solid. The effective transport tensors $D = D(\epsilon, \rho_s, T)$ and $\tilde{D} = \tilde{D}(\epsilon, \rho_s, T)$ are defined through kinetic cell closure problems and $K = K(\epsilon)$ is defined through elliptic cell closure problems ([3],[4]). More precisely these closure problems are defined on the fluid phase $Y_f(t)$ of the unit cell Y for D and $\tilde{D}$, and on the solid phase $Y_s(t)$ of the unit cell Y for K. For instance, the cell closure problem defining D is

$$\begin{aligned}
-L(f_0\beta_i) + v\cdot\nabla_y(f_0\beta_i) &= \frac{-f_0}{\rho_0}v_i \text{ in } Y_f(t) && (6)\\
\beta_i(y,v)_{v\cdot n>0, y\in\Gamma_Y(t)} &= \int_{w\cdot n<0} |w\cdot n|\beta_i(w)M(T)dw &&
\end{aligned}$$

where f_0 is the absolute Maxwellian distribution with density ρ_g and temperature T and L is the linearized collision operator used in the Boltzmann equation. In order to uncouple the different scales, we make the following assumption:

[4]Now at IFP, Reservoir Engineering Division, Department of Numerical Simulation of Flow in Porous Media, 92852 Rueil-Malmaison

(H) *We assume that in every unit cell of the material the solid phase traces during its evolution the same intrinsic sequence* $Y_s(\tau)$.
Of course in a particular simulation each unit cell will trace this intrinsic sequence at its own rate which depends on the macroscopic state it encounters. With this assumption the architecture of the approach is composed of the following set of nested models (and associate computing tools):

(i) *micro-scale:* the intrinsic sequence of solid phase traced by unit cells is computed by a level set method and can be parametrized by the porosity when the sequence $Y_s(t)$ is increasing (as in CVI, for instance). The results is a data base $\{Y_f(\epsilon_j)\}_{\{j\}}$.

(ii) *micro/macro-scale :* for each value of the porosity ϵ_j, for discrete values of ρ_g and T the various cell closure problems are solved on $Y_f(\epsilon_j)$ and a data base of effective transport coefficients is obtained : $\left\{D(\epsilon^j, \rho_g^k, T^l)\right\}_{\{j,k,l\}}$.

(iii) *macro-scale :* At the macroscopic scale, for engineering purpose (for instance in order to analyse the effect of reactor control parameters in the CVI process), the above transport model is used with geometry, initial and boundary conditions corresponding to the considered configuration. The model uses the data base created by the micro/macro-scale computing tool (ii).

The macroscopic transport model has been derived for transitional flows inside the pore. However we can prove that this model is consistent with usual ones in limit regimes. More precisely, in the limit of dense flows $\tilde{D}_{ij}T/D_{ij}\rho_g \rightarrow 1$ and furthermore $J = -(B/\mu)\nabla p$ so that we recover the Darcy law as constitutive law for the flow. Furthermore, for simple geometry such as pipes, the tensor D gives in the rarefied limit the well-known Knudsen diffusion tensor.

Numerical results

The basic computing tools of the hierarchy have been developed and validated ([4]). The solution of the cell closure problems has been tested on realistic sample of materials. Figure 1 shows the porous structure of a C/C composite preform deduced from a Synchrotron-X Micro Tomography. It is described by $50 \times 50 \times 50$ voxels.

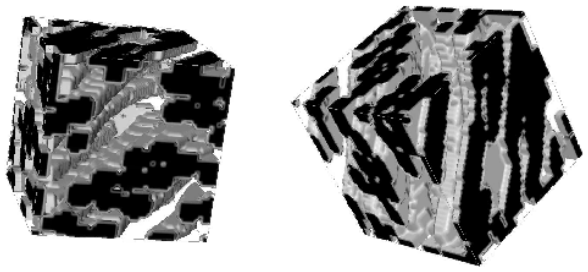

Figure 1: C/C composite preform (SXMT data from LCTS)

On Figure 2 the principal directions of the effective coefficient D computed with the micro/macro-scale model are drawn over a section of the preform. The principal direction corresponding to the larger eigenvalue follows the main direction of the pores, proving that the model is able to extract relevant information on the flow even in a complex geometry (computing the tensor D leads to solve systems with 1 700 000 unknowns). Our approach has been used for the simulation of pyrolysis

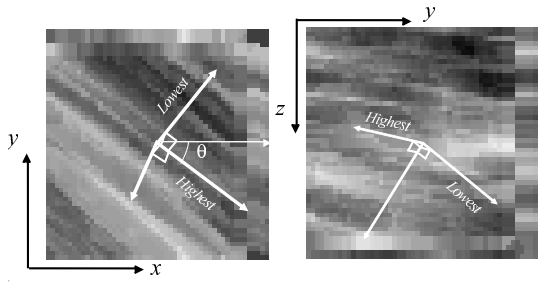

Figure 2: Principal direction of the tensor D

in a carbon-phenolic composite material with a simplified microstructure. Figure 3 shows the position of the pyrolysis front at a given time and the velocity of the interface between the solid and fluid phases. This simulation uses the three sub-models of the hierarchy ((i), (ii) and (iii)).

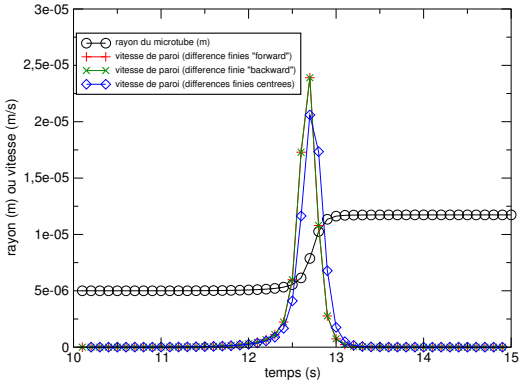

Figure 3: Pyrolysis front and velocity of the interface

References

[1] N. Reuge, G. Vignoles (2005): Modeling of isobaric-isothermal chemical vapor infiltration: effect of reactor control parameters on a densification, *Journal of Materials Processing Technology*, **166**, 15–29.

[2] J. Guo (2004): *Pyrolysis of Wood Powder and Gasification of Wood-derived Char*, Ph. D. Thesis, Technische Universiteit Eindhoven.

[3] P. Charrier, B. Dubroca (2003): Asymptotic transport model for heat and mass transfer in reactive porous media, *SIAM Journal on Multiscale Modelling and Simulation*, **2**, 124–157.

[4] C. Preux (2006) : Modélisation et calcul du transfert de masse et de chaleur dans un milieu poreux réactif en évolution structurale et applications. *Ph. D. Thesis, Université Bordeaux 1*.

Part VII

Homogenization of Elastic and Inelastic Behaviour

Numerical Assessment of Charles Bridge in Prague: An Uncoupled Multi-Scale Approach

J. Zeman[1*], **J. Novák**[1], **M. Šejnoha**[1,2], **J. Šejnoha**[1,2]

[1]Department of Mechanics, Faculty of Civil Engineering, Czech Technical University in Prague
Thákurova 7, 166 29 Prague 6, Czech Republic
zemanj@cml.fsv.cvut.cz, novakj@cml.fsv.cvut.cz

[2]Centre for Integrated Design of Advanced Engineering Structures
Thákurova 7, 166 29 Prague 6, Czech Republic
sejnom@fsv.cvut.cz, sejnoha@fsv.cvut.cz

Summary: In this contribution, a numerical study of a two-span segment of Charles Bridge in Prague is presented. The analysis itself is executed in a fully staggered manner, both in terms of material modeling as well as the assessment of external actions on the structure. The results of the model are validated in terms of typical displacements of parapet walls and crack distribution and opening due to a combined effect of temperature change, dead load and water pressure. In overall, the analysis has provided a valuable estimate of the load-bearing capacity of the structure providing the basis for the optimal planning of remedial measures.

Introduction

Charles Bridge in Prague is one of the listed monuments having the paramount historical importance. Since its completion in 1406, it has experienced several extensive damages, mainly due to repeated floods and water erosion. These were followed by reconstruction, rehabilitation and strengthening measures, which resulted in a large technological and material variability inside the bridge body.

The present study was initiated by the need of a reliable assessment of the current state of the bridge and the extent of the intended reconstruction works. Of course, a certain compromise, based on a careful engineering judgment, must be made between the theoretical appeal of the computational model and necessary simplifications due to limited data available [1]. Even under such restrictions, however, the modern computational tools and methods can provide a reliable basis for diagnostics of historical structures and possible rehabilitation works, especially when compared with linear elastic models [2].

In the ideal case, the analysis to be performed should be (i) *multi-scale* due to heterogeneity of the structure on several spatial scales, (ii) based on *non-linear material models* taking into account quasi-brittle response of masonry materials, (iii) *multi-physical* to incorporate climatic effects on the structure and the interaction of the bridge with water, (iv) *time-dependent* to cover the behavior of the bridge in different periods of the year and (v) *three-dimensional* as the bridge is a very massive structure.

Clearly, such an analysis is not currently feasible, not only from the viewpoint of theoretical and numerical difficulties, but simply due the amount of information required to capture the interaction within the sub-systems. The pragmatic approach adopted in this work is to “decouple” the analysis into independent simplified parts, which are solved using appropriate specialized numerical tools. Outputs of these sub-problems then serve as inputs for a detailed non-linear mechanical simulation allowing us to assess their impact on the overall behavior of the bridge.

Geometrical model of structure

The analyzed two-dimensional segment was decomposed into a number of quasi-homogeneous parts. The partitioning was derived mainly from heterogeneity of the structure resulting from construction and re-construction steps. In addition, the model was refined in the vicinity of surfaces to correctly represent the temperature gradients. Moreover, to capture structure-subsoil interaction, the model incorporates finite element mesh of the layered subsoil, see Fig. 1 as an example.

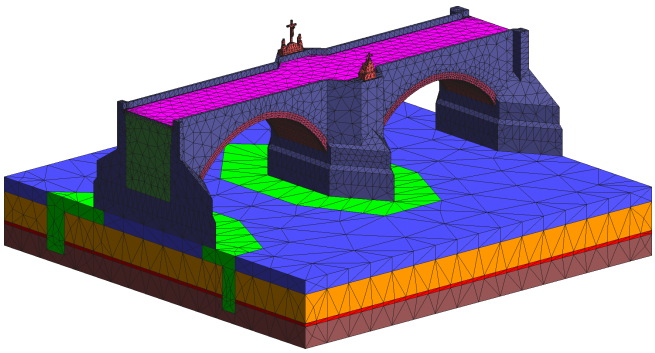

Figure 1: Finite element mesh of the two-span model

Material modeling

Non-linear mechanical behavior of individual materials forming the structure was described using a quasi-brittle three-dimensional constitutive model *CC3DNonLinearCementitous* implemented in the ATENA computer code [4]. The model assumes small strains and initial isotropy of a material, tensile behavior is governed by the Rankine-type criterion while in compression, the Menetrey-Willam yield condition is used. The objectivity in the strain-softening regime is ensured by the crack band model with mesh adjusted softening modulus. A particular material is described using five well-defined input parameters: tensile and compressive strengths, Young’s modulus,

Poisson's ratio, fracture energy and the coefficient of thermal expansion.

When dealing with a heterogeneous part of the structure, however, the previous description applies to individual constituents only. To this end, the parameters characterizing the "smeared" response of selected parts of the structure were extracted from the first-order homogenization simulations executed on representative periodic unit cells. A detailed discussion of individual steps supported by numerical-experimental validation can be found in [3].

External actions

In the present days, when the bridge is open to pedestrians only, the dominant actions on the structure result from its self-weight and annual temperature changes. Introduction of both actions into the model is briefly summarized bellow.

Self-weight Due to a massive character of the structure, the self-weight presents the far most important permanent action. Even more importantly, it turns out that the definition of the computational model plays a central role in getting meaningful results. When the bridge is loaded by the self-weight as a whole body (without taking into account stages of construction), the results of a linear elastic analysis predict the appearance of tensile stresses in the vaults of the bridge. Obviously, this is an incorrect answer indicating the global failure of the bridge even in the construction stage. Therefore, a more detailed model of the construction progress is required when considering the self-weight effects. Owing to the lack of detailed historical data on this subject, a three-stage procedure was used to apply the dead load. The refined model now shows realistic distribution of stresses and crack patterns.

Temperature change The temperature fields inside the structure were based on a two-dimensional coupled heat and mass transfer simulation performed in the finite volume code DELPHIN [5]. Obtained results were validated against in-situ measured temperature profiles; the maximum difference found was $\approx 5°C$. Using the extremal two-dimensional data, the temperature distribution on the bridge surfaces as well as inside the bridge filling were determined. These values were subsequently used to define boundary conditions for a linear stationary three-dimensional heat transfer analysis and the resulting temperature profiles were introduced into the mechanical model.

Example of analysis results

The reported loading combination involves self-weight of the structure, water pressure due to normal water level and the summer temperature change. The steep temperature change gradients result in an extensive array of cracks at the interface between parapet walls and irregular stone masonry filling, see Fig. 2. The maximum predicted crack opening displacement is 0.7 mm. We can also identify two dominant areas of smaller cracks (with crack opening displacement up to 0.2 mm), the

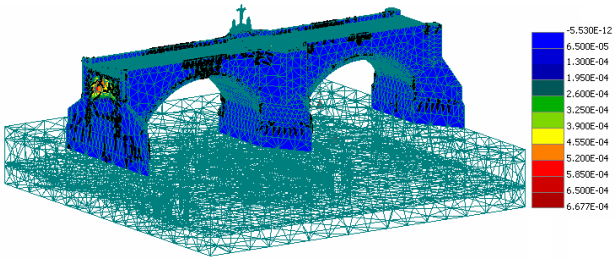

Figure 2: Crack patterns due to positive temperature change

first within the interface between pavement and parapet walls and the second one on the surface of masonry in the mid-span.

The results also allow us to provide an explanation for several important failures located mainly at the oblique part of the parapet wall. Two dominant mechanisms can be identified : (i) increased displacements of parapet walls in the vicinity of the buttress, (ii) high compressive stresses due to restraining effects of the neighboring parts of the structure. It is worth noting that despite a number of simplifying assumptions adopted in the analysis, the predicted crack pattern and their width comply rather well with in-situ observations.

Conclusions

- The computational homogenization approaches, when carefully validated with small-scale tests, can provide a rational procedure for feeding material models with reliable data without a need of large-scale destructive experiments.
- The performed assessment shows that the bridge is currently stable and safe for all load combinations both locally and globally. This conclusion justifies the "minimal" variant of the remedial measures that are currently in progress.

This work was supported by the reasearch plan MSM 6840770003 of the Ministry of Education of the Czech Republic.

References

[1] P. B. Lourenço (2002): Computations of historical masonry structures, *Progress in Structural Engineering and Materials*, **4**, 301–319.

[2] A. Carpinteri, S. Invernizzi, G. Lacidogna (2006): Numerical Assessment of Three Medieval Masonry Towers Subjected to Different Loading Conditions, *Masonry International*, **19**, 65–76.

[3] J. Šejnoha, M. Šejnoha, J. Zeman, J. Sýkora, J. Vorel (2007): A mesoscopic study on historic masonry, *Computers & Structures*, submitted.

[4] V. Červenka, L. Jendele, J. Červenka (2006): *ATENA Program Documentation*, Červenka Consulting, Prague.

[5] J. Grünewald (2000): *DELPHIN 4.1–Documentation, Theoretical fundamentals*, TU Dresden.

Two-Scale Computational Approaches for Masonry Structures with Localisation of Damage and their Extension to Flexural Effects

B. Mercatoris, T. J. Massart*, A. Diaby

Université Libre de Bruxelles
Building, Architecture & Town Planning Dept. (BATir) CP 194/2
Avenue F.D. Roosevelt 50, 1050 Brussels, Belgium
bmercato@ulb.ac.be, thmassar@batir.ulb.ac.be, adiaby@batir.ulb.ac.be

Summary: This contribution discusses the formulation of two-scale computational frameworks for masonry structures. The heterogeneous nature of masonry coupled to its periodic stacking of quasi-brittle constituents leads to preferential damage patterns. Their influence can be incorporated in structural computations using computational homogenisation concepts. The ingredients needed to couple structural and constituents scales are introduced for the case of planar structures, and their extension to flexural effects on masonry walls is discussed. A first tentative of a coupled two-scale framework for masonry plates is presented.

Introduction

The formulation of macroscopic constitutive laws for the behaviour of masonry is a complex task, due to its strongly heterogeneous mesostructure which considerably influences its overall mechanical behaviour. Due to the quasi-brittle nature of its constituents, this results in initial and damage-induced (evolving) anisotropy properties, accompanied with localisation of damage. In its structural use, such a material may be subjected to cracking, leading to localisation of damage at both the structural and fine scales. Closed-form laws have therefore been developed for equivalent anisotropic media for elastic and cracking behaviour [1], later applied for modelling plate failure [2]. The use of such models in the cracking regime is however impeded by their costly and cumbersome identification. As a complementary approach to closed-form constitutive relations, the multi-scale computational strategies aim at solving this issue by deducing a homogenised response at the structural scale from a representative volume element (RVE), based on constituents properties and averaging theorems.

Computational homogenisation

Computational homogenisation approaches allow to identify homogenised continuum properties from the constituents constitutive behaviour of a heterogeneous mesostructure. In a computational context, in each (macroscopic) point of the structural scale discretisation, a sample of the mesostructure is used to determine the material response. For this purpose the local macroscopic strain measure is applied in an average sense to the mesostructure and the resulting mesostructural stresses are determined numerically. The averaging of these mesostructural stresses and the condensation of the mesostructural tangent stiffness to the homogenised tangent stiffness then furnish the macroscopic material response associated with the macroscopic point. This concept, which is also known as multilevel-FEM has been used before to model heterogeneous polymeric systems and other materials, see e.g. [3], and is illustrated in Fig. 1. The definition of such a nested scheme essentially requires the definition of four ingredients: (i) a fine scale constitutive setting for the constituents, (ii) the definition of a representative mesostructural sample, (iii) the choice of a macroscopic representation, and (iv) the set-up of scale transitions linking structural and fine scale quantities.

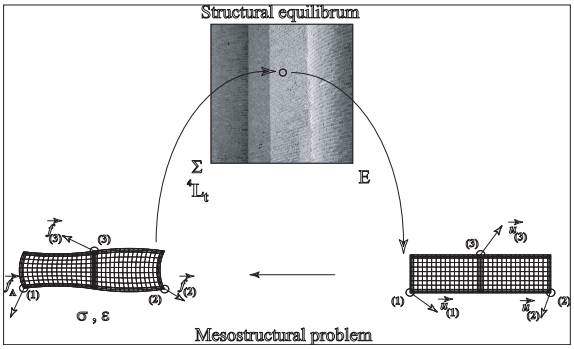

Figure 1: Multi-scale computational scheme.

Multiple-scale treatment of damage localisation

In order to incorporate damage localisation effects at both the structural and fine scales, this approach has to be adapted, by carefully selecting the above-mentioned features. For in-plane loaded structures, in which both fine and coarse scale descriptions follow similar kinematical assumptions, these adaptations have been proposed recently in [4].

In this approach, the homogenised tangent stiffness is used to detect the occurrence of structural scale damage localisation. A continuous-discontinuous multi-scale enhanced scheme is then proposed, in which the localising behaviour at the fine scale of constituents is modelled using available closed-form descriptions (e.g. cohesive zones, non-local damage). A well-posed macroscopic description is preserved upon macroscopic localisation detection by embedding discontinuous localisation bands with mesostructurally motivated properties and width, see Fig. 2. At a macroscopic point, a localising band (b) is embedded into an unloading region (s) with an average strain decomposition rule given by

$$\begin{aligned} \mathbf{E}^b &= \mathbf{E} + f^s \left(\vec{m}\vec{n}\right)^{sym} \\ \mathbf{E}^s &= \mathbf{E} - f^b \left(\vec{m}\vec{n}\right)^{sym} \end{aligned} \tag{1}$$

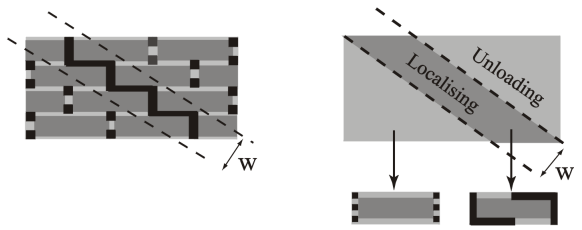

Figure 2: Computational homogenisation-based embedded discontinuity.

where f^b, f^s represent the respective volume fractions of the subregions and $\vec{m}$ is a strain jump. Based on these macroscopic strains applied in an average sense to unit cells, computational homogenisation is used to obtain the response of the macroscopic point from the behaviour of each region. As an additional equation, the traction is required to remain continuous at the interface between the localising and unloading regions

$$\vec{n}.\left(\boldsymbol{\Sigma}^b - \boldsymbol{\Sigma}^s\right) = \vec{0} \tag{2}$$

Two-scale computational framework for flexural effects

This framework can be extended to plate formulations, where higher order kinematical quantities such as curvatures appear at the structural scale. This requires to adapt the structural scale description as well as the scale transitions. At the structural scale, a Reisner-Mindlin description is used. A strong discontinuity approach for plates at failure, as proposed in [5], is used upon macroscopic localisation. The kinematics of the shell description is then generalised by considering an element-based enrichment (a displacement jump) $\{\xi\}$, see Fig. 3, added to the regular part of the displacement field according to

$$\{u_e\} = \{u\} + [\Psi]\{\xi\} \quad \text{with} \quad [\![\Psi]\!] = 1 \tag{3}$$

where the deflection and rotations dofs are collected in $\{u\}$, and $[\Psi]$ represents a set of functions exhibiting a unit jump along a curve Γ_d. Based on the discretisation of the regular and discontinuous parts of the displacement field, the generalised strains (transverse shear and curvatures) in the bulk of the material are obtained as

$$\{\varepsilon_b\} = [B]\{d\} + [G]\{\xi\} \tag{4}$$

where $[G]$ is a set of strain operator associated to the displacement jumps [5].

In order to determine the additional displacement jump fields, the weak form of equilibrium is solved together with a continuity condition on generalised stresses (moments and resultant forces) along the discontinuity Γ_d

$$\int_{\Gamma_d} \left[\delta\vec{\xi}_\theta \cdot \left(\vec{M}_d - \mathbf{m}\cdot\vec{n}\right) + \delta\xi_w \left(V_d - \vec{v}\cdot\vec{n}\right)\right] d\Gamma = 0 \tag{5}$$

where the stress resultants in the bulk are given by

$$\begin{cases} \vec{M} &= \mathbf{m}\cdot\vec{n} \\ V &= \vec{v}\cdot\vec{n} \end{cases}$$

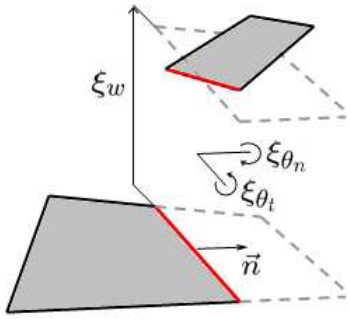

Figure 3: Kinematics of shell discontinuity.

and where $\vec{M}_d$ and V_d represent the generalised stresses in the discontinuity. In contrast with the closed-form evolution laws used in [5] for the discontinuity behaviour, this structural scale description is here coupled with the computational homogenisation concepts to set up a nested computational procedure for flexural effects. Prior to localisation, the generalised stresses are obtained numerically from a RVE computation based on extended scale transition rules. The generalised tangent stiffness $[C^{tan}]$ is also obtained, from which structural scale localisation is detected according to the criterion

$$\det\left(C^{tan}\right) = 0 \tag{6}$$

Upon localisation, the bulk material is assumed to unload elastically along the secant stiffness, while the behaviour of the discontinuity is still deduced from the scale transition

$$\{\dot{\sigma}_d\} = [C_d]\{\dot{\xi}\} \tag{7}$$

The implementation details of this framework will be given, and its results will be illustrated to show that mesostructurally motivated preferential damage orientations can be incorporated into structural plate computations in a natural fashion.

References

[1] P. B. Lourenço, R. de Borst, J. G. Rots (1997): A plane stress softening plasticity model for orthotropic materials, *Int. J. Num. Meth. Engng.*, **40**, 4033-4057.

[2] P. B. Lourenço (2000): Anisotropic softening model for masonry plates and shells, *J. Struct. Engrg. ASCE*, **126**, 1008-1016.

[3] R. J. M. Smit (1998): Toughness of heterogeneous polymeric systems. A modelling approach. *PhD Thesis*, Eindhoven University of Technology, The Netherlands, 1998.

[4] T. J. Massart, R. H. J. Peerlings, M. G. D. Geers (2007): An enhanced multi-scale approach for masonry wall computations with localization of damage, *Int. J. Num. Meth. Engng.*, **69**, 1022–1059

[5] F. Armero, D. Ehrlich (2006): Finite element methods for the multi-scale modeling of softening hinge lines in plates at failure, *Comp. Meth. Appl. Mech. Engrg.*, **195**, 1283–1324.

Overall Yield Strength Domain of Out-of-Plane Loaded Brick Masonry: Comparison of Homogenization Theory Predictions to Experimental Results

J. Dallot, K. Sab*, D. Berg

Institut Navier, LAMI (ENPC / LCPC), Ecole Nationale des Ponts et Chaussées
6 & 8 avenue Blaise Pascal, 77455 Marne-la-Vallée Cedex 2, France
dallot@lami.enpc.de, sab@lami.enpc.fr, berg@lami.enpc.fr

Summary: The aim of this paper is to provide a comparison between the results of a homogenization procedure for the determination of the ultimate loads of out-of-plane loaded masonry walls and the results of a new experimental set up.

Introduction

In a previous paper, Sab [2] suggested a homogenization procedure for the yield design of thin periodic plates has been proposed. Applied to masonry walls, this procedure leads to a Love-Kirchhoff homogeneous plate model. Hence, it does not take into account shear stresses. In [3] Sab et al. developed the above mentioned approach for both thin and thick periodic brickwork plates taking into account the effect of out-of-plane shear forces on the yield strength domain. The periodic brickwork is made of 3D infinitely resistant blocks connected by Mohr-Coulomb interfaces (cohesion c and friction angle φ). According to the homogenization procedure with shear effects, the panel is modeled as an homogeneous Reissner-Mindlin plate subject to in-plane and out-of-plane loads. The homogenized yield surfaces are obtained semi-analytically in terms of c, φ and the geometric characteristics of the microstructure (block dimensions and pattern). They are additional and complementary to the in-plane anisotropic yield surfaces found by De Buhan and de Felice [1]. There is a need to compare these theoretical surfaces to experimental results. Hence, the purpose of this communication is to adopt the homogenized model and to compare its results to the first ones of a new experimental set up developed for this purpose.

Experimental set up

A reduced scale rectangular brickwork-like plate (in-plane dimensions 660x462mm) is subjected to in-plane uniform prestresses and to an increasing out-of-plane force applied in its center as shown in Fig. 1. The bricks are all made of the same wooden material (in-plane dimensions 49x19mm). The design of the bricks has been made very carefully in order to obtain the same roughness for all faces and consequently the same frictional behavior at the interfaces ($c = 0$ and φ is uniform). The in-plane forces are all equal: $T_i = T$, $i = 1, 2, 3, 4$. They are applied through 4 elastic springs which are attached to two pairs of opposite sliding metallic boundaries as shown in Fig. 1. The out-of-plane force is an increasing vertical weight V applied on a small region which is situated at the center of the plate (the two in-plane directions of the plate are actually the two horizontal directions, hence the plate is also submitted to its own weight). Two thicknesses of the blocks are tested: 19mm and 30mm. For each type of blocks, the limit load $V_{\lim}$ is measured for several values of the horizontal force T (cf. Figs. 2b and 3b). As expected, it is found that $V_{\lim}$ is proportional to $(T - T_w)$ where T_w is the in-plane force corresponding to the failure of the plate under its own weight. Moreover, it is observed that the failure modes are different: shear mode for thick blocks (Fig. 3b) and bending mode for thin blocks Fig. 2b).

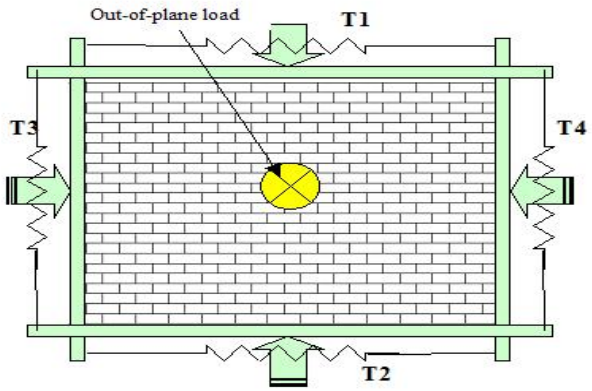

Figure 1: Experimental set up.

Perspectives

Using the observed failure modes, the kinematic method for the determination of the limit load of a homogeneous Reissner-Mindlin plate will be used in order to give a prediction of T_w and of the ratio $V_{lim}/(T - T_w)$ for both the thin plate and thick the plate. These theoretical values will be compared to the experimental ones.

References

[1] De Buhan, P., De Felice, G. (1997): A homogenization approach to the ultimate strength of brick masonry. *Journal of the Mechanics and Physics of Solids*, **45**, 1085–1104.

[2] Sab, K. (2003): Yield design of thin periodic plates by a homogenization technique and an application to masonry walls. *C.R. mécanique*, **331**, 641–646.

[3] Sab K., Cecchi A., Dallot J. (2007): Determination of the Overall Yield Strength Domain of Out-of-Plane Loaded Brick Masonry. *International Journal of Multiscale Computational Engineering*, to appear.

(a)

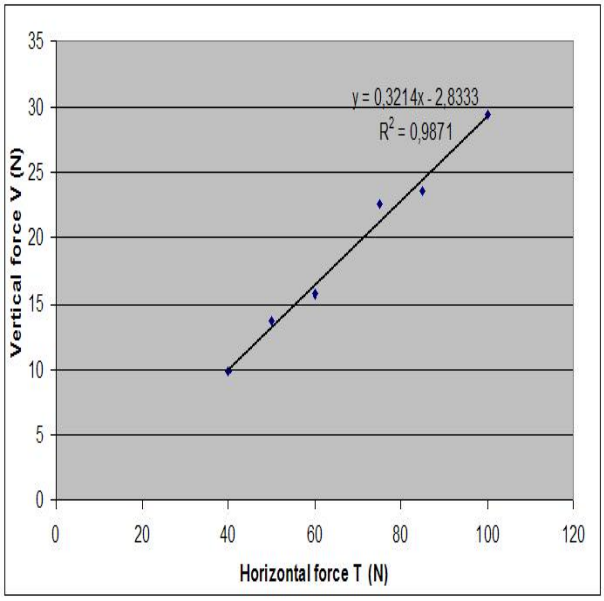

(b)

Figure 2: Ultimate load for thin plates: (a) bending failure mode, (b) results for 6 values of the horizontal force T. Linear regression.

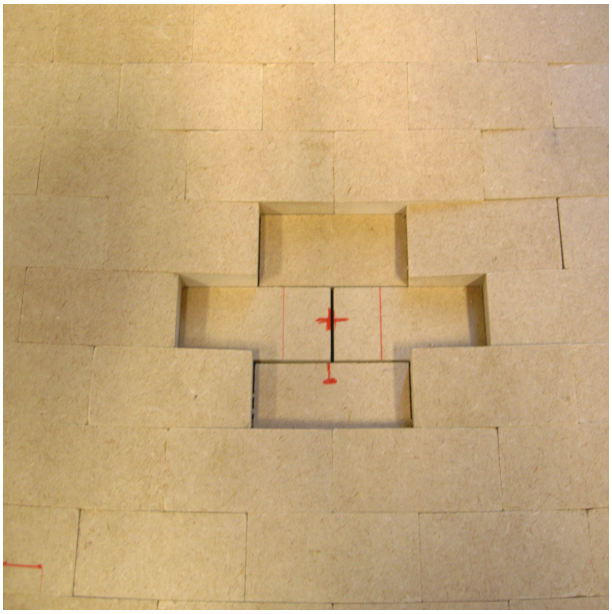

(a)

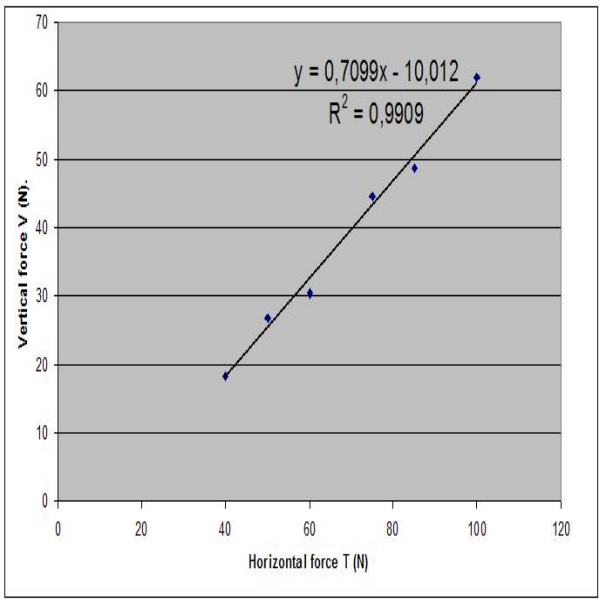

(b)

Figure 3: Ultimate load for thick plates: (a) shear failure mode, (b) results for 6 values of the horizontal force T. Linear regression.

Random Field Models of Heterogeneous Media via Microstructural Quantification

M. Lombardo[1*], **J. Zeman**[2], **M. Šejnoha**[2]

[1]Department of Civil Engineering, University of Messina
C.da di Dio, 98166 Messina, Italy
mlombardo@ingegneria.unime.it

[2]Department of Mechanics, Czech Technical University in Prague
Thákurova 7, 166 29 Prague 6, Czech Republic
sejnom@fsv.cvut.cz, zemanj@cml.fsv.cvut.cz

Summary: The goal of this contribution is to demonstrate that the elements of quantitative characterization of random microstructures can be efficiently used in order to generate the random field description tailored to a specific geometry distribution. The elastic analysis of an irregular masonry panel via Stochastic Finite Element Method is included.

Introduction

The mechanical behavior of random media is a relevant research topic in a wide variety of applied mechanics fields, such a composite materials, geotechnical engineering and biomechanics. There are cases when the classical continuum mechanic approach is insufficient to model adequately materials with a microstructure. A common feature of these media is the random spatial arrangement of components forming the heterogeneous microstructure. A useful way to take into account this randomness is its stochastic characterization.

For many engineering applications, two different approaches are available to the modeling of random heterogeneous materials. The first one, based on the well-established homogenization theories, essentially replaces the heterogeneous body by a homogeneous equivalent with unknown properties. The characteristics of a fictitious homogenized material are determined from the analysis of a statistically representative sample of the material in question.

The alternative methods employ the techniques of stochastic continuum mechanics. In this context, the spatial distribution of material parameters is described by a given random field. Although the latter method is generally preferable to the homogenization techniques, its major disadvantage is that the random field is often introduced without a clear link to the underlying microstructure. If the microstructure can be related to the spatially varying material property fields, characterization and simulation of uncertain mechanical properties can be done [1].

The goal of this contribution is to demonstrate that the elements of quantitative characterization of random microstructures can be efficiently used to generate the random field description tailored to a specific geometry distribution.

Probabilistic numerical methods are most appropriate tools to analyse these stochastic structures, since they incorporate information concerning the random fluctuations of input parameters and permit conclusions concerning the fluctuations of the output parameters. The statistics of the structure response can be then obtained using the classical Stochastic Finite Element Method (SFEM). The basic assumption is that the material properties are described by a random field [2]. Using the theory of composite materials, the random fields of the mechanical properties are defined by means of the corresponding stochastic field that describes the microstructure. The mechanical properties are assumed to be known through their second-order statistics and are assumed to vary continuously over the space. This approach takes into account the correlation function obtained from a procedure that uses the statistical descriptors of the random geometry [3, 4]. This method starts from the analysis of a sample image that is digitally reduced to a binary image; then, the statistical descriptors of the random geometry are evaluated and finally the random field describing the mechanical properties is characterized by means of the evaluation of its fundamental quantities (for example, the correlation functions).

The issue of representing the random process used to model the random material properties is crucial to the SFEM. The Karhunen-Loève (KL) expansion is utilized for this purpose [5].

A KL expansion provides a second-moment characterization of a random process $H(\boldsymbol{x},\theta)$, function of the position vector $\boldsymbol{x}$ defined over the domain D and with θ belonging to the space of random events Ω, in terms of deterministic orthogonal function and uncorrelated random variables as follows:

$$H(\boldsymbol{x},\theta) = \mu(\boldsymbol{x}) + \sum_{i=1}^{M} \sqrt{\lambda_i}\,\xi_i(\theta)\,\varphi_i(\boldsymbol{x}) \qquad (1)$$

where $\mu(\boldsymbol{x})$ is the mean of the process, λ_i and $\varphi_i(\boldsymbol{x})$ are the eigenvalues and eigenfunctions of the covariance function, $\xi_i(\theta)$ is a set of uncorrelated random variables and M is the number of KL terms.

The second level of representation involves the solution process. Since the analysis is conducted in the context of Finite Element analysis, the solution process consists of a vector random process whose members represent the random solution at the nodes of the mesh.

Principles of the method are exemplified through an elastic analysis of the irregular masonry panel depicted in Fig. 2. Fig. 1 shows the result obtained by a software developed to evaluate the statistical descriptors of microstructure.

References

[1] S. Torquato (2002): *Random heterogeneous materials: Microstructure and macroscopic properties.* Springer-Verlag.

[2] E. Vanmarcke (1998): *Random fields: Analysis and Synthesis.* MIT Press.

[3] J. Gajdošík, J. Zeman, M. Šejnoha (2005): Qualitative analysis of fiber composite microstructure: Influence of boundary conditions. *Probabilistic Engineering Mechanics*, **21**, 317-329.

[4] G. Falsone, M. Lombardo (2006): About the stochastic representation of the mechanical properties of irregular masonry panel. In *Computational Stochastic Mechanics 5*, Rhodos (Greece), in Press.

[5] R. Ghanem, P. D. Spanos (1991): *Stochastic finite element: a spectral approach.* Springer Press, Berlin.

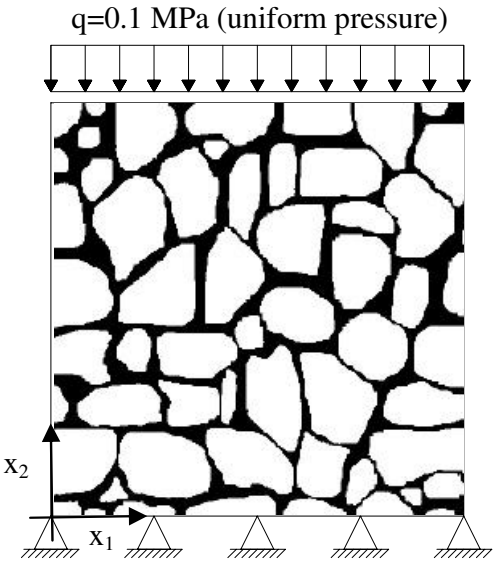

Figure 2: Loading and boundary condition on finite element model.

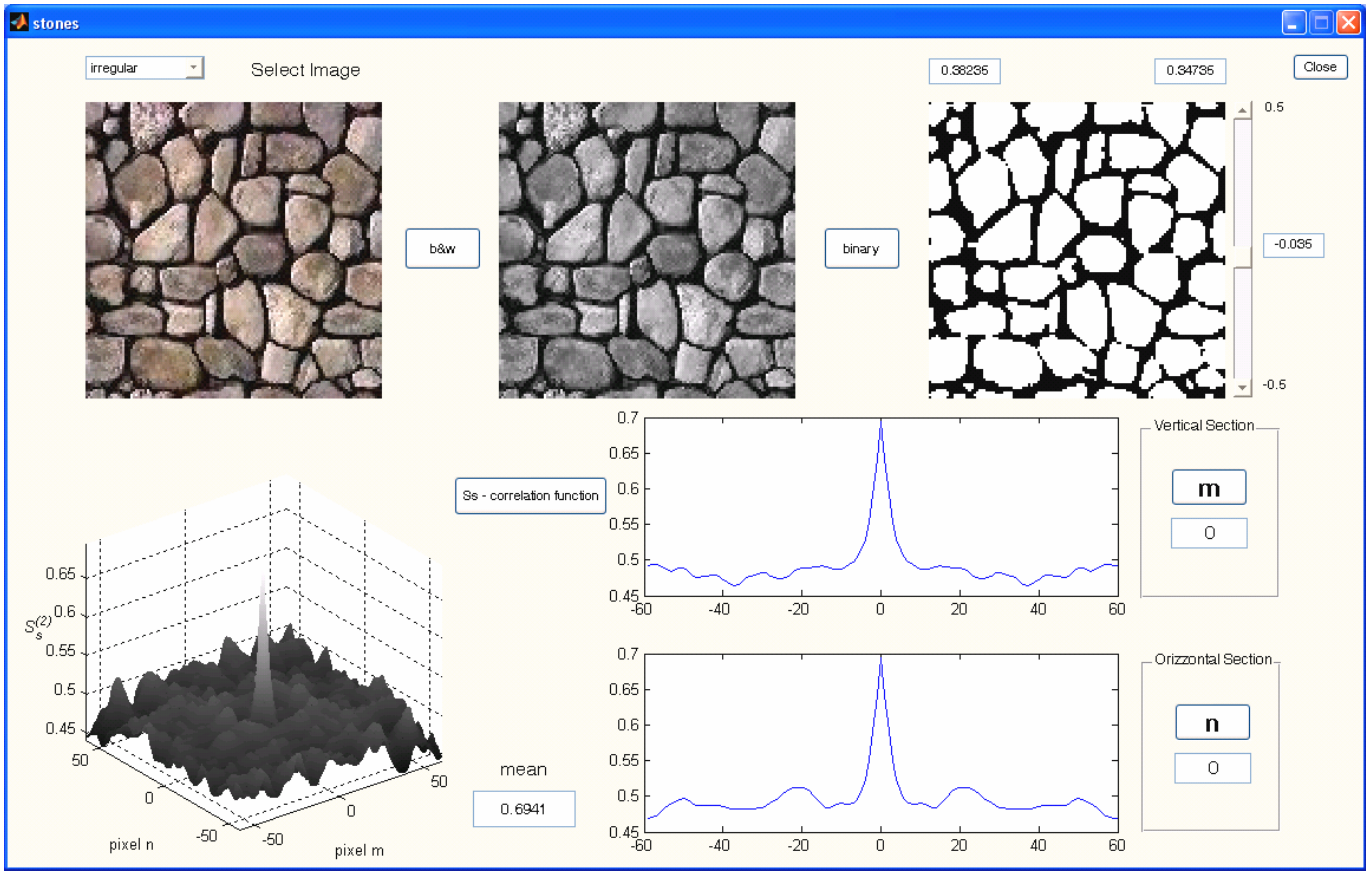

Figure 1: Example of the program used to obtain correlation function for a chaotic masonry panel.

Towards Confined Granular Multiscale Methods

H. A. Meier[1*], **E. Kuhl**[2], **P. Steinmann**[1]

[1]Department of Mechanical Engineering
University of Kaiserslautern, 67659 Kaiserslautern, Germany
homei@rhrk.uni-kl.de, ps@rhrk.uni-kl.de

[2]Department of Mechanical Engineering
Stanford University, Stanford, CA 94305-4040, USA
ekuhl@stanford.edu

Summary: Over the last few years, granular and granular-like media have been gaining a tremendous interest in computational mechanics [9, 10]. Based on their discontinuous nature, an appropriate method is needed to simulate the behavior of particulate media. The discrete element method (dem) [1, 2] provides the perfect means to do so, but also includes the drawback of high computational costs if the number of simulated particles (nop) grows towards infinity. To overcome this drawback a multiscale method is used, restricting the number of particles by introducing a geometric periodic representative volume element (rve). The discontinuous confined granular media are placed on the microscale level simulated by the means of the dem. A finite element method is used on the macroscale level to discretize the overall continuum. Quantities between the different scales are related by the use of averaging theorems, see [5].

Generation of geometric periodic representative volume element

The evolution process of the periodic representative volume element is based on the Lubachevsky-Stillinger algorithm [4] developed in the context of computational chemistry. This algorithm is known to produce highly packed particle assemblies including periodic boundaries, see [6, 7].

Starting with a periodic boundary box of dimensions, $\mathsf{l}_{\mathsf{rve}} \times \mathsf{l}_{\mathsf{rve}}$ particles with radii zero are randomly inserted. Provided with a random velocity $\boldsymbol{v}_i$, as well as a unique particle growth rate g_i related to a given grain size distribution the algorithm is started. Using an event driven method to step forward in time, particles collide and their radii r_i grow depending on the elapsed time, see (1).

$$^{n+1}r_i = {}^{n}r_i + g_i\,\Delta t \qquad \forall \quad i \in \{1,\dots \mathsf{nop}\} \tag{1}$$

Correspondingly, the volume fraction ϕ, i.e. the volume occupied by the particles per volume of the periodic boundary box, is directly related to the prescribed growth rates.

Demanding a constant individual particle velocity between the collision events, the well known Euler formula is applied. With this the position of particle i at time ^{n+1}t is calculated by:

$$^{n+1}\boldsymbol{x}_i = {}^{n}\boldsymbol{x}_i + \Delta t\,{}^{n}\boldsymbol{v}_i \qquad \forall \quad \boldsymbol{x}_i\,,\boldsymbol{v}_i \in \mathbb{R}^{\mathsf{dim}} \tag{2}$$

The events, collisions between two particles i and j, are treated by an enhanced purely elastic impact law between bodies of equal mass, resulting in:

$$\begin{aligned} {}^{+}_{n+1}v_{n_i} &= \mathsf{min}\left\{ {}^{-}_{n+1}v_{n_i}\,,{}^{-}_{n+1}v_{n_j} \right\} - g_i\,, \\ {}^{+}_{n+1}v_{n_j} &= \mathsf{max}\left\{ {}^{-}_{n+1}v_{n_i}\,,{}^{-}_{n+1}v_{n_j} \right\} + g_j\,. \end{aligned} \tag{3}$$

Here, v_{n_i} represents the normal particle velocity with respect to the collision direction. Quantities prior to the contact are indicated by $\overset{-}{(\bullet)}$, whereas $\overset{+}{(\bullet)}$ represents quantities posterior to the collision. A finished geometric periodic volume element is shown in Fig. 1. The driving frame is spanned by the particles in

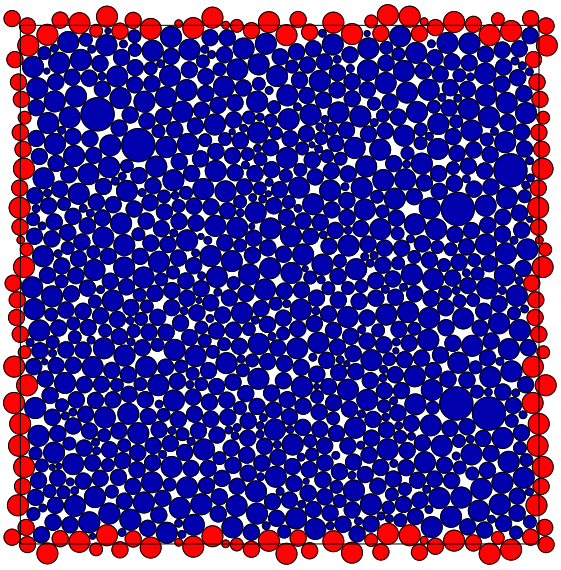

Figure 1: Geometric periodic volume element containing 1000 primary particles and their periodic images. Boundary particles belonging to the driving frame are colored in red. The periodic boundary box is illustrated by a black box. The final volume fraction reached is approximately $\phi \approx 0.84761$.

the boundary set $\mathscr{B}$, colored in red. The boundary frame can be considered to be a closed ordered sequence of the boundary particles, resulting into a closed hull.

$$\mathscr{B} := \left\{ i \in \{1,\dots,\mathsf{nop}\} : \overline{B}_{R_i}\left({}^{0}\boldsymbol{x}_i\right) \cap \partial\mathsf{rve} \neq \emptyset \right\} \tag{4}$$

The remaining particles belong to the inner particle set $\mathscr{I}$, driven by the particles on the boundary. A summary of the input parameters is given in Table 1.

Table 1: 1000 primary particles, quartz sand, see [8]

grain ∅ $[mm]$	mass % [%]	volume % [%]	particle % [%]	particle [/]
0.315	0.00	0.00	0.0000	0
0.250	2.50	2.50	0.6227	6
0.160	39.72	39.72	24.1531	242
0.125	44.22	44.22	44.0557	441
0.100	9.58	9.58	14.9131	149
0.063	3.70	3.70	14.5119	145
0.050	0.28	0.28	1.7435	17

Microscale level computation

Using the previous outlined method to produce a geometric periodic granular representative volume element allows to directly start the computation on the microscale level. Note that due to the generation process, a stable and nearly force free particle assembly is created, which is kept intrinsically stable by the definition between primary particles and their images.

The deformation process is driven by a deformation gradient tensor $\boldsymbol{F}$, applied on the boundary frame particles in a periodic matter, see (5). Additionally, the previous definition of the boundary frame allows to differentiate between linked and unlinked neighbors in the boundary frame particle set which has influence on the force calculation.

$$ {}^{n+1}\boldsymbol{x}_{i,\oplus} - {}^{n+1}\boldsymbol{x}_{i,\ominus} = \boldsymbol{F}\left[{}^{n}\boldsymbol{x}_{i,\oplus} - {}^{n}\boldsymbol{x}_{i,\ominus}\right] \quad \forall\, i \in \mathscr{B} \tag{5} $$

Here $\oplus$ and $\ominus$ refer to the split of the boundary frame into a positive and negative side.

Relating any particle and its images in a direct manner to the deformation gradient tensor ensures the exclusion of rigid body translations and rotations of the granular assembly.

The use of only penalty type laws to position the boundary frame particles underlines the characteristics of the applied periodic boundary conditions with regards to their softness. To solve the described boundary value problem at the microscale level a dynamic relaxation method is utilized, overcoming the loss of regularity of the stiffness matrix during deformation.

Homogenization

Inserting the geometric periodic granular rve on the microscale level, having a finite element model on the macroscale level, allows to calculate confined granular materials with a minimum of computational effort. The connection between the two scales is accomplished by applying averaging theorems, see [3].

The complete homogenization cycle can be outlined as follows: The macroscopic deformation gradient at each integration point is used on the microscale level to drive the boundary frame particles. Completing this task leads to an output of a stress tensor on the microscale level, which is returned to the macroscale level.

References

[1] P. A. Cundall, O. D. L. Strack (1978): The Distinct Element Method as a Tool for Research in Granular Media, *Report to the National Science Foundation Concerning NSF Grant ENG76-207 11, PART I*.

[2] P. A. Cundall, O. D. L. Strack (1979): The Distinct Element Method as a Tool for Research in Granular Media, *Report to the National Science Foundation Concerning NSF Grant ENG76-207 11, PART II*

[3] J. Dettmar, C. Miehe (2004): A framework for micro-macro transitions in periodic particle aggregates of granular materials, *Computer Methods in Applied Mechanics and Engineering*. **193**, 225–256.

[4] B. D. Lubachevsky, F. H. Stillinger (1990): Geometric properties of random disk packings, *Journal of Statistical Physics*, **60**, 561–583.

[5] H. A. Meier, E. Kuhl, P. Steinmann (2006): Failure of granular materials at different scales - microscale approach, *PAMM*, **6**, 399–400.

[6] H. A. Meier, E. Kuhl, P. Steinmann (2006): On Discrete Modeling and Visualization of Granular Media, In *'Visualization of Large and Unstructured Data Sets', GI-Edition, Lecture Notes in Informatics*, eds. Hagen H, Kerren A, Dannenmann P., pp. 165–175.

[7] H. A. Meier, E. Kuhl, P. Steinmann (2006): A note on the generation of periodic granular microstructures based on grain size distribution curves, submitted for publication.

[8] T. Wichtmann (2005): Explicit accumulation model for non-cohesive soils under cyclic loading, *Schriftreihe des Institutes für Grundbau und Bodenmechanik der Ruhr-Universität Bochum, Heft 38*.

[9] T. I. Zohdi (2005): Modeling and direct simulation of near-field granular flows, *International Journal of Solids and Structures*, **42**, 539–564.

[10] T. I. Zohdi (2005): Charge-induced clustering in multi-field particulate flow, *International Journal for Numerical Methods in Engineering*, **62**, 870–898.

Influence of Boundary Conditions on Simulated Overall Effective Properties of Cancellous Bone

D. H. Pahr*, P. K. Zysset

Institute of Lightweight Design and Structural Biomechanics
Gusshausstrasse 27-29, 1040 Vienna, Austria
pahr@ilsb.tuwien.ac.at

Summary: High-resolution finite element models of trabecular bone can be used to study trabecular structure-function relationships, elasticity, multiaxial strength, and tissue remodelling in more detail than experiments. Appropriate boundary conditions have to be applied on Representative Volume Elements (RVE) and "apparent" instead of "effective" overall elastic properties can be computed. Beside effects of the RVE size, scan/analysis resolution, segmentation process, etc. the type of the applied BCs might have a strong influence on the predicted elastic properties. This study provide some answers concerning these errors by comparing different boundary condition types (displacement controlled, mixed BCs, periodic Bcs), different RVEs (original and mirrored-periodic RVE), and various bone densities (BVTV 6,5% - 37,6%). Finally, the Young's moduli, shear moduli, and Poisson's ratios are computed and the errors are compared.

Introduction

While multi-axial and off axis properties of trabecular bone play an important role in fracture and prosthesis design, experimental data on multi-axial properties are limited due to technical difficulties. Use of high-resolution finite element models [1] can avoid these problems if they are sufficiently accurate.

Beside other factors, the applied boundary conditions have an influence on the predicted elastic properties. Huet [2] introduces the notion "apparent" properties. Comparisons of different BCs were previously done by Kowalczyk [3] but only for idealized periodic structures and two type of BCs (uniform displacement and periodic) were investigated.

The objective of this study is to study real bone geometries instead of idealized and introduce a new BCs type. The apparent stiffness tensors are obtained from FEM RVE analyses where uniform displacements, mixed BCs, and periodic BCs are applied on the models. Additionally, the "anisotropic" bone RVEs are mirrored to get "orthotropic" samples and results for different BCs compared with the original one.

Boundary conditions

Hill [4] showed that all necessary and sufficient conditions of the equivalence between the energetically and mechanically defined properties of elastic materials are contained in the so-called Hill condition:

$$\langle \boldsymbol{\sigma} : \boldsymbol{\varepsilon} \rangle = \langle \boldsymbol{\sigma} \rangle : \langle \boldsymbol{\varepsilon} \rangle \tag{1}$$

This condition means that the average ($\langle \dots \rangle = \int_V \dots dV$) of the product of the stress $\boldsymbol{\sigma}$ and strain tensors $\boldsymbol{\varepsilon}$ equals the product of their averages. Using the Gauss theorem the Hill condition can be generalized to nonlinear heterogeneous materials [5]:

$$\langle \boldsymbol{\sigma} : \boldsymbol{\varepsilon} \rangle - \langle \boldsymbol{\sigma} \rangle : \langle \boldsymbol{\varepsilon} \rangle = 0 \qquad \Leftrightarrow \tag{2}$$

$$\int_{\partial B} \big(\boldsymbol{t} - \langle \boldsymbol{\sigma} \rangle \cdot \boldsymbol{n}\big) \cdot \big(\boldsymbol{u} - \langle \boldsymbol{\varepsilon} \rangle \cdot \boldsymbol{x}\big) dS = 0\,, \quad \forall \boldsymbol{x} \in \partial B$$

where ∂B is the boundary of a the RVE and $\boldsymbol{t}$, $\boldsymbol{u}$, $\boldsymbol{n}$, $\boldsymbol{x}$ are the traction, displacement, normal and radius vector, respectively. For an infinite homogeneous body this condition is trivially satisfied, but for a finite heterogeneous body it requires that the body is loaded in a specific way on its boundary ∂B. This is satisfied by three different types of boundary conditions for random media [6]:

1. Uniform displacement (Dirichlet) boundary condition
$$\boldsymbol{u}(\boldsymbol{x}) = \boldsymbol{\varepsilon}^0 \cdot \boldsymbol{x} \qquad \forall \boldsymbol{x} \in \partial B \tag{3}$$
2. Uniform traction (Neumann) boundary condition:
$$\boldsymbol{t}(\boldsymbol{x}) = \boldsymbol{\sigma}^0 \cdot \boldsymbol{n} \qquad \forall \boldsymbol{x} \in \partial B \tag{4}$$
3. Uniform displacement-traction (orthogonal mixed) boundary condition:
$$\big(\boldsymbol{t}(\boldsymbol{x}) - \langle \boldsymbol{\sigma} \rangle \cdot \boldsymbol{n}\big) \cdot \big(\boldsymbol{u}(\boldsymbol{x}) - \langle \boldsymbol{\varepsilon} \rangle \cdot \boldsymbol{x}\big) \qquad \forall \boldsymbol{x} \in \partial B \tag{5}$$

where $\boldsymbol{\varepsilon}^0$ and $\boldsymbol{\sigma}^0$ denote constant tensors, prescribed a priori on the RVE. From the strain and stress average theorems it follows that $\boldsymbol{\varepsilon}^0 = \langle \boldsymbol{\varepsilon} \rangle$, $\boldsymbol{\sigma}^0 = \langle \boldsymbol{\sigma} \rangle$. Each of these BCs results in different "apparent" stiffness tensors. For uniform displacement BCs the stiffness tensor $\boldsymbol{C}^d$ is introduced:

$$\langle \boldsymbol{\sigma} \rangle = \boldsymbol{C}^d : \boldsymbol{\varepsilon}^0\,, \tag{6}$$

and for force controlled BCs the compliance tensor $\boldsymbol{S}^t$:

$$\langle \boldsymbol{\varepsilon} \rangle = \boldsymbol{S}^t : \boldsymbol{\sigma}^0 \tag{7}$$

Hazanov [7] showed that displacement and traction BCs provide bounds for the stiffness $\boldsymbol{C}^{dt}$ based on mixed BCs:

$$[\boldsymbol{S}^t]^{-1} \leq \boldsymbol{C}^{dt} \leq \boldsymbol{C}^d \tag{8}$$

where this inequality is understood in terms of quadratic forms.

In the case of periodic micro structures ([8]) the boundary must always appear in parallel pairs denoted as k^+ and k^- and for the corresponding boundary it has to be fulfilled that:

$$\boldsymbol{u}(\boldsymbol{x})^{k^+} - \boldsymbol{u}(\boldsymbol{x})^{k^-} = \boldsymbol{\varepsilon}^0 \cdot \Delta \boldsymbol{x}^k \qquad \forall \boldsymbol{x} \in \partial B^k \tag{9}$$

where $\Delta \boldsymbol{x}^k$ is a constant distance between corresponding surfaces.

Voxel model

Six bone samples are extracted from a human proximal femur and scanned with a resolution of 26 μm on a μCT40. From these data's, cubical voxel models are cropped (edge length of 5.2 mm), rotated such that the global x, y, z coordinate system is aligned with the orthotropic axis (see [1]), and resampled with a factor of 2 (BVTV $< 20\%$) or 3 (BVTV $> 20\%$). The dataset is segmented and the hexahedral voxel models are generated for ABAQUS (Fig. 1, left). The BVTV of the samples is 6.52%, 10.7%, 12.25%, 15.76%, 20.76%, and 37.61%. A second type of model is genered by mirroring the 5.2 mm cubical RVEs along x, y, and z axis (Fig. 1, right). Thus a periodic orthotropic microstructure is obtained.

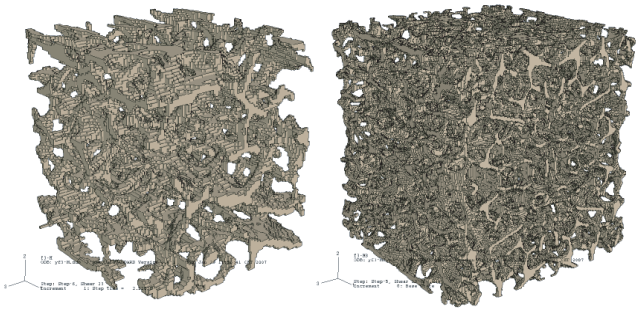

Figure 1: Cubical FEM model with 5.2 mm (left) and mirrored (periodic) cube with 10.4 mm edge length (right). BVTV=12.25%.

All models are analyzed using uniform displacement and mixed BCs. In the case of the mirrored (big) FEM periodic BCs are applied additionally. Six independent load cases (3×uniaxial tension, 3×shear) are analyzed.

Results

For the big FEM models, the mixed boundary conditions give exactly the same result as the periodic BCs (=reference solution). The uniform displacement BCs (="upper bound") show important overestimation of elastic material parameters (Fig. 2), where the errors are higher for the shear moduli and decrease with increasing BVTV.

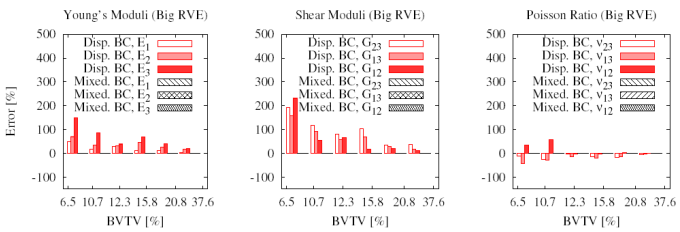

Figure 2: Error in the Young's moduli, shear moduli, and Poisson's ratio for the big (10.4 mm) FEM model. The results are related to the results with periodic BCs.

A similar but more pronounced trend is visible for the small RVE (Fig. 3). The uniform displacement BCs yield fully anisotropic stiffness tensors, while mixed BCs give only orthotropic stiffness tensors. The error between the results of the small and big RVE in the case of mixed BCs is negligible. Force controlled BCs (lower bound) give in the present case

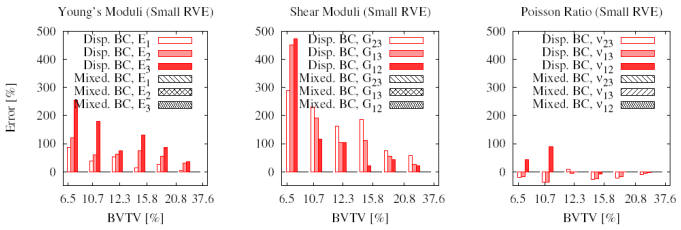

Figure 3: Error in the Young's moduli, shear moduli, and Poisson's ration for the small (5.4 mm) FEM model. The results are related to the results from the big RVE with periodic BCs.

of a porous media "zero" stiffnesses and, therefore, are not included.

Discussion

Orthogonal mixed BCs can be realized only in at least orthotropic materials (i.e. the bone RVE have to be rotated before the FEM analysis). But mixed BCs are the best choice because they give the same overall elastic properties as periodic BCs.

References

[1] B. Van Rietbergen, A. Odgaard, J. Kabel, R. Huiskes (1996): Direct mechanics assessment of elastic symmetries and properties of trabecular bone architecture. *Journal of Biomechanics*, **29**, 1653–1657.

[2] C. Huet (1990): Application of variational concepts to size effects in elastic heterogeneous bodies. *Journal of the Mechanics and Physics of Solids*, **38**, 813–841.

[3] P. Kowalczyk (2003): Elastic properties of cancellous bone derived from finite element models of parameterized microstructure cells. *Journal of Biomechanics*, **36**, 961–972.

[4] R. Hill (1963): Elastic properties of reinforced solids: Some theoretical principles. *J. Mech. Phys. Solids*, **11**, 127–140.

[5] S. Hazanov (1999): On apparent properties of nonlinear heterogeneous bodies smaller than the representative volume. *Acta Mechanica*, **134**, 123–134.

[6] M. Ostoja-Starzewski (2006): Material spatial randomness: From statistical to representative volume element. *Probabilistic Engineering Mechanics*, **21**, 112–132.

[7] S. Hazanov, C. Huet (1994): Order relationships for boundary conditions effect in heterogeneous bodies smaller than the representative volume. *Journal of the Mechanics and Physics of Solids*, **42**, 1995–2011.

[8] D. H. Pahr (2003): *Experimental and Numerical Investigations of Perforated FRP-Laminates.* Fortschritt-Berichte VDI Reihe 18 Nr. 284. VDI-Verlag, Düsseldorf, Germany.

Numerical Modelling of Large Deforming Foam Materials by the Computational Homogenization Method

V. Lukeš*, E. Rohan

Dept. of Mechanics, University of West Bohemia, Pilsen
Univerzitní 22, 306 14 Plzeň, Czech Republic
lukes@kme.zcu.cz, rohan@kme.zcu.cz

Summary: In this paper we treat large deforming solids with inclusions filled by a compressible ideal gas. This simplified model can represent such widely used materials as polymer foams, etc. Our mathematical model is based on the two-scale homogenization procedure, where the material model at the macroscopic scale is described in terms of the homogenized (effective) material parameters obtained by solving the local microscopic problems. The parallel computational strategy is proposed to solve the large number of the local microscopic subproblems.

Introduction

The problem of computing large deformations in a heterogeneous media ([3], [4]) is characterized by non-uniform change in the microstructure, the macroscopic properties depend on the spatial position. The system of governing equations is nonlinear and the multi-scale analysis becomes fully coupled, it results in a sequence of the macroscopic and the local microscopic problems.

The assumption of periodicity is crucial for the application of the homogenization method. The microstructure is assumed to be formed as a periodic lattice generated by a representative volume element (RVE) which reflects geometrical arrangement of the structure at the microlevel, see Fig. 1.

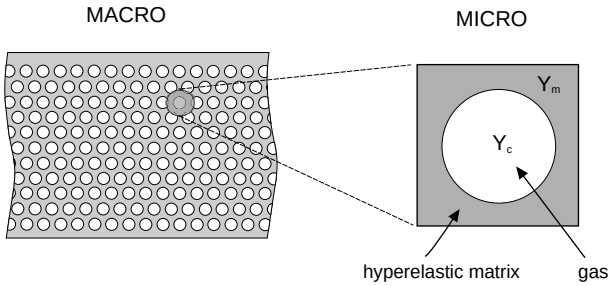

Figure 1: Macro- and micro-scale, structure of the RVE.

Two scale homogenized model

The homogenization procedure ([1]) is applied to the micro-model based on the hyperelastic material model (matrix) and adiabatic process of the ideal gas (inclusion). The incremental updated Lagrangian formulation is used for linearization of the finite deformation problem, cf. [3]

The microscopic representative cell Y is decomposed as $Y = \overline{Y_m \cup Y_c}$, where Y_m is the matrix and Y_c is the inclusion. The Cauchy stress in the matrix is given by the strain energy function (neo-Hookean or Mooney-Rivlin model) whereas in the inclusion the shear stress is not defined and the pressure is derived from formula for the ideal gas

$$p\,V^{\kappa} = \text{const.} \tag{1}$$

Local microscopic problem

The following local cell problems (in discretized form) are solved to compute the corrector functions χ_i^{kl} for displacements, π^{kl} for the pressure in the matrix and $\bar{\pi}^{kl}$ for the pressure in the inclusion

$$\begin{bmatrix} {}^{\mu}\boldsymbol{K} & -{}^{\mu}\boldsymbol{K}_p & {}^{\mu}\boldsymbol{K}_{p0} \\ -{}^{\mu}\boldsymbol{K}_p^T & {}^{\mu}\boldsymbol{I}_m & \\ {}^{\mu}\boldsymbol{K}_{p0}^T & & {}^{\mu}\boldsymbol{I}_c \end{bmatrix} \begin{bmatrix} \boldsymbol{\chi}^{kl} \\ \boldsymbol{\pi}^{kl} \\ \bar{\boldsymbol{\pi}}^{kl} \end{bmatrix} = \begin{bmatrix} {}^{\mu}\boldsymbol{K}\,\boldsymbol{\Pi}^{kl} \\ -{}^{\mu}\boldsymbol{K}_p\,\boldsymbol{\Pi}^{kl} \\ -|Y_c|\,\delta_{kl} \end{bmatrix}, \tag{2}$$

where ${}^{\mu}\boldsymbol{K}$ is the tangent stiffness matrix, ${}^{\mu}\boldsymbol{K}_p$ and ${}^{\mu}\boldsymbol{K}_{p0}$ are matrices corresponding to the pressure terms, ${}^{\mu}\boldsymbol{I}_m$ and ${}^{\mu}\boldsymbol{I}_c$ involve the compressibility parameters of the matrix and inclusion, $\boldsymbol{\Pi}_i^{kl} = \delta_{ik}\,y_l$.

The microstructure must be updated at each macro-iteration step using the macroscopic deformation, this updating process does not result in an equilibrated microscopic configuration. In order to satisfy equilibrium conditions, we must find correct displacement and pressure fields using the ULF algorithm. It means to solve the system (2) (with different right-handside terms) iteratively for the (micro)increments $\delta\boldsymbol{u}$, $\delta\boldsymbol{p}$, $\delta\bar{\boldsymbol{p}}$, see Fig. 2.

Global macroscopic problem

The correctors $\boldsymbol{\chi}_i^{kl}$, $\boldsymbol{\pi}^{kl}$ and $\bar{\boldsymbol{\pi}}^{kl}$ determine the homogenized stiffness coefficients $\mathcal{Q}_{ijkl}$

$$\mathcal{Q}_{ijkl} = \frac{1}{|Y|}\left[\left(\boldsymbol{\Pi}^{kl} - \boldsymbol{\chi}^{kl}\right)^T {}^{\mu}\boldsymbol{K}\,\left(\boldsymbol{\Pi}^{ij} - \boldsymbol{\chi}^{ij}\right)\right] + \\ + \bar{p}^0\left(\delta_{jk}\delta_{il} - \delta_{ij}\delta_{kl}\right), \tag{3}$$

where $\bar{p}^0$ is the inclusion pressure.

In order to constitute the macroscopic subproblem we have to define the averaged (averaging over the microscopic domain) stress $\mathcal{S}_{ij}$

$$\mathcal{S}_{ij} = \frac{1}{|Y|}\left[\int_{Y_m} \sigma_{ij}\,dY - \bar{p}^0\,\delta_{ij}\,|Y_c|\right]. \tag{4}$$

At the global macroscopic level the goal is to find the macroscopic increment of displacements $\Delta \boldsymbol{u}^0$, it is obtained by solving the macroscopic system involving the homogenized stiffness coefficients $\mathcal{Q}_{ijkl}$ ($^M\boldsymbol{K} = {}^M\boldsymbol{K}(\mathcal{Q})$) and the averaged stress $\mathcal{S}_{ij}$ ($f = f(f_{\text{extern}}, \mathcal{S})$)

$$^M\boldsymbol{K}\,\Delta u^0 = \boldsymbol{f}. \tag{5}$$

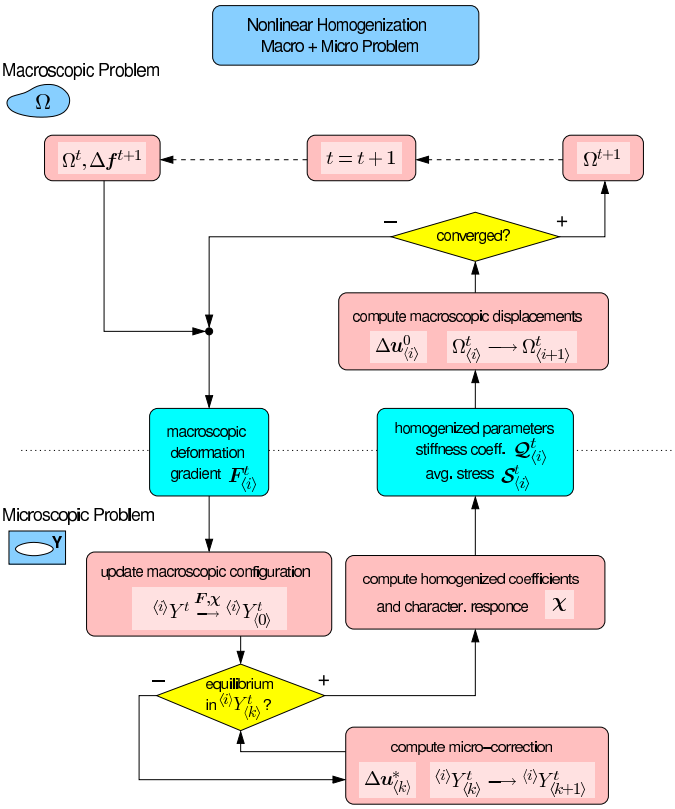

Figure 2: Macro-micro computational algorithm.

Parallel strategy

The resolution of the coupled microscopic subproblems presents solving the system of linear equations in each integration point of the macroscopic problem. In the case of 3D structures the number of microproblems is very large and resolution time enormous. The resolution time can be reduced using a parallel algorithm.

For the parallel computation we use a cluster of Linux machines communicating via the MPI library. We assign one computational node (master) to solve the macroscopic problem and the others (slaves) work on the microscopic ones as demanded by the master. Since data needed to communicate between the master and the slaves are quite small we achieve nearly linear speedup, cf. Fig. 3.

Acknowledgment: The research is supported by the project MSM 4977751303 of the Czech Republic.

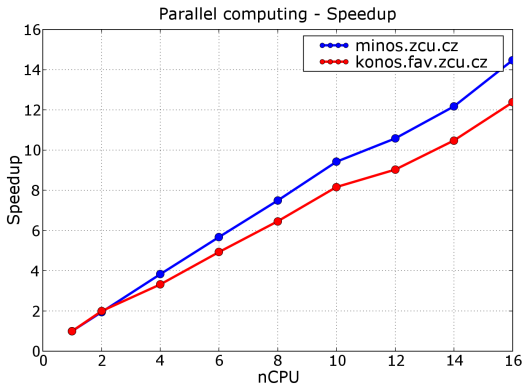

Figure 3: Speedup: 3D problem; 1280 microscopic subproblems × 5 macro-iterations; cluster MINOS and KONOS.

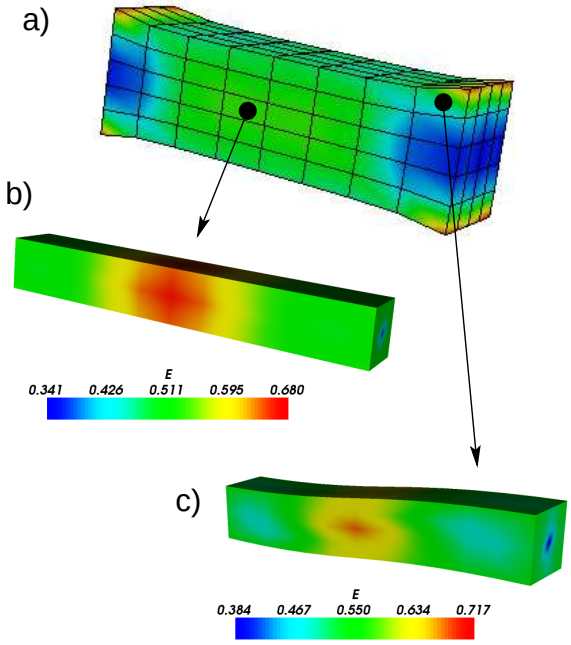

Figure 4: a) Macroscopic deformation, b) and c) microscopic deformation at two different points of the macrodomain.

References

[1] D. Cioranescu, P. Donato (1999): *An Introduction to Homogenization*. Oxford University Press, Oxford.

[2] B. Markert (2005): *Porous Media Viscoelasticity with Application to Polymeric Foams*. Universität Stuttgart, Stuttgart.

[3] E. Rohan, R. Cimrman, V. Lukeš (2006): Numerical modelling and homogenized constitutive law of large deforming fluid saturated heterogeneous solids. *Int. J. of Computers & Structures*, **84**, 1095–1114.

[4] N. Takano, Y. Ohnishi, M. Zako, K. Nishiyabu (2000): The formulation of homogenization method applied to large deformation problem for composite materials. *Int. J. of Solids and Structures*, **37**, 6517–6535.

'Universal' Microstructural Patterns in Cortical and Trabecular, Extracellular and Extravascular Bone Materials, Quantified through Multiscale Continuum Microelasticity

Ch. Hellmich*, A. Fritsch

Vienna University of Technology, Institute for Mechanics of Materials and Structures
Karlsplatz 13/202, A-1040 Wien, Austria
christian.hellmich@tuwien.ac.at, andreas.fritsch@tuwien.ac.at

Summary: This paper describes a multiscale homogenization technique valid for the anisotropic elasticity of bone materials across various species and observation scales.

Bone materials are characterized by an astonishing variability and diversity. Still, because of 'architectural constraints' due to once chosen material constituents and their physical interaction, the fundamental hierarchical organization or basic building plans of bone materials remain largely unchanged during biological evolution (Gould and Lewontin, 1979). Such universal patterns of microstructural organization govern the mechanical interaction of the elementary components of bone [hydroxyapatite, collagen, water; with directly measurable tissueindependent elastic properties (Katz and Ukraincik, 1971; Cusack and Miller, 1979)], which are here quantified through a multiscale homogenization scheme (Zaoui, 2002; Fritsch and Hellmich, 2006) delivering effective elastic properties of bone materials: At a scale of 10 nm, long cylindrical collagen molecules, attached to each other at their ends by $\sim$ 1.5 nm long crosslinks and hosting intermolecular water inbetween, form a contiguous matrix called wet collagen [Fig. 1(a)]. At a scale of several hundred nanometers, wet collagen and mineral crystal agglomerations interpenetrate each other, forming the mineralized fibril (Fig. 1(b)]. At a scale of 5-10 microns [Fig. 1(d)], the extracellular solid bone matrix is represented as collagen fibril inclusions embedded in a foam [Fig. 1(c)] of largely disordered (extrafibrillar) mineral crystals (Hellmich and Ulm, 2002; Hellmich et al., 2004). At a scale above the ultrastructure, where lacunae are embedded in extracellular bone matrix, the extravascular bone material is observed [Fig. 1(e)]. Model estimates predicted from tissue-specific composition data gained from a multitude of chemical and physical tests (Lees, 1987) agree remarkably well with corresponding acoustic stiffness experiments (Lees et al., 1983) across a variety of cortical and trabecular, extracellular and extravascular materials. Besides from reconciling the well-documented, seemingly opposed concepts of 'mineral-reinforced collagenmatrix' (Currey, 1969) and 'collagen-reinforced mineral matrix' (Crolet et al., 1993; Hellmich and Ulm, 2002) for bone ultrastructure, this approach opens new possibilities in the exploitation of computer tomographic data for nano-to-macro mechanics of bone organs.

References

[1] J. Crolet, B. Aoubiza, A. Meunier (1993): Compact bone: numerical simulation of mechanical characteristics. *Journal of Biomechanics*, 26, 677–687.

[2] J. Currey (1969): The relationship between the stiffness and the mineral content of bone. *Journal of Biomechanics*, 2, 477–480.

[3] S. Cusack, A. Miller (1979): Determination of the elastic constants of collagen by Brillouin light scattering. *Journal of Molecular Biology*, 135, 39–51.

[4] A. Fritsch, C. Hellmich (2006): 'Universal' microstructural patterns in cortical and trabecular, extracellular and extravacular bone materials: Micromechanics-based prediction of anisotropic elasticity. *Journal of Theoretical Biology*, 244, 597–620.

[5] S. Gould, R. Lewontin (1979):The spandrels of SanMarco and the Panglossian paradigm: a critique of the adaptionist program. *Proceedings of the Royal Society of London, Series B*, 205, 581–598.

[6] C. Hellmich, J. F. Barthélémy and L. Dormieux (2004): Mineral-collagen interactions in elasticity of bone ultrastructure – a continuum micromechanics approach. *European Journal of Mechanics A-Solids*, 23, 783–810.

[7] C. Hellmich, F. J. Ulm (2002): Are mineralized tissues open crystal foams reinforced by crosslinked collagen? – some energy arguments. *Journal of Biomechanics*, 35, 1199–1212.

[8] J. Katz, K. Ukraincik (1971): On the anisotropic elastic properties of hydroxyapatite. *Journal of Biomechanics*, 4, 221–227.

[9] S. Lees (1987): Considerations regarding the structure of the mammalian mineralized osteoid from viewpoint of the generalized packing model. *Connective Tissue Research*, 16, 281–303.

[10] S. Lees, J. Ahern, M. Leonard (1983): Parameters influencing the sonic velocity in compact calcified tissues of various species. *Journal of the Acoustical Society of America*, 74, 28–33.

[11] A. Zaoui (2002): Continuummicromechanics: Survey. *Journal of Engineering Mechanics (ASCE)*, 128, 808–816.

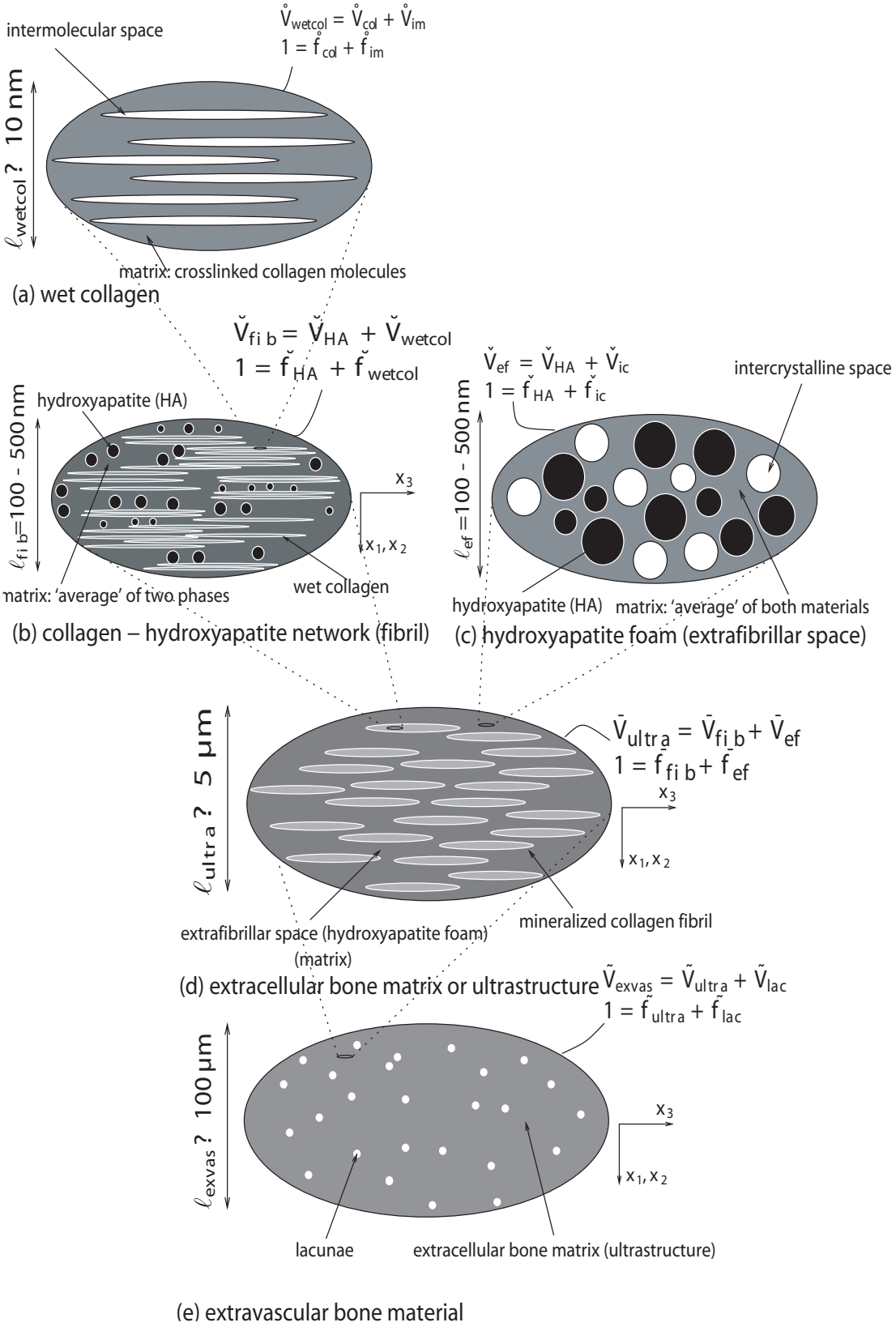

Figure 1: Micromechanical representation of bone material by means of a five-step homogenization procedure (Fritsch and Hellmich, 2006).

Multiscale Characterization and Modeling of Creep and Autogenous Shrinkage of Early-Age Cement-Based Materials

C. Pichler[1], **R. Lackner**[1,2*]

[1]Institute for Mechanics of Materials and Structures
Vienna University of Technology
Karlsplatz 13/202, A-1040 Vienna, Austria
{Christian.Pichler,Roman.Lackner}@tuwien.ac.at

[2]FG Computational Mechanics
Technical University of Munich
Arcisstraße 21, 80333 Munich, Germany
Lackner@bv.tum.de

Summary: Concrete is a partially saturated, porous medium gaining strength and stiffness in the course of the hydration process, i.e., the chemical reaction between anhydrous cement and water. Inelastic material behavior of concrete such as *viscoelasticity* (time-dependent deformation under sustained loading) and *autogenous shrinkage* [bulk deformation of the (closed) cement-based material system associated with capillary depression of the pore liquid] are affected by the hydration extent. Unlike material models formulated exclusively at the macroscopic scale of observation, multiscale models allow the explicit link of complex macroscopic behavior to its respective origin at finer scales of observation with a sound physical / chemical basis of the employed constitutive laws at these finer scales. Whereas finer-scale composition (and its history) is accessible through recently developed hydration models for the main clinker phases in ordinary Portland cement (OPC) [1], a *multiscale* model for the prediction of autogenous-shrinkage deformations and basic creep of early-age cement-based is presented in this paper.

The proper description of the mechanical behavior of concrete is essential for the reliable prediction of the performance and safety of structures made of plain, reinforced, and/or prestressed concrete. At early ages, the beneficial increase of the stiffness and strength of concrete in the course of hydration is accompanied by autogenous-shrinkage deformations and significant creep under loading. Opposed to material models formulated exclusively at the so-called macroscale, i.e., the scale of structural analysis, capturing the mentioned characteristics of early-age concrete in a phenomenological manner, a multiscale model (see Figure 1) for the prediction of autogenous-shrinkage deformations and basic creep of early-age concrete is developed in this paper, covering:

- *Experimental characterization at finer scales of observation.*
  Nanoindentation (NI), characterized by driving a tough (usually a diamond) tip into the ground and polished sample surface, is employed for experimental characterization at the micrometer range. Based on the obtained NI-test results, the creep behavior of calcium-silicate-hydrates (CSH) is found to be of logarithmic type [4].

- *Identification of basis mechanical properties of the material phases encountered at finer scales of observation from NI-test results*
  Lacking analytical solutions for conical indentation into materials showing viscoelastic-plastic behavior, numerical results are used to construct solutions for (i) viscoelastic indentation and (ii) viscoelastic-cohesive indentation in dimensionless form. These relations are employed for identification of material properties from NI-test data [6, 2].

- *Upscaling schemes for elastic and viscoelastic material behavior.*
  Classical homogenization schemes for upscaling of elastic properties based on continuum micromechanics, e.g., the Mori-Tanaka scheme, are expanded towards consideration of (i) eigenstresses for upscaling of autogenous-shrinkage deformations [5] and (ii) viscoelastic behavior of CSH for upscaling of creep properties [3]. As regards the latter, the Laplace-Carson transformation of the Mori-Tanaka scheme is employed.

- *Experimental verification of upscaling schemes.*
  In order to assess the quality of the developed upscaling schemes, results from (i) autogenous-shrinkage experiments conducted at the laboratory of the Institute for Mechanics of Materials and Structures, Vienna University of Technology [5], and (ii) creep experiments taken from the open literature [3] are employed. The developed multiscale model links the logarithmic type creep behavior observed at the macroscale to finer scales, considering the continuously changing finer-scale composition as well as the stiffening effect of inclusions and the compliant effect of (partially saturated) pores at the different observation scales.

- *Application to shotcrete tunnel analysis.*
  Finally, the multiscale model is employed to specify the early-age properties of shotcrete within a so-called hybrid analysis of a shotcrete tunnel lining, allowing consideration of the actual mix design and the conditions at the construction site. The performed hybrid analysis provides access to the level of loading $\bar{\mathcal{L}}$ of the tunnel support structure, which is illustrated for one cross-section of Lainzer tunnel near Vienna, Austria (see Figure 2).

Thus, by using the developed multiscale model in structural analysis, the actual composition and (microstructural) loading of early-age concrete can be considered. Moreover, since the link between the macroscopic behavior of the material and its composition is established, performance-based optimization of the mix design is possible.

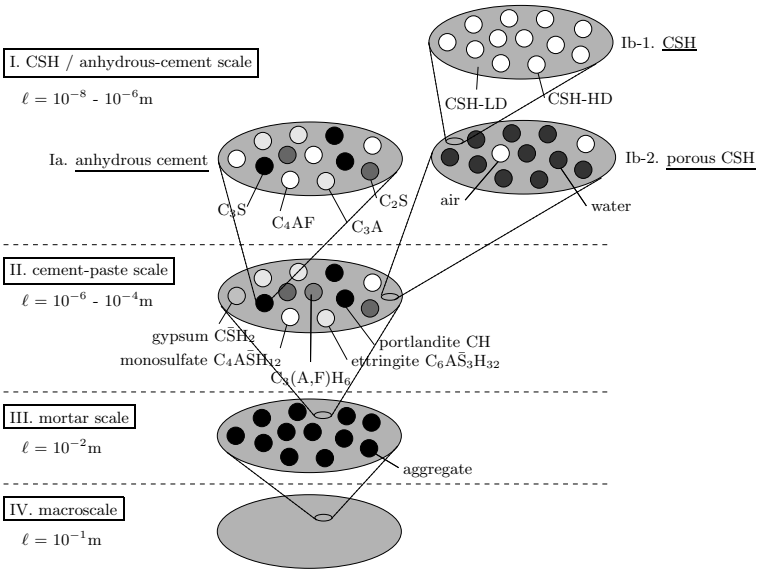

Figure 1: Scales of observation for upscaling of creep and shrinkage properties of cement-based materials [ℓ = size of representative volume element (RVE)]

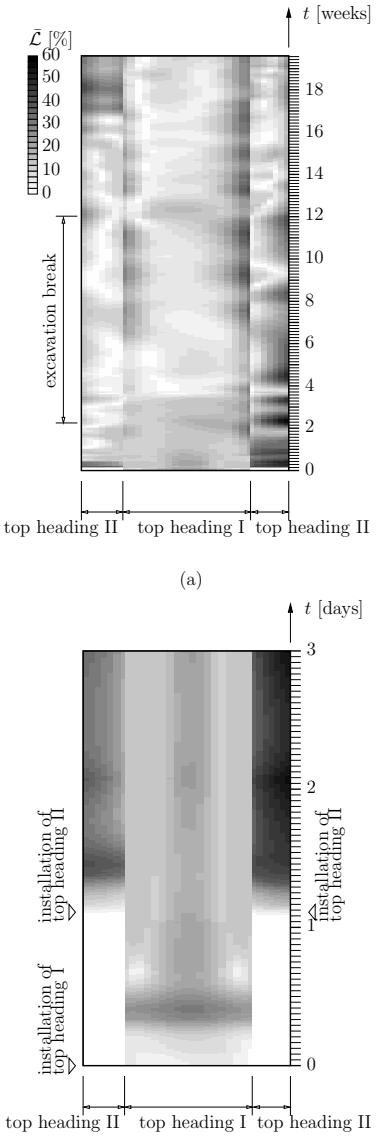

Figure 2: History of distribution of $\bar{\mathcal{L}}$ in shotcrete lining at considered MCS (top view): for a time span of (a) 4.5 month and (b) 3 days after application ($t = 0$ refers to the time instant of installation of top heading I)

References

[1] O. Bernard, F.-J. Ulm, and E. Lemarchand (2003): A multiscale micromechanics-hydration model for the early-age elastic properties of cement-based materials, *Cement and Concrete Research*, **33**, 1293–1309.

[2] Ch. Pichler (2007): *Multiscale characterization and modeling of creep and autogenous shrinkage of early-age cement-based materials*, PhD thesis, Vienna University of Technology.

[3] Ch. Pichler and R. Lackner (2007): A multiscale micromechanics model for early-age basic creep of cement-based materials, *Engineering Fracture Mechanics*, Submitted for publication.

[4] Ch. Pichler and R. Lackner (2007): Nanoindentation of ordinary portland cement paste: Identification of basic mechanical properties, *Strain*, Accepted for publication.

[5] Ch. Pichler, R. Lackner, and H. A. Mang (2007): A multiscale micromechanics model for the autogenous-shrinkage deformation of early-age cement-based materials, *Engineering Fracture Mechanics*, **74**, 34–58.

[6] Ch. Pichler, R. Lackner, and F.-J. Ulm (2006): Scaling relations for viscoelastic-cohesive indentation – identification of material properties from instrumented indentation. In G. Meschke, R. de Borst, H.A. Mang, and N. Bicanic, editors, *Computational Modelling of Concrete Structures – Proceedings of EURO-C 2006*, pages 191–202, Mayrhofen, Austria, Taylor and Francis Group, London.

Computational Homogenization for Discrete Micro-Structures Including Damage

S. Ricker[1]*, **A. Menzel**[2], **P. Steinmann**[1]

[1]Chair of Applied Mechanics
Postfach 3049, 67653 Kaiserslautern, Germany
sricker@rhrk.uni-kl.de, ps@rhrk.uni-kl.de

[2]Institute of Mechanics and Control Engineering
Paul-Bonatz-Str. 9–11, 57076 Siegen, Germany
menzel@imr.mb.uni-siegen.de

Summary: Within this work we focus on the extension of the computational homogenization scheme – or the FE^2-Method – towards the simulation of discrete micro-systems, especially structural elements on the micro-level. Furthermore, a damage model monitoring local softening and failure is incorporated.

Motivation

The past years have been marked by a growing significance in so-called multi-scale and homogenization methods. This is motivated by the fact that a wide class of engineering materials possess a heterogeneous micro-structure like, for instance, metal foams, alloys or composite materials, which become more and more important due to their diverse competitiveness to classical materials. On account of these micro-structures, it is not sufficient to simulate the macroscopic behavior of such materials with pre-assumed (overall) material parameters, or rather constitutive-law-based standard methods. Therefore, the main goal of the homogenization method applied is to define macroscopic material behavior, e.g. stress-strain relations, based on the underlying micro-structures. The coupling of the length scales is based on the following relations between the macroscopic and microscopic deformations and stresses:

$$\boldsymbol{F}_M = \frac{1}{\mathcal{V}_0}\int_{\mathcal{V}_0} \boldsymbol{F}_m \,\mathrm{d}V_0 = \frac{1}{\mathcal{V}_0}\int_{\partial\mathcal{V}_0} \boldsymbol{x}\otimes\boldsymbol{N}\,\mathrm{d}A_0 \quad (1)$$

$$\boldsymbol{P}_M = \frac{1}{\mathcal{V}_0}\int_{\mathcal{V}_0} \boldsymbol{P}_m \,\mathrm{d}V_0 = \frac{1}{\mathcal{V}_0}\int_{\partial\mathcal{V}_0} \boldsymbol{t}_0\otimes\boldsymbol{X}\,\mathrm{d}A_0\,. \quad (2)$$

In this work we apply the so-called computational homogenization scheme which is suitable for the coupling between a macroscopic continuous system simulated via FE methods and various micro-systems. For an overview of the coupling with continuous FE simulated micro-systems via first-order deformation gradients at small strains see e.g. [1] or for the large strain case see [2, 3], whereby the latter also focuses on non-linear history dependent material behavior. An extension of these first-order homogenization is given by the so-called higher-order homogenization schemes – see [4] – which are also able to incorporate the length scales of the underlying micro-structures.

The advantages of the (first-order) computational homogenization scheme applied here can be shortly summarized as follows: It is applicable to the small and the large strain case both on the micro- and macro-structure. Furthermore, it is possible to include nonlinear material behaviors on the micro-level. The micro-level may be simulated with various techniques like for instance FE methods, lattice statics or molecular dynamics. On top of that, the homogenization procedure can be coupled with interface formulations which can for instance be used for simulations of delamination processes.

Discrete micro-structures

The present work deals with the extension of the continuous micro-systems – presented in the references – to discrete micro-systems. Accordingly, the underlying micro-structure in each macroscopic integration point is considered as a structural setting – see Fig. 1 for an illustration of the relation between the macroscopic and the microscopic level.

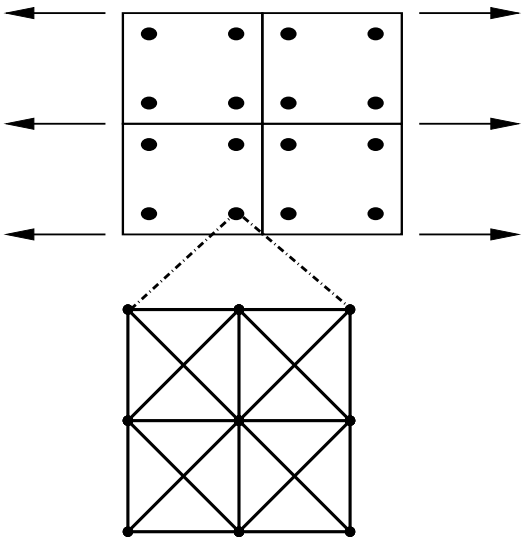

Figure 1: Connection between Macro- and Micro-Level.

Preliminary studies focus especially on truss structures which represent systems where mass points under certain loadings may quasi-statically interact with their immediate neighbors via springs – see e.g. the work by Friesecke and Theil [5] for such a system constrainted by the Cauchy-Born rule. To give an ex-

ample, we here refer to a truss element, so that

$$\boldsymbol{F}^e_m = \lambda^e_m \, \boldsymbol{n}^e \otimes \boldsymbol{N}^e \; , \; \boldsymbol{P}^e_m = P^e_m \, \boldsymbol{n}^e \otimes \boldsymbol{N}^e \, . \qquad (3)$$

with $\|\boldsymbol{n}^e\| = \|\boldsymbol{N}^e\| = 1$ and $\lambda^e = \frac{l^e}{L^e}$

The influence of different admissible boundary conditions – necessary to perform the macro-micro transition – on the homogenized macroscopic quantities will additionally be highlighted. Boundary conditions are admissible if they satisfy the so-called Hill-Mandel condition requiring that the variation of the work performed on the macro-level should be equal to the volume average of the variation of the work on the micro-level. Due the equilibrium of forces at the inner nodes this condition simplifies in the discrete form to a sum over all resulting forces in the trusses and the nodal displacements at the boundary nodes:

$$\boldsymbol{P}_M \; : \; \delta \boldsymbol{F}_M = \frac{1}{\mathcal{V}_0} \sum_{\text{bc-nodes}} \sum_{\text{trusses}} \boldsymbol{f}^{res} \cdot \delta \boldsymbol{u}_m . \qquad (4)$$

Examples for such boundary conditions are linear displacements or constant tractions on the boundary, or periodic displacements and antiperiodic tractions. According to these boundary conditions, deformation or load, respectively, is applied to the micro-structure via, e.g., the macroscopic deformation gradient tensor in a deformation-driven scheme.

In the special case of discrete microstructural settings it should be pointed out that in equations (1) and (2) the boundary integral may be replaced by a discrete sum over all boundary nodes:

$$\boldsymbol{F}_M = \frac{1}{\mathcal{V}_0} \sum_{\text{bc-nodes}} \boldsymbol{x} \otimes \boldsymbol{N} \qquad (5)$$

$$\boldsymbol{P}_M = \frac{1}{\mathcal{V}_0} \sum_{\text{bc-nodes}} \sum_{\text{trusses}} \boldsymbol{f}^{res} \otimes \boldsymbol{X} \, , \qquad (6)$$

whereby $\boldsymbol{f}^{res}$ exhibits the resulting force at each boundary node emerged from the boundary conditions applied.

Damage model

In addition to the extension towards discrete micro-structures, a damage model has been incorporated into the homogenization scheme. The damage model applied to the micro-level simulates a continuous decrease in material stiffness. Thus a softening effect is observed until total failure occurs in the material at local macroscopic integration points. In order to implement this damage formulation a damage variable d is introduced, whereby $0 \leq d \leq 1$. Adopting a strain-based formulation, compare [6], the algorithmic update results in

$$\kappa^{n+1} = \max \left(\bar{W} \left(\boldsymbol{F}^{n+1}_m \right) , \kappa^n , \kappa^0 \right) \qquad (7)$$

$$d^{n+1} = \phi \left(\kappa^{n+1} \right) , \qquad (8)$$

wherein $\bar{W}$ denotes the effective strain energy – taking the reduced format $\bar{W} \left(\lambda^e_m \right)$ for a truss element – and ϕ is assumed as

$$\phi \left(\kappa \right) = 1 - \exp \left(h \left[\kappa^0 - \kappa \right] \right) . \qquad (9)$$

Accordingly, the Piola stress is derived from

$$\boldsymbol{P}_m = \partial_{\boldsymbol{F}_m} W \left(d, \boldsymbol{F}_m \right) \qquad (10)$$

$$\text{with } W \left(d, \boldsymbol{F}_m \right) = \left[1 - d \right] \bar{W} \left(\boldsymbol{F}_m \right) . \qquad (11)$$

Outlook

Concerning future research, the truss formulation on the micro-level will be extended to beam structures – see e.g. [7]. Furthermore, the presented damage model may be extended towards the simulation of defects contained in the microscopic specimen which enables the comparison with atomistic simulations, for example with lattice statics based on pair potentials or the embedded atom method.

References

[1] C. Miehe, A. Koch (2002): Computational Micro-to-Macro Transitions of Discretized Microstructures Undergoing Small Strains. *Archive of Applied Mechanics*, **72**, 300–317.

[2] C. Miehe (2003): Computational Micro-to-Macro Transitions of Discretized Microstructures of Heterogeneous Materials at Finite Strains Based on the Minimization of Averaged Incremental Energy. *Computer Methods in Applied Mechanics and Engineering*, **192**, 559–591.

[3] V. Kouznetsova, W. A. M. Brekelmans, F. P. T. Baaijens (2001): An Approach to Micro-Macro Modeling of Heterogeneous Materials. *Computational Mechanics*, **27**, 37–48.

[4] V. Kouznetsova, M. G. D. Geers, W. A. M. Brekelmans (2002): Multi-Scale Constitutive Modelling of Heterogeneous Material with a Gradient Enhanced Computational Homogenization. *International Journal for Numerical Methods in Engineering*, **54**, 1235–1260.

[5] G. Friesecke, F. Theil (2002): Validity and Failure of the Cauchy-Born Hypothesis in a Two-Dimensional Mass-Spring Lattice. *Journal of Nonlinear Science*, **12**, 445–478.

[6] J. C. Simo, J. W. Ju (1987): Strain- and Stress-based Continuum Damage Models: I. Formulation. *Journal of Solids and Structures*, **23**, 821–840.

[7] T. Ebinger, H. Steeb, S. Diebels (2005): Modeling Macroscopic Extended Continua with the Aid of Numerical Homogenization Schemes. *Computational Materials Science*, **32**, 337–347.

Part VIII

Instabilities, Anisotropy, Enhanced Continua

Why Does a Domain of Bifurcation Exist in Granular Materials?

F. Nicot[1,3*], **L. Sibille**[2,3], **F. Darve**[2,3]

[1]Cemagref, Unité de Recherche Erosion Torrentielle Neige et Avalanches
Grenoble, France
francois.nicot@grenoble.cemagref.fr

[2]Laboratoire Sols Solides Structures, UJF-INPG-CNRS
Grenoble, France

[3]RNVO Research Group "Natural Hazards and Structure Vulnerability"

Summary: This contribution examines the relation between both microscopic and macroscopic second-order works. It is shown that the vanishing of the microscopic second-order work, related to a material or a geometrical cause, may induce the vanishing of the macroscopic second-order work, indicating that the mechanical state of the specimen is unsustainable.

Both experimental and numerical investigations ascertain that for nonassociated materials such as granular assemblies a broad domain exists, strictly within the plastic limit, where different failure modes can coexist (Darve and Laouafa, 2000 and 2002; Darve *et al*., 2004; Darve and Vardoulakis, 2005). We focus herein on the notion of loss of sustainability, which was recently shown to be a proper mode of bifurcation (Nicot *et al*., 2006). Given a mechanical rate-independent system in equilibrium under prescribed control parameters, the mechanical state is reputed unsustainable if and only if the system can reach spontaneously (namely, without change in the control parameters) another mechanical state. We establish in a very general manner that such bifurcation modes, characterized by a development of kinetic energy, are detected by the vanishing of the second-order work, defined in a semi-Lagrangian formalism as the inner product between the Piola-Kirchoff stress tensor of the first kind and the velocity gradient tensor (Nicot *et al*., 2006).

Specializing our investigation to granular materials, these theoretical predictions were perfectly confirmed from recent discrete element simulations. For this purpose, a granular sample, in a given mechanical state (such that an incremental loading direction leading to the vanishing of the second-order work exists) after a given loading history, was considered. The prescribed control parameters are imposed to remain constant. It was shown that any infinitesimal perturbation applied to any granule induces a dramatic increase in the kinetic energy of the assembly, leading to the collapse of the material. If the same experiment is carried out by considering a mechanical state such that no incremental loading direction leading to the vanishing of the second-order work exists, then no amplification in the kinetic energy of the system is observed (Sibille *et al*., 2007).

Starting from micromechanical considerations, we show that both macroscopic (on the specimen scale) and microscopic (on contact scale) second-order works are related through a fundamental multiscale relation (Nicot *et al*., 2007). This relation expresses that the macroscopic second-order work for the whole granular assembly is equal the sum of the microscopic second-order works computed on each contact, with respect to the frame attached to each contact. This relation is at the basis of our microstructural investigation. In particular, it was established that two main causes are responsible for the vanishing of the macroscopic second-order work:

- A material cause, related to the plastic behavior of some contacts.
- A geometrical cause, related to the deletion of contacts.

In particular two-dimensional conditions, the vanishing of the microscopic second-order work implies that an unloading along the normal direction of the contact occurs, and that the incremental tangential displacement is higher than a positive limit value function of the incremental normal displacement (Nicot and Darve, 2006). As verified from simulations carried out using a micro-mechanical model (Nicot and Darve, 2005; Darve and Nicot, 2005a and 2005b), conditions for the vanishing of the macroscopic second-order work are less restrictive in two dimensions than in three dimensions.

In conclusion, the microscopic second-order work may vanish only if the considered nonopening contact is in a plastic regime and is subjected to a normal release. However, and particularly in three-dimensional conditions, the microscopic second-order work is likely to be positive even though the contact behaves plastically. It should be emphasized that the microscopic second-order work cannot vanish in a compressive situation. Thus, on a grain assembly scale, the second-order work is expected to remain positive along confined loading paths such as oedometric loading (i.e., one-dimensional compression).

Opening the contact can also contribute to the vanishing of the microscopic second-order work. This is an outstanding feature of granular materials, where sudden collapses may occur, and inducing significant rearrangements between grains. This feature was well-recognized from both experimental investigations (Oda *et al*., 1982) and numerical simulations based on a discrete element method (Bardet, 1994). In order to tackle this question, it is relevant to consider that the granular assembly can be split into two distinct regimes. Indeed, it has been established that a granular medium can be considered as composed of two distinct phases (Horne, 1965; Radjai *et al*., 1998). Specific patterns for grains that are joined by contacts transmitting high contact forces may be developed within the gran-

ular assembly. Since these patterns are responsible for the ability of the medium to transmit local forces, they are denoted force chains (or solid paths, using the terminology adopted by Horne). These chains constitute the so-called strong phase. In the vicinity of these chains, a network of weak contacts exists, associated with low contact forces; similarly, this network constitutes the so-called weak phase. However, force chains are likely to collapse abruptly; this is particularly true for rounded particles since particle rotations may occur. Indeed, it is well-known that particle rolling is to a large extent responsible for the so-called buckling effect (Oda, 1982, and more recently, Tordesillas and Walsh, 2002). The collapse of force chains induces substantial structural rearrangements, directing bursts of kinetic energy of the assembly. This geometrical "instability" can be detected by the vanishing of the second-order work. Furthermore, it has also been established (Radjai *et al*, 1998) that the low normal contact forces that exist within the weak phase may justify that several contacts are in the plastic regime, possibly leading to the vanishing of the microscopic second-order work for these contacts.

In conclusion, it was established that the vanishing of the second-order work has two origins. A geometrical origin essentially concerns the strong phase and is related to important changes in the structure resulting from the collapse of force chains. A material origin could be linked to the sliding between adjoining granules that mainly occurs within the weak phase.

References

[1] Darve, F., and Laouafa, F. (2000): Instabilities in granular materials and application to landslides. Mechanics of Cohesive-frictional Materials, Vol. 5, n ° 8, pp. 627-652.

[2] Darve, F., and Laouafa, F. (2002): Constitutive equations and instabilities of granular materials. *In* Modelling and mechanics of granular and porous materials, Capriz *et al*. eds., Birkhauser publ., pp. 3-43.

[3] Darve, F., Servant, G., Laouafa, F., and Khoa H.D.V. (2004): Failure in geomaterials, continuous and discrete analyses. Comp. Methods Appl. Mech. Engrg., Vol. 193, pp. 3057-3085.

[4] Darve, F., and Vardoulakis, I. (2005): Instabilities and degradations in geomaterials. Darve and Vardoulakis Eds., Springer publ.

[5] Darve, F., and Nicot, F. (2005a): On incremental non linearity in granular media: phenomenological and multiscale views (Part I). Int. J. Num. Anal. Methods in Geomechanics. Vol. 29, pp. 1387-1409.

[6] Darve, F., and Nicot, F. (2005b): On flow rule in granular media: phenomenological and multi-scale views (Part II). Int. J. Num. Anal. Methods in Geomechanics. Vol. 29, pp. 1411-1432.

[7] Nicot, F., and Darve, F. (2005): A multiscale approach to granular materials. Mechanics of Materials, Vol. 37 (9), pp. 980-1006.

[8] Nicot, F., and Darve, F. (2006): Micro-mechanical investigation of material instability in granular assemblies. Int. J. of Solids and Structures, Vol. 43, pp. 3569-3595.

[9] Sibille, L., Nicot, F., Donze, F., and Darve, F. (2007): Material instability in granular assemblies from fundamentally different models. Int. J. Num. Anal. Methods in Geomechanics, *in press*.

[10] Nicot, F., Darve, F., and Khoa, H.D.V. (2006): Bifurcation and second-order work in geomaterials. Int. J. Num. Anal. Methods in Geomechanics, *in press*.

[11] Nicot, F., Sibille, L., Donzé, F., and Darve, F. (2007): From microscopic to macroscopic second-order works in granular assemblies. Mechanics of Materials, *in press*.

[12] Oda, M., Konishi, J., and Nemat-Nasser, S. (1982) : Experimental evaluation of strength of granular materials, effects of particle rolling. Mechanics of Materials, Vol. 1, pp. 269-283.

[13] Tordesillas, A., and Walsh, D. C. (2002): Incorporating rolling resistance and contact anisotropy in micromechanical models of granular media. Powder Technology, Vol. 124, pp. 106-111.

[14] Radjai, F., Wolf, D., Jean, M., and Moreau, J.J. (1998): Bimodal character of stress transmission in granular packing. Physical Review Letters, Vol. 80, n ° 1, pp. 61-64.

[15] Horne, M.R. (1965): The behaviour of an assembly of rotund, rigid cohesionless particles – I, II. Proc. Royal Society London, Vol. 286, pp. 62-97.

[16] Bardet, J.P. (1994): Observations on the effects of particle rotations on the failure of idealized granular materials. Mechanics of Materials, Vol. 18, pp. 159-182.

Anisotropic Damage Model with Micro-Cracks Closure Effect for Seismic Applications

R. Desmorat*, A. Souid, F. Ragueneau

LMT-Cachan, ENS Cachan / Univ. Paris 6 / CNRS
61 av. du président Wilson, F-94235 Cachan Cedex, France
desmorat@lmt.ens-cachan.fr

Summary: An anisotropic damage model has been recently proposed for concrete with a quite reduced numbers of material parameters and with good numerical properties [1]. The dissymmetry tension/compression in such a model is due to the damage induced anisotropy. The quasi-unilateral conditions of microcracks closure were written in this initial model mainly built for monotonic applications on the hydrostatic stresses only. The present work proposes a better modeling of the microcracks closure effect. A proper 3D thermodynamics framework is used to recover both hydrostatic and shear stiffness in compression. Seismic applications are then described using multifibre beam analysis.

Introduction

Damage in quasi-brittle materials is anisotropic. Many research efforts have been made to model loading induced damage anisotropy, at different scales, leading to popular models [2]. But an important difficulty remains in most modeling approaches: the numerical cost and the model robustness. In quasi-static this point is not so crucial, but it becomes critical for dynamics applications as in earthquake engineering. On the basis of an anisotropic damage model recently proposed [1, 4] for concrete with a quite reduced numbers of material parameters and with good numerical properties (no need of an iterative process at the Gauss point level), one focuses next on phenomenological modeling for non monotonic applications of the microcracks closure effect and stiffness recovery in compression.

Thermodynamics potential

One considers Ladevèze's framework for anisotropic damage [5] in order to build a Gibbs potential $\rho\psi^\star$, with ρ the density, which can be continuously differentiated,

$$\begin{aligned}\rho\psi^\star \;=\; & \frac{1+\nu}{2E}\left[tr\left(\boldsymbol{H}\boldsymbol{\sigma}_+^D\boldsymbol{H}\boldsymbol{\sigma}_+^D\right) + \langle\boldsymbol{\sigma}^D\rangle_- : \langle\boldsymbol{\sigma}^D\rangle_-\right] \\ & + \frac{1-2\nu}{6E}\left[\frac{\langle tr\,\boldsymbol{\sigma}\rangle_+^2}{1-tr\,\boldsymbol{D}} + \langle tr\,\boldsymbol{\sigma}\rangle_-^2\right] \end{aligned} \tag{1}$$

where the notation $\langle . \rangle_-$ stands for the negative part, in terms of principal values for tensors, where ^{D} denotes the deviatoric part and where the effective damage tensor is set as $\boldsymbol{H} = (\mathbf{1}-\boldsymbol{D})^{-1/2}$. A single thermodynamics damage variable is used but which acts fully for "tension" and partially for "compression" (note that the state of stress can be 3D). In order to keep the differentiability feature of Gibbs energy a special positive part $\boldsymbol{\sigma}_+^D$ is built with the eigenvalues λ^I and the corresponding eigenvectors $\vec{T}^I$ of $(\boldsymbol{H}\boldsymbol{\sigma}^D)$ [5, 3]. The vectors $\vec{T}^I$ and λ^I are given by the eigenvalue problem

$$\boldsymbol{\sigma}^D\vec{T}^I = \lambda^I\boldsymbol{H}^{-1}\vec{T}^I \tag{2}$$

in which the normalization $\vec{T}^{I\,T}\boldsymbol{H}^{-1}\vec{T}^J = \delta_{IJ}$ is made. The positive part $\boldsymbol{\sigma}_+^D$ is then defined as

$$\boldsymbol{\sigma}_+^D = \sum_{I=1}^{3}\left[\boldsymbol{H}^{-1}\vec{T}^I\right]\left[\boldsymbol{H}^{-1}\vec{T}^I\right]^T\langle\lambda^I\rangle_+ \tag{3}$$

expression which simplifies in case of proportional loading as $\boldsymbol{\sigma}_+^D = \langle\boldsymbol{\sigma}^D\rangle_+$, the classical positive part of the deviatoric stress tensor. The elasticity law derives from Gibbs potential as $\boldsymbol{\epsilon}^e = \rho\,\partial\psi^\star/\partial\boldsymbol{\sigma}$ or:

$$\begin{aligned}\boldsymbol{\epsilon}^e = & \frac{1+\nu}{E}\left[(\boldsymbol{H}\boldsymbol{\sigma}_+^D\boldsymbol{H})^D + \langle\boldsymbol{\sigma}^D\rangle_-^D\right] \\ & + \frac{1-2\nu}{3E}\left[\frac{\langle tr\,\boldsymbol{\sigma}\rangle_+}{1-tr\,\boldsymbol{D}} + \langle tr\,\boldsymbol{\sigma}\rangle_-\right]\mathbf{1}\end{aligned} \tag{4}$$

It is continuous (all 3D stress tensor components are continuous even in non proportional loading) and takes into account the quasi-unilateral effect.

Damage criterion and damage law

A damage criterion f defines the elasticity domain as $f<0$ and damage growth as $f=0$ for any loading including tension and compression. The criterion was of the form $f = \hat{\epsilon} - \kappa(tr\,\boldsymbol{D})$ in the initial model with $\hat{\epsilon}$ Mazars equivalent strain and κ a consolidation function,

$$\kappa(tr\,\boldsymbol{D}) = a\cdot\tan\left[\frac{tr\,\boldsymbol{D}}{aA} + \arctan\left(\frac{\kappa_0}{a}\right)\right] \tag{5}$$

introducing the damage threshold κ_0 and A, a as damage parameters. A response equivalent in both monotonic tensile and compressive cases is gained by setting:

$$f = \hat{\epsilon} - \kappa\left(\frac{\boldsymbol{D}:\langle\boldsymbol{\epsilon}\rangle_+}{\max\,\epsilon_I}\right) \tag{6}$$

with $\max\,\epsilon_I$ the maximum positive extension. Expression (6) allows for tensile damage deactivation in compression. Last, damage induced anisotropy is modeled through the damage law [6]

$$\boldsymbol{D} = \dot{\lambda}\langle\boldsymbol{\epsilon}\rangle_+ \tag{7}$$

of damage governed by the positive extensions. The damage multiplier $\dot{\lambda}$ is gained from the consistency condition $f = 0$, $\dot{f} = 0$.

An example of the stress-strain response in cyclic tension is given in Fig. 1. The stiffness recovery in compression after a damaging tension can be noticed.

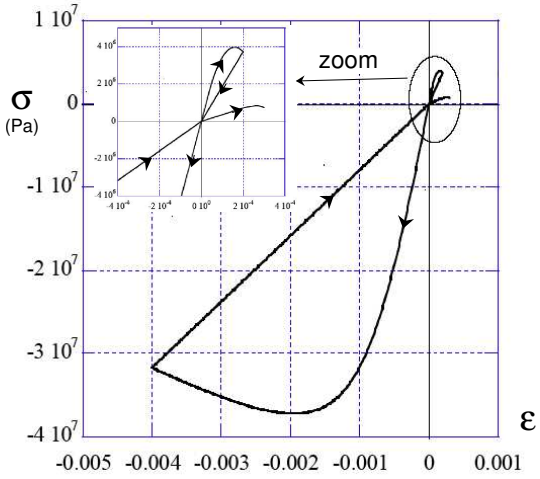

Figure 1: Tension-compression-tension

Discussion and applications

The anisotropic damage model proposed is 3D and has quite a reduced number of material parameters (5 including the 2 elasticity parameters) due to the fact that the damage anisotropy is responsible for the dissymmetry tension/compression. The present model recovers the initial anisotropic model in monotonic cases making the identification simple. It ensures the stresses continuity in 3D, the stiffness recovery (unilateral effect). Seismic applications take advantage of such a modeling as a single set of parameters is used for both tension and compression and as the non monotonic response is gained by a classical numerical scheme solving nonlinear differential equations. Using multifibre beam analysis only the 1D version of the model needs to be implemented, work which has been done in CEA Cast3m Finite Element code.

References

[1] R. Desmorat (2004): Modèle d'endommagement anisotrope avec forte dissymétrie traction/compression, *5è journées RF2B*, Liège, Belgium, 5-6 July.

[2] Z.P. Bazant and P. C. Prat (1998): Microplane model for brittle plastic material: I. Theory and II. Verification, *Journal of Engineering Mechanics ASCE*, **114**, 1672–1702.

[3] J. Lemaitre, R. Desmorat (2005): *Engineering Damage Mechanics:Ductile, Creep, Fatigue and Brittle Failures*, Springer.

[4] R. Desmorat, F. Gatuingt, F. Ragueneau (2007): Nonlocal anisotropic damage model and related computational aspects for quasi-brittle materials, *Engineering Fracture Mechanics*, in press.

[5] P. Ladevèze (1993): On an anisotropic damage theory, Proc. CNRS Int. Coll. 351 Villars-de-Lans (1983), Failure criteria of structured media, J.P. Boehler Ed., pp. 355–363.

[6] J. Mazars and Y. Berthaud and S. Ramtani (1990): The unilateral behavior of damaged concrete, *Engineering Fracture Mechanics*, **35**, 629–635.

Modeling of Textural Anisotropy in Granular Materials with Stochastic Micro-Polar Hypoplasticity

J. Tejchman

Gdansk University of Technology, 80-952 Gdansk-Wrzeszcz, Poland
tejchmk@pg.gda.pl

Summary: The paper deals with a numerical analysis of the effect of textural anisotropy on the behaviour of cohesionless granular materials with consideration of shear localization. For a simulation of the mechanical behavior of a granular material during a monotonous deformation path, an isotropic micro-polar hypoplastic constitutive model was used. To describe textural effects, spatially correlated random fields of the initial void ratio were subject to rotation against the horizontal axis. The results were compared with those obtained with an anisotropic micro-polar constitutive model. The calculations were carried out with a dense granular specimen during plane strain compression under constant lateral pressure.

Introduction

Granular materials are heterogeneous and discrete systems composed of grains with different shape, size, roundness and roughness. Thus, their behaviour is influenced by the orientation of grains with respect to the direction of sedimentation. This inherent anisotropy due to texture (fabric) is called a traverse isotropy since the material has a rotational symmetry with respect to one of the co-ordinates axes. The plane perpendicular to the orientation direction is called bedding plane and it is a plane of isotropy.
The laboratory experiments on plane strain compression show evidently that the orientation of the bedding plane relative to the principal stress directions has a pronounced effect on the stress-strain behaviour [1]. The shear stiffness, peak friction angle and average volume change are usually larger and strain corresponding to the peak value are smaller for loading perpendicular to the bedding plane than for loading parallel to it. The inclination of the shear zone with respect to the bottom becomes smaller. For large monotonic shearing, the stress ratio approaches a stationary value [1], i.e. anisotropy vanishes at residual state (critical state) at large shear deformation due to the so-called SOM-effect (swept out of memory effect). The DEM simulations seem to confirm also this SOM-effect in granular bodies.
In this paper, a novel approach was attempted to describe textural anisotropy with isotropic micro-polar hypoplasticity. First, the initial void ratio in the granular specimen was distributed stochastically by using a random correlated field. Next, this field was rotated by different angles to simulate the specimen preparation process in laboratory experiments, which was characterized by the angle between the filling and loading direction [1]. An isotropic micro-polar hypoplastic constitutive model was used, which is able to describe the essential properties of granular materials during shear localization in a wide range of pressures and densities. In addition, the numerical results from the isotropic model were compared with three different anisotropic micro-polar constitutive models [2-4]. The effect of this rotation on the spontaneous shear zone formation in dense sand during plane strain compression under constant lateral pressure was numerically investigated with the finite element method.

Constitutive model

Non-polar hypoplastic constitutive models describe the evolution of the effective stress tensor depending on the current void ratio, stress state and rate of deformation by isotropic non-linear tensorial functions. A striking feature pertinent to hypoplasticity is that the constitutive equation is incrementally non-linear in deformation rate. The hypoplastic models are capable of describing a number of significant properties of granular materials, e.g. non-linear stress-strain relationship, dilatant and contractant volumetric change, stress level dependence, density dependence and material softening. A further feature of hypoplastic models is the inclusion of critical states, in which grain aggregate can deform continuously at constant stress and constant volume. In contrast to plastic models, a decomposition of deformation into elastic and plastic parts, the formulation of yield surface, plastic potential, flow rule and hardening rule are not needed. The hallmark of these models are their simple formulation and procedure for determining the material parameters with standard laboratory experiments.
It has been shown that hypoplastic constitutive models without a characteristic length cannot describe realistically shear localization [5]. A characteristic length can be introduced into hypoplasticity by means of micro-polar, non-local and second-gradient theory [5]. In this paper, a micro-polar theory was adopted. A micro-polar model makes use of rotations and couple stresses, which have clear physical meaning for granular materials. In the calculations, micro-polar isotropic hypoplastic model was used [3,5]. The constitutive relationship requires ten material parameters [3].

Input data and FE-implementation

FE-calculations of plane strain compression tests were performed with a sand specimen with initial dimensions of h_o=140 mm (height), b=40 mm (width) and l=1.0 m (depth due to plane strain calculations). 3584 triangular elements were used. The quadrilateral elements composed of four diagonally crossed triangles were used to avoid volumetric locking due to dilatancy effects. The height of the finite elements was not larger than five times mean grain diameter to properly capture shear localization. A quasi-static deformation was imposed through a constant vertical displacement increment prescribed at nodes

along the upper edge of the specimen. The boundary conditions of null shear stress were imposed at the top and bottom of the specimen. To preserve the stability of the specimen against horizontal sliding, the node in the middle of the top edge was kept fixed. As the initial stress state, a K_0-state was assumed. Next, a confining pressure of σ_c=200 kPa was prescribed.
A spatially correlated distribution of the initial void ratio e_o was assumed in the granular specimen in the form of a two-dimensional Gaussian stochastic field. Randomness of the initial void ratio was described by the following homogeneous correlation function [6]:

$$K(x_1, x_2) = s_d^2 \, e^{-\lambda_{x_1} \Delta x_1} (1 + \lambda_{x_1} \Delta x_1) e^{-\lambda_{x2} \Delta x_2} (1 + \lambda_{x_2} \Delta x_2)$$

where Δx_1 and Δx_2 are the distances between two field points along the horizontal axis x_1 and vertical axis x_2, λ_{x1} and λ_{x2} are the decay coefficients characterizing a spatial variability of the specimen properties while the standard deviation s_d represents their scattering. The simulation process was divided into three stages [8]. First, the four corner random values were generated. Next, a propagation scheme with a growing number of points covered a defined base scheme of the field mesh. In the third stage, the base scheme was appropriately shifted, and the next group of unknown random values was simulated. The base scheme was translated so as to cover the entire field nodes. For the sake of simplicity, only single realizations were performed in the first step with the initial void ratio e_o =0.65 in the specimen. The standard deviations should be assumed based on experimental data. Due to the lack of experimental data, however, one assumed two different standard deviations $s_d = 0.05$ (small scatter) and $s_d = 0.10$ (large scatter). One assumed strongly correlated fields in the horizontal direction ($\lambda_{x1} = 1$) and weakly correlated fields in the vertical one ($\lambda_{x2} = 3$). A strongly correlated field implied a small variation of e_o. Therefore, the density in the horizontal direction was close to a uniform distribution. Next, the generated random fields were rotated by the angle $\theta = 0^o$ and $\theta = 90^o$ against the horizontal axis x_1 to simulate the filling process in laboratory tests (θ = bedding plane inclination).
The numerical results for three different spatially correlated random fields of the initial void ratio (with $\lambda_{x1} = 1$, $\lambda_{x2} = 3$ and $s_d = 0.05$) rotated by $\theta = 0^o$, $\theta = 45^o$ and $\theta = 90^o$ are depicted in Figs. 1 and 2. The normalized load-displacement curves are shown in Fig.1 (P = resultant vertical force on the top, u_2^t = vertical displacement of the top boundary). The deformed FE-meshes with the distribution of the equivalent total strain $\bar{\varepsilon} = \sqrt{\varepsilon_{ij}\varepsilon_{ij}}$ are demonstrated in Fig. 2 (ε_{ij} = strain tensor).
The normalized overall vertical force in the granular specimen is the largest for the rotation angle θ=0^o, smaller for θ=45^o and the smallest for the angle θ=90^o (as in the experiments [1]). One shear zone occurs inside of the specimen which crosses the specimen and whose location is caused by a stochastic distribution of the initial void ratio. The shear zone thickness is insignificantly influenced by the rotation angle θ (it slightly increases with increasing θ). By making use of Cosserat rotations the shear zone thickness is about 8-9 mm [(16-18)$\times d_{50}$]. The shear zone inclination against the bottom always decreases slightly with increasing angle θ from 54^o (θ=0^o) down to 50^o (θ =90^o).

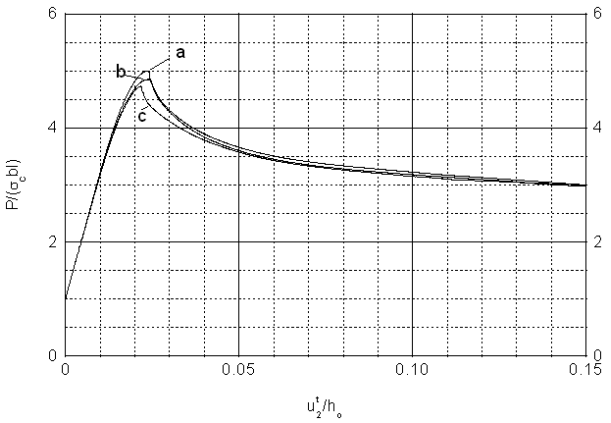

Figure 1: Effect of the rotation angle θ on the normalized load-displacement curve with stochastic distribution of e_o using isotropic micro-polar hypoplastic model [3] ($\lambda_{x1} = 1$, $\lambda_{x2} = 3$, $s_d = 0.05$): a) $\theta = 0^o$, b) $\theta = 45^o$, c) $\theta = 90^o$.

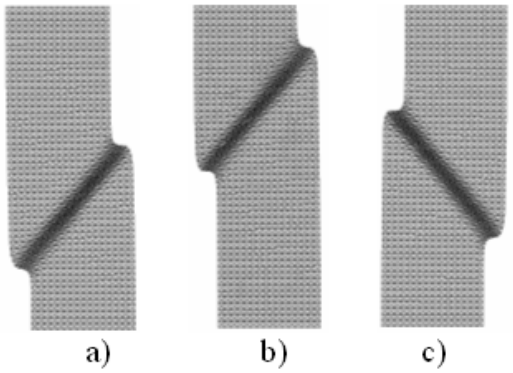

Figure 2: Deformed meshes with the distribution of equivalent total strain at residual state ($\lambda_{x1} = 1$, $\lambda_{x2} = 3$, $s_d = 0.05$): a) $\theta = 0^o$, b) $\theta = 45^o$, c) $\theta = 90^o$.

References

[1] F. Tatsuoka, M. S. A. Siddiquee, T. Yoshida (1994): Testing methods and results of element tests and testing conditions of plane strain model bearing capacity tests using air-dried dense Silver Leighton Buzzard sand. *Internal Report of the Tokyo University*, 1–120.

[2] J. Tejchman (2005): Investigations of shear localization in granular bodies within an anisotropic micro-polar hypoplasticity. *Archives of Hydro-Engineering and Environmental Mechanics*, 52, 85–106.

[3] J. Tejchman, A. Niemunis (2006): FE-studies on shear localization in an anistropic micro-polar hypoplastic granular material. *Granular Matter*, 8, 205–220.

[4] J. Tejchman, E. Bauer, W. Wu (2007): Effect of fabric anisotropy on shear localization in sand during plane strain compression. *Acta Mechanica* (in press).

[5] J. Tejchman (2004): Influence of a characteristic length on shear zone thickness in hypoplasticity with different enhancements. *Computers and Geotechnics* 31, 595–611.

[6] H. Walukiewicz, E. Bielewicz, J. Gorski (1997): Simulation of nonhomogeneous random fields for structural applications. *Computers and Structures*, 64, 491–498.

Localization of Deformation and Pore Pressure in Two-Phase Modified Cam-Clay Plasticity Model

J. Pamin*, A. Stankiewicz

Cracow University of Technology, Department of Civil Engineering
ul. Warszawska 24, 31-155 Cracow, Poland
e-mail: jpamin@L5.pk.edu.pl, A.Stankiewicz@L5.pk.edu.pl

Summary: The modified Cam-clay plasticity is employed in a two-phase soil modelling. A simple Laplacian-enhancement of the theory is discussed. The influence of permeability and fluid phase compressibility on shear band instabilities is investigated. The mesh-sensitivity of localization simulations is verified.

Introduction

The influence of the fluid phase on instabilities in two-phase soil modelling is a subject of ongoing research, see for instance [1, 2, 3, 4, 5, 6]. The solid-fluid interaction can influence the critical load level for which an instability occurs as well as the direction and width of the localization band. The two-phase modelling of soil involves a gradient term via the Darcy's law. However, its effect is strongly dependent on the permeability coefficient and thus some localization limiter still seems necessary. Moreover, the constitutive description plays an important role in the solid-fluid coupling. This issue is investigated in the paper within the formulation based on a gradient-enhanced modified Cam-clay model.

Two-phase modelling

Soil is a multiphase material which consists of a solid skeleton and voids filled with fluids (usually water and air). In this paper soil is described as a two-phase medium (solid + water) which, with the assumption of incompressibility of solid grains, is governed by the following two equations:

$$\boldsymbol{\nabla}\cdot\boldsymbol{\sigma}_t+\hat{\rho}\boldsymbol{g}=\boldsymbol{0} \tag{1}$$

$$\boldsymbol{\nabla}\cdot\dot{\boldsymbol{u}}+\boldsymbol{\nabla}\cdot\boldsymbol{v}_d-n\dot{\theta}_f=0 \tag{2}$$

where $\boldsymbol{\sigma_t}$ - total stress tensor for the porous medium, $\hat{\rho}$ - saturated density of the solid-fluid mixture, $\boldsymbol{g}$ - gravitation vector, $\boldsymbol{u}$ - displacement vector, $\boldsymbol{v}_d$ - Darcy's velocity, n - porosity and θ_f - volumetric strain of compressible fluid. Equation (1) represents the balance of momentum and eq. (2) the balance of mass. They require appropriate boundary conditions and the rate eq. (2) requires an initial condition as well.

We note that the balance of the medium is maintained by the total stress, while the deformation and limit states of saturated soil are governed by the effective stress tensor $\boldsymbol{\sigma}$ defined as $\boldsymbol{\sigma}=\boldsymbol{\sigma_t}+\boldsymbol{I}p_f$ with unit tensor $\boldsymbol{I}$ and pore pressure p_f.

Gradient-dependent modified Cam-clay model

The modified Cam-Clay model, originated in [7], is commonly accepted as reliable for a large class of soils. It belongs to critical state models and describes the behaviour of the soil skeleton, since the constitutive equations are written in terms of effective stresses. This plastic model, combined with nonlinear elasticity, is capable of reproducing the essential physical properties of soils, including hardening/softening and contraction/dilatation. In particular, dilatation due to large preconsolidation involves softening and negative excess pore pressure.

The yield function for the gradient-dependent modified Cam-clay model is written as:

$$f(\boldsymbol{\sigma},\Lambda,\nabla^2\Lambda)=q^2+M^2p\left[p-p_c(\Delta\theta^{\mathrm{p}})+g\nabla^2\Lambda\right] \tag{3}$$

where $q=\sqrt{3J_2}$, J_2 - second invariant of the deviatoric effective stress tensor, M- function of the internal friction angle, p - effective pressure acting on the soil skeleton, p_c - (positive) measure for the current degree of overconsolidation, θ^{p} - volumetric part of the plastic strain tensor, dependent on plastic multiplier Λ, and g - positive gradient influence factor. The algorithmic implementation of the model is based on [8] and presented in [9].

Discretization of three-field formulation

To combine the problem of pore pressure evolution with the gradient-enhanced plasticity modelling of the solid skeleton, the weak forms of equations (1-3) are required. Upon discretization of the displacements $\boldsymbol{u}$, plastic multiplier Λ and excess pore pressure p_f, one obtains the incremental matrix problem:

$$\begin{bmatrix}\boldsymbol{K}_{uu} & \boldsymbol{K}_{u\Lambda} & -\boldsymbol{K}_{up}\\ \boldsymbol{K}_{\Lambda u} & \boldsymbol{K}_{\Lambda\Lambda} & \boldsymbol{0}\\ \boldsymbol{K}_{up}^{\mathrm{T}} & \boldsymbol{0} & \boldsymbol{K}_{pp}\end{bmatrix}\begin{Bmatrix}\Delta\bar{\boldsymbol{u}}\\ \Delta\bar{\boldsymbol{\Lambda}}\\ \Delta\bar{\boldsymbol{p}}\end{Bmatrix}=\begin{Bmatrix}\boldsymbol{f}_{ext}-\boldsymbol{f}_{\mathrm{int}}\\ \boldsymbol{f}_{\Lambda}\\ \Delta t\Delta\boldsymbol{f}_p\end{Bmatrix} \tag{4}$$

in which $\boldsymbol{K}_{uu}$ is the classical tangent stiffness operator, $\boldsymbol{K}_{u\Lambda}$ and $\boldsymbol{K}_{\Lambda u}$ are equilibrium-plasticity coupling matrices, $\boldsymbol{K}_{\Lambda\Lambda}$ is the gradient-dependent yield condition matrix, $\boldsymbol{K}_{up}$ is deformation-pore pressure coupling operator, $\boldsymbol{K}_{pp}$ results from pore pressure discretization of eq. (2) and involves explicitly the time increment Δt. The right-hand side vector contains residual terms of the discrete nonlinear problem, cf. [10].

Influence of fluid phase on localization

In this paper the influence of the fluid phase on soil instabilities is investigated using the local and gradient-enhanced modified Cam-clay model. The numerical investigation is focused

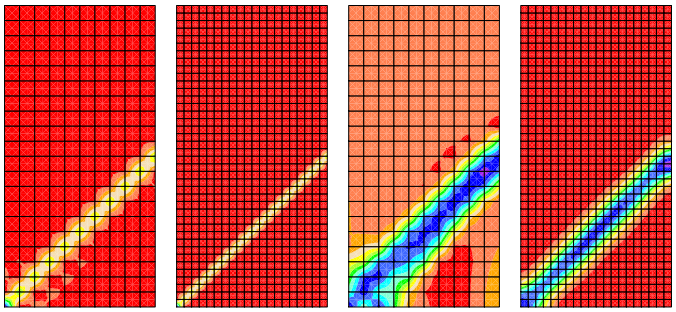

Figure 1: Biaxial compression test for local Cam-clay model: vertical strain (left) and pore pressure (right) distribution for coarse and medium meshes.

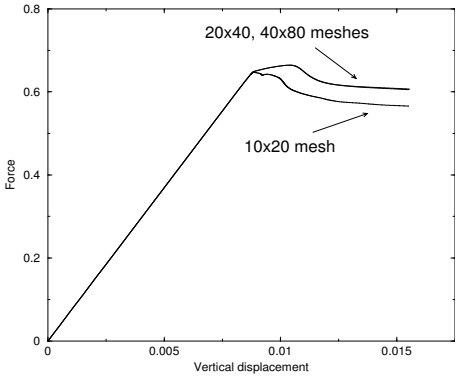

Figure 2: Biaxial compression test for two-phase medium with gradient-dependent Cam-clay model: load-deformation curves

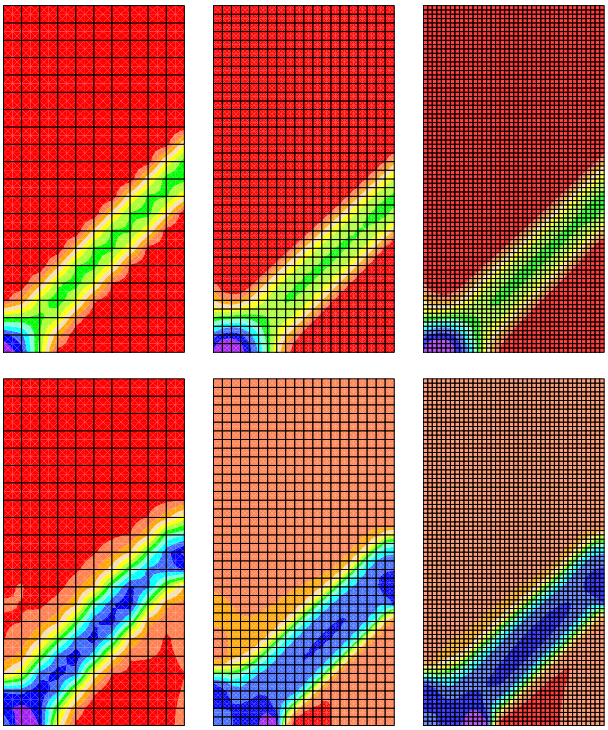

Figure 3: Vertical strain distribution (top) and pore pressure distribution (bottom).

on shear banding localization in the classical plane strain biaxial compression test. It turns out that deformations obtained for various values of permeability coefficient are sensitive to the discretization density unless gradient regularization is employed. Some stabilizing effect of the fluid phase is observed only in the pore pressure distribution, see Fig. 1.

Figure 2 shows the load-deformation diagrams obtained for the two-phase medium using the gradient-dependent model. Figure 3 shows the vertical strain and pore pressure distributions for three mesh refinements and proves that the adopted gradient enhancement provides an effective regularization.

The physical consequences of the gradient enhancement and the influence of fluid compressibility are also investigated in the paper. The reasons for inconsistent conclusions from the results presented in [5] and [10] are discussed.

References

[1] B.A. Schrefler, L. Sanavia, and C.E. Majorana (1996): A multiphase medium model for localisation and post-localisation simulation in geomechanics, *Mechanics of Cohesive-Frictional Materials*, **1**, 95–114.

[2] J. Larsson (1999): *On the modeling of porous media with emphasis on localization*, Ph.D. dissertation, Chalmers University of Technology, Gothenburg.

[3] A. Benallal and C. Comi (2003): On numerical analyses in the presence of unstable saturated porous materials, *International Journal for Numerical Methods in Engineering*, **56**, 883–910.

[4] H.W. Zhang and B.A. Schrefler (2004): Particular aspects of internal length scales in strain localisation analysis of multiphase porous materials, *Computer Methods in Applied Mechanics and Engineering*, **193**, 2867–2884.

[5] Scarpas A. Liu, X. and Blaauwendraad J. (2005): Numerical modelling of nonlinear response of soil. part 2: Strain localization investigation on sand, *International Journal of Solids and Structures*, **42**, 1883–1907.

[6] R. de Borst and M.-A. Abellan (2006): Dispersion and internal length scales in strain-softenig two-phase media, In G. Meschke et al., editors, *Proc. EURO-C 2006 Int. Conf. Computational Modelling of Concrete Structures*, pages 549–556, London/Leiden, Taylor & Francis.

[7] K.H. Roscoe and J.B. Burland (1968): On the generalized behaviour of 'wet' clay, In *Engineering plasticity*, volume 48, pages 535–609, Cambridge, Cambridge University Press.

[8] A. Groen (1997): *Three-dimensional elasto-plastic analysis of soils*, Ph.D. dissertation, Delft University of Technology, Delft.

[9] A. Stankiewicz and J. Pamin (2006): Gradient-enhanced Cam-clay model in simulation of strain localization in soil, *Foundations of Civil and Environmental Engineering*, **7**, 293–318.

[10] A. Stankiewicz and J. Pamin (2006): Finite element analysis of fluid influence on instabilities in two-phase cam-clay plasticity model, *Computer Assisted Mechanics and Engineering Sciences*, **13**, 669–682, 2006.

Wave Dispersion in Heterogeneous Materials Using a $\mathcal{C}^0$-Implementation of Gradient Elasticity

T. Bennett*, **H. Askes**

University of Sheffield
Dept. of Civil & Structural Engineering, Mappin Street, Sheffield, S1 3JD, United Kingdom
T.Bennett@Sheffield.ac.uk, H.Askes@Sheffield.ac.uk

Summary: Wave propagation through heterogeneous materials is dispersive, that is, the propagation velocity of the harmonic wave components depends on the wave number. A homogeneous continuum material model can be used to represent a heterogeneous medium, and wave dispersion can be modelled by including additional gradients of certain state variables. Particularly suited for a realistic description of wave dispersion are those formats of gradient elasticity that incorporate so-called micro-inertia (related to intrinsic time scales); other terms related to micro-stiffness (and intrinsic length scales) may also be present in the formulation. A widespread use of gradient elasticity in large-scale applications is hampered by the often stringent continuity requirements imposed on the numerical interpolation scheme. Gradient elasticity formulations are normally fourth-order partial differential equations in terms of the displacements and require therefore continuity of the primary unknowns as well their first derivatives. In this contribution, we will revisit the general gradient elasticity formulation that includes micro-inertia as well as micro-stiffness, and we will re-formulate this theory such that the continuity requirements are $\mathcal{C}^0$, rather than $\mathcal{C}^1$. This enables a straightforward implementation of this particular theory.

Introduction

In their linear form, the constitutive equations of gradient elasticity are written as [2, 3]

$$\sigma_{ij} = C_{ijkl}\left(\varepsilon_{kl} - \ell_s^2 \varepsilon_{kl,mm}\right) \tag{1}$$

where σ is the stress, C contains the elastic moduli, ε is the strain defined as the symmtric gradient of the displacements u, and subscripts following a comma denote a derivative with respect to a spatial coordinate. The newly introduced material parameter ℓ_s is a material length scale and it represents the underlying microstructure.

Models can be derived for which strain singularities are avoided, realistic dispersion is predicted and the additional parameters can be expressed in terms of microstructural properties. For this class of models the constitutive equations can be written as

$$\sigma_{ij} = C_{ijkl}\left(\varepsilon_{kl} - \ell_s^2 \varepsilon_{kl,mm}\right) + \rho \ell_m^2 \ddot{u}_{i,j} \tag{2}$$

where ρ is the mass density, a superimposed dot denotes a time derivative, and two length scales have appeared: ℓ_s related to higher-order stiffness and ℓ_m related to higher-order inertia.

Ultimately a numerical implementation based on discretisation must be attempted. The field equations according to Eq. (2) are of the fourth order in the displacements and therefore the shape functions must be at least $\mathcal{C}^1$-continuous. The need for a $\mathcal{C}^1$ implementation of Eq. (2) can be avoided by applying an operator split as discussed in detail by Ru and Aifantis [3]. In this paper, the model according to Eq. (2) will be reformulated along similar lines such that it can be implemented straightforwardly by means of the finite element method.

The Ru-Aifantis theorem

Solution strategies will be sought that facilitate the numerical solution of gradient elasticity problems. Firstly, the static case is considered. The equilibrium equations associated with the static form of gradient elasticity of Eq. (1) can be cast in terms of displacements as

$$C_{ijkl}\left(\frac{u^g_{k,jl} + u^g_{l,jk}}{2} - \ell_s^2 \frac{u^g_{k,jlmm} + u^g_{l,jkmm}}{2}\right) = 0 \tag{3}$$

where body forces are not considered. A superscript g has been used for the displacements to indicate that gradient dependence is present. Solving these fourth-order equations (analytically or numerically) can be a tedious task, however Eq. (3) can be rearranged as [3]

$$C_{ijkl}\,\frac{u^a_{k,jl} + u^a_{l,jk}}{2} = 0 \tag{4}$$

where the auxiliary displacements u^a are defined as

$$u^a_i = u^g_i - \ell_s^2 u^g_{i,mm} \tag{5}$$

The auxiliary displacements are obtained from Eq. (4) which takes the format of classical elasticity — indeed u^a can be identified as the classical elasticity displacements in statics. Next, the gradient-dependent displacements u^g are obtained by solving the non-homogeneous Helmholtz equation (5) where u^a is used as a source term. Not does this only offer a tremendous simplification in analytical solution methods, also the continuity requirements imposed on the shape functions in numerical methods have become less strict: $\mathcal{C}^0$-continuous, rather than the cumbersome $\mathcal{C}^1$-continuous, shape functions suffice. Eqs. (4) and (5) can be used instead of Eq. (3) while capturing the same material response — this is known as the Ru-Aifantis theorem [3].

When dynamic loading conditions are imposed, Eq. (2) rather than Eq. (1) should be used so that a realistic dispersive behaviour is obtained. The equations of motion in terms of u^g

then read

$$\rho\left(\ddot{u}_i^g - \ell_m^2 \ddot{u}_{i,mm}^g\right) = \\ = C_{ijkl}\left(\frac{u_{k,jl}^g + u_{l,jk}^g}{2} - \ell_s^2 \frac{u_{k,jlmm}^g + u_{l,jkmm}^g}{2}\right) \quad (6)$$

The goal is now to accomplish a simplification of Eq. (6) similar to that of Eq. (3), such that a formulation results for which C^0-continuous interpolations suffice.

In the case that $\ell_m \neq \ell_s$ it is not possible to rewrite the left-hand-side and the right-hand-side of Eq. (6) with a single substitution in the spirit of Eq. (5). Since the fourth-order spatial derivatives appear in the right-hand-side, the auxiliary displacements u^a are substituted on this side, hence

$$\rho\left(\ddot{u}_i^g - \ell_m^2 \ddot{u}_{i,mm}^g\right) = C_{ijkl}\frac{u_{k,jl}^a + u_{l,jk}^a}{2} \quad (7)$$

in conjunction with Eq. (5). Now, the system is fully coupled as both variables u^a and u^g appear in both expressions. However, a further elaboration is made by taking the second time derivative of Eq. (5):

$$\ddot{u}_i^a = \ddot{u}_i^g - \ell_s^2 \ddot{u}_{i,mm}^g \quad (8)$$

A symmetric formulation can now be obtained by multiplying Eq. (8) with ℓ_m^2/ℓ_s^2, the result is used to replace the $\ddot{u}_{i,mm}^g$ term in Eq. (7), and multiplying Eq. (8) with $\rho(1-\ell_m^2/\ell_s^2)$, the result is to be used instead of Eq. (5). With these substitutions, the symmetric set of coupled equations reads

$$\rho\left(\frac{\ell_m^2}{\ell_s^2}\,\ddot{u}_i^a - \frac{\ell_m^2 - \ell_s^2}{\ell_s^2}\,\ddot{u}_i^g\right) = C_{ijkl}\frac{u_{k,jl}^a + u_{l,jk}^a}{2} \quad (9)$$

together with

$$\rho\left(-\frac{\ell_m^2 - \ell_s^2}{\ell_s^2}\,\ddot{u}_i^a + \frac{\ell_m^2 - \ell_s^2}{\ell_s^2}\,\ddot{u}_i^g - \left(\ell_m^2 - \ell_s^2\right)\ddot{u}_{i,mm}^g\right) = 0 \quad (10)$$

Note that in this case, the auxiliary displacements u^a cannot be interpreted as the displacements of classical elasticity.

Discretised system of equations

The field equations are now discretised taking into account the derived boundary conditions. Adopting the usual matrix-vector notation, the weak form of Eq. (9) is written as

$$\int_\Omega \delta\boldsymbol{u}^T \rho\left(\frac{\ell_m^2}{\ell_s^2}\,\ddot{\boldsymbol{u}}^a - \frac{\ell_m^2 - \ell_s^2}{\ell_s^2}\,\ddot{\boldsymbol{u}}^g\right)\mathrm{d}V - \int_\Omega \delta\boldsymbol{u}^T \mathbf{C}\mathbf{L}\boldsymbol{\varepsilon}^a\,\mathrm{d}V = 0 \quad (11)$$

where $\delta\boldsymbol{u}$ is a vector of test functions and $\mathbf{L}$ is a differential operator. Integrating the last term of Eq. (11) by parts leads to

$$\int_\Omega \delta\boldsymbol{u}^T \rho\left(\frac{\ell_m^2}{\ell_s^2}\,\ddot{\boldsymbol{u}}^a - \frac{\ell_m^2 - \ell_s^2}{\ell_s^2}\,\ddot{\boldsymbol{u}}^g\right)\mathrm{d}V + \int_\Omega \delta\boldsymbol{\varepsilon}^T \mathbf{C}\boldsymbol{\varepsilon}^a\,\mathrm{d}V = \\ = \int_{\Gamma_n} \delta\boldsymbol{u}^T \boldsymbol{t}\,\mathrm{d}S \quad (12)$$

where the prescribed tractions $\boldsymbol{t}$ have been substituted on the relevant part of the boundary Γ_n. Similarly, Eq. (10) is cast in its weak format according to

$$\int_\Omega \delta\boldsymbol{v}^T \rho\Big(-\frac{\ell_m^2 - \ell_s^2}{\ell_s^2}\,\ddot{\boldsymbol{u}}^a + \frac{\ell_m^2 - \ell_s^2}{\ell_s^2}\,\ddot{\boldsymbol{u}}^g - \\ - \left(\ell_m^2 - \ell_s^2\right)\nabla^2\ddot{\boldsymbol{u}}^g\Big)\mathrm{d}V = 0 \quad (13)$$

with $\delta\boldsymbol{v}$ a vector of test functions. The last contribution is integrated by parts, which gives

$$\int_\Omega \delta\boldsymbol{v}^T \rho\left(-\frac{\ell_m^2 - \ell_s^2}{\ell_s^2}\,\ddot{\boldsymbol{u}}^a + \frac{\ell_m^2 - \ell_s^2}{\ell_s^2}\,\ddot{\boldsymbol{u}}^g\right)\mathrm{d}V + \\ + \sum_{\xi=x,y,z}\int_\Omega \frac{\partial\boldsymbol{v}^T}{\partial\xi}\rho\left(\ell_m^2 - \ell_s^2\right)\frac{\partial\ddot{\boldsymbol{u}}^g}{\partial\xi}\mathrm{d}V = 0 \quad (14)$$

Homogeneous natural boundary conditions have been assumed by which the boundary integral cancels.

The two vectors of trial functions $\boldsymbol{u}^a$ and $\boldsymbol{u}^g$ are discretised as $\boldsymbol{u}^a = \mathbf{N}_a\mathbf{u}^a$ and $\boldsymbol{u}^g = \mathbf{N}_g\mathbf{u}^g$. The test functions $\delta\boldsymbol{u}$ and $\delta\boldsymbol{v}$ are also discretised with shape functions $\mathbf{N}_a$ and $\mathbf{N}_g$, respectively. Discretisation in time is performed using the constant acceleration variant of the Newmark scheme.

A more thorough exposition of the formulation, along with examination of the boundary conditions and a numerical example, is given in [1].

References

[1] H. Askes and T. Bennett, E. C. Aifantis: A new formulation and C^0-implementation of dynamically consistent gradient elasticity. *International journal for numerical methods in engineering* (accepted for publication).

[2] E. C. Aifantis (1992): On the role of gradients in the localization of deformation and fracture. *Int. J. Engng. Sci.*, **30**, 1279–1299.

[3] C. Q. Ru, E. C. Aifantis (1993): A simple approach to solve boundary-value problems in gradient elasticity, *Acta Mech.*, **101**, 59–68.

Part IX

Microplane Models

Nano-Mechanics Based Size Effect on Safety Factors and Lifetime of Quasibrittle Structures

Z. P. Bažant

Northwestern University, 2145 Sheridan Road, CEE
Evanston, IL 60208, USA; z-bazant@northwestern.edu

Summary: For quasibrittle structures failing at macro-fracture initiation, there exists a size effect not only on the mean strength of structure but also on the type of its strength distribution, which varies from Gaussian (normal) to Weibullian as the size increases.There are serious consequences for the safety factors and structural lifetime.

Motivation and problem

The uncertainty in the understrength (or capacity reduction) parts of safety factors, which are still essentially empirical, is much larger than the typical errors of modern computer analysis of structures. This problem is paramount importance for quasibrittle structures. Its resolution would yield greater benefits than most refinements in computational mechanics. Purely empirical, statistically based, safety factors are adequate for structures whose failure is either purely ductile or purely brittle because the type of cumulative probability distribution function (cdf) of structure strength is independent of structure size and geometry, and is either Gaussian (normal) or Weibullian. Not so for structures consisting of quasibrittle materials, which include, at normal scale, concrete, fiber-polymer composites, tough ceramics, rocks, sea ice, wood, etc., at normal scale, and many more at the scale of MEMS and thin films. For such structures, which are the focus of this lecture, the cdf continuously varies from nearly Gaussian to Weibullian as the structure size increases, and also depends on the structure geometry. Quasibrittle structures are characterized by a fracture process zone that is not negligible compared to the cross-section dimensions of the structure. As firmly established by now, the mean strength of quasibrittle structures failing at fracture initiation does not scale as a power law but varies with the structure size as a gradual transition between two asymptotic size effect laws of power law type—one of them deterministic (or energetic), based stress redistribution due to a large fracture process zone, and the other statistical, based on the weakest-link model and Weibull theory or random material strength. In this lecture, it is argued that the safety factors for such structures, which have generally been considered as size independent and purely empirical, must also be considered to depend on the structure size as well as shape. Furthermore, the dependence of structural lifetime on structure size (at fixed nominal stress) must be considered to deviate, for such structures, from the power law predicted by Weibull theory, and the type of cdf of structure lifetime to be size dependent. The safety factors must ensure an extremely low failure probability, $\leq 10^{-6}$. For such a low probability, direct experimental verification by strength histograms is impossible. A physically based theory whose experimental verification is indirect is, therefore, required.

Conspectus of main results

Recently it has been shown that the cdf of strength can be derived from the Maxwell-Boltzmann distribution of atomic thermal energies and the stress-dependence of activation energy of interatomic bond breaks (Fig. 1a). The analysis indicates that the far-left tail of every cdf of strength of a representative volume element (RVE) of any material must be a power law. For ductile (plastic) materials, the power-law tail is so remote that it plays no role, but not for quasibrittle materials. The cdf of strength of quasibrittle structures of positive geometry (which are the structures failing at fracture initiation) can be modelled as a chain (or series coupling) of RVEs (Fig. 1e). It is demonstrated that the RVE must be modelled by neither a chain nor a bundle. Rather, it must be statistically represented by a hierarchical model consisting of bundles (or parallel couplings) of only 2 long sub-chains, each of them consisting of sub-bundles of 2 or 3 long sub-sub-chains of sub-sub-bundles, etc., until the nano-scale of atomic lattice is reached. The power-law character of the cdf tail is indestructible. It is transmitted through all the scales from nano to macro while its exponent is gradually raised from 1 on the atomistic scale to a value equal, on the RVE scale, to the Weibull modulus (typically between 10 and 50). The physical meaning of Weibull modulus is shown to be the minimum number of cuts needed to separate the hierarchical model into two halves, which should be equal to the number of dominant cracks needed to break the representative volume element (RVE) of material. Thus the model indicates the Weibull modulus m to be governed by the packing of inhomogeneities within a RVE. It is also shown that the RVE cannot be defined in the classical sense but must be understood as the smallest material volume whose failure causes failure of the whole structure (of positive geometry). The model indicates that the cdf of RVE strength must have a broad Gaussian (or error function) core, onto which a power-law tail of an exponent equal to the Weibull modulus is grafted at the failure probability of about 0.001, if the structure is quasibrittle. The model predicts how the grafting point, separating the Gaussian and Weibullian parts, moves to higher failure probabilities as the structure size increases, and also how the grafted cdf depends on the temperature, lifetime (or load duration, loading rate) and activation energy (which in turn is affected by aggressive chemical species). On a large enough scale (equivalent to at least 1000 RVEs), quasibrittle structures must follow the Weibull distribution with, necessarily, a zero threshold. Thus the cdf of structure strength changes from predominantly Gaussian for small sizes to predominantly Weibull for large sizes (Fig. 1a,e). It is widely agreed that engineering structures must generally be designed to ensure failure probability $P_f \leq 10^{-6}$. Since the point of $P_f = 10^{-6}$ is, for the Weibull distribution, about twice as far from the mean than it is for the Gaussian distribution of the same mean and variance (Fig. 1a), the understrength

part of the safety factor must be approximately doubled when passing from very small to very large structures (Fig. 1d). This serious consequence, unique to quasibrittle structures, has not been considered in the design of large concrete structures or large composite parts of aircraft made of composites. On the other hand, the coefficient of variation of quasibrittle structures, unlike perfectly brittle structures, decreases with structure size (Fig. 1d). This behavior may partly or fully offset the need for a larger safety factor. The experimental histograms with kinks, which were previously thought to require the use of a finite threshold, are shown to be fitted much closer by the proposed chain-of-RVEs model with a zero threshold (Fig. 1c). For not too small structures, the model is shown to represent, in the mean sense, essentially a discrete equivalent of the previously developed nonlocal Weibull theory, and to match the mean size effect law previously obtained from this theory by asymptotic matching (Fig. 1e). The chain-of-RVEs model (Fig. 1e) can be verified and calibrated from the mean size effect curves, as well as from the kink locations (Fig. 1c) on experimental strength histograms for sufficiently different specimen sizes. Strength histograms for specimens of one size (Fig. 1a) are not sufficient. The mean stochastic response agrees with the cohesive crack model, crack band model and nonlocal damage models. Analysis of some major structural collapses, e.g., the devastating failures of Malpasset dam and Schoharie Creek Bridge on New York Thruway, reveals that the size effect (on both the mean nominal strength σ_N and the safety factor) must have been a significant contributing factor. The tolerable abutment displacement of that ill-fated record-slender and record-tall arch dam would today be about four-times smaller than that deemed tolerable according to the standard design procedures at the time of design. Finally, the new theory also indicates that, for quasibrittle structures, the definitions of Cornell and Hasofer-Lind reliability indices in FORM and SORM need to be modified.

References

[1] Z. P. Bažant and S. D. Pang (2006): Mechanics based statistics of failure risk of quasibrittle structures and size effect on safety factors. *Proc. of the National Academy of Sciences*, **103**, 9434–9439.

[2] Z. P. Bažant and S. D. Pang (2006): Activation energy based extreme value statistics and size effect in brittle and quasibrittle fracture. *J. of the Mechanics and Physics of Solids*, **54**, in press.

[3] Z. P. Bažant (2004): Scaling theory for quasibrittle structural failure. *Proc., National Academy of Sciences*, **101**, 14000–14007.

[4] Z. P. Bažant (2005): *Scaling of Structural Strength*, 2nd updated edition, Elsevier, London.

[5] Z. P. Bažant, M. Vořechovský, D. Novák (2007): Asymptotic prediction of energetic-statistical size effect from deterministic finite element solutions. *J. of Engrg. Mechanics ASCE*, **128**, 153–162.

[6] Z. P. Bažant, M. Vořechovský, D. Novák (2007): Energetic-Statistical Size Effect Simulated by SFEM with Stratified Sampling and Crack Band Model."*Int. J. of Numerical Methods in Engineering*, in press.

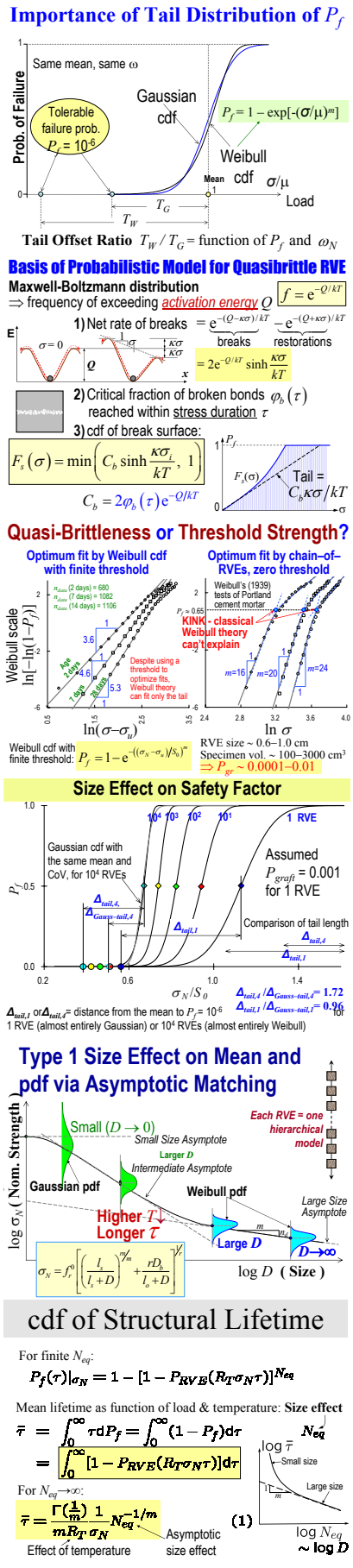

Figure 1: Explanations of concept and properties of activation energy based chain-of-RVEs model.

Microplane Model for Composite Laminates

G. Cusatis[1*], Z. P. Bažant[2], A. Beghini[3]

[1]Department of Civil and Environmental Engineering, Rensselaer Polytechnic Institute
4048 Johnsson Engineering Center, 110 Eighth St, Troy, NY, USA
cusatg@rpi.edu

[2]Department of Civil and Environmental Engineering, Northwestern University
2145 Sheridan Rd., Evanston, IL, USA
z-bazant@northwestern.edu

[3]Skidmore, Owings & Merril LLP
224 S. Michigan Av., Chicago, IL, USA
alessandro.beghini@som.com

Summary: This paper presents the spectral stiffness microplane (SSM) model, which is a general constitutive model for composite laminates, able to simulate the orthotropic stiffness, pre-peak nonlinearity, failure envelopes, post-peak softening and fracture. The model is verified by comparisons with experimental data for uniaxial and biaxial tests of unidirectional and multidirectional laminates

Introduction

Various theories can be found in the literature for the description of the mechanical behavior of fiber-polymer composites [1]. These theories, however, generally neglect the quasibrittle character of these materials. In quasibrittle fracture, the crack tip is surrounded by a nonlinear zone (fracture process zone) that is not negligible compared to the cross section dimension of the structures. The fracture process zone (FPZ) at crack tip occupies almost the entire nonlinear zone and undergoes softening damage instead of plastic deformation typical of ductile behavior. The stress along the FPZ is nonuniform and the stress decreases with crack opening gradually, due to discontinuous cracking in the FPZ, crack bridging by fibers, and frictional pullout of inhomogeneities.

The present paper summarizes the outcome of a recent research effort [2, 3] in which a complete theory for the mechanical behavior of fiber-polymer laminates has been formulated in the framework of the microplane model. A constitutive law is first developed for laminates with unidirectional reinforcement. Subsequently, general laminates with multidirectional reinforcement are modeled as an overlay of lamina with unidirectional reinforcements of different orientations.

Microplane model mormulation with spectral decomposition

By exploiting the spectral decomposition theorem, the material stiffness matrix can be decomposed [4] as follows:

$$\mathbf{E} = \sum_I \lambda_I \mathbf{E}_I \tag{1}$$

where λ_I are the eigenvalues of the stiffness matrix and $\mathbf{E}_I$ define a set of matrices constructed through the diadic products of the eigenvectors of the materials stiffness matrix. The matrices $\mathbf{E}_I$ also decompose the stress and strain vectors into energetically orthogonal modes, which are called eigenstresses and eigenstrains. In the case of isotropic materials, these orthogonal modes represents the volumetric and deviatoric deformation modes.

By projecting the eigenstrains on a generic microplane of a kinematically constrained microplane model [5], it is possible to decompose the microplane strain vector into orthogonal components ($\boldsymbol{\varepsilon}_{\mathcal{P}I}$, microplane eigenstrains) that can be used to drive the constitutive behavior at the microplane level. From the microplane eigenstrains, the microplane eigenstresses, $\boldsymbol{\sigma}_{\mathcal{P}I}$, can be calculated according to suitable constitutive relations for the normal and shear components of each eigenmode. The macroscopic stress tensor may then be computed from the principle of virtual work, which reads:

$$\boldsymbol{\sigma} = \frac{3}{2\pi} \sum_I \int_\Omega \mathbf{E}_I \boldsymbol{\mathcal{P}}^T \boldsymbol{\sigma}_{\mathcal{P}I} \mathrm{d}\Omega \tag{2}$$

where Ω is the surface of a unit hemisphere, $\boldsymbol{\sigma}$ is the contraction of the stress tensor into a six-dimensional vector, and $\boldsymbol{\mathcal{P}}$ is the macro-micro projection operator.

In [2] and [3], the approach highlighted above has been fully developed with reference to unidirectional (transversely isotropic) composite laminates. In this case, four orthogonal modes exist and each mode can be approximately associated with a specific failure mode. This observation greatly simplifies the formulation of the constitutive behavior at the microplane level.

Calibration and validation

An extensive calibration and rigorous validation of the presented model is still under way. Nevertheless, preliminary results [2, 3] are promising and the developed theory seems to be able to capture the most relevant aspects of the behavior of composite laminates. Fig. 1 shows the comparison between the microplane simulation, the well known Tsai-Wu criterion [7],

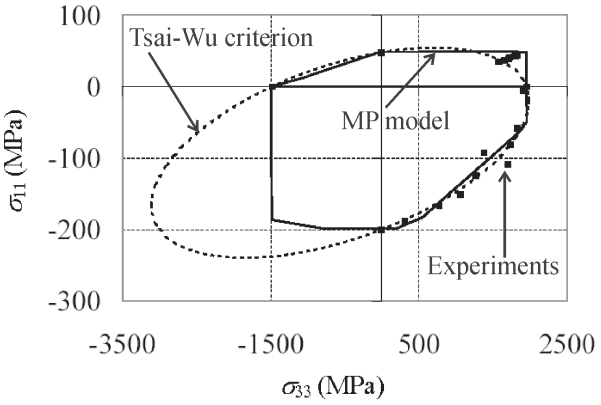

Figure 1: Comparison between numerical simulations (solid line), Tsai-Wu criterion (dashed line), and experimental results (points) from [6] for the biaxial failure envelope of a unidirectional laminate.

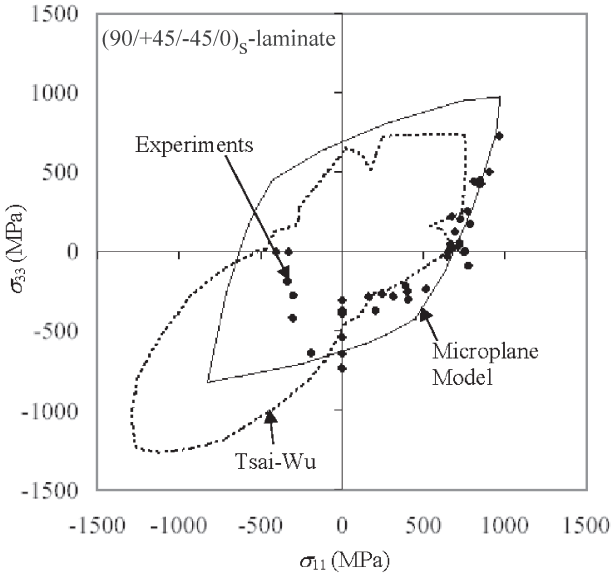

Figure 2: Comparison between numerical simulations (solid line), Tsai-Wu criterion (dashed line), and experimental results (points) from [6] for multiaxial failure envelope for a multidirectional laminate.

and the experimental results (published in [6]) for the biaxial failure envelope of a unidirectional laminate.

The developed and calibrated microplane model for unidirectional laminates can be then used for the simulation of multidirectional laminates. A widely used laminate lay-up is $(90/+45/-45/0)_S$, which is quasiisotropic. The behavior of this multidirectional laminate is here simulated assuming each ply to be governed by the microplane model for unidirectional laminates.

Fig. 2 shows the comparison between the experiments, the microplane model prediction and the prediction of the Tsai-Wu criterion. The microplane model theory agrees very well with the experimental data in the tension-tension quadrant of the envelope. For the tension-compression quadrant, the prediction is less accurate but still satisfactory. However, marked disagreement is found in the compression-compression quadrant, in which both the microplane model and the Tsai-Wu criterion severely overestimate the laminate strength.

Conclusions

1. The spectral decomposition theorem, applied to the material stiffness matrix, is a powerful tool to analyze generally anisotropic materials.

2. The present SSM (spectral stiffness microplane) model describes well the experimentally observed behavior of fiber composites, not only for uniaxial stress-strain curves, but also for multiaxial failure envelopes.

3. The main advantage of the SSM model is that one and the same model can simulate the orthotropic stiffness, failure envelopes and the post-peak behavior, which include strain-softening damage and fracture mechanics aspects. This further implies that the SSM model must be able to automatically predict the energetic size effect.

4. The SSM model can be implemented as a material subroutine in finite element codes, either implicit or explicit. From experience with microplane models for concrete, the kinematically constrained formulation is known to be very stable in finite element analysis.

References

[1] I. M. Daniel, and O. Ishai (1994): *Engineering Mechanics of Composite Materials*. New York: Oxford University Press.

[2] G. Cusatis, A. Beghini, and Z. P. Bažant (2007): Spectral Stiffness Microplane Model for QuasiBrittle Composite Laminates: I. Theory. *J. Appl. Mech.*, ASME, in press.

[3] A. Beghini, G. Cusatis, and Z. P. Bažant (2007): Spectral Stiffness Microplane Model for QuasiBrittle Composite Laminates: II. Calibration and Validation. *J. Appl. Mech.*, ASME, in press.

[4] P. S. Theocaris, and D. P. Sokolis (1999): Spectral decomposition of the linear elastic tensor for monoclinic symmetry. *Acta Crystallographica*, **A55**, 635–647.

[5] Z. P. Bažant, and B. H. Oh (1985): Microplane model for progressive fracture of concrete and rock. *J. Eng. Mech.*, ASCE, **111**, 559–582.

[6] P. D. Soden, M. J. Hinton, and A. S. Kaddour (2002): Biaxial test results for strength and deformation of a range of E-glass and carbon fibre reinforced composite laminates: failure exercise benchmark data. *Composites Science and Technology*, **62**, 1489–1514.

[7] S. W. Tsai, and E. M. Wu (1972): A general theory of strength for anisotropic materials. *J. Composite Matls.*, **5**, 58–80.

Modeling of Wood in the Framework of Microplane Theory

J. Ožbolt

University of Stuttgart, Institute of Construction Materials
Pfaffenwaldring 4, 70569 Stuttgart, Germany
ozbolt@iwb.uni-stuttgart.de

Summary: The paper describes modeling of initial anisotropy of wood in the framework of microplane theory. The performance of the proposed model is demonstrated on one numerical example. In the example a 3D finite element analysis of a wooden specimen loaded in tension is carried out at the meso scale. The results are compared with the test results and the comparison shows reasonably good agreement.

Introduction

In engineering practice there is an obvious need for a model, which is able to realistically predict the response of materials with strong initial anisotropy, such as wood. Initial anisotropy is a consequence of the material structure, i.e. by nature the material has different properties in different directions (e.g. wood, fiber composite materials, etc.). In the present paper the microplane material model, which accounts for initial as well as damage induced anisotropy, is considered as a possible modeling alternative to the classical macroscopic models, which are based on the theory of tensorial invariants. The concept of the microplane model is based on the following fundamental assumption:

$$\Psi^M = \frac{3}{4\pi}\int_\Omega \Psi^m f(\boldsymbol{n}) d\Omega \qquad (1)$$

in which Ω represents the surface of the unite sphere, $\boldsymbol{n}$ is direction of the microplane, Ψ^m is the microplane free energy, Ψ^M is the macroscopic Helmholz free energy and $f(\boldsymbol{n})$ is empirical weighting function which controls the contribution of a single microplane to the macroscopic response of the material. Knowing or assuming Ψ^m and $f(\boldsymbol{n})$ it is possible to calculate macroscopic response from microplane responses using differential form of (1).

Initial anisotropy in the microplane model

There are two possibilities to account for initial anisotropy in the microplane model. The first, relatively simple one, is to set function $f(\boldsymbol{n})$ in (1) to be dependent on the orientation of the microplane normal relative to known weak direction(s) **w** (see Fig. 1). When the microplane direction coincides with the weak direction $f(\boldsymbol{n})$ = 0 and when it is perpendicular to it $f(\boldsymbol{n})$ = 1. Once the function $f(\boldsymbol{n})$ is known, the anisotropy is automatically accounted for. Here is the main difficulty to identify $f(\boldsymbol{n})$ from experiments. The second, more general possibility takes the advantage of the microplane formulation in which the uniaxial microplane constitutive laws ($\sigma_m = \partial\Psi^m/\partial\varepsilon_m$) are defined for each plane separately. The material anisotropy results automatically when these laws are adopted as a function of the microplane orientation. In the here used model the first approach was adopted.

To account for the anisotropy of wood, without discrete modeling of its structure, two coordinate systems were considered: (i) the local coordinate system (x,y,z), in which the analysis is carried out, and (ii) the material coordinates (X,Y,Z), which define the orientation of the material structure (see Fig. 2). The origin of the material coordinates coincides with the center of the cross-section of a tree.

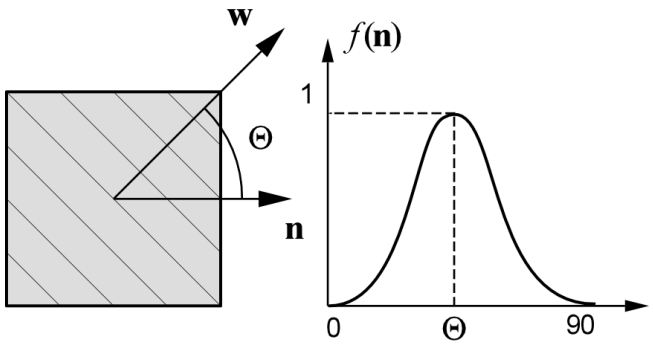

Figure 1: Orientation of weak direction.

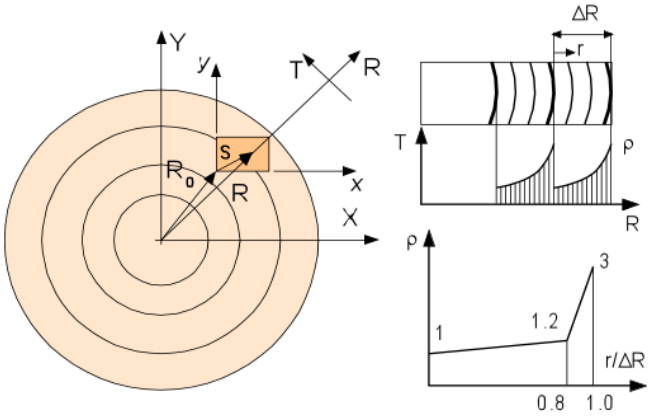

Figure 2: Position of the specimen in the cross-section of a tree and variation of density in the radial direction.

To account for three dominant directions of the wood structure (R-radial, T-tangential and L-parallel to the grain), two weak directions are defined by their unit vectors $\mathbf{w}_R$ and $\mathbf{w}_T$ (see Fig. 2) and one strong direction (parallel to the grain) is defined by $\mathbf{w}_L$. The resulting function $f(\boldsymbol{n})$, which controls the initial anisotropy in (1), is calculated as:

$$\begin{aligned} f(\boldsymbol{n}) &= f(\boldsymbol{n})_R \cdot f(\boldsymbol{n})_T \cdot f(\boldsymbol{n})_L \\ \text{with: } f(\boldsymbol{n})_R &= 1 - |\cos(\Theta_R)|^{\alpha_R} \\ f(\boldsymbol{n})_T &= 1 - |\cos(\Theta_T)|^{\alpha_T} \\ f(\boldsymbol{n})_L &= |\cos(\Theta_L)|^{\beta_L} \end{aligned} \qquad (2)$$

where Θ is the angle between the microplane orientation $\boldsymbol{n}$ and the corresponding orientation of the material weak or strong planes (R, T and L, see Fig. 2), respectively. Parameters α ($0 \leq \alpha \leq 1$) and β ($\beta \geq 1$) in (2) are empirical. Together with the basic microplane parameters, as defined in [2], they control the relation between initial stiffness and strength in the three dominant directions of the material.

Numerical example

The performance of the model is illustrated on one numerical example. In the example 3D finite element analysis of a wooden specimen loaded in uniaxial tension was carried out. The finite element discretization was performed using eight-node solid finite elements (see Fig. 3). The average element size in the zone of interest was 0.30 mm. To assure mesh objective results the crack band method was used. The analysis was performed at the meso scale, i.e. the size of the specimen in the companion experiment by Dill-Langer et al. [1] was roughly 10 mm. Due to the small specimen size and high level of anisotropy of wood, the homogenization of the material properties, typically used for macroscopic analysis, was not possible.

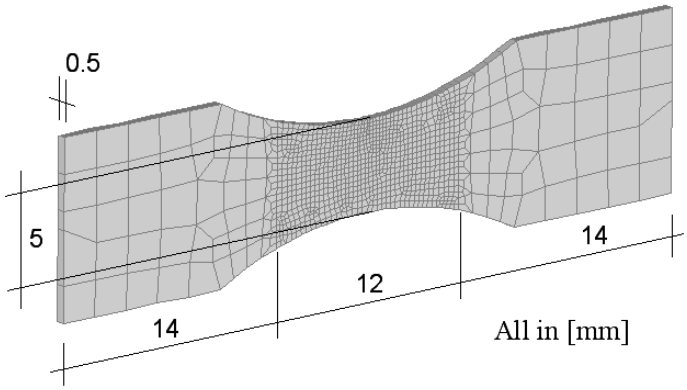

Figure 3: Geometry of the specimen and 3D finite element discretization.

The identification of the model parameters is not straightforward. Two levels of identification procedures were performed: (i) identification of average macroscopic properties of wood, which are typically required for macroscopic finite element analysis and (ii) identification of parameters that are needed for the analysis at the meso scale. The macroscopic set of model parameters can be used only if the specimen size is sufficiently large. For wood this is the case if the minimal specimen dimension is approximately larger than 50 mm. However, in the tests performed in [1] the specimen size was of the order of 10 mm and the size of the finite elements should be less than 1 mm. This implies that analysis at the meso scale needs to be carried out in order to account for the fact that over the width of the year ring ΔR (see Fig. 2), the size of which is roughly 1.5 mm, there is a large difference in the density of the wood. Consequently, the mechanical properties of the wood inside the ring varies considerably. To account for this, an additional internal variable ρ was introduced. Its value varies between 1 and 3 (see Fig. 2). The stiffness and the strength at the microplane level are assumed to be proportional to ρ.

The microplane model parameters obtained from the first level of calibration (macroscopic) were modified such that the resulting strength and the stiffness obtained from the meso analysis were similar to that obtained from the meso experiment on unnotched specimens loaded in the radial and tangential directions, respectively. The parameters α_R, α_T and β_L were assumed to be independent of the type of the analysis. It is interesting to observe that the resulting microplane parameters were such that the strength and the areas under the constitutive stress-strain curves (fracture energies) were in the meso analysis smaller than the corresponding macroscopic values. This is a consequence of the fact that the meso type of experiment (analysis) accounts only for local effects. The interaction over a distance is not accounted for. Consequently, as expected, the parameters of the model used in the meso analysis are not representative for macro analysis.

Results and conclusions

Similar to the experiment [1], after reaching maximum resistance the load drops immediately to zero, which indicates a brittle type of failure. The distribution of maximum principal strains on the hardening part of the load-displacement curve (20% of the peak load) is shown in Fig. 4a. The figure clearly reproduces the structure of wood, i.e. due to the lower density and strength of the younger part of the year rings, strains start to localize into these zones. Close before the peak load the crack propagates from the notch tip in the radial direction until it hits a ring of older wood. Subsequently, in the post-peak region the crack propagates along the direction of the year ring (see Fig. 4b). Similar crack propagation was observed in the experiment (Fig. 4c). It can be concluded that the presented model is able to predict the complex failure mechanism of wood at the meso scale without a need for the adopting the finite element mesh to the internal structure of the wood.

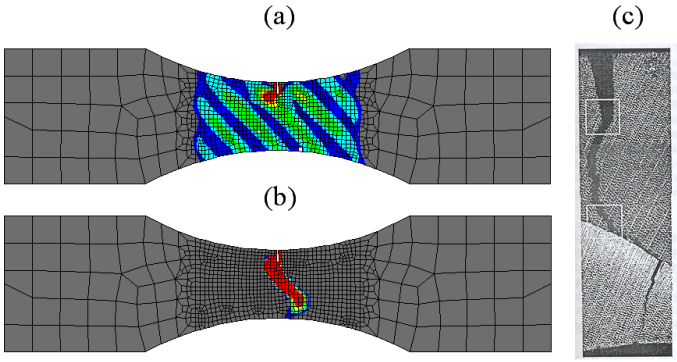

Figure 4: Localization of max. principal strains: (a) before peak load, (b) after peak load and (c) in the experiment [1].

References

[1] G. Dill-Langer, S. Lütze and S. Aicher (2002): Microfracture in Wood monitored by Confocal Laser Scanning Microscopy. *J. Wood Sci. Tech.*, **36**, 487–499.

[2] J. Ožbolt, Y.-J. Li, and I. Kožar (2001): Microplane model for concrete with relaxed kinematic constraint. *Int. J. of Solids and Structures*, **38**, 2683–2711.

Microplane Model for Soft Tissue

F. C. Caner*, **I. Carol**

Universitat Politecnica de Catalunya
School of Civil Engr., C. Jordi Girona 1-3, 08034 Barcelona, Spain
ferhun.caner@upc.edu, ignacio.carol@upc.edu

Summary: We summarize the microplane model for soft tissue and demonstrate the application of the model for human annulus fibrosus. Recently Peng et. al. [1] and Guo et. al. [2] showed that, the classical anisotropic hyperelastic constitutive models for soft tissue which do not account for the fiber-matrix shear interaction cannot simulate the behavior human annulus fibrosus. In this study, we show that the microplane model for soft tissue adjusted for human annulus fibrosus can accurately simulate the behavior of annulus fibrosus without fiber-matrix interaction. A comparison of results obtained from *(i)* a fiber-matrix parallel coupling model without the fiber-matrix interaction, *(ii)* the same model with fiber-matrix interaction, and *(iii)* microplane model for soft tissue adapted to annulus fibrosus is presented.

Introduction

Recently, two papers, [1] and [2], have been submitted for publication in which the fiber-matrix interaction is shown to be indispensable for simulating mechanical behavior of annulus fibrosus by optimally fitting various experimental data from literature and contrasting the results obtained from the model with fiber-matrix interaction against those from the model without any such interaction. In this study, microplane model for soft tissue published in [4] is adapted for annulus fibrosus by incorporating two fiber families in accordance with the physiology of the lamellae. To be able to provide a fair comparison, the 1D fiber constitutive law is kept the same as in [1], except for the material parameters, which have to be readjusted because of the 3D angular fiber distribution employed in the microplane model. The constitutive model for the matrix is neo Hookean in this model as well [5, 6]. In contrast, there is no explicit fiber-matrix interaction employed in microplane model for soft tissue. However, there is indeed interaction of distributed fibers provided automatically by construction of the model.

Microplane constitutive model for soft tissue

Isotropic incompressible neo-Hookean microplane model. The formulation for isotropic compressible neo Hookean microplane model was developed in [5] as part of a framework for hyperelastic microplane models and the anisotropic hyperelastic microplane model for blood vessel tissue was developed in [4]. In these formulations, the macroscopic free energy per unit volume, denoted $\rho_0\Psi$, is assumed to be integral of microplane free energies per unit area of a unit hemisphere Ψ_Ω, i.e.

$$\frac{2\pi R^3}{3}\rho_0\Psi = \int_\Omega \Psi_\Omega \mathrm{d}\Omega \tag{1}$$

Here $R = 1$ is the radius of the unit hemisphere, Ω denotes the surface of the unit hemisphere, ρ_0 is the mass density, Ψ is the macroscopic free energy per unit mass per unit volume, Ψ_Ω is the microplane free energy per unit area given by

$$\Psi_\Omega\left(\lambda_D, \lambda_J\right) = \mu_0\left(\frac{\lambda_D^2}{2} + \frac{\lambda_D^{-3}}{2} - \frac{5}{6}\right) + \frac{1}{3}g(J) \tag{2}$$

in which, μ_0 is the material constant, λ_D is distortional stretch and $J = \det F$ is the volume change with $F = \partial x/\partial X$ being the deformation gradient tensor and $g(J)$ is the volumetric energy function. The microplane stretch is defined as

$$\lambda_N = \lambda_D\lambda_J = \sqrt{\mathbf{N}\cdot\mathbf{C}\cdot\mathbf{N}} \tag{3}$$

where $\lambda_J = J^{1/3}$ is the volumetric stretch, $\mathbf{N}$ is the microplane normal vector, $\mathbf{C}$ is the right Cauchy-Green tensor. The volumetric energy function is given by

$$g(J) = \frac{\lambda_0}{2}\left(J + \frac{1}{J} - 2\right) \tag{4}$$

It can be shown that substitution of Eqs. 2, 3 and 4 into Eq. 1 results in

$$\rho_0\Psi = \frac{\mu_0}{2}\left(I_1^D - 3\right) + g(J) \tag{5}$$

where I_1^D is the first invariant of $\mathbf{C^D} = J^{2/3}\mathbf{C}$.

Collagen fibers: Anisotropic microplane model. In [6] it is reported that under a microscopic study of arterial tissue, a directional distribution of densely packed collagen structures is observed. The probability density function corresponding to the distribution of orientation of cell nuclei (and thus that of the collagen fibers) in a human aortic media in 2-D reported in that study is given in Fig. 1. To facilitate the computations, the discrete data points are fitted with a convenient probability density function given by

$$\phi(\mathbf{N}) = \Phi(\theta) = c_1\exp\left(c_2\theta^2\right) \tag{6}$$

where θ is the angle in radians measured from the circumferential direction. Thus, the proposed microplane constitutive law with a continuous representation of fiber directions in 3D can be expressed as

$$\boldsymbol{\Sigma} = \frac{3}{2\pi}\int_\Omega\left[\left(\frac{\Sigma_D}{\lambda_D\lambda_J^2} + \phi(\mathbf{N})\Sigma_F\right)\mathbf{N}\otimes\mathbf{N} - \frac{\Sigma_D}{3}\lambda_D\mathbf{C^{-1}}\right]\mathrm{d}\Omega + \Sigma_J\lambda_J\mathbf{C^{-1}} \tag{7}$$

where the fiber stress is $\Sigma_F = \partial\Psi^F/\partial\lambda_F$ in which $\lambda_F^2 = \mathbf{N}\cdot\mathbf{C}\cdot\mathbf{N}$ and $\Psi^F = C_2(\lambda_F^2 - 1)^2 + C_3(\lambda_F^2 - 1)^2$ if $\lambda_F > 1$, $\Psi^F = 0$ if $\lambda_F < 1$.

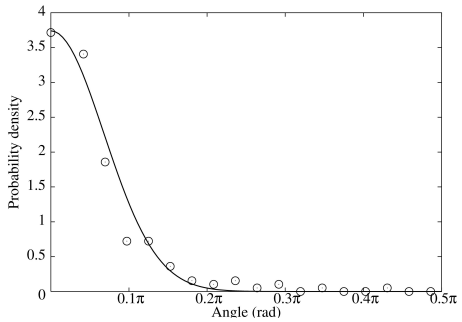

Figure 1: The distribution of orientation of cell nuclei (and thus of collagen fibers) in aortic media (taken from [6]).

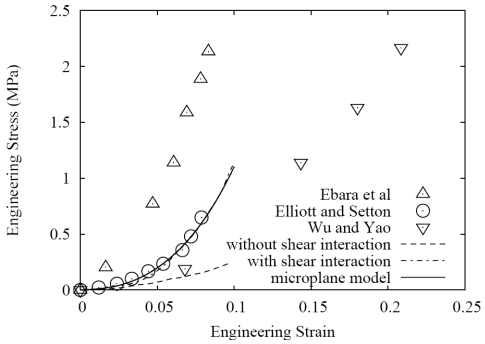

Figure 2: Tensile behavior of multi-layer human anterior outer annulus fibrosus; inter-fiber angle is $60°$.

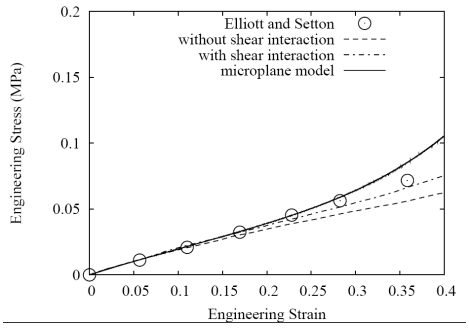

Figure 3: Tensile behavior of multi-layer human anterior outer annulus fibrosus; inter-fiber angle in loading direction is $120°$.

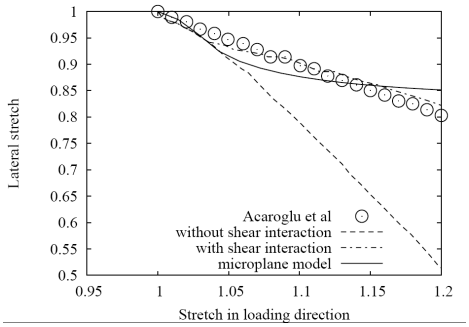

Figure 4: Inter-fiber angle change vs stretch in loading direction in multi-layer annulus fibrosus; inter-fiber angle in load direction is $60°$.

Discussion of results

The predicted mechanical response from fiber-matrix parallel coupling model *(i)* without shear interaction, *(ii)* with shear interaction, and *(iii)* microplane model for annulus fibrosus, are demonstrated in Figs. 2–5. The plot in Fig. 2 shows that the material properties of annulus fibrosus show significant differences due to factors such as age, lifestyle and diseases. In this study we chose to fit the one by Elliott and Setton [3], because they also provide equivalent data in the perpendicular direction, as shown in Fig. 3. These two figures are simultaneously fitted to calibrate the material constants as $C_2 = 0.45$ MPa, $C_3 = 82.6$ MPa for the parallel coupling and as $\mu_0 = 0.068$ MPa, $C_1 = 6$ MPa, $C_2 = 4000$ MPa, $c_1 = 20.5$ and $c_2 = -80$ for the microplane model. All other test data are simulated with the material parameters being fixed. In Fig. 4, microplane model performs as well as the parallel coupling model with interaction even though it does not have the explicit formulation for interaction, but the performance of the model without the interaction may be considered not acceptable. In Fig. 5 microplane model performs similar to parallel coupling model with shear interaction; that without the interaction performs poorly.

References

[1] X. Q. Peng, Z. Y. Guo and B. Moran 2006: An anisotropic hyperelastic constitutive model with fiber-matrix interaction for the human annulus fibrosus. *J. of Applied Mechanics*, **73**, 815–824.

[2] Z. Y. Guo, X. Q. Peng and B. Moran (2006): A composites-based hyperelastic constitutive model for soft tissue with application to the human annulus fibrosus. *J. of the Mechanics and Physics of Solids*, **54**, 1952–1971.

[3] D. M. Elliott, L. A. Setton (2001): Anisotropic and inhomogeneous tensile behavior of the human annulus fibrosus: Experiments measurement and material model predictions. *J. of Biomechanical Engineering*, **123**, 256–263.

[4] F. C. Caner, I. Carol (2006): Microplane constitutive model and computational framework for blood vessel tissue. *J. of Biomech. Eng. – Transactions of the ASME*, **128**, 419–427.

[5] I. Carol, M. Jirásek and Z. P. Bažant (2004): A framework for microplane models at large strain, with application to hyperelasticity. *Int. J. Solids Structures*, **41**, 511–557.

[6] G. A. Holzapfel (2003): Structural and numerical models for (visco) elastic response of arterial walls and residual stresses. *Biomech. of soft tissue in card. sys.*, 109–184.

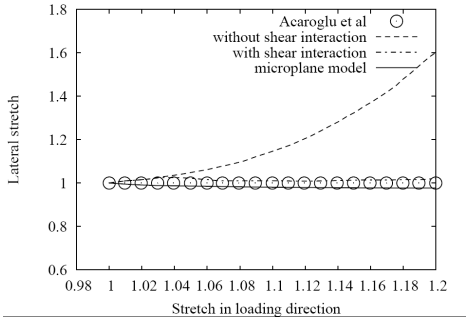

Figure 5: Stretch in through-thickness vs stretch in load direction in multi-layer annulus fibrosus; inter-fiber angle in load direction is $60°$.

An Approach for a Constitutive Relation for Skeletal Ligaments Using a Microplane Model

A. E. Blangino*, S. Valente, M. Barba

Gabinete de Biomecánica, Dep. of Mechanical Engineering, Faculty of Engineering, University of Buenos Aires
Paseo Colón 850 (1063) Buenos Aires, Argentina
eblangi@fi.uba.ar, sergiovalente@fibertel.com.ar, martingbarba@gmail.com

Summary: The connective tissue in ligaments is composed mainly of collagen fibrils, with contributions from trapped water and mucopolysaccharide ground substance matrix. In this work we develop constitutive relations for the skeletal ligament material based on the microplane formulation at large strain. New microplane strain measures are tested to take into account the fiber stretch. We compare our results with classical macroscopical formulations.

Introduction

The skeletal ligaments are short bands of tough fibrous connective tissue binding bones together across joints. The tissue is formed by an amorphous matrix with collagen bands across it. Ligaments typically sustain uniaxial loads and therefore the constituent collagen fibers are highly aligned, showing nonlinear properties in the primary loading direction.

There are several works devoted to characterize the mechanical response of ligaments to uniaxial loads (partial reviews in [1, 2]).

Mathematical models of ligament behavior are, in general, characterized as phenomenological (containing exponential or bilinear functions selected to best fit uniaxial stress-strain data) or structural (based on the structure or microstructure of tissue components). Both type of characteristics can be incorporated in hyperelastic models (into the strain energy function).

The amorphous matrix (quasi-fluid with random inclusions) is modeled as non-linear isotropic and the oriented collagen fibers allow to capture the anisotropy of the mechanical response. Some models include also the fiber-matrix interactions [3].

The hyperelastic formulation is used in the traditional (tensorial) context to establish the mathematical model for the material behavior. To capture the transversal isotropy of the material, five invariants (I_i, $i = 1, \dots 5$) introduced by Spencer [4] are used ($\boldsymbol{C}$ is the the right Cauchy Green tensor and a^0 the fiber direction in the reference configuration):

$$I_1 = \mathrm{tr}\boldsymbol{C}, I_2 = \frac{1}{2}\left[(\mathrm{tr}\boldsymbol{C})^2 - \mathrm{tr}\boldsymbol{C}^2\right], I_3 = \det \boldsymbol{C}$$

$$I_4 = a^0.\boldsymbol{C}.a^0, I_5 = a^0.\boldsymbol{C}^2.a^0$$

I_1, I_2 and I_3 are associated with the isotropic matrix (as usual, we assume it incompressible, I_3 = 1), I_4 enables us to take into account the interaction between the fibers stretch and the bulk matrix and I_5 let us to include shear fiber-matrix interactions.

As the ligaments can be considered as incompressible, only four invariants are needed in the formulation.

The smart use of the invariants allows good agreements with the observed characteristics (a bilinear model [3] or a derivable one [5, 6] combining Mooney-Rivlin hyperelasticity with exponential stretching). These models are based on a macroscopic formulation.

The aim of this work is to develop a model for the material of the ligaments, based on the microplane theory [7].

Constitutive equations for a transversally isotropic elastic material

This study takes into account finite deformations at macroscopical level. The Lagrangian formulation is used because the Green Lagrange strain tensor $\mathbf{E}$ and the second Piola Kirchhof stress tensor $\boldsymbol{\Sigma}$ are energetically conjugates in the hyperelastic formulation [7].

With the usual notation ($\boldsymbol{F}$ for the deformation gradient, $\boldsymbol{C}$ as above, for the right Cauchy Green tensor) let $\rho_0\Psi$ be the free energy density per unit volume. According to the microplane theory, it can be written as [7]

$$\rho_0\Psi = \frac{3}{2\Pi}\int_{\Omega} \Psi_\Omega \left(E^{(N)}, N\right) d\Omega \qquad (1)$$

with $\Psi_\Omega = \Psi^{(N)}$ the free energy for the microplane (defined by the normal vector N) and $E^{(N)}$ a suitable set of microplane strain measures functionally related. When the microplane strain measures are specified, the macroscopic stresses can be computed as:

$$\boldsymbol{\Sigma} = \frac{\partial(\rho_0\Psi)}{\partial \boldsymbol{E}} = \frac{3}{2\Pi}\int_{\Omega} \Sigma^{(N)} \bullet \frac{\partial E^{(N)}}{\partial E} d\Omega \qquad (2)$$

being $\Sigma^{(N)} = \partial\Psi_\Omega/\partial E^{(N)}$, the microplane stresses.

It is accepted that, for ligaments, $\rho_0\Psi$ can be expressed as [2, 3]:

$$\rho_0\Psi = F_1(I_1, I_2) + F_1(I_4) + F_1(I_1, I_2, I_4, I_5) \qquad (3)$$

where F_1 represents the material response of the (isotropic) matrix. F_2 accounts for the fibers' stretch and F_3 is the contribution from the interaction between fibers and ground substance.

In this work we develop an expression for the microplane strain energy that recovers the Neo-Hookean model for the amorphous matrix and depends on the direction a^0 of the fibers. It has the following general form:

$$\Psi^{(N)} = E_\lambda \left(\frac{\lambda_N^2}{2} + \frac{\lambda_N^{-3}}{3} - \frac{5}{6}\right) + \left|a^0.N\right| f(\lambda_a) \qquad (4)$$

with E_λ constant (calibrated experimentally), $\lambda_N = |N.\boldsymbol{F}|$ the microplane stretch of the matrix fiber initially aligned with the microplane normal N, and $f(\lambda_a)$ a suitable function of the collagen fiber stretch λ_a.

The first term in the right hand side of (4) leads to the (well known) Neo-Hookean model, as is demonstrated in [7].

Two possibilities for the functional form of f are analyzed. The results are compared with those published.

References

[1] Y. C. Fung (1993): Mechanical Properties of Living Tissues. 2nd ed. Springer Verlag.

[2] J. Weiss, J. Gardiner (2001): Computational Modeling of Ligament Mechanics , *Critical reviews in Biomechanical Engineering*, **29**, 1–70.

[3] H. A. Guerin, D. Elliot (2005): The Role of Fiber-Matrix Interactions in a Nonlinear Fiber-Reinforced Strain Energy Model of Tendon. *Journal of Biomechanical Engineering*, **27**, 45–350.

[4] A. J. M. Spencer (1984): Constitutive Theory for StronglyAnisotopic Solids. In *Continuum Theory of the Mechanics of Fibre-Reinforced Composites*, A.M.J. Spencer ed, Springer Verlag, New York, 1–32.

[5] J. Weiss, J. Gardiner, K. Quapp (1995): Material model for the Study of soft Tissue Mechanics. In *Proc. International Conference on Pelvic and Lower Extremity Injuries*, Wash. DC, December 4-6, 249–261.

[6] K. Quapp, J. Weiss (1998): Material characterizationof human medial collateral ligament.ASME *J. Biomech. Eng.*, **120**, 757–763.

[7] I. Carol, M. Jirásek, Z. P. Bažant (2004): A framework for microplane models at large straisn, with apllication to hyperelasticity. *International Journal of Solid and Structures*, **41** , 511-557.

Elastoplastic Microplane Model for Cohesive-Frictional Materials: Application to Geotechnical Engineering Problems

F. A. Sánchez, P. C. Prat*

Technical University of Catalonia (UPC)
Jordi Girona 1-3 – Edif. D2, 08034 Barcelona, Spain
tunnel_borer@yahoo.com, pere.prat@upc.edu

Summary: This paper deals with the application of the microplane theory within the framework of general elastoplasticity to the field of geotechnical engineering. Microplane theory, combined with other constitutive laws such as elastoplasticity and damage, holds a great potential for advanced material modelling. However, the application of the elastoplasticity theory within the constitutive framework of microplanes, adequate to represent the real behaviour of geotechnical materials, has proven to be a complex problem. In this paper the main characteristics of a microplane elastoplastic constitutive law which reproduces well the overall response for complex kinds of behaviour, typical of geological materials will be discussed.

Constitutive modelling of cohesive-frictional, quasi-brittle materials such as concrete has experienced a great progress and reached an important degree of refinement through the development of algorithms such as the M4 and M5 models of Bažant and co-workers [1–8]. However, such models utilise a considerable amount of non-dimensional, fixed and non-fixed adjustable parameters, which for the case of concrete have been identified after long trial and verification processes. Some geologic materials, particularly rocks, exhibit many of the constitutive features observed also in concrete. However, due to the large number of variables that played a role in the geological processes that formed such materials, it seems almost impossible trying to identify all the parameters that would be necessary to represent the material's behaviour with a microplane model. Moreover, geological materials range from hard rocks, of quasi-brittle behaviour, to soft rocks or soils which exhibit a more plastic behaviour. A general model for this wide collection of materials would have no practical engineering applications unless its behaviour can be modelled with only a limited number of easily-measurable parameters.

The aim of the research summarized in this paper is the development of an engineering application based on the microplane theory adequate to solve practical geotechnical problems such as excavations, slopes, earth and rockfill dams, etc. One way of achieving this, taking the advantages of microplane modelling, consists in defining a microplane elastoplastic constitutive law whose yield criterion is based on parameters that can be easily related to those of some classical invariant-based macroscopic model. A fundamental feature to achieve is that the microplane model parameters can be automatically calculated from typical geotechnical engineering data like friction angle, cohesion and tensile strength. This requires a very good knowledge of the relations between the microplane parameters and the macroscopic response of the model. However, the application of the elastoplasticity theory within the constitutive framework of microplanes, adequate to represent the real behaviour of geotechnical materials has proven to be a complex problem. A proposal for the coupling of elastoplasticity and microplane theory has already been presented by the authors [9, 10]. Its fundamental features, and application to solving boundary value problems, are to be extended in the present paper.

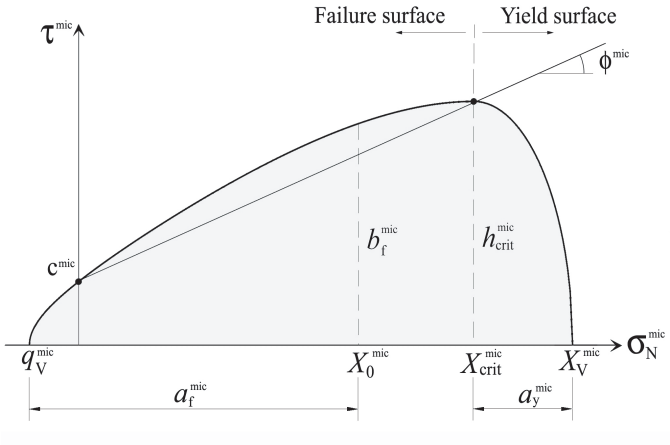

Figure 1: Yield surface on the τ-σ_N plane for each microplane.

A crucial point of the coupled microplane-elastoplasticiy formulation of a material model is the understanding of how the microplane constitutive equations are linked to the macroscopic response, not only in terms of parameters, but also in terms of the shape of the macroscopic yield surface deduced from the integrated microplane plastic stresses. In this paper we will discuss the main characteristics of a microplane elastoplastic constitutive law which reproduces well the overall response for complex kinds of behaviour, typical of geological materials. For this purpose a three yield surface (one for tension, one for cohesive-frictional response and one for volumetric yielding), fully elastoplastic formulation will be presented. Fig. 1 shows the yield surface defined for each microplane on the τ-σ_N stress space. After integration, the macroscopic yield surface shown in Fig. 2, in the principal stress space, is obtained.

In the first part of the paper some classical rock mechanics laboratory tests will be simulated via finite element models (solving the boundary value problem) in order to study the capability of the algorithm to represent the progressive plastification and failure of the rock samples and the relation of such plastic phenomena with the orientation of different planes within the material matrix. A main objective of the experiments is the establishment of the relations between microplane input parameters and the local and global failure response of the samples,

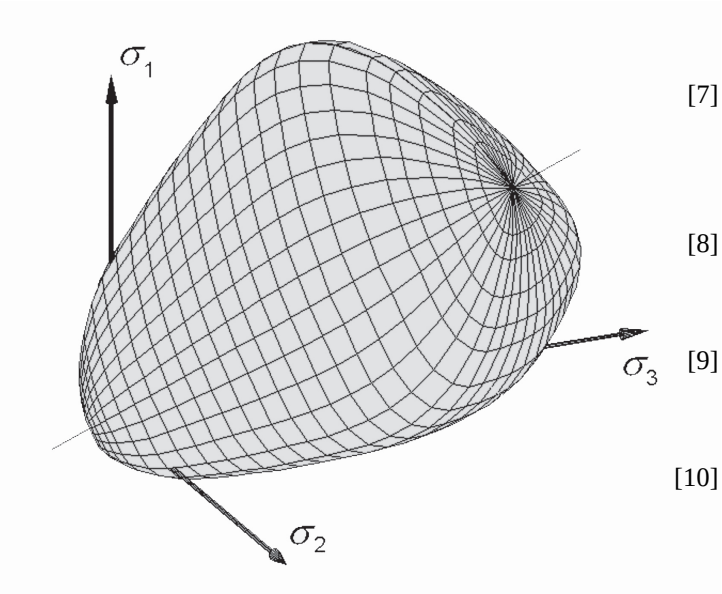

Figure 2: Macroscopic yield surface in the principal stress space.

as well as its deformational processes.

In the second part, the potential of the model for simulating anisotropy (inherent and/or induced) will be tested. The algorithm allows the user to define any number of inherent anisotropy directions not necessarily coinciding with the exact orientation of particular microplanes. Then, the anisotropic parameters are distributed on the microplanes assigning different weights according to their proximity to the anisotropy directions. Again, some classical laboratory tests will be simulated with a general finite element code.

References

[1] Z.P. Bažant, F.C. Caner (2005): Microplane model M5 with kinematic and static constraints for concrete fracture and anelasticity. I: Theory. *Journal of Engineering Mechanics-ASCE*, **131**, 31–40.

[2] Z.P. Bažant, F.C. Caner (2005): Microplane model M5 with kinematic and static constraints for concrete fracture and anelasticity. II: Computation. *Journal of Engineering Mechanics-ASCE*, **131**, 41–47.

[3] Z. P. Bažant, G. di Luzio (2004): Nonlocal microplane model with strain-softening yield limits. *International Journal of Solids and Structures*, **41**, 7209–7240.

[4] Z. P. Bažant, G. S. Zi (2003): Microplane constitutive model for porous isotropic rocks. *International Journal for Numerical and Analytical Methods in Geomechanics*, **27**, 25–47.

[5] F. C. Caner, Z.P. Bažant (2000): Microplane model M4 for concrete: I. Formulation with work-conjugate deviatoric stress. *ASCE J. Engrg. Mech.*, **126**, 944–953.

[6] Z. P. Bažant, F. C. Caner, I. Carol, M. D. Adley, S. A. Akers (2000): Microplane model M4 for concrete: II.Algorithm and calibration. *ASCE J. Engrg. Mech.*, **126**, 954–961.

[7] Z. P. Bažant, Y. Xiang, M. D. Adley, P. C. Prat, S. A. Akers (1996): Microplane model for concrete: I. Stress-strain boundaries and finite strain. *ASCE J. Engrg. Mech.*, **122**, 245–262.

[8] Z. P. Bažant, Y. Xiang, P. C. Prat (1996): Microplane model for concrete: II. Data delocalization and verification. *ASCE J. Engrg. Mech.*, **122**, 263–268.

[9] F. Sánchez, P.C. Prat (2005): Elastoplasticity within the framework of microplane models. Part I: Basic concepts, in *IACMAG-11*. Pàtron Editore: Torino, Italy, 489–496.

[10] F. Sánchez, N. A. González (2005): Elastoplasticity within the framework of microplane models. Part II: Applicable models for their use in geotechnical analyses, in *IACMAG-11*. Pàtron Editore: Torino, Italy, 497–504.

Microplane Model and Solidification-Microprestress Theory for Early Age Concrete Behavior

G. Di Luzio[1*], **G. Cusatis**[2]

[1]Department of Structural Engineering, Politecnico di Milano
Plazza Leonardo da Vinci, 32, 20133, Milano, Italy
diluzio@stru.polimi.it

[2]Department of Civil and Environmental Engineering, Rensselaer Polytechnic Institute
4048 Johnsson Engineering Center, 110 Eighth St, Troy, NY, USA
cusatg@rpi.edu

Summary: This paper presents a constitutive model for early age concrete behavior that is formulated through the amalgamation and extension of two existing models: 1) the microplane model M4, and 2) the microprestress-solidification theory. The resulting constitutive model is able to simulate the main features of concrete behavior, such as creep, shrinkage, thermal deformation, cracking, and damage from the beginning of the hydration process up to the complete maturity.

Introduction

In concrete constructions a great effort is nowadays made to ensure the durability and the functionality of the structures being built. Cracking due to shrinkage and to thermal effects is one of the cause of major concern, particulary at early ages. This kind of non-structural cracks can induce major structural problems and/or mar the appearance of monolithic constructions. In addition, reinforcing steel may become exposed to oxygen and moisture that lead to an increased chance of corrosion.

The work presented in this paper is part of a research effort aiming at the formulation of a hygro-, thermal-, chemical-, and -mechanical computational framework for the simulation of concrete mechanical behavior at the early age and beyond. Such a framework will enable the design and construction of more durable and more functional reinforced concrete structures. The hygro-thermal-chemical problem (not discussed herein) is solved by choosing temperature, relative humidity as the primary variables governed trough standard mass and energy balance equations. The hydration processes are assumed to influence the solution of the hygro-thermal problem through the evolution of the hydration degree, which describes the hydration rate as a function of chemical affinity. The hygro-thermal-chemical problem is then coupled with the mechanical problem where a suitable constitutive law is adopted. The main features of this constitutive law is described in the following.

Early age constitutive model

In absence of high confining pressure, concrete strain can be additively decomposed into several components: the instantaneous strain, ϵ_i, the viscoelastic strain, ϵ_{ev}, the purely viscous strain, ϵ_f, the inelastic strain (due to cracking and damage), ϵ_{cr}, the free shrinkage strain, ϵ_{sh}, and the thermal strain, ϵ_T.

The instantaneous strain is the strain that appears immediately after the application of loads and, it can be considered time and age independent. The viscoelastic strain models the visco-elastic properties of the solid gel of calcium silicate hydrates and it can be described effectively according to the solidification theory [6] in which the aging of concrete is modeled through the volume growth of a non-aging constituent: $\dot{\epsilon}(t) = \dot{\gamma}(t)/v(t)$. The function $v(t)$ approximately describes the volume fraction of solidified material during the hydration processes and the variable $\dot{\gamma}(t)$ is the viscoelastic strain in the cement gel, which is assumed to be fully recoverable upon unloading. The purely viscous strain (flow strain) ϵ_f is the completely irrecoverable part of the creep strain, which can be described through the microprestress theory [4, 3]. The rate of the viscous strain is formulated as a power function of the so-called microprestress *S*, which is an average measure of the self-equilibrated micro-stresses acting across the slip planes represented by the hindered adsorbed water layers in the microstructure of the cement paste. The microprestress theory can accurately describe long-term aging, as well as drying creep and transitional thermal creep [3].

Damage and cracking strain is modeled through the microplane model M4 [1, 10], in which the constitutive relation is formulated in terms of stress and strain vectors acting on several microplanes with different orientation in a certain material point. The microplane strains are obtained through projection of the strain tensor (kinematic constraint) and the stress tensor is obtained by a weak enforcement of the equilibrium (principle of virtual work). The model is rate dependent and the rate-dependence is based on the activation energy concept [2]. To prevent pathological spurious mesh sensitivity, the concept of crack band model [5] is also adopted. A realistic aging model has been established in which the mechanical properties act as internal-like variables, and their evolution laws must at least be formulated in terms of hydration degree and temperature. In this work, the microplane model M4 has been extended in order to take into account the effect of aging on concrete strength and brittleness. Following the approach proposed in [8] the microplane material parameters are made dependent on both hydration degree and temperature. Both hydration degree and temperature are obtained from the solution of a coupled hygro-thermal-chemical problem.

The rate of the free shrinkage strain (shrinkage of a stress-free volume of material) is assumed to be proportional to the change

of relative humidity and the rate of the thermal strain is assumed to be proportional to the change of temperature.

Numerical examples

The numerical algorithm developed by Di Luzio [10] to incorporate the early age mechanical model into the numerical solution of coupled hygro-thermo-chemo-mechanical problems is adopted in this work. In the following, two numerical examples are used to validate the overall computational framework. The first one deals with the simulation of the response of concrete specimens, both in sealed and drying conditions, loaded at different ages [7]. The simulation of companion specimens subjected only to humidity variations is also carried out (Fig. 1). In the second example the effect of the aging on the mechanical properties is simulated with reference to the experimental investigation of Khan et al. [11] (Fig. 2). The examples show that the proposed model is a promising tool for analysis of concrete structures starting from the initial stages of the hydration process up to the complete maturation. Extensive calibration and validation of the model is ongoing.

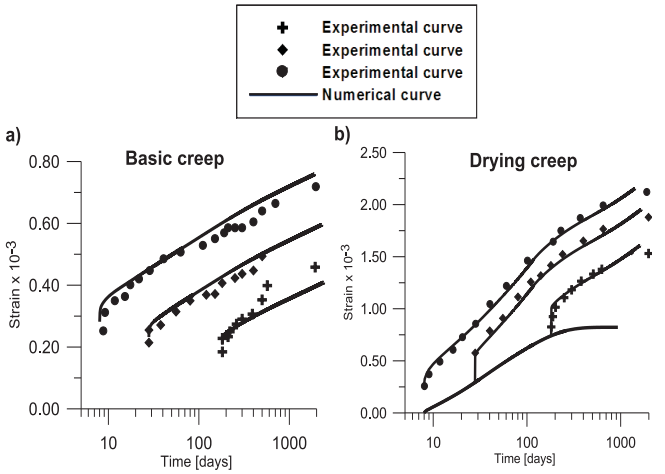

Figure 1: Comparison between numerical results and experimental results by Bryant and Vadhanavikkit [7] concerning the response of concrete specimens loaded at the age of 8, 28, 84 and 182 days: a) sealed specimen (basic creep); and b) unsealed specimen (drying creep).

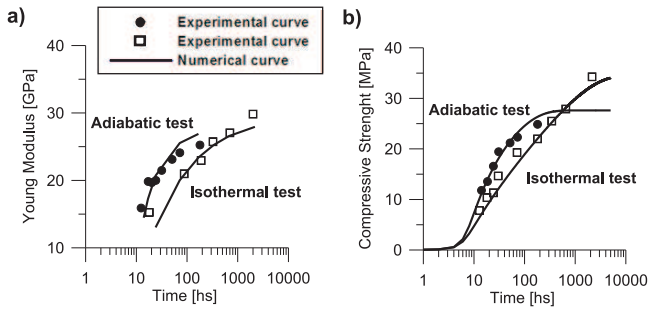

Figure 2: Numerical vs experimental results (Khan et al. [11]) relevant to the effect of aging on Young modulus and compressive strength.

Conclusion

This paper describes a thermo-chemo-mechanical model that accounts for many of the features observed in the behavior of concrete at early ages. The short-term mechanical behavior is based on the microplane model M4 extended to include the phenomenon of aging. The long-term mechanical behavior is based on the microprestress-solidification theory. The capabilities and potentialities of the model are shown by performing simulations of some available experimental data with a good agreement between the numerical and the experimental results.

References

[1] Z. P. Bažant, F. Caner, I. Carol, M. Adley, S. A. Akers (2000): Microplane Model M4 for Concrete I.: formulation with work-conjugate deviatoric stress. *Journal of Engineering Mechanics*, **126**, 944–953.

[2] Z. P. Bažant, F. Caner, M. Adley, S. A. Akers, (2000): Fracturing rate effect and creep in microplane model for dynamics. *Journal of Engineering Mechanics*, **126**, 962–970.

[3] Z. P. Bažant, G. Cusatis, L. Cedolin (2004): Temperature Effect on Concrete Creep Modeled by Microprestress-Solidification Theory. *Journal of Engineering Mechanics*, **130**, 691–699.

[4] Z. P. Bažant, A. B. Hauggaard, S. Baweja, F. J. Ulm (1997): Microprestress-solidification theory for concrete creep I.: Aging and drying effects. *Journal of Engineering Mechanics*, **123**, 1188–1194.

[5] Z. P. Bažant, B.-H. Oh (1983): Crack band theory for fracture of concrete. *Material and Structures*, **16**, 155–177.

[6] Z. P. Bažant, S. Prasannan (1989): Solidification theory for concrete creep I.: formulation. *Journal of Engineering Mechanics*, **115**, 1691–1703.

[7] A. H. Bryant, C. Vadhanavikkit (1987): Creep, shrinkage-size, and age at loading effects. *ACI Materials Journal*, 117–123.

[8] M. Cervera, J. Olivier, T. Prato (1999): A thermo-chemo-mechanical model for concrete I.: hydration and aging. *Journal of Engineering Mechanics*, **125**, 1018–1027.

[9] G. Di Luzio (2007): A numerical model for concrete time-dependent fracturing. Submitted to *Journal of Engineering Mechanics*.

[10] G. Di Luzio (2007): A symmetric over-nonlocal microplane model M4 for fracture in concrete. *International Journal of Solids and Structures* (in press).

[11] A. A. Khan, W. D. Cook, D. Mitchell (1995): Early age compressive stress-strain properties of low-medium, and high-strength concretes. *ACI Material Journal*, **92**, 617–624.

Microplane M4 Model for Fiber Reinforced Concrete

M. T. Kazemi*, I. Zakeri

Sharif University of Technology
Tehran, Iran
kazemi@sharif.edu, zakeri@mehr.sharif.edu

Summary: In this paper, an extension of the Microplane model M4 is presented. The stress-strain boundaries are modified and new boundaries are defined. It is assumed that fibers act in parallel with the concrete matrix. By adapting the sub-material algorithm, which is used in microplane model M4 for plain concrete, a new code was generated for the modeling of Fiber Reinforced Concrete (FRC) under uniaxial tension and compression. The enhanced microplane model M4 predictions agree with the existing uniaxial tension and compression experimental data for FRC.

Introduction

In recent years, the microplane model was developed and widely used for concrete and other quasi brittle materials. In this work, an extension of the Microplane model M4 is presented for Fiber Reinforced Concrete (FRC). By adding fibers, the mechanical behavior of concrete, such as crack resistance and fracture toughness, is enhanced. If the fiber content is in the range of 0.2 to 2 percent of concrete volume, it is called low content FRC. As it can be seen from previous works, the pre peak tension and compression behavior of low content FRC is the same as the plain concrete, but its post peak behavior is differed by the more ductile behavior of FRC than plain concrete [1,2]. In this paper, the Microplane M4 model was developed for prediction of FRC behavior under uniaxial tension and compression. The enhanced microplane model M4 can simulate the behavior of FRC with high fiber content, too. The prediction has a good agreement with the existing experimental data in both pre peak and postpeak regions.

Review of basic relations of microplane model

The microplane constitutive model is defined by a relation between the stresses and strains acting on a plane having an arbitrary orientation, characterized by its unit normal n_i [3]. The basic hypothesis, which is ensures stability of post peak strain softening [4], is that the strain vector on the microplane is the projection of macroscopic strain tensor. Therefore:

$$\varepsilon_N = N_{ij}\varepsilon_{ij} \tag{1}$$

$$\varepsilon_M = M_{ij}\varepsilon_{ij}, \qquad \varepsilon_L = L_{ij}\varepsilon_{ij} \tag{2}$$

where ε_N is normal strain on microplane and ε_M and ε_L are shear strains on microplane. In equations (1) and (2), $N_{ij} = n_i n_j, M_{ij} = (m_i n_j + m_j n_i)/2,\ L_{ij} = (l_i n_j + l_j n_i)/2$ (repetition of the subscript implies summation). The kinematic constraint relates strains on the micro level (microplane) and macro level (continuum). Therefore, the static equilibrium can be enforced approximately by principle of virtual work [4] written for surface Ω of the unit hemisphere:

$$\frac{2\pi}{3}\sigma_{ij}\delta\varepsilon_{ij} = \int(\sigma_N\delta\varepsilon_N + \sigma_M\delta\varepsilon_M + \sigma_L\delta\varepsilon_L)d\Omega \tag{3}$$

The most general constitutive relations on the microplane level, is considering the microplane stresses as a function of its strain [4]. The general relation of stress-strain boundaries are:

$$\sigma_N \le F_N(\varepsilon_N) \tag{4}$$

$$F_V^-(\varepsilon_V) \le \sigma_V \le F_V^+(\varepsilon_V) \tag{5}$$

$$F_D^-(\varepsilon_D) \le \sigma_D \le F_D^+(\varepsilon_D) \tag{6}$$

$$|\sigma_M| \le F_T(\sigma_N, \varepsilon_V) \tag{7}$$

$$|\sigma_L| \le F_T(\sigma_N, \varepsilon_V) \tag{8}$$

The relation of this boundaries can be found in [4] in more details.

Enhanced microplane M4 model for FRC

By adding fiber in low content, the concrete shows more ductile behavior in post peak region. Microplane model can reproduce the macroscopic inelastic behavior with using simple relation between stresses and strains which are acting on planes with arbitrary orientation. Thus, for considering the effect of fibers in concrete, we assume that they act in parallel with the matrix. Therefore we can say:

$$\sigma_N = \sigma_N^m + \sigma_N^f \tag{9}$$

$$\sigma_L = \sigma_L^m + \sigma_L^f \tag{10}$$

$$\sigma_M = \sigma_M^m + \sigma_M^f \tag{11}$$

In these relations, the superscript m and f are implies matrix and fiber, respectively.

For this simulation, we should define the boundaries for fibers the same as the boundaries for concrete, which are defined in [4]. We assume that fibers incrementally elastic in their boundaries and they can not violet their boundaries. According to previous works, the FRC up to a specific percentage of fiber content has a same stress and strain peak as plain concrete [2]. This behavior enforced to define restriction fiber content in normal stress boundary of fiber. We called it threshold percent, α. For instance the normal boundary for fiber can be formulated as below:

$$\begin{aligned}\sigma_N^{bf} &= F_N(\varepsilon_N, \alpha, x) = xE_f k_{f4} c_1 \langle x - \alpha\rangle A \\ &\quad + \langle \varepsilon_N - c_1 c_2 k_1\rangle x E_f k_{f1} c_1 A\end{aligned} \tag{12}$$

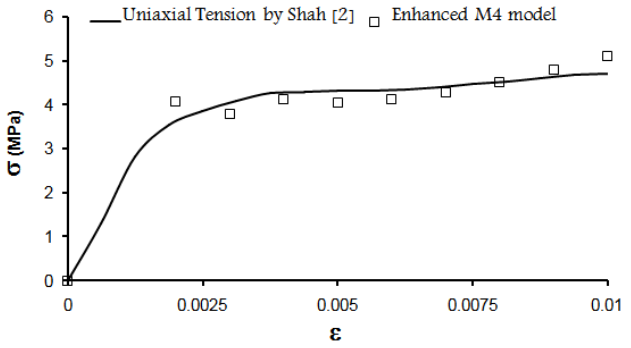

Figure 1: Uniuaxial tension test data of Shah [2] and optimized fit with enhanced M4 model.

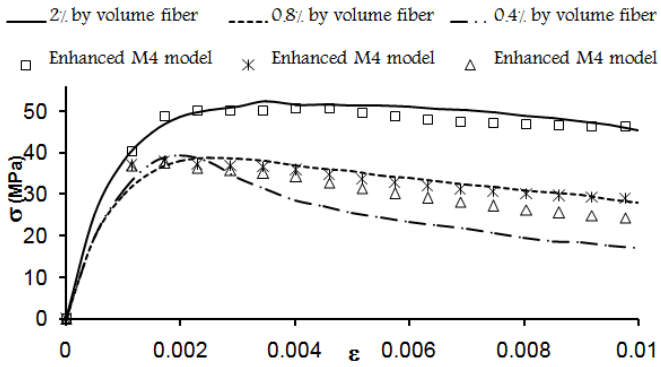

Figure 2: Uniaxial compression tests data from Shah [2] and optimized fits with enhanced M4 model.

where:

$$A = \exp\left(-\frac{\langle \varepsilon_N - c_1 c_2 k_1 \rangle}{k_1 c_3 + c_4 \langle -\frac{\sigma_V}{\varepsilon_V} \rangle}\right) \tag{13}$$

In these equations, the parameters c_i are constant parameters, which are defined in more details in [4], E_f is fiber Young modulus, k_f are fitting parameters, which are defined the various concrete behavior, and x is fiber content. The first term of equation (12) defines the change in pre peak behavior of FRC according to the threshold percent and the second term is defined the post peak behavior. The volumetric and deviatoric boundary can be the same as for concrete.

Predicting of test results

To examine the accuracy of the enhanced microplane M4 model, simulation of uniaxial tension and compression test are conducted. For this purpose, we use the uniaxial test result which of Shah [2]. In this experiment, the specimen had 2% fiber content and the fibers are smooth steel fiber with 25 mm length and 0.43 mm diameter. As Fig. 1 illustrates, the model has a good agreement with the test result.

We also used uniaxial compression test which of Shah [2] with various percent of fiber content. Fig. 2 illustrates the good prediction of the uniaxial compression behavior with different content of fibers. As it is expected, by increasing the fiber content, the peak point is also affected and the post peak region is more ductile.

Conclusion

By assuming parallel action for fiber and matrix, and defining new boundaries for fiber, the uniaxial test results of FRC with different fiber content can be predicted. The good agreement between the enhanced microplane M4 model and the test data, interest us that this model is good established and can be used for FRC.

References

[1] F. Li (1998): *Fracture characterization of fiber reinforced concrete in uniaxial tension*, Ph.D thesis, Hong Kong University of Science and Technology.

[2] P. N. Balaguru and S. P. Shah (1992): *Fiber-reinforced cement composites*, McGraw-Hill, Singapor.

[3] Z. P. Bažant, F. C. Caner, I. Carol, M. D. Adley and S. A. Akers (2000): Microplane model M4 for concrete. I: formulation with work-conjugate deviatoric stress, *Journal of Engineering Mechanics*, ASCE, **126**, 944–952.

[4] Z. P. Bažant (1984): Microplane model for strain controlled inelastic behavior,*Mechanics of Engineering Materials*, C. S. Desaei and R. H. Gallagher, eds., Chapter 3, Wiley, London, 45–49.

Inverse Procedure for the Parameters Identification of the Microplane Material Model

B. Deliktas[1*], **F. C. Caner**[2], **M. Ornek**[3]

[1]Mustafa Kemal University
Department of Civil Engineering, Mustafa Kemal University, 31040, Hatay, Turkey
bdeliktas@mku.edu.tr

[2]Univ. Politecnica de Catalunya
Jordi Girona 1-3, Ed.D2 D.305, Barcelona 08034, Spain
ferhun.caner@upc.es

[3]Cukurova University
Department of Civil Engineering, Cukurova University, Adana, Turkey
mornek@cukurova.edu.tr

Summary: This paper presents a method and requirements of material parameter identification for the Microplane material model. The procedure, applied here to identify microplane model parameters from the experimental data is based on inverse analysis approach, which consist of minimizing the function representing the differences between the experimental data and data computed by material model. Two numerical processes are implemented here is based on interaction of two numerical tools; an optimization code(GA90)and the microplane material model driver.

Introduction

Since the concrete is one of the most commonly used material in engineering structures, it is very crucial for the structures to develop a reliable and robust model for the mechanical behavior of the concrete. Nowadays based on the micromechanics and computational algorithms the complex behavior of concrete can be simplified and modeled successfully. Recently a variety of theoretical models have been proposed and discussed in the referenced literature to describe the wide range of the inelastic behavior of concrete [13, 14]. Among the many of them, Microplane model developed by Bazant and coworkers [8, 9, 7] is one of the reliable and robust model that accurately predict the complex behavior of the concrete under various loading conditions. For an accurate modeling of the material behavior of concrete a certain number of model parameters are necessary, depending on the model used. The problem is that concrete is more complex than the most other materials. The graphical characterization of its nonlinear triaxial behavior necessitates the curves for at least 7 different characteristic types of responses, and the curve fitting of each of these responses necessitates no less than 3 or 4 parameters. Looking at it from the view point of microstructure, to characterize its geometry at several scales, the mechanical properties of all the constituents, their mutual bonding, defects, and pores, one needs at least 25 parameters [10]. In the case of microplane model there are mainly 29 parameters that seem to be adjusted to the experimental data for a given concrete. This large number of parameters which significantly influence the material behavior must be identified accordingly such that the accurate behavior of the material can be obtained. Every constitutive equation has its own method for parameter identification. In conventional approaches, the model of interest is first approximated and its parameters are identified sequentially through the curve fitting approach. However, this is not possible for models where parameters are not easy to identify directly by some features in the test results. Adding to this difficulty it is the fact that the most of the material parameters lack their obvious or direct physical interpretation and they differ in scale for a given model. Also, even under load histories in simple laboratory tests, many parameters will highly interact with each other, affecting the model response predicted. Then a systematic and objective computer based procedure for parameter identification is necessary [4, 5, 3, 2].

In this paper we , therefore, propose to use EAs for identifying the parameter set to the microplane model. The advantage of the proposed approach is that parameter can be identified without any divergence in every case.

Parameter identification of microplane model

Although microplane model contains many parameters, all of them except four have have fixed values for all types of concretes. The fixed parameters are those for which the optimization yielded nearly the same values for different concretes. They are denoted as $c_i, (i = 1, \ldots 17)$. The typical four free materials parameters, denoted as k_i $(i = 1, \ldots 4)$ are very crucial and they need to be adjusted for any given type of concrete. In the inverse analysis the parameter identification problem can be formulated to find the parameter set (vector) $\boldsymbol{x} \in X$ by iteratively changing input values until the simulated output values match the measured data (vector) $\boldsymbol{y} \in \Psi$. This input-output relation may be expressed as follows [1]

$$\boldsymbol{y} = \psi(\boldsymbol{x}) + \boldsymbol{e} \tag{1}$$

where $\boldsymbol{e} \in \Psi$ is the error measure. This error measure given in equation (1) is minimized with respect to material parameters

and its expression is defined as

$$\begin{cases} \text{Minimize} \quad e(\boldsymbol{x}) = 0 \quad \boldsymbol{x} \in R^n \\ \text{subject to constraints} \\ c_i^{eq}(\boldsymbol{x}) = 0 \qquad\qquad i = 1 \ldots n_{eq} \\ c_i^{in}(\boldsymbol{x}) \leq 0 \qquad\qquad i = 1 \ldots n_{eq} \\ \boldsymbol{L} \leq \boldsymbol{x} \leq \boldsymbol{U} \end{cases} \tag{2}$$

where $\boldsymbol{x}$ is a vector with n unknown parameters. The constraints can be nonlinear equations and n_{eq} is the number of equality and n_{in} is the number of inequality constraints. $\boldsymbol{L}$ and $\boldsymbol{U}$ are lower and upper limits for the parameters. Bruhms and Anding [6] give the following definition for an error measure as

$$e(\boldsymbol{p}) = \frac{1}{2}\boldsymbol{r}^T\boldsymbol{G}\boldsymbol{r} \tag{3}$$

where $\boldsymbol{G}$ is diagonal matrix with individual standard deviation errors for the measured data. The vector $\boldsymbol{r}$ has a square of the difference between computed and experimentally obtained stress $r_i = (\sigma_e - \sigma_c)_i^2$ at different strains or times. The matrix $\boldsymbol{G}$ can be used also to make the error non-dimensional and include scaling factor, $\boldsymbol{w}(\epsilon)$. Now the objective function of this parameter identification problem can be written as

$$f = \min \sum (\sigma_e - \sigma_c)_i^2 G_{ij} (\sigma_e - \sigma_c)_j^2 \tag{4}$$

This objective function clearly depends on the measured data and the model in use. (EAs)where genetic algorithms(GAs) have been most successfully used to minimize such an objective function, which quantifies the fit between computed results and the experiments.

Analysis and Discussions

It is very important that these parameters be identified correctly in order to predict material behaviors accurately. In summary, the processes of material parameters identification problem consists of the constitutive equations of the model, initial condition,material parameters of the model, and the experimental conditions.The model parameters have been optimized so as to make the responses very close to the typical test data exit, especially those from triaxial tests at various confining pressures. The numerical process implemented here is based on the interaction of two numerical tools; an optimization code (Ga90 and material model driver(IFED90 [10]) The performance of the proposed identification method is investigated with the actual experimental data from literature [11, 12] and more comprehensive test data from the Waterways Experimental Stations (WES). The experimental data consists of the uniaxial(unconfined) compression test [11], three triaxial compression tests each with a lateral confinement of 34.5 MPa, 68.9 MPa, 103.4 MPa and 172.4 MPa [12], and confined compression test. Parameters vector $\boldsymbol{x} = [k_1, k_2, k_3, k_4, c_1, c_2, c_2, c_3, c_4, c_5, c_6, c_7, c_8, c_9, c_{10}, c_{11}, c_{12}, c_{13}, c_{14}, c_{15}, c_{16}, c_{17}]$ are identified.

References

[1] T. Furukawa and G. Yagawa (2001): Inelastic constitutive parameter identification using evolutionary algorithm with continuous individuals, *International Journal of Numerical Methods in Engineering*, **40**, 1071–1090.

[2] C. L. Bellego, J. F. Dube, G. P. Cabot and B. Gerard (2003): Calibration of nonlocal damage model from size effect tests, *European Journal of Mechanics A/Solids*, **22**, 33–46.

[3] T. Furukawaand and G. Yagawa (2004): Inverse procedure for parameters identification of continuum damage models, *Inverse Problems, Designs and Optimization Symposium*.

[4] R. Mahnken (2000): A comprehensive study of a multiplicative elastoplasticity model coupled to damage including parameter identification *Computers & Structures*, **74**, 179–200.

[5] V. Slowik, B. Villmann and T. Villmann, Computational aspects of inverse analyses for the determination strain softening curves of concrete *Computer Methods in Applied Mechanics and Engineering*, **74**, 179–200.

[6] O.T. Bruhns and D.K. Anding (1999): On the simultaneous of model parameters used in constitutive laws for inelastic material behavior *International Journal of Plasticity*, **15**, 1311–1340.

[7] Z. Bazant and P.C. Prat (1988): Microplane model for brittle plastic material I: Theory, *ASCE Journal of Engineering Mechanics*, **114**, 1672–1688.

[8] Z. Bazant, F.C. Caner, M.D. Adley and S.A. Akers (2000): Microplane model M4 for concrete I: Formulation with work conjugate deviatoric stress *ASCE Journal of Engineering Mechanics*, **126**,944–953.

[9] Z. Bazant, F.C. Caner, M.D. Adley and S.A. Akers (2000): Fracturing rate effect and creep in microplane model for dynamics *ASCE Journal of Engineering Mechanics*, **9**, 962–970.

[10] Bazant Z. and Caner F.C. (2000): Microplane model M4 for concrete II: Algorithm and calibration *ASCE Journal of Engineering Mechanics*.

[11] J.G.M van Mier (1986): Multiaxial strain-softening of concrete:Part I: Fracture, Part II: Load Histories *Materials and Structures*, **19**, 179–200.

[12] G.G. Balmer (1984): Shearing strength of concrete under high triaxial stress-computation of Mohr's envelope as a curve, *Sruct. Res. Lab Report No:SP-23*, Denver,CO.

[13] S. Ananiev and J. Ozbolt (2004): Plastic damage model for concrete, In In V.Li, C.K.Y. Leung, K.J Villam and S.L.Billington Eds., *Fracture Mechanics of Concrete Structures*, 271–278.

[14] P. Grassl, K. Lundgren and Gylltoft (2002): Concrete in compression: Plasticity theory a novel hardening law, *International Journal of Solid and Structures*, **39**, 5205–5223.

Estimation of Microplane Model Parameters from Experiments in Uniaxial Compression

A. Kučerová, M. Lepš*, J. Němeček

Czech Technical University in Prague, Faculty of Civil Engineering
Thákurova 7, 166 29 Prague 6, Czech Republic
anicka@cml.fsv.cvut.cz, leps@cml.fsv.cvut.cz, jn@cml.fsv.cvut.cz

Summary: A new procedure based on layered feed-forward neural networks for the microplane material model parameters identification is proposed in the present paper. It is based on the inverse mode of the inverse analysis. Novelties are usage of the Latin Hypercube Sampling method for the generation of training sets, a sensitivity analysis and a genetic algorithm-based training of a neural network by an evolutionary algorithm. Advantages and disadvantages of this approach together with possible extensions are thoroughly discussed and analyzed.

Introduction

The problem of an inverse analysis appears in many engineering tasks. Generally speaking, the aim of an inverse analysis is to rediscover unknown inputs from the known outputs. In common engineering applications, a goal is to determine original conditions and properties from physical experiments or, equivalently, to find a set of parameters for a numerical model describing the experiment. Therefore, existence of such numerical model is assumed in this work and the task is to find parameters of the model to match its outputs to experimental data.

In overall, there are two main philosophies to solution of this problem. *A forward* (classical) mode/direction is based on the definition of an error function of the difference between outputs of the model and experimental measurements. A solution comes with the minimum of this function. The main advantage of this approach is that the forward mode is general in all possible aspects and is able to find an appropriate solution if such exists.

The biggest disadvantage of the forward mode is the need for a huge number of error function evaluations, especially when employing derivative-free optimization algorithms to error minimization. This problem can be managed by two approaches: the first one is based on parallel decomposition and parallel implementation, the second one employs a computationally inexpensive approximation or interpolation methods.

The second philosophy, *an inverse* mode, assumes existence of an inverse relationship between outputs and inputs. If such relationship is constructed, then the retrieval of desired inputs is a matter of seconds. This is of a great value especially for repeated identification of one model.

On the contrary, the main disadvantage is an extremely demanding search for the inverse relationship. Nowadays, artificial neural networks [1, 2] are commonly used due to their ability to approximate complex non-linear functions and their straightforward implementation and utilization.

Microplane model

Concrete is one of the most frequently used materials in civil engineering. Nevertheless, as a highly heterogeneous material, it shows very complex non-linear behavior, which is extremely difficult to describe by a sound constitutive law. Consequently, a numerical simulation of response of complex concrete structures remains a very challenging and demanding topic in engineering computational modeling.

One of the most promising approaches to modeling of concrete behavior is based on the microplane paradigm, see [3] for the most recent version of this family of models. It is a fully three-dimensional material law that incorporates tensional and compressive softening, damage of the material, supports different combinations of loading, unloading and cyclic loading along with the development of damage-induced anisotropy of the material. As a result, the material model presented in [3] is fully capable of predicting behavior of real-world concrete structures, once provided with proper input data, see [4] for more details. The major disadvantages of this model are, however, a large number of phenomenological material parameters and a high computational cost associated with structural analysis even in a parallel implementation [4].

Although the authors of the model proposed a heuristic calibration procedure [3], it is based on the trial-and-error method and provides a guide to determination of selected material parameters. In particular, a certain type of concrete is described by eight parameters: Young's modulus E, Poisson's ratio ν, and other six parameters (k_1, k_2, k_3, k_4, c_3, c_{20}), which do not have a simple physical interpretation, and therefore it is difficult to determine their values from experiments. Hence, a reliable and inexpensive procedure for identification of these parameters is demanded.

Proposed algorithm

In the view of potential improvements proposed in a recent work on soft computing methods [5], a new methodology based on artificial neural networks for the microplane parameter identification is proposed in the present contribution. In order to be able to asses the reliability of identified material parameters, results of a stochastic sensitivity study based on the Latin Hypercube Sampling (LHS) method [5] are presented first. Different tests, proposed in [3], are simulated numerically and used to determine, which model parameters can be reliably identified from these tests. In the next step, a neural network-based

procedure is presented for identification of material parameters. More precisely, a fully connected feed-forward layered neural network with bias neurons is used. A crucial point here is the generation of a training set used to determine weights of individual neurons [7]. To this end, the LHS method is again employed as it allows using a limited number of computational simulations while ensuring the representativeness of the generated training set [5]. The training procedure itself is based on a real-coded genetic algorithm SADE [6, 8] that has outperformed the traditional Backpropagation algorithm [9]. Moreover, the parameters with the highest sensitivity were estimated as the first. In the next step, they were used to improve quality of remaining, less sensitive, parameters. Finally, the application of the proposed identification procedure to the back analysis of laboratory experiments is presented to show performance of the method, see Fig. 1.

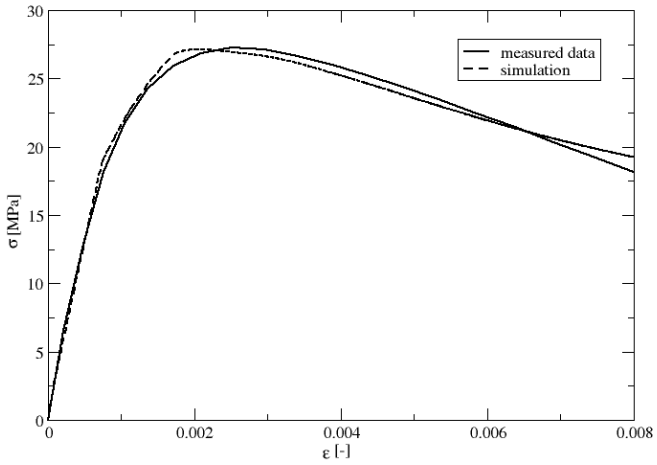

Figure 1: Comparison of measured data and results of final simulation of the uniaxial test.

As the best results, we can highlight the fact that the sensitivity analysis shows not only the influence of individual parameters but also approximately predicts the errors produced by the neural network. Although the obtained predictions from the neural network are still not identical with the desired ones, they can be further improved by much longer training process and/or by changing the topology of a neural network. Nevertheless, the main advantage of the proposed approach can be still employed – the trained neural network can be used for the next estimation phase in the future without the need of expensive numerical simulations.

Acknowledgement

The financial support of this work by research project of the Czech Ministry of Education, MSM 6840770003, is gratefully acknowledged.

References

[1] S. Haykin (1998): *Neural Networks: A Comprehensive Foundation*. Prentice Hall.

[2] Ch. Bishop (1995): *Neural Networks for Pattern Recognition*. Clarendon Press, Oxford.

[3] Z. P. Bažant, F. C. Caner, I. Carol, M. D. Adley, S. A. Akers (2000): Microplane model M4 for concrete. Part I: Formulation with work-conjugate deviatoric stress, Part II: Algorithm and calibration, *Journal of Engineering Mechanics-ASCE*, **126**, 944–961.

[4] J. Němeček, B. Patzák, D. Rypl, Z. Bittnar (2002): Microplane models: Computational aspects and proposed parallel algorithm, *Computers and Structures*, **80**, 2099–2108.

[5] D. Novák, D. Lehký (2006): ANN inverse analysis based on stochastic small-sample training set simulation, *Engineering Applications of Artificial Intelligence*, **19**, 731–740.

[6] O. Hrstka, A. Kučerová (2004): Improvements of real coded genetic algorithms based on differential operators preventing the premature convergence, *Advances in Engineering Software*, **35**, 237–246.

[7] F. Tong, X. Liu (2004): On training sample selection for artificial neural networks using number-theoretic methods. *Proceedings of the Fourth International Conference on Engineering Computational Technology*. Civil-Comp Press, Stirling, Scotland.

[8] O. Hrstka, A. Kučerová, M. Lepš, J. Zeman (2003): A competitive comparison of different types of evolutionary algorithms, *Computers and Structures*, **81**, 1979–1990.

[9] J. Drchal, A. Kučerová, J. Němeček (2002): Optimizing synaptic weights of neural networks, In Topping, B. and Bittnar, Z., editors, *Proceedings of the Third International Conference on Engineering Computational Technology*, Stirling, United Kingdom. Civil-Comp Press.

Part X

Modelling of Transport Properties

A Multiscale Approach to the Modelling of Grout Transport and Fluid Flow During Permeation Grouting

F. Bouchelaghem*

Institute of Mechanics, Laboratory of Mechanics, Materials and Structures
5 place Jussieu, 75005 Paris, France
fatiha.bouchelaghem@univ-orleans.fr

Summary: A multi-scale approach is employed to model the transport of a cement-based grout in a porous matrix. Periodic homogenization is used to derive the average grout concentration and fluid flow equations, as well as the macroscopic flow and transport parameters. Particular attention is paid to the filtration of cement grains occurring on the solid skeleton surface. The numerical computations performed using the Finite Element Method allow to compare different deposition modes with several 3D microstructures, and to confront the macroscopic response with experimental interstitial pressures and filtrated mass data.

Introduction

Grouting of a micro-cement suspension within a saturated soil is studied when grout filtration is taking place on the solid skeleton surface. As filtration can entail a rapid clogging of the pore flow channels, it may considerably reduce the grouting efficiency or even compromise the whole grouting process. Clogging processes are highly dependent on details of the pore structure as well as on the deposit morphology, and existing macroscopic models [2, 3] do not allow to express the effect of the complex soil microstructure, nor to identify the mechanisms favouring the filtration at the level of the pores.

In consequence, in order to develop a realistic model for the transport of a cement-based grout within a saturated porous medium in the presence of filtration, the Homogenization of Periodic Media (HPM) method is used, which naturally takes into account the heterogeneity of the porous matrix microstructure.

Model description

The macroscopic porous domain to be grouted is assumed to contain sand grains, grout filtrated on the sand grains surface, and residual voids filled with the flowing fluid phase, in such a way that a Representative Elementary Volume (REV) can be defined which size is small compared to the macroscopic volume. As the medium is assumed to be periodical, the REV coincides with the periodic cell. With l a characteristic length of the period and L the macroscopic lengthscale, the separation of scales is written as follows [1, 4]:

$$\varepsilon = \frac{l}{L} \ll 1 \tag{1}$$

Condition (1) introduces two independent dimensionless space variables $y = X/l$, $x = X/L$, where X is the physical space variable. x is the macroscopic space variable and y is the microscopic space variable describing the local scale. As a result, each unknown physical quantity ϕ is looked for in the form of a double scale asymptotic expansion [1, 4]:

$$\begin{aligned} \phi(x,y) &= \phi^{(0)}(x,y) + \varepsilon\phi^{(1)}(x,y) + \varepsilon^2\phi^{(2)}(x,y) + ..., \\ x &= \varepsilon y \end{aligned} \tag{2}$$

Furthermore, the porous medium studied is assumed to be saturated and nondeformable, meaning that the fluid-solid interface movement takes only place under the effect of grout deposition. Grout is assumed to be miscible with water initially present within the interstitial space, and as the resulting grout suspension is highly concentrated in cement, the fluid phase density depends on the grout concentration. For the same reason, the fluid phase viscosity and the diffusion coefficient vary with the grout concentration.

The dimensionless Navier-Stokes equations, the fluid continuity equation and the transport equation describe the problem at the microscopic scale:

$$\begin{aligned} &\mu\Delta_y\mathbf{v} + (\lambda+\mu)\nabla_y(\nabla_y\cdot\mathbf{v}) - \varepsilon^{-1}\nabla_y p = \\ &\varepsilon\rho\frac{\partial\mathbf{v}}{\partial t} + \varepsilon^2\rho(\mathbf{v}\cdot\nabla_y)\mathbf{v} \end{aligned} \tag{3}$$

$$\varepsilon\frac{\partial\rho}{\partial t} + \nabla_y\cdot(\rho\mathbf{v}) = 0 \tag{4}$$

$$\varepsilon^2\frac{\partial c}{\partial t} + \nabla_y\cdot(-\mathbf{D}\nabla_y c + \varepsilon c\mathbf{v}) = 0 \tag{5}$$

In the previous equations, $\mathbf{v}$ is the fluid velocity vector, p is the interstitial fluid pressure. ρ and μ represent respectively the density and the viscosity of the fluid phase, while c is the grout concentration and $\mathbf{D}$ is the diffusion tensor of the grout component within the fluid phase.

The filtration boundary conditions on the solid-fluid interface surface Γ_{sf}:

$$(-D\nabla_y c + \varepsilon c\mathbf{v})\cdot\mathbf{n} = \varepsilon\rho\mathbf{v}\cdot\mathbf{n} = \varepsilon^2\alpha c \tag{6}$$

$$\mathbf{v}\cdot\mathbf{t} = 0 \tag{7}$$

are complemented by the conditions of periodicity for all the dimensionless transport and flow variables. α is the grout filtration coefficient, $\mathbf{n}$ is the unit outward normal vector, and $\mathbf{t}$ the unit tangent vector on Γ_{sf}.

Asymptotic expansions of the form (2) are introduced for the physical variables of the problem in order to obtain the macroscopic description. After inserting the differentiation rule and the asymptotic expansions in the normalized local description (3)–(7), components corresponding to the same powers of ε are identified in the equations and the problems to be solved on the periodic cell can be derived at the successive orders of approximation.

The homogenization procedure leads to the macroscopic flow and grout transport equations:

$$\phi\frac{\partial\rho^{(0)}}{\partial t}+\nabla_x\cdot\left(-\frac{\rho^{(0)}\mathbf{K}^{\hom}}{\mu^{(0)}}\nabla p^{(0)}\right) = -\alpha c^{(0)}S_{fs}$$

$$\phi\frac{\partial c^{(0)}}{\partial t}+\nabla_x\cdot\left(c^{(0)}\left\langle\mathbf{v}^{(0)}\right\rangle-\mathbf{D}^{\hom}\nabla c^{(0)}\right) = -\alpha c^{(0)}S_{fs}$$

$\phi=\Omega_f/\Omega$ and $S_{fs}=\Gamma_{sf}/\Omega$ are respectively the macroscopic porosity and the specific surface of the granular arrangement, while $\mathbf{K}^{\hom}$ and $\mathbf{D}^{\hom}$ are respectively the effective permeability and diffusion tensors, which relate the microscopic and macroscopic descriptions and are introduced by the upscaling process in a straightforward manner. $\left\langle\mathbf{v}^{(0)}\right\rangle$ is the volume average of the microscopic velocity vector.

The resulting formulation has been implemented in a Finite Element solving procedure. As the parameters $\mathbf{K}^{\hom}$ and depend on the grout concentration and the evolution of the interstitial space available to flow, a program has been developed in Matlab which solves the macroscopic fluid flow and transport equations concurrently with the local boundary problems defined for $\mathbf{K}^{\hom}$, $\mathbf{D}^{\hom}$and the porosity ϕ on the periodic cell. The 3D microstructures considered and the different deposition modes, which can be surfacic, intergranular or a combination of both, are illustrated in Fig. 1.

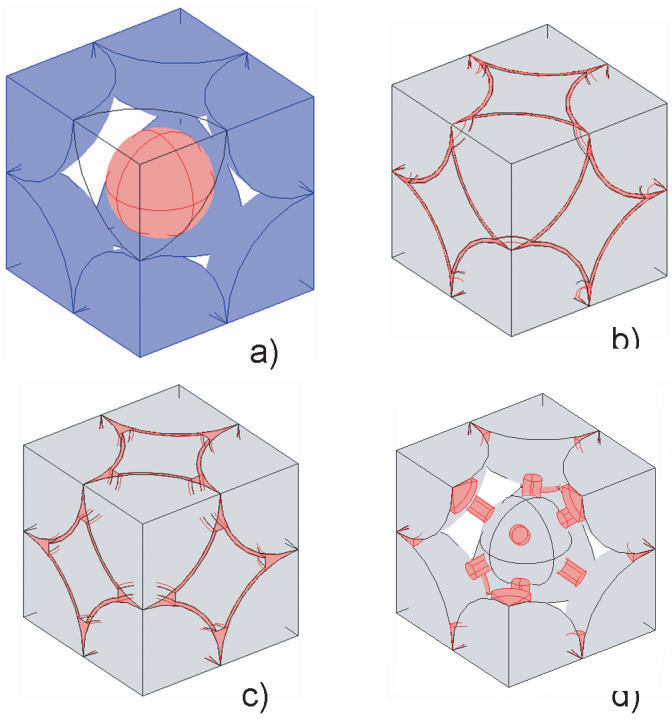

Figure 1: 3D microstructures employed to compute the macroscopic permeability : a) initial granular arrangement b) surface deposition c) and d) intergranular deposition.

One-dimensional soil grouting simulations

The model performance is confronted with existing soil column grouting experiments presented in [2] and [4], as illustrated in Fig. 2. Pressure increase takes place in two main steps separated by an intermediate stabilized stage. As explained in [2], during the first stage water initially filling the interstitial space is replaced by the cement-based grout under no significant filtration, while the cement filtration is responsible for the second phase of pressure increase. The numerical pressures display the same kind of evolution, and the best agreement between experiment and computation is obtained when intergranular deposition mode is dominant. The same conclusion is reached concerning mass intake comparisons.

Conclusion

The effective governing equations for fluid pressure and grout concentration capture the macroscopic behaviour observed during one-dimensional grouting experiments, and although the microstructures retained to describe the filtration mechanisms are rather simple, they lead to realistic effective permeability predictions, without need to resort to any phenomenological permeability function.

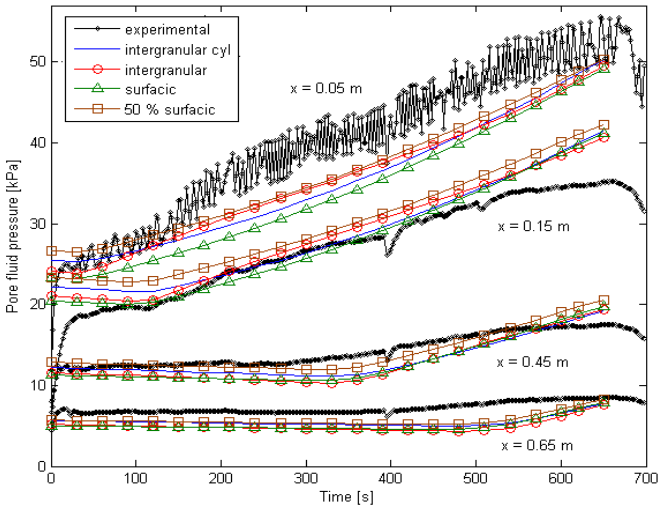

Figure 2: One-dimensional soil grouting. Comparison between experimental and numerical pressures.

References

[1] J. L. Auriault, J. Lewandowska (1996): Diffusion-adsorption-advection macrotransport in soils, *Eur. J. of Mechanics A/ Solids*, **15**, 681–704.

[2] F. Bouchelaghem, L. Vulliet (2001): Mathematical and numerical filtration-advection-dispersion model of miscible grout propagation in saturated porous media. *Int. J. for Numerical and Anal. Methods in Geomechanics*, **25**, 1195–1227.

[3] Z. Saada, J. Canou, L. Dormieux, J. C. Dupla, S. Maghous (2005): Modelling of cement suspension flow in granular porous media. *Int. J. for Num. and Analytical Methods in Geomechanics*, **29**, 691–711.

[4] E. Sanchez-Palencia (1980): *Non-Homogeneous Media and Vibration Theory*, Lecture Notes in Physics, 127, Springer-Verlag, Berlin.

Two-Scale Modelling of Water Transport Mechanisms in Internally Cured Concrete

M. Wyrzykowski[1*], D. Gawin[1], F. Pesavento[2]

[1]Dept. of Building Physics and Building Materials, Tech. University of Lodz
Al. Politechniki 6, 93-590 Lodz, Poland
mw@robobat.pl, gawindar@p.lodz.pl

[2]Dept. of Structural and Transportation Engineering, University of Padova
Via F. Marzolo 9, 34131 Padova, Italy
pesa@dic.unipd.it

Summary: A novel, mechanistic-type numerical model of concrete at early ages [1] has been used for two-scale modelling of the hygro-thermal phenomena in internally cured maturing concrete. The model is used for analysis of the concrete behaviour at the meso-scale, where the material is treated as a composite made of inclusions of internal water reservoirs surrounded by the maturing mortar. The internal moisture source terms and moisture transport properties are then up-scaled into the macro-scale, at which the material is treated as a continuum and analysed in the full range of hydration-related phenomena. The simulations results are compared to some published experimental data concerning performance of internally cured, maturing concrete.

Mechanistic-type model of concrete

The presented model of maturing concrete has been recently used for macro-scale modelling of a wide range of chemical, hygro-thermal, and mechanical phenomena, accompanying hydration of cement, e.g. [1]. Now, the efforts focus on the use of the model for two-scale modelling of concrete, i.e. at the meso- and macro-scale (see also [2]). For the sake of brevity, only a brief description of the model assumptions is given here (for more details see [1]).

The balance equations for phases and interfaces are developed at the micro-level and then volume-averaged, by means of the Hybrid Mixture Theory by Hassanizadeh and Gray (see [1]) in order to obtain their macroscopic formulation. The constitutive laws are introduced directly at the macro-scale, where evolution of some material properties is governed by the hydration degree. The final governing equations of the model, i.e. mass, energy and momentum balances are written in terms of the chosen primary variables: gas pressure, capillary pressure, temperature and displacements, and the hydration degree as an internal variable. The equations are discretized in space by means of FEM and implemented into the computer code HMTRA-FRESH, [1]. Concrete is treated as a deformable, multiphase porous material. All the phase changes are taken into account as well as the generalized, complex chemical reactions. The mass and energy transport mechanisms are considered for specific phases of concrete. Full coupling between hygro-thermo-mechanical phenomena and the chemical reactions during cement hydration is assumed. Coupled influence of the relative humidity and temperature on the hydration process evolution, and further on macroscopic properties of the material allow us to analyse their non-linearity due to aging.

The mechanical behaviour of the model, in particular shrinkage and creep strains are described in terms of the effective stress principle, developed by Gray and Schrefler for media with a well-developed internal surface (i.e. cementitious composites), see [1]. The effective stress accounts both for the external load and the internal load exerted by the pore fluids on the solid skeleton, rising with the decrease of pores relative humidity. Finally, creep is modelled by means of the microprestress-solidification theory by Bazant *et al*. [3], modified in such a way that the total stresses are replaced with the effective ones. Thanks to such an assumption it is possible to model the coupling between creep and autogenous shrinkage strains in the absence of any external load.

Two-scale modelling concept

Although the model as described in the previous section was successfully validated for the macro-scale problems related to autogenous phenomena, [1], in the case of internal curing further model developments are necessary. It seems, that the only reasonable way in this case is to use the two-scale modelling concept which involves description of coupled heat and moisture transport at two scales: meso- and macroscopic. Our approach is based on the so-called numerical homogenization. The effective properties of the macro-scale, i.e. homogenous model, Fig. 1c, in particular water mass source due to internal 'water reservoirs', are obtained by scaling up the results, Fig. 1b, simulated for the Representative Elementary Volume (REV), Fig. 1a, at the meso-scale. The REV is modelled as consisting of two porous materials: an inclusion of saturated 'water reservoir', visible in the edge of the cutting, surrounded by the mortar, Fig. 1a, which are treated as homogenous. In concrete technology practice, the 'reservoirs' are supplied by introducing into mortar saturated light weight aggregates (LWA) or super absorbent polymers (SAP), [4].

In this paper, the linkage between the both scales is considered in one direction only, i.e. up-scaling. The up-scaling scheme allows for determining the effective properties and the mass source term in the homogenized moisture balance equation based on the results of the meso-level analysis. The numerical homogenization of the effective properties is done as follows:

– the thermal conductivity and intrinsic permeability of internally cured mortar is obtained from the analysis of heat and water flows in the REV;

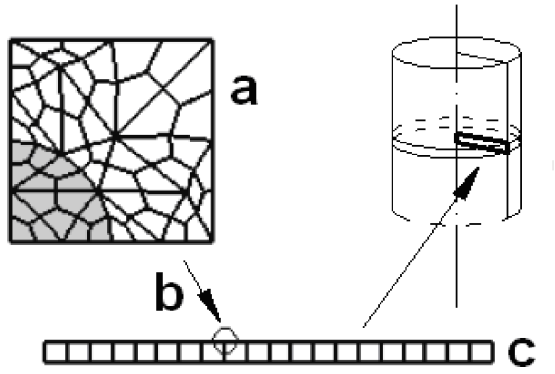

Figure 1: The scheme of scale-linkage and FEM meshes used in numerical simulations.

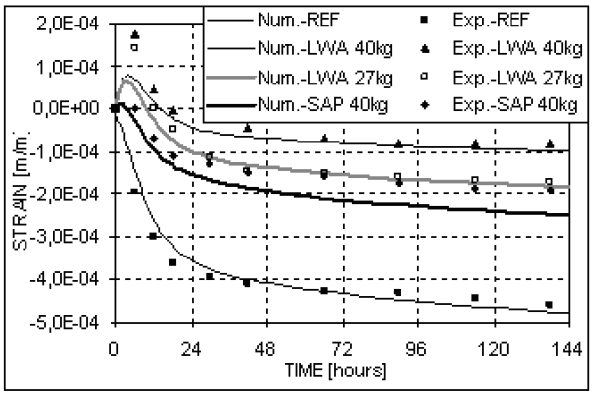

Figure 2: Results of the numerical meso-level simulations compared with the experimental data [4] concerning autogenous strains of concretes modified with different amounts of LWA or SAP. The masses refer to the amount of water per 1 m^3.

– the sorption isotherm of the medium is modified, using the volume-averaged results obtained at the meso-level for the REV being in the state of hygro-thermal equilibrium;

– the hydration process evolution equation is modified by changing the viscosity parameter in the relation describing the normalized chemical affinity, influencing the hydration rate, [1].

The up-scaling of the water transport from the internal 'water reservoir' into maturing mortar is done by introducing an additional water source term into the macro-scale mass balance equation. This term is assumed as a volume averaged (considering the ratio of volume occupied by LWA or SAP) derivative of the water mass loss from LWA (or SAP) with respect to the hydration degree of the mortar (i.e. the evolution-governing variable of the model).

At the macro-level, the real specimen is modelled by means of the strip cut off of the cylinder specimen (Fig. 1c) with the dimensions and boundary conditions described with respect to the real experiment. The analysis is carried out with the modified properties for the full range of phenomena accompanying cement hydration.

Simulation results

In order to illustrate the possibilities of the model the numerical example based on the experimental work by Craeye and De Schutter [4] has been carried out in accordance with the scheme described in the previous section. The authors of the experiment measured the linear deformations of the high performance concretes modified by means of addition of various types and amounts of LWA or SAP. The autogenous strains of internally cured samples were then compared to the reference ones showing the improved performance of the former due to internal curing.

In Fig. 2 some exemplary results of our simulations are presented. The results concern the strains computed directly at the meso-level. As can be seen, a good agreement was obtained for the simulations of concrete with LWA. Some discrepancy is visible only in the case of initial swelling. However, one should notice that the initial period of material behaviour cannot be yet modelled by the assumed mathematical model, mainly due to great complexity of physical phenomena in fully saturated maturing concrete. In the case of simulations of concrete with SAP greater shrinkage was predicted by the model than that observed in reality. This is the main problem which further developments of the model should be focused on. As proved by our numerical analysis, a part of influence of SAP on the material performance (especially on the decrease of RH and on the material strains) cannot yet be modelled by the described model. This in particular concerns the phenomena related to the modifications of inner-structure caused by SAP in reality.

However, as proved by the examples presented, the phenomena of water transport from the internal sources during concrete curing and the material deformations can be analysed with the presented model using the two-scale modelling scheme, thus a further research in this field will be carried out.

References

[1] D. Gawin, F. Pesavento, B. A. Schrefler (2006): Hygro-thermo-chemo-mechanical modelling of concrete at early ages and beyond. Part I: Hydration and hygro-thermal phenomena, Part II: Shrinkage and creep of concrete. *Int. J. Num. Meth. Engng*, **67**, 299–331, 332–363.

[2] M. Wyrzykowski, D. Gawin, F. Pesavento, P. Lura (2006): Multi-scale modelling of autogenous strains of an internally cured cementitious material. In *Proc. Int. RILEM Conf. Volume Changes of Hardening Concrete: Testing and Mitigation*, Lyngby, PRO 52, 137–146.

[3] Z. P. Bazant, A. B. Hauggaard, S. Baweja, F.J. Ulm (1997): Microprestress-solidification theory for concrete creep. I: Aging and drying effects. *Journal of Engineering Mechanics ASCE*, **123**, 1188–1194.

[4] B. Craeye, G. De Schutter (2006): Experimental evaluation of mitigation of autogenous shrinkage by means of a vertical dilatometer for concrete. In *Proc. Int. RILEM Conf. Volume Changes of Hardening Concrete: Testing and Mitigation*, Lyngby, PRO 52, 21–30.

Micro-Macro Thermo-Mechanical Modeling of Heterogeneous Materials

I. Özdemir*, W. A. M. Brekelmans, M. G. D. Geers

Eindhoven University of Technology, Department of Mechanical Engineering
P.O. Box 513, 5600 MB Eindhoven, The Netherlands
I.Ozdemir@tue.nl, W.A.M.Brekelmans@tue.nl, M.G.D.Geers@tue.nl

Summary: This contribution introduces a multi-scale framework for the thermomechanical analysis of heterogeneous solids. The principles of the method rely on a two-scale computational homogenization approach which is applied successfully for the stress analysis of multi-phase solids under purely mechanical loading. The present paper extends this methodology to heat conduction and thermomechanical problems. The flexibility of the method permits one to take into account local microstructural heterogeneities and thermal and mechanical anisotropy, including nonlinearities which might arise at some stage of the loading history. The resulting complex microstructural response is transferred back to the macro level in a consistent manner. A proper macro to micro transition is established in terms of the microscopically applied boundary conditions and likewise a micro to macro transition is formulated in the form of consistent averaging relations. A nested finite element solution procedure within the operator split formalism is outlined and the effectiveness of the approach is demonstrated by an illustrative example problem.

Introduction

Materials with a high thermomechanical resistance are indispensable in many engineering applications. Refractories used in furnace linings, thermal coatings and microelectronic components are just a few examples indicating the wide range of applications where a structure is exposed to strong temperature changes and cycles. The materials selected for heat isolation purposes are generally far from being homogeneous due to their multiphase, porous microstructure. Under severe thermal conditions, it is well documented that the relevant damage mechanisms originate from the induced stress gradients, the thermal expansion anisotropy and the non-uniformity and mismatches between the constituents at the meso or micro level.

Modeling framework

To incorporate the underlying mechanisms more transparently in our modeling effort and to investigate the interaction of mechanical and thermal fields and its consequences from a microstructural perspective, a multi-scale analysis approach for thermomechanical problems is proposed within the framework of computational homogenization. Computational homogenization is a multi-scale strategy in which the material response is obtained from the underlying microstructure by solving a boundary value problem defined on a representative volume element of the microstructure (RVE) where characteristic physical and geometrical properties of the fine scale (different phases, internal boundaries, flaws etc.) are embedded. The scale bridging from macro to micro is achieved by the formulation of consistent RVE boundary conditions in terms of macroscopic quantities passed to the micro level (RVE input, step I in figure 1). Then, the microscopic field excited by the prescribed boundary conditions is resolved by a proper discretization technique applied to the micro-scale BVP (step II in figure 1). The resulting microscopic quantities are used to extract the macroscopic quantities (step III in figure 1) via a consistent averaging scheme. Furthermore, the relation between infinitesimal variations of the RVE output quantities in relation to infinitesimal variations of the input quantities are extracted, i.e. the tangent operator.

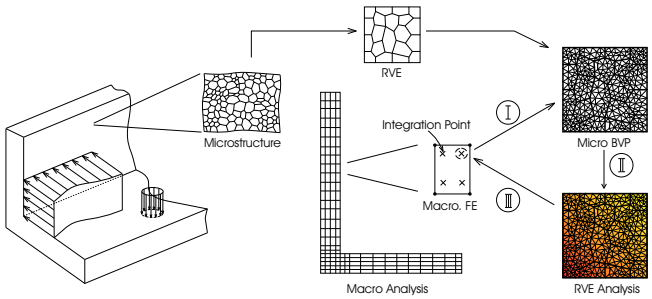

Figure 1: Schematic representation of the computational homogenization scheme

In what follows, the subscript capital 'M' denotes macroscopic quantities whereas a lower case 'm' will be the indicator for microscopic quantities, including some differential operators, e.g. the gradient operator $\vec{\nabla}_M$ or $\vec{\nabla}_m$.

Within a geometrically nonlinear continuum framework, in the absence of body forces and internal heat sources, the balance equations to be satisfied at the micro level take the standard form,

$$\vec{\nabla}_m \cdot \boldsymbol{\sigma}_m = \vec{0} \tag{1a}$$

$$\vec{\nabla}_m \cdot \vec{q}_m = 0 \tag{1b}$$

with $\vec{q}_m$ the microscopic heat flux and σ_m the microscopic Cauchy stress in the microstructural components. The heat flux $\vec{q}_m$ and the stress σ_m are related to the gradients of the temperature and the displacements by proper constitutive relations. At the micro level, it is assumed that a steady-state temperature profile is reached instantaneously due to the negligibly small size of the representative volume element (RVE), which is typically the point of departure in any first order homogenization scheme.

At the macro level the balance equations have the general form,

$$\vec{\nabla}_M \cdot \boldsymbol{\sigma}_M = \vec{0} \tag{2a}$$

$$(\rho c_v)_M \dot{\theta}_M + \vec{\nabla}_M \cdot \vec{q}_M = 0 \tag{2b}$$

where θ_M is the temperature at macro level. This system is completed with proper macroscopic boundary conditions. Explicit constitutive relations for $\vec{q}_M$ and σ_M are not required. Instead, the macroscopic quantities are extracted from the response of the underlying microstructure in a consistent way.

The thermal energy consistency of micro and macro levels is assured by enforcing the condition

$$\theta_M (\rho c_v)_M = \frac{1}{V} \int_V \theta_m (\rho c_v)_m dV \tag{3}$$

$$\text{with } (\rho c_v)_M = \int_V (\rho c_v)_m dV$$

which also guarantees a unique temperature profile. The mechanical and thermal excitation of the microstructure is prescribed in terms of the macroscopic deformation gradient $\mathbf{F}$ and the temperature gradient $\vec{\nabla}_M \theta_M$ through macro-to-micro scale bridging relations

$$\mathbf{F}_M = \frac{1}{V} \int_V \mathbf{F}_m dV \tag{4a}$$

$$\vec{\nabla}_M \theta_M = \frac{1}{V} \int_V \vec{\nabla}_m \theta_m dV \tag{4b}$$

which constitute basis to specify the boundary conditions at the micro level, in combination with periodicity assumptions.

With the prescribed boundary conditions in terms of macroscopic quantities, the micro level problem is solved by the finite element method. Upon the solution, the macroscopic quantities are extracted from the micro level as simple volume averages,

$$\boldsymbol{\sigma}_M = \frac{1}{J} \mathbf{P}_M \mathbf{F}_M^T \text{ with } \mathbf{P}_M = \frac{1}{V} \int_V \mathbf{P}_m dV \tag{5a}$$

$$\vec{q}_M = \frac{1}{V} \int_V \vec{q}_m dV \tag{5b}$$

where $\mathbf{P}$ stands for the first Piola-Kirchhoff stress tensor and $J = \det \mathbf{F_M}$. Equations (5) are derived from the micro-macro virtual work equivalency (macrohomogeneity condition) and the entropy consistency condition. The tangent operators used in the incremental-iterative solution of the macroscopic balance equations are extracted through a condensation procedure from the microstructural system of equations as outlined in [1] and [2].

Solution algorithm

The coupled thermo-mechanical problem is solved by the operator split approach in which the coupled problem is split into two sub-problems, namely (1) the thermal equilibrium problem with a fixed displacement and hence a fixed stress field and (2) the mechanical equilibrium problem with a fixed temperature field. The solution of the micro-BVP is embedded in the macroscopic solution algorithm which leads to a nested finite element procedure as presented in [1] and [2]. The framework is constructed in such a way that damage evolution and coupling between the fields through damaging of the microstructure can be incorporated in the model.

The two scale nested solution procedure is implemented and a simple illustrative example is presented in figure 2. A planar structure made of a two-phase material is exposed to a linearly increasing temperature loading at the free (right) end. The analysis reveals microscopic thermal and mechanical field quantities in addition to macroscopic ones. With this method, it is straight forward to investigate the effect of the microstructural morphology on the resulting macroscopic response. The approach becomes superior particularly when the coupling between the micro and macro scales becomes stronger, e.g. in case of a temperature sensitive microstructural response or in case of materials with evolving microstructure, for which asymptotic homogenization or unit cell based approaches are not appropriate.

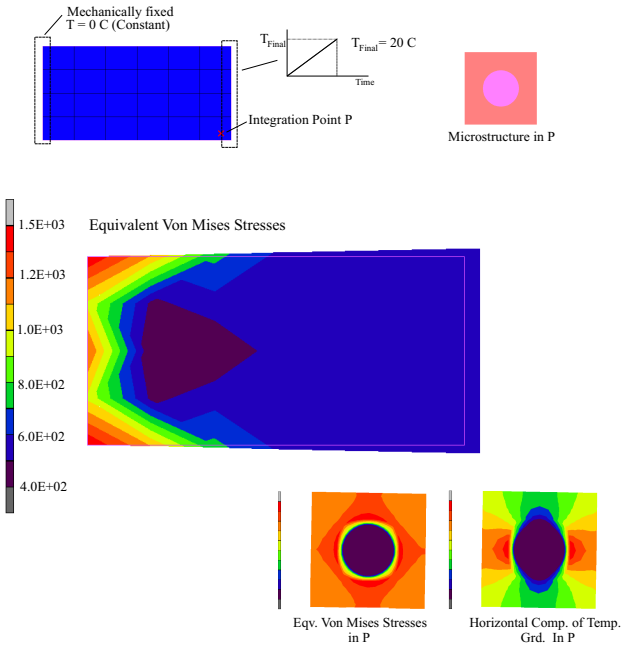

Figure 2: Illustrative Example

Conclusively, with the framework introduced, the influence of microstructural evolution (e.g. damage and microcracking) on the mechanical and thermal fields and their interaction can be effectively taken into account. This enables the modeling and enhances the understanding of damage phenomena and opens the possibility to identify some interesting mechanisms of failure initiation and field interaction effects which cannot be easily captured and described without incorporating the relevant microstructural details, as done here.

References

[1] V.G. Kouznetsova, W.A.M. Brekelmans, F.P.T. Baaijens (2001): An approach to micro-macro modeling of heterogeneous materials, *Comp. Mech.*, **27**, 37–48.

[2] I. Özdemir, W.A.M. Brekelmans, M.G.D. Geers (2006): Computational homogenization for heat conduction in heterogeneous solids, *Int. J. Num. Methods Eng.*, accepted.

Effective Conductivity of Random Heterogeneous Materials by a Local Method

Y. Hakobyan[1], **K. Papoulia**[2*], **M. Grigoriu**[3]

[1] Department of Physics, Cornell University
Ithaca, NY 14853, U.S.A.
yh77@cornell.edu

[2] Department of Civil and Environmental Engineering, University of Waterloo
Waterloo, ON N2L 3G1, Canada
papoulia@civmail.uwaterloo.ca

[3] School of Civil and Environmental Engineering, Cornell University
Ithaca, NY 14853, U.S.A.
mdg12@cornell.edu

Summary: This paper describes a method for finding effective material properties of random heterogeneous materials based on a local solution of transport equations. We apply the method to calculate the effective conductivity of several microstructures, and assess the accuracy of the method.

Introduction

Global properties of nominally identical material specimens can differ significantly because microstructural properties generally exhibit notable spatial random variation, indicating that these properties are random quantities. The specimen to specimen variation of global properties can be significant if, for example, the scale of fluctuation of microstructural properties and the specimen size have a similar order of magnitude.

Global properties are typically measured in the laboratory, become deterministic as the specimen size increases indefinitely, and provide material constants for mathematical models of continuum mechanics and other fields. There are many methods for calculating global material properties, referred to as effective properties. Many of these methods are reviewed in [2], and applied to a broad range of microstructures.

Our objective is to present a method for finding effective material properties of nonhomogeneous materials based on a local solution of transport equations. We apply the method to calculate the effective conductivity of several microstructures, and assess the accuracy of the method. The method extends results in [1], [2], and [3].

Effective material properties

Consider a microstructural specimen occupying a bounded set D in $\mathbb{R}^d$, $d = 1, 2, 3$, whose electric or thermal conductivity is $\sigma(\boldsymbol{x}) > 0$ at $\boldsymbol{x} \in D$. Suppose the specimen is subjected to a flux $\gamma(\boldsymbol{x})$. The steady state temperature or electric potential $u(\boldsymbol{x})$ in the specimen is the solution of

$$\nabla \left(\sigma(\boldsymbol{x})\, \nabla\, u(\boldsymbol{x})\right) = -\gamma(\boldsymbol{x}), \quad \boldsymbol{x} \in D. \tag{1}$$

The effective conductivity σ_{eff} of the specimen in D is the conductivity of a virtual homogeneous specimen that occupies the set D and is equivalent to the original specimen in some sense. For example, if D is a sphere $S_d(r)$ of radius $r > 0$, we require that the solutions of Eq. (1) at $\boldsymbol{x} = \mathbf{0}$ for the original and the virtual specimen coincide. The equality of these solutions yields σ_{eff}.

We can solve Eq. (1) for the original and virtual specimens by finite difference, finite element, or other traditional numerical method. Alternatively, Monte Carlo techniques can be used to solve Eq. (1) and find σ_{eff} for two-phase materials with homogeneous phases. For example, the effective conductivity can be approximated from the average time required by many walkers moving randomly in space with fixed steps and speeds depending on the local phase conductivities. Special provisions are made for situations in which during a step the boundary between two distinct phases is crossed ([1], [2]). Though easily coded, these methods are not efficient in computational time, especially for samples with very small inclusions; also, the methods cannot be used in the case of continuously varying conductivity (functionally graded materials).

The developments in this paper follow a Monte Carlo method proposed by Grigoriu [3]. The method is extended to heterogeneous materials and can be used to find effective properties of arbitrary microstructures. The method is based on properties of diffusion processes, the Itô formula for continuous semimartingales, and the relationship between the functional form of the differential operator in Eq. (1) and the infinitesimal generator of diffusion processes.

Consider [3] a stochastic differential equation defining a $\mathbb{R}^d$-valued state $\mathbf{X}$, called an Îto process,

$$d\mathbf{X}(t) = \mathbf{a}(\mathbf{X}(t))\, dt + \mathbf{c}(\mathbf{X}(t))\, d\mathbf{B}(t),\ t >= 0, \tag{2}$$

where $\mathbf{B}$ is a Brownian motion in $\mathbb{R}^d$ and the (d,1) and (d,d) matrices $\mathbf{a}$ and $\mathbf{c}\mathbf{c}^T$ are real-valued functions defined on $\mathbb{R}^d$. Define the drift and diffusion coefficients of $\mathbf{X}$ by

$$a_k(\boldsymbol{x}) = \frac{\partial \sigma(\boldsymbol{x})}{\partial x_k},\ k = 1, \ldots, d \text{ and } \mathbf{c}(\boldsymbol{x}) = \sqrt{2\sigma(\boldsymbol{x})}\, i, \tag{3}$$

where i is the (d,d) identity matrix. For simplicity of numerical computation, we choose to work with spherical samples $D = S_d(r)$, d-dimensional spheres of radius r, with a homogeneous Dirichlet boundary condition, i.e. $u(\boldsymbol{x}) = 0$ for $\boldsymbol{x} \in \partial D$.

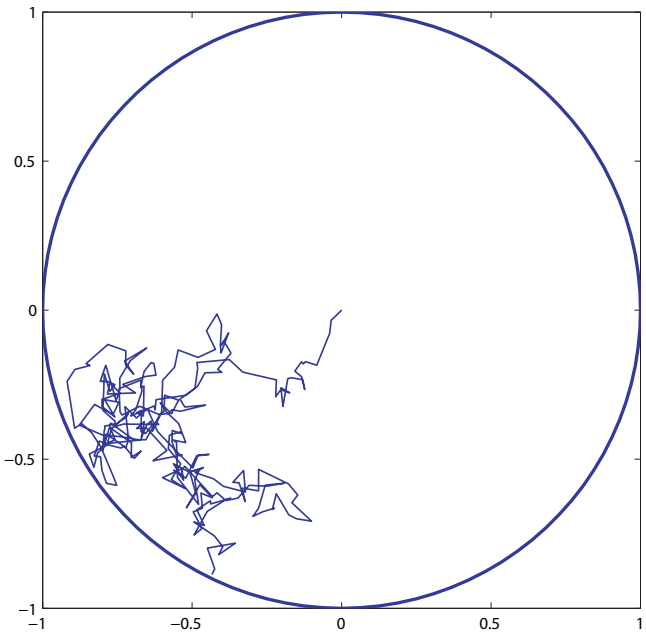

Figure 1: Example of a random walk in a homogeneous material with $\Delta t = 0.001$ in two dimensions.

Let $T(r)$ be the first time when $\mathbf{X}$, starting at an initial state $\mathbf{X}(0) = 0$, exits $D = S_d(r)$ and assume that $\gamma(\boldsymbol{x}) = 1$. The effective conductivity for a heterogeneous material is then given by [3]

$$\sigma_{eff} = \frac{r^2}{2\,d\,E[T(r)]}, \tag{4}$$

where $E[]$ denotes expectation value. The generation of samples of the Îto process $\mathbf{X}$ can be based on a finite difference approximation.

Consider a random walk method (RWM) of a particle, which moves with a fixed time-step Δt, according to the formula

$$\boldsymbol{x}_2 = \boldsymbol{x}_1 + \mathbf{a}(\boldsymbol{x}_1)\,\Delta t + \mathbf{c}(\boldsymbol{x}_1)\,randn(d,1)\,\sqrt{\Delta t}, \tag{5}$$

where $\boldsymbol{x}_1 \in \mathbb{R}^d$ is the initial point, i.e., the point at which the particle starts its motion and $\mathbf{a}$, $\mathbf{c}$ are given by (3), while $randn(d,1)$ stands for a d-length column of normally distributed random numbers. The total time to exit from the sample for the i-th random walker is $T_i = \sum \Delta t$. The effective conductivity of a spherical sample is calculated by [3]

$$\sigma_{eff} = \frac{r^2}{2\,d\,\hat{T}}, \tag{6}$$

with $\hat{T} = \sum_{i=1}^{N} T_i/N$ being the mean (over N random walks) time a particle spends while travelling in the sample. Fig. 1 shows an example of random walks in a homogeneous sample. (Time steps in the nonhomogeneous case are too small for visual output.)

We observe that the effectiveness and accuracy of (5) reduces significantly in the case the two terms depending on the conductivity and its derivative have different orders of magnitude. We suggest a modification to (5), whereby we introduce a parameter ϵ, which controls the value of the two terms. We call this approach a modified random walk method (MRWM).

For a fixed value of ϵ, we choose the time-step as $\Delta t = min[\epsilon/a, (\epsilon/c)^2]$, where a, c are the absolute values of the corresponding vectors in (3), for which comparable contributions from the two terms in (5) are obtained.

As an example of a hypothetical heterogeneous material, consider the thermal or electrical conductivity given by an exponential function in two dimensions

$$\sigma(r) = e^{10r^2},\ r = \sqrt{x^2 + y^2} \in [0,1], \tag{7}$$

and assume Dirichlet boundary conditions, i.e. $u(1) = 0$. We study the dependence of effective conductivity on parameters Δt and N for the random walk algorithm and (ϵ, N) for the modified algorithm. We find that the modified algorithm approximates the true value of σ_{eff} more accurately than the original random walk method for a given number N of samples if we choose the parameter ϵ of the modified random walk method to be on the same order as $\sqrt{\Delta t}$, where Δt is the parameter of the original RWM.

We extend the method to discontinuous cases such as spherical and thin elliptical inclusions and provide comparison to finite element results. Though we solve the conductivity problem (1) with Dirichlet boundary conditions, the approach can be modified to solve partial differential equations with mixed boundary conditions as well [4].

References

[1] E. J. Garboczi, L. M. Schwartz and D. P. Bentz (1995): Interfacial transport in porous media: application to dc electrical conductivity of mortars. *Journal of Applied Physics*, **78**, 5898–5908.

[2] S. Torquato (2001): *Random heterogeneous materials: microstructure and microscopic properties*. Springer-Verlag, New York (Interdisciplinary Applied Mathematics, Vol. 16).

[3] M. Grigoriu (2002): *Stochastic Calculus: Applications in Science and Engineering*. Springer-Verlag, Boston.

[4] M. Grigoriu, K. Papoulia (2005): Effective conductivity by a probability-based local method. *Journal of Applied Physics*, **98**, issue 3.

Part XI

Plasticity, Damage and Fracture of Heterogeneous Materials

Determination of a Macroscopic Plastic Yield Behaviour of Porous Materials

V. Monchiet, E. Charkaluk, D. Kondo*

Laboratoire de Mécanique de Lille. UMR8107 CNRS, Lille, France
Vincent.monchiet@ed.univ-lille1.fr, eric.charkaluk@@univ-lille1.fr, djimedo.kondo@@univ-lille1.fr

Summary: This paper investigates a 3D micromechanical modelling of ductile porous materials composed of a rigid perfectly plastic matrix containing prolate or oblate cavities. For this purpose, we consider an eshelby-like trial velocity field in the standard limit analysis of porous materials (Gurson, 1977) as well as in its extensions to the case where voids are non spherical. The obtained approximate pressure-sensitive criterion is exact for hydrostatic loading and presents several original features : it is valid for arbitrary loadings and gives very good predictions for low stress triaxility (in particular purely deviatoric loadings) in which case they agree with the (nonlinear) Hashin - Shtrikman bound established by Ponte-Castaneda and Suquet (1998). Significant improvements of the existing Gurson-type criteria, particularly those dealing with penny-shaped cracks, are obtained. Finally, we indicate how these new results immediately apply to poroplastic behavior (saturated porous material).

Motivation of the study

The modeling of the behavior of ductile porous media has been the subject of important researches in nonlinear mechanics of materials. In his pioneering work, Gurson [4] developed a limit analysis approach of a hollow sphere which constitutes an upper bound for a composite spheres assemblage. Later, the Gurson model has been extended in order to take into account the voids shapes (see review by Gologanu et al. [3]). Alternatively, by using variational techniques (reviewed by Ponte Castaneda and Suquet [7]), rigorous nonlinear Hashin-Shtrikman upper bounds have been derived for plastic porous media with various voids shapes. An important observation is that the Gurson model violates the corresponding upper bound for low values of the stress triaxiality $T = \Sigma_h/\Sigma_{eq}$. However, its predominance over the non linear Hashin-Shtrikman bound is still observed for high stress triaxialities. A possible method to improve the predictions of the original limit analysis of Gurson (and in fact the subsequent models for non spherical voids), already used by some authors, consists in considering refined trial velocity fields. Still, due to the limitation of trial velocity fields which have been explored in the past studies, it seems that there is need for new investigations in this domain. The main objective of this study is to develop a limit analysis approach based on Eshelby-like velocity fields and to derive a new expression of the yield function of the porous medium.

Basic concepts and methodology

The calculations have been performed in the general case of prolate and oblate voids. By doing so, the new results can also be compared to those which can be found Gologanu et al. [3]. As in [3], consider then a spheroidal prolate or oblate cavity with semi-axes a_1 (along $\underline{e}_3$), and b_1 (along $\underline{e}_1$ and $\underline{e}_2$) embedded in a cell which has the shape of a confocal spheroid with the semi axes a_2 (along $\underline{e}_3$), and b_2 (along $\underline{e}_1$ and $\underline{e}_2$) (Fig. 1). $a_1 > b_1$ corresponds to a prolate cavity while $b_1 > a_1$ is associated to an oblate one. Let us denote c the focal distance and

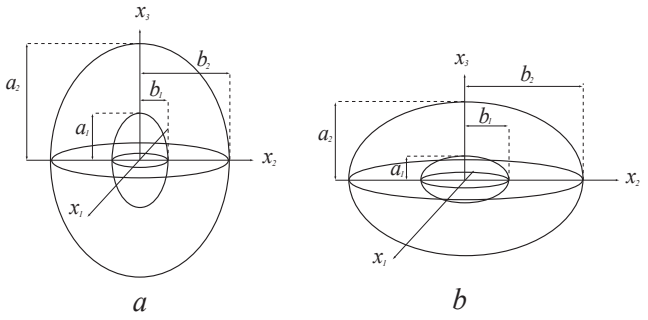

Figure 1: Studied cell for (a) a prolate and (b) an oblate spheroidal void embedded in a confocal spheroid relative to a Cartesian coordinate system (x_1, x_2, x_3).

e_1 the eccentricity defined by:

$$\begin{aligned} c &= \sqrt{a_1^2 - b_1^2}; \quad e_1 = \frac{c}{a_1} \quad (prolate) \\ c &= \sqrt{b_1^2 - a_1^2}; \quad e_1 = \frac{c}{b_1} \quad (oblate) \end{aligned} \tag{1}$$

The porosity f and the void shape parameter S are given by:

$$f = \frac{a_1 b_1^2}{a_2 b_2^2};\ S = \ln\left(\frac{a_1}{b_1}\right) \tag{2}$$

The determination of the macroscopic criterion is made by considering, as classically, a velocity field $\underline{v}$ in the matrix, decomposed into a first field, $\mathbf{A}.\underline{x}$, corresponding to uniform strain rate $\mathbf{A}$, and an heterogeneous field, denoted $\underline{v}^E$, which describes void expansion and shape changes. For $\underline{v}^E$, we propose to consider the exterior point Eshelby solution ([2], see also [6]) adapted here to an incompressible viscous fluid containing a spheroidal inclusion. By the consideration of these new fields which are discussed, an approximate expression of the macroscopic dissipation is obtained (see [5]). Since the considered velocity field introduces some unknown kinematical parameters, a minimization procedure has to be performed in order to determine the macroscopic dissipation $\Pi(\mathbf{D})$, $\mathbf{D}$ being the macroscopic strain rate tensor. A detailed presentation of the computation is provided in [5].

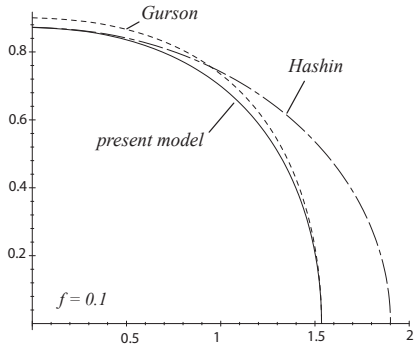

Figure 2: Yield surface of the porous material: case of spherical void: Σ_{eq}/σ_0 as function of Σ_m/σ_0; comparison of the proposed model (3) with the Gurson yield locus and the nonlinear Hashin-Shtrikman bound. Porosity $f = 0.1$.

Examples of results

New expressions of the macroscopic criteria of the porous medium (with prolate and oblate cavities) are derived from $\Pi(\mathbf{D})$. It is shown that the obtained results significantly improve existing criteria for ductile porous media. Moreover, for low stress triaxialities, these new results agree with the (non linear) Hashin-Shtrikman bound (see [7]). For illustration purpose, consider here the particularly simple case of a porous medium with spherical cavities. In this case, f being the porosity and σ_0 the yield stress of the solid matrix, the obtained macroscopic criterion takes the form :

$$\frac{\Sigma_{eq}^2}{\sigma_0^2} + 2f\cosh\left\{\frac{1}{\sigma_0}\sqrt{\frac{9}{4}\Sigma_h^2 + \frac{2}{3}\Sigma_{eq}^2}\right\} - 1 - f^2 = 0 \qquad (3)$$

At the difference of the Gurson's criterion, (3) provides also the strongly remarkable property that the deviatoric equivalent stress Σ_{eq} enters with the hydrostatic stress Σ_h in the $cosh$ term. For low values of Σ_h, the nonlinear Hashin-Shtrikman bound is recovered (see Fig. 1).

It is also shown that in the general case of a spheroidal cavity, the developped approach leads also to some improvements of existing models, particularly in the case of the cracked plastic medium. As an example of illustration, consider a porous medium with prolate or oblate voids (including penny-shaped cracks) subjected to an axisymetic load. The obtained results are shown on Fig. 2 and are compared to numerical results provided by [3].

Extension to fluid saturated porous media

The results provided in the present study can be readily extended to the case of saturated cavities by a fluid at pressure P. Indeed, in this case, the boundary value problem to be solved involves application of P at the internal surface $\lambda = \lambda_1$. Thanks to the plastic incompressibility of the solid matrix (Von Mises material), it follows that the new problem can be recast in the same form as for the dry porous material by replacing $\mathbf{\Sigma}$ by $\mathbf{\Sigma}' = \mathbf{\Sigma} + \mathbf{1}P$. Clearly enough, the macroscopic criterion in the context of poroplasticity, can be obtained from the previous results by adopting the Terzaghi's effective principle. A full discussion of this point can be found in [1].[3]

[3] By nonlinear homogenization techniques, [1] has shown that for Drucker-Prager matrix the Terzaghi's effective stress principle cannot be applied.

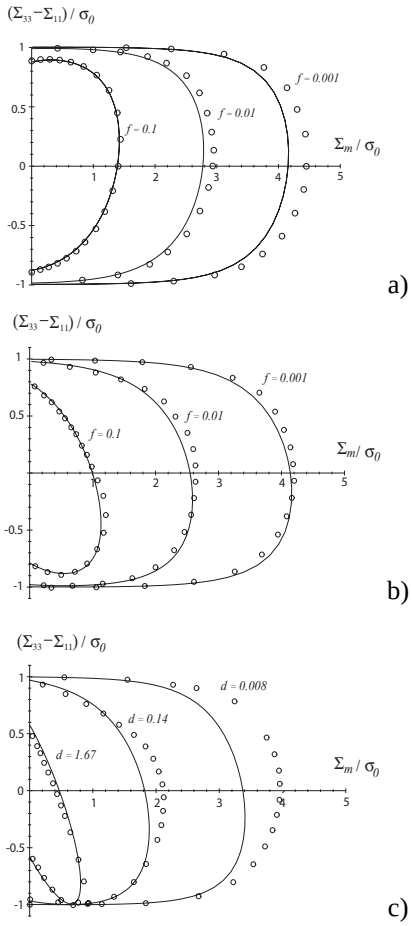

Figure 3: Yield surface of the porous material: a) case of prolate void, $a_1/b_1 = 5$, b) case of oblate void, $b_1/a_1 = 5$, c) case of penny shaped cracks (oblate cavities with $b_1/a_1 \to 0$). Comparison of the proposed model and "numerical" results obtained by Gologanu et al. (1997).

References

[1] L. Dormieux, D. Kondo, F.-J. Ulm (2006): *Microporomechanics*, Wiley.

[2] J. D. Eshelby (1957): The determination of the elastic field of an ellipsoidal inclusion, and related problem. *Proc. R. Soc. Lond.* A 241, 376-396

[3] M. Gologanu, J.B. Leblond, G. Perrin and J. Devaux (1997): Recent extensions of Gurson's model for porous ductile metals. *Continuum Micromechanics*, ed. P. Suquet, Springer Verlag.

[4] A.L. Gurson (1977) : Continuum theory of ductile rupture by void nucleation and growth: Part I. - Yield criterion and flow rules for porous ductile media. *J. Eng. Mat. Tech.*, **99**, 2–15.

[5] V. Monchiet, E. Charkaluk and D. Kondo (2007): An improvement of Gurson-type models of porous materials by using Eshelby-like trial velocity fields. *C.R. Mécanique*, to be published.

[6] T. Mura (1987): *Micromechanics of Defects in Solids*. Martinus Nijhoff, Dordrecht.

[7] P. Ponte-Castañeda, P. Suquet (1998): Nonlinear composites. *Adv. Appl. Mech*, **34**, 171–302.

Modeling the Evolution of Microstructure in Single and Dual Phase Polycrystalline Metals under Large Plastic Deformation

A. Butz, M. R. Ripoll, O. I. Benevolenski*

Fraunhofer Institute for Mechanics of Materials
Woehlerstraße 11, D-79108 Freiburg, Germany
butz@iwm.fhg.de, rod@iwm.fhg.de, bene@iwm.fhg.de

Summary: This contribution is concerned with the microstructural modeling of single and dual phase polycrystalline metals and its evolution during large plastic deformation. Representative volume elements (RVEs) are used in combination with a crystal plasticity model. The applicability of this approach is demonstrated on example of two technical applications.

Introduction

Microstructure evolution of polycrystalline metals under large plastic deformation during production processes significantly affect their mechanical properties such as formability [1], toughness and fatigue resistance. In this contribution are considered two practically important examples, namely, drawing of tungsten wire for the lighting industry and rolling of high strength dual phase steels for automotive applications. Representative volume elements (RVE) with single crystal plasticity describing individual grains are used in order to take into account the specific morphological aspects.

Crystal plasticity model

Grains in the polycrystalline aggregate are modelled within the framework of crystal plasticity, see for example [2]. This physically based theory describes plastic flow as the result of the movement of dislocations (namely slip) in a continuum way. This means that plasticity is the result of continuous shearing (slip) along various well-defined lattice planes. A slip system α is defined by the unit normal $m_i^{(\alpha)}$ to the slip plane and the unit vector $s_i^{(\alpha)}$ in the slip direction.

The theory is formulated in the framework of large deformation. The total deformation gradient F_{ij} can be decomposed as

$$F_{ij} = F^*_{ik} F^p_{kj}, \tag{1}$$

where F^*_{ij} denotes plastic shear and F^p_{ij} accounts for elastic stretching and rotation of the lattice. The rate of change of the plastic deformation gradient is given by

$$\dot{F}^p_{ik} F^{p^{-1}}_{kj} = \sum_\alpha \dot{\gamma}^{(\alpha)} s_i^{(\alpha)} m_j^{(\alpha)}. \tag{2}$$

The rate of the stretching tensor D_{ij} can be also decomposed into parts due to lattice deformation (*) and plastic slip (p):

$$D_{ij} = D^*_{ij} + D^p_{ij} \tag{3}$$

The flow rule based on Schmid's law is determined by the Schmid tensor $P_{ij}^{(\alpha)}$ and the shear rate $\dot{\gamma}^{(\alpha)}$ on the slip system α in form of a power law

$$\begin{aligned} D^p_{ij} &= \sum_{\alpha=1}^{n} P_{ij}^{(\alpha)} \dot{\gamma}^{(\alpha)} \\ P_{ij}^{(\alpha)} &= \frac{1}{2}(s_i^{*(\alpha)} m_j^{*(\alpha)} + m_i^{*(\alpha)} s_j^{*(\alpha)}) \\ \dot{\gamma}^{(\alpha)} &= \dot{a}\, \text{sign}\, \tau^{(\alpha)} \left| \frac{\tau^{(\alpha)}}{g^{(\alpha)}} \right|^{1/n} \end{aligned} \tag{4}$$

where $\tau^{(\alpha)}$ stands for the resolved shear stress on the slip system α, for instance

$$\tau^{(\alpha)} = s_i^{*(\alpha)} \sigma_{ij} m_j^{*(\alpha)} = P_{ij}^{(\alpha)} \sigma_{ij}, \tag{5}$$

where $\dot{a}$ denotes a reference shear rate and n the material rate sensitivity. $g^{(\alpha)}$ means the slip system hardness. The value of each $g^{(\alpha)}$ for γ = 0 has to be specified and is denoted with the symbol τ_0.

The strain hardening obeys the following evolution law:

$$\dot{g}^{(\alpha)} = \sum_\beta h_{\alpha\beta} \dot{\gamma}^{(\beta)} \tag{6}$$

with the hardening matrix $h_{\alpha\beta}$, where $h_{\alpha\alpha}$ stands for self-hardening on system α while $h_{\alpha\beta}$ ($\alpha \neq \beta$) describes the latent-hardening rate of system α. A simple form is used for $h_{\alpha\alpha}$ [2]

$$h_{\alpha\alpha} = h(\gamma) = h_0 \sec h^2 \frac{h_0 \gamma}{\tau_s - \tau_o}, \tag{7}$$

(without summation over α),

where h_0 represents the initial hardening rate and τ_s stands for the saturation strength. The latent hardening modulus is given by

$$h_{\alpha\beta} = q h(\gamma) \text{ for } \alpha \neq \beta \tag{8}$$

with the latent hardening parameter q.

Crystal plasticity is implemented as a user material subroutine UMAT, based on [3], in the finite element code ABAQUS.

Representative volume element

The use of RVEs provides a detailed insight into the material heterogeneities. The RVEs account for grain shape and lattice orientation and offer a practical way for predicting grain

morphology evolution, texture development and intergranular stresses. The geometrical microstructure is build up using Voronoï tessellations discretized using finite elements. Each grain of the RVE possesses a given crystal structure and lattice orientation. The crystal structure determines the number and type of potentially active slip systems. The initial lattice orientation of the grain is prescribed to represent the desired initial texture. The grains deform according to the single crystal plasticity constitutive equations.

The periodic boundary conditions are used in order to minimize the constraint effects. This means that the displacement vectors of two equivalent points a and b are coupled by the macroscopic deformation gradient $\bar{F}_{ij}$ [4]

$$u_i^b - u_i^a = \bar{F}_{ij}\left(x_{j0}^b - x_{j0}^a\right) - \left(x_{i0}^b - x_{i0}^a\right), \qquad (9)$$

where x_{i0}^a, x_{i0}^b indicate the position of a point pair in the non-deformed configuration.

Drawing of tungsten wires

Tungsten wires are drawn in successive steps until they reach a diameter suitable to be used as lamps filaments. During the drawing process the wires undergo severe plastic deformation that leads to a sharp <110> fibre texture. The well established texture induces single grains to deform by plane strain elongation [5]. This anisotropic deformation causes that initially equiaxed grains tend to develop and elliptical shape in the wire cross section. The major axes of the ellipses are given by the initial orientation of the $[1\bar{1}0]$ directions, perpendicular to the wire axis and randomly rotated around it [6].

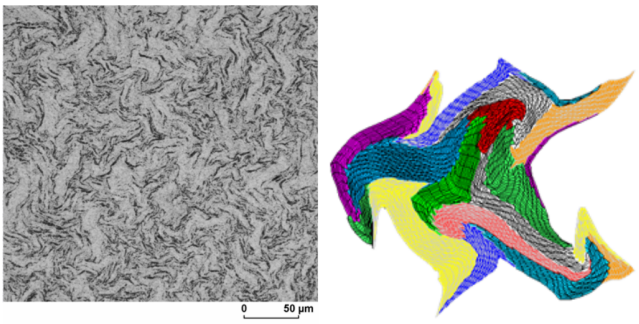

Figure 1: Grain curling in a tungsten wire. a) Structure observed in the cross section, b) simulated microstructure using a RVE.

This fact enhances mutual accommodation of neighbouring grains that bend around each other and create a characteristic pattern in the cross-section of the wire, known as grain curling or "Van Gogh sky structures", Fig. 1. This heterogeneous strain deformation at the microscopic level produces locally high stress concentrations that might explain the well-known tendency of BCC wires to develop longitudinal intergranular cracks known as splits [7, 8].

Rolling of dual phase steels

Dual phase steels demands an explicit representation of the microstructure during plastic deformation for a realistic simulation of the rolling process. The typical morphology of dual phase steels is characterized by a ferritic matrix and a martensitic phase which is localized within the interspaces of the ferrite grains. For the modeling of this morphology the previously described representative volume elements are used. An additional and new procedure is proposed to place the martensitic phase at the proper positions. A volume fraction of up to 25 percent martensite is assumed. Each grain inside the RVE deforms according to single crystal plasticity as illustrated before.

It is expected, that the advantageous mechanical properties of dual phase steels may be partly attributed to the specific spatial distribution of the martensitic phase. Therefore, this aspect will be examined in detail by comparing RVE models with varied arrangement of the martensitic phase. The results will be discussed and employed to propose an appropriate RVE model for the numerical simulation of the rolling of dual phase steel sheets.

References

[1] W. Schmitt, O. Benevolenski, T. Walde, A. Krasowsky (2005): Material characterization for simulation of sheet metal forming. In Proc. *VIII International Conference on Computational Plasticity*, COMPLAS VIII, E. Onate and D.J. Owen (Eds.) Barcelona.

[2] R. J. Asaro (1983): Micromechanics of Crystals and Polycrystals, *Adv. Appl. Mech.*, **23,** 1–115.

[3] Y. G. Huang (1991): *A User-material Subroutine Incorporating Single Crystal Plasticity in the ABAQUS Finite Element Program*, Harvard Univ., Rep. MECH-178.

[4] M. Nygårds, P. Gudmundson (2002): Three-dimensional Periodic Voronoi Grain Models and Micromechanical FE-Simulations of a Two-phase Steel, *Comp. Mater. Sci.*, **24,** 513–519.

[5] W. F. Hosford (1964): Microstructural Changes During Deformation of [011] Fiber-Textured Metals, *Trans. AIME*, **230,** 12–15.

[6] J. Očenášek, M. Rodriguez Ripoll, S. M. Weygand and H. Riedel: Multi-grain finite element model for studying the wire drawing process, *Computational Materials Science*, in press.

[7] P. F. Browning, C. L. Briant, K. Rajan, B. A. Knudsen (1995): An Analysis of Splitting Failures During the Drawing of Tungsten Wire, *Engineering Failure Analysis* **2,** 105–115.

[8] J. Gil Sevillano, D. González, J. M. Martínez-Esnaola (2006): Heterogeneous deformation and internal stresses developed in BCC wires by axisymmetric elongation, *Materials Science Forum*.

A Covariant Continuum Theory of Solids with Distributed Defects

A. Yavari[1*], **A. Ozakin**[2]

[1]School of Civil and Environmental Engineering
Georgia Institute of Technology, Atlanta, GA 30332, USA
arash.yavari@ce.gatech.edu

[2]Georgia Tech Research Institute, Atlanta, GA 30332, USA
arkadas.ozakin@gtri.gatech.edu

Summary: In this paper we first review the efforts in both physics and mechanics literatures on using non-Riemannian geometries in modelling continua with distributed defects. Building on the ideas from the last few decades we introduce a field theory of solids with distributed defects. In our theory, evolution of defects is represented by a dynamic reference manifold with time-varying metric and torsion. We will develop a covariant theory by postulating the invariance of energy balance under spatial and material diffeomorphisms of the ambient and material spaces.

Introduction

It is known that, in principle, it is possible to investigate a crystalline solid with a large number of defects in a continuum framework. Since the 1950s researchers have known that continuum mechanics of solids with distributed defects has a close connection with the differential geometry of manifolds with a Riemannian metric and torsion—a subject in mathematics that has found a wide range of applications in physics and engineering. For example, dislocation and disclination density tensors are closely related to torsion and curvature of a material connection, respectively. However, in spite of many efforts in the past decades, still a complete continuum theory of solids with distributed defects, capable of modeling defects and their evolution is missing.

In this seminar we first review the efforts in both physics and mechanics literatures on using non-Riemannian geometries in modeling continua with distributed defects. Building on the ideas from the last few decades we introduce a field theory of solids with distributed defects. In our theory, evolution of defects is represented by a dynamic reference manifold with time-varying torsion, curvature and non-metricity (see Fig. 1). We will develop a covariant theory by postulating the invariance of energy balance under spatial and material diffeomorphisms of the ambient and material spaces. We study the Lagrangian field theory of bodies with defects and consider both conservative and dissipative cases. Finally, we will make a connection between phenomenological plasticity and the geometric theory.

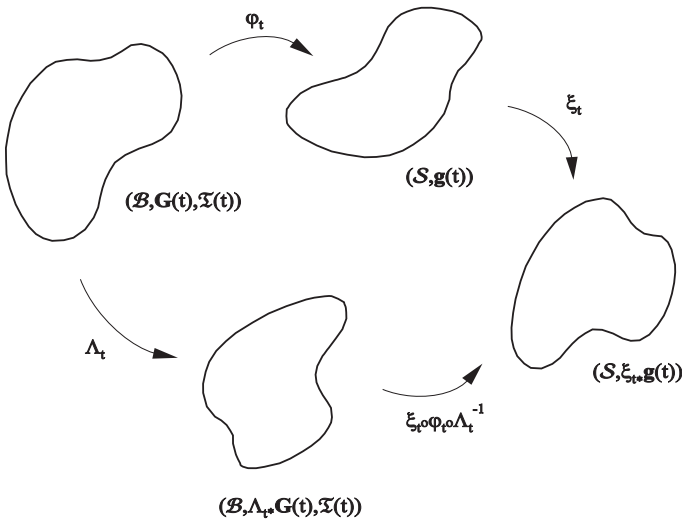

Figure 1: Spatial and material reframings of a continuum with distributed defects.

References

[1] B. A. Bilby, R. Bullough, and E. Smith (1955): Continuous distributions of dislocations: a new application of the methods of non-Riemannian geometry, *Proceedings of the Royal Society of London*, **A231**, 263–273.

[2] K. Kondo (1955): Geometry of elastic deformation and incompatibility, *Memoirs of the Unifying Study of the Basic Problems in Engineering Science by Means of Geometry* (K. Kondo, ed.), vol. 1, Division C, Gakujutsu Bunken Fukyo-Kai, 5–17.

[3] E. Kröner, (1996): Dislocation theory as a physical field theory, *Mechanica*, **31**: 577–587.

[4] E. J. Marsden and T. J. R. Hughes (1983): *Mathematical Foundations of Elasticity*, Dover, New York.

[5] A. Yavari, J. E. Marsden and M. Ortiz (2006): On the spatial and material covariant balance laws in elasticity, *Journal of Mathematical Physics*, **47**, 85–112.

Stochastic and Finite Element Modelling of 3D Heterogeneity in Geo-Engineering

M. A. Hicks*, J. D. Nuttall, W. A. Spencer

School of Mechanical, Aerospace and Civil Engineering, The University of Manchester
Sackville Street, Manchester, M60 1QD, United Kingdom
Michael.Hicks@manchester.ac.uk, Jonathan.Nuttall@student.manchester.ac.uk, William.Spencer@postgrad.manchester.ac.uk

Summary: This paper reports the use of finite elements and random fields for quantifying the effects of heterogeneity in geo-engineering. It starts by justifying the need for 3D simulations, through comparing the results of 2D and 3D analyses of failure in a long slope cut in clay. It then discusses the implications for geo-engineering in general; in particular, with regard to parallel computing and the need to model heterogeneity over a range of scales in many geo-environmental applications.

Introduction

This paper uses random field theory to model the heterogeneity of geo-materials and finite elements to quantify the influence of that heterogeneity on geo-structural response. The point-wise variation in material properties is defined by a probability distribution, mean (μ) and coefficient of variation (V), whereas the spatial correlation is characterised by an exponential covariance function and scale of fluctuation (θ). The random fields have been generated using local average subdivision (LAS) [1] and the finite element coding is based on [2].

Geotechnical example

The influence of heterogeneity of undrained shear strength (c_u) on the stability of a long slope cut in clay is investigated. It is an extension of previous 2D studies [3, 4, 5, 6], and follows a stochastic (Monte Carlo) approach, involving multiple realisations. Each realisation involves the generation of a random field of c_u, and the subsequent analysis of the problem using finite elements.

Fig. 1 examines the influence of the spatial correlation of c_u on reliability, R, versus global factor of safety, F, for a 1:1 slope, 5 m high and 100 m long, with V = 0.3 and $\theta_v = 1$ m [7]. F is based on the mean c_u, whereas R is given by,

$$R = \left(1 - \frac{N_f}{N}\right) \times 100 \qquad (1)$$

in which N is the total number of realisations and N_f is the number of realisations in which slope failure occurs. The figure compares results for different ratios of the horizontal to vertical scales of fluctuation ($\xi = \theta_h/\theta_v$).

The large difference between the 2D, Fig. 1(a), and 3D, Fig. 1(b), solutions is attributed to two factors: the infinite θ along the length of the slope, implicit in the plane strain assumption, and the inability of the 2D case to account for different failure mechanisms. In particular, 3D modelling revealed three principal failure modes [7]: for large values of θ_h, relative to the slope dimensions, the slope fails along its length and the solution is equivalent to the 2D case; for intermediate θ_h, independent and sometimes multiple failures can occur, Fig. 2; and, for small θ_h, the slope fails along its length, but the solution is not equivalent to the 2D case (rather, it tends to the deterministic solution based on μ).

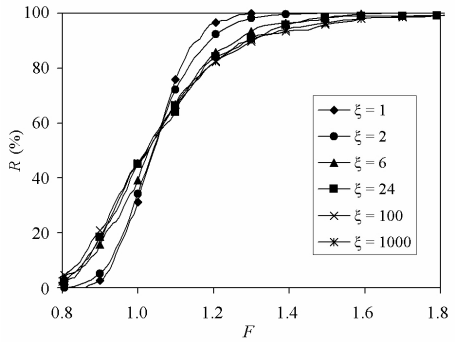

(a) 2D solution

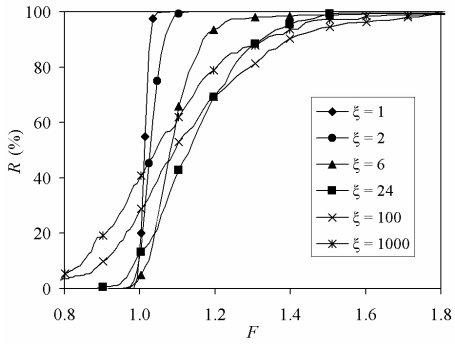

(b) 3D solution

Figure 1: Reliability versus factor of safety for a long slope.

Geo-environmental implications

The geotechnical analogy may be extended to applications in geo-environmental engineering. These are often characterised by very large domains, and by heterogeneity at multiple scales. For contaminant transport and bio-remediation, there is also the possibility of transient point and spatial statistics; e.g. due to changes in void spaces arising from bio-chemical reactions. As for the 3D slope example, fine mesh discretisations are needed for modelling spatial variability, whereas multiple realisations are needed to account for uncertainty in spatial distributions.

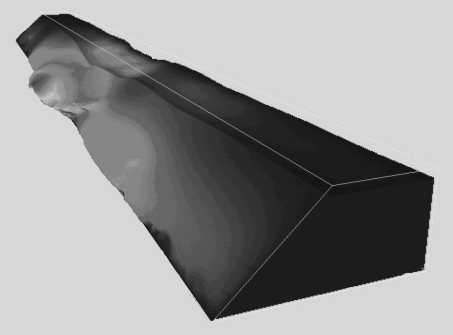

Figure 2: 3D failure in a long slope.

There are two possible strategies for tackling such problems:

The first is parallel computing [2], which may be used at two levels. For "smaller domains", the realisations can be shared across processors, whereas, for larger domains, individual realisations can also be shared. Note that the finite element requirements are optimised by assigning random field values to element sampling points, rather than to elements themselves [3, 4, 5, 6, 7]. Hence, in this paper, 8 random field cell values have been mapped onto each 20-node brick element. An advantage of LAS is that very large random fields are generated quickly, but, for larger problem domains, each field will still need to be generated in parallel due to the storage requirement. For example, Fig. 3 shows an anisotropic random field that has been generated over 4 processors.

The second (more complicated) possibility for modelling large heterogeneous systems is up-scaling, in which the problem is subdivided into different levels of heterogeneity. Hence, the overall domain is discretised to adequately reflect the largest heterogeneity scale, with the constitutive behaviour of each "cell" at that level being defined by the behaviour of smaller discretised domains at the next level down the heterogeneity scale, and so on. The overall system would then account for heterogeneity down to the smallest scale, but with a much reduced overall finite element requirement.

Conclusion

2D computer models in geo-engineering are often an over-simplification of the real problem. This paper has considered a simple geotechnical problem that would usually be idealised as 2-dimensional, and shown that heterogeneity and 3D aspects cannot be ignored.

Parallel computing has obvious potential for the modelling of large heterogeneous systems. However, as geo-environmental problems are often measured in km, and heterogeneity can be present at many scales, up-scaling techniques may also be needed.

Acknowledgement

This work is funded by the Engineering and Physical Sciences Research Council (Grant References GR/T11975/01 and EP/D037247/1).

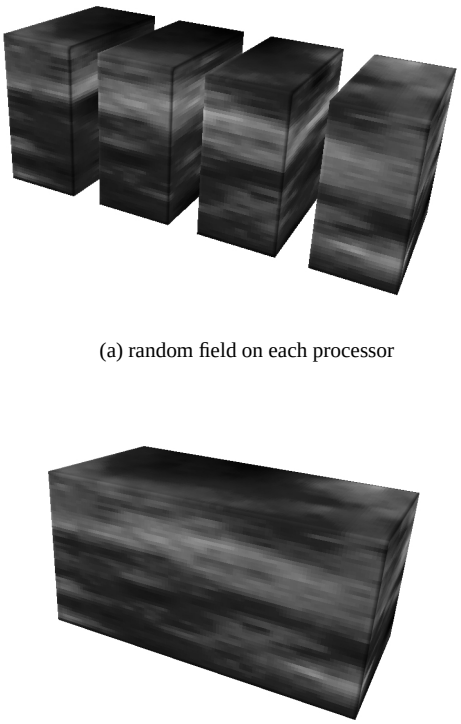

(a) random field on each processor

(b) full random field

Figure 3: Random field generation using 4 processors.

References

[1] G. A. Fenton, E. H. Vanmarcke (1990): Simulation of random fields via local average subdivision. *ASCE Journal of Engineering Mechanics*, **116**, 1733–1749.

[2] I. M. Smith, D. V. Griffiths (2004): *Programming the finite element method* (4th ed). John Wiley & Sons, Chichester.

[3] M. A. Hicks, K. Samy (2002): Influence of heterogeneity on undrained clay slope stability. *Quarterly Journal of Engineering Geology and Hydrogeology*, **35**, 41–49.

[4] M. A. Hicks, K. Samy (2002): Influence of anisotropic spatial variability on slope reliability. In *Proc. Eighth Int. Symp. on Numerical Models in Geomechanics*, Rome, 535–539.

[5] M. A. Hicks, K. Samy (2002): Reliability-based characteristic values: A stochastic approach to Eurocode 7. *Ground Engineering*, **35**, 30–34.

[6] M. A. Hicks, K. Samy (2004): Stochastic evaluation of heterogeneous slope stability. *Italian Geotechnical Journal*, **38**, 54–66.

[7] W. A. Spencer, M. A. Hicks (2007): A 3D finite element study of slope reliability. In *Proc. Tenth Int. Symp. on Numerical Models in Geomechanics*, Rhodes, in press.

Adaptive Time-Stepping Algorithm Exploiting the Combined Effect of Softening and Spatial Variability of Material Parameters

J. Jeřábek[1*], R. Chudoba[1], M. Vořechovský[2], M. Mombartz[1]

[1]Chair of Structural Statics and Dynamics, RWTH Aachen University
Mies-van-der-Rohe-Str. 1, 52074 Aachen, Germany
{jakub.jerabek,rch}@lbb.rwth-aachen.de, mmombartz@imb.rwth-aachen.de

[2]Institute of Structural Mechanics, Brno University of Technology
Veveří 95, 602 00 Brno, Czech Republic
vorechovsky.m@fce.vutbr.cz

Summary: The aim of the present work is to provide an efficient numerical framework for studying the interplay between the statistically and deterministically introduced length-scale. This paper gives an outline of adaptive nonlinear FE-algorithm focused on applications where the damage evolution gets driven by spatial variability of material properties at some length scale.

Introduction

The statistical length scale, i.e. the spatial measure of variability of material parameters can act as a localization limiter of the failure process in quasi-brittle materials. In other words, the combination of strain-softening behavior with spatially non-uniform material parameters affects the volume involved in the stress redistribution. This fact has been utilized in the formulation of an adaptive strategy governed by the correct reflection of stress redistribution in the damage zone occurring during the failure process.

The usual damage/plasticity framework is used to formulate the extension of the standard time-integration algorithm. The refinement/coarsening strategy is controlled by the relative distance to the inelastic range at each material point. This variable controls both the time- and space- resolution of the discretization. In particular, the formulation renders (1) general criteria for controlling the time-step and (2) spatially defined mesh resolution control function (MRCF). The constructed MRCF reflects the variability of arbitrary material parameters affecting both stiffness and strength.

In this abstract we explain the construction of MRCF in principle and sketch the control flow in a general time-stepping algorithm. The presentation shall address the connected issues of state variable transfer and the choice of the softening material model in a more detail.

Mesh resolution control function

The mesh control is based on the assumption that the used material model introduces a loading function

$$f(\boldsymbol{\varepsilon}, \boldsymbol{\kappa}, \boldsymbol{\theta}) \leq 0 \tag{1}$$

representing the transition to an inelastic zone, where $\boldsymbol{\varepsilon}$, $\boldsymbol{\kappa}$ and $\boldsymbol{\theta}$ represent the spatially varying fields of strain, internal variables and material properties.

Regarding a time-step $n+1$, iteration k and a quadrature point $x_I \in \Omega_I$ the loading function has the form

$$f_{I,n+1}^{(k)} = f(\boldsymbol{\varepsilon}_{I,n+1}^{(k)}, \boldsymbol{\kappa}_{I,n}, \boldsymbol{\theta}_I) \gtreqless 0 \tag{2}$$

that is normally followed by evaluation of trial stresses, return mapping and evaluation of the equilibrium residual. In the present algorithm we require that prior to this evaluation the loading function must not be violated:

$$f_{I,n+1}^{(k)} = f(\boldsymbol{\varepsilon}_{I,n} + \eta_I^{(k)} \Delta\boldsymbol{\varepsilon}_{I,n+1}^{(k)}, \boldsymbol{\kappa}_{I,n}, \boldsymbol{\theta}_I) \leq 0 \tag{3}$$

The parameter $\eta_I^{(k)}$ is introduced to adjust the time step before proceeding with the next iteration. Assuming that the material response is linear within the elastic domain and realizing that the internal variables $\boldsymbol{\kappa}$ are frozen during the iteration, Eq. (3) can be rewritten as:

$$f_{I,n} + \eta_I^{(k)} (f_{I,n+1}^{(k)} - f_{I,n}) \leq 0 \tag{4}$$

with $f_{I,n}$ representing the value of loading function from the last equilibrated step. Collecting the material points experiencing loading

$$\Omega_K = \{I | f_{I,n} < f_{I,n+1}^{(k)}\},$$

the scaling factor adjusting the step such that Eq. (3) holds is obtained as

$$\eta_K^{(k)} = \frac{f_{I,n}}{f_{K,n} - f_{K,n+1}^{(k)}}, \ \forall K \in \Omega_K \tag{5}$$

Note that η_K is positive. The global scaling factor is obtained by identifying the infimum of η_K over the subset of all points with loading

$$\lambda^{(k)} = \inf_{K \in \Omega_K} \eta_K^{(k)} \tag{6}$$

This factor is used twice: (1) to adjust the next iteration step and (2) to evaluate the distance from inelastic zone in each material point (compare Eq. (4)):

$$f_{I,n} + \lambda^{(k)} (f_{I,n+1}^{(k)} - f_{I,n}) \geq -\epsilon \tag{7}$$

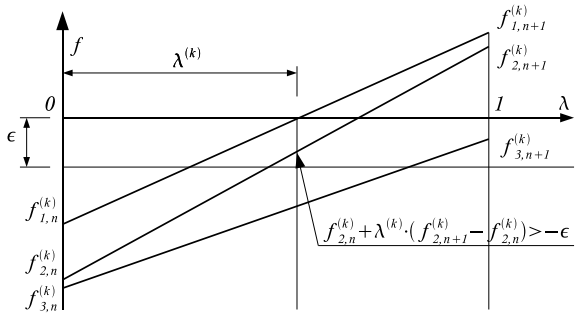

Figure 1: Illustration of the step scaling of loading function f in k-th iteration loading step $n+1$ in three material points.

Realizing that the left-hand-side is negative, this condition identifies the points near the inelastic range in terms of the threshold value ϵ (see Fig. 1). With the help of Heaviside function H this condition provides a mapping from the spatial domain to binary variable $\Omega_I \rightarrow [0,1]$ indicating zones with the onset of inelasticity

$$\phi_I^{(k)} = H\left(f_{I,n} + \lambda^{(k)}(f_{I,n+1}^{(k)} - f_{I,n}) + \epsilon\right) \tag{8}$$

In these zones we require the mesh to sufficiently resolve the variability of material parameters represented by an autocorrelation length l_ρ. In particular, the zones near to the onset of inelasticity ($\phi_I = 1$) must be discretized with elements of size $h_I \leq l_\rho/n_\rho$. Here n_ρ specifies the number of elements required within the autocorrelation length l_ρ. The zones to be refined within the current mesh are indicated by the binary mapping $\Omega_I \rightarrow [0,1]$:

$$\zeta_I^{(k)} = H\left(h_I^{(k)} - l_\rho/n_\rho\right) \tag{9}$$

The MRCF is then constructed as a product of the functions representing the proximity to inelasticity (8) and the mesh density requirement (9) at a quadrature point I

$$\psi_I^{(k)} = \phi_I^{(k)}\zeta_I^{(k)} \tag{10}$$

Further extensions of the MRFC are possible including coarsening and user-specified requirements on the mesh resolution.

Extension of time-stepping procedure

The application of MRCF introduces an additional inner loop within the equilibrium iteration keeping track of the mesh resolution. The basic requirement is that there are no points with $\psi_I^{(k)} = 1$ when accepting the next equilibrium state.

In particular, the solution to the discretized boundary value problem is obtained by the standard iterative time-stepping algorithm proceeding as follows. Let $(\bullet)_{n+1}^{(k)}$ be the value of variable $(\bullet)$ at the k-th iteration during the load step in $[t_n, t_{n+1}]$. Accordingly,

i let $\Delta\boldsymbol{d}_{n+1}^{(k)}$ be the vector of displacement increments at the k-th iteration, and let

$$\boldsymbol{d}_{n+1}^{(k)} = \boldsymbol{d}_n + \Delta\boldsymbol{d}_{n+1}^{(k)} \tag{11}$$

be the total value of the vector $\boldsymbol{d}$. The strain field can be computed by

$$\boldsymbol{\varepsilon}_{n+1}^{(k)} = \boldsymbol{B}\boldsymbol{d}_{n+1}^{(k)} \tag{12}$$

ii given the strain field, compute the stresses $\boldsymbol{\sigma}_{n+1}^{(k)}$ in terms of the current material model.

iii Evaluate $\lambda^{(k)}$ and $\psi_I^{(k)}$
IF $\exists\psi_I^{(k)} = 1$:
REMESH, TRANSFER state variables and
GO TO **i**

iv evaluate the global internal force vector $\boldsymbol{F}^{\mathrm{int}}(\boldsymbol{\sigma}_{n+1})$;

v check equilibrium: if equilibrium is satisfied for $\boldsymbol{\sigma} = \boldsymbol{\sigma}_{n+1}^{(k)}$ then $(\bullet)_{n+1}^{(k)}$ is the solution; otherwise, continue; and

vi determine $\Delta\boldsymbol{d}_{n+1}^{(k)}$, set $k \leftarrow k+1$, and go to step **i**.

The adaptive extension is handled completely in point **iii**. The remeshing is performed hierarchically using the parent-child relation to transfer the state variables in a targeted way. State transfer is performed by interpolating the state variables in the coarse mesh before entering the inelastic regime. Therefore, no path dependence may occur due to the variable transfer. Such a case may, however, arise if the diffusion error is large. The way how to treat such case shall be addressed in the presentation.

Conclusions

The pilot formulation and verification of the framework has been presented recently using one-dimensional example with simple hardening plasticity material [2]. Here, we extend the concept to strain-softening failure. The procedure shall be demonstrated on more complex examples with different scales of spatial variability. The efficiency shall be compared with the overkill discretization of the problem.

The presented adaptive extension serves as a basis for efficient Monte-Carlo simulations of non-linear problems with quasi-brittle material behavior allowing us to study the role of the statistical and deterministic length scales in the simulation of the localized failure. When choosing a particular material model with strain-softening in connection with spatially varying material parameters the question arises, whether or not the two scales interact or are exchangeable at least in some range. This question belongs to the general discussion on hierarchy of length scales [1].

References

[1] H. Stang, J. F. Olesen, P. N. Poulsen, L. Dick-Nielsen (2006): Application of the cohesive crack in cementitious materials modelling. In *EURO-2006, Computational Modelling of Concrete Structures*, 443–448.

[2] M. Vořechovský, R. Chudoba, J. Jeřábek (2006): Adaptive probabilistic modeling of localization, failure and size effect of quasi-brittle materials, In C. A. Mota-Soares, editor, *ECCM10*, page 286 (abstract), full papers on CD-ROM.

Numerical Prediction of the 3D Fracture Propagation in the Proximal Femur

T. Ch. Gasser*, **M. Auer**

Royal Institute of Technology (KTH), Department of Solid Mechanics.
Osquars backe 1, SE–100 44 Stockholm, Sweden.
tg@hallf.kth.se, mauer@kth.se

Summary: Bone can be regarded as a quasi brittle material, where a significant non-linear zone develops ahead the crack tip. Within this paper we utilize the strong discontinuity approach to predict failure propagation in the proximal part of the femur under compressive loading. A geometrically detailed 3D finite element model, which accounts for inhomogeneous fracture properties, has been applied, and the achieved computational results are compared to experimental data available in the literature.

Motivation and Background

Fracture of the proximal femur is accompanied by surgical complexity and high socio-economical costs, such that, it is under extensive scientific investigation and a large number of 3D Finite Element computations have been proposed in the literature. Nevertheless, less attention has been given to the numerical prediction of the onset and progress of fracture of a patient specific 3D model of the proximal femur.

Bone tissue consists mostly of collagen and mineral in the form of hydroxyapatite crystals [1] and the heterogeneous structure of bone tissue causes non-linear fracture zones ahead the tip. In particular, collagen fiber bridging causes non-linear zones of the dimension of millimeters, and hence, linear elastic fracture mechanics does no longer apply [5].

The present work applies the strong discontinuity approach and models fracture of the proximal femur under compressive loading, where the existence of a fracture process zone is postulated. We assume that mode I failure properties are applicable to characterize the mixed mode situation present and employ an isotropic (discrete) constitutive description of the cohesive zone [2].

Modeling assumptions

Strong discontinuity kinematics

We follow the strong discontinuity approach and assume a discontinuity $\partial\Omega_{0\mathrm{d}}$ in the displacement field separating the body into two sub-bodies, where Ω_{0+} and Ω_{0-} denote the referential sub-domains occupied by the them. The orientation of the discontinuity at a material point $\mathbf{X}_\mathrm{d} \in \partial\Omega_\mathrm{d}$ is defined by the unit direction vector $\mathbf{N}$ and the displacement at a material point $\mathbf{X}$ is assumed to be $\mathbf{u}(\mathbf{X}) = \mathbf{u}_\mathrm{c}(\mathbf{X}) + \mathcal{H}(\mathbf{X})\mathbf{u}_\mathrm{e}(\mathbf{X})$. Here $\mathbf{u}_\mathrm{c}$ and $\mathbf{u}_\mathrm{e}$ are regular and enhanced displacement fields and $\mathcal{H}(\mathbf{X})$ denotes the *Heaviside* function, with the values 0 for $\mathbf{X} \in \Omega_{0-}$ and 1 for $\mathbf{X} \in \Omega_{0+}$. According to that definition and the use of $\mathrm{Grad}\,\mathcal{H}(\mathbf{X}) = \delta_\mathrm{d}\mathbf{N}(\mathbf{X}_\mathrm{d})$ the corresponding deformation gradient $\mathbf{F}(\mathbf{X}) = \mathbf{I} + \mathrm{Grad}\,\mathbf{u}(\mathbf{X}) = \mathbf{I} + \mathrm{Grad}\,\mathbf{u}_\mathrm{c}(\mathbf{X}) + \mathcal{H}\mathrm{Grad}\,\mathbf{u}_\mathrm{e}(\mathbf{X}) + \delta_\mathrm{d}(\mathbf{X})\mathbf{u}_\mathrm{e}(\mathbf{X}) \otimes \mathbf{N}(\mathbf{X}_\mathrm{d})$ is defined. Here we have introduced the *Dirac-delta* functional δ_d with $\delta_\mathrm{d} = 0$ and $\delta_\mathrm{d} = \infty$ for $\mathbf{X} \notin \partial\Omega_{0\,\mathrm{d}}$ and $\mathbf{X} \in \partial\Omega_{0\,\mathrm{d}}$, respectively.

Variational formulation

The underlying variational formulation is based a single-field variational principle, i.e. $\int_{\Omega_0} \mathrm{Grad}\,\delta\mathbf{u} : \mathbf{P}(\mathbf{F})\mathrm{d}V - \delta\Pi^{\mathrm{ext}}(\delta\mathbf{u}) = 0$, where $\mathbf{P}(\mathbf{F})$ and $\delta\mathbf{u}$ denote the first Piola-Kirchhoff stress tensor and the admissible variation of the displacement field. With $\delta\mathbf{u} = \delta\mathbf{u}_\mathrm{c} + \mathcal{H}\delta\mathbf{u}_\mathrm{e}$ the variational principle renders two spatial variational statements

$$\int_{\Omega_-} \mathrm{sym}(\mathrm{grad}_\mathrm{c}\delta\mathbf{u}_\mathrm{c}) : \boldsymbol{\sigma}_\mathrm{c}\mathrm{d}v + \int_{\Omega_+} \mathrm{sym}(\mathrm{grad}_\mathrm{e}\delta\mathbf{u}_\mathrm{c}) : \boldsymbol{\sigma}_\mathrm{e}\mathrm{d}v - \\ -\delta\Pi^{\mathrm{ext}}_\mathrm{c}(\delta\mathbf{u}_\mathrm{c}) = 0, \tag{1}$$

$$\int_{\Omega_+} \mathrm{sym}(\mathrm{grad}_\mathrm{e}\delta\mathbf{u}_\mathrm{e}) : \boldsymbol{\sigma}_\mathrm{e}\mathrm{d}v + \int_{\partial\Omega_\mathrm{d}} \mathbf{t}\cdot\delta\mathbf{u}_\mathrm{e}\mathrm{d}s - \\ -\delta\Pi^{\mathrm{ext}}_\mathrm{e}(\delta\mathbf{u}_\mathrm{e}) = 0, \tag{2}$$

where $\mathrm{d}v$ and $\mathrm{d}s$ are the spatial volume and surface elements, respectively. Here, $\boldsymbol{\sigma}_\mathrm{c}$ and $\boldsymbol{\sigma}_\mathrm{e}$ denote the Cauchy stress tensors and $\mathbf{t} = \mathbf{T}\mathrm{d}S/\mathrm{d}s$ is the Cauchy traction vector associated with a fictitious discontinuity $\partial\Omega_\mathrm{d}$, i.e. the mapping of $\partial\Omega_{0\mathrm{d}}$ to the current configuration. Algorithmic issues including a consistent linearization of the statements (1) and (2) are given in [2] and references therein.

Cohesive constitutive formulation

Bone fracture causes significant non-linear zones ahead the crack tip [5] and the associated complex irreversible changes on the microstructure are lumped into a discrete cohesive zone, which are mechanically defined by the cohesive potential

$$\psi(\widehat{\mathbf{u}} \otimes \widehat{\mathbf{u}}, \delta) = \frac{t_0}{2\delta}\exp(-a\delta)i_1. \tag{3}$$

Here $i_1 = \widehat{\mathbf{u}} \cdot \widehat{\mathbf{u}}$ is the first invariant of the symmetric tensor $\widehat{\mathbf{u}} \otimes \widehat{\mathbf{u}}$, t_0 denotes the cohesive strength of bone tissue and the non-negative parameters a and δ characterize the softening properties of the cohesive zone. According to the procedure by *Colleman* and *Noll*, the first Piola Kirchhoff traction is defined by

$$\mathbf{T} = \frac{\partial\psi}{\partial\widehat{\mathbf{u}}} = \frac{t_0}{\delta}\exp(-a\delta)\widehat{\mathbf{u}}, \tag{4}$$

and the introduction of the mode I fracture energy $\mathcal{G}_I = \int_0^\infty \mathbf{T} \cdot \mathrm{d}\widehat{\mathbf{u}} = \int_0^\infty t_0 \delta^{-1} \exp(-a\delta) \widehat{\mathbf{u}} \mathrm{d}\widehat{u} = t_0/a$ gives the relation $a = T_0/\mathcal{G}_I$ for the introduced material parameter a.

Crack tracking algorithm

A critical task to apply the introduced concept within a numerical frame is the geometrical representation of the crack surface and tracking its propagation. Especially for 3D, the development of crack-tracking algorithms is an active research area in computational mechanics, and different crack-tracking schemas are under discussion.

Herein, we use the recently proposed two step predictor-corrector schema [2]; the predictor step generates a failure surface according to the *Rankine* failure criterion, while the corrector step smoothes it and avoids the development of topological difficulties. Hence, the corrector step draws in non-local information of the existing crack, which is realized by fitting a polynomial surface $Z(X, Y)$ locally to the crack surface defined by the predictor step. To this end n_R points on the crack surface (located in the vicinity of the material point of interest) are considered and the coefficients of the polynomial surface are defined by minimizing the least-square problem

$$\Phi = \sum_{i=1}^{n_R} (Z_i - Z(X_i, Y_i))^2 \rightarrow \min, \tag{5}$$

where X_i, Y_i, Z_i denote the components of the considered points on the crack surface. Subsequently, the orientation of the discontinuity $\mathbf{N}$ in the k-th finite element is adapted (corrected) to the normal onto the polynomial surface $Z(X, Y)$ [2].

The numerical model and its predictions

The numerical example presented herein follows closely the experimental investigation discussed in [4], where a proximal part of about 20.0 cm of the femur is loaded until failure. We used the geometry of the proximal part of a standardised femur and the generated finite element mesh has been slightly refined at those regions were failure was expected. Boundary and loading conditions are chosen according to the experimental study [4] and arc-length method has been applied to solve the problem.

We assume a homogeneous elastic stiffness, defined by the Young's modulus 10.0 GPa of and the Poisson's ratio of 0.35, which is in accordance with reported mechanical properties of femural bone [1]. In order to account for the different strength of cancellous and cortical bone, the cohesive strength t_0 is assumed to vary from 3.0 MPa at the top of the femoral head and 35.0 MPa at the femoral shaft. The mode-I fracture energy has been assumed to be constant $\mathcal{G}_I = 1.5$ kJ/m^2 and further modeling details are given in [3]

The predicted crack formation is shown in Figure 1; it is found to be in good agreement with the experimental study [4]. Apart from that, the predicted ultimate load of 7800.0 N is close to the experimental value of 8400 N reported in the same study.

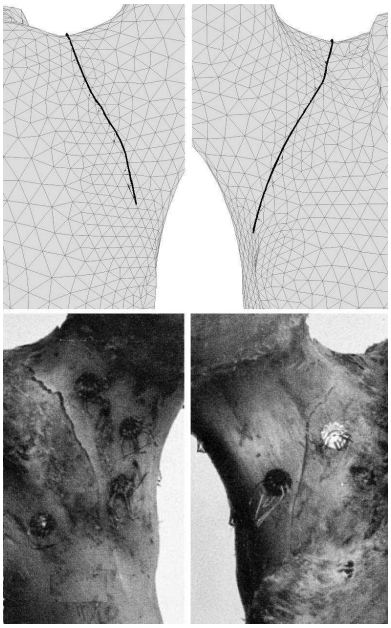

Figure 1: Predicted crack formation of the proximal femur in comparison with results of the experimental study [4].

Conclusions

The concept of strong discontinuities has be applied to predict fracture of the proximal femur, which gave a detailed insight into the mechanisms of femoral fracture under compressive loading. The proposed approach utilizes a cohesive fracture model and a 3D crack-tracking algorithm within the Finite Element Method, which renders an efficient and stable numerical concept. Although the heterogeneity of bone density has been captured in a very rough manner, the predictions of the presented model agreed nicely with available experimental data.

References

[1] S. C. Cowin (2001): *Bone mechanics handbook*. CRC Press, Boca Raton, Florida.

[2] T. C Gasser and G. A. Holzapfel (online): 3D crack propagation in unreinforced concrete. A new smoothing algorithm for tracking 3D crack surfaces. *Comput. Meth. Appl. Mech. Eng.*

[3] T. C. Gasser and G. A. Holzapfel (in press): A numerical framework to model 3-d fracture in bone tissue with application to failure of the proximal femur. *In:* T. Belytschko, A. Combescure, R. de Borst (eds.): *Discretization Methods for Evolving Discontinuities*. Heidelberg. Springer-Verlag.

[4] T. Ota, I. Yamamoto, and R. Morita (1999): Fracture simulation of femoral bone using finite-element method: How a fracture initiates and proceeds. *Bone and Mineral Metabolism*, **17**, 108–112.

[5] Q.D. Yang, B.N. Cox, R.K. Nalla, and R.O. Ritchie (2006): Re-evaluating the toughness of human cortical bone. *Bone*, **38**, 878–887.

A Regularized XFEM Formulation for Process Zone Modelling

E. Benvenuti*, A. Tralli

Engineering Department, University of Ferrara
via Saragat, 1- 44100 Ferrara, Italy
elena.benvenuti@unife.it, antonio.tralli@unife.it

Summary: A new finite element scheme for modelling fracture is presented, which extends to the case of elastodamaging interfaces the approach for elastic interfaces developed by the authors in reference [1]. The process zone is modelled as a soft elastodamaging layer, whose thickness introduces a characteristic length scale into the continuum model. When the characteristic length is finite, an extended FE model with a finite process zone is obtained. When the characteristic length vanishes, a crack model with a cohesive traction-separation law is recovered. The associated finite element formulation is based on the partition if unit property of the standard interpolation functions (e.g. [2]), and can be seen as an extended finite element formulation (XFEM) with a regularized kinematics. Some results obtained for a DCB test and a plate subjected to shear load are synthetically presented.

Introduction

Interfaces with finite or zero thickness are of great interest in structural mechanics applications. In this work, a soft and thin layer whose thickness is a model parameter is embedded in a body. Let us consider a two-dimensional body Ω with smooth boundary $\partial\Omega$, subjected to prescribed displacements $\mathbf{u} = \bar{\mathbf{u}}$ on $\partial\Omega_u$ and to given surface load distribution $\bar{\mathbf{F}}$ on $\partial\Omega_f$. The domain is divided by an internal surface $\partial\Omega_d$ with normal $\mathbf{n}$ and tangent $\mathbf{t}$ into two disjoint sub-domains Ω^+ and Ω^-, so that $\Omega \equiv \Omega^+ \bigcup \Omega^-$. Furthermore, a layer of thickness $2L_\rho$ is obtained by shifting $\partial\Omega_d$ by an offset $L_\rho/2$ with $L_\rho > 0$ in the $\mathbf{n}^+$ and the $\mathbf{n}^-$ directions, respectively (Fig. 1).

We assume that the displacement field $\mathbf{u}$ is characterized by a bounded jump $[\mathbf{u}(\boldsymbol{x})] = \mathbf{u}^+(\boldsymbol{x}) - \mathbf{u}^-(\boldsymbol{x})$ across the surface $\partial\Omega_d$, where $\mathbf{u}^+$ and $\mathbf{u}^-$ denote the restrictions of $\mathbf{u}$ to $\partial\Omega_d^+$ and $\partial\Omega_d^-$, respectively. The vector field

$$\mathbf{a}(\boldsymbol{x}) = \mathcal{H}_\rho(d(\boldsymbol{x})) \tag{1}$$

is introduced, where $d(\boldsymbol{x})$ is the signed distance function. The function $\mathcal{H}_\rho$ is a smooth approximation of the Heaviside function $\mathcal{H}$, which can be defined as $\mathcal{H}(\boldsymbol{x}) = -1$ if $d(\boldsymbol{x}) \cdot \mathbf{n} < 0$ and $\mathcal{H}(\boldsymbol{x}) = 1$ if $d(\boldsymbol{x}) \cdot \mathbf{n} > 0$. Function $\mathcal{H}_\rho$ is continuous with continuous derivatives, The length of the regularization is the decaying length L_ρ, that is related to ρ and depends on the type of function $\mathcal{H}_\rho$ that is adopted. As ρ vanishes, $\mathcal{H}_\rho$ reproduces the Heaviside function $\mathcal{H}(\boldsymbol{x})$.

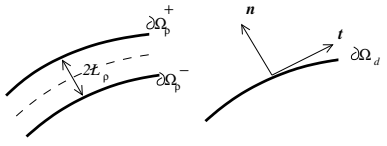

Figure 1: Layer of thickness L_ρ

Finite element formulation

Let the domain Ω be discretized into $\mathcal{M}$ non over-lapping finite elements $\Omega \equiv \bigcup_{i=1}^{\mathcal{M}} \Omega_i$ connected at $\mathcal{N}$ nodes. The displacement $\mathbf{u}$ and the jump $\mathbf{a}$ are modelled as independent fields. The primal fields $\mathbf{v}$ and $\mathbf{a}$ are approximated as

$$\mathbf{v} \approx \mathbf{N}\mathbf{V}\,, \quad \mathbf{a} \approx \mathbf{N}\mathbf{A} \tag{2}$$

where vectors $\mathbf{V} = \{\mathbf{v}_1, \mathbf{v}_2, \ldots, \mathbf{v}_\mathcal{N}\}$ and $\mathbf{A} = \{\mathbf{a}_1, \mathbf{a}_2, \ldots, \mathbf{a}_\mathcal{N}\}$ collect the $\mathcal{N}$ nodal values, and the same polynomial shape functions $\mathbf{N} = \{\mathbf{N}_1, \mathbf{N}_2, \ldots, \mathbf{N}_\mathcal{N}\}$, are adopted for both $\mathbf{v}$ and $\mathbf{a}$. The total displacement field is approximated as

$$\mathbf{u} = \mathbf{N}\mathbf{V} + \mathcal{H}_\rho \mathbf{N}\mathbf{A} \tag{3}$$

The latter expression satisfies the local Partition of Unity property of standard finite element interpolation functions. The same regularized kinematics was exploited in reference [3]. The associated strains are

$$\boldsymbol{\varepsilon}^{(0)} = \mathbf{B}\mathbf{V}\,, \quad \boldsymbol{\varepsilon}^{(1)} = \mathcal{H}_\rho \mathbf{B}\mathbf{A}\,, \quad \boldsymbol{\varepsilon}^{(2)} = \delta_\rho(\mathbf{N}\mathbf{A} \otimes_s \mathbf{n}) \tag{4}$$

where $\delta_\rho = d(\mathcal{H}_\rho(s))/d\,s$.

A crucial point is the constitutive modelling of the stress which are fields work-conjugated to the strain components

$$\boldsymbol{\sigma}^{(0)} = \mathbb{D}^{(0)}(\boldsymbol{\varepsilon}^{(0)} + \boldsymbol{\varepsilon}^{(1)})\,, \; \boldsymbol{\sigma}^{(1)} = \boldsymbol{\sigma}^{(0)}\,, \; \boldsymbol{\sigma}^{(2)} = \mathbb{D}^{(2)}\boldsymbol{\varepsilon}^{(2)} \tag{5}$$

where $\mathbb{D}^{(0)}$ the elastic constitutive operator of the bulk. Isotropic damage governed by the scalar $\omega^{(2)}$ is associated to the cohesive stress $\boldsymbol{\sigma}^{(2)}$ through the elastodamaging constitutive operator $\mathbb{D}^{(2)} = (1 - \omega^{(2)})^2\mathbb{E}^{(2)}$.

Damage evolution is governed by the following set of loading-unloading conditions:

$$\phi = Y^{(2)} - \tilde{Y}^{(2)} \leq 0 \quad \dot{\omega}^{(2)} \geq 0 \;\; \phi\dot{\omega}^{(2)} = 0 \tag{6}$$

where $Y^{(2)}$ is the damage energy release rate and $\tilde{Y}^{(2)}$ is the damage threshold.

Following [4], $\mathbb{D}^{(2)}$ is obtained starting from the knowledge of the real thickness of the layer t and the constitutive operator $\mathbb{D}^c$ of the given real interface as follows [1]

$$\mathbb{D}^{(2)} = \frac{\mathbb{D}^c}{t\delta_\rho} \text{ such that } \boldsymbol{\sigma}^{(2)} = \frac{\mathbb{D}^c}{t}(\mathbf{N}\mathbf{A} \otimes_s \mathbf{n}) \tag{7}$$

Let us assume virtual variations $\tilde{\mathbf{v}}$ and $\tilde{\mathbf{a}}$ and the associated virtual strains $\tilde{\boldsymbol{\varepsilon}}^{(0)}$, $\tilde{\boldsymbol{\varepsilon}}^{(1)}$, $\tilde{\boldsymbol{\varepsilon}}^{(2)}$

$$\int_\Omega \boldsymbol{\sigma}^{(0)} \cdot \tilde{\boldsymbol{\varepsilon}}^{(0)} + \boldsymbol{\sigma}^{(1)} \cdot \tilde{\boldsymbol{\varepsilon}}^{(1)}\, d\Omega + \int_{\Omega_\rho} \boldsymbol{\sigma}^{(2)} \cdot \tilde{\boldsymbol{\varepsilon}}^{(2)} d\Omega = \mathcal{L}_{ext} \tag{8}$$

where the external work $\mathcal{L}_{ext} := \int_{\partial\Omega^p} \mathbf{N}^t\mathbf{F}^t\tilde{\mathbf{v}}dS$. After replacement of the constitutive laws, and considering as given the solution at the instant t_n, at the instant t_{n+1}, the equilibrium equations can be rephrased into the matrix form

$$\begin{pmatrix}\mathbf{K}_{vv} & \mathbf{K}_{va}\\ \mathbf{K}_{av} & \mathbf{K}_{aa}\end{pmatrix}\left\{\begin{array}{c}\mathbf{v}\\ \mathbf{a}\end{array}\right\}\Big|_{n+1} = \left\{\begin{array}{c}\int_{\Omega^f}\mathbf{N}^t\mathbf{F}^t\,dS\\ \mathbf{0}\end{array}\right\}\Big|_{n+1} \quad (9)$$

where

$$\mathbf{K}_{vv} = \int_\Omega \mathbf{B}^t\mathbb{D}^{(0)}_{n+1}\mathbf{B}\,d\Omega \quad (10a)$$

$$\mathbf{K}_{va} = \mathbf{K}^t_{av} = \int_\Omega \mathbf{B}^t\mathbb{D}^{(0)}\mathbf{B}\mathcal{H}_\rho\,d\Omega \quad (10b)$$

$$\mathbf{K}_{aa} = \int_\Omega \mathcal{H}^2_\rho\mathbf{B}^t\mathbb{D}^{(0)}\mathbf{B}\,d\Omega + \int_{\Omega_\rho}\delta_\rho\bar{\mathbf{N}}^t\frac{\mathbb{D}_c}{t}\bar{\mathbf{N}}\,d\Omega \quad (10c)$$

and $\varepsilon^{(2)} = \bar{\mathbf{N}}\mathbf{A}$.

It can be shown that the work carried out by the stress $\boldsymbol{\sigma}^{(2)}$ by the strain $\boldsymbol{\varepsilon}^{(2)}$ converges to the work of the traction for the displacement discontinuity as ρ tends to zero (see reference [1]).

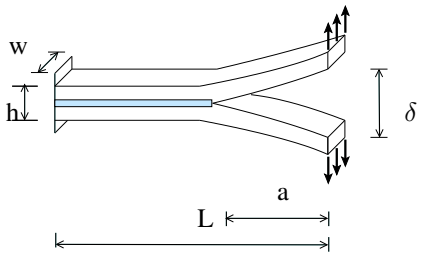

Figure 2: Double cantilever beam: $L = 100$ mm, $a = 30$ mm, $h = 6$ mm; the constitutive parameters are $E = 135300$ N/mm^2 and $\nu = 0$

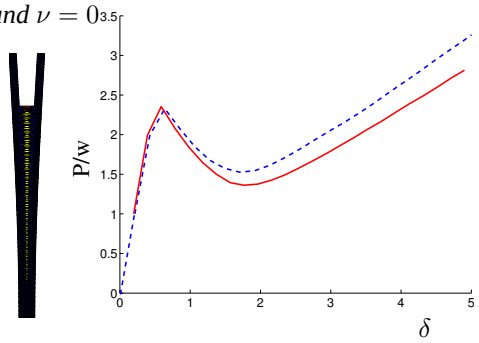

Figure 3: Double cantilever beam with a internal elasto-damaging layer: a) damaged deformed mesh; b) load per unit width versus opening displacement for $\rho = 0.01$ (blue-dashed line) mm and $\rho = 0.008$ mm (red-continuous line); the initial damage threshold is $\tilde{Y}^{(2)} = 1$ Nmm^2 and $E_c/t = E/10^5$.

Results

A discussion on the most appropriate quadrature techniques can be found in Reference [1]. Here, three-noded triangles with a grid of 13 quadrature points has been adopted. The opening and shearing components of the displacement jump define the modes and can be simultaneously present in the general case of mixed-mode delamination. However, the effectiveness of the proposed methodology has been tested simulating a mode I crack growth in double cantilever beams and a mode II crack growth in a plate subjected to plane strain state. In the first case, the specimen of Fig. 2 has been tested. The load per unit of width has been plotted versus the opening displacement by assuming $\rho = 0.01$ mm and $\rho = 0.008$ mm in Fig. 3. The second test has been carried out on a plane strain plate subjected to a made II loading. The influence of the adopted internal scale and of the mesh size is shown in Fig. 4; the profiles in continuous line refer to the extra-fine mesh, those in dashed line to a fine mesh.

Conclusive remarks

A general approach has been presented that makes it possible to deal with delamination problems and to model the transition from continuous to discontinuous failure. By decreasing the values of the characteristic length L_ρ and by changing the constitutive matrix associated to the process zone, a cohesive "spring-type" interface which transmits the traction vectors and allows for discontinuous displacements is recovered when the thickness vanishes [4]. In the most general case, a process zone of finite width placed either intra- or extra-element can be explicitly accounted for. Other important issues like a proper modelling of the process zone as a function of the damage level and the transition from continuous damage to crack are the subject of an undergoing research.

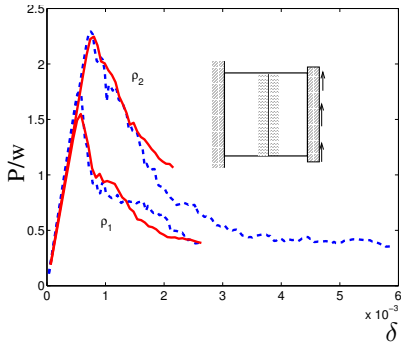

Figure 4: Mode II loading: load-displacement profile of a 10mm×10mm plate for $\rho_1 = 0.01$ mm and $\rho_2 = 0.02$ mm; the constitutive parameters are $E = 135300$ N/mm^2 and $\nu = 0$; the initial damage threshold is $\tilde{Y}^{(2)} = 1$N/mm^2 and $E_c/t = E/10^5$.

References

[1] E. Benvenuti, A. Tralli, G. Ventura (2007), A regularized XFEM model for the transition from continuous to discontinuous displacements, submitted.

[2] N. Moes, T. Belytschko (2002): Extended finite element method for cohesive crack growth, *Engineering Fracture Mechanics*,**69**,813–833.

[3] B. Patzák, M. Jirásek (2003). Process zone resolution by extended finite elements. *Engineering Fracture Mechanics*,**70**, 957–977.

[4] Z. Hashin (1990): Thermoelastic properties and conductivity of carbon/carbon fiber composites, *Mechanics of Materials*, **8**, 293–308.

Structured Meshes for Heterogeneous Materials Failure Model

S. Melnyk*, J. B. Colliat, M. Hautefeuille, A. Ibrahimbegović

Ecole Normale Supérieure de Cachan, LMT,
61, avenue de président Wilson, 94235 Cachan, France
{melnyk, colliat, hautefeuille, ai}@lmt.ens-cachan.fr

Summary: In this work we discuss the Finite Elements Method using the embedded discontinuity of strain and displacement fields, which can handle the problem of localized failure in heterogeneous materials by using structured (regular) meshes. On the chosen 2D model problem we develop all the pertinent details of the finite element approximation. With such a modeling in hand we also presented how to take into account for the variability of the geometrical description at the meso-scale level.

The majority of materials used in the civil engineering and the mechanical engineering are composed of several phases. Along the life, structures are often cracked, and therefore it is not possible to neglect cracking of the structure during computations. In this work we present an approach which makes possible to take into account for cracks propagation in materials composed of several phases.

Many methods of simulation (including the Finite Element Method) are using mesh refinement in conformity with the various phases of modeled material. In this case, a typical element contains only one phase some leading to complex meshes and a rather high number of elements. One also risks to have distorted elements that can lead to a badly conditioned problem because the form and the size of inclusions and voids of the real structures are not obvious (see [10, 1, 3]). This kind of representation is generally too expensive in computation time but gives a solution with high accuracy.

In addition, some methods of resolution (e.g. for the macroscopic method see [5]) give less accurate solution compared to the previous ones but are much efficient in computation time. For these methods, a typical element represents several phases with different behaviors (elastoplastic, damage, etc...). Here an element consists of two various phases, leading to a jump of strain inside the element, which is represented by a discontinuity of strains field. The interface between the two phases also takes into account a debonding and therefor it is also represented by a discontinuity of displacements field [4].

In order to represent two discontinuities (displacement and strain) we use the Incompatible Modes Method (see [9, 7]). We introduce two complementary modes, one for the displacements discontinuity and another for the strain discontinuity (see [6]). In this way we enhance only elements that contain two phases. The elements are enhanced locally and the total number of unknowns remains still the same.

The second important point of this work, cement-based materials, such as concrete or mortar, can be modelled at different scales, depending on the objectives and the physical mechanisms to be accounted for. Namely, for engineering applications and computations at the structure scale (macro-scale), such materials might be considered as homogeneous, and their properties obtained by using the key concept of RVE (see [2, 8]) to obtain phenomenological models of inelastic behavior (e.g. see [10, 1, 3]) The main advantage of those models is their robustness and small computational cost, hence this approach is widely spread. On the other hand, such phenomenological models are based on a set of ”material” parameters which ought to be identified, mainly from experiments performed with prescribed load paths. This methodology leads to a set of parameters which is linked to the chosen load-path, which will not be adapted to another path, thus leading to a non-predictive macromodel.

We illustrate the possibilities provided by the use of structured mesh representation and the efficient computation capabilities of the proposed model for dealing with random heterogeneities. To that end, we consider herein a porous material (typical of many cement-based material) at a meso-scale level. At this scale we assume that such a material is characterized by a two-phase microstructure with a solid phase and a fluid phase. The former will be referred as the ”matrix” and the latter is supposed to represent the voids or inclusions. Depending on the number of inclusions their sizes and positions, the non-linear macroscopic response of such a material will vary. In other words, the macroscopic characteristics, such as Young’s modulus or the yield stress, will be influenced by the meso-scale geometry. Our goal here is to carry out numerically study of the variations of the macroscopic characteristics upon the inclusion sizes and positions. The key point for this study is that the variability introduced into the model is only strictly restricted to the specimen geometry, whereas the mechanical characteristics of the two phases are deterministic and remain constant during all the process.

In particular, the matrix phase is supposed to be accurately modelled by an elastic-perfectly plastic model based upon the Drucker-Prager criterion. The voids are represented by a simple linear isotropic elasticity model with very small value Young’s modulus.

References

[1] K. J. Bathe (1996): *Finite Element Procedures*, Prentice Hall.

[2] M. Bornert, T. Bretheau and P. Gilormini (2001): *Homogéneisation en mécanique des matériaux*, volume I, II, Hermes-Sciece, Paris.

[3] A. Ibrahimbegovic (2006): *Nonlinear Computational Solid Mechanics*, Hermes-Science Publication, Paris, 2006, in French.

[4] A. Ibrahimbegovic, D. Brancherie (2003): Combined hardening and softening constitutive model of plasticity: precursor to shear slip line failure, *Comp. Mechanics*, **31**, 88–100.

[5] A. Ibrahimbegovic, D. Markovic (2003): Strong coupling methods in multiphase and multiscale modeling of inelastic behavior of heterogeneous structures, *Comp. Meth. Appl. Mech. Eng.*, **192**, 3089–3107.

[6] A. Ibrahimbegovic, S. Melnyk (2007): Embedded discontinuity finite element method for modeling of localized failure in heterogeneous materials with structured mesh: an alternative to extennded finite element method, *Comp. Mechanics*.

[7] A. Ibrahimbegovic, E. L. Wilson (1991): A modified method of incompatible modes, *Communications in Applied Numerical Methods*, **7**, 187–194.

[8] T. Kanit, S. Forest, I. Galliet, V. Mounoury and D. Jeulin (2003): Determination of the size of the representative volume element for random composites: statistical and numerical approach, *Int. J. Solid Struct.*, **40**, 3647–3679,.

[9] E. L. Wilson, R. L. Taylor, W. P. Doherty, J. Ghaboussi (1973): Incompatible displacement models, *Numerical and Computer Methods in Structural Mechanics*, 43–57, Academic Press, New York.

[10] O. C. Zienkiewicz and R. L. Taylor (2005): *The Finite Element Method, 6th edition, Volumes 1 and 2*, Elsevier, Oxford.

Investigations of Size Effect in Tensile Fracture of Concrete Using a Lattice Model

J. Kozicki*, J. Tejchman

[1]Gdansk University of Technology, Faculty of Civil and Environmental Engineering
80-952 Gdansk-Wrzeszcz, Poland
kozicki@pg.gda.pl, tejchmk@pg.gda.pl

Summary: Lattice model was used to model fracture processes in concrete at the meso-level. Concrete was described as a three-phase material including aggregate, interfacial transition zone and cement matrix. The calculations were carried out for concrete specimens of a different size subject to uniaxial extension.

Introduction

A realistic description of the fracture process is of major importance to ensure safety of the structure and to optimize the behavior of material. The phenomenon of the propagation of the fracture process in brittle materials can be modelled with continuous and discrete models. The lattice models are the simplest discrete models to simulate the development and propagation of fracture in brittle materials consisting of a main crack with various branches, secondary cracks and microcracks. They allow a straightforward implementation of the material heterogeneity which is projected on a lattice and corresponding properties are assigned to relevant lattice elements.

The intention of the paper is to describe and to understand the mechanism of fracture in concrete specimens during uniaxial extension. In contrast to other lattice models [1, 2], a geometric type lattice model was used what is a novelty [3, 4]. Owing to that, the computational effort was significantly reduced. The calculations were performed with concrete considered as three-phase material (aggregate, cement matrix and interfacial transition zone). Attention was paid to the effect of the specimen size on its strength during uniaxial tension.

Lattice model

In our 2D-lattice model, the quasi-brittle material was discretized in the form of a triangular grid including beam elements (as in the lattice model described in [1, 2]). The distribution of beams was assumed to be completely random analogously to a Voronoi's construction scheme (Fig. 1). First, a triangular grid was created in the material with the side dimensions equal to g. In each triangle of the grid, additional interior squares were assumed with an area of s×s. Next, one point was selected at random within these interior squares. Later, all points inside of squares were connected with neighboring ones within a distance of $r_{\max}$ to create a non-uniform mesh of beams, where the maximum beam length was $r_{\max}$ (e.g. $r_{\max} = 2g$), the minimum beam length was $r_{\min}$ (e.g. $r_{\min} = 0.1g$ for $s = 0.6g$) and the minimum angle between beams was assumed to be α (e.g. $\alpha = 20^{\circ}$). A uniform triangular mesh could be obtained with parameter $s = 0$. Using this grid generation method, the beams could cross each other in two dimensional calculations but they did not intersect each other in three-dimensional analyses. The beams possessed a longitudinal stiffness described by the parameter k_l (which controlled the changes of the beam length). The beams were treated as only geometric lines and the model was of a kinematic type, i.e. the calculations of beam displacements were carried out on the basis of the consideration of successive geometry changes of beams due to translation, rotation and deformation (normal and bending). Thus, the global stiffness matrix was not built and the calculation method had a purely explicit character. The displacement of the center of each beam was calculated as the average displacement of two end nodes belonging to the beam from the previous iteration step: The displacement vector of each beam node was calculated by averaging the displacements of the end of beams belonging to this node caused by translation, rotation, normal and bending deformations. The node displacements were calculated successively during each calculation step, beginning first from beams subject to prescribed displacements. A beam was removed from the lattice if the local critical tensile strain ε_{min} was exceeded. All presented numerical calculations were strain controlled. To perform them, the self-written program was used.

Numerical results

The 2D calculations of a deterministic size effect in concrete specimens during uniaxial tension were performed with a three-phase concrete specimen composed of aggregates, cement matrix and interfacial zones. The beams were distributed non-uniformly ($\alpha = 20^{\circ}$, $s = 0.6g$, $g = 1$ mm, $r_{max} = 2g$). The minimum beam length was about 0.3 mm and the maximum one was about 2 mm. The following material parameters were used for the cement matrix, aggregate and bond: $p_m = k_b/k_l = 0.7$ (with $k_l = 0.01$) and local $\varepsilon_{min} = 0.2\%$ for cement matrix, $p_m = k_b/k_l = 0.7$ (with $k_l = 0.03$) and local $\varepsilon_{min} = 0.133\%$ for aggregate and $p_m = k_b/k_l = 0.7$ (with $k_l = 0.007$) and local $\varepsilon_{min} = 0.05\%$ for bond, respectively. The aggregate density was assumed to be 50%. The mean aggregate diameter was taken as $d_{50} = 3.5$ mm (for the aggregate size of the range 2-8 mm). First, a grading curve was chosen. Next, certain amounts of particles with defined diameters were generated according to this curve. Finally, the spheres describing aggregates were randomly placed in the specimen preserving the particle density and a certain assumed mutual minimum distance. Five simulations were performed for each case. The interfacial zones were added by assigning different properties to the beams which directly connected the aggregate with the cement matrix. Their width changed between 0.3–2 mm. The

moduli of elasticity were: E=60 GPa (aggregate), E=20 GPa (cement matrix) and E=14 GPa (bond), respectively. Thus the interface had the lowest strength.

To investigate a deterministic size effect, the calculations were carried out with two different rectangular concrete specimens using the same beam distributions: 10×10 cm^2 and 20×20 cm^2 (Figs. 2 and 3). The results show that the specimen strength and ductility increase with decreasing specimen size (as in the experiment [5]) while the crack pattern remains similar. In turn, the fracture energy decreases.

Conclusions

The lattice model is very useful in studying and understanding the phenomenon of the crack formation and crack propagation during uniaxial tension since it can reproduce fracture processes observed in real laboratory experiments. Owing to this, novel (stronger and better) engineering materials can be developed. By using an elastic–purely brittle local fracture law at the particle level of the material, global softening behavior is obtained.

The heterogeneous 2D lattice model for concrete used in the paper requires 4 material parameters $k_l, k_b, E, \varepsilon_{min}$ for each material phase and 4 grid parameters g, s, α and r_{max} related to the distribution, quantity and length of beams.

The obtained results of crack patterns and stress-strain curves for a three-phase concrete material during uniaxial tension are qualitatively in agreement with experimental ones for concrete.

The material composition has a significant effect on the material behaviour, in particular the particle density and distribution of weak bond zones. The strength and pre-peak nonlinearity decrease with increasing aggregate density and decreasing mean aggregate diameter during uniaxial tension. The material ductility increases when the aggregate density increases. The vertical strain corresponding to the peak increases with decreasing particle density. At the low particle content debonding occurs extensively near the isolated aggregates. At the high particle density, percolation of bond zones occurs, and the condition for

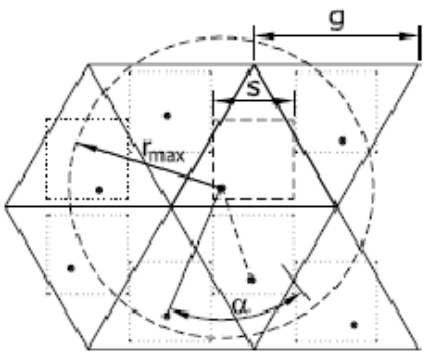

Figure 1: Scheme to assume a non-uniform distribution of beams in the lattice (s = size of interior squares, r_{max} = maximum beam radius, α = minimum angle between two beams, g = size of triangular grid).

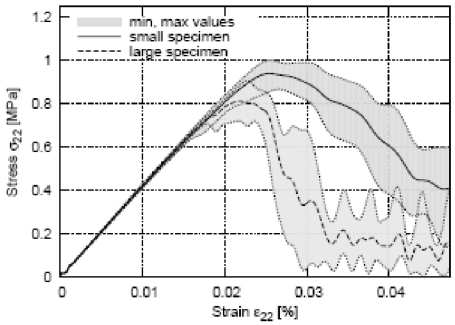

Figure 2: Deterministic size effect of 2D concrete specimens subject to uniaxial extension with sizes 10×10 cm^2 (small specimen) and 20×20 cm^2 (large specimen) (σ_{22} - vertical normal stress, ε_{22} vertical normal strain).

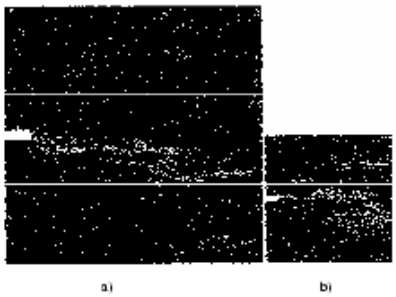

Figure 3: Fracture in concrete specimens of different sizes: 20×20 cm^2 (a) and 10×10 cm^2 (b).

macro-crack nucleation and growth occurs. The pre-peak nonlinearity cannot be ignored at low particle density. The macro-crack process occurs before the maximum load.

The simulations of a deterministic size effect show a decrease of nominal strength with increasing specimen size as well as an increase of fracture energy with size.

References

[1] E. Schlangen, E. J. Garboczi (1997): Fracture simulations of concrete using lattice models: computational aspects. *Engineering Fracture Mechanics*, **57**, 319–332.

[2] G. Lilliu, J. G. M. van Mier (2003): 3D lattice type fracture model for concrete. *Engineering Fracture Mechanics*, **70**, 927–941.

[3] J. Kozicki, J. Tejchman (2006): 2D lattice model for fracture in brittle materials. *Archives of Hydro-Engineering and Environmental Mechanics*, **53**, 137–155.

[4] J. Kozicki, J. Tejchman (2006): Modelling of fracture process in brittle materials using a lattice model. In *Computational Modelling of Concrete Structures, EURO-C 2006* (eds. G. Meschke, R. de Borst, H. Mang. N. Bicanic), Taylor and Francis, 301–307.

[5] M. R. A. van Vliet (2000): Size effect in tensile fracture of concrete and rock. *PhD thesis*, University of Delft.

Part XII

Microstructure Characterization and Reconstruction

Polyether Polyurethane Foams under Multiaxial Loading: Experiments and Model

G. Gioia*, **X. Dai, T. Sabuwala**

Department of Mechanical Science and Engineering
University of Illinois at Urbana-Champaign
1206 West Green St. Urbana IL 61801, USA

Summary: We measured the mechanical response of soft open-cell polyether polyurethane solid foams of different densities subjected to a set of multiaxial loading cases. Then, we formulated a mean-field unit-cell model of the foams and compared the predictions of the model with the experimental results.

Introduction

Solid polymeric foams are light cellular materials which are employed in numerous applications. They come in two varieties: rigid and soft. Rigid polymeric foams are stiff and brittle. In the aeronautical industry, rigid polymeric foams are the most commonly used materials in the cores of structural panels. On the other hand, soft polymeric foams may be deformed elastically to extremely high strains. In packaging, soft polymeric foams are very effective at shielding fragile products from the jolts associated with transportation and handling. These foams are also widely used in car seats, where they are ideally suited to provide comfort to the occupant and, in the event of a crash, to help keep the occupant safe.

Our interest here is in soft, open-cell polymeric foams. These foams are manufactured by promoting the growth of numerous gas bubbles within a solid layer of soft, elastic polymer such as polyether polyurethane. As the bubbles grow, the layer of polymer expands anisotropically, mostly along a direction normal to the plane of the layer—the so-called *rise direction*. The microstructure of open-cell polymeric foams consists of a three-dimensional network of slender bars of similar length and cross-section. This network may be modeled as a periodic array of cells or identical groupings of bars—the open cells of the foam. Because the bars of the cells are slender and elastic, they undergo large rotations and displacemets without breaking, and soft open-cell polymeric foams are highly nonlinear elastic materials. Even under service conditions, these foams display a complex phenomenology that may include configurational transitions and heterogenous fields.

Experiments

We conducted a series of tests of open-cell polyether polyurethane foams for several different loading cases including uniaxial compression along the rise direction; uniaxial compression along two mutually perpendicular transverse directions (both normal to the rise direction); uniaxial tension along the rise direction; compression along the rise direction superposed to shear; and compression along the rise direction superposed to hydrostatic pressure. For each loading case, we performed tests with foam specimens of five different densities ranging from 50.3 to 220.5 $\mathrm{kg/m^3}$. For each test we measured the mechanical response; in a few tests, we also took pictures of the surface of the specimen and used the Digital Image Correlation (DIC) technique to compute the strain fields on the surface of the specimen.

In this abstract we discuss just a few examples of our experimental results. For uniaxial compression along the rise direction, the mechanical response of relatively high density foams displayed a monotonically increasing stress whereas the mechanical response of relatively low density foams displayed the type of stress plateau associated with the occurrence of a phase transition. For these relatively low density foams, measurements computed using the DIC technique showed that heterogeneous, two-phase strain fields accompanied the stress plateaus, as expected [2]. On the other hand, for uniaxial compression along any of the two transverse directions tested, the mechanical response did not display stress plateaus, not even for the least dense foam. The DIC results computed for the least dense foam showed homogeneous strain fields at all stages in the test, confirming the absence of a configurational phase transition.

Model

We used the experimental results to calibrate a mean-field model. This model may be implemented in a general purpose finite element program; it is a triaxial generalization of the uniaxial mean-field model of reference [1]. In the model, a unit cell composed of several bars is cut off from an idealized, perfectly periodic open-cell foam. Then, the unit cell is deformed in accord with the applied mean field, and the attendant stress tensor is computed by energy minimization. To deform the unit cell in accord with the applied mean field, the tips of the bars of the cell (where the cell was attached to the rest of the idealized foam) are subjected to a set of displacements affine with the prevalent deformation gradient. The tips of the bars are left to rotate freely.

The unit cell is characterized using several physically meaningful material or geometric parameters whose values may be readily estimated for a given foam.

Predictions versus experimental results

To compare the predictions of the model with our experimental results, we superpose plots of the predicted and measured curves of stress versus strain (up to 15%) for all the loading cases and for all the foam densities tested. In all instances, we compute all the predicted curves using a single set of model parameters. We show that with a suitable choice of parameters

the model gives predictions that compare favorably with our experimental results for all loading cases. For some loading cases and foams of relatively low density, the model predicts stress plateaus and heterogeneous strain fields in agreement with our experimental results.

Acknowledgements

We gratefully acknowledge the National Science Foundation for financial support under grant CMS-0092849 (Ken P. Chong, Program Manager).

References

[1] G. Gioia, Y. Wang, and A. M. Cuitiño (2001): The energetics of heterogeneous deformation in open-cell solid foams. *Proceedings of the Royal Society of London*, **457**, 1079–1096.

[2] Y. Wang, G. Gioia, and A. M. Cuitiño (2000): The deformation habits of compressed open-cell solid foams *Journal of Engineering Materials and Technology*, **122**, 376–380.

The Condualistic Approach for Modelling the Geometry of Heterogeneous Materials

M. Moesen*, S. V. Lomov, I. Verpoest

Department of Metallurgy and Materials Engineering (MTM), K.U. Leuven
Kasteelpark Arenberg 44 B-3001 Heverlee, Belgium
maarten.moesen@mtm.kuleuven.be, stepan.lomov@mtm.kuleuven.be, ignaas.verpoest@mtm.kuleuven.be

Summary: This paper presents the condualistic approach for modelling heterogeneous materials in 2D and 3D. It allows an arbitrary number of phases, which can be combined into larger phases at several stages of the modelling process. We show how sketching the interior of each phase permits to define parametric phase boundaries (1) which respect the sketched interiors such that (2) their geometry can vary significantly while their topology remains fixed and (3) whose parameters span a convex space, well-suited for optimization. The approach is illustrated with examples of trabecular bone and biomimetic bone scaffolds.

Problem statement

This paper presents a new approach, the condualistic approach, to the computer-aided modelling and representation of the meso-scale geometry of heterogeneous materials. Geometric models play a key role in understanding the functional behaviour of these materials at the macro-scale as they provide, together with material properties, the input for simulations of for example mechanical behaviour or permeability.

However, generating geometric models which are suitable for simulation is not a sinecure. Firstly because of the complexity of the materials themselves we would like to make the modelling procedure as simple and as close to the structure as possible. Secondly because of the presence of multiple, possibly adjacent phases between which the phase boundaries must be unique and well-defined interfaces. Thirdly, a modeller is often not only interested in one geometric realization, but in different realizations for which some parameters are kept constant and others are varied over some different distribution. The presented approach enables parametric modelling, but moreover allows to vary the geometry significantly without changing the topology.

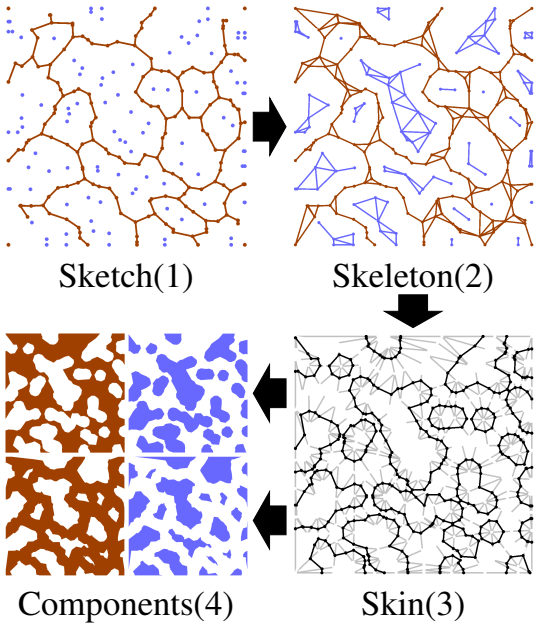

Figure 1: Overview of the condualistic modelling process

Condualistic modelling

Overview The condualistic modelling approach proceeds in four steps, as shown in figure 1. In the first step the modeller defines the phases constituting the material and provides for each phase a sketch of its interior. In the second step from these sketches a skeleton is computed, which is a simplicial complex defining the topology of and between the phases of the material. In the third step the skin is computed, which is a set of parametric surfaces representing the phase boundaries. In the fourth step, both the skeleton and the skin are combined into solid representations of the phases. The algorithms and data structures used in this approach are implemented in a 2D and 3D C++ library.

Condualism The first step in condualistic modelling is to define all the homogeneous components of the material, which are represented by regions. A region may simply be thought of as a color or a tag representing a homogeneous component of the material such as a phase. Actually, the region abstraction is introduced to avoid the physical meaning attached to the term 'phase'. In various steps of the modelling process, regions can be aggregated (taken together) into larger regions, which to some extent enables multiscale modelling.

The term '-dualistic' is chosen because all regions are treated in a symmetrical manner and are considered as complementary entities constituting the whole material. The prefix 'con-' stresses the fact that different adjacent regions either define a boundary between these regions or are aggregated into a larger region.

Sketch The sketch (figure 1.1) is a representation of the *interior* of all regions, consisting of primitives such as points and line segments, whose 'color' represents the region to which it belongs. Certain guidelines and rules apply for these primitives. Firstly, primitives of different regions must not intersect each other, because this would mean that the overlapping points belong to the interior of more than one region simultaneously. Secondly, the primitives must span the volume to model, i.e.

the model volume is the convex hull of all primitives. Thirdly, primitives belonging to the same connected component in a region may be disconnected but must be close enough to each other to ensure that they are connected later on in the skeletonizing step.

Skeleton Next, using the Delaunay triangulation, the skeleton is computed. In this process, no points or line segments disappear from the sketch, but points which are natural neighbours and have the same region are connected (compare figure 1.1 and 1.2). Similarly, natural neighbouring points having different regions indicate the presence of a phase boundary between these points. This results for each region in a set of well-defined disconnected networks, called skeleton components, which define the structure of the material.

Skin From the skeleton the skin is computed, which is a set of parametric polyhedral surfaces representing the boundary between two adjacent regions. The vertexes of these surfaces are parametric but restricted to degrees of freedom (gray lines in figure 1.3) which on the one hand allow the surface to deform in the complete space between the skeleton components, but on the other hand ensure that no skeleton component is ever intersected by the skin. Thus the geometry of the skin may vary significantly, while its topology is fixed and defined by the skeleton.

Moreover, the degrees of freedom have straightforward geometrical meaning, and the parameters which define the skin are all defined between 0 and 1, spanning a convex space, well-suited for numerical optimization.

Components Finally, using the skeleton and the skin, the modeller may define solid components of each region or some parts of each region. These solid components are parametric, because the skin is also parametric, allowing different geometrical realizations having the same structure, as shown in figure 1.4. Because the skin provides well-defined interfaces between adjacent regions, solid components of different regions fit perfectly into each other, and interpenetration problems are avoided.

On the one hand, the resulting model can be used to measure and even optimize geometrical characteristics such as the volume fraction or the surface area to volume ratio, which can be expressed as functions of the skin parameters. On the other hand, they may be exported to free-form fabrication models, used to generate BEM surface meshes or FEM volume meshes, or be simply converted to 2D or 3D digital images (pixel/voxel representation) of arbitrary resolution.

Examples In this presentation, the approach will be illustrated. The first example is a simple synthetic model of a granular material, illustrating the ability to define and aggregate multiple regions. The second example is a model representing a unit cell of trabecular bone, showing how to design sketches to yield a certain skeleton. The third example (figure 2) is a digital image-based reconstruction of a biomimetic titanium bone scaffold, to assess that the condualistic modelling approach is able to realistically represent complex microstructures with a limited number of degrees of freedom and computation time.

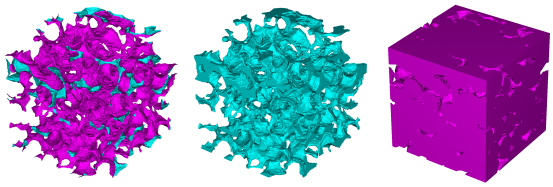

Figure 2: Skin and components of a titanium bone scaffold [1]

Related work

A vast number of (1) digital image-based and (2) CAD-based tools exists for generating geometrical models [2], as well as (3) a number of medial representations.

Digital image-based or voxel representations are commonly used to represent heterogeneous materials, they represent multiple phases simultaneously and are often acquired from real samples using 3D scanning techniques. However, they have limited resolution and their number of parameters increases at a cubic rate, making them less suited for geometrical modelling and optimization. It was our objective to propose a resolution independent representation which has a better scalable number of parameters, which have more clear geometrical meaning and preserve a predefined topology.

CAD-based modelling using Constructive Solid Geometry (CSG) or boundary representations, is also used to generate parametric, resolution independent geometric models. However, we observed that for complex structures this process quickly becomes labour intensive and error-prone, especially when multiple adjacent phases have to be modelled. Therefore we propose to model the phase interiors, which is less complex and yields more insight in the material structure, leaving the intricate job of defining the phase boundaries to the computer. Nevertheless we acknowledge that drawing good sketches and finding suitable parameters may not be straightforward.

Perhaps most closely related to our work are medial representations and skin surfaces [3] which allow to model solid bodies using a representation of their interiors. While the theory developed for these techniques is useful for our purposes, they themselves focus on representing a single phase, and representing multiple adjacent phases becomes tedious.

References

[1] T. Van Cleynenbreugel, H. Van Oosterwyck, J. Vander Sloten, J. Schrooten (2002): Trabecular bone scaffolding using a biomimetic approach. *Journal of Materials Science: Materials in Medicine*, **13**, 1245-1249

[2] F.-E. Wolter, N.Peinecke and M. Reuter (2004): Geometric Modeling of Complex Shapes and Engineering Artifacts. In *Encyclopedia of Computational Mechanics, Volume 1: Fundamentals*, 475-495,

[3] N. G.H. Kruithof (2006): Envelope Surfaces: Surface Design and Meshing. *PhD Thesis*, Rijksuniversiteit Groningen

Sampling Sphere Distribution: A Novel Method to Quantify Structural Anisotropy of Trabecular Bone in Unsegmented Images

P. Varga*, P. K. Zysset

Institute of Lightweight Design and Structural Biomechanics, Vienna University of Technology
Gusshausstrasse 27-29, A-1040 Vienna, Austria
vpeter@ilsb.tuwien.ac.at, philippe.zysset@ilsb.tuwien.ac.at

Summary: A novel sampling sphere distribution (SSD) method based on mobile sampling spheres is developed for describing microstrustural anisotropy of trabecular bone using grayscale images. Efficient implementation of SSD on segmented and unsegmented 3D μCT images of anatomically diverse human trabecular bone samples is demonstrated. The second order fabric tensor of SSD corresponds well with the one derived from the mean intercept length (MIL) method applied on segmented images. The results of SSD are extended to higher order approximations and their robustness with respect to sampling sphere radius and image resolution is examined.

Introduction

Architectural anisotropy (or fabric) and the mechanical properties of cancellous bone are closely related (review: [1]). The increasing resolution of non-invasive imaging techniques such as CT or MRI allows to assess trabecular architecture *in vivo* which may be exploited to predict mechanical properties for clinical diagnostics, treatment or follow up. In fact, architectural anisotropy can be adequately described by a positive definite second order tensor called fabric tensor.
There are well-known and widely used methods to compute this fabric tensor. Mean intercept length (MIL) is an interface-based, while volume orientation (VO), star length distribution (SLD) and star volume distribution (SVD) are volume-based methods to identify main trabecular orientations (review: [2]). They were all shown to be good predictors of mechanical anisotropy, but all of them require segmented images. The thresholding procedure to generate these binary images is an important and delicate step, especially for low resolution images where the voxel size is larger than the dimension of the structural elements (partial volume effect). To circumvent this problem, grayscale images could be used directly to quantify architectural anisotropy. Recent publications showed different approaches along this idea.
For instance, Fast Fourier Transform was applied on radiographic images to quantify trabecular orientation in 2D [3]. Wald et al. presented a 3D autocorrelation function to measure its orientational dependence assuming bone as a quasi-periodic structure [4]. The relationship of the latter method with MIL or other measures of anisotropy remains unknown. Saha et al. introduced the tensor scale method (TSD) for computing the local orientation of small structures such as trabeculae [5]. The orientation is based on the axes of an ellipse fitted to the local density distribution and homogenization scheme of this local measure is proposed to provide global orientation anisotropy.
The goal of this study is to develop, validate and test an efficient and robust method to quantify architectural anisotropy based on grayscale images in a region of interest (ROI) of trabecular bone.

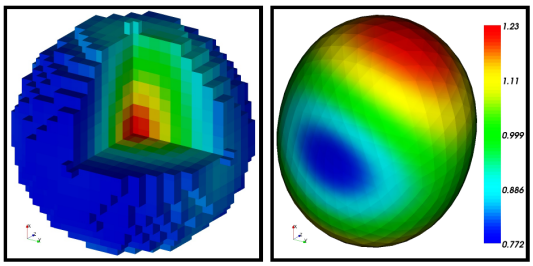

Figure 1: Left: the filled container sphere with $1/8$ of its volume removed to show the internal density distribution in colors; right: the corresponding second order tensor.

Method

The sampling sphere distribution (SSD) method is designed for unsegmented 3D images with positive density values. We assume the ROI to be a closed convex set within such an image. The basic idea of the method is to sample the ROI density (grayscale) with spheres over a periodic grid. The sampling spheres are free to move from the initial grid positions and get attracted by the center of gravity of the local density distribution. This way, the spheres move towards the center or junction of the heterogeneities to capture their orientation. After convergence of their motion, their content is collected and summed up into a container of identical shape. The size of the sampling spheres must be determined according to the characteristic size of the underlying structure (e.g. trabecular spacing). Finally, the densities of the container are made symmetric with respect to its center which becomes the center of gravity of the distribution.
The spatial distribution of density in the spherical container is then approximated with generalized Fourier series leading to a normalized orientation distribution function (ODF) on the container surface:

$$SSD(\mathbf{n}) = g + \mathbf{G} : \mathbf{F} + \mathbb{G} : \mathbb{F} + ... \qquad (1)$$

Only even-ranked tensors of the ODF appear due to the central symmetry. The second order approximation exhibits at least orthotrophic symmetry and leads to the definition of a fabric tensor characterized by three eigenvalues m_i and three orthogonal eigenvectors $\mathbf{m}_i$ (Fig. 1). Higher order approximations allow

to describe more complex ODFs with lower symmetries. As black and white images can be considered as a special case of a grayscale image and the method can also be applied on binary data. This property ensures a basis of control and comparison with the methods based on segmented images.

Results

The method was tested on μCT images with 26 μm isotropic resolution(μCT40, Scanco) of 18 human trabecular bone biopsies. The samples were selected from 6 anatomical locations: femoral trochanter, femoral neck, T10 vertebra, L2 vertebra, radius and calcaneus, with a broad range of volume fraction and degree of anisotropy (MIL) computed with the associated software. The fabric tensor of the second order results of the SSD was compared to the fabric tensor of MIL. The analysis of the eigenvectors showed that in case of samples with higher degree of anisotropy (DA) the mean deviation from the main eigendirection of MIL is 3.30 ± 3.52 degrees (15 samples). As expected in the case of smaller DA, this angular deviations increase and become indeterminate when two or three eigenvalues degenerate. As shown in Fig. 2, a strong linear relationship was found between the respective eigenvalues with $R^2 = 0.964$.

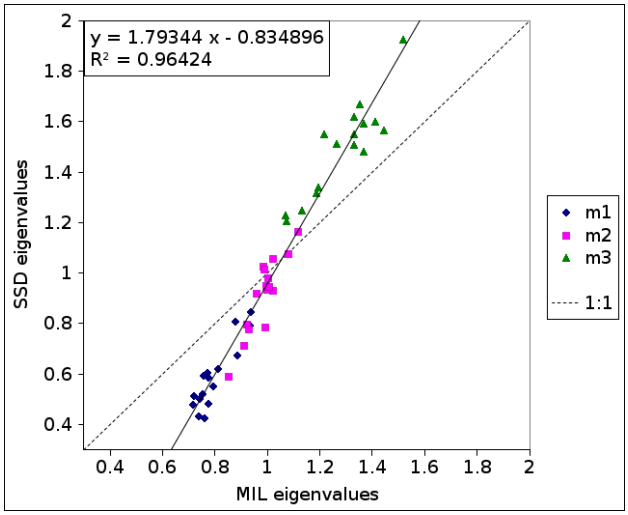

Figure 2: Eigenvalues of MIL and SSD for 18 samples.

When using segmented images, the eigenvalues and eigenvectors remained close to those obtained with grayscale images. In particular, a strong linear relationship was obtained between their eigenvalues ($R^2 = 0.971$), angular deviation of the eigendirections was 2.56 ± 2.21 degrees for the main direction (15 samples).
Additional tests were performed to examine robustness of the method with respect to image resolution. When coarsening the images to 52μm and 104μm resolution, the eigenvalues kept a strong linear relationship with the original ones, the coefficient of determination being $R^2 = 0.996$ and $R^2 = 0.974$ respectively.
Despite the mentioned guideline to select the appropriate sampling sphere size, its influence on the fabric tensor was examined and found to be quite negligible. In order to verify the potential of SSD to describe more complex orientation patterns, the image of an artificial orthogonal grid structure that exhibits cubic symmetry was created and analyzed with a 4^{th} order approximation. As expected, a more detailed ODF with cubic symmetry was obtained that emphasized the three main orientations of this grid.

Discussion

A novel three-dimensional SSD method is proposed to describe the architectural anisotropy of a trabecular bone ROI. The application on μCT graylevel images of a broad range of human trabecular morphologies is demonstrated. Fortunately, the SSD method was found to be robust with respect to its unique parameter, the sampling sphere diameter. This favourable property suggests that the method is not exceedingly sensitive to trabecular spacing. The second order results of SSD showed an excellent correlation with the results of the MIL method considered as a gold standard for segmented images. Current fabric-elasticity models based on MIL eigenvalues can therefore also be used with SSD data. As suggested by the 4^{th} order approximation of an artificial structure, SSD contains more information than MIL and is in this sense closer to SLD. Interestingly, the results of SSD on segmented and unsegmented images are very similar, which is a further demonstration of the robustness of this novel method. The implemented version of SSD is computationally efficient: for example, the analysis of a $270 \times 270 \times 600$ voxel region takes less than 1 minute on a standard PC for a standard sampling sphere size.
While FFT is restricted to 2D images so far, ACF is applicable exclusively on rectangular ROIs. TSD provides an elliptical approximation of volume orientation and has not been compared with MIL. It is therefore difficult to compare the performance of SSD with these other methods.
To conclude, SSD is an efficient and robust tool for characterization of fabric in grayscale images of human trabecular bone. The extension of the SSD method to *in vivo* clinical CT systems will be undertaken in a close future.

References

[1] P. K. Zysset (2003): A review of morphology–elasticity relationships in human trabecular bone: Theories and experiments, *Journal of Biomechanics*, **36**, 1469–1485.

[2] A. Odgaard (1997): Three-Dimensional Methods for Quantification of Cancellous Bone Architecture, *Bone*, **20**, 315–328.

[3] B. Brunet-Imbault, G. Lemineur, C. Chappard, R. Harba, C. L. Benhamou (2005): A new anisotropy index on trabecular bone radiographic images using the fast Fourier transform, *BMC Medical Imaging*, **5**.

[4] M. J. Wald, B. Vasilic, P. K. Saha, F. W. Wehrli (2005): Study of trabecular bone microstructure using spatial autocorrelation analysis, *Medical Imaging 2005*, Proc. of the SPIE, **5746**, 291–302.

[5] P. K. Saha, F. W. Wehrli, (2004): A robust method for measuring trabecular bone orientation anisotropy at in vivo resolution using tensor scale, *Pattern Recognition*, **37**, 1935–1944.

Reconstruction of Multi-Phase Microstructure from Computer Tomography

D. Rypl*, Z. Bittnar

Czech Technical University in Prague, Faculty of Civil Engineering, Department of Mechanics
Thákurova 7, 166 29 Prague, Czech Republic
drypl@fsv.cvut.cz, bittnar@fsv.cvut.cz

Summary: The present paper deals with the modelling of microstructure initially represented by a digital image obtained from Computer Tomography or any other similar scanning device. In the digital representation, the boundary voxels are identified and then replaced by a semi-regular triangulation of the same resolution of the image. This triangulation is then subjected to recursive subdivision to recover a smooth surface of the microstructure which is then retriangulated according to a user specified resolution. The performance of the proposed approach is shown on an example.

Introduction

Modern technologies as computer tomography (CT) or magnetic resonance tomography (MRT) offer a powerful nondestructive technique for digital representation of opaque solid objects. This voxel based representation can be discretized using for example the marching cubes algorithm [1]. The resolution of the resulting triangulation, however, is strongly dependent on the resolution of the digital representation which might be either too coarse (without important features being captured) or too fine (with unimportant features captured by excessive number of elements). To make the fine discretization appropriate for numerical analysis, it has to be further processed. One choice [2] is to adapt the triangulation by successive modifications using a set of geometrical and topological operators according to the desired resolution. Alternatively, the digital representation may be first used to derive a smooth representation which is then subjected to triangulation of a variable resolution. In [3], the smooth representation is recovered using the spherical harmonic analysis. However, this method is limited to star-shaped objects without internal voids and cannot be therefore applied to a general microstructure. In the present work, the smooth representation is reconstructed using a recursive subdivision interpolating technique [4].

Digital representation of microstructure

The three-dimensional digital representation that comes out from CT or similar scanning devices can be interpreted as sequence of two-dimensional gray scale digital images corresponding to (but not necessarily physically taken at) parallel cuts through a three-dimensional object. Each digital image consists of the grid of pixels of gray scale value related to a specific property (e.g. density). Assuming that the pixel in each image is of the shape of a square and that the individual cuts are at the distance corresponding to the edge length of that square, then the digital representation is described by a set of gray scale cubes - voxels. Clearly, the amount of data to be handled by the voxel based representation grows cubically with the increasing resolution, which makes this representation prohibitively memory demanding. It is therefore apparent, that an alternative representation of the microstructure with variable resolution and handling much smaller amount of data is desirable.

Microstructure reconstruction

In this work, the multi-phase microstructure is represented by a variable size surface triangulation that is reconstructed from the initial digital representation. Firstly, the gray scale digital representation is thresholded into voxels of appropriate discrete values of gray corresponding to individual phases of the processed microstructure. In the next phase, the boundary voxels (and their boundary sides) of individual phases are identified. Note that this boundary voxel representation is slightly modified in order to eliminate small features that might disturb the smooth representation of microstructure surface that is to be recovered. A triangulated boundary representation is then obtained from the boundary voxel representation by replacing the boundary sides of boundary voxels by semi-regular triangulation with nodes at the centres of those boundary sides. Note that care must be taken to handle some special topological cases. In this triangulated boundary representation, the individual surfaces (and their boundary curves) bounding individual phases of the microstructure are identified and then subjected to recursive interpolating subdivision [4, 5] yielding a C^1 continuous surface. In the final phase, the individual smooth boundary surfaces are triangulated using the Advancing Front Technique [6]. Since there is available no global mapping of the recovered surfaces, the discretization is performed directly in 3D space on the surface. Note that the resolution of the final triangulation is independent of the resolution of the initial digital representations and is driven mainly by the user specification and properties (curvature) of the recovered smooth representation.

Example

The proposed algorithm is demonstrated on the example of a two-phase microstructure. In Fig. 1, the original voxel based representation of a single phase is displayed. The surface mesh reconstructed over the microstructure of that phase is then shown in Fig. 2.

Conclusions

This paper has presented an approach for the reconstruction of a multi-phase microstructure from the digital representation ob-

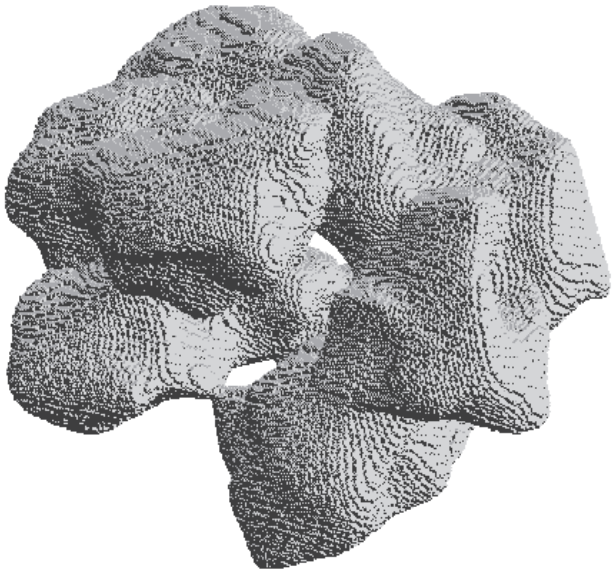

Figure 1: Voxel representation of a microstructure.

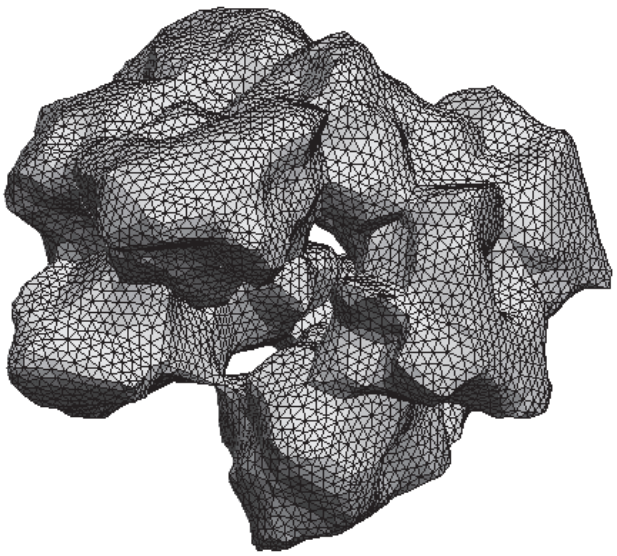

Figure 2: Surface mesh reconstructed over the microstructure.

tained from CT. It is beneficial in the sense that it is capable to handle complex topologies and its final resolution is independent of the resolution of the digital representation. Although only the surface representation has been treated in this work, the reconstructed surface triangulation can be easily employed for the solid triangulation of the microstructure, again with variable resolution. However, while the shape of the microstructure is captured quite precisely, the volume fractions of individual phases exhibits some discrepancies when compared to the initial digital representation. This also implies that statistical distribution of individual phases is not reconstructed optimally. From this point of view, the future research is to be focused on further enhancement of the quality of the reconstruction, especially in the quantitative sense.

Acknowledgment

This work was supported by the Ministry of Education of the Czech Republic project No. MSM 6840770003. Its financial assistance is gratefully acknowledged.

References

[1] W. E. Lorensen, H. E. Cline (1987): Marching cubes: A high resolution 3D surface construction algorithm. *Computer Graphics*, **21**, 163-169.

[2] P. Frey (2000): About surface remeshing. In *Proceedings of 9th International Meshing Roundtable*.

[3] E. J. Garboczi (2002): Three-dimensional mathematical analysis of particle shape using X-ray tomography and spherical harmonics: Application to aggregate used in concrete. *Cement and Concrete Research*, **32**, 1621-1638.

[4] D. Zorin, P. Schröder, W. Sweldens (1996): Interpolating subdivision for meshes with arbitrary topology. In *Computer Graphics Proceedings (SIGGRAPH '96)*, 189–192.

[5] N. Dyn, J. A. Gregory, A. Levin (1987): A four-point interpolatory subdivision scheme for curve design. *Computer Aided Geometric Design*, **4**, 257–268.

[6] D. Rypl, Z. Bittnar (2004): Triangulation of 3D surfaces reconstructed by interpolating subdivision. *Computers and Structures*, **82**, 2093–2103.

Elastic Properties of Finely Twinned Martensitic Structures Determined by Resonant Ultrasound Spectroscopy

L. Bicanová[1,2*], H. Seiner[1,2], P. Sedlák[1,2], M. Landa[1], L. Heller[1]

[1]Institute of Thermomechanics, Academy of Sciences of the Czech Republic
Dolejškova 5, Prague 8, CZ 182 00, Czech Republic

[2]Faculty of Nuclear Sciences and Physical Engineering, Czech Technical University in Prague
Trojanova 13, Prague 2, CZ 120 00, Czech Republic
Bicanova@it.cas.cz, hSeiner@it.cas.cz, pSedlak@it.cas.cz, ML@it.cas.cz, Heller@it.cas.cz

Summary: This paper presents a novel method for determination of all independent elastic coefficients of single variants of martensite from RUS measurements of finely twinned crystals.

Introduction

Elastic coefficients of the martensitic phase of the shape memory alloys, as well as the thermal dependencies of these coefficients near the transition temperatures, are crucial parameters for the interpretation and understanding of the mechanism of the shape memory effect. All independent elastic coefficients of the martensitic phase can be determined by the resonant ultrasound spectroscopy (RUS) from a simply shaped specimen of single variant of martensite.

Resonant ultrasound spectroscopy [1] is a well-known technique for study of elastic properties of solids based on the inversion of natural frequencies of free elastic vibration of a small specimen. However, automatic and reliable resonance detection and its classification, stability of the inversion procedure, initial guess independence, and its accuracy estimation, is still a hard nut of this technique, especially in the case of high anisotropic and low symmetric solids with general crystallographic orientation. We have recently introduced several improvements of the RUS technique [2] :

1) The standard Ritz method was adopted for the calculation of resonance frequencies of a parallelepiped (generalized prism) specimen with arbitrary orientation of crystallographic axes.

2) Reliable mode identification and, thus, well stability of resonance inversion was achieved by the displacement field measurement on the vibrated specimen using scanning Laser-Doppler interferometry (Figs. 1, 2).

3) Efficiency of the inverse computation was improved by deriving the analytical expression of the gradient and the Hessian of the objective function.

4) The accuracy and reliability of the presented method are investigated using a Monte Carlo simulation.

However, for some shape memory alloys, the single variants are difficult to obtain, whereas the martensites of these alloys naturally form fine twinned structures, consisting of parallel laminae of different variants.

Therefore, it is suggested to extend this approach also for determination of all independent elastic coefficients of single variants of martensite from RUS measurements of finely twinned crystals. The proposed algorithm is based on homogenization of the elastic properties, using a geometrical ray model of elastic wave propagation in a laminated structure (shown schematically in Fig. 3). The direct evaluation of the homogenized elastic properties from coefficients of the single variants is illustrated on synthetic input data (CuAlNi), as well as on real experimental results.

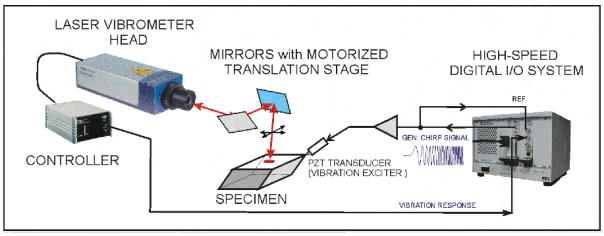

Figure 1: Experimental set-up.

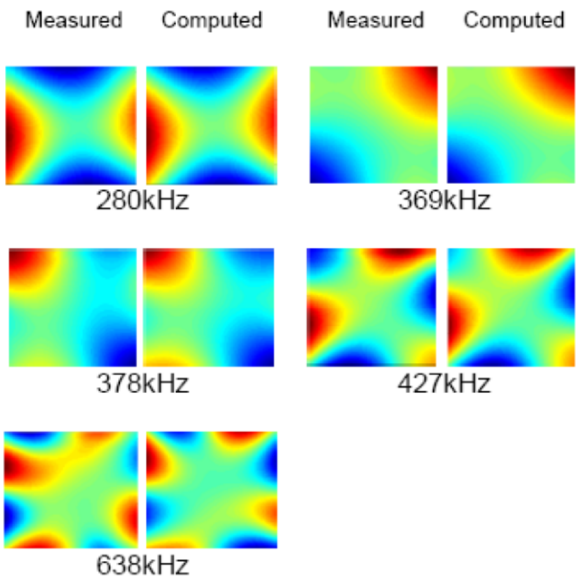

Figure 2: Example of comparison of measured and computed shapes of eigenmodes of a CuAlNi martensitic single crystal specimen.

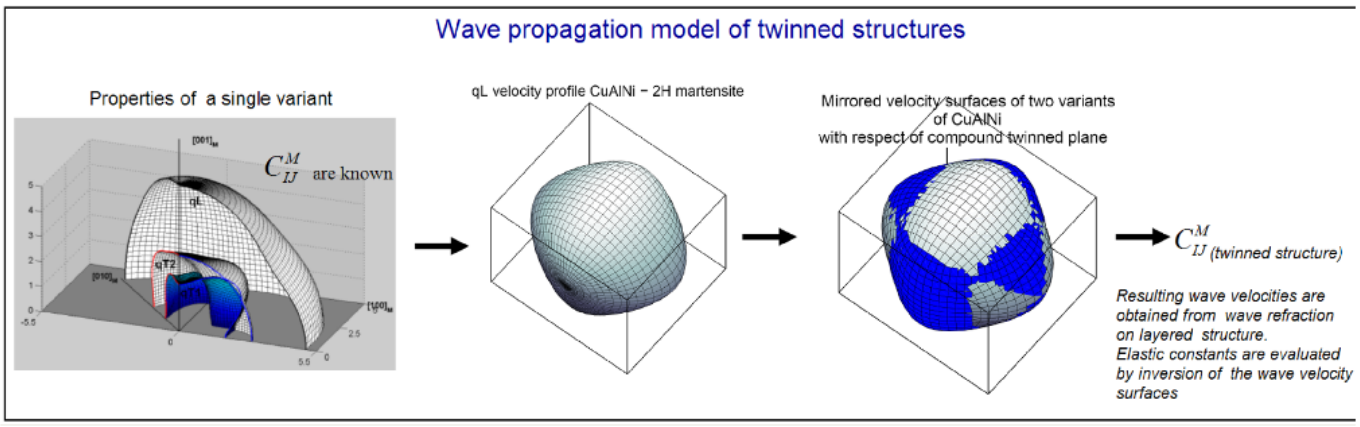

Figure 3: The principle of homogenization of the elastic properties, using a geometrical ray model of elastic wave propagation.

Experimental results

The result are shown in Table 1, where the coefficients of the single variant (<1% of other variants) are compared to measured and evaluated elastic coefficients for finely twinned martensite, containing approximately 10% of a mirrored variant. The coefficients of a single variant are in good agreement with the results from pulse-echo measurements published by authors in [3]. The theoretical effective coefficients of the twinned structure were computed by an algorithm based on the Snell-Descartes law. Especially in the diagonal coefficients C_{11}, C_{22} and C_{33}, the agreement between measured and evaluated elastic coefficients is satisfactory. However, the symmetry of the twinned structure deviates from orthotropy, which may be the reason for the discrepancy in determined shear coefficients.

Table 1: Effective elastic coefficiens measured and evaluated of finely twinned martensite of CuAlNi.

Elastic coefficient	Relative contents of the mirrored variant [%]		
GPa	$< 1\%$	$\approx 10\%$	10% evaluated
C_{11}	185.3	191.2	189.7
C_{22}	151.3	150.5	150.7
C_{33}	241.9	236.4	236.0
C_{44}	63.2	64.2	63.5
C_{55}	23.9	24.1	25.5
C_{66}	62.0	62.0	61.1
C_{23}	88.0	98.2	92.2
C_{13}	67.0	64.9	65.3
C_{12}	141.8	138.8	140.7

Concluding remarks

The inversion procedure for determination of elastic coefficients of anisotropic solids was generalized for an arbitrary oriented nonrectangular parallelepiped. The procedure was also stabilized by using a novel hybrid architecture of the optimizing algorithm, which utilizes analytical expressions of the Hessian of the minimized error function. Laser interferometry was used for association of measured frequencies to particular eigenmodes. The agreement between measured and computed shapes of the eigenmodes confirms the reliability of obtained elastic coefficients.

Applicability of the proposed method for a general parallelepiped enabled this method to be also used for determination of effective elastic properties of finely twinned martensitic structures. As a testing material, the CuAlNi alloy was chosen again. However, the main possible income of such measurements lies in experimental investigation of naturally twinned materials, such as NiMnGa, where the single crystals of pure martensitic variants cannot be easily prepared.

Acknowledgement

Supports from the Marie-Curie Research Training Network MULTIMAT (MRTN-CT-2004-505226), the project No. 101/06/0768 of the Czech Science Foundation and the institutional project of IT ASCR, v.v.i. CEZ:AV0Z20760514 are greatly acknowledged.

References

[1] A. Migliori, J. L. Sarrao, W. M. Visscher, T. M. Bell, M. Lei, Z. Fisk, and R. G. Leisure (1993): "Resonant ultrasound spectroscopic techniques for measurement of the elastic moduli of solids," *Physica B* 183, 1–24.

[2] H. Seiner, P. Sedlák, M. Landa (2006): Improvement of the Inversion Procedure in Resonant Ultrasound Spectroscopy for Generally Oriented High Anisotropic Crystals. *Proceedings of 2006 IEEE International Ultrasonics Symposium*, October 3-6, 2006, Vancouver (Canada), CD-ROM.

[3] P. Sedlák, H. Seiner, M. Landa, V. Novák, P. Šittner and Ll. Mañosa (2005): "Elastic constants of bcc austenite and 2H orthorhombic martensite in CuAlNi shape memory alloy," *Acta Materialia* 53, 3643–3661.

Part XIII

Microscale Modelling of Cementitious Materials

Relationships of Cement Paste Mineralogy to Porosity and Mechanical Properties

T. Matschei[1*], D. Herfort[2], B. Lothenbach[3], F. P. Glasser[1]

[1]University of Aberdeen, Old Aberdeen, AB24 3UE Scotland, UK
t.matschei@abdn.ac.uk, f.p.glasser@abdn.ac.uk
[2]Aalborg Portland Group, Denmark
DHE@aalborgportlandgroup.com
[3]EMPA, Swiss Federal Laboratories for Materials Testing and Research, CH-8600 Dbendorf, Switzerland
barbara.lothenbach@empa.ch

Summary: Applied thermodynamics has been developed as a tool to calculate the mineralogy of hydrated Portland cement and to determine the impact of limestone (calcite) additions. The results are used to relate chemical and mineralogical properties to engineering parameters, such as porosity and strength.

Introduction

In the early 20th century, the science base for inorganic cements became decoupled from mainstream materials sciences. This has led to relative isolation from other relevant areas of research. Thus little quantitative progress has been made on the relationships between, on the one hand, physical chemistry, including mineralogical and microstructural aspects, and on the other, engineering properties of Portland cement. This is unfortunate as much of the man-made infrastructure depends on Portland cement products and, increasingly, on economic use and long performance life of construction. Predictions of the properties of the hardened product rely heavily on empirical correlations and accumulated experience. Examples include the relationships between water content and strength of hardened concrete first demonstrated by Feret about 1900 [1]. But these models are of limited applicability and often lack theoretical justification. To progress, it is necessary to return to fundamentals. We begin by developing models of cement mineralogy based on the thermodynamics of hydration. It has been necessary to develop a new thermodynamic database [2, 3]. Although some features of cement hydration are metastable, these can be included in models. The calculated mineralogical development can be used to calculate the space filling achieved by solids. The hydrates occupy less volume than the reactants and the resulting pore space weakens the matrix.

Experimental

Calculations have been made using GEMS [4], a software to minimise the free energy of a given system. GEMS computes mass balances, giving the composition of the aqueous phase as well as tabulating coexisting solids. From the amount and molar volumes of the phases, the specific volume of solids and aqueous phase can be calculated.; "total porosity" is defined by the amount of excess mixing water which is not chemically bound in the cement hydrates and the estimated chemical shrinkage of the cement paste. Air voids are not considered. The calculations of Fig 1 use a model cement composition consisting of initially 69 wt.-% CaO, 22 wt.-% SiO_2, 4.5 wt.-% Al_2O_3 and 4.5 wt.-% $CaSO_4$ ($\sim$2.6 wt.-% SO_3). 100 g of cement are blended with increasing quantities of limestone ($CaCO_3$). Thus the initial amounts of several of the cement's main chemical components (SiO_2, Al_2O_3 and $CaSO_4$) diminish due to dilution. The water:binder ratio was kept constant at 0.5 by mass (including $CaCO_3$). A hydration degree of 100% and a constant temperature of 25 ˚C were assumed.

Results and discussion

Fig. 1 shows the mineralogical evolution, with calcite addition, and the specific volume of the solids. It is obvious that mineralogical changes influence the solids volume significantly. It is important to note that the mineralogical changes occurring upon adding calcite to cement do not just involve carbonate-containing phases, e.g. calcite and carboaluminates, but markedly affect the amounts of other phases, notably ettringite and portlandite: sulfate, displaced from monosulfoaluminate in the course of its conversion to carboaluminates, is incorporated into ettringite (AFt), a low-density, water rich phase with high molar volume. As shown in Fig. 1 the resulting ettringite increases the molar volume of the cement solids and binds liquid water. A more detailed explanation of mineralogical changes due to the addition of limestone to cement is given in [5–7]. Herfort [8] has demonstrated in similar unpublished studies the evolution of compressive strength and porosity of a cement blended with low contents of reactive limestone. The cement composition is similar to that of the model cement used in calculation of Fig. 1. It is apparent that the *calculated* porosity changes of the model cement correlate very well with the *measured* compressive strength of mortar samples (Fig. 2). The minimum calculated porosity and maximum compressive strength occur at about 2 wt% calcite.

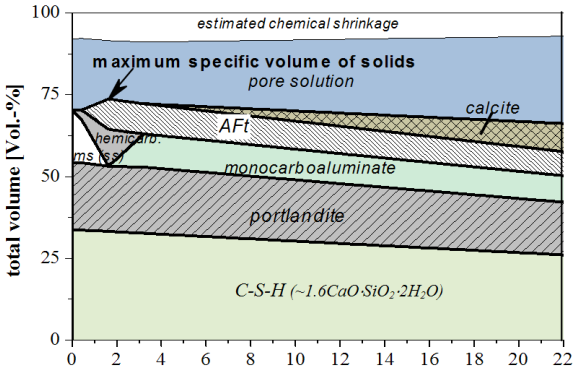

Figure 1: Volume changes of hydrate phases and pore solution of a hydrated model cement with fixed sulfate ratio (SO_3/Al_2O_3 $\sim$0.7) in dependence of changing carbonate contents.

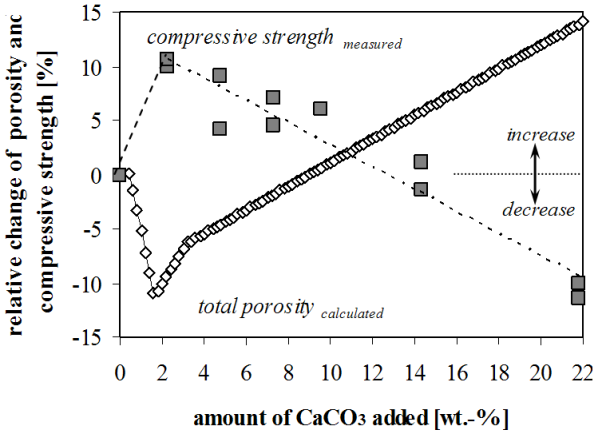

Figure 2: Comparison of relative changes of calculated porosity of model cement paste ($SO_3/Al_2O_3 \sim 0.7$) and relative changes of measured 1 year compressive strength of mortars ($SO_3/Al_2O_3 \sim 0.7$, w/c=0.5; strength data were taken from Herfort [8]).

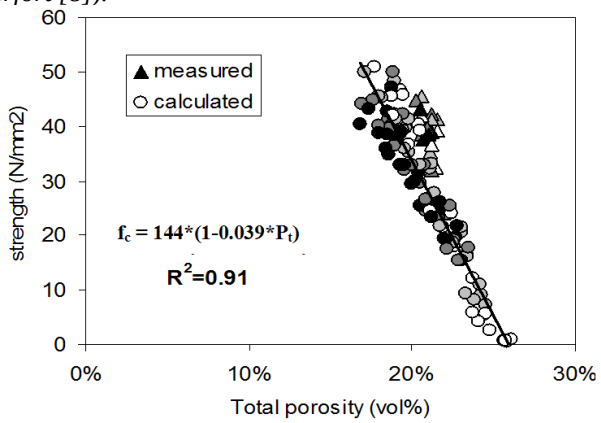

Figure 3: Calculated total porosity of mortar samples compared to measured compressive strength f_c (figure taken from Lothenbach et al. [3]).

Up to about 3 wt.% calcite is calculated to react with the model cement, with any excess behaving as an inert filler. But up to ∼ 10 wt.-% calcite added to the model cement will improve the space filling properties, decreasing total porosity and increasing compressive strength relative to the cement-only benchmark. Thus controlled limestone blending shows promise to improve the physical space filling of pastes, reducing free porosity while also decreasing the clinker content. Limestone has traditionally been regarded as an inert filler and the strength-enhancement effect -if any- attributed to improved packing arising from optimised granulometric properties of the mix. However this paper has shown that some, perhaps much, of the limestone is reactive and that mineralogical changes have a great impact on the space filling and related physical and mechanical properties of the hydrated matrix. Thus both, physical and mineralogical aspects have to be considered to achieve optimum performance of the cement. However similar space filling in plain Portland cements are also related to time and temperature of hydration. As shown by Lothenbach et al. [3], there is a strong dependency between calculated porosity and compressive strength. Porosity is difficult to measure in cement systems, different methods giving different results. Calculation enables an unambiguous basis for determining intrinsic porosity and, as Fig. 3 shows, agrees reasonably well with measured values. Thus it is possible to calculate porosities of cement pastes together with the hydrate mineralogy and link these calculations with mechanical properties, e.g. strength.

Conclusion

Empirical models used in civil engineering to predict cement and concrete properties are generally restricted to narrow fields of application of known performance, and cannot adequately explain the effect of changes in chemical or mineralogical composition such as the additional of limestone. This paper develops new paradigms linking chemical and mineralogical constitution with physical and mechanical properties. Microstructure is not yet included. The studies reported here represent just the first steps in establishing quantitative links between cement chemistry and mineralogy with physical and mechanical properties. The chosen example has shown that calcite at low concentrations is consumed by reaction with cement and the reaction products enhance space filling and strength. Theory and experiment are in good accord: the predicted benefit is significant to industry and enables the more economic use of energy-rich cement clinker. Moreover we anticipate that other space-filling strategies can be developed. Thus the more scientific approach described here represents a step forward and can be used as a basis to drive research.

Acknowledgement: The support of NANOCEM, a European industrial/academic partnership for fundamental research on cementitious materials, is acknowledged.

References

[1] F. M. Lea (1970): The Chemistry of Cement and Concrete. 3rd Edition, Edward Arnold Publishers Ltd.

[2] T. Matschei, B. Lothenbach, F. P. Glasser (2007): Thermodynamic properties of cement hydrates in the system $CaO-Al_2O_3-SiO_2-CaSO_4-CaCO_3-H_2O$. Submitted to *Cement and Concrete Research*

[3] B. Lothenbach, T. Matschei, Mschner, G, F. P. Glasser (2007): Thermodynamic modelling of the effect of temperature on the hydration and porosity of Portland cement. Submitted to *Cement and Concrete Research*.

[4] D. Kulik, U. Berner, E. Curti (2003): Modelling chemical equilibrium partitioning with the GEMS-PSI code. *PSI Scientific Report 2003*, Vol. IV, 109–122.

[5] T. Matschei, B. Lothenbach, F. P. Glasser (2007): The AFm-phase in Portland cement. *Cement and Concrete Research*, **37**, 118–131.

[6] T. Matschei, B. Lothenbach, F. P. Glasser (2007): The role of calcium carbonate in cement hydration. *Cement and Concrete Research*, in press.

[7] T. Matschei, F. P. Glasser (2006): Zum Einfluss von Kalkstein auf die Zementhydratation. *Zement, Kalk, Gips*, **59**, 78–86.

[8] D. Herfort (2004): Relationship between Strength, Porosity and Cement Composition. Unpublished paper, Nanocem workshop on the “Relation between Microstructure and Mechanical Properties”, Czech Technical University, Prague.

Thermodynamic Modelling of the Effect of Temperature on the Hydration and Porosity of Portland Cement

B. Lothenbach

Empa, Laboratory for Concrete & Construction Chemistry
Überlandstrasse 129, CH-8600 Dübendorf, Switzerland
barbara.lothenbach@empa.ch

Summary: Temperature influences the composition of the solid and liquid phase. The conversion of ettringite and monocarbonate to monosulphate was observed experimentally in Portland cements at approximately 50 ˚C, which agrees well with the results of thermodynamic modeling. These changes of the composition of the hydrate assemblage decrease the volume of solids present, increase the porosity and thus influence negatively compressive strength.

Influence of temperature

Higher temperatures lead initially to a fast hydration of Portland cements and to a high early compressive strength. However, the 28 and 91 day strength of mortar and concrete samples is found to be reduced at higher temperature (see Figure 1), although the observed degree of hydration is similar to that achieved in the temperature range 5-50 ˚C.

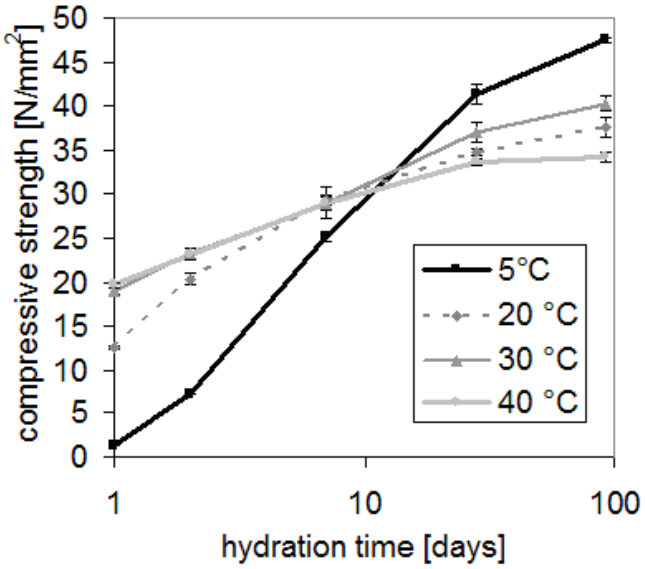

Figure 1: Compressive strength (in N/mm2; standard deviation indicated by bars) as a function of time.

At higher temperatures, the precipitating hydrates are distributed inhomogenously resulting in a coarser porosity, denser C-S-H, and the morphology of ettringite is more equant. In addition, at 50 ˚C or above, monosulfate is increasingly formed at the expenses of ettringite and monocarbonate [1]. Temperature also influences the composition of the pore solution. The concentrations of many of the ions present remain little changed but sulphate concentrations increase and aluminium concentrations decrease at higher temperatures.

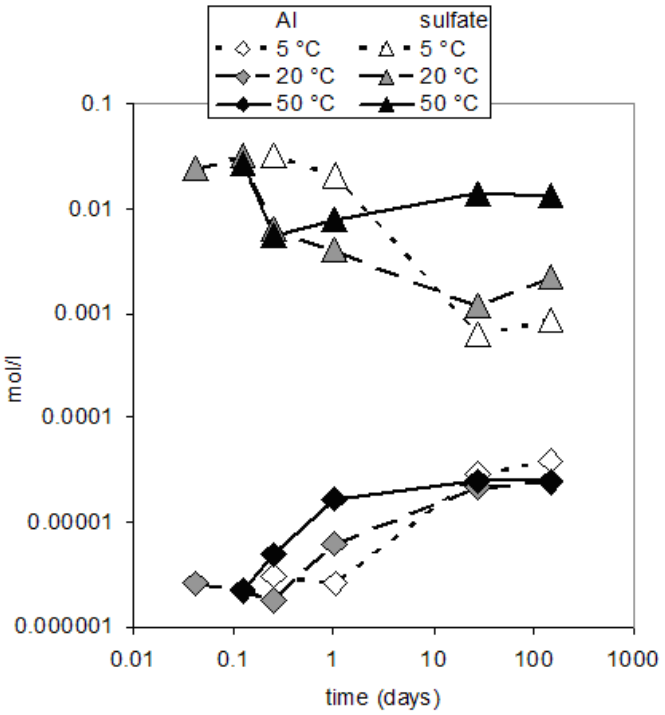

Figure 2: Measured concentrations in the pore solutions of a cement hydrated at 5, 20, 50 ˚C. The lines are intended as eye guides only.

Thermodynamic modelling

The composition of the phase assemblage and the pore solution of Portland cements hydrated between 0 and 60 ˚C can be modelled as a function of time and temperature [2]. The results of thermodynamic modelling show a good agreement with experimental data. At 5 and at 20 ˚C, a similar phase assemblage was calculated to be present, while at approximately 50 ˚C, thermodynamic calculations predict the conversion of ettringite and monocarbonate to monosulphate.

Modelling showed that in Portland cements which have an Al_2O_3/SO_3 ratio of > 1.3 (bulk weight), above 50 ˚C monosulphate and monocarbonate are present (cf. Figure 3). In Portland cements which contain less Al ($Al_2O_3/SO_3 < 1.3$), above 50 ˚C monosulphate and small amounts of ettringite are expected to persist.

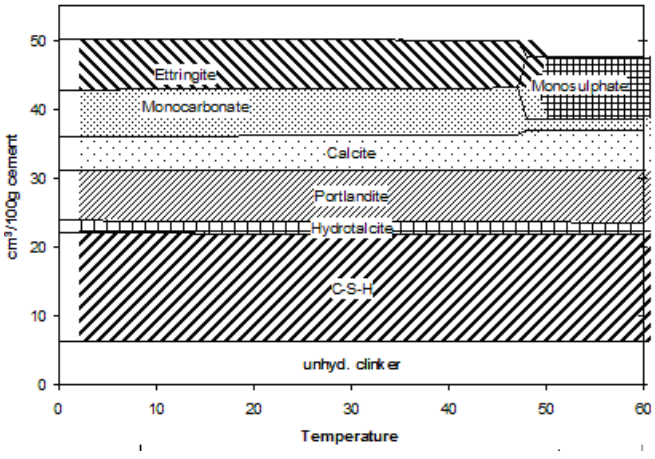

Figure 3: Calculated volume of hydrates in a Portland limestone cement as a function of temperature assuming a dissolution of 75 % of the clinker phases.

A good correlation between calculated porosity and measured compressive strength is observed (cf. Figure 4). A weak dependence of the calculated porosity on the temperature was observed, which disappeared when different densities of C-S-H at different temperatures were assumed. This indicates that other factors such as the heterogeneous distribution of the hydration products and differences in morphology of the hydrates (e.g. longer ettringite needles at lower temperature) play only a minor role for the strength development while the primary factor influencing strength is the degree of space filling or, conversely, the capillary porosity of the system as e.g. demonstrated by Verbeck and Helmuth [3].

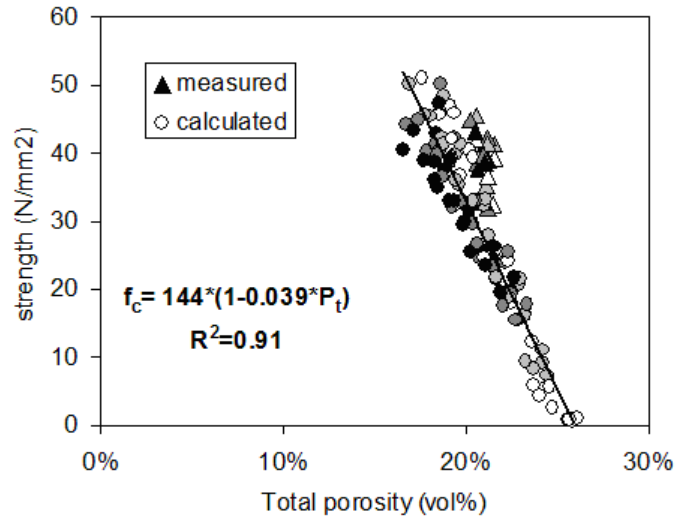

Figure 4: Calculated total porosity of mortar samples compared to measured compressive strength. White data points indicate data from mortars hydrated at 5 ˚C, light grey refers to 20 ˚C, dark grey to 30 ˚C and black to 40 ˚C.

Conclusions

Temperature influences both the composition of the aqueous and the solid phase. Monosulphate instead of ettringite and monocarbonate is formed around 50 ˚ C; the sulphate concentration in the pore solution increases with higher temperatures. The results of thermodynamic modelling show a good agreement with the experimental data. At both 5 and 20 ˚C, a similar phase assemblage was calculated to be present. The thermodynamic calculations predicts the conversion of ettringite and monocarbonate to monosulphate at approximately 50 ˚C, which agrees well with experimental observations in Portland cements [1, 4].

The changes of the composition of the hydrate assemblage with increasing temperature decreases the volume of solids present in the hydrating cement, increases the porosity and thus influences negatively compressive strength. A good correlation between calculated porosity and measured compressive strength was observed.

References

[1] B. Lothenbach, F. Winnefeld, C. Alder, E. Wieland, P. Lunk (2007): Effect of temperature on the pore solution, microstructure and hydration products of Portland cement pastes, *Cement and Concrete Research*, **37**, 483-491.

[2] B. Lothenbach, T. Matschei, G. Möschner, F. Glasser: Thermodynamic modeling of the effect of temperature on the hydration and porosity of Portland cement, *Cement and Concrete Research*, submitted.

[3] G. J. Verbeck, R. H. Helmuth (1968): Structure and physical properties of cement paste. *Proc. 5th Int. Symp. Chem. Cem.*, Tokyo, 1–32.

[4] A. N. Christensen, T. R. Jensen, J. C. Hanson (2004): Formation of ettringite, $Ca_6Al_2(SO_4)_3(OH)_{12}.26H_2O$, AFt, and monosulfate, $Ca_4Al_2O_6(SO_4).14H_2O$, AFm-14, in hydrothermal hydration of Portland cement and of calcium aluminum oxide - calcium sulfate dihydrate mixtures studied by in situ synchrotron X-ray powder diffraction, *Journal of Solid State Chemistry*, **177**, 1944–1951.

Multiscale Heat Conduction Model for Hydration Heat of Concrete

V. Šmilauer*, T. Krejčí

CTU in Prague, Faculty of Civil Engineering, Department of Mechanics
Thákurova 7, Prague 6, 166 29, Czech Republic
vit.smilauer@fsv.cvut.cz, krejci@fsv.cvut.cz

Summary: This paper presents the multiscale model of concrete heat evolution. Cement hydration model CEMHYD3D is used at the micrometer scale, controlled with actual temperature from macroscale concrete level which is computed by means of heat conduction differential equation. Effects of cement chemical composition, fineness and initial temperature are examined in more detail. The validation shows considerable impact of heat of hydration on temperature evolution, especially in massive structures.

Introduction

The hydration of concrete is an exothermic process, contributing to temperature rise of concrete structure under normal circumstances. Concrete, as a multicomponent material, may be considered as hydrating cement paste with inert aggregates, enabling the multiscale modeling at the micrometer resolution of cement paste [1]. The effect of temperature is mainly twofold; an initiation of thermal stress and changing the hydration kinetics.

The thermal stress originates due to internal or external confinement, typically when new concrete is placed on a rock foundation. Possible cracks cause a decay in structure and they will never close up in the future [1]. Precise prediction of heat distribution through the structure will be explored in more detail. The basis for proper problem formulation is based on a nonstationary, diffusion-type, differential heat-flow equation:

$$-\nabla^T \boldsymbol{q}(\boldsymbol{x}) + Q(\boldsymbol{x},t) = \rho(\boldsymbol{x}) c_v(\boldsymbol{x}) \frac{\partial T(\boldsymbol{x},t)}{\partial t} \quad (1)$$

$$\boldsymbol{q}(\boldsymbol{x}) = -\lambda(\boldsymbol{x}) \nabla T(\boldsymbol{x}) \quad (2)$$

where $\boldsymbol{q}(\boldsymbol{x})$ is a heat flux, $Q(\boldsymbol{x},t)$ represents a heat source, $\rho(\boldsymbol{x})$ stands for material density, $c_v(\boldsymbol{x})$ is specific heat capacity and $\lambda(\boldsymbol{x})$ is heat conductivity of isotropic material. Dirichlet, Neumann and Cauchy boundary conditions and initial conditions may be associated with Eq. (1). The principle of virtual temperatures allows numerical solution of Eq. (1) via FEM and explicit or implicit time discretization.

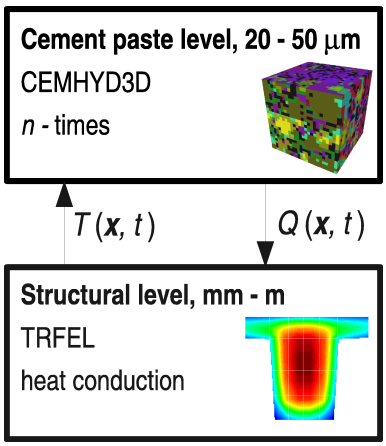

Figure 1: Coupling between cement paste and structural level

The heat source represents the hydration heat of concrete, which is strongly influenced with actual temperature. Therefore, it is necessary to couple hydration model at the microscale with structural model at macroscale in terms of temperature and hydration heat, Fig. 1.

CEMHYD3D hydration model is used for the modeling of heat evolution in a cement paste microstructure [2]. The model allows to include various chemical composition of cement, cement fineness, water regime of curing and the effect of temperature history. The microstructure is built from voxels $1 \times 1 \times 1$ μm, each of them representing one chemical phase, Fig. 2.

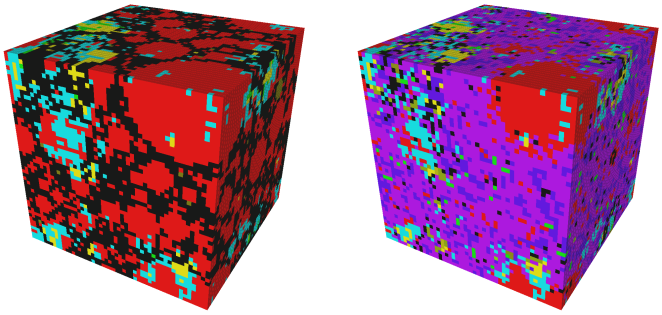

Figure 2: Microstructure 50 × 50 × 50 μm, $w/c = 0.25$, used for generation of hydration heat, initial (left) and at the degree of hydration of 0.63 (right). Red = C_3S, cyan = C_2S, green = C_3A, yellow = C_4AF, black = porosity, violet = C-S-H, blue = CH

Basic chemical reactions are included in CEMHYD3D hydration model. All implemented chemical reactions produce certain amount of heat. The reactions are partially reversible and the total amount of heat is calculated from consumed clinker minerals and other chemical phases. For example, the hydration of silicates is implemented as

$$C_3S + 5.3H \rightarrow C_{1.7}SH_4 + 1.3CH, \quad 517\ \mathrm{J/g}, \quad (3)$$

$$C_2S + 4.3H \rightarrow C_{1.7}SH_4 + 0.3CH, \quad 262\ \mathrm{J/g}, \quad (4)$$

where the heat is related to the amount of C_3S or C_2S. Ordinary Portland cement releases approximately 500 J/g.

The representative volume element (RVE) corresponds to the CEMHYD3D's microstructure, Fig. 2. The modeling of temperature effect is based on the Arrhenius equation

$$\frac{\tau(T)}{\tau(T_0)} = \exp\left[\frac{E_a}{R}\left(\frac{1}{T_0} - \frac{1}{T}\right)\right], \quad (5)$$

where τ is the characteristic time, T and T_0 are arbitrary and some reference temperature of hydration, R is the universal gas constant and E_a is the apparent activation energy. It is a well-known fact that a temperature rise of 10°C in concrete causes approximately two times hydration speedup.

Results

The validation aimed at the quantification of following effects in slab and massive-like constructions:

- RVE size due to its randomness and the impact on the heat of hydration,
- chemical composition of Portland cement,
- saturated and sealed water environment,
- initial temperatures,
- water/cement ratio.

The heat evolution on a bridge cross section of "TT" shape was simulated as the representative of slab and massive parts. The bridge is composed from 350 mm thick slab and two beams 1200 x 2100 mm. The 2D heat conduction problem was discretized with 156 finite elements. Heat generation on each element is simulated on RVE size of 50 × 50 × 50 μm.

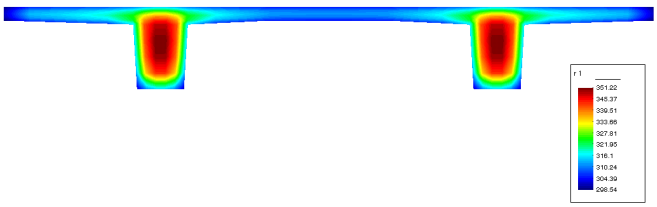

Figure 3: Temperature distribution after 26 h of hydration, ordinary Portland cement CEM I 42.5 R, 300 kg/m^3, water/cement ratio 0.5, initial temperature 20°C

The multiscale model of cement hydration coupled with macroscopic heat conduction provides valuable tool for modeling of temperature distribution on structures. The reasonable size of RVE 50 × 50 × 50 μm of cement microstructure was found. All simulations testify that hydration heat is critical in massive parts where heat conduction is slow and small surface fraction is not effective in cooling. The factors having impact on the temperature inside concrete structures were found in the following order:

- initial temperature and outer temperature after the hydration has started,
- cement fineness,
- chemical composition of cement,
- water/cement ratio.

We gratefully acknowledge financial support from the grants MSM 6840770003 and GAČR 103/03/D145.

References

[1] K. Maekawa, R. P. Chaube, T. Kishi (1999): *Modeling of Concrete Performance.* E & FN SPON (London).

[2] D.P. Bentz (2005): *CEMHYD3D: A Three-Dimensional Cement Hydration and Microstructure Development Modeling Package. Version 3.0.* Building and Fire Research Laboratory Gaithersburg, Maryland 20899.

On the Appropriateness of Various Constitutive Models for Nanoindentation of Cement Paste

J. Němeček*, P. Kabele and Z. Bittnar

Czech Technical University in Prague
Thákurova 7, 166 29 Prague 6, Czech Republic
jiri.nemecek@fsv.cvut.cz, petr.kabele@fsv.cvut.cz, bittnar@fsv.cvut.cz

Summary: This paper concerns on experimental and numerical investigations of cement paste. Multiple nanoindentation experiments with emphasis on creep effects and including cyclic loading were carried out in this study. Limitations of using traditional elastic solution in simple loading cases was shown. The paper concerns also on the appropriateness of conventional methods used for evaluation of micromechanical properties and it investigates possibilities of the use of enhanced methods for better description of the nanoindentation process. Several models based on analytical visco-elastic solution and finite element model with general visco-elasto-plastic constitutive relation were proposed. The models were used for simulation of nanoindentation and for estimation of material parameters of hydrated phases of cement paste at micrometer scale.

Introduction

Cement is the main binding component of concrete and other cementitious composites. The development of various experimental techniques, namely nanoindentation, made possible to access also its mechanical properties at submicron length scales. Nanoindentation is based on the direct measurement of the load-displacement relationship using a very sharp tip pressed into the material. Nowadays, nanoindentation is widely used for assessment of micro-mechanical behavior of thin films, metals, plastics and other materials. Several works can be found also for cement-like materials, e.g. [1, 2].

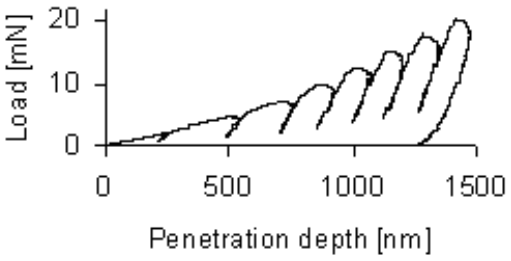

Figure 1: Example of multi-cycle loading with increasing load and no holding period at the peaks.

Nanoindentation of cement pastes

In contrast to usual indentation on metals, for example, cement paste is much more complex and also time-dependent material. From the microstructural point of view, cement paste is a heterogeneous material with several material phases. The most important are the hydrated phases (C-S-H gels) for which the material properties are assessed in this study. Cement paste also exhibits significant creep that can affect evaluation of its elastic properties using standard procedures [3]. Ignoring creep in the evaluation of results can lead to overestimation of elastic properties. Simulation of indentation process and comparison with experimental data can answer the question on the appropriateness of different constitutive relations and the underlying material behavior.

Experiments

Cement paste samples were prepared and tested by means of nanoindentation. Only hydrated phases were considered for the evaluation of results. Several types of loading were prescribed:

(i) one-cycle loading (loading, holding and unloading) (Fig. 3b),

(ii) multi-cycle loading to increasing loads without holding periods at peaks (Fig. 1),

(iii) cyclic loading with long holding periods at the peak (Fig. 3c).

Experiments were carried out in a large load range to cover also wide ranges of penetration depths.

Analysis of indentation data and their numerical simulation

Traditionally, only elastic parameters are evaluated from nanoindentation experiments. In this case, unloading part of the load-displacement curve is supposed to be elastic and an analytical solution is used for assessment of elastic modulus, for example [3]. However, the material behavior does not always fulfill such a strong assumption. It can be seen in Fig. 1 that the loading curve contains a bulge at the beginning of unloading in each cycle. It shows the role of creep that is present even on the unloading branch. It leads to spurious size effect on the evaluation of elastic properties using standard procedures based on elasticity [3] as shown in Fig. 2. On the other hand, using long holding periods significantly reduces this kind of spurious size effect (Fig. 2). Generally, material response may contain also inelastic deformations and more precise material models are needed for its description.
Recently, an analytical solution based on visco-elasticity was derived by Vandamme and Ulm [4]. This kind of model was

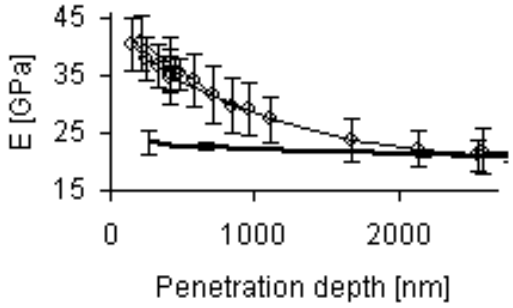

Figure 2: Size effect on the elastic modulus evaluated with Oliver-Pharr method [3] ignoring creep effects (thin line) and using long holding periods (thick line).

found to be suitable for simple (one-cycle) experiments. Viscous parameters can be found easily in this case from the creep in holding period (Fig. 3a) and the overall material response is described well (Fig. 3b). However, for a general case of multi-cycle experiments this model fails because it cannot describe also plastic deformations that are present in subsequent loading cycles (Fig. 3c.). Since the loading path was too complicated for the analytical solution [4] simplified loading history without intermediate unloading was used. It is the reason why no cyclic loading is shown in the simulation in Fig. 3c. However the numerical response does not wrap the experimental curve as it was expected. Using the same material parameters lead to underestimation of deformation in this experiment.

It motivated us to construct the finite element model with more complex constitutive laws and with the possibility of setting an arbitrary loading history. Multi-cycle experiments were qualitatively captured by using constitutive relation containing not only creep (viscous part) but also plastic strains (Fig. 3d). However, parameters of this qualitatively most suitable elastic-plastic-creep model are difficult to obtain. Presently, the possibility of using a more sophisticated method of parameter identification based on genetic algorithms is being researched.

Conclusions

Based on the experimental evidence it was found that standard evaluation procedures based on elasticity [3] lead to spurious size effect on elastic properties for cement paste. It is caused by the presence of creep in the initial part of the unloading branch. In case of using long dwell period at peak loads this effect can be significantly decreased.
An analytical visco-elastic solution [4] can be successfully used for simulation of one-cycle experimental curves. Material parameters are, in this case, obtained by nonlinear fitting of creep curve during holding period. The same model applied for more complex type of experiment with cyclic loading leads to underestimation of deformations.
General FE model with visco-elasto-plastic constitutive relation can qualitatively match also multi-cyclic experimental loading paths. However, parameters of this qualitatively most suitable model are difficult to obtain. Presently, the possibility of using genetic algorithms for parameter identification is investigated.

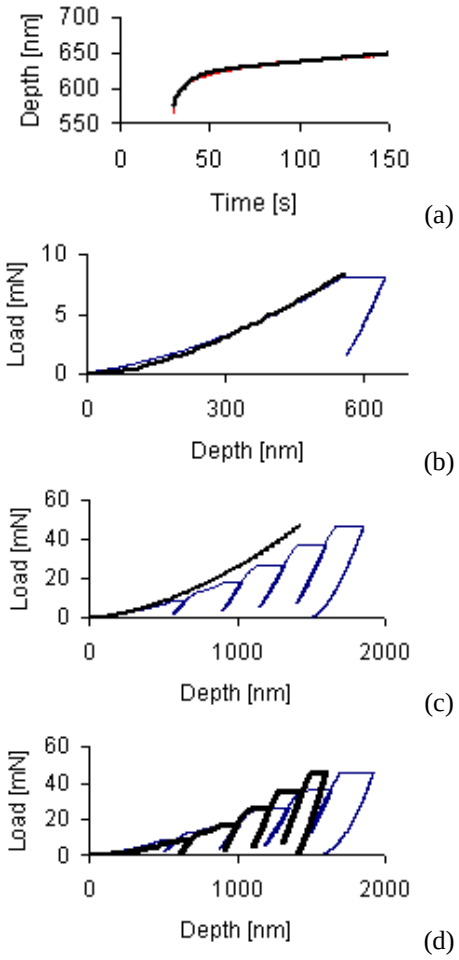

Figure 3: Experimental curves (thin lines) and numerical responses (thick lines): (a) holding period (creep), (b) one-cycle loading, (c) multi-cycle loading modeled by viscoelasticity, (d) multi-cycle experiment modeled by visco-elasto-plastic model.

Acknowledgements

Support of the Ministry of Education of the Czech Republic (project MSM 6840770003) is gratefully acknowledged.

References

[1] Constantinides, G., Ulm F. J., Van Vliet K. (2003): On the use of nanoindentation for cementitious materials. *Materials and Structures* 36, 191–196.

[2] Constantinides, G., Ulm F. J. (2004): The effect of two types of C-S-H on the elasticity of cement-based materials: Results from nanoindentation and micromechanical modeling. *Cement and Concrete Research* 34, 67–80.

[3] Oliver W. C., Pharr G. M. (1992): An improved technique for determining hardness and elastic modulus using load and displacement sensing indentation experiments. *Journal of Material Research* 7, 1564–1583.

[4] Vandamme M., Ulm F. J. (2006): Visco-elastic solutions for conical indentation. *Int. J. of Solids and Structures* 43, 3142–3165.

Multiscale Experimental Investigation of Deterioration of Fiber-Cementitious Composites in Aggressive Environment

P. Kabele*, L. Novák, J. Němeček, J. Pekař

CTU in Prague, Faculty of Civil Engineering
Thákurova 7, Praha 6, Czech Republic
petr.kabele@fsv.cvut.cz, jiri.nemecek@fsv.cvut.cz

Summary: In the present paper, we experimentally investigate the effects of chloride exposure and calcium leaching on the mechanical properties on various levels of microstructure of fiber-cementitious composites. The levels include fiber-matrix interface, matrix itself, and cohesive crack traction due to fiber bridging. The performed tests show consistent effects across different scales.

Introduction

Application of strain hardening fiber reinforced cementitious composites (SHCC) is often seen as one of possible ways to improve durability of concrete and reinforced concrete (R/C) structures, especially of those exposed to harsh environment [8]. These materials, which are also called high performance fiber reinforced cementitious composites (HPFRCC), are characteristic by the ability to sustain significant straining under increasing load in tension. The overall deformation is mostly attributed to formation and opening of a large number of distributed sub-parallel matrix cracks bridged by fibers – a process called multiple cracking. From the durability point of view, it is important that the widths of these cracks remain in the sub-millimeter range, even when the overall strain attains the level of several percent. The composite is then much less susceptible to ingress of water and aggressive agents from the environment than ordinary R/C would be at the same structural deformation.

The conditions that a brittle-matrix composite with discontinuous fibers has to satisfy to achieve multiple cracking have been rigorously studied and set forth by several authors in the past (e.g. [5], [2]). In simple words, existence of multiple cracking is determined by sufficiently low matrix cracking strength and sufficiently strong crack-bridging action of fibers. The former is related to the size of initial matrix flaws and the matrix fracture toughness, while the latter mostly depends on fiber volume fraction and alignment, fiber strength, and fiber-matrix bond strength. For the sake of simple production and application of the composites, it is desirable to use low volume fraction of short random fibers. Engineered Cementitious Composites (ECC) [3] represent a class of SHCC materials whose microstructure (micromechanical parameters of fiber, matrix, and their interface) is consciously optimized so as to achieve strain hardening behavior even with fiber volume fraction as low as 2%. As we have discussed in the first paragraph, when ECCs are used to improve structural durability, the composites' ability to undergo damage in the form of multiple cracking under severe environmental conditions is essential. Since the overall mechanical behavior of ECC materials is closely related to their tailored microstructure, this ability can be estimated if the effects of aggressive environment on mechanical phenomena that take place at the microscale, are known. In the present study, we experimentally investigated the effects of chloride exposure and calcium leaching on the mechanical behavior on various levels of the composites' microstructure. Note that in the real world, chloride attack usually occurs due to use of deicing salt for road maintenance or in seashore and marine structures. Leaching can take place in structures exposed to soft water or water containing ions like SO_4^{2-}, NH_4^+ underground structures, sewers, dams, etc.

Specimen preparation and treatment

Material composition used in the tests was derived from the standard PVA-ECC type M45 developed at the University of Michigan [7]. However higher water/cement ratio was used to achieve sufficient workability with constituents available in the Czech Republic. The composite contained 2% by volume of PVA fibers.

Specimens were prepared by casting and, in case of fracture tests (see below), cutting from larger plates. Consequently, some pieces were kept in room conditions as reference (O-series), while others were exposed to chloride attack (S-series) and yet others to calcium leaching (N3-series and N6-series). Chloride attack was induced by 10 cycles of 5-days immersion in a saturated solution of NaCl at 20 ^{o}C and 2-days drying in oven at 50 ^{o}C. Leaching was preformed by immersing the samples for 70 days into 3 mol/l (N3-series) or 6 mol/l (N6-series) water solution of NH_4NO_3 at room temperature. After the chemical exposure, the specimens were left covered in room conditions for about one month before being tested.

Fiber pullout tests

In order to estimate the basic bond properties of fiber-matrix interface, single-fiber pullout tests were conducted [1]. A fiber, partially embedded (typically 2-4 mm) into cylindrical matrix specimens (27 mm high, 32 mm in diameter), was pulled out in axial direction under displacement control. Pullout force P and pullout displacement Δ were monitored and recorded. The measured force was correlated with model described in ref. [4], from which chemical bond strength G_d and frictional bond strength τ_0 were calculated. Figure 1 shows that both chloride and nitrate attacks significantly reduce the chemical bond strength. On the other hand, frictional bond is decreased only by nitrate, while chloride exposure causes its slight increase.

Nanoindentation

To gain a better understanding of the phenomena observed in the pullout tests, nanoindentation of the fiber-matrix interfacial transition zone (ITZ) was carried out [6]. Figure 2 shows that in control specimens (O), the local elastic modulus increases as

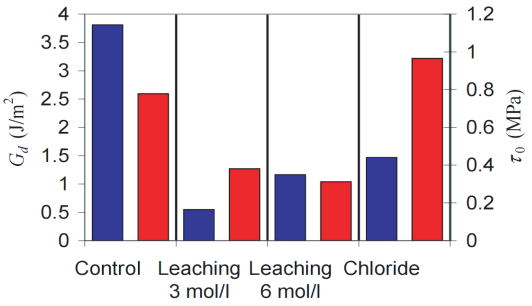

Figure 1: Effect of chemical exposure on chemical bond (left columns) and frictional bond (right columns).

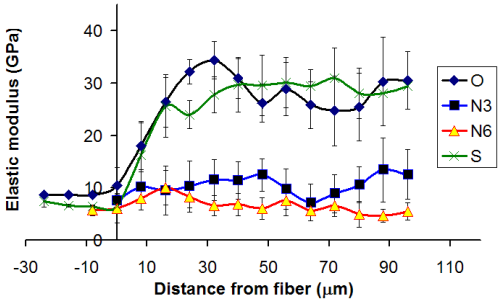

Figure 2: Effect of chemical exposure on the matrix local elastic modulus.

the distance from the fiber increases, before attaining a stable value at about 30 μm from the fiber. This can be attributed to higher porosity of the ITZ close to the fiber. This tendency is almost unaffected by chloride attack (S). On the other hand, nitrate causes degradation of the matrix by calcium leaching, which manifests itself by low modulus even farther from the fiber.

Fracture tests

Matrix fracture toughness is another important micromechanical parameter, since it controls initiation of multiple cracks from matrix defects. Fracture tests on small 3-point bending notched beams (150×20×12 mm) with notch size close to the largest intrinsic flaw (5 mm) were carried out. From the load at initiation of crack propagation, the matrix fracture toughness was estimated. Fig. 3 shows that the fracture toughness is almost unaffected by chloride treatment. Exposure to nitrate causes a severe decrease of this parameter.

From the peak loads attained in these tests, we also calculated the modulus of rupture. Since the peak load is mostly determined by the cohesive traction acting between crack surfaces, we obtained qualitative information on the effectiveness of fiber bridging on a single crack. Fig. 3 indicates that the bridging effectiveness significantly degrades due to exposure to nitrate, while chloride causes only a slight decrease.

Concluding remarks

The performed tests showed consistent effects of aggressive environment on fiber-cementitious composites across different scales. Exposure to nitrates (calcium leaching) strongly degrades the cementitious matrix, which results in reduction of fiber bond, matrix toughness, and cohesive crack-bridging traction. Chloride treatment almost does not affect the matrix properties. It causes slight change in fiber bond properties, which results in small decrease of the bridging traction.

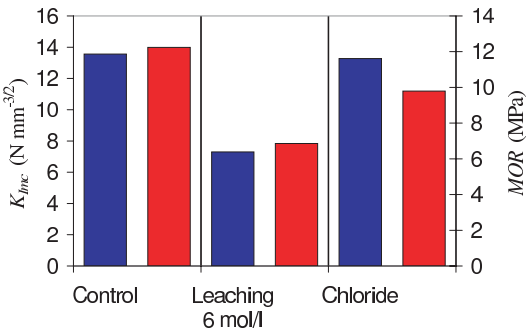

Figure 3: Effect of chemical exposure on matrix fracture toughness K_{Imc} (left columns) and composite modulus of rupture (right columns).

Acknowledgments

The presented research has been supported by the Czech Science Foundation grant GACR 103/05/0896 and the Ministry of Education, Youth and Sports of the Czech Republic contract MSM6840770003. The accelerated chloride treatment was carried out in collaboration with RWTH Aachen University.

References

[1] P. Kabele, L. Novák, J. Němeček, L. Kopecký (2006): Effects of chemical exposure on bond between synthetic fiber and cementitious matrix, *Proc. Int. Conference on Textile Reinforced Concrete*, Aachen, 2006, RILEM.

[2] V. C. Li, H. C. Wu (1992): Conditions for pseudo strain-hardening in fiber reinforced brittle matrix composites, *Journal of Applied Mechanics Review* **45**, 390–398.

[3] V. C. Li (2003): On Engineered Cementitious Composites (ECC) – a review of the material and its applications, *Journal of Advanced Concrete Technology* **1**, 215–230.

[4] Z. Lin, T. Kanda, V. C. Li (1999): On interface characterization and performance of fiber-reinforced cementitious composites, *Concrete Science and Engineering* **1**, 173–184.

[5] A. E. Naaman, S. P. Shah (1979): Fracture and multiple cracking of cementitious composites, *Fracture Mechanics Applied to Brittle Materials, ASTM STP 678*, American Society for Testing and Materials, 183–201.

[6] J. Němeček, P. Kabele, L. Kopecký, Z. Bittnar (2007): Effect of chemical exposure on fiber reinforced cementitious matrix, *Proc. SEMC 200*, South Africa, to appear.

[7] S. Wang, V. C. Li (2005): Polyvinyl alcohol fiber reinforced engineered cementitious composites: material design and performances, *Proc. Int. Workshop on High Performance Fiber Reinforced Cementitious Composites in Structural Applications*, Honolulu, RILEM, CD-ROM, also available at www.hpfrcc-workshop.org.

[8] F. H. Wittmann (2006): Specific aspects of durability of strain hardening cement-based composites, *Restoration of Buildings and Monuments* **12**, 109-118.

Part XIV

Posters

Numerical Modeling of the Rate-Dependent Response of Filled Rubber

B. Marvalová*

Technical University of Liberec
Hálkova 6, 46117 Liberec, Czech Republic
bohda.marvalova@tul.cz

Summary: The rate-dependent behavior of filled rubber is investigated in compression regimes. The viscosity-induced rate-dependent effects are described. The parameters of a constitutive model of finite strain viscoelasticity are determined by nonlinear optimization methods. The material model is implemented into finite element code and the viscoelastic stress response of carbon-black filled rubber at large strains in relaxation, creep and cyclic loading is simulated.

Model of viscoelastic material at finite strains

Rubber materials are applied in various branches of mechanical engineering because of their damping properties. The modelling and FEM simulations of the structural response require a constitutive model which captures the complex material behaviour.

The ground-stress response of filled rubber is usually modelled in the phenomenological framework of finite elasticity by Mooney-Rivlin or Ogden models, or by Aruda and Boyce model in terms of the micromechanically based kinetic theory of polymer chain deformations.

Beside the elastic response the filled rubber shows also the finite viscoelastic overstress response which is apparent in creep and relaxation tests. Cyclic loading tests show a typical frequency-dependent hysteresis as well where the width of the hysteresis increases with increasing stretch rates.

The constitutive theory of finite linear viscoelasticity is a major foundation for modeling rate-dependent material behaviour based on the phenomenological approach. In this approach, a suitable hyperelasticity model is employed to reproduce the elastic response and the inelastic overstress is determined by an evolution equation.

The origin of the material model of finite strain viscoelasticity used in our work is the concept of Simo [1,2]. The finite element formulation of the model was elaborated by Holzapfel [3] and used by Holzapfel & Gasser [4] for the simulation of the viscoelastic deformation of fibre reinforced composite material undergoing finite strains. The model is based on the theory of compressible hyperelasticity with the decoupled representation of the Helmholtz free energy function composed of the volumetric and the isochoric elastic parts and of the dissipative potential responsible for the viscoelastic contribution [5]. The 2^{nd} Piola-Kirchhoff stress with volumetric, isochoric and overstress terms reads:

$$\boldsymbol{S} = \boldsymbol{S}^{\infty}_{VOL} + \boldsymbol{S}^{\infty}_{ISO} + \sum_{\alpha=1}^{m} \boldsymbol{Q}_{\alpha} \qquad (1)$$

The evolution equation for the overstress $\boldsymbol{Q}_{\alpha}$ is in the form:

$$\dot{\boldsymbol{Q}}_{\alpha} + \frac{\boldsymbol{Q}_{\alpha}}{\tau_{\alpha}} = \dot{\boldsymbol{S}}_{ISO\alpha}, \qquad \boldsymbol{S}_{ISO\alpha} = \beta^{\infty}_{\alpha} \boldsymbol{S}^{\infty}_{ISO} \qquad (2)$$

where β^{∞}_{α} is the nondimensional strain energy factor [1] and τ_{α} is the relaxation time.

We assumed slightly compressible material, the volumetric and isochoric (Mooney-Rivlin) parts of Helmholtz free energy function were chosen in the form:

$$\begin{aligned} \Psi^{\infty}_{VOL}(J) &= \frac{1}{d}(J-1)^2, \\ \Psi^{\infty}_{ISO}(\bar{\boldsymbol{C}}) &= c_1(\bar{I}_1 - 3) + c_2(\bar{I}_2 - 3) \end{aligned} \qquad (3)$$

The viscoelastic behaviour was modelled by use of $\alpha = 2$ relaxation processes. The relaxation times τ_1, τ_2, the free energy factors $\beta^{\infty}_1, \beta^{\infty}_2$, the parameters c_1, c_2 and d were determined experimentally from the relaxation tests of rubber specimens in compression.

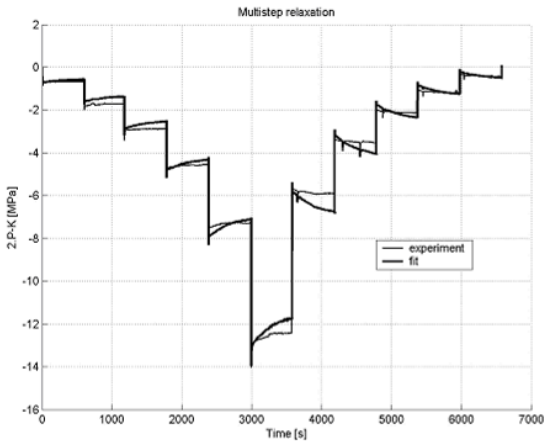

Figure 1: Multistep relaxation experiment.

Experiment

All tests were performed in the compression regime at constant ambient temperature under strain control. Blocks of filled rubber 44 x 27 x 22 mm were used as specimens. Prior to an actual test, each virgin specimen was subjected to a pre-loading process to remove the Mullins' softening effect.

The relaxation behaviour at different strain levels was examined in simple-step and in multi-step relaxation tests. The strain rate of 0.05 mm/s was applied during the loading path. The stress relaxation was recorded for 1200 s. Fig. 1 shows the time histories of stress at different strain levels in the multi-step relaxation test.

The stresses measured at the termination points of the relaxation periods are approximate values of the equilibrium stress. The difference between the current stress and the equilibrium stress is the overstress.
Fig.1 compares the experimental data of a multistep relaxation test and the curves fitted to the proposed material model by nonlinear least squares method. All curves reveal the existence of a very fast stress relaxation during the first 10 seconds followed by a very slow rate of relaxation.
Comparing the results obtained at different strain levels, it can be seen that relaxation tests carried out at higher strain levels possess larger over-stresses and subsequently show a faster stress relaxation than those at lower strain levels with lower over-stresses.
The seven material parameters were calculated by nonlinear optimization methods in Matlab. First the parameters c_1, c_2 and d were determined from the equlibrium stresses, then the parameters $\beta_1^\infty, \beta_2^\infty$ and τ_1, τ_2 were determined from the relaxation data. Fig.1 compares the experimental data of a multistep relaxation test and the curves fitted with the proposed material model.

Finite element simulation

We implemented the material model in the Lagrangian configuration into Comsol Multiphysics. The Structural Mechanics and PDE modules were used for the calculation of time dependent response of a rubber block in creep, relaxation and cyclic loading.
The application mode type plane strain in Structural Mechanics Module, the time dependent analysis and the Mooney-Rivlin hyperelastic material were chosen for the calculation of the equilibrium response.
The components of the isochoric stress rate $\dot{\boldsymbol{S}}_{ISO}^{\infty}$ were derived in Symbolic Toolbox in Matlab and added to the scalar expressions in Comsol. PDE module was used for the integration of the evolution equation (2).
The results of the simulations of the compressive loading at different strain rates and of the cyclic loading at Figs. 2 and 3 show the good qualitative agreement with experimental time dependent behaviour of filled rubbers.

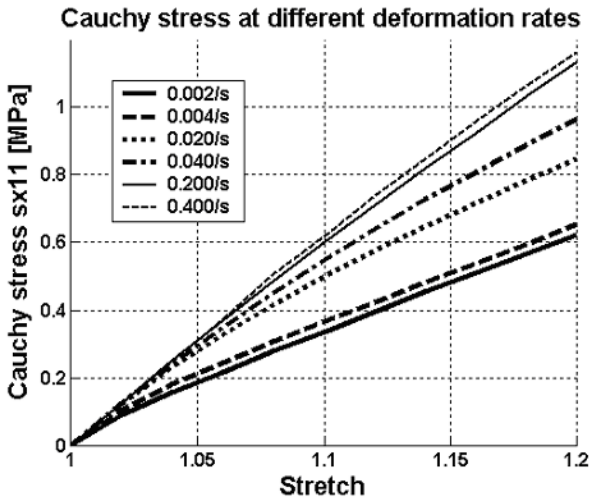

Figure 2: Simulation of the compression at different strain rates.

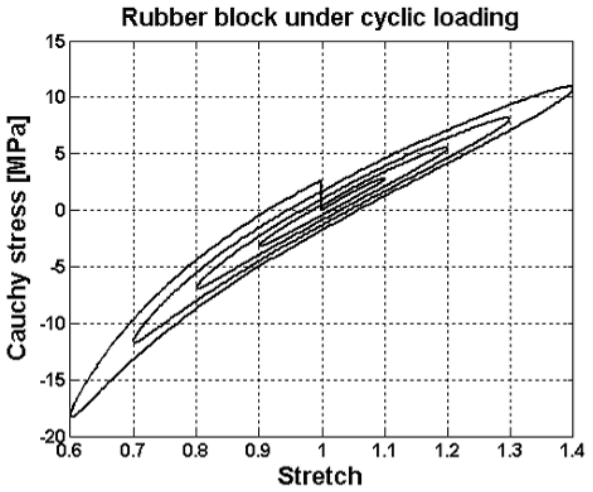

Figure 3: Simulation of the cyclic loading.

Acknowledgement

The author gratefully acknowledges the funding provided by the Czech Grant Agency GACR, grant No.101/05/2669.

References

[1] J. C. Simo (1987): On a fully three dimensional finite strain viscoelastic damage model: formulation and computational aspects. *Comput. Meth. Appl. Mech. Eng.* **60**, 153–173.

[2] S. Govindjee, J. C. Simo (1992): Mullins' effect and strain amplitude dependence of the storage modulus. *Int. Journal of Solids and Structures* **29**,1737–1751.

[3] G. A. Holzapfel, (1996): On large strain viscoelasticity: continuum formulation and finite element application to elastomeric structures, *Int. J. Numer. Meth. Eng.* **39**, 3903–3926

[4] G. A. Holzapfel, T. C. Gasser (2001): A viscoelastic model for fiber-reinforced composites at finite strains. Continuum basis, computational aspects and applications. *Computer Meth. Appl. Mech. Eng.* **190**, 4379–4430

[5] G. A. Holzapfel (2000): *Nonlinear Solid Mechanics*. Wiley, N.Y.

Multiscale Modeling and Simulation of Fiber Reinforced Composites: Macroscopic Properties vs. Microscopic Features

V. Sansalone[1]*, **P. Trovalusci**[2]

[1]Laboratoire de Biomécanique et Biomatériaux Ostéo-Articulaires, CNRS UMR 7052, Université Paris 12
61, Av. Du Général de Gaulle, 94010 Créteil Cedex, France.
vittorio.sansalone@univ-paris12.fr

[2]Dipartimento di Ingegneria Strutturale e Geotecnica, Università La Sapienza
Via Gramsci 53, 00197 Roma, Italy
patrizia.trovalusci@uniroma1.it

Summary: This paper focuses on the modeling of a fiber-reinforced composite material, by means of a micropolar continuum. The macroscopic constitutive relation is obtained by a multiscale procedure, bridging the continuum with a lattice-type micromodel. Numerical results show the influence of the morphological and constitutive micro-features on the macroscopic response.

Introduction

Mechanical response of composite materials is strongly influenced by the microstructural features of the material. From the engineering point of view, it is important to set up effective macroscopic mechanical models, without resorting to an explicit description of the microstructure.

Micropolar continua [1] have been found to be suitable for modeling a large class of fiber-reinforced composite materials, namely when the reinforcements are much stiffer than the emebedding matrix: fibre reinforced polymers [2], masonry-like materials [3], bones ultrastructure [4]. However, the constitutive characterization of such continua is tricky, since it depends not only on the constitutive properties of the microconstituents but also on their arrangement.

To obtain the appropriate macroscopic constitutive description, we used a two-scale homogenization based on a principle of energy equivalence. The resulting formal expression is insensitive to the specific geometrical and constitutive assumptions at the microscale, and that makes the procedure quite general.

In this study we explore how the microscopic ingredients influence the macroscopic properties of the fiber-reinforced material, focusing on both morphological (size and orientation of the fibers) and constitutive (No-Tension vs. Coulomb-like response of the matrix) issues.

Two-scale model for fiber-reinforced composites

Our reference material is a composite characterized, at the microscopic level, by short, stiff fibres embedded in a deformable matrix. We assume perfect adhesion between the fibres and the matrix. Our modeling is based on a two-scale description of the material. At the microscale, we consider a periodic microstructure, where the module is a *lattice-type model* (Fig. 1): the fibers (represented by the dark shaded bars in the figure and labeled a, b, ..., in the following) are described as rigid bodies. They interact with each other by a set of springs, represented by thick segments in the figure, which are the only deformable elements and describe the effect of the matrix. At the macroscale, the equivalent continuum turns out to be a *micropolar continuum*, where material particles are described by a displacement field, $\boldsymbol{u}$, and by a skew-symmetric 2-tensor field, W, representing the microrotation of the fibres.

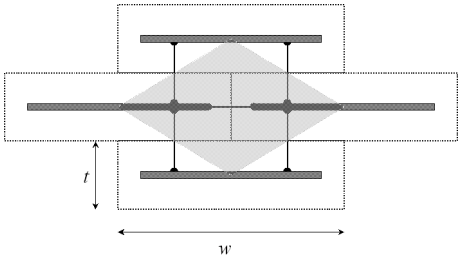

Figure 1: Sketch of the orthotropic lattice adopted as micromodel. Light shaded area represents the periodic module.

A suitable choice of the macroscopic constitutive relation is a crucial point. Here, the idea is to describe the macroscopic response explicitly resorting to the microstructure, in a truly multiscale, computationally-oriented setting. The key assumptions of the procedure are: **(a)** the admissible deformations for the module are considered homogeneous; **(b)** the average strain energy of the module, ϕ_μ, is equal to the strain energy density of the macromodel, ϕ_M.

Then, it is possible to identify the macroscopic stress measures, namely the Cauchy stress S and the couple-stress $\boldsymbol{S}$, in terms of the actions at the microscale, namely the force $\mathbf{t}^{\mathsf{ab}}$ and the couple C^{ab} exchanged between all the pairs of fibers a and b.

$$S = \mathcal{H}_S(\mathbf{t}^{\mathsf{ab}}, \mathrm{C}^{\mathsf{ab}}), \quad \boldsymbol{S} = \mathcal{H}_{\boldsymbol{S}}(\mathbf{t}^{\mathsf{ab}}, \mathrm{C}^{\mathsf{ab}}). \tag{1}$$

The homogenization operators $\mathcal{H}_S$ and $\mathcal{H}_{\boldsymbol{S}}$ *do* depend on the morphology of the module but *do not* depend on the constitutive assumptions at the microscale.

In turn, the micro-actions $\mathbf{t}^{\mathsf{ab}}$ and C^{ab} are computed from the relative displacement $\mathbf{u}^{\mathsf{ab}}$ and rotation W^{ab} of the fibers:

$$\mathbf{t}^{\mathsf{ab}} = \mathfrak{t}\left(\mathbf{u}^{\mathsf{ab}}, \mathrm{W}^{\mathsf{ab}}\right), \quad \mathrm{C}^{\mathsf{ab}} = \mathfrak{C}\left(\mathbf{u}^{\mathsf{ab}}, \mathrm{W}^{\mathsf{ab}}\right), \tag{2}$$

where $\mathfrak{t}$ and $\mathfrak{C}$ are constitutive maps, and $\mathbf{u}^{\mathsf{ab}}$ and W^{ab} are computed by affine expansion of the fields $\boldsymbol{u}$ and W.

Numerical simulations

The micropolar model is well suited to describe the dependency of the macroscopic response on the morphology of the microstructure. We show that considering the test case in Fig. 2: a beam of length L and height $H = L/10$, in plane-strain, four-point bending loading condition. The elastic strain energy $\Phi := \int \phi_M$ (a synthetic measure of the deformability of the system) is reported as a function of the scale factor $\lambda := w/L$, for three different orientations of the fibers. The mechanical response strongly depends on both the orientation and the size of the fibers. Other morphological factors, like the aspect ratio of the module (here $w/t = 10$), are not considered in this study, but they would likely influence the overall behaviour as well. In the same figure, dashed straight lines refer to the corresponding (anisotropic) Cauchy model, which is clearly unable to show any scale effect. Moreover, it can not be even considered the limit case of the micropolar continuum while $\lambda \to 0$.

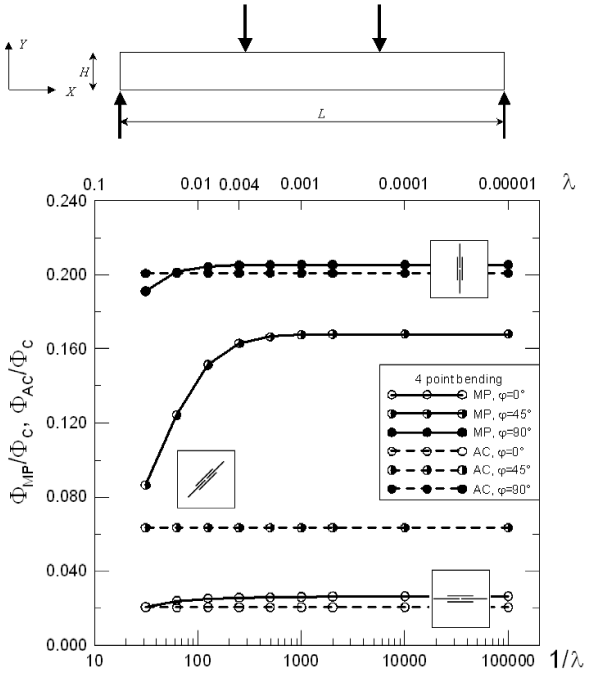

*Figure 2: (*Top*) Geometry and loads. (*Bottom*) Plot of the strain energy vs. the orientation and the size of the fibers; Φ_{MP}: micropolar model; Φ_{AC}: Cauchy model; Φ_C: bare matrix.*

An important feature of the proposed approach is the *uncoupling of models* at different scales. Since both the (strain-)localization and the (stress-)homogenization operator are not influenced by the specific constitutive assumptions at the microscale, the micromodel can be formulated independently. Then, a very few effort must be done to study the macroscopic effects of different microscopic constitutive ingredients. As a toy problem, we studied a "wall" on an inclined plane, subjected to its weigth, Fig. 3. At the microscale, we assumed for the springs a No-Tension and a Coulomb-like [3] constitutive behaviour, respectively. In the former case, the microrotation field is very smooth, while in the latter a band appears in the microrotation map, corresponding to a high vertical gradient of fibres rotation. Under and over this band, microrotations realized in the Coulomb-like model attain values much lower and much higher than the No-Tension model, respectively.

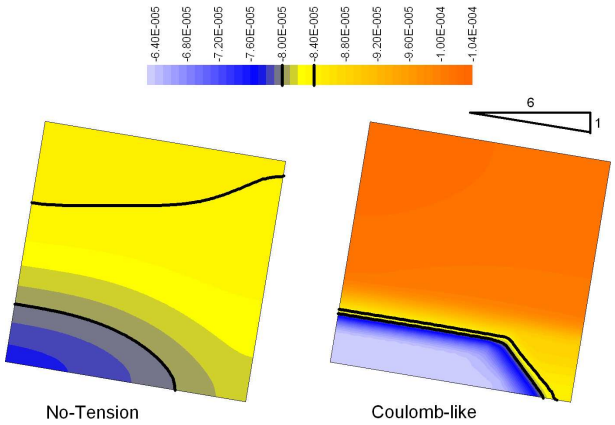

Figure 3: Microrotation map for a wall subjected to its weigth. Comparison between No-tension and Coulomb-like model.

Final remarks

In this work we studied the response of a target fiber-reinforced composite (epoxy matrix reinforced with short, stiff glass fibres) by a multiscale approach. At the macroscopic level, the body is described by a micropolar continuum, while at the microscale a lattice periodic cell is adopted. The model is well suited for describing the effect of the microstructural features on the macroscopic response. We considered in the numerical simulations both morphological and constitutive issues. Such features are very important for understanding the relation between the microscopic structure and the macroscopic properties of the material, and therefore for an optimum design of the microstructure.

The multiscale approach provides a mechanically funded basis to build up equivalent continua endowed with the parameters suitable for describing different microstructures. The macroscopic constitutive relation is implicitly recovered by a numerical homogenization: this leads to a clear *uncoupling* of the modeling at the two scales, which makes the proposed framework quite general and suitable for further extensions.

References

[1] G. Capriz (1989): *Continua with Microstructure*. Springer-Verlag, Berlin.

[2] V. Sansalone, P. Trovalusci, F. Cleri (2006): Multiscale modelling of materials by a multifield approach: Microscopic stress and strain distribution in fiber-matrix composites. *Acta Materialia*, **54**, 3485–3492.

[3] P. Trovalusci, R. Masiani (2003): Non-linear micropolar and classical continua for anisotropic discontinuous materials. *Int. J. Solids Structures*, **40**, 1281–1297.

[4] I. Jäger, P. Fratzl (2000): Mineralized collagen fibrils: A mechanical model with a staggered arrangement of mineral particles. *Biophysical Journal*, **79**, 1737–1746.

The Theory of Plasticity, Involving Micro Strains: Modelling of Inelastic Deformation of Geomaterials

Yu. A. Chernyakov, V. P. Shneider[1], **A. S. Polischuk***

[1]Dnipropetrovsk National University
Naukovy, 13, Dnipropetrovsk, 49050, Ukraine
chernyakova@fregat.dp.ua, shneider_vova@mail.ru, tensorx@yandex.ru

Summary: In work the variant of the theory of the plasticity involving micro strains, directed on the account of features of inelastic behavior of geomaterials is given. Influence of the first and the third invariants of stress tensor on process of deformation is considered. Comparison of numerical finite-element calculations with experimental data for triaxial tests is made.

Introduction

In works [1-3] the theory of plasticity, considering micro strains, has been offered for metals, in it the big role was devoted to account of internal micro stresses which arise on borders of grains owing to heterogeneity of plastic deformation. Such approach was allowed to describe main effects of process of plastic deformation of metals at complex loading [4] even at essential simplifications.

In the given work generalization of the theory of the plasticity involving micro strains is presented, which allow to describe inelastic deformation of geomaterials. The same idea about non-uniform granular structure of the representative macro volume consisting of micro particles of various sizes and various orientations is put in the basis of the model. In suggested variant of the theory the mechanism of micro fracture [3] leading to strain softening is accepted as the basic mechanism of inelastic deformation. A measure of micro fracture is tensor σ_k^f, which is coaxial with directing deviator α, fixing a direction in deviatoric space. As a result of such generalization we come to the theory which considers influence of the first and the third invariants of stress tensor on plastic deformation and fracture.

Formulations of the theory

We will write down the local law of strain softening in the form of

$$\boldsymbol{\sigma}_k + \boldsymbol{\sigma}_k^f = \tilde{\boldsymbol{G}} : \boldsymbol{\varepsilon}_k \tag{1}$$

where $\boldsymbol{\varepsilon}_k$, $\boldsymbol{\sigma}_k$, $\boldsymbol{\sigma}_k^f$ are tensors of micro strain, micro stress and stress of micro fracture of k-th particles accordingly.

The law of development of micro fracture stress of each particle is set in the form of:

$$\dot{\boldsymbol{\sigma}}_k^f = \dot{\sigma}_k^f \boldsymbol{\mu}_k, \qquad \boldsymbol{\mu}_k = \boldsymbol{\varepsilon}_k / \varepsilon_k, \tag{2}$$

where ε_k is the local limit of micro fracture in strain space ($\varepsilon_k(0) = \varepsilon_{k0}$), $\boldsymbol{\mu}_k$ is directing tensor, defining a direction of rate of change of micro fracture stress which is also represented coaxial with $\boldsymbol{\alpha}$ (directing deviator, fixing a direction in deviatoric space):

$$\boldsymbol{\mu}_k = m_1 \boldsymbol{e} + m_2 \boldsymbol{\alpha} + m_3 \boldsymbol{\alpha} \cdot \boldsymbol{\alpha} \tag{3}$$

The law of change of limit of micro fracture can be set in a following general view

$$\dot{\boldsymbol{\varepsilon}}_k = \sum_n \boldsymbol{E}_{kn} \dot{\boldsymbol{\sigma}}_n^f \equiv \left\langle E_{kn} \dot{\sigma}_n^f \right\rangle \tag{4}$$

where E_{kn} is the function of influence defining the contribution of n-th particle in change of micro fracture limit of k-th particle and symbol $\langle\ \rangle$ represent averaging throughout all micro particles. In special cases this relation can be simplified up to

$$\dot{\varepsilon}_k = \begin{cases} E_1 \dot{\sigma}_k^f + E_2 \dot{\boldsymbol{\sigma}}^f : \boldsymbol{\mu}_k + E_3 \left\langle \dot{\sigma}_k^f \right\rangle, & \boldsymbol{\mu}_k = \boldsymbol{\mu}_{k'} \\ E_2 \dot{\boldsymbol{\sigma}}^f : \boldsymbol{\mu}_k + E_3 \left\langle \dot{\sigma}_k^f \right\rangle, & \boldsymbol{\mu}_k \neq \boldsymbol{\mu}_{k'} \end{cases} \tag{5}$$

where $\boldsymbol{\mu}_{k'}$ is direction of active micro fracture.

For an establishment of connection of local laws of micro- and macroscopical deformation we shall take advantage of relations of Kroner's type:

$$(\dot{\boldsymbol{\sigma}} - \dot{\boldsymbol{\sigma}}_k) = \tilde{\boldsymbol{A}} : (\dot{\boldsymbol{\varepsilon}}_k - \dot{\boldsymbol{\varepsilon}}) \tag{6}$$

where $\tilde{\boldsymbol{A}}$ is tensorial function of the fourth rank of micro- and macro condition of material. The relations (6) allows to receive a number of widespread approaches in polycrystalline modeling with particular choice of function $\tilde{\boldsymbol{A}}$, for instance, approaches of type of Taylor, Voigt, Reuss, Eshelby, Kroner, advanced self-consistent models.

Stress of macro fracture is defined as the sum of micro fracture stresses of all micro particles:

$$\dot{\boldsymbol{\sigma}}_f = \sum_k \dot{\sigma}_k^f \boldsymbol{\mu}_k \tag{7}$$

Resulting formula

From here it is possible to receive

$$\dot{\boldsymbol{\sigma}}^f = -\dot{\boldsymbol{\varepsilon}} : \quad \left(\left\langle \frac{\tilde{\boldsymbol{D}}_4}{D_1} : \boldsymbol{\mu}_k \boldsymbol{\mu}_k \right\rangle + D_5 \left\langle \frac{\tilde{\boldsymbol{D}}_4}{D_1} : \boldsymbol{\mu}_k \right\rangle \left\langle \frac{\boldsymbol{D}_3}{D_1} : \boldsymbol{\mu}_k \right\rangle \right) : \\ : \quad \left(\tilde{\boldsymbol{I}} - \left\langle \frac{D_2}{D_1} \boldsymbol{\mu}_k \boldsymbol{\mu}_k \right\rangle - D_5 \left\langle \frac{D_2}{D_1} \boldsymbol{\mu}_k \right\rangle \left\langle \frac{D_3}{D_1} \boldsymbol{\mu}_k \right\rangle \right)^{-1} \tag{8}$$

where

$$D_1 = 1 - E_1 \boldsymbol{\mu}_k : (\tilde{\boldsymbol{A}} + \tilde{\boldsymbol{G}}) : \boldsymbol{\mu}_k \quad (9)$$

$$D_2 = 1 + E_2 \boldsymbol{\mu}_k : (\tilde{\boldsymbol{A}} + \tilde{\boldsymbol{G}}) : \boldsymbol{\mu}_k \quad (10)$$

$$D_3 = E_3 \boldsymbol{\mu}_k : (\tilde{\boldsymbol{A}} + \tilde{\boldsymbol{G}}) : \boldsymbol{\mu}_k \quad (11)$$

$$\tilde{\boldsymbol{D}}_4 = \tilde{\boldsymbol{A}} + \tilde{\boldsymbol{G}} \quad (12)$$

$$D_5 = \left(1 - \left\langle \frac{D_3}{D_1} \right\rangle\right)^{-1} \quad (13)$$

Here $\langle\ \rangle$ means averaging of the quantities, which is carried out only on active particles ($\sqrt{\boldsymbol{\varepsilon_k} : \boldsymbol{\varepsilon_k}} = \varepsilon_k$ and $\dot{\sigma}_k^f > 0$).

Results

Last relation defines resolving equation of the theory of the plasticity involving micro fractures. Algorithms of identification of universal parameters of the theory on the basis of accessible base experiments are presented in the work. On the basis of the presented model algorithms of numerical calculations by final elements method are developed. Results of comparison of numerical modeling with experimental data for triaxial tests of geomaterials are shown in the work.

References

[1] Yu. I. Kadashevich, V. V. Novozhilov (1968): On the effect of micro pre-stresses in the theory of plasticity. *Eng. J. Solids Mechanics*, **3**, 81–91. (in Russian)

[2] Yu. I. Kadashevich, V. V. Novozhilov, Yu. A. Chernyakov (1985): Theory of plasticity including micro strains. *Proc. of USSR AS*, **284**, 821–823. (in Russian)

[3] Yu. I. Kadashevich, Yu. A. Chernyakov (1992): Theory of plasticity, taking into account micro stresses. *Advances in Mechanics*, **15**, 3–39.

[4] V. P. Shneider, Yu. A. Chernyakov (2006): The development of micro deformations theory: the account of polycrystalline material grain sizes. In *Proceedings of third international conference Multiscale Material Modeling*, Freiburg (Germany), 530–533.

On Connection of the Theory of Micro Strains with Microplane Models

Yu. A. Chernyakov, V. P. Shneider

Dnipropetrovsk National University
Naukovy, 13, Dnipropetrovsk, 49050, Ukraine
chernyakova@fregat.dp.ua, shneider_vova@mail.ru

Summary: In the given work the description of the theory of micro strains is given. Close connection of the theory with microplane theories is shown. Lacks and advantages of both approaches to the description of plastic deformation of metals are analyzed.

Introduction

In work [1] the theory of micro strains which was the further development of the approaches stated in works of Novozhilov and his collaborators [2, 3] is stated. Interrelations between this theory and other theories of plasticity, in particular slip theories, physical theories of plasticity, structural models, have been established. In the given work the interrelation of the theory of micro strains with the microplane theories, which have received last time intensive development in the appendix to plasticity of metals [4, 5], is analyzed.

Main features of theory of micro strains

Scheme of the theory of micro strains, consists in assumption that the representative macro volume is consisting of final number of the interconnected micro particles. The stress-strain state of each micro particle is defined by micro stresses and micro strains. Thus there is accepted that there are exists at least two levels of the characteristic sizes: macro level defined by the size of representative macro volume, and micro level which characteristic size is defined by the size of micro particles. We shall note that in the theory the size of a micro particle is not fixed. By virtue of it the concept "micro particle" is purely conventional and only reflects the fact of existence of two characteristic levels at construction of constitutive relations.

Let us note the basic features of the theory of micro strains which distinguish it from other plasticity theories with structure. The first, there is enough detailed account of the internal stresses arising between various particles in a material. Physical nature of such stresses is connected with discrepancy of plastic deformation from grain to grain. The phenomenological approach to their account allows to abandon from necessity of experiments for definition of physical constants and allows to define them from macroscopical behavior. The second feature of the given theory is generalization of tensor of micro plastic strain on tensor of a general view that allows to construct the theory of plasticity of the polycrystals in deviatoric space, differing from the theory of plasticity of polycrystals in the same degree as a condition of plasticity of the Tresca and Mises. In the third, in the theory of micro strains the big attention is given to interference of plastic strains of individual particles. This moment also is a key at establishment of interrelation with other theories. With special choice of the law of interference of micro strains it is possible to receive the scheme of deformation like in microplane model.

Formulation of theory of micro strains

System of resolving equations of the theory of micro strains represented in the form [1-3] of

$$\boldsymbol{\sigma} = \tilde{\boldsymbol{G}} : (\boldsymbol{\varepsilon} - \boldsymbol{\varepsilon}_p) \quad (1)$$

$$\boldsymbol{\sigma} = \boldsymbol{\tau} + \boldsymbol{\rho} \quad (2)$$

$$\boldsymbol{\tau} = \tau \boldsymbol{\alpha} \quad (3)$$

$$\dot{\boldsymbol{\varepsilon}}_p = \dot{\varepsilon}_p \boldsymbol{\alpha} \quad (4)$$

$$\boldsymbol{\rho}(\boldsymbol{\alpha}, t) = \int_{\Omega} R(\boldsymbol{\alpha}, \boldsymbol{\alpha}') \boldsymbol{\varepsilon}_p(\boldsymbol{\alpha}', t) \mathrm{d}\Omega \quad (5)$$

$$\langle \boldsymbol{\sigma} \rangle - \boldsymbol{\sigma} = A \left(\boldsymbol{\varepsilon}_p - \langle \boldsymbol{\varepsilon}_p \rangle \right) \quad (6)$$

As a result of transformations we come to one integral equation

$$\boldsymbol{\sigma} : \boldsymbol{\alpha} = \tau_0 + \int_{\Omega} R_1(\boldsymbol{\alpha}, \boldsymbol{\alpha}') \varepsilon_p(\boldsymbol{\alpha}', t) \mathrm{d}\Omega \quad (7)$$

from which it is necessary to find intensity of micro plastic strain $\varepsilon_p(\boldsymbol{\alpha}', t)$ and domain of active micro plastic deformations $\boldsymbol{\alpha}' \in \Omega$. Macro plastic strain is defined then under the formula

$$\langle \boldsymbol{\varepsilon}_p \rangle = \int_{\Omega_\alpha} \varepsilon_p(\boldsymbol{\alpha}', t) \boldsymbol{\alpha}' \mathrm{d}\Omega \quad (8)$$

Interrelation with microplane theory

Now let us assume

$$\boldsymbol{\alpha} = (\boldsymbol{n} \otimes \boldsymbol{m} + \boldsymbol{m} \otimes \boldsymbol{n})/2 \quad (9)$$

i.e. we shall consider, that micro plastic strain occurs as a result of plastic slip on planes with normal $\boldsymbol{n}$ in the direction $\boldsymbol{m}$.

Then the resolving equation will become

$$\tau_{nm} = \tau_0 + \int_{\Omega} R_{nm}(\boldsymbol{n}, \boldsymbol{m}, \boldsymbol{n'}, \boldsymbol{m'}) \gamma(\boldsymbol{n'}, \boldsymbol{m'}, t) \mathrm{d}\Omega \quad (10)$$

This equation can be treated as the generalized resolving equation of slip theory. In particular it is shown in [3], that from last relation at

$$R_{nm}(\boldsymbol{n}, \boldsymbol{m}, \boldsymbol{n'}, \boldsymbol{m'}) = \delta(\boldsymbol{1} - \boldsymbol{n} \cdot \boldsymbol{n'} \boldsymbol{m} \cdot \boldsymbol{m'}) F(\gamma_{nm}) \quad (11)$$

the theory of Batdorf-Budiansky follows. Let us assume now

$$R_{nm}(\boldsymbol{n},\boldsymbol{m},\boldsymbol{n'},\boldsymbol{m'}) = R_n(\mathbf{1}-\boldsymbol{n}\cdot\boldsymbol{n'})R_m(\boldsymbol{m}\cdot\boldsymbol{m'}) \quad (12)$$

and $R_n(\mathbf{n}\cdot\mathbf{n}') = \delta(\mathbf{1}-\mathbf{n}\cdot\mathbf{n}')$, $R_m(\mathbf{m}\cdot\mathbf{m}') = \mathbf{m}\cdot\mathbf{m}'$, then it is easy to show, that on a plane with normal $\mathbf{n}$ the active direction always will be directed along tangential stress acting on this plane

$$\boldsymbol{m} = \boldsymbol{\sigma}_T = \boldsymbol{\sigma}\cdot\boldsymbol{n} - \sigma_N\boldsymbol{n} = (\boldsymbol{e}-\boldsymbol{n}\otimes\boldsymbol{n})\cdot(\boldsymbol{\sigma}\cdot\boldsymbol{n}) \quad (13)$$

and we obtain known [4, 5] relations of microplane model for metals:

$$\boldsymbol{\varepsilon}_p = \frac{3}{4\pi}\int\limits_{\Omega_n}\boldsymbol{\varepsilon}_{Tr}\cdot(\boldsymbol{n}\otimes\boldsymbol{\delta}+\boldsymbol{\delta}\otimes\boldsymbol{n})\mathrm{d}\Omega_n \quad (14)$$

Conclusions

Thus, in the given work it is shown, that microplane theories is one of subclasses of the theory of micro strains. Series of numerical calculations of plastic deformations of metals at complex loading has been lead for finding-out of quantitative and qualitative differences of both approaches. It is shown, that results are close enough at active loading. For complex cyclic loading the modified theory of micro strains [6] is used and the modified microplane theory is constructed, allowing to describe ratcheting.

References

[1] Yu. I. Kadashevich, V. V. Novozhilov (1968): On the effect of micro pre-stresses in the theory of plasticity. *Eng. J. Solids Mechanics* **3**, 81–91. (in Russian)

[2] Yu. I. Kadashevich, V. V. Novozhilov, Yu. A. Chernyakov (1985): Theory of plasticity including micro strains. *Proc. of USSR AS* **284**, 821–823. (in Russian)

[3] Yu. I. Kadashevich, Yu. A. Chernyakov (1992): Theory of plasticity, taking into account micro stresses. *Advances in Mechanics* **15**, 3–39.

[4] I. Carol, Z. P. Bazant (1997): Damage and plasticity in microplane theory. *Int. J. Solids Srructures* **34**, 3807–3835.

[5] M. Brocca, Z. P. Bazant (2000): Microplane constitutive model and metal plasticity. *Appl. Mech. Rev* **53**, 265–281.

[6] V. P. Shneider, Yu. A. Chernyakov (2006): The development of micro deformations theory: the account of polycrystalline material grain sizes. In *Proceedings of third international conference Multiscale Material Modeling*. Freiburg (Germany), 530–533.

Medical Image Processing and Biomechanical Analysis of Fibula Bone

C. Radu*, I. C. Roca

Faculty of Mechanical Engineering, Transylvania University of Brasov
Str. Grui, Bl. 9, Sc. B, Ap. 5, Zrnesti, Brasov, Romania
ciprian1_radu@yahoo.com, ilcrosca@unitbv.ro

Summary: This article briefly outlines the conceptual basis of biomechanics analysis and discusses a number of the key technical considerations involved, specifically from the standpoint of effective modelling of biomechanical systems. The purpose of this paper is to perform a biomechanical analysis of a human ankle joint and fibula bone by determining the reaction forces in static conditions using inverse dynamic method. Also this paper treats some theoretical aspects of a finite element analysis of a human fibular bone to validate the applicability of the finite element technique to this kind of complex structures.

Ankle joint reaction forces in static conditions

Using an inverse dynamics approach the reaction forces in the ankle joint can be calculated, where the anthropometrical data of 70 kg person are used as input data for biomechanical system [2].

Inverse dynamic method presumes some conditions:

- the human body is divided in segments;
- each segment is rigid and it has a fixed mass located as a point mass at its center of mass (which will be the center of gravity in the vertical direction);
- the location of each segment's center of mass remains fixed;
- the length of each segment remains constant;
- the friction force in the joint is null.

By using the stance phases of foot to the ground (Fig. 1), we can calculate the reaction forces and net joint moment in the ankle [2].

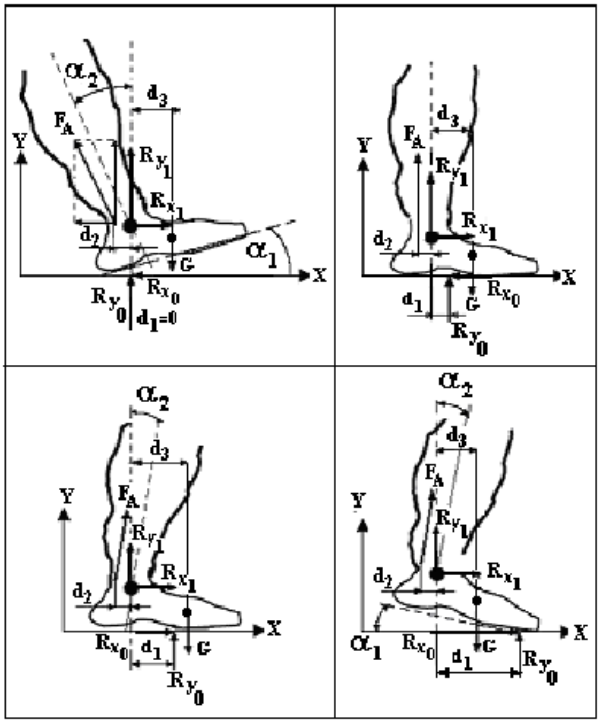

Figure 1: The foot contact fazes with the ground: 10%, 25%, 45%, 70%.

3D reconstruction of human fibula

The proposed solution is based on a method witch combine the imagine processing techniques and 3D computer graphics. The method adopted for visualization is the conversion of 2D image slice data, as grey value images. The resolution can vary from 0.2 to 1 mm. The program also generates high-resolution 3D renderings in different colours directly from the slice information. Contrast enhancement can be carried out interactively to improve the model. The segmentation mask can be displayed in a different colour on top of the image [1, 2].

The steps to obtain the human fibula 3D model are:

1. Import of all processor data witch are represented by 2D thomographic slice. The number o 2D slices are 72 and the height of each one is one millimeter. These 2D slices belong to a person with a weight of 70 kg.
2. Thresholding means that the segmentation object (visualized by a colored mask) will contain only those pixels of the image with a value higher than or equal to the threshold value. A low threshold value makes it possible to select the soft tissue of the scanned patient. With a high threshold, only the very dense parts remain selected. Detection of bone tissue can be obtained by using the optimal gray value, established between minimum value of 2080 and maximum value of 3056 Hounstield units.
3. The 3D representation of the ankle articulation and fibular bone (Fig. 1). As it can be seen in the picture below, the left hand said model represents the human ankle articulation and on the right hand said the fibular bone [1].

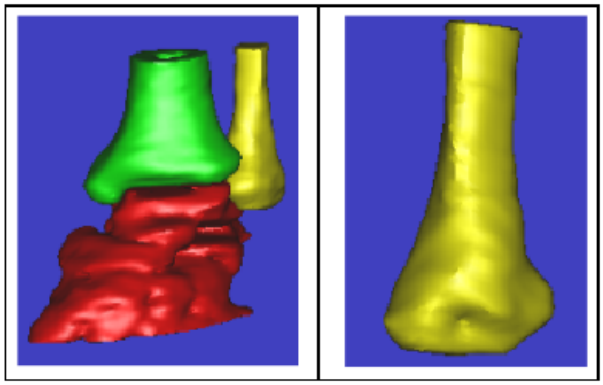

Figure 2: 3D representation of ankle joint and fibular bone.

Finite element analysis of human fibula

Finite element studies generally involve few stages. The first phase, known as preprocessing, involves prescribing the mesh geometry, specifying the material property distributions, and designating the loading [3]. The bone is modeled as nonhomogenous, orthotropic and linear elastic material. This means that the bone elastic modulus vary between 33% (when the density is 1.5 g/cm^3) and 62% (when the density is 2 g/cm^3) and has the higher value on axial direction then transversal and longitudinal direction. On the axial direction the elastic modulus is 19.34 GPa, on the transversal direction the value is 11.23 GPa and on the longitudinal direction the value is 9.74 GPa. Also the Poisson coefficient (ν_x = 0.31; ν_y = 0.18; ν_z= 0.18) and tensile strength (σ_x = 4.32 GPa;σ_y = 3.57 GPa; σ_z = 3.57 GPa) are different on the X, Y, Z directions [2–5].

In this case, when the material is orthotropic (composite material), for accurate results I have used ten node tetrahedral elements with the element mesh size of 2 mm. The finite element software has generated for fibular model a number of 498,910 nodes and 361,404 elements [2].

The 3D model is constrained on the superior part and on the inferior part is subjected with a compression force of 112.6 N. The compression force is the 1/6 part of the total reaction force witch acts in a human ankle having a weight of 70 kg [2].

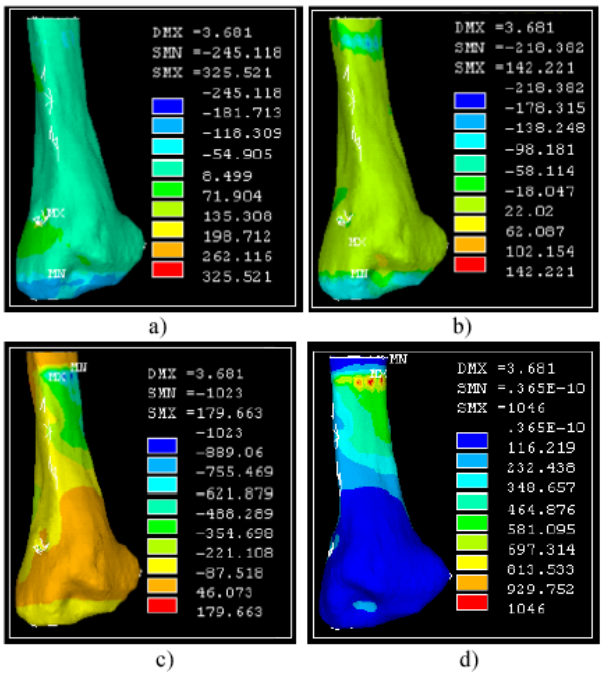

Figure 3: The finite element analysis results: a) the stress on the x direction (Sx); b) the stress on the y direction (Sy); the stress on the z direction (Sz); d) equivalent stresses.

References

[1] A. Watt (1995): *3D Computer Graphics*, Addison Wesley, England.

[2] C. Radu (2005): Improvements Apported to the Biomechanical Systems Modeling. In *Second Report of the PhD. thesis: Improvements Apported to the Prosthetic Elements by Rapid Prototyping*, Brasov.

[3] D. Thomas (2004): Finite Element Modeling in Musculoskeletal Biomechanics. In *Journal of Applied Biomechanics*, University of Iowa.

[4] J. H. Keyak, H.B. Skinner (1992): Three-dimensional finite element modeling of bone. *Journal of Biomedical Engineering*.

[5] W. A. M. Brekelmans, H. W. Poort, T. J. J. H. Sloof (1972): A new method to analyze the mechanical behavior of skeletal parts. *Acta Orthopaedica Scandinavica*.

Low Frequency Approximation for Recovering Relaxed Viscoelastic Parameters of Bones

L. Le Marrec[1*], J.-P. Groby[2], A. Wirgin[3], L.R. Rakotomanana[1]

[1]IRMAR, Université de Rennes 1, Campus de Beaulieu, 35042 Rennes cedex, France
loic.lemarrec@univ-rennes1.fr, lalaonirina.rakotomanana-ravelonarivo@univ-rennes1.fr

[2]CMAP, Ecole polytechnique, 91128 Palaiseau cedex, France
groby@cmapx.polytechnique.fr

[3]LMA, 31 chemin Joseph-Aiguier 13402 Marseille cedex 20, France
wirgin@lma.cnrs-mrs.fr

Summary: Bone characterization is still a relevant problem due to the complexity of bone tissue. Bones are composed of complex porous media at the microscopic scale and at macroscopic scales we deal with homogenized properties, that have to be determined. A first approximation of long bones consists in considering the cortical part to be filled with an isotropic, linear, viscoelastic medium, and neglecting the trabecular part. The configuration in the sagittal plane takes the form of a circular viscoelastic cylinder, placed in a softer viscoelastic medium. Considering circular section, the problem is analytically solved in the frequency domain, providing the direct problem. Inverse problem is focused on the low frequency problem in order to retrieve relaxed properties of the cortical bone. The algorithm is based on the low frequency approximation of the analytical solution of our problem. In particular, we show how low frequency approximation can be relevant to highlight the ill posed character of the inverse problem.

Introduction

We are concerned by cortical bones in the appendicular portion of long bones. Cortical bone is arranged as bundles of osteon packed tightly together. Bone is a highly heterogenous porous anisotropic media at both micro and macro scale. As we deal with wavelengths large compared to the size of bundles of osteon, homogenized models involving homogenized parameters are appropriate. Because of the low porosity of cortical bones ($3-5\%$), we are dealing with a viscoelastic medium [1] to model cortical tissue. We show how we could solve the problem of the diffraction of a cylindrical incident wave striking a viscoelastic tube (representative of the cortical bone), by an analytical method.
Finally, we consider the low frequency approximation of the analytical solution and show how it can used to solve explicitly, but partially, the inverse problem of the recovery of mechanical parameters of the long bones.

Direct problem

Measurement and material ingredient We consider that the medium M^0, occupying the host domain Ω_0 (the surrounding domain and the medullar cavity) is viscoelastic such that $\rho^0 = 1030$ kg·m^{-3}, $\left(c_S^0\right)_R = 200$ m·s^{-1}, $Q_S^0 = 100$, $\left(c_P^0\right)_R = 1500$ m·s^{-1}, $Q_P^0 = 150$, values which are representative of muscles [2].
In the appendicular part, cortical bone is transversally isotropic and cancelous bones are neglected. The bone is solicited by an incident P wave radiated by a line source located in the surrounding medium. We assume that the excited portion of the bone is sufficiently long for the latter to be assimilated with an infinitely-long cylinder. In such case, we are dealing with a 2-D viscoelastic diffraction problem.
Heterogeneity and porosity of cortical bone are accounted by considering medium M^1 filling Ω_1 (cortical ring) to be a homogenized viscoelastic solid such that $\rho^1 = 1850 kg.m^{-3}$, $\left(c_S^1\right)_R = 1800$ m·s^{-1}, $Q_S^1 = 30$, $\left(c_P^1\right)_R = 3050$ m·s^{-1}, $Q_P^0 = 50$ ([2]). Note that in such model, dissipation in the cortical bone is of particular interest for osteoporosis diagnosis.
Finally, we consider a circular tubes (inner radius r_{ext} and outer radius r_{in}). This is consistant with the low frequency approximation that would be used.

Governing equations We solve the scattering problem in an analytical manner. The problem is to determine the field in the subdomain Ω_0. We are dealing with the Fourrier transform of the scalar and vectorial potentials, respectively $\phi(\mathbf{x},\omega)$ and $\boldsymbol{\psi}(\mathbf{x},\omega) = \psi(\mathbf{x},\omega)\mathbf{i}_3$ related to the diplacement $\mathbf{u}^j$ through $\mathbf{u}^j(\mathbf{x},\omega) = \nabla\phi^j(\mathbf{x},\omega) + \nabla \wedge \boldsymbol{\psi}^j(\mathbf{x},\omega)$ These potentials verify Helmholtz equation (with source terms at $\mathbf{x^s} = (r^s,\theta^s)$ for scalar potential). In the cylindrical coordinate system, these potentials satisfy the displacement and the traction continuity conditions on the outer and inner interfaces and the outgoing wave condition.
The viscoelastic properties are expressed by complex wave number depending on frequency and on the relaxed material parameters.

Field representations The incident P wave is radiated by a line source located at $\mathbf{x^s} = (r^s,\theta^s)$. Incident, scattered and transmitted fields are represented thanks to cylindrical functions. For exemple, in the case of scattered fields (satisfying

radiation condition) :

$$\begin{cases} \phi^{0d} = \sum_{m=0}^{\infty} a_m^0 \epsilon_m H_m^{(1)}(k_\phi^0 r)\cos\left(m\left(\theta-\theta^s\right)\right) \\ \psi^{0d} = \sum_{m=0}^{\infty} b_m^0 \epsilon_m H_m^{(1)}(k_\psi^0 r)\sin\left(m\left(\theta-\theta^s\right)\right) \end{cases} \quad (1)$$

wherein $H_m^{(1)}()$ are the m-th order and the first kind Hankel function and $\epsilon_0 = 1$, $\epsilon_{m>0} = 2$. Our goal being to express the coefficients a_m^0 and b_m^0, this is done by first expressing the continuity of the boundary conditions at each interface and by using the orthogonality relations of the above $\cos m(\theta-\theta^s)$ functions, secondly by inverting the system.

Low frequency approximation We follow the approach exposed in [3]. We first define $\chi = k_\phi^0 r_{ext}$ and $e = \dfrac{r_{int}}{r_{ext}}$. We assume that χ is small enough (i.e., $0 < \chi \ll 1$) for it to be true for all the arguments of all cylindric functions in the system expressing the continuity condition. This authorizes use of the small-argument asymptotic forms :

$$\begin{aligned} &H_0^{(1)}(\zeta) \sim \frac{2\mathrm{i}}{\pi}\ln\zeta \;;\; H_m^{(1)}(\zeta) \sim -\frac{\mathrm{i}(m-1)!}{\pi}\left(\frac{\zeta}{2}\right)^{-m} \\ &J_m(\zeta) \sim \frac{1}{m!}\left(\frac{\zeta}{2}\right)^{m} \;;\; \zeta\to 0,\; m=0,1,... \end{aligned} \quad (2)$$

After a series of algebraic manipulations, the following asymptotic form of a_m^0 and b_m^0 are found (for $m > 1$ the terms are negligible in regards to χ^2):

$$\begin{aligned} &a_0^0 = \tilde{a}_0^0\cdot\chi^2 + O\left(\chi^4\right) \;,\; a_1^0 = \tilde{a}_1^0\cdot\chi^2 + O\left(\chi^4\right) \\ &b_1^0 = \tilde{b}_1^0\cdot\chi^2 + O\left(\chi^4\right) \end{aligned} \quad (3)$$

wherein

$$\begin{aligned} \tilde{a}_0^0 &= \frac{\mathrm{i}H_0^{(1)}\left(k_\phi^0 r^s\right)}{4}\frac{\mathrm{i}\pi}{4}F(\Pi_R^0,\Pi_R^1,\Pi_R^2,\mu_R^0,\mu_R^1,\mu_R^2,e) \\ \tilde{a}_1^0 &= \frac{\mathrm{i}H_1^{(1)}\left(k_\phi^0 r^s\right)}{4}\left(\frac{\mathrm{i}\pi}{8}\right)G(\rho^0,\rho^1,\rho^2,e) \\ \tilde{b}_1^0 &= \sqrt{\frac{\Pi_R^0}{\mu_R^0}}\times\tilde{a}_1^0 \end{aligned} \quad (4)$$

where, the function F and G are independ of the frequency and are given in Apendix.
Eq. (4) only involves the Lamé coefficients of the relaxed parameters Π_R^j and μ_R^j, $j = 0,1,2$ because $\lim_{\omega\to 0}\Pi^j(\omega) = \Pi_R^j$ and $\lim_{\omega\to 0}\mu^j(\omega) = \mu_R^j$. Then, by employing the low frequency approximation, we deal with the static characteristics of the involves media and not at all with their frequency behavior (i.e. the quality factors).

Inverse problem

Recovering the scattering coefficients At a point $\mathbf{x} = (r,\theta)$, the low frequency approximation of the diffracted potentials in the host solid becomes (to second order in χ)

$$\begin{aligned} \phi^{0d}(\mathbf{x},\omega) &\approx \left(\tilde{a}_0^0 H_0^{(1)}\left(k_\phi^0 r\right) + 2\tilde{a}_0^1 H_1^{(1)}\left(k_\phi^0 r\right)\cos\left(\theta-\theta^s\right)\right)\chi^2 \\ \psi^{0d}(\mathbf{x},\omega) &\approx 2\tilde{b}_1^0 H_1^{(1)}\left(k_\psi^0 r\right)\chi^2\sin\left(\theta-\theta^i\right) \end{aligned} \quad (5)$$

We are considering that a multi-frequency scattered field is available all around the bone in a circular ring of radius b. Making use of the orthogonality relations we uncouple the different order of the cylindrical decomposition, and we define:

$$\begin{aligned} \mathcal{I}_m^\phi(\omega) &= \int_{\theta^i}^{\theta^i+\pi}\phi^{0d}(b,\theta,\omega)\cos m\left(\theta-\theta^i\right)\frac{d\theta}{\pi} = a_m^0 H_m^{(1)}\left(k_\phi^0 b\right) \\ \mathcal{I}_m^\psi(\omega) &= \int_{\theta^i}^{\theta^i+\pi}\psi^{0d}(b,\theta,\omega)\sin m\left(\theta-\theta^i\right)\frac{d\theta}{\pi} = b_m^0 H_m^{(1)}\left(k_\psi^0 b\right) \end{aligned} \quad (6)$$

The inversion is then obtained by extrapolating the previous parameters to their zero frequency limit. In a second step the mechanical parameters are obtained trough the equation:

$$\begin{aligned} \lim_{\omega\to 0}\mathcal{I}_0^\phi(\omega) &= \tilde{a}_0^0 H_m^{(1)}\left(k_\phi^0 b\right)\chi^2 = \mathcal{F}\times F \\ \lim_{\omega\to 0}\mathcal{I}_1^\psi(\omega) &= \tilde{b}_1^0 H_m^{(1)}\left(k_\psi^0 b\right)\chi^2 = \mathcal{G}\times G \end{aligned} \quad (7)$$

Where F and G are the preceding equation of the material parameters of bones and host media, and $\mathcal{F}$ and $\mathcal{G}$ are complex function of known coefficients (measurements parameters and host material properties).
These relations show that the field is a nonlinear function of the material parameters. Knowing e, we could only retrieve the density ρ^1 and get an equation relating Π_R^1 and μ_R^1.

Conclusion

The last relations shows that the low-frequency perturbation scheme enables an explicit (partial) solution of the inverse problem of the reconstruction. Supposing that the host media and the external radius is known, we are interested in 4 bone parameters (three material static parameters of the bone specimen : Π_R^1 , μ_R^1 ρ^1 and thickness e) but only two of them can be imaged through low frequency measurement using such model.

Apendix

$$\begin{aligned} &F(\Pi_R^0,\Pi_R^1,\Pi_R^2,\mu_R^0,\mu_R^1,\mu_R^2,e) = \{ \\ &\left(\Pi_R^1-\mu_R^1-\Pi_R^2+\mu_R^2\right)\left(\Pi_R^0-\mu_R^0+\mu_R^1\right)e^2 + \\ &\left(\Pi_R^0-\mu_R^0-\Pi_R^1+\mu_R^1\right)\left(\Pi_R^2-\mu_R^2+\mu_R^1\right)\}/\{ \\ &\left(\Pi_R^1-\mu_R^1-\Pi_R^2+\mu_R^2\right)\left(\mu_R^0-\mu_R^1\right)e^2 + \\ &\left(\Pi_R^1-\mu_R^1+\mu_R^0\right)\left(\Pi_R^2-\mu_R^2+\mu_R^1\right)\} \\ &G(\rho^0,\rho^1,\rho^2,e) = \frac{\left(\rho^2-\rho^1\right)e^2+\rho^1-\rho^0}{\rho^0} \end{aligned} \quad (8)$$

References

[1] V. Morochnik, J.P. Bardet (1996): Viscoelastic approximation of poroelastic media for wave scattering problems., *Soil Dynam.Earthqu.Engrg.*, **15**, 337–346.

[2] E.L. Masen, H.J. Sathoff, J.A. Zagzebski (1983): Ultrasonic shear wave properties of soft tissues and tissue-like materials. *J.Acoust.Soc.Am.*, **74**, 1346–1355.

[3] Z.E.A. Fellah, J.-P. Groby, E. Ogam, T. Scotti, A. Wirgin (2005): Acoustic identification of a poroelastic cylinder. *ArXiv, physics/0511242*

Phase Interaction in a Heterogeneous Material on Macro- and Nanoscale: Numerical Approach

A. S. Kravchuk[1*], **P. Neittaanäki**[2]

[1]Moscow State University (Informatics and Instruments)
Stromynka, 20, Moscow 107846, Russia
kravchuk_ biocom@mail.ru

[2]Department of Mathematical Information Technology
P.O. Box 35 (Agora), FIN-40014 University of Jyväskylä, Finland
pn@mit.jyu.fi

Summary: This paper describes some results obtained for the contact problems arising in mathematical modeling of the heterogeneous materials. Variational method developed in the previous work for the friction contact problem is used in the macroscale. In the nanoscale a molecular dynamic and static approach is proposed and realized as well as a hybrid model.

Introduction

This work is devoted to the development of numerical methods for finding of the contact stress interaction at the separation boundary of two different phases in a heterogeneous material, as well for stresses and strains near this boundary. Two material models are used: traditional continuum model for an elastic solids, and molecular dynamic and/or quasi-static models. In the 1st kind problems the contact interaction is investigated for the following conditions at the separation boundary: continuous contact, increasing or decreasing contact without- and with Coulomb friction, adhesion contact with failure, i.e., with crack propagation. The solution methods are given in [1]. A generalization consists of the development of algorithms onto two deformed body. At nanoscale level two models are used: the first one is two lattices composed from different kind of particles, the second model is a homogeneous lattice (nanocoating) interacting with an elastic body. First kind problem are solved by the molecular dynamic methods [2], Newtons iteration are used for quasi-static problem solution. A newness of this part consists of development of a hybrid model which a continuum and discrete particles with long-range interaction are used simultaneously.

Mathematical setting and discretization

Let Ω_1 and Ω_2 be two deformed solids (two homogeneous phase) in contact, and Σ_C be the separation boundary. In an internal point of Ω_1 and Ω_2 the equilibrium equations hold. The following boundary condition holds at the any point of Σ_C :

1. contact displacement and forces (scalar product of the stress tensor to the external unit normal vector) are equal one to other for the continuous contact,
2. impenetrability condition and non positiveness of the contact pressure holds for the frictionless increasing or decreasing contact, with zero tangential contact force,
3. in a friction contact problem the Coulomb friction law holds on Σ_C.

Discretization with respect to the spatial variables is made with the boundary element method (BEM), using the fundamental solution for 2D problems, Boussinesq and Cerruti formulae for 3D problems. The finite difference approximation is used for the discretization with respect to load parameter to take into account the history of a loading. Equations for a lattice are the traditional 2^{nd} Newton law equations, with the forces defined by a potential of the long-range interaction. Verlet integration algorithm is used [2].

Examples

In the frame of the contact problem for two elastic bodies the following mechanical phenomena were found.

- There exists a critical angle between the separation boundary and the boundary of the domain $\Omega_1 \cup \Omega_2$: when a current value of such angle exceed this critical value then an unbounded increase of the contact stresses take place with the movement to the point of intersection of the mentioned two boundary; this phenomenon was analyzed for 2D problems.
- The contact stresses depends on the loading history when the Coulomb friction is taken into account; this dependence was detected for 2D- and 3D friction contact problems.
- The tangential contact stress is smooth if we use step-by-step algorithm for the friction contact problem, and it has a discontinuous derivative if we do not take into account a loading history.

Some interesting results of this part of work are presented in Figs. 1–2. The curves in Fig. 1 relate to 2D problem and show the distribution of the normal contact pressure of the contact interaction between a rigid rough fragment of the broken reinforced fiber in the deformed matrix of a composite material. The Coulomb friction law is used. It can be seen that there exists a concentration of the contact stresses near the end of

the fiber. Theoretically this stress tends to infinity when we approach to fiber ends. Solid curves in Fig. 1 correspond to Galin's and Spence's solution, dotted lines represent the numerical solution obtained with BEM. Note that for a small length of the fiber fragment the numerical solutions are almost the same that the analytical ones.

Fig. 1 shows some results of the numerical solution of a 3D friction contact problem for a fragment of the cylindrical rigid rough fiber contacting with the plan layers. The contact stresses increase when we approach to the ends of a fragment. Theoretically there exists the limit equal to infinity. The presented friction stresses are the modulus $|\vec{\sigma}_T|$ of the friction stress vector (Euclidean norm). Note that the solution is obtained for 10 steps of the external load being an approach of the layers. A sections of the surface $|\vec{\sigma}_T(x, y)|$ by a plane parallel to the cylinder axis is a smooth curve with a maximum corresponding to the separation point of the stick and slip domains. Note that for one loading step this curve is not smooth.

A theory of interaction of a coating with a coated material at the nanoscale is proposed. This theory is based on the molecular static and molecular dynamic approach [2]. Some results of the numerical experiments are shown in Fig. 3. Theses results relate to a chain composed from two different kinds of atoms: atoms numbered 0,1,2,..., N_1 correspond to Cu, atoms $N_1, ..., N_2$ correspond to Ag. Atom No "0" is fixed, atom No "$N_1 + N_2$" is loaded by a given displacement, and there exists a gap between N_1 and N_2-th atoms. The calculation was made for Morse's potential with the constants (and dimensionalities of all the quantities) taken in [2]. The number of the load steps is equal to 1000 for maximal displacement of the last atom equal to 25. The solid curves correspond to 500 steps, the dotted curves, (a) for the force acting on the atom No "I" from right, and (b) for the displacement of the atom, correspond to the final state of the system with the gap equal to 1. It can seen that the destroyed bond correspond to the junction point of two materials. Note that inside two fragments of chain the displacements are a linear functions and the interaction force is constant. Then we can use the equation of a deformed continuum in such a subdomains. Only near the ends of the chain and near the junction point of two different materials we must use the molecular static (or dynamic) approach. Some applications of the molecular dynamic approach to a biomedical nanotechnology were investigated too.

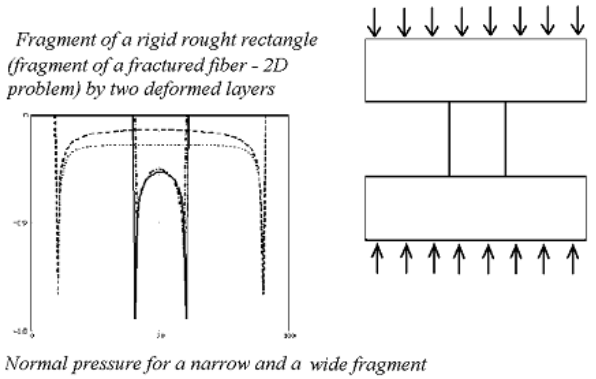

Figure 1: Distribution of the normal contact stresses.

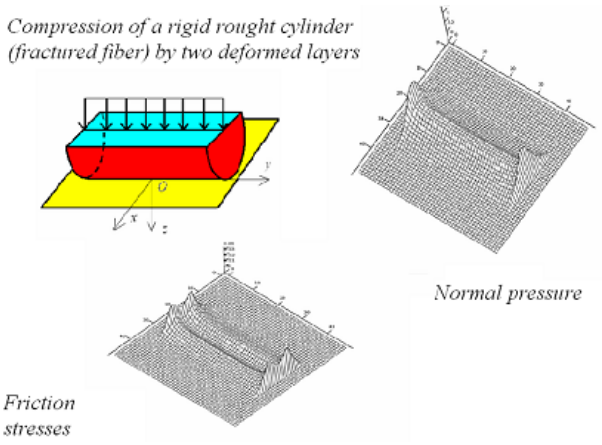

Figure 2: Distribution of the contact stresses.

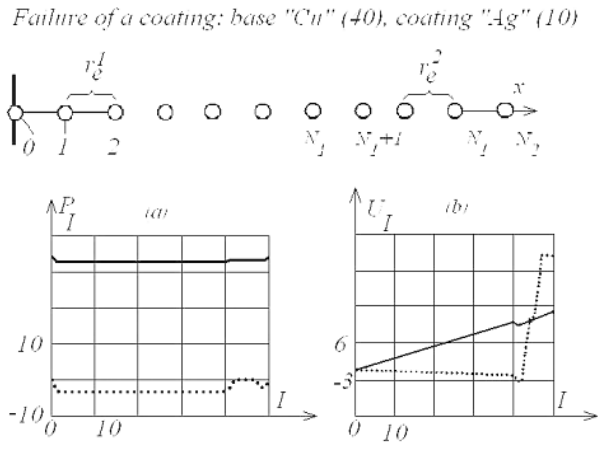

Figure 3: Displacements and forces in an atom chain (one-dimensional model of a nanocoating).

Acknowledgements

This work was partly supported by the Tekes MASI program (Finnish Academy of Sciences), and grant No 05-01-00591, SS-1245.2006.1 of the National Scientific Foundation of Russia.

References

[1] A. S. Kravchuk, P. Neittaanmäki (2007): *Variational and Quasi-variational Inequality in Mechanics.* To appear in Springer.

[2] M. Rieth (2003): *Nano-Engineering in Science and Technology.* World Scientific Press, New Jersey etc.

Numerical Solution of Newtonian and Non-Newtonian Fluids in the Branching Channel

R. Keslerová*, K. Kozel

CTU in Prague, Fac. of Mechanical Engineering, Dept. of Technical Mathematics
Karlovo nám. 13, 121 35 Praha 2, Czech Republic
kozelk@fsik.cvut.cz, keslerov@marian.fsik.cvut.cz

Summary: This paper describes the numerical solution of Newtonian and non-Newtonian fluid flows in two dimensional and three dimensional branching channel. Viscous incompressible laminar fluid flow is considered. The system of generalized Navier-Stokes equations and the continuity equation presents the mathematical model. This unsteady system (repared by artificial compressibility method) is solved numerically using finite volume method in conjuction with multistage Runge-Kutta method. The numerical results for three dimensional case are presented.

Mathematical model

Firstly, we consider the non-Newtonian flows. The generalized system of two dimensional Navier-Stokes equations and continuity equation for incompressible laminar flows in conservative form is

$$\tilde{R}W_t + F_x + G_y = \frac{\tilde{R}}{\mathrm{Re}}(R_x + S_y), \quad \mathrm{Re} = \frac{q_\infty l}{\nu}, \tag{1}$$

where q_∞ is reference velocity value and

$$W = \mathrm{col}\|p, u, v\|, \quad \tilde{R} = \mathrm{diag}\|0, 1, 1\|, \tag{2}$$

$$F = \mathrm{col}\|u, u^2 + p, uv\|, \quad G = \mathrm{col}\|v, uv, v^2 + p\|, \tag{3}$$

$$R = \mathrm{col}\|0, g_{11}, g_{21}\|, \quad S = \mathrm{col}\|0, g_{12}, g_{22}\|. \tag{4}$$

We used one of the known non-Newtonian models

$$g_{ij} = 2 \mid e \mid^r e_{ij}, \qquad e_{ij} = \frac{1}{2}\left(\frac{\partial u_i}{\partial x_j} + \frac{\partial u_j}{\partial x_i}\right). \tag{5}$$

For Newtonian fluids (special form of the previous system with $r = 0$) the system of Navier-Stokes equations and continuity equations for incompressible laminar flows reads

$$\tilde{R}W_t + F_x + G_y = \frac{\tilde{R}}{\mathrm{Re}}\Delta W. \tag{6}$$

Numerical solution

The artificial compressibility method is used to find steady state solutions. Then we can rewrite system (1) (non-Newtonian fluids) or (6) (Newtonian fluids) as

$$W_t = -(\tilde{F}_x + \tilde{G}_y) \tag{7}$$

where

$$\tilde{F} = F - \frac{1}{\mathrm{Re}}F^v, \quad \tilde{G} = G - \frac{1}{\mathrm{Re}}G^v$$

F and G are inviscid fluxes defined by (3) and F^v and G^v are viscous fluxes represented right hand side in the systems (1) and (6).

The system of equations (7) is integrated over D_{ij} (finite volume cells). After applying mean value and Green's theorems we get

$$W_t \mid_{ij} = -\frac{1}{\mu_{ij}} \oint_{\partial D_{ij}} \tilde{F}\mathrm{d}y - \tilde{G}\mathrm{d}x. \tag{8}$$

The integrals on the right hand side are numerically approximated by

$$W_t \mid_{ij} = -\frac{1}{\mu_{ij}} \sum_{k=1}^{4} \tilde{F}_{ij,k}\Delta y_k - \tilde{G}_{ij,k}\Delta x_k. \tag{9}$$

The system of ordinary differential equations (9) is solved by finite volume method. We used multistage Runge-Kutta method as numerical method for this system

$$\begin{aligned} W_{ij}^n &= W_{ij}^{(0)} \\ W_{ij}^{(r)} &= W_{ij}^{(0)} - \alpha_r \Delta t \overline{R} W_{ij}^{(r-1)} \\ W_{ij}^{n+1} &= W_{ij}^{(m)} \qquad\qquad r = 1, \ldots, m, \\ \overline{R}W_{ij}^n &= RW_{ij}^n - DW_{ij}^n, \end{aligned} \tag{10}$$

where for our computations we used $m = 3$, three-stage Runge-Kutta coefficients $\alpha_1 = \alpha_2 = 0.5,\ \alpha_3 = 1$.

The steady residual RW_{ij} is defined by

$$\begin{aligned} RW_{ij} = \frac{1}{\mu_{ij}} \sum_{k=1}^{4} \Bigg[&\left(F_k - \frac{1}{\mathrm{Re}}F_k^v\right)\Delta y_k - \\ &- \left(G_k - \frac{1}{\mathrm{Re}}G_k^v\right)\Delta x_k \Bigg], \end{aligned} \tag{11}$$

the term DW_{ij} presents the artificial viscosity of Jameson's type (for details see, e.g., [2])

In order to satisfy the stability condition the time step is chosen as (for details see, [1]):

$$\Delta t = \min_{i,j,k} \frac{\mathrm{CFL}\ \mu_{ij}}{\rho_A \Delta y_k + \rho_B \Delta x_k + \frac{2}{\mathrm{Re}}\left(\frac{(\Delta x_k)^2 + (\Delta y_k)^2}{\mu_{ij}}\right)}, \tag{12}$$

$$\rho_A = \mid \hat{u} \mid + \sqrt{\hat{u}^2 + 1} \qquad \rho_B = \mid \hat{v} \mid + \sqrt{\hat{v}^2 + 1},$$

$\mid \hat{u} \mid, \mid \hat{v} \mid$ are the maximal values of the components of velocity vector inside the computational domain.

The computation is performed until the value of the L^2-norm of residual satisfes Rez $W_{ij}^n \leq \epsilon_{ERR}$ with ϵ_{ERR} small enough

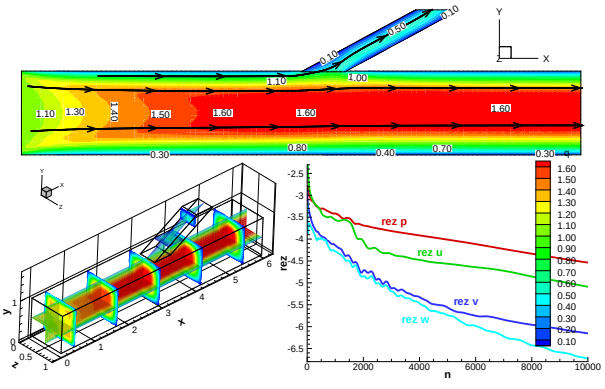

Figure 1: Velocity isolines of 3D channel for non-Newtonian fluids.

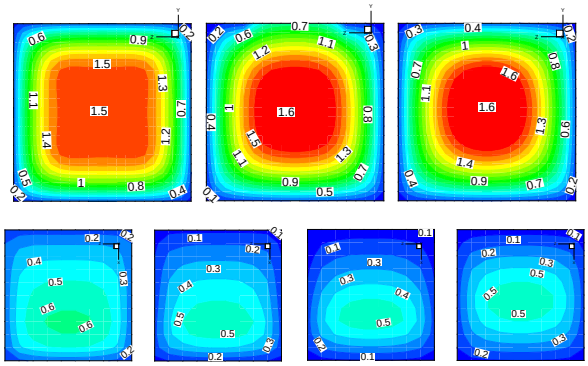

Figure 2: Velocity magnitude distribution in the cuts of 3D channel from Fig. 1.

(MN denotes the number of grid cells in the computational domain), where

$$\text{Rez } W_{ij}^n = \sqrt{\frac{1}{MN}\sum_{ij}\left(\frac{W_{ij}^{n+1} - W_{ij}^n}{\Delta t}\right)^2}. \qquad (13)$$

Numerical results

We present the numerical results for 3D branching channel. Fig. 1 and Fig. 2 show the fluid velocity distribution and cuts of main and branching parts of the channel for the non-Newtonian fluids in 3D channel, Reynold's number is defined by Re $= q_\infty 4S_1/\mu O$, Re = 300 for this case. In the Fig. 3 and Fig. 4 the velocity isolines and cuts of both parts of the channel for Newtonian fluids with the Reynold's number 300 is shown. The history of convergence of the residuals of the vector $W = (p, u, v, w)^T$ is presented. By the symbol q the velocity magnitude is denoted, i.e. $q = \sqrt{u^2 + v^2 + w^2}$.

Acknowledgements: This work was partly supported by grant A100190505 and Research Plan MSM 68 40770003.

References

[1] R. Dvořák, K. Kozel (1996): *Mathematical Modelling in Aerodynamics*. CTU Prague.

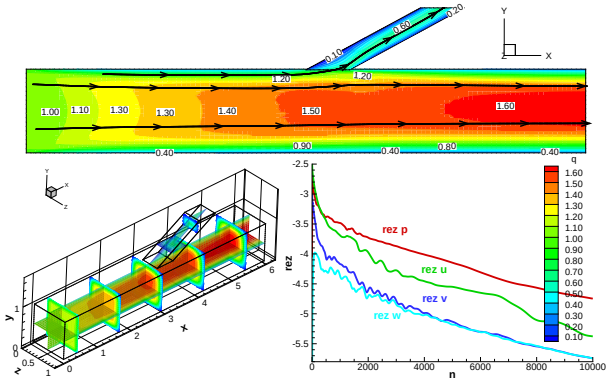

Figure 3: Velocity isolines of 3D channel for Newtonian fluids.

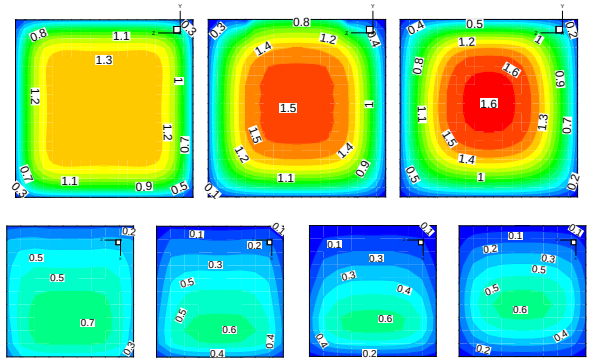

Figure 4: Velocity magnitude distribution in the cuts of 3D channel from Fig. 3.

[2] R. C. Swanson, E. Turkel (1997): Multistage Schemes with Multigrid for Euler and Navier-Stokes Equations. *NASA Technical Paper 3631*.

[3] R. Keslerová, K. Kozel (2006): Numerical Solution of Incompressible Laminar Flows. *Proc. The 13th International Conference on Fluid Flow Technologies CMFF'06*, Budapest, Hungary.

A Cellular Model of Viscoelastic Material

F. Moravec*, M. Müller, M. Holeček,

Department of Mechanics
University of West Bohemia in Pilsen, Husova 11, 306 14 Plzeň, Czech Republic
fanny@kme.zcu.cz, holecek@kme.zcu.cz

Summary: The viscoelastic behaviour of a material of which microstructure is formed of elastic balls floating in a viscoelastic matrix is studied. The model is based on expressions of the elastic and the dissipative potentials resulting from the work and the power of forces developed at the micro-scale during reconfiguring between micro-constitutents.

Introduction

Viscoelastic behaviour is typical of a number of materials such as polymers and biological tissues. These materials have memory but typically this memory fades with time. Assuming the time fading to be enough important, the short time history of the deformation can be represented by the rate of deformation [1]. General constitutive law for a material where stress at a given material point depends on deformation and on the rate of deformation at that point, is

$$\mathbf{S}(t) = p\mathbf{C}^{-1} + 2\frac{\partial W^e(\mathbf{C})}{\partial \mathbf{C}} + 2\frac{\partial W^v(\dot{\mathbf{C}}, \mathbf{C})}{\partial \dot{\mathbf{C}}}. \qquad (1)$$

Herein the deformation is assumed to be isochoric ($\sqrt{\det \mathbf{C}} = 1$, $\mathbf{C}$ is the right Cauchy-Green strain tensor) and p in the hydrostatic pressure. The key question when modeling viscoelastic material is consequently "which" expressions have to be chosen for the elastic and the dissipative potentials W^e and W^v? It is clear that these expressions should reflect the reality of material constitution: they define the "constitutive" law of material behaviour. Unfortunately it is impossible to take all aspects of the material microstructure into account in a reasonable model. For instance, here, the microstructure is averaged to model the heterogeneous material as a material where microstructure is constituted of inclusions floating in a matrix. In what follows, the term "balls" is preferred over "inclusions" because the balls will be considered to be smoother than the matrix. Moreover balls are assumed to be incompressible. The elastic behaviour of such a material has been already studied in details in [2]. In this paper viscoelasticity is included to the material behaviour assuming the matrix to be viscous. Material model includes some internal variables in terms of lengths sizes of balls and distances between balls. In addition to the macroscopic constitutive law (1), the study asks for the laws governing the time evolution of these internal variables. They are given by the compensation at the micro-scale between the elastic forces due to the stretching of the elastic components and the viscous force due to the fluid movement in matrix. Work and power of these forces are essential quantities for the constitutive law. They are used to define the expressions of the elastic and the dissipative potentials.

Expressions of potentials

Thanks to the determinism of the considered material microstructure, the elastic and the dissipative potentials occurring in the expression (1) can be expressed as functions of the macroscopic deformation and of the microscopic configuration. The microscopic configuration is governed by sizes c_i of balls and the distances Δ_i between balls, $i = 1 \dots 3$ (see Figure 1) so that $W^e = W^e(\mathbf{F}, c_i, \Delta_j)$ and $W^v = W^v(\mathbf{F}, \dot{\mathbf{F}}, c_i, \Delta_j)$. Changes in these internal variables' values lead to microscopic material restructuring. Micro-restructuring is accompanied by development of forces at the micro-scale. These forces are of two kinds. Elastic forces are due to the extension or the contraction of elastic components. Viscous forces are implied by the fluid movement of the matrix. Then, the main idea of this work was to express the elastic and the dissipative potentials as the densities of the work and of the power of these forces, respectively. For simplicity, the model of linear springs is used for averaging the elastic components. Elastic forces are forces developed by the contraction or the extension of springs:

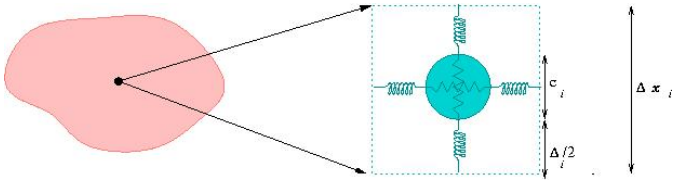

Figure 1: Material which microstructure is formed of 'balls and springs'.

$$f^e = K(h - h^{(0)}), \qquad (2)$$

where f^e is force, K is rigidity and h and $h^{(0)}$ are current and rest lengths, respectively. The work w^e of the force f^e is then

$$w^e = \int f^e \mathrm{d}h = \frac{K}{2}(h - h^{(0)})^2. \qquad (3)$$

The elastic potential W^e is defined as the density of the sum of works developed in all elastic components within a representative volume element (RVE). With $h = c_i$ in balls and $h = \Delta_i$ between balls, $i = 1 \dots 3$, we obtain

$$W^e = \frac{1}{2V_{\mathrm{rve}}} \sum_{i=1}^{3} \left(K_i^c (c_i - c_i^{(0)})^2 + K_i^{\Delta} (\Delta_i - \Delta_i^{(0)})^2 \right), \qquad (4)$$

where K_i^c and K_i^{Δ} are the rigidity of the elastic reinforcement of the cell and of the matrix respectively, along the i^{th} direction; the superscript index $^{(0)}$ is used for rest lengths. V_{rve} is the volume of each RVE; it remains constant during any deformation since the material is incompressible.

Viscous forces are reaction forces to the movement of the matrix due to the compression or the aspiration of the fluid between two balls surfaces. Viscous force developed during a compression or an aspiration of fluid between two identical surfaces depends on the fluid viscosity η, the thickness h between the two surfaces, the relative velocity $\dot{h}$ between the two surfaces and the common area S of the surfaces. In agreement with the dimensional analysis we can write

$$f^v = \eta \dot{h} \frac{S^\alpha}{h^{2\alpha-1}}, \tag{5}$$

where α is a positive dimensionless number. The power w^v of f^v is:

$$w^v = \int f^v \mathrm{d}\dot{h} = \frac{\eta \dot{h}^2 S^\alpha}{2h^{2\alpha-1}}. \tag{6}$$

The dissipative potential W^v is defined as the density of the sum of all viscous powers developed in the matrix. With $h = \Delta_i$ and $S = c_j c_k$, t reads

$$W^v = \frac{\eta}{2V_{\mathrm{rve}}} \left(\frac{(c_2 c_3)^\alpha}{\Delta_1^{2\alpha-1}} \dot{\Delta_1}^2 + \frac{(c_3 c_1)^\alpha}{\Delta_2^{2\alpha-1}} \dot{\Delta_2}^2 + \frac{(c_1 c_2)^\alpha}{\Delta_3^{2\alpha-1}} \dot{\Delta_3}^2 \right). \tag{7}$$

Internal variables

When the sample undergoes a mechanical loading, every RVE deforms. Expressing the gradient of deformation in local coordinate

$$F_{ij} = \delta_{ij} \lambda_i, \tag{8}$$

the external deformation of the RVE is given by the principal stretches λ_i. Namely its lengths sizes Δx_i can be related to the reference ones $\Delta x_i^{\mathrm{ref}}$m

$$\Delta x_i = \lambda_i \Delta x_i^{\mathrm{ref}}. \tag{9}$$

Nevertheless, for any fixed macro-deformation, an inner restructuring within the RVE may occur moving the c_i and Δ_i values. The current values of these internal variables are given solving ordinary differential equations that result for the forces compensation at micro-scale

$$\mathcal{F}^e + \mathcal{F}^v = 0. \tag{10}$$

The forces $\mathcal{F}^e$ and $\mathcal{F}^v$ diverge from the forces f^e and f^v. Indeed, the latter ones consider the micro-variables as independent from each other,

$$f^e(\xi) = V_{rve} \frac{\partial W^e}{\partial \xi}, \tag{11}$$

$$f^v(\xi) = V_{rve} \frac{\partial W^v}{\partial \dot{\xi}}, \tag{12}$$

where $\xi = c_i$ or Δ_i. In reality, the internal variables c_i and Δ_j are not independent from each other but they are linked together by the following two equations. The ball's volume preservation holds the product

$$V_c \equiv c_1 c_2 c_3, \tag{13}$$

which is constant, and three geometric relationships

$$c_i + \Delta_i = \Delta x_i, \ i = 1 \ldots 3, \tag{14}$$

have to be fulfilled at any time. The dependence between micro-variables is induced by using the total derivative. For instance, working with the variable Δ_1, the total elastic contribution is given by

$$\mathcal{F}^e(\Delta_1) = V_{rve} \frac{dW^e}{d\Delta_1} = \\ = V_{rve} \left(\frac{\partial W^e}{\partial \Delta_1} + \frac{d\Delta_j}{d\Delta_1} \frac{\partial W^e}{\partial \Delta_j} + \frac{dc_i}{d\Delta_1} \frac{\partial W^e}{\partial c_i} \right), \tag{15}$$

and the total viscous contribution is:

$$\mathcal{F}^v(\Delta_1) = V_{rve} \frac{dW^v}{d\dot{\Delta}_1} = \\ = V_{rve} \left(\frac{\partial W^v}{\partial \dot{\Delta}_1} + \frac{d\dot{\Delta}_j}{d\dot{\Delta}_1} \frac{\partial W^v}{\partial \dot{\Delta}_j} + \frac{d\dot{c}_i}{d\dot{\Delta}_1} \frac{\partial W^e}{\partial \dot{c}_i} \right). \tag{16}$$

Replacing the potentials W^e and W^v by their expressions (4) and (7), the forces compensation (10) leads to an ordinary differential equation for Δ_1 that can be numerically solved. In fully 3D modeling, this equation does not suffice to characterize the current configuration of the micro-structure, but is has to be coupled with a second equation written by considering a second micro-variable, e.g. Δ_2. However if the deformation is plane or if it respects transverse isotropy symmetry, then that equation suffices.

The domain of material application is very large. For instance, the model can be applied to the phenomenon of stress relaxation. The restructuring between the micro-constituents of the tissue may explained the delay in stress response. The model could be also useful in biomechanics. Biological tissues are generally assumed to be incompressible and viscoelastic. Their microstructure is very complex but for a very simple approximation the model of balls may mimic the occurrence of biological cells.

Acknowledgement This work has been supported by the Czech Grant Agency, grant number 106/05/0219.

References

[1] D. P. Pioletti, L. R. Rakotomanna (2000): Non-Linear viscoelastic laws for soft biological tissues. *European Journal of Mechanics and Solids*, **19**, 749–759.

[2] M. Holeček, F. Moravec (2006): Hyperelastic model of a material which microstructure is formed by "balls and springs". *International Journal of Solids and Structures*, **43**, 7393–7406.

Reconstruction of Cement Paste Microstructure Using Image Analysis

K. Forstová*, J. Němeček

Czech Technical University in Prague
Thákurova 7, 166 29 Prague 6, Czech Republic
katerina.forstova@fsv.cvut.cz, jiri.nemecek@fsv.cvut.cz

Summary: Presented work deals with the reconstruction of cement paste microstructure for the purpose of simulation of its micromechanical behavior. Two-dimensional real images of cement paste captured by environmental scanning electron microscope (ESEM) were employed for this reconstruction in two and also three dimensions. Thresholded images were converted to binary representation that allowed using statistical descriptor (autocorrelation function). Computed examples proved good efficiency of the reconstruction algorithms.

Introduction

Hydrated cement paste is a heterogeneous material at microscale which consists of three main phases- hydration products, unhydrated clinkers and pores. There are several known models for the reconstruction of its microstructure. For example, the Powers model can describe newly formed phases in the quantitative way. In order to reconstruct the cement microstructure also spatially, more sophisticated model has to be used. Such model, based on voxel structure, was developed by Bentz (CEMHYD3D, [3]). In this model, the primary microstructure is generated using statistical descriptor in the form of autocorrelation function.

After the iteration process that includes dissolution, diffusion, transport of chemicals and phase percolation the three-dimensional microstucture of hydration products is generated.

Methods

The final goal of the presented work is to elaborate an efficient numerical algorithm for the simplified (three-phase) microstructure reconstruction of a particular cement paste sample using real ESEM images. For this purpose images captured by the back-scattered electron (BSE) detector of ESEM were used. Contrast in BSE images is produced by the variation of atomic number within the scanned area of the specimen surface. This variation corresponds to the different material phases. The resulting image displays phases in the grey scale. Typical image of the cement paste contains black color that represents empty pores (they have zero reflectivity), white color of unhydrated clinker minerals (they contain calcium and silica and they have high reflectivity) and grey levels that can be assigned to various hydration products (C-S-H gels, calcium hydroxide, ettringite etc.). So far, there has not been found a way how to distinguish between the hydrated phases just according to the grey level. For the purpose of the simplified model, the complex microstructure was treated like a three-phase medium. Hydrated phases, clinkers and pores were selected from the image using thresholding levels. Since the tresholding was done manually (according to the chemical composition from ESEM), the results are necessarily dependent on this intentional choice.

Reconstruction algorithm in two dimensions

The proposed reconstruction algorithm is based on the binary representation of the real microstructure. To provide a general statistical descriptor of such a system it is useful to characterize each member of an ensemble by a random stochastic function characteristic function $\chi_r(\kappa, \alpha)$, which is equal to one when a point x lies in the material phase r in the sample α a and equal to zero otherwise [1]. Then, the one-point probability S_r function gives the probability that a point x will be found in a given phase r and the two-point probability function S_{rs} stands for the probability that the points x and y will be located phases r and s, respectively:

$$S_r(x) = P(\chi_r(x) = 1) \tag{1}$$

$$S_{rs} = P(\chi_r(x)\chi_s(y) = 1) \tag{2}$$

For the case of statistically homogeneous and ergodic media, information contained in the one-point probability function reduces to the volume fraction of a given phase. In addition, the two-point probability function then depends on $x - y$ distances and it can be obtained from the relation

$$S_{rs}(x,y) = \frac{1}{WH} IDFT\left\{DFT\left\{\chi_r(x,y)\right\}\overline{DFT\left\{\chi_s(x,y)\right\}}\right\} \tag{3}$$

where W is the width of image, H is the height of image, $\chi_r(x,y)$ is the characteristic function of phase r, $\chi_s(x,y)$ is the characteristic function of phase s, DFT and $IDFT$ stand for the direct and inverse Fourier transform and overline denotes the complex conjugate [1].

The process of the reconstruction of a real microstructure starts with the replacement the grey-scale image with a binary one. In this way a two-phase reference system is created (e.g. pores and other phases, Fig. 1a). The two point probability (autocorrelation) function is represented by a matrix with the same dimensions as the source binary image [2]. The second step is to use a random checkerboard with volume fraction of the reference system as the initial structure (Fig. 1b). The structure is then altered by a phase interchange of two randomly selected pixels. The resultant two-point probability function of the intermediate (new) system is calculated. Then the series of iterative steps in which always two pixels are altered is carried out. The convergence of the iteration is controlled by the difference of norms of autocorrelation functions between the previous and the new

images. The matrix norm of the autocorrelation function can be written as:

$$\|A\| = \left(\sum_{i=1}^{W} \sum_{j=h}^{W} a_{xy} \right)^{1/2} \quad (4)$$

The iteration loop is stopped after reaching a specified tolerance limit (Fig. 1d). The iterative process is depicted in Fig. 3a.

Reconstruction algorithm in three dimensions

Similarly to two dimensions, $S_{rs}(x, y)$ is computed from 2-D binary image. However, for 3-D reconstruction it has to be converted to $S(d)$ format since for an isotropic media the autocorrelation function should only be a function of the distance $d = \|x-y\|$ [3]. In this case, the autocorrelation function forms a two-column matrix. The first column contains the distance between two points in the same phase and the second column expresses the average probability that two points in certain distance are in the same phase.

In our algorithm an initial 3-D microstructure is created using a Gaussian noise (which was taken from CEMHYD3D algorithm). It has a probability density function of the normal distribution as the Gaussian noise. Then, the convolution mask of two images is computed. It involves the multiplication of a group of pixels in the input image (created with the Gaussian noise) with an array of pixels in a convolution mask (specified by the autocorrelation function). The output value produced in a spatial convolution operation is a weighted average of each input pixel and its neighboring pixels in the convolution mask. Initial 3-D microstructure is also filtered by a convolution mask maintaining periodic boundaries. The newly created microstructure is thresholded in order to convert each pixel into black or white. The resulting 3-D microstructure is produced so that it has very similar autocorrelation function as the input 2-D image (Fig. 3b).

Examples

In order to verify the reliability of the proposed algorithm, an example of 2-D reconstruction was computed on the artificial image (Fig. 1). Although the final image does not match exactly the reference one it is very similar in terms of similar autocorrelation functions and it also respects periodic boundary conditions. Using lower-order correlation functions leads to non-uniqueness of the solution that is caused by i ncomplete morphological information. On the other hand, the computational algorithm is simple, although also time-consuming.
An example of 3-D reconstruction of the real 2-D image is presented in Fig. 2. For the comparison, the graph of autocorrelation functions for the reference and reconstructed structures is presented in Fig. 3b.

Summary

To summarize, algorithms for 2-D and 3-D reconstruction of random microstructure of cement paste using image analysis and two-point probability function was presented. However, it is clear that even if the correlation function of the reference and reconstructed images are in good agreement, it is not ensured that both images will match each other. An extension to higher-order correlation functions and applying various boundary conditions to the resulting system that will match better is possible. It is planned to use the result of this work as an input for finite element analysis of the micromechanical properties of cement paste.

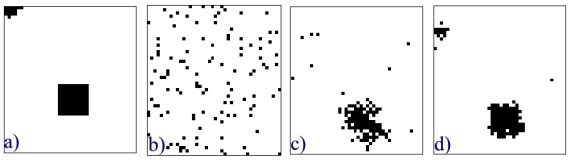

Figure 1: 2-D reconstruction: a) reference system, b) initial image, c) intermediate image after 3 000 steps, d) final image (after 10 000 steps).

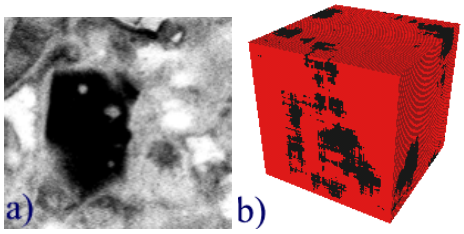

Figure 2: 3-D reconstruction: a) reference 2-D image, b) resulting 3-D microstructure 100x100x100 μm.

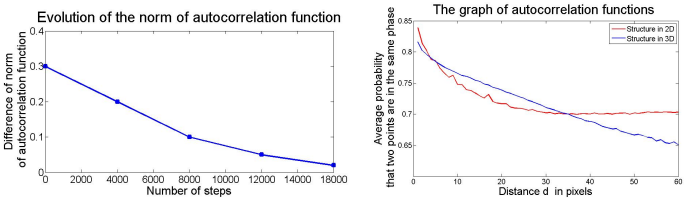

(a) (b)

Figure 3: (a) Evolution of the norm of autocorrelation function for 2-D example in Fig. 1, (b) the graph of autocorrelation functions for reference system (red) and structure in 3D (blue).

Acknowledgments: Supports of the Czech Grant Agency (GAČR 103/06/1856) and of the Ministry of Education of Czech Republic (MSM 6840770003) are gratefully acknowledged.

References

[1] S. Torquato, G. Stell (1982): Microstructure of two-phase random media.I. The n-point probability functions, *Journal of Chemical Physics*, **77**, 2071-2077.

[2] S. Torquato, C. L. Y. Yeong (1998): Reconstructing random media. *Physical Review E*, **57**, 495–506.

[3] D. P. Bentz (2000): CEMHYD3D: A Three-Dimensional Cement Hydration and Microstructure Development Modeling Package. Version 2.0.NISTIR 6485, U.S. Dept. of Commerce.

Systemization of Constitutive Models and Identification of their Parameters

J. Burša*, P. Janíček

Institute of Solid Mechanics, Mechatronics and Biomechanics, FME, Brno University of Technology
Technická, CZ 61669 , Brno, Czech Republic
bursa@fme.vutbr.cz, janicek@fme.vutbr.cz

Summary: This paper defines a variety of general constitutive laws for various substances and creates a systematic overview of various types of constitutive models. It deals with identification of parameters of hyperelastic isotropic and anisotropic constitutive models from various types of mechanical tests in greater detail and presents results achieved with a biaxial testing machine for soft tissues.

Introduction

For many years, linear elastic constitutive model (Hooke´s law) was sufficient for technical practice. More sophisticated models of our up-to-date computer age enable us, among others, to model also more complex material behaviour described by various mathematical formulas constitutive models. Many of these constitutive models are presented e.g. in [1] in their mathematical as well as graphical form. However, it appears to be useful to complete the dependencies presented in [1] and to systemize all the constitutive models into several basic categories and to express the relations among them explicitly.

Basic categories of constitutive models

In mechanics in the common sense, constitutive models are mathematical descriptions of mutual dependencies between acting loads (or stresses) and deformation of bodies (or deformation rate), including time dependencies, i.e., among others creep and relaxation responses. Constitutive dependencies can be defined as follows:

Constitutive dependencies are causal dependencies among tensors of stresses and strains and quantities derived of them by mathematical operations, with accounting of time dependencies.

In the sense of this definition, the simplest idealized states of matter (rigid solid, perfect fluid, perfect gas) can be understood as basic constitutive models. On the other side, a number of rather complex constitutive models have been formulated till now, with various components of their behaviour (elastic, plastic, viscous); the simpler models can be derived of them as their special cases. Therefore it is useful to systemize all the constitutive models into several hierarchical levels.

- **Basic constitutive models.** This level consists of the constitutive relations for rigid solid, perfect fluid and perfect gas (and plasma, if there are any).
- **Simple constitutive models.** This level consists of models describing the behaviour of matters that differ from the above “perfect” ones by one certain property only, e.g. linear elastic solid, viscous fluid etc.
- **Combined constitutive models.** This level consists of models created by combination of two or more simple constitutive models. They use, among others, reological models to describe e.g. the behaviour of viscoelastic, elastic-plastic, viscoplastic and elastic-viscoplastic matters.

A schematic overview of some most frequent constitutive models with mutual relations among them is presented in Fig. 2. The three above levels of constitutive models are distinguished by different colours in this scheme.

Identification of constitutive parameters

The more complex constitutive models and identification of their parameters require also more complex mechanical testing. In our institute, a machine for various types of biaxial tests was produced recently; it is presented in Fig. 1.

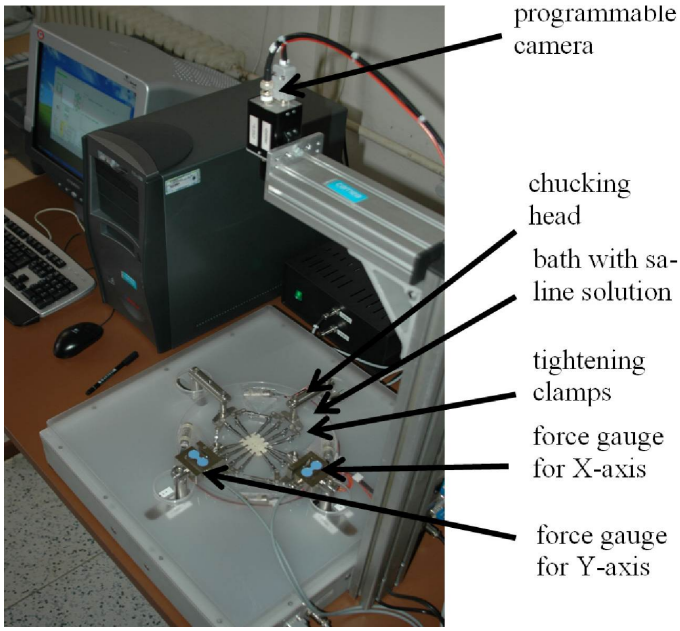

Figure 1: Biaxial testing machine for polymers and soft tissues.

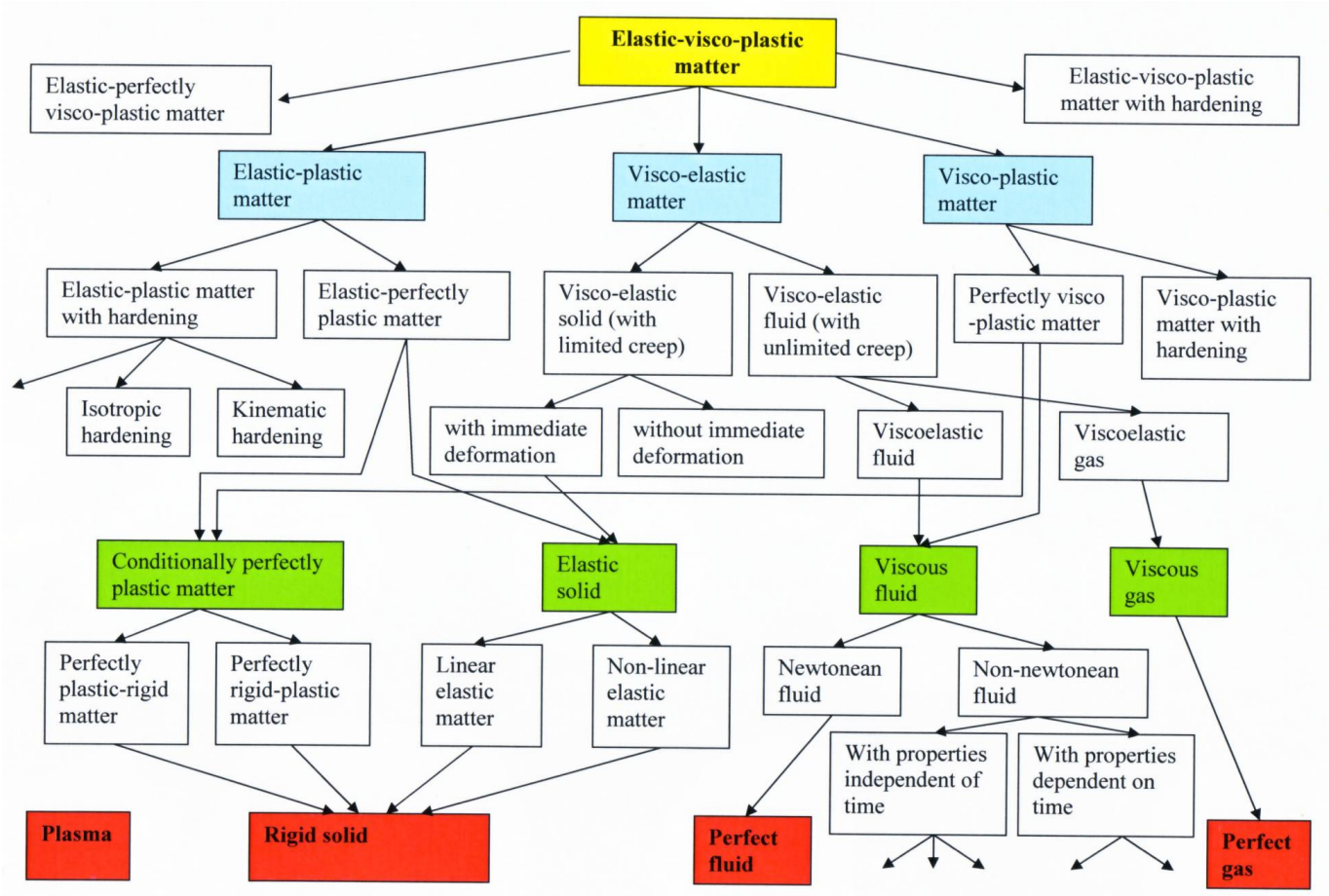

Figure 2: Systematic scheme of constitutive models.

Conclusion

Some results of tests realized with this machine and parameters of constitutive models identified on the base of these tests will be published in the paper.

References

[1] J. Lemaitre, J.-L. Chaboche (1994): *Mechanics of Solid Materials*. Cambridge University Press.

A Model for Concrete at High Temperatures

J. Hartikainen, R. Kouhia, T. Manninen*

Laboratory of Structural Mechanics, Helsinki University of Technology
P.O. 2100, FI-02015 TKK, Finland
juha.hartikainen@ttk.fi, reijo.kouhia@ttk.fi, timo.manninen@ttk.fi

Summary: In the present paper, a preliminary version of a fully coupled non-linear multi-phase mathematical model based on continuum thermodynamics is presented for simulation of hygro-thermo-mechanical behaviour of moist, partially saturated concrete at high temperatures. The hygro-thermal behaviour of concrete is highly complex phenomenon which is influenced by cracking of concrete. The couplings between hygro-thermo-mechanical responses are dealt with by a consistent constitutive approach choosing proper expressions for the Helmholtz free energy and the dissipation potential.

Introduction

In the present paper, a thermodynamically consistent model to describe the behaviour of concrete at elevated temperatures is presented. The model is based on the theory of mixtures and the principles of continuum mechanics and macroscopic thermodynamics [1, 2, 3, 4, 5]. In the model, the following phenomena are taken into account:

- the reversible thermoelastic behaviour of concrete,
- damaging of concrete,
- transport of water, water vapour and air in the porous cement paste,
- adsorption of water into the cement gel,
- phase change between water and water vapour and
- diffusion of water vapour in the gaseous component.

Thermomechanical theory

The concrete is considered as a multiconstituent system consisting of a solid skeleton (s), liquid water (l) and a gaseous component (g) of water vapour (v) and air (a).

The volume fractions of the solid, liquid and gaseous components are defined as

$$\beta_k = \frac{\mathrm{d}V_k}{\mathrm{d}V}, \qquad k \in \{\mathrm{s},\mathrm{l},\mathrm{g}\}\,, \tag{1}$$

where $\mathrm{d}V_k$ is the volume of component *k* and $\mathrm{d}V$ the reference volume. Since the water vapor and air belong to the same gaseous component, their relative proportions are measured via the molar fractions ζ_v and ζ_a such that

$$\zeta_\mathrm{v} \equiv \zeta = \frac{n_\mathrm{v}}{n_\mathrm{v}+n_\mathrm{a}}, \qquad \zeta_\mathrm{a} \equiv 1-\zeta = \frac{n_\mathrm{a}}{n_\mathrm{v}+n_\mathrm{a}}, \tag{2}$$

where n_k is the mole number of constituent k. The molar volume fractions, ξ_k, are defined as

$$\xi_\mathrm{s} = \beta_\mathrm{s}, \quad \xi_\mathrm{l} = \beta_\mathrm{l}, \quad \xi_\mathrm{v} = \zeta_\mathrm{v}\beta_\mathrm{g} \equiv \zeta\beta_\mathrm{g}, \quad \xi_\mathrm{a} = \zeta_\mathrm{a}\beta_\mathrm{g}. \tag{3}$$

Apparently the molar volume fractions satisfy the constraints

$$\sum_k \xi_k = 1, \quad \xi_k \geq 0, \quad k \in \{\mathrm{s},\mathrm{l},\mathrm{v},\mathrm{a}\}. \tag{4}$$

The molar volume fractions ξ_k relate the the apparent densities ρ_k to the intrinsic (bulk) densities $\bar{\rho}_k$ according to

$$\rho_k = \xi_k\bar{\rho}_k, \quad k \in \{\mathrm{s},\mathrm{l},\mathrm{v},\mathrm{a}\}. \tag{5}$$

The state of motion of constituent k at an arbitrary instant of time t is described by a velocity field $\boldsymbol{v}_k(\boldsymbol{x},t)$, where $\boldsymbol{x}$ is the vector of spatial coordinates. The motion the solid component can be described more conveniently by its displacement field $\boldsymbol{u}_\mathrm{s} \equiv \boldsymbol{u}(\boldsymbol{x},t)$.

The deformations are described either by the rate of deformation

$$\boldsymbol{d}_k = \tfrac{1}{2}\big[\nabla\boldsymbol{v}_k + (\nabla\boldsymbol{v}_k)^\mathsf{T}\big], \quad k \in \{\mathrm{s},\mathrm{l},\mathrm{v},\mathrm{a}\} \tag{6}$$

or by the strain

$$\boldsymbol{\varepsilon}_\mathrm{s} \equiv \boldsymbol{\varepsilon} = \tfrac{1}{2}\big[\nabla\boldsymbol{u} + (\nabla\boldsymbol{u})^\mathsf{T}\big]. \tag{7}$$

The material time derivative of a quantity following the movement of constituent k is determined by the operator

$$\frac{\mathrm{d}_k}{\mathrm{d}t} = \frac{\partial}{\partial t} + \boldsymbol{v}_k\cdot\nabla. \tag{8}$$

The velocity $\boldsymbol{v}_\mathrm{s}$ is then obviously the material time derivative $\mathrm{d}_\mathrm{s}\boldsymbol{u}/\mathrm{d}t$.

Because constituents have in general different velocities at the same macroscopic point of the mixture, a reference velocity field $\boldsymbol{v}_*(\boldsymbol{x},t)$ is introduced in order to establish the fundamental principles for the mixture. The material time derivative with respect to the reference movement can be expressed as follows

$$\frac{\mathrm{d}_k}{\mathrm{d}t} = \frac{\mathrm{d}_*}{\mathrm{d}t} + \boldsymbol{v}_{k*}\cdot\nabla, \tag{9}$$

where $\boldsymbol{v}_{k*}$ is the relative velocity of the constituent k with respect to the reference velocity: $\boldsymbol{v}_{k*} = \boldsymbol{v}_k - \boldsymbol{v}_*$.

The balance law of linear momentum and the conservation laws of mass and energy for the concrete can be expressed as follows [2]:

$$\boldsymbol{m}_\mathrm{s} + \boldsymbol{m}_\mathrm{l} + \boldsymbol{m}_\mathrm{v} + \boldsymbol{m}_\mathrm{a} = 0, \tag{10}$$
$$\theta_\mathrm{s} = 0, \tag{11}$$
$$\theta_\mathrm{l} + \theta_\mathrm{v} = 0, \tag{12}$$
$$\theta_\mathrm{a} = 0, \tag{13}$$
$$\ell_\mathrm{s} + \ell_\mathrm{l} + \ell_\mathrm{v} + \ell_\mathrm{a} = 0, \tag{14}$$

where the linear momentum production rate $\boldsymbol{m}_k$ the mass production rate θ_k, and the energy production rate ℓ_k for con-

stituents $k \in \{\mathrm{s}, \mathrm{l}, \mathrm{v}, \mathrm{a}\}$ are defined as

$$\boldsymbol{m}_k = \rho_k \frac{\mathrm{d}_k \boldsymbol{v}_k}{\mathrm{d}t} + \theta_k \boldsymbol{v}_k - \nabla\cdot\boldsymbol{\sigma}_k - \rho_k \boldsymbol{g}, \tag{15}$$

$$\theta_k = \frac{\partial \rho_k}{\partial t} + \nabla\cdot(\rho_k \boldsymbol{v}_k), \tag{16}$$

$$\ell_k = \rho_k \frac{\mathrm{d}_k e_k}{\mathrm{d}t} + (e_k - \tfrac{1}{2}\boldsymbol{v}_k\cdot\boldsymbol{v}_k)\theta_k - \boldsymbol{\sigma}_k\!:\!\boldsymbol{d}_k + \boldsymbol{m}_k\cdot\boldsymbol{v}_{k*} + \nabla\cdot\boldsymbol{q}_k - r_k. \tag{17}$$

where $\boldsymbol{\sigma}_k$ is the Cauchy stress tensor, e_k the specific internal energy, $\boldsymbol{q}_k$ the heat flux vector, r_k the external energy supply of constituents, $k \in \{\mathrm{s}, \mathrm{l}, \mathrm{v}, \mathrm{a}\}$ and the acceleration of gravity is denoted as $\boldsymbol{g}$.

According to the second principle of thermodynamics the entropy production should always be positive. Introducing the absolute temperature T and the specific entropy s_k of constituent *k*, the entropy inequality for the concrete can be stated as

$$T(\gamma_\mathrm{s} + \gamma_\mathrm{l} + \gamma_\mathrm{v} + \gamma_\mathrm{a}) \geq 0, \tag{18}$$

where the entropy production rate γ_k of constituent *k* is defined as follows

$$\gamma_k = \rho_k \frac{\mathrm{d}_k s_k}{\mathrm{d}t} + s_k\theta_k + \nabla\cdot\left(\frac{\boldsymbol{q}_k}{T}\right) - \frac{r_k}{T}. \tag{19}$$

Constitutive relations

The thermodynamic state and the material behaviour are defined in terms of variables of state and dissipation through the Helmholz free energies and the dissipation potential. The variables defining the thermodynamic state are the absolute temperature T, which is assumed to be uniform for all constituents, the strain tensor $\boldsymbol{\varepsilon}$ and the damage tensor $\boldsymbol{D}$, which takes into account microfracturing of the solid component, as well as the intrinsic densities $\bar{\rho}_\mathrm{s}$, $\bar{\rho}_\mathrm{l}$, $\bar{\rho}_\mathrm{v}$ and $\bar{\rho}_\mathrm{a}$ and the molar volume fractions ξ_s, ξ_l, ξ_v and ξ_a. The variables defining the dissipation behaviour in turn are the heat flux, $\boldsymbol{q} = \boldsymbol{q}_\mathrm{s} + \boldsymbol{q}_\mathrm{l} + \boldsymbol{q}_\mathrm{v} + \boldsymbol{q}_\mathrm{a}$, the rate of damage, $\dot{\boldsymbol{D}} \equiv \mathrm{d}_\mathrm{s}\boldsymbol{D}/\mathrm{d}t$, and the relative velocities $\boldsymbol{v}_\mathrm{ls}$, $\boldsymbol{v}_\mathrm{vs}$ and $\boldsymbol{v}_\mathrm{as}$. Reversible material behaviour is described by means of the Helmholz free energies

$$\psi_\mathrm{s} = \psi_\mathrm{s}(T, \boldsymbol{\epsilon}, \boldsymbol{D}, \bar{\rho}_\mathrm{s}, \xi_\mathrm{s}, \xi_\mathrm{l}, \xi_\mathrm{v}, \xi_\mathrm{a}), \tag{20}$$

$$\psi_\mathrm{v} = \psi_\mathrm{v}(T, \bar{\rho}_\mathrm{v}, \xi_\mathrm{s}, \xi_\mathrm{l}, \xi_\mathrm{v}, \xi_\mathrm{a}), \tag{21}$$

$$\psi_\mathrm{l} = \psi_\mathrm{l}(T, \bar{\rho}_\mathrm{l}, \xi_\mathrm{s}, \xi_\mathrm{l}, \xi_\mathrm{v}, \xi_\mathrm{a}), \tag{22}$$

$$\psi_\mathrm{a} = \psi_\mathrm{a}(T, \bar{\rho}_\mathrm{a}, \xi_\mathrm{s}, \xi_\mathrm{l}, \xi_\mathrm{v}, \xi_\mathrm{a}), \tag{23}$$

whereas irreversible material behaviour is characterised through the dissipation potential

$$\phi = \phi(\boldsymbol{q}, \dot{\boldsymbol{D}}, \boldsymbol{v}_\mathrm{ls}, \boldsymbol{v}_\mathrm{vs}, \boldsymbol{v}_\mathrm{as}\,;\, T, D, \bar{\rho}_\mathrm{v}, \xi_\mathrm{s}, \xi_\mathrm{l}, \xi_\mathrm{v}, \xi_\mathrm{a}). \tag{24}$$

The thermodynamically admissible constitutive relations are derived from the Helmholz free energies and the dissipation potential by exploiting the entropy inequality (18) as follows. Introducing the Legendre transformations

$$T^{-1}\psi_k = T^{-1}e_k - s_k, \quad k \in \{\mathrm{s}, \mathrm{l}, \mathrm{v}, \mathrm{a}\}, \tag{25}$$

postulating the representation of the power of dissipation

$$T(\gamma_\mathrm{s} + \gamma_\mathrm{l} + \gamma_\mathrm{v} + \gamma_\mathrm{a}) = \frac{\partial\phi}{\partial\boldsymbol{q}}\cdot\boldsymbol{q} + \frac{\partial\phi}{\partial\dot{\boldsymbol{D}}}\!:\!\dot{\boldsymbol{D}} + \frac{\partial\phi}{\partial\boldsymbol{v}_\mathrm{ls}}\cdot\boldsymbol{v}_\mathrm{ls} + \frac{\partial\phi}{\partial\boldsymbol{v}_\mathrm{vs}}\cdot\boldsymbol{v}_\mathrm{vs} + \frac{\partial\phi}{\partial\boldsymbol{v}_\mathrm{as}}\cdot\boldsymbol{v}_\mathrm{as} \tag{26}$$

and taking into account the field equations (11)-(17) yield the relevant constitutive equations, see [6].

Concluding remarks

A rather general formulation for the analysis of hygro-thermo-mechanical behaviour of concrete at elevated temperatures is presented. The resulting model is capable of describing the following phenomena: the thermoelastic and damaging behaviour of concrete, transport of water, water vapour and air in the porous cement paste, adsorption of water into the cement gel and diffusion of water vapour in the pores. In addition, the model takes into account the phase change between liquid water and water vapour.

Further improvements to the model will include:

- shrinkage of concrete due to the loss of adsorbed and chemically bound water during heating,
- inclusion of a model for transient thermal creep and
- model for the plastic behaviour of concrete, that is mainly due to the relative sliding of the microdamaged material surfaces.

Moreover, numerical implementation of the model is under development.

Acknowledgements. This research has been supported by the Academy of Finland (decision number 210622).

References

[1] M. Frèmond, M. Mikkola (1991): Thermomechanical modelling of freezing soil. *Ground Freezing* (Proc. 6th int. symp. on ground freezing, Beijing, China), 17–24.

[2] J. Hartikainen, M. Mikkola (1997): Thermomechanical model of freezing soil by use of the theory of mixtures. *Proc. of the Finnish Mechanics Days* (Oulu, Finland), 1–23.

[3] M. Mikkola, J. Hartikainen (2001): Mathematical model of soil freezing and its numerical implementation. *International Journal for Numerical Methods in Engineering*, **52**, 543–557.

[4] P. Jussila (2006): Thermomechanics of Porous Media – I: Thermohydraulic model for compacted bentonite. *Transport in Porous Media*, **62**, 81–107.

[5] M. Frémond (2002): *Non-Smooth Thermomechanics*, Springer, Berlin.

[6] J. Hartikainen, R. Kouhia, T. Manninen (2006): A model for concrete at high temperatures. *The IX Finnish Mechanics Days* (Lappeenranta, Finland), 683–691.

On Approximation of Non-Newtonian Fluid Flow by the Finite Element Method

P. Sváček

CTU, Faculty of Mechanical Engineering, Department of Technical Mathematics
Karlovo náměstí 13 121 35 Praha 2, Czech Republic
svacek@marian.fsik.cvut.cz

Summary: In this paper the problem of numerical approximation of non-Newtonian fluid flow with free surface is considered. Various industrial slurries are concentrated mixtures of very small particles and grains in water. Generally, these suspensions are non-Newtonian fluids exhibiting a yield stress that needs to be overcome for the flow to take place, cf. [1], [2]. Recently it has become possible to simulate a broad variety of flows with many different constitutive equations. The use of the finite element method for non-Newtonian flows was studied, e.g., by [4] or [6]. The main interest is paid to the proper simulation of non-Newtonian fluid flow. The developed numerical procedure is applied on the solution of several free surface problems.

Introduction

The study of dynamics of fluids which do not belong to the class of Newtonian fluids is important problem mainly in many industrial applications, cf. [2]. The Newton's law of viscosity is simply inadequate for the description of macromolecular liquids as well as various mixtures (e.g., fresh concrete, mortar), where the viscosity coefficient can drammatically vary with the change of fluid's rate of strain. Recall that the incompressible fluids are characterized by two material constants: the density ρ and the viscosity μ. The experimental description of the incompressible non-Newtonian fluid is far more complicated, cf. [1]. In this paper we address the rheological models of fluids from the class of so-called *time independent fluids/generalised Newtonian fluids*, where the local viscosity coefficient depends only on recent local values of the rate of shear and do not exhibit memory effects.

The mathematical description of this problem consists of the continuity equation, Navier-Stokes system of momentum equations and the constitutive equation for the specified fluid. The constitutive equation is not linear and thus even for very low convection, the generalization of the Stokes problem is nonlinear even if the convective terms ommited.

The addressed problem is the numerical simulations of the flow of the fresh concrete. Concrete in its fresh state can be thought as a fluid, provided that a certain degree of flow can be achieved and that the concrete is homogeneous. The description of flow of a fluid use concepts such as shear stress and shear rate. Concrete as a fluid is most often assumed to behave like a Bingham fluid, cf. [1]. In this case the fluid is characterized by two parameters: yield stress and plastic viscosity. The parameters of the model can be found by rheological methods and depends on the ingredients quality of the concrete. Naturally, the model can not describe the qualitative state and chemical changes of the concrete, but for the fresh state it can provide useful approximation.

Furthermore, the problem with free surface needs to be approximated. The fluid surface is not known apriori, but it is part of the solution. The widely used methods can be characterized either as the interface capturing or the interface tracking methods, cf. [5].

The mathematical problem is discretized by the finite element method. The stabilization procedure is based on modification of Galerkin Least Squares method acording to [3].

Constitutive equations

The Cauchy stress tensor σ consists of the normal stress components (pressure p) and the extra stress tensor $\boldsymbol{\tau'}$, i.e.

$$\boldsymbol{\sigma} = -p\mathbb{I} + \boldsymbol{\tau'} \tag{1}$$

The relation between the deviatoric components $\boldsymbol{\tau'}$ of the Cauchy stress tensor and the rate of strain tensor depends on the physical properties of the modeled fluid. In the case of Newtonian fluid the relation is linear. Strictly speaking no fluid can be considered as Newtonian, but for micromolecular fluids (air, water) the Newtonian fluid description is very good approximation of the real fluid. On the other hand, for the macromolecular polymer fluids as well as for the mixtures of small particles and water (as concrete) the model of the Newtonian fluid is inappropriate. In this case the nonlinear relation between the deviatoric components and the strain tensor can be employed.

In the case when the fluid does not include memory effects and its viscosity depends only on local value of the shear stress, the fluid can be characterized as the generalized Newtonian fluid, see, e.g., [1], [2]. The generalized form of the Newtonian law of viscosity is described by the constitutive equation

$$\boldsymbol{\tau'} = \mu\,\mathbb{D} \tag{2}$$

where the viscosity function $\mu = \mu(\dot\gamma)$ depends on the shear rate $\dot\gamma$ given by

$$\dot\gamma = \sqrt{2\sum_{ij} d_{ij}^2} \tag{3}$$

The employed models of the generalized Newtonian fluids are *Power law fluid* with the constitutive equation $\mu = \mu_0\dot\gamma^{\alpha-1}$ or the *Bingham* fluid with two parameters τ_0 - yield stress, μ - plastic viscosity. Hence $\tau = \tau_0 + \mu\dot\gamma$.

Two phase formulation

In order to describe the free surface flow in complex geometries, where the fluid motion can meet boundaries far from the

initial configuration, the model is described with the aid of two phase flows (let us distinguish the two phases as fluid and gas). The initial configuration with the given fixed walls is filled with two fluids, where the first one is the fluid of our interest and the other one is the surrounding gas which fills up the remaining room of the configuration. The two fluids with densities $\rho^{(k)}$, the fluid velocities $\mathbf{v}^{(k)}$, pressures $p^{(k)}$ and the viscosities $\mu^{(k)}$ are considered. The domain occupied by the k-th fluid at time t is denoted by $\Omega_t^{(k)}$. From conservation laws the system of equations holds

$$\rho^{(k)}\frac{\partial v_i^{(k)}}{\partial t} + \rho^{(k)}\sum_j \frac{\partial\left(v_i^{(k)}v_j^{(k)}\right)}{\partial x_j} + \frac{\partial p^{(k)}}{\partial x_i} = \sum_j \frac{\partial}{\partial x_j}\left(\mu^{(k)}d_{ij}\right) + \rho^{(k)}f_i$$

on the domain $\Omega_t^{(k)}$ for $k = 1, 2$. The system is equipped with boundary conditions and an initial condition.

Furthermore, on the interface $\Gamma_{\mathcal{I}_t}$ the kinematic condition $\mathbf{v}^{(1)} = \mathbf{v}^{(2)}$ and the dynamic condition $\boldsymbol{\sigma}^{(1)}\cdot\mathbf{n} = \boldsymbol{\sigma}^{(2)}\cdot\mathbf{n}$ are precribed (no surface tension is assumed).

Following [5] we can introduce the functions ρ, μ and $\mathbf{v}$ defined on the computational domain $\Omega = \Omega_t^{(1)} \cup \Omega_t^{(2)}$ as $\rho = \rho_k$, $\mu = \mu_k$ and $\mathbf{v} = \mathbf{v}^{(k)}$ on $\Omega^{(k)}$. Then the following formulation of the problem can be given

$$\rho\frac{\partial v_i}{\partial t} + \rho\sum_j \frac{\partial\left(v_i v_j\right)}{\partial x_j} + \frac{\partial p}{\partial x_i} = \sum_j \frac{\partial\left(\mu d_{ij}\right)}{\partial x_j} + \rho f_i \qquad (4)$$

and

$$\rho\nabla\cdot\mathbf{v} = 0$$

on the domain Ω.

Level set method

The free surface modelling can met difficulties caused by either the mathematical modelling (e.g. the moving interface, physical transfer process through the surface) or the numerical approximation (e.g. approximation of the moving interface, discontinuity of physical quantites - density, viscosity, pressure - across the interface). The methods of free surface approximation can be divided to two classes the *interface tracking methods* (the interface is approximated exactly) or the *interface capturing methods* (the fluid volume is tracked rather then interface).

In this paper the level set method is employed, see, e.g., [5]. The equation (4) is coupled with the transfer equation for the additional level set function function φ

$$\frac{\partial\varphi}{\partial t} + \nabla\cdot(\mathbf{v}\varphi) = 0 \qquad (5)$$

where the meaning of the function φ at a point $\mathbf{x}$ indicates whether it is occupied by the fluid ($\varphi > 0$) or by the gas ($\varphi < 0$). The surface is identified by the equation $\varphi = 0$.

The density, viscosity and velocity can be given with the aid of Heaviside function $H(\varphi)$ as

$$\rho = \rho_1 + H(\varphi)\left(\rho_2 - \rho_1\right) \qquad \mu = \mu_1 + H(\varphi)\left(\mu_2 - \mu_1\right)$$

In the numerical approximation the regularized Heaviside function H_ϵ is employed, where the thickness of the interface can be regulated through the parameter ϵ. The reinitialization step of the level set algorithm is needed in order to insure that the level set function φ remains a distance function through the computation.

The equation

$$\frac{\partial\varphi}{\partial t} + \nabla\cdot(\mathbf{v}\varphi) = 0 \qquad (6)$$

is discretized with the aid of finite element method. The first order piecewies linear reconstruction is applied.

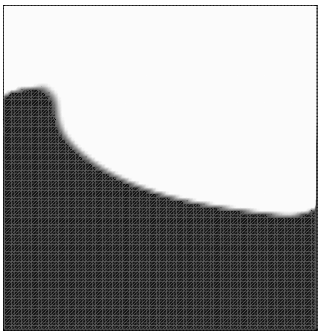

Figure 1: Numerical simulation of the standing wave problem. The density ρ is depicted.

Acknowledgment. This research was supported under grant No. 201/05/P142 of the Grant Agency of the Czech Republic and under the Research Plan MSM 6840770003 of the Ministry of Education of the Czech Republic.

References

[1] R. B. Bird, R. C. Armstrong, and O. Hassager (1987): *Dynamics of polymeric liquids, Volume 1: Fluid Mechanics*, John Wiley & Sons.

[2] R. P. Chhabra and J. F. Richardson (1999): *Non-newtonian flow in the process industries*, Butterworth-Heinemann.

[3] T. Gelhard, G. Lube, M. A. Olshanskii, and J.-H. Starcke (2005): Stabilized finite element schemes with LBB-stable elements for incompressible flows, *Journal of Computational and Applied Mathematics*, **177**, 243–267.

[4] H.-C. Huang, Z.-H. Li, and A. S. Usmani (1999): *Finite Element Analysis of Non-Newtonian Flow : Theory and Software*, Springer-Verlag.

[5] S. R. Ransau (2002): *Solution methods for incompressible viscous free surface flows: A literature review*, Technical Report 3/2002, Norwegian University of Science and Technology, Trondheim.

[6] J. N. Reddy (2004): *Introduction to nonlinear finite element analysis*, Oxford University Press.

Numerical Modelling of a Shape Memory Alloy/Elastomer Composite

Y. Chemisky*, V-L. Tahiri, A. Eberhardt, E. Patoor

Laboratoire de Physique et Mécanique des Matériaux, UMR CNRS 7554
Ile du Saulcy, 57045 METZ CEDEX 01, France
chemisky@univ-metz.fr, tahiri@univ-metz.fr

Summary: Due to their biocompatibility and remarkable properties, such as large reversible strains and shape memory effect, Nickel-Titane Shape Memory Alloys (SMA) are increasingly used in biomedical engineering. Combining such materials with an elastomer gives enhanced possibilities of active composite applications. In this study, a Finite Element Method is used to model the behaviour of a pseudoelastic SMA wire embedded in an elastomer ribbon. The SMA behaviour is described using a constitutive law based on micromechanical considerations, while a hyperelastic model is used for the elastomer. A good correlation is observed between numerical and experimental results.

Introduction

In SMA/elastomer devices, multiphysic couplings of the SMA material confer adaptiveness to the composite structure, which behaviour depends on thermomechanical conditions. Since the late 90's, many SMA/elastomer applications developed in the fields of robotics [1], biomimetics or load transmission [2], have showed the interest of the elastomer mechanical contribution to the global response of the composite. In this work, a "snake-like"-shaped NiTi wire embedded in a photoelastic elastomer matrix is studied. Behaviours of both materials are described by means of thermodynamic potentials. So as to assess the validity of the model used, and the structural interaction effects between the constituents of the composite, FEM calculation results are compared to experimental quantitative and qualitative results.

Materials and testing conditions

A 0.2 mm diameter NiTi wire (50.6% at. Ni) was cold-worked at 22% then heated at 350 ˚ C for 15 minutes, to get a pseudoelastic behaviour of the SMA at room temperature. As for the elastomer matrix, commercial glue was selected for its photoelastic properties and easy processing. The NiTi wire was embedded in a 1mm x 10mm x 70mm elastomer ribbon to obtain a flat composite, which allows to use photostress analysis experiments to visualise stress fields near the wire/matrix interface. To obtain less than 3% strain in the SMA for 10% elongation of the composite, predimensional calculations led to the design of a 1 mm radius "snake-like"- shape (see Fig. 3) for the NiTi wire. All tensile tests were carried out at room temperature at a constant elongation rate of 10%.min^{-1}. Several material parameters were identified from tensile tests on SMA wire and elastomer ribbon separately.

Constitutive law of the components

To describe the behaviour of complex SMA structures, a macroscopic thermomechanical constitutive law was developed by Peultier *et al*. [3], from results obtained within a micromechanical approach (see Fig. 1) using self consistent method [4]. The model is based on a thermodynamical description of the phase transformation. An evolution criterion of martensite volume fraction denoted by f is derived from the following thermodynamical potential:

$$F_f = \sigma_{ij} \cdot \varepsilon_{ij}^T - B(T - T_0) - H_{var} \cdot f - H_{grain} \cdot f \cdot (\varepsilon_{ij}^T)^2 \quad (1)$$

where ε_{ij}^T is the mean transformation strain, T_0 is the mean transformation temperature, and B is a material parameter. H_{var} and H_{grain} denote intervariant and intergranular interaction coefficients respectively. This model was implemented in the ABAQUS FEM code through a User Material (UMAT) subroutine.

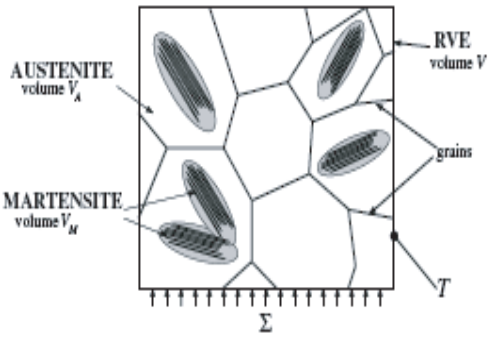

Figure 1: Representative volume element (RVE) of a polycrystalline SMA [3].

To describe the behaviour of the elastomer, the following Moonley-Rivlin potential was chosen:

$$\Psi = C_{10}(I_1 - 3) + C_{01}(I_2 - 3) \quad (2)$$

where C_{10} and C_{01} are material constants, I_1 and I_2 are the first and second strain tensor invariants. Note that this model is currently used in FEM simulations [5]. Moreover, to complete this hyperelastic model, the hysteresis phenomenon was taken into account using Bergström and Boyce law [6]. Both previous modellings of the elastomer were already implemented in the ABAQUS FEM code.

Comparison of numerical and experimental results

Tensile tests on separate SMA and elastomer and on the SMA/elastomer composite allow to quantify structural interaction effects between the constituents, as well as to assess the validity of the FEM model used.

On Fig. 2, the experimental response of the composite compared with the sum of the responses obtained for separate components shows that structural interactions increase the stiffness of the composite.

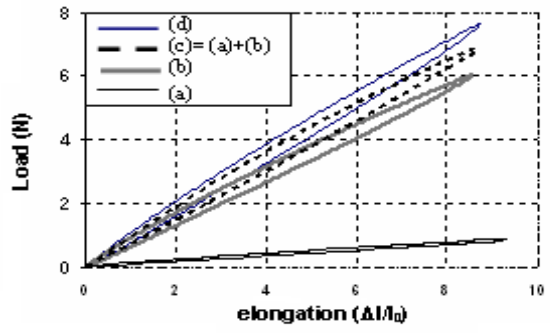

Figure 2: Experimental responses of: (a) SMA; (b) elastomer; (c) sum of (a) and (b); (d) composite.

Fig. 3 (experimental qualitative results) shows strongly heterogeneous stress fields, induced by structural interactions between the constituents of the composite.

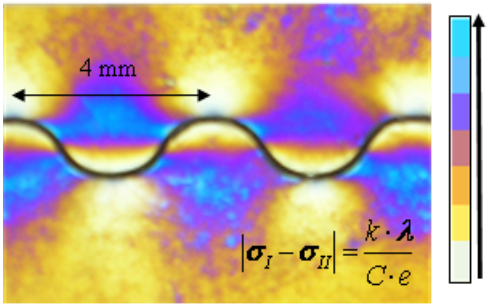

Figure 3: Photoelasticimetry results: each color of area corresponds to a mean stress level.

Fig. 4 (numerical quantitative results) shows similar stress field shapes. The good correlation observed between both kinds of results proves that the FEM model used correctly describes structural interaction effects.

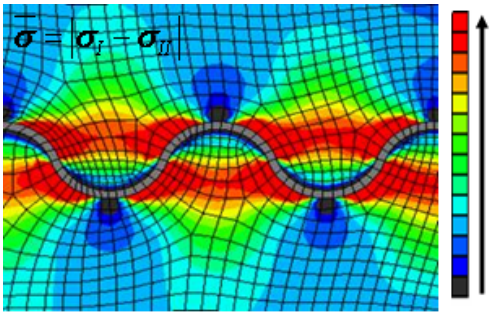

Figure 4: PFEM results: mean stress field in the middle plane of the composite.

Concerning the global response of the composite, Fig. 5 shows that experimental and numerical responses are very close on loading, as well as on the second part of unloading. The discrepancy observed (at most 10% on load values) at the beginning of unloading arises from the Bergström and Boyce law description of the hysteresis for the elastomer. On the whole, the present FEM modelling of the composite gives satisfactory results.

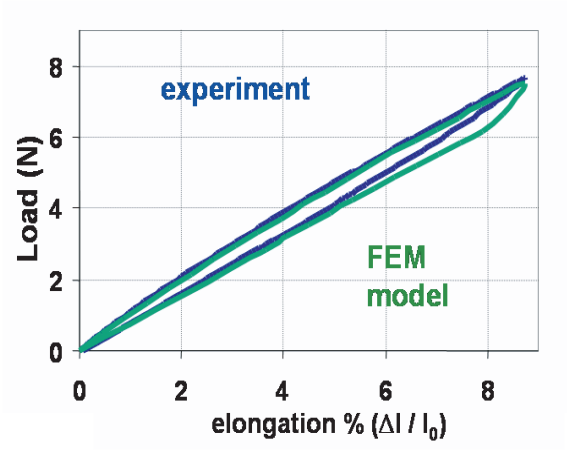

Figure 5: Experimental and numerical responses of the composite.

Conclusions

In the present study, the behaviour of an SMA/elastomer composite was modelled using thermodynamic potentials for both materials. FEM calculation results were successfully compared with experimental results obtained under tension loading at room temperature.

In further works, a complete thermomechanical constitutive law for SMAs will be optimized, including shape memory effects. Moreover the development of SMA/elastomer composites for biomedical applications is envisaged (e.g. active fabrics), involving either pseudoelasticity or two way shape memory effect of a “snake-like”-shaped NiTi wire.

References

[1] K. Escher, E. Hornbogen, M. Mertmann (1993): in Proceedings of ICOMAT-92, *Monterey Institute for Advanced Studies, Montery, California*, 1289–1294.

[2] K. Neuking, A. Abu-Zarifa, S. Youcheu-Kemtchou, G. Eggeler (2005): Polymer/NiTi composites, Fundamental aspects, Processing and Properties, *Advanced Engineering Materials*, **7**, 1014–1023.

[3] B. Peultier, T. Ben-Zineb, E. Patoor (2006): Macroscopic constitutive law of shape memory alloy thermomechanical behaviour. Application to structure computation by FEM *Mechanics of Materials*, **38,** 510–524.

[4] E. Patoor, A. Eberhardt, M. Berveiller (1996): Micromechanical modelling of superelasticity in shape memory alloy, *J. Phys. IV*, col. C1 **6**, 277–292.

[5] C. Gsell, A. Coupard, Génie mécanique des caoutchoucs (1997), *Gsell & Coupard Ed.*, APOLLOR-INPL.

[6] J. S. Bergström, M. C. Boyce (1998): Constitutive modelling of the large strain dependant behavior of elastomers. *J. Mech. Phys. Solids*, **46**, 931–954.

Implementation of Non-Local Integral Models into commercial FE-Methods

J. Bobiński*, J. Tejchman

Faculty of Civil and Environmental Engineering, Gdansk University of Technology
Narutowicza 11/12, 80-226 Gdansk, Poland
bobin@pg.gda.pl, tejchmk@pg.gda.pl

Summary: This paper presents hints useful in the implementation of non-local models of the integral type into a commercial FEM program Abaqus/Standard. First, strain localisation and a regularisation method in the form of a non-local theory is briefly discussed. Then, gathering of the non-local global data is described. The modelling of notches and symmetry of the specimen is presented. Advantages and shortcomings of the proposed method are outlined.

Strain localisation

In quasi-brittle materials after the peak the phenomenon of strain softening occurs. A gradual decrease of carrying stresses with increasing strains takes place. In concrete it can be observed both in tension and compression. The deformations localise in small areas in the form of cracks or shear zones. Unfortunately, classical FE-simulations with materials with softening are not able to properly model strain localisation. The obtained results suffer from a mesh sensitivity. The reason is that differential equations of motion change their type and the boundary value problem is ill-posed. To capture realistically strain localisation, a characteristic length of microstructure has to be included. It restores a well-posedness of the boundary value problem and enables to obtain an objective numerical solution. There are many different methods of regularisation e.g. micro-polar, viscous, strain gradient or non-local ones.

Non-local theory

To regularise boundary value problems in brittle materials with a constitutive law defined within the continuum mechanics, a non-local theory was chosen. It is based on a spatial averaging of a tensor or scalar state variable (describing the material degradation) in a certain neighbourhood of a given material point. The non-locality is used mainly in damage mechanics, plasticity, coupled damage and plasticity, but also it has been already applied to smeared crack models, microplane models, hypoplasticity and lattice models. For simplicity, we will restrict ourselves only to the two first constitutive models.

In damage mechanics, usually the definition of the equivalent strain measure $\tilde{\varepsilon}$ is replaced by its non-local counterpart defined as [2]

$$\bar{\varepsilon}(\boldsymbol{x}) = \int_V \alpha(\boldsymbol{x},\boldsymbol{\xi})\tilde{\varepsilon}(\boldsymbol{\xi})\,\mathrm{d}\boldsymbol{\xi}, \tag{1}$$

where $\boldsymbol{x}$ are the coordinates of the considered point, $\boldsymbol{\xi}$ denotes the coordinates of the surrounding points and a function α is equal to

$$\alpha(\boldsymbol{x},\boldsymbol{\xi}) = \frac{\alpha_0\left(\|\boldsymbol{x},\boldsymbol{\xi}\|\right)}{\int_V \alpha_0\left(\|\boldsymbol{x},\boldsymbol{\zeta}\|\right)\,\mathrm{d}\boldsymbol{\zeta}}. \tag{2}$$

As a weighting function α_0, the Gauss distribution can be assumed

$$\alpha_0(r) = \frac{1}{l\sqrt{\pi}} e^{-\left(\frac{r}{l}\right)^2}, \tag{3}$$

where r is a distance between two points and l denotes a characteristic length of microstructure. It should be noted that averaging is restricted only to a small area around the considered point. In plasticity, a slightly modified formula is used to define the non-local hardening (softening) parameter $\widehat{\kappa}$ [3]

$$\widehat{\kappa}(\boldsymbol{x}) = (1-m)\kappa(\boldsymbol{x}) + m\int_V \alpha(\boldsymbol{x},\boldsymbol{\xi})\kappa(\boldsymbol{\xi})\,\mathrm{d}\boldsymbol{\xi}, \tag{4}$$

where κ is a local value of a softening parameter and m is a constant greater than 1.

FE-modelling

Researchers involved in advanced numerical modelling of materials have to choose between two solutions. First option is to write their own FE-code or modify and extend existing programs with a source code available (like FEAP or OOFEM [4]). The last program is especially interesting because it includes some non-local damage models. As an alternative, one of commercial FE-methods as Abaqus, Adina, Ansys or MSC Marc with an unavailable source code can be applied. The use of a commercial package (like Abaqus/Standard [1]) limits a programming effort at one side but at the other side it creates some additional problems in an implementation of non-typical subroutines. The non-local theory requires some numerical tricks to achieve a successful implementation into the Abaqus/Standard program.

Gathering data

The first problem is to collect the required data. To calculate non-local parameters from equations (1) and (4), the coordinates of integration points, local quantities to be averaged ($\tilde{\varepsilon}$ or κ) and area of finite elements have to be known. The first two ones are available directly in integration points (procedure `UMAT` in Abaqus). The area of elements can be calculated by defining user's elements (procedure `UEL` in Abaqus). Alternatively, one can use so called 'element characteristic length' (related to the volume of finite elements) which is available in the procedure `UMAT`.

In standard commercial programs, the information about elements or integration points is available locally, i.e. only in a considered element (point). A non-local model requires information from all integration points at the same time. It can be

done by storing the data in tables defined with the aid of the COMMON block. In general, the data gathering can be achieved using 3 different ways:

- **Double mesh** – two meshes are used (one mesh with standard elements using user's material law (procedure UMAT) and second mesh defined by the user's elements (procedure UEL) (Fig. 1). The elements in the second mesh are attached to the same nodes as the main finite elements from the first mesh. They have no stiffness, so they do not influence the FE-results. Their task is to collect the required data only. This option can be used when the user controls the order, at which the procedures UMAT and UEL are called during iterations (in some programs there is an internal order of elements despite their numbers).

- **Odd and even iterations** – iterations are conceptually divided into odd (when the data is collected), and into even ones (when non-local calculations are performed). Between odd and even iterations, the same node configuration is imposed.

- **Values form previous step** – non-local quantities are estimated on a basis of values from the previous step (in which they are all known). This method, unfortunately, can not be applied to non-local damage models.

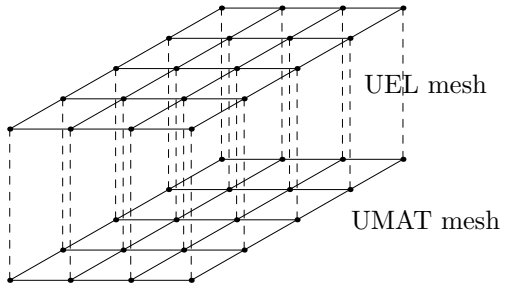

Figure 1: Definition of the double mesh.

Symmetry and notches

Two other problems should be also taken into consideration when applying non-local models. The first case occurs when one utilises the symmetry (simulations concern only a half of the problem). For integration points in the neighbourhood of the axis of symmetry, the reflected points should be also taken into account (Fig. 2). The most universal method to consider the symmetry axis is to define an additional truss element (with no stiffness) and to "mirror" the information for points which are located closer than interaction radius R.

The second problem arises when modelling notches. In this case, an non-local interaction between points at the opposite side of the notch should be avoided (Fig. 3). Again an information about the geometry of the notch can be provided by defining additional truss elements with no stiffness.

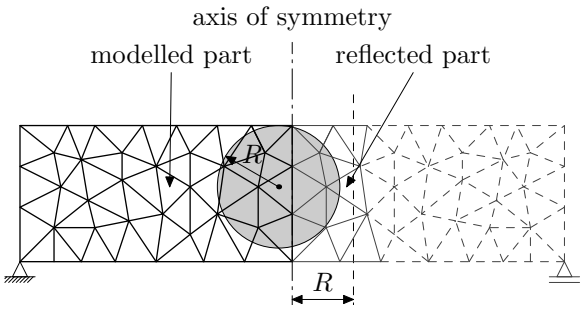

Figure 2: Symmetry of problem.

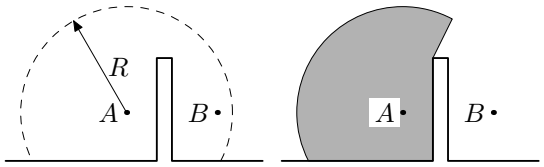

Figure 3: Interaction between points at the opposite side of notch.

Final remarks

The presented implementation methods of non-local models into commercial FE-packages enable to minimise the programmer's effort and to use all benefits of the program. However, a major drawback concerning a global stiffness matrix should be mentioned. It is impossible to define a non-local tangent stiffness matrix in damage models (local secant matrix can be used) what reduces the convergence speed. Moreover, in Abaqus/Standard, a global stiffness matrix is defined and factorised in each iteration. In turn, in non-local plasticity, an elastic global stiffness matrix is used during the whole loading history.

Acknowledgements

The numerical calculations were performed on supercomputers of the Academic Computer Centre in Gdansk TASK.

References

[1] Abaqus (1998): *Abaqus Theory Manual*. Hibbitt, Karlsson & Sorensen, Inc.

[2] G. Pijaudier-Cabot, Z. P. Bažant (1987): Nonlocal damage theory. *Journal of Engineering Mechanics ASCE*, **113**, 1512–1533.

[3] R. B. J. Brinkgreve (1994): *Geomaterial Models and Numerical Analysis of Softening*. PhD Thesis, Delft University of Technology.

[4] B. Patzák, Z. Bittnar (2001): Design of object oriented finite element code. *Advances in Engineering Software*, **32**, 759–767.

Some Considerations about Elasticity of the Eye-Lens Microstructure

M. Baritz*, G. Deliu

University Transilvania, Brasov, Romania
mbaritz@unitbv.ro, deliumec@unitbv.ro

Summary: This paper presents some considerations about the elastic behavior of the human eye-lens. Establishing a model of it we were studying, in different research modules, the optical and elastic characteristics of the eye-lens microstructure. This study it is very important to analyze the visual accommodation process of the natural eye-lens in different conditions.

In the first part of the paper they are presented some aspects about the natural eye-lens analyze from optical point of view for modeling and studying the accommodation phenomena, for establishing the iso-indicial surfaces, the shape and the dimensions of them.

Using the Moore model it is possible to establish the index equation like this:

$$n = n_o(z) + n_1(z)\,\xi + n_2(z)\,\xi^2 + ... \qquad (1)$$

This relation was developed and applied to the microstructure of the eye-lens in the ten layers which make an assembly of nine bonded lens.

In this research work for modeling the behavior of the eye-lens in different situation was adopted the Moore equation, to which, also, was calculated the values for n_i in two situations: paraxial and extra-axial fields and for the accommodation process with the limits of this accommodation power (0-12) dpt.

The iso-indicial surfaces are presented in Fig. 1, supposing that they have the same thickness on the optical axis in accommodation ($d_a/10$) and non-accommodation state ($d_{na}/10$).

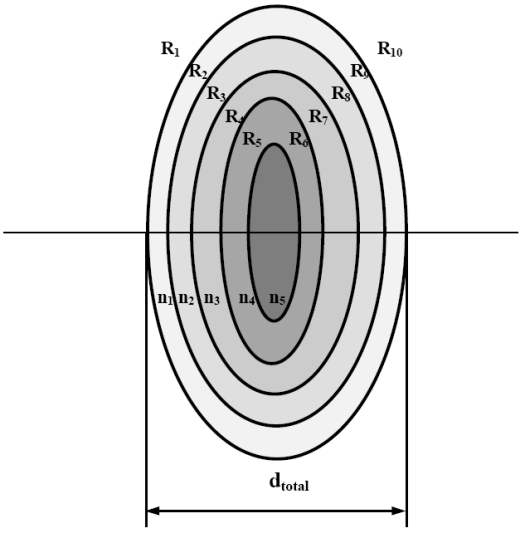

Figure 1: The view of the eye-lens multilayers model.

By this calculation, in the center of the system $O(0,0)$ one can obtain, in both state of the vision process (accommodation and non-accommodation) the same refractive index $n_a(0,0) = n_{na}(0,0) = 1.406$, which they are in correspondence with the Gullstrand ideal values for the eye-lens center.

Some considerations about analyze and modeling of the eye-lens by elastic behavior theory of the components surfaces are presented in the second part of the paper

We consider the micro-structure of the eye-lens being accomplished by elastic, multilayer material, axial symmetrical and uniform in each layer.

The study of the elastic behavior of the eye-lens layers by adopting the model of the thin curvilinear plate was the most realistic model for analyze and modeling the natural behavior of them.

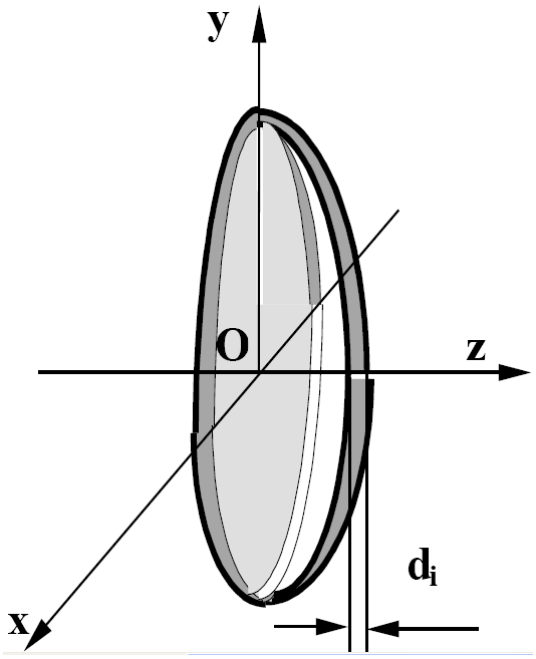

Figure 2: The model of the eye-lens layer like curvilinear plate.

For that analyze and modeling process, each layer was assimilated with a thin curvilinear plate ($d_i = 0.4(0.36)$ mm $<<$ $D_u = 8.5$ mm), which are defined by a median curvilinear surface.

It was considered, also, that each layer takes part of a spherical surface, with axial symmetry but with variable thickness in the zOy and xOy planes.

Some initial hypothesis for simplifying the modeling process and for deformations values calculation of this surface were introducing at the beginning:

- the material for each eye-lens layer has homogeny and

isotropy qualities and the behavior of each plate's element does not depend of the position and the orientation, but only depends of the forces on him;

- the deformations of the material are in the proportionality zone and the elasticity module is the same in all directions (for each of the layers);
- the thickness of the plate was considered very small comparing with the curvature radius of the median surface.

There are two sections for these kind of layer surfaces, perpendicular between them, but having, one of them, the maximum curvature radius and the other one, the minimum radius, named principal curvatures.

For the calculation of the sectional efforts into the dioptrically surface of the eye-lens it is necessary to isolate a surface element and to write the equilibrium equations for it.

The equations system is :

$$\begin{aligned} N_{\phi\theta}\frac{\partial r}{\partial \phi} + \rho_1 \frac{\partial N_\theta}{\partial \theta} + r\frac{\partial N_{\phi\theta}}{\partial \phi} + N_{\theta\phi}\rho_1 \cos\phi + p_x r \rho_1 &= 0 \\ N_\phi \frac{\partial r}{\partial \phi} + r\frac{\partial N_\phi}{\partial \phi} + \rho_1 \frac{\partial N_{\theta\phi}}{\partial \theta} - N_\theta \rho_1 \cos\phi + p_y r \rho_1 &= 0 \\ \frac{N_\phi}{\rho_1} + \frac{N_\theta}{\rho_2} + p_z &= 0 \end{aligned}$$

The unknowns from the equations system are N_ϕ, N_θ, $N_{\theta\phi} = N_{\phi\theta}$ named *sectional efforts* of the plate (model of the eye-lens layer).

After this calculation and modeling of the elastic behavior of all eye-lens thin curvilinear plates, the deformation of all layers was observed from interior to exterior (Fig. 5).

Also was establishing that the center of the eye-lens model had no deformation, remaining immobile, this "eye-lens quality" having a very big importance and showing that the visual accommodation process is made by the external layers, more elastic and flexible ones.

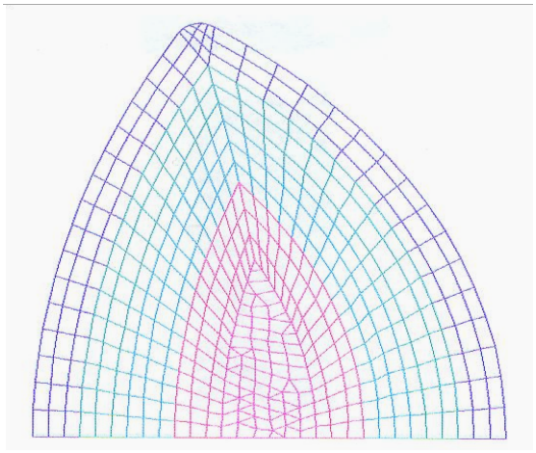

Figure 3: The eye-lens model in initial conditions (without deformation) with 10 layers.

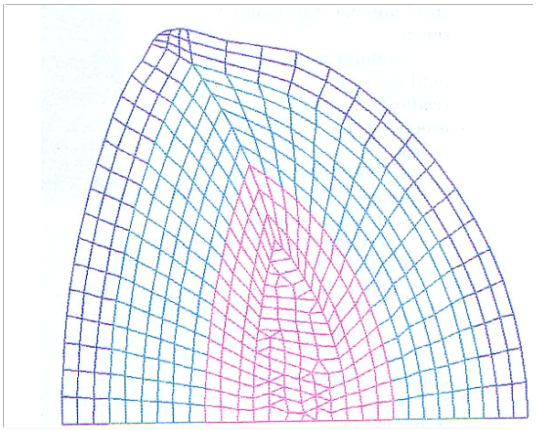

Figure 4: The eye-lens model after deformation with 10 layers.

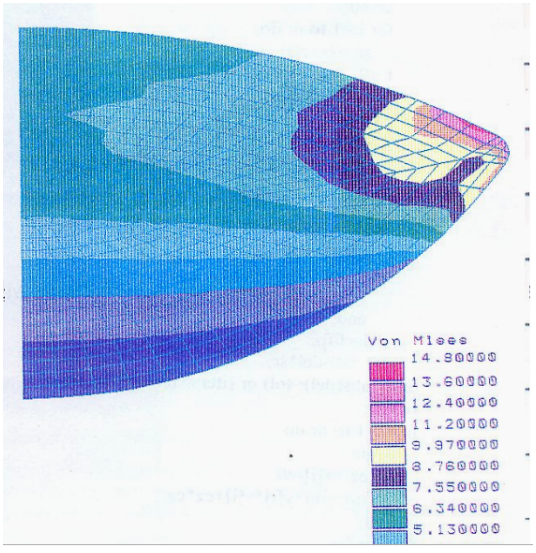

Figure 5: The limits of the eye-lens behavior modeling.

References

[1] M. Baritz (2002): *Studiul profilelor speciale prin metode complementare*, Ed. Infomarket, Brasov, Romania.

[2] D. R. Mocanu et al. (1976): *Analiza exprimentala a tensiunilor*, Ed. Tehnica Bucuresti, Romania.

[3] H. H. Emsley (1980): *Visual Optics*, Butterworths, London, England.

[4] Gh. Deliu (2002): *Mechanics for Engineering Students*, Ed. Albastra, Romania.

Variational Reduction for the Transport Equation

M. Picq, J. Pousin*

Camille Jordan Mathematical Institute INSA de Lyon
Address 20 Av. A. Einstein F-69100 Villeurbanne Cedex, France
martine.picq@insa-lyon.fr, jerome.pousin@insa-lyon.fr

Summary: Asymptotic partial decomposition has been studied in [1] for an elliptic problem in the case of geometrical heterogeneous domains when the right hand side does not depend on the shrinking variable. In this work we consider the Transport equation in an heterogeneous domain with a general right hand side. Introducing a variational reduction type method and dealing with a constrained formulation of the problem, we show that the problem can be reduced to a 2D-1D problem.

Introduction

Let us consider the Transport equation in the following domain Q:

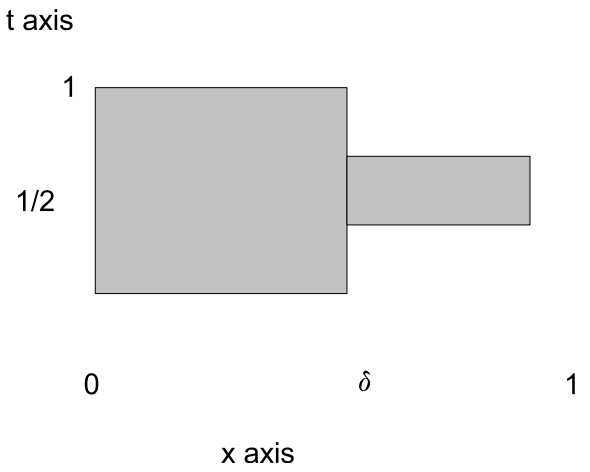

Figure 1: Heterogeneous domain Q.

Let $f \in C^0(Q;\mathcal{R})$ a continuous function, $a \in C^1(Q;\mathcal{R})$ be given, we define the function $\beta = \begin{pmatrix} 1 \\ a(t,x) \end{pmatrix}$ and we assume a to be bounded from below by a positive number. We look for

$$\begin{array}{c} u \in H(\beta,Q) = \{\rho \in L^2(Q), \\ div(\beta\,\rho) \in L^2(Q), \rho\,|_{Q_-} \in L^2(\partial Q_-, |(\beta/n)|\; d\sigma)\} \end{array} \tag{1}$$

verifying:

$$(\beta/\nabla u)_2 = \frac{\partial u}{\partial x} + a(t,x)\frac{\partial u}{\partial x} = f \tag{2}$$

The boundary conditions are fixed to be zero on ∂Q_-. Due to the heterogeneous domain, the Transport equation can be reduced to an ordinary differential equation in the thin part of the domain. This can be proved with the partial asymptotic decomposition method [1] when the function f is only a function of x. A numerical method based on finite element is given in [2].

In this work, we would like to consider the general case where the function f depends on (t,x) variables. Let Γ_ϵ be defined by: $\Gamma_\epsilon = (\frac{1}{2}-\epsilon, \frac{1}{2}+\epsilon) \times \{\delta\}$.

The variational reduction method consists in introducing a product space $H(\beta,Q_1) \times (M(\Gamma_\epsilon) \bigotimes_0 H^1(\delta,1))$ where $M(\Gamma_\epsilon) = vec(q_j)_{j=0}^m$. Introduce the unbounded operator:
$\frac{d}{dt} : D(\frac{d}{dt}) \subset L^2(\Gamma_\epsilon) \to L^2(\Gamma_\epsilon)$
$d(\frac{d}{dt}\varphi,\psi) = (\frac{d}{dt}\varphi/\psi)_{\Gamma_\epsilon}\ \forall \psi \in L^2(\Gamma_\epsilon)$.

We assume that $M(\Gamma_\epsilon) \subset Ker\frac{d}{dt}$ and that the $q_j's$ are orthogonal with respect to both the $L^2(\Gamma_\epsilon, a(\cdot,\delta)dt)$ scalar product and the $L^2(\Gamma_\epsilon)$ scalar product. When the function a is time-independent, one can choose $q_0(t) = 1$; and $q_k(t) = \sin(k\pi[\frac{t-\frac{1}{2}}{\epsilon}+1])$ for $1 \le k \le m$. Then we look for a solution $(u_1, u_{2_M}) = \sum_{j=0}^m q_j(t)u_{2_j}(x))$.
Consider now a weak formulation of the problem in $Q \setminus Q_1$: $\forall\, q \in M(\Gamma_\epsilon)$

$$\begin{array}{c} \int_\delta^1 \int_{\frac{1}{2}-\epsilon}^{\frac{1}{2}+\epsilon} \partial_t u_{2M} q(t)\varphi(x)\,dtdx \\ -\int_\delta^1 \int_{\frac{1}{2}-\epsilon}^{\frac{1}{2}+\epsilon} u_{2M} q(t)\partial_t(a(t,x)\varphi(x))\,dtdx \\ -\int_{\frac{1}{2}-\epsilon}^{\frac{1}{2}+\epsilon} u_{2M} a(t,\delta)\varphi(\delta)q(t)\,dt \\ = \int_\delta^1 \int_{\frac{1}{2}-\epsilon}^{\frac{1}{2}+\epsilon} f(t,x)q(t)\varphi(x)\,dtdx,\ \forall \varphi \in H^1(\delta,1); \varphi(1) \\ = 0 \end{array} \tag{3}$$

The decomposed problem reads: find (u_1, u_{2_M}) verifying (3) and :

$$\begin{array}{l} (\beta/\nabla u_1)_2 = f \text{ in } Q_1; \\ \forall q \in M(\Gamma_\epsilon)\, b(u_1 - u_{2_M}, q) = \\ = \int_{\{x=\delta\}} (u_1(t,\delta) - u_{2_M}(t,\delta))q(t)a(t,\delta)\,dt = 0. \end{array} \tag{4}$$

The matching conditions on the interface are imposed with a weak formulation. Now, let us specify the equations for the case where a is time-independent. Problem (3) is then expressed in differential form as: $j = 0$

$$\begin{array}{c} a(x)\partial_x u_{2M_0}(x) = \frac{1}{\epsilon}\int_{\frac{1}{2}-\epsilon}^{\frac{1}{2}+\epsilon} f(t,x)\,dt; \\ u_{2M_0}(\delta) = \frac{1}{\epsilon}\int_{\frac{1}{2}-\epsilon}^{\frac{1}{2}+\epsilon} u_1(t,\delta)\,dt \end{array} \tag{5}$$

and for $1 \le j \le m$

$$\begin{array}{c} a(x)\partial_x u_{2M_j}(x) = \frac{1}{\epsilon}\int_{\frac{1}{2}-\epsilon}^{\frac{1}{2}+\epsilon} f(t,x)\sin(j\pi[\frac{t-\frac{1}{2}}{\epsilon}+1])\,dt \\ u_{2M_j}(\delta) = \frac{1}{\epsilon}\int_{\frac{1}{2}-\epsilon}^{\frac{1}{2}+\epsilon} u_1(t,\delta)\sin(j\pi[\frac{t-\frac{1}{2}}{\epsilon}+1])\,dt \end{array} \tag{6}$$

For $j = 0$, let ϵ go to zero, we get the classical zero order homogenized problem. In the case with a velocity $a(\cdot,\cdot)$ regular

and time-dependent, for the zero order term we get:

$$\begin{array}{c} a(\frac{1}{2},x)\partial_x u_{2M_0}(x) = f(\frac{1}{2},x)\,, \delta < x < 1 \\ u_{2M_0}(\delta) = u_1(\frac{1}{2},\delta) \end{array} \tag{7}$$

Now let us introduce a test case. We set $a(t,x) = 50x + \exp(t)$, $f(t,x) = x + x\exp(\frac{t}{2})$, and the problem is discretized in Q_1 with a finite difference method. The time step equals the space step and is equal to 0.25×10^{-2}. In Figure 1, the solution is depicted for $\epsilon = 2 \times 10^{-2}$.

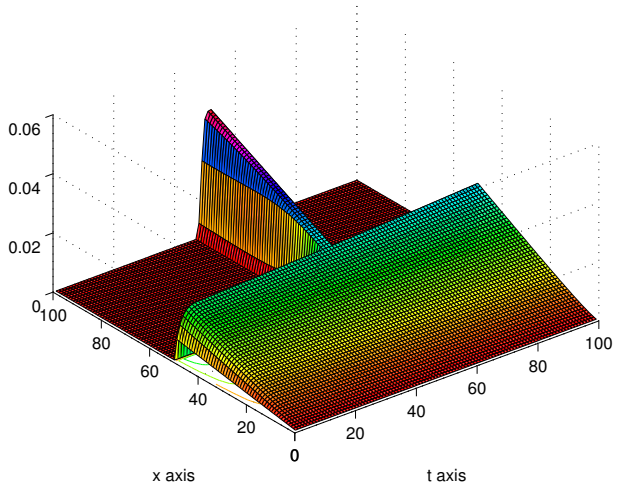

Figure 2: Finite difference computed solution.

In Figure 2 the zero order (7) approximation is used for the solution in domain $Q \setminus Q_1$.

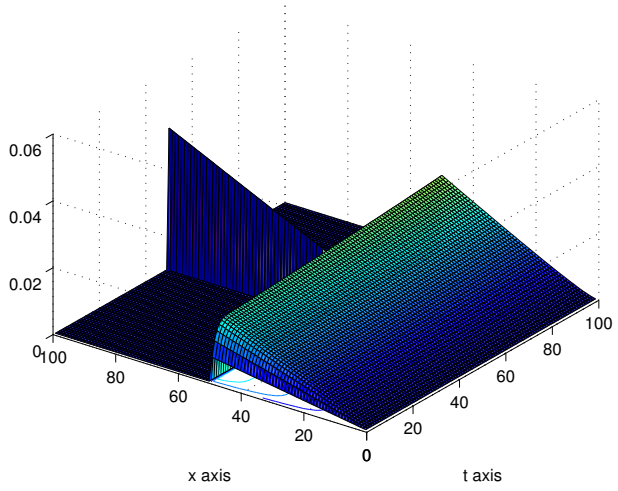

Figure 3: Zero order computed solution.

Let us mention that in the case where the domain $Q \setminus Q_1$ is too thin, classical numerical methods do not work anymore. For example, we need more than ten points in the thickness of the thin domain $Q \setminus Q_1$. In the following Figure, $\epsilon = 0.83 \times 10^{-2}$, and we can see some discrepancy between the classical finite difference solution and the zero order approximation.

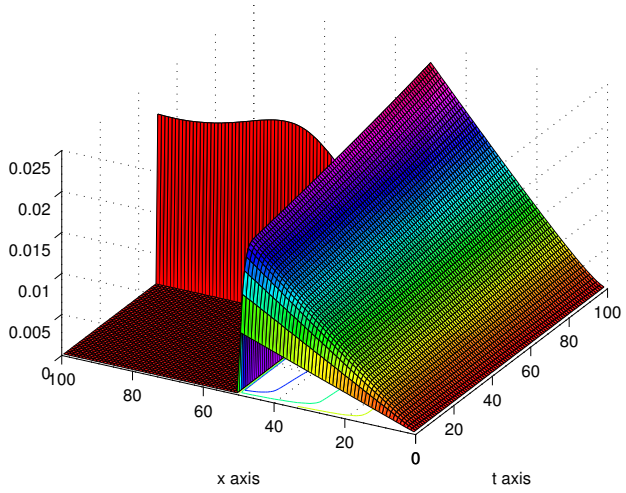

Figure 4: Thinner case: FD computed solution.

References

[1] G. P. Panasenko (2005): Multi-scale modelling for structures and composites, *Springer Verlag*.

[2] F. Fontviele, G. Panassenko, J. Pousin (2007): *F.E.M. implementation for the asymptotic partial decomposition*, to appear in Applicable Analysis.

Mathematical and Numerical Modelling of Focal Ischemia

M. Perego[1*], A. Veneziani[1], E. Agostoni[2], S. Salsa[1]

[1]MOX (Modeling and Scientific Computing), Dipartimento di Matematica "F. Brioschi", Politecnico di Milano, Via Bonardi 9, I - 20133 Milano, Italy
mauro.perego@polimi.it, alessandro.veneziani@polimi.it, sandro.salsa@polimi.it

[2]Neuroscience Department, A. Manzoni Hospital, Lecco, Italy
e.agostoni@libero.it

Summary: This paper concerns mathematical and numerical modelling of focal ischemia in tridimensional geometries. The proposed model includes a space dependent description of the blood dynamics assuming that the vascular tissue is a porous medium and a description of ion disorder and tissue damage rate caused by a reduction in the flow rate.

Introduction

Relevance of a deep comprehension of the brain tissue damage mechanisms during focal ischemia has been realized since a long time (see [3, 2, 7, 10]). Besides the set up of therapies for stopping tissue degeneration in the ischemic penumbra, a possible outcome is the understanding of the failure of actions that in other districts yield good results. For instance, fibrinolythic therapies, that in the coronary districts works, in the neurological context can lead to dangerous blood hemorrhages. A possible approach for having a deeper insight of these phenomena is to resort to mathematical models and numerical simulations (see [3, 2, 7, 10]). The main difficulties in this context concern:

1. intrinsic complexity of the phenomena at hand, that involve interacting fluid and biochemical dynamics; this is typically reflected into the complexity of the associated mathematical models, given by systems of partial and ordinary differential and sometimes algebraic equations;
2. complexity of the geometries at hand that can play a relevant role (see [8]);
3. parameters identification and evaluation (see [7, 1]).

These difficulties affect the set up of reliable numerical models. Numerical simulations presented in the literature are so far limited to 2D geometries and use a lumped average parameter to describe the cerebral blood flow, obeying an ordinary differential (see [2]) or an algebraic (see [7]) equation.

The aim of the present work is twofold. The first goal, following the guidelines of the model proposed in [2, 1, 4] including dynamics for intra and extra cellular potassium and calcium ions (see [1]) and of some heuristic indices for the tissue integrity and the metabolic stores, is to give a more rigorous model for the ions dynamics and include a precise description of the fluid dynamics. More precisely, on one hand, by means of "average volume" techniques (see [5, 6]) we present a model accounting for local dynamics in an average way, giving a mesoscale picture of the ion concentrations and of the tissue integrity; on the other hand, we include a space dependent description of the blood dynamics assuming that the vascular tissue is a porous medium. For this reason, we replace the ordinary differential equation of the flow in the original model of [2] with the Darcy law for porous media. The basic idea is that the permeability is a function of the integrity of the tissue. The more precise formulation of the hemodynamics will allow the simulation of the possible action of fibrinolytic therapies and subsequent hemorrhage.
The second goal is to present numerical simulation of the phenomena at hand in 3D, by means of ad hoc finite element code.

Model

The whole model is composed by two main parts: the biochemical one, describing the behavior of potassium and calcium concentrations and the tissue damage, and the fluid-dynamics one describing blood flow.
The biochemical part is formed by four partial differential equations, describing the intracellular and extracellular concentrations of potassium and calcium and by two ordinary equations, one describing the energy reserve (E) of the tissue and the other describing an heuristic index (I) representing the damage rate of the tissue. Each ion concentration follows a system of two differential equations (the first for the extracellular concentration (C_e) and the second for the intracellular concentration (C_i)):

$$\begin{cases} \dfrac{\partial C_e}{\partial t} - D_e \Delta C_e = J_C, \\ \dfrac{\partial C_i}{\partial t} - D_i \Delta C_i = -J_C. \end{cases} \tag{1}$$

J_C is the ion flux through cell membrane and is a function of ion concentrations and of the energy reserve (E). In our model we rearranged the membran flux equation proposed in [1] in order to describe the ischemic case.
The fluid dynamics part is constituted by an elliptic equation, derived by Darcy law:

$$\boldsymbol{q} = -K(I)\,\nabla\varphi \tag{2}$$

where $\boldsymbol{q}$ is the blood mean velocity, φ is the piezometric head, and K, which is a function of the tissue integrity, is the conducibility of the porous medium. The conducibility K increases when the tissue is injured (see [11]).

Results

As a sample of our results, we show two simulations in very simple geometries. In the first example we consider a sphere and we impose a flux which is null in the centre and reaches the physiological value at the sphere surface. Figure 1 shows the extracellular potassium concentration. As expected, the ischemia induces the release of potassium in the extracellular space, which spreads in the form of periodic waves (*Spreading Depression* phenomenon). Figure 2 shows the tissue integrity, at different time istants. As expected the injuried area grows with the passing of time ($I = 0$ means necrotic tissue, while $I = 1$ means intact tissue). In the second example we consider a cylinder with an artery placed along its axis. Figure 3 shows specific blood flow rate; on the left side the brain is in physiological conditions, while on the right it's simulated a reperfusion of the artery after being occluded for a long time. The increased flux could be correlated with an hemorrhage risk.

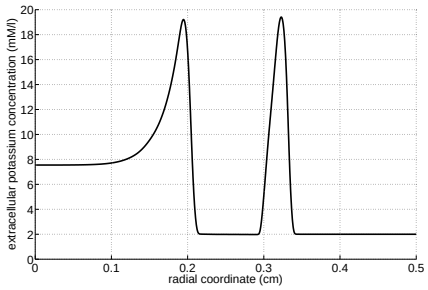

Figure 1: Extracellular potassium concentration versus the radial coordinate at time $t = 4min$.

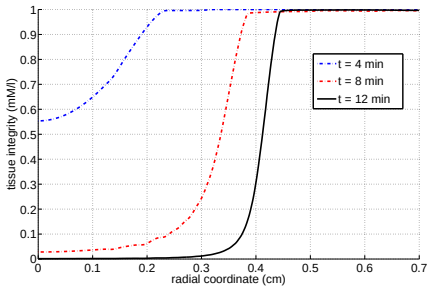

Figure 2: Tissue integrity versus the radial coordinate at different time instants.

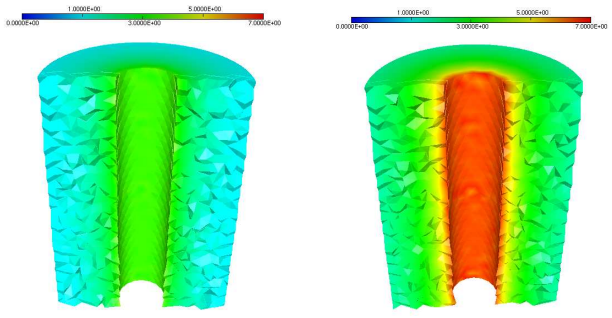

Figure 3: Specific blood flow rate in physiological and pathological case.

The numerical results presented here show at a qualitative level possible dynamics that can be induced by the combination of biochemical events induced by the stroke and the reperfusion of the occluded vessels. The quantitative validation of the model used here is complicated by the difficulties in collecting experimental data. Nevertheless, it represents an important development of the present work.

References

[1] H. C. Tuckwell, R. M. Miura (1978): A mathematical model for spreading cortical depression. *Biophysics Journal*, **23**, 257–276.

[2] E. Ruppin, E. Ofer, J. A. Reggia, K. Revett, S. Goodall (1999): Pathogenic mechanism in ischemic damage: a computational study. *Computers in Biology and Medicine*, **29**, 39–59.

[3] K. Revett, E. Ruppin, S. Goodall, J. A. Reggia (1998): Spreading depression in focal ischemia: a computational study. *Journal of Cerebral Blood Flow and Metabolism*, **18**, 998–1007.

[4] L. Dai (1997): Lattice Boltzmann equation models for migration of ions in the brain and their applications. *PhD Thesis*.

[5] S. Whitaker (1969): Fluid motion in porous media. *Industrial and Engineering Chemistry*, **61**, 15–28.

[6] F. K. Lehner (1979): On the validity of Fick's law for transient diffusion through a porous medium. *Chem. Engin. Sci.*, **34**, 821–825.

[7] M. A. Dronne, J. P. Boissel, E. Grenier, H. Gilquin, M. Cucherat, M. Hommel, E. Barbier, G. Bricca (2004): Mathematical Modelling of an Ischemic Stroke: an Integrative Approach. *Acta Biotheoretica*, **52**, 255–272.

[8] M. A. Dronne, E. Grenier, H. Gilquin, M. Hommel, J. P. Boissel (2004): Influence of brain geometry on spreading depressions: a computationnal study. *Preprint*.

[9] E. Grenier, M. A. Dronne, H. Gilquin (2004): Modelization of spreading depressions following Nedergaard. *Preprint*.

[10] A. C. G. Almeida, H. Z. Texeira, M. A. Duarte, and A. F. C. Infantosi (2004): Modeling Extracellular Space Electrodiffusion During Leão's Spreading Depression. *Biomedical Engineering*, **51**, 450–458.

[11] P. A. Fraser, A. D. Dallas (1993): Permeability of disrupted cerebral microvessel in the frog. *Journal of physiology*, **461**, 619–632.

Heterogeneous Interface Numerical Solution by Field Boundary Element Method

V. Minutolo, E. Ruocco*

Department of Civil Engineering, Second University of Naples (SUN), Engineering Faculty
via Roma 9, Aversa, Ce, 81031, Italy
vincenzo.minutolo@unina2.it, eugenio.ruocco@unina2.it

Summary: To analyse graded materials with Boundary Element Method a particular fundamental solution is required, conversely when standard Kelvin's solution is used, Field Boundary Integral Equation arises. The formulation is effective when one deals with multiregion structures where two or more regions are linked by graded interfaces. The Field Boundary Elements have to be used only at the interfaces whilst constant material regions require only Boundary Elements. It is shown that the procedure is simple and stable and some case studies are discussed in detail.

Introduction

Constitutive behaviour of Functionally Graded Material (FGM) [1-3] depends on both composition and material structure gradual change over the volume, resulting in corresponding changes on the properties of the material. The variations of material components are intentionally designed and tailored in order to optimize the performance in a particular application, or under a specific set of functional requirements. In the simplest FGMs, two different material ingredients change gradually from one to the other.

The FGM concept is applicable to almost all engineering fields. Examples of a variety of actual and forthcoming applications to transport systems, energy conversion systems, cutting tools, machine parts, semiconductors, optics and bio-systems are widely available in literature, comprehensive reviews of FGM research can be found in.
First examples of FGMs are available in nature: examining biological load carriers such as animal bones, it has been observed that internal pattern has optimal shape with respect to principal stress directions and shear stress magnitude, it is produced by self-optimizing system, activated by biological sensors that detect external mechanical stimuli producing deposition and absorption of solid component of the skeleton tissue responsible of remodelling process. Analogous optimization characterizes the growth some plant stems, where position, size, number of holes constituting nutrient ducts and fibres assembly give rise to optimal structural pattern with respect to resistance, elasticity and ductility. Due to complications that arise to mechanical formulation of FGM, computational analysis is an effective method to design, and to understand FGM behaviour.

The Boundary Integral Equation Method (BIEM) has not been widely applied to graded material since it is rather difficult to obtain the fundamental solution except for simple variation of constitutive properties [4-6]. Solution for some particular kind of variability is available where the analytical solution for exponential variation is obtained.
The main disadvantage of BIEM treatment of FGM consists of the requirement of ad hoc solution for any possible variation of the material elasticity and inhibit its use into general purpose codes; consequently present authors developed a formulation that uses the fundamental solution of homogeneous material, say classical Kelvins solution, to deal with FGM. The work allows representing the response of heterogeneous material by means of Field Boundary Element Method (FBEM). The proposed formulation can handle both isotropic and anisotropic materials and is able to represent homogeneous and heterogeneous elasticity.

Unlike BEM, the formulation requires field discretization and contains domain unknowns. This disadvantage disappears if the material gradation reduces to a small part of the structure, say interfaces, joints etc., while the main part is homogeneous (Fig. 1). The structure can be analysed by pure Boundary Element almost everywhere except that on the small graded part where Field Boundary Element are required.

In the proposed work the good agreement with analytical result is shown and the accuracy of the method is tested with respect to FEM that allows the calculation of FGM but gives less accurate results than FBEM when high gradient of stress arises and high distorted mesh are used for the structure modelling. In these cases FBEM gives its best results

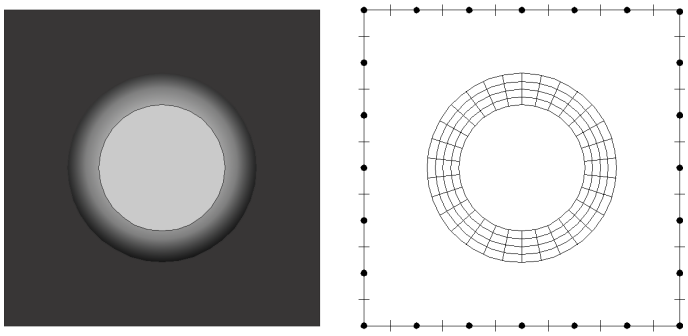

Figure 1: FGM interface and FBEM discretization. Atomistic and various continuum models for carbon-nanotubes.

FBEM formulation

Elastic relationship of FGM assumes that elastic coefficients vary within the structure accordingly to a prescribed function, isotropic material depend on two parameters, namely Young modulus E and Poisson ratio, ν. Commonly Poisson ratio variation can be neglected due to the little interval it has to belong

to:

$$\nu \in (-1, 0.5) \tag{1}$$

From equation (1), the elastic relationship is simplified introducing a scalar field $\gamma(x)$, depending on the position x in the structure, that multiply elastic tensor c of the material.

$$\sigma_{ij} = \gamma(x)\, c_{ijhk} \varepsilon_{hk} \tag{2}$$

where σ_{ij} are the stress and ε_{hk} the strain components. Equation (2) represents a scalar varying isotropic FGM.

An elastic structure, V, satisfy the Field Boundary Integral Equation [7]

$$\gamma \mathbf{k} \cdot \mathbf{u} = \int_{\partial V} \tilde{\mathbf{u}} \cdot \mathbf{t} dS - \int_{\partial V} \gamma \tilde{\mathbf{t}} \cdot \mathbf{u} dS + \int_{\bar{V}} \tilde{\boldsymbol{\sigma}} \cdot \mathbf{u} \cdot \nabla \gamma dV \tag{3}$$

where the volume integral is defined over the part $\bar{V}$ of the structure where the heterogeneous law (2) holds (i.e. $\nabla\gamma \neq 0$). In (3) $\tilde{\mathbf{u}}$, $\tilde{\mathbf{t}}$ and $\tilde{\boldsymbol{\sigma}}$ are the kernels corresponding to displacement, traction and stress of the Kelvin's solution of the homogeneous elastic unbounded space under one point load [8].

Equation (3) is solved by collocation on the boundary of the structure and on internal elements of graded part $\bar{V}$.

The proposed example concern a multi-region elastic plate constituted by a square with a circular inclusion. Taking as reference the young modulus of the Kelvin solution, E_0, the inclusion modulus is assumed equal to $E_i = 2E_0$ and the surrounding plate modulus $E_s = 8E_0$.

Ramped and stepped variation of the Young modulus is assumed within a circular region around the inclusion to model FGM interface. The plate is subjected to axial tensile load.

In Fig. 2, on the left, the drawing of the structure is reported where it can be seen the variation of the elastic modulus for both variation schemes. On the right the normal stress is plotted along the middle line of the plate, it can be seen that the stress increases approaching the graded zone, thus it suddenly decreases across the FGM area reducing to $1/4$ of the outer stress due to the corresponding reduction of the elasticity. It is evident that ramped model of the interface result into discontinuous plot of the stress that overcame the continuous result. Conversely the ramped model describes, with good agreement, the smoothing effect produced by graded interface.

Contour plots in Fig. 2, describe axial stress within the structure. On the left hand contour plot ramped interface results are depicted, it can be seen that the stress increases since the inclusion edge along horizontal diameter and decrease inside the inclusion. Along vertical diameter it is shown that vertical stress decreases to the same value resulting into the inclusion. The contours show the smooth behaviour of the stress and highlight the effect of FGM presence. The left hand side plot represents the contour of the vertical stress for the ramped interface case where the jumps of the stress are evident.

To solve the proposed structure only the boundary of the plate, the two boundaries of the interface and the interface domain have been discretised, notice that for ramped representation two or more inclusion have to be introduced.

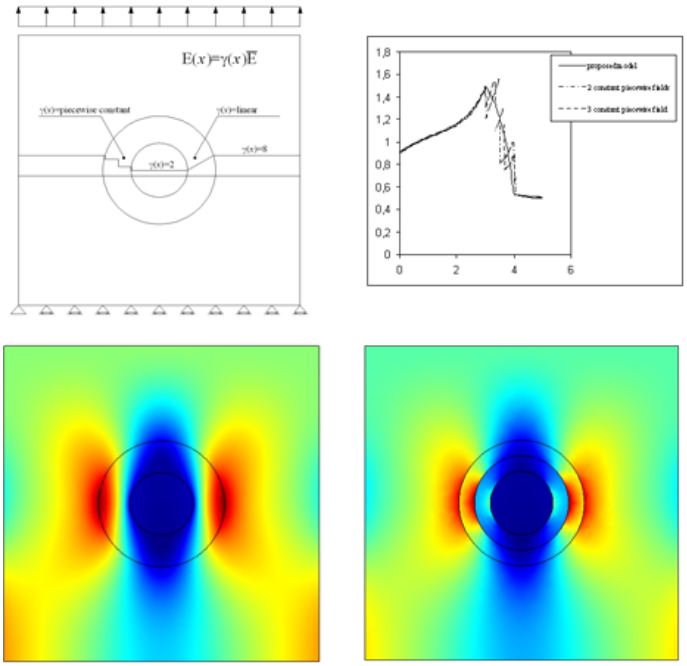

Figure 2: Geometry, boundary condition and σ_y results for ramped and stepped interface.

References

[1] J. R. Zuiker (1995): Functionally Graded Materials. Choice of Micromechanics Model and Limitation in Property Variation, *Composites engineering*, **5**, 807–819.

[2] B. Ilshner, (1996): Processing-Microstructure-Property Relationships in Graded Materials *J. Mech. Physics Solids*, **44**, 647-656.

[3] J.-H. Kim, G. Paulino (2002): Isoparametric Graded Finite Elements for Nonhomogeneous Isotropic and Orthotropic Materials, *J. Appl. Mechanics*, ASME, **69**, 502–514.

[4] Ch. Zhang, J. Sladek, V. Sladek (2005): Antiplane crack analysis of a functionally graded material by a BIEM, *Computational Materials Science*, **32**, 611–619.

[5] G. Paulino, A. Sutradhar, L. J. Gray (2002): Boundary Element Method for Functionally Graded Materials, P*roc. IABEM 2002*, Austin, Texas.

[6] M. I. Azis, D. L. Clements (2001): A boundary element method for anisotropic inhomogeneous elasticity, *I.J. of Solids and Structures*, **38**, 5747–5763.

[7] V. Minutolo, E. Ruocco (2005): Boundary element modelling and optimisation of structures made of functionally graded materials, *Proc. Of VI Inter. Conference on Boundary Element Techniques*, Montreal.

[8] L. C. Wrobel, M. H. Aliabadi (2002): *The Boundary Element Method*, Wiley.

Modelling the Mechanical Properties of Electro-Spun Non-Wovens for Tissue Engineering Starting from a Single Fibre Experiment

D. Jaeger[1*], B. Henrich[1], J. Schischka[2], J. Bagdahn[2], R. Jaeger[1], M. Moseler[1]

[1]Fraunhofer Institute for Mechanics of Materials
Wöhlerstr. 11, 79108 Freiburg, Germany
dj@iwm.fhg.de, henr@iwm.fhg.de, mos@iwm.fhg.de, jae@iwm.fhg.de

[2]Fraunhofer Institute for Mechanics of Materials
Heideallee 19, 06120 Halle, Germany
jan.schischka@iwm.fhg.de, jb@iwm.fhg.de

Summary: Non-wovens made by the electrostatic spinning process have potential applications as scaffolds in tissue engineering. Besides biocompatibility and high porosity, they have to posses a sufficient mechanical strength. Furthermore, stresses transmitted by the scaffold to the growing tissue can play an important role in stimulation tissue growth (mechanotransduction). The mechanical properties can be adjusted by varying the fibre orientation in the non-woven.
The used materials and cell biological experiments are cost intensive and therefore simulations are an important alternative to the elaborate spinning process. Mechanical experiments on a microscale silicon waver-chip are undertaken for the determination of the mechanical properties of a single fibre. Aim of the current study is to measure and simulate the mechanical properties of differently orientated non-wovens, starting from a single fibre experiment.

Materials and method

In the electro spinning process, ultra-thin fibres are pulled out of a polymer solution or melt by using a strong electrostatic field. Differently aligned non-wovens were electro-spun out of two polymeric systems: poly- (L-lactic acid) (PLLA) and poly-(DL-lactic acid) PDLA 96/4.

The degree of alignment of the fibres was determined by evaluating SEM images of the non-wovens with an image processing routine. The C++ routine employs a 2D-Fast Fourier Transform (FFT) routine. The angular distribution of the 2D-FFT grey scale spectrum was fitted with a Cauchy distribution. The width of the Cauchy distribution is used as indicator for the degree of fibre orientation.

Uniaxial tensile tests on the non-wovens were carried out with an EnduraTec Elf 3200 mechanical testing system. Experiments were carried out with specimens with different degrees of fibre alignment.

The single fibre's mechanical behavior is tested on a specially developed miniaturized tensile tester, which can be operated with a needle manipulator. Several hundred "one way" testing devices were etched on a silicon chip.

A molecular dynamic model (MD) was used for the simulation of the non-woven. The results of the simulation were compared with the experimental data. Of special interest are the internal effects, as fibre contact and the resulting sliding forces. The cell diffusion into the non-woven as well as the transport of degradation products out of the non-woven are also in the focus of investigation.

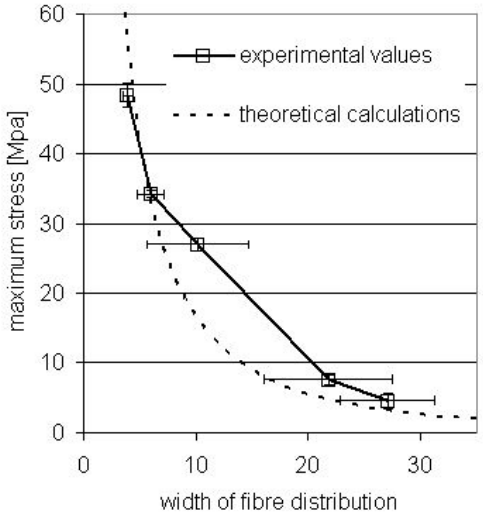

Figure 1: Experimental and calculated values for the maximum stress vs. the width of the fibre distribution.

Results and discussion

Non-wovens based on the mentioned polymer systems were fabricated. The fibre diameter is about one μm. The mechanical properties of the non-wovens depend strongly on their degree of fibre orientation. In Fig. 1, the maximally achieved stress under uniaxial load is plotted versus the degree of orientation of the non woven. The variation of the maximum stress as a function of the degree of alignment was estimated by a basic model assuming linear fibres.

Single fibre tensile tests were carried out on a micro-chip (Fig. 2). The evaluation of the stress-strain-curves is still under investigation.

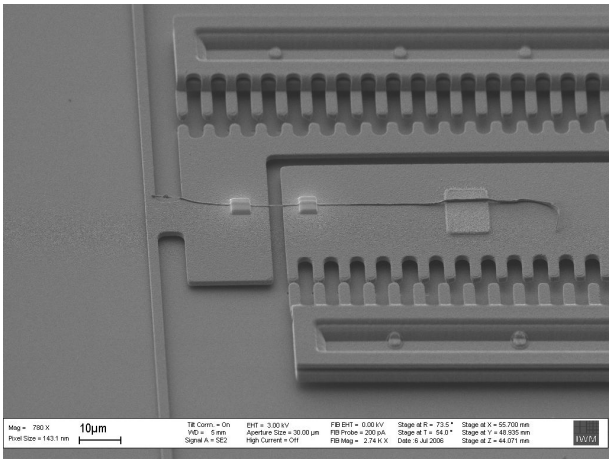

Figure 2: A micro chip with a uniaxial single fibre testing device.

An elementary model for the non-woven could be generated (Fig. 3). Within the non-woven simulation the fibres are Cauchy-distributed around a main orientation. In the simulation Lennard-Jones-Like-Potentials are describing the interactions between the fibres. The forces between the fibres segments are approximated with spring-like-forces.

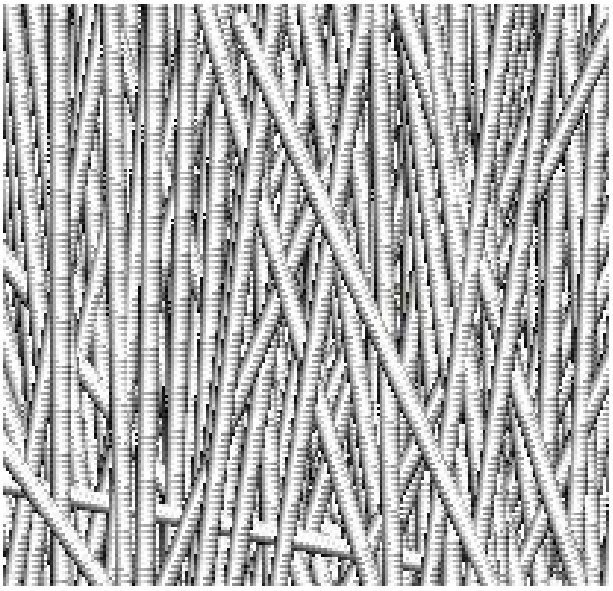

Figure 3: Model of Cauchy distributed fibres in a non-woven.

The experimentally obtained results were compared to the theoretical calculations and the simulation. The calculations were in agreement with the mechanical behaviour of the materials.

Summary

The method used for the evaluation of the degree of fibre orientation verifies the SEM-observation. The experimental results show that non-wovens with different degree of orientation and defined mechanical properties can be prepared in a controlled fashion. Future work will focus on a modelling of the transport phenomena in the non-wovens.

Optimization Based Back Analysis of Tunnel Stability

P. P. Procházka, A. E. Yiakoumi*

Czech Technical University in Prague, Faculty of Civil Engineering
Thákurova 7, 166 29 Prague 6, Czech Republic
petrp@fsv.cvut.cz

Summary: In certain previous papers of authors coupled numerical experimental modeling was based on minimization of functional describing steepest descend mode of differences of measured and computed values of stresses or displacements at selected points. In this way nonlinear model in numerical analysis can be improved using eigenparameters as design parameters in optimization. In this paper 2D problem is solved with moving patches (support subdomains) with uniformly introduced eigenstrains.

Introduction

Using a very powerful tool, Transformation field analysis (TFA), back analysis of structures can be regarded as seeking optimal distribution of eigenparameters in domain of definition. Unit impulses of these quantities enable one to find material properties from comparison of results from experimental studies and numerical analysis at selected points, as was done in many papers on geomechanical problems, [1, 3]. The only problem occurs: Find optimal distribution of patches (subregions), where eigenstrains are introduced or considered. This is a problem of combined optimization, where the principal variables depend on subdomains (patches), the uniform distribution (this is one of possible approximations) of eigenparameters is assumed. This problem is not easy to solve, as the optimization of principal variables must be iterated, and a reasonable tool for it should be find out. One of such tools can serve Inverse variational principles, which hold the volume of the domain as constant, and design variables are subdomains, [2].

Idea of TFA involvement to the formulation

This section is focused on formulation of the general procedure using the TFA. It may be done in terms of many modern numerical methods. First, let us consider that the body Ω under consideration (part of a structure, element, and system of more elements, composite) behaves linearly, i.e. Hooke's linear law is valid in the entire body. When the problem is correctly posed, the displacement vector, strain and stress tensors can be obtained from the Navier equations, kinematical equations, and linear Hooke's law.

In the second step we select points, where the measured values are available, either from experiments in laboratory, or from in situ measurements. We also select points A_r, or disjoint regions (subdomains) $\Omega_r, r = 1, ..., n$, from the body under study, and apply there successively unit eigenparameter impulses (either eigenstresses or eigenstrains) to get an influence tensors (matrices). Moreover, let the set of points where the measured values are known be $B_s, s = 1, ..., m$. Then the real stress $(\sigma)^s$ at B_s is a linear hull of stress $(\sigma^{ext})^s$ at B_s due to external loading and eigenstrains $(\mu)^r$ and $(\varepsilon^{pl})^r$, or eigenstress $(\lambda)^r$ and relaxation stress $(\sigma^{rel})^r$at A_r (similar relations are valid for overall strain field ε or displacements u):

$$\begin{aligned}
(\sigma_i)^s &= (\sigma_i^{ext})^s + (P_{ik}^{\sigma})^{sr}(\mu_k)^r + (Q_{ik}^{\sigma})^{sr}(\varepsilon_k^{pl})^r, \text{ or} \\
(\sigma_i)^s &= (\sigma_i^{ext})^s + (R_{ik}^{\sigma})^{sr}(\lambda_k)^r + (T_{ik}^{\sigma})^{sr}(\sigma_k^{rel})^r \quad (1) \\
(u_i)^s &= (u_i^{ext})^s + (P_{ik}^{u})^{sr}(\mu_k)^r + (Q_{ik}^{u})^{sr}(\varepsilon_k^{pl})^r, \text{ or} \\
(u_i)^s &= (u_i^{ext})^s + (R_{ik}^{u})^{sr}(\lambda_k)^r + (T_{ik}^{u})^{sr}(\sigma_k^{rel})^r \quad (2)
\end{aligned}$$

where the influence tensors P, Q, and also R and T may be identical, as any eigenparameter may stand for the plastic or relaxation parameter (say, eigenstrain may stand for plastic strain, which is obvious from (1) and (2)). The strain and stress components are written in vector form. Note that it holds: $\lambda = -L\mu$, where L is the elastic stiffness tensor.

The first relations in (1) and (2) describe the initial strain method while the second relations in those equations formulate the initial stress method.

From the above equations it immediately follows that it holds, for example:

$$\begin{aligned}
(\sigma_i)^s &= (S_{ik}^{\sigma})^s + (P_{ik}^{\sigma})^{sr}(\mu_k)^r \\
(u_i)^s &= (S_{ik}^{u})^s + (P_{ik}^{u})^{sr}(\mu_k)^r \quad (3)
\end{aligned}$$

i.e., the influence of plasticity is hidden in the first terms of right hand sides of (3). From (3) two possibilities obviously appear: Either plastic effects disappear in the first terms of r.h.s. of (3) or they are considered there. Certain starting plastic rules involved in (3) are discussed in [3].

On the other hand measured stresses $(\sigma_i^{meas})^s$, or measured displacements $(u_i^{meas})^s$ are available in a discrete set of points. A natural requirement is formulated in terms of steepest descent type "error functionals" I, which express that the values of measured and computed values be as close as possible:

$$\begin{aligned}
I_\sigma[(\mu_k)^r] = [(\sigma_i)^s - (\sigma_i^{meas})^s]^2 &\longrightarrow \text{minimum} \\
I_u[(\mu_k)^r] = [(u_i)^s - (u_i^{meas})^s]^2 &\longrightarrow \text{minimum} \quad (4)
\end{aligned}$$

where sum is taken over i and s. Differentiating I by $(\mu_\alpha)^\beta$ yields a linear system of equations for $(\mu_k)^r$:

$$(A_{\alpha k})^{\beta r}(\mu_k)^r = Y_\alpha^\beta, \quad \alpha = 1, ..., 6, \quad \beta = 1, ..., m \quad (5)$$

Inverse variational principles

Following extended primary variational principles one can write the energy functionals on the whole domain Ω as:

$$\Pi = \tfrac{1}{2}a(u,u) - [p,u] \quad \longrightarrow \quad \text{minimum} \tag{6}$$

where a(.,.) is an energetic norm and [.,.] is the scalar product on the boundary Γ of Ω, with p being prescribed traction. Let us divide Ω into disjoint subregions Ω_r, union of them is Ω. Then (6) can be rewritten as

$$\Pi = \sum \tfrac{1}{2}a_r(u,u) - [p,u] \quad \longrightarrow \quad \text{minimum} \tag{7}$$

where a_r(.,.) is an energetic norm on each Ω_r and the sum is taken over r.
Let now sets Ω_r fulfill the requirement that they are mutually disjoint and sum of their closure covers Ω. Then the problem appears not properly defined. In order to ensure that the problem is correctly posed, the volumes (or areas in 2D) have to be bounded. The functional (6) then has to be improved as:

$$\begin{aligned} \Pi(u,\Omega) \quad = \quad & \sum \left[\tfrac{1}{2}a_r(u,u) + \omega_r \left(\int_\Omega d\Omega_r - C_r \right) \right] \\ & -[p,u] \quad \longrightarrow \quad \text{stationary} \end{aligned} \tag{8}$$

where C_r is a measure of Ω_r, see [4], and ω_r are the Lagrangian multipliers. The internal energy is a sum of integrals over appropriate domains Ω_r of a potential $(W)^r$, which in our case reads as:

$$(W)^r = (\sigma_i)^r[(\varepsilon_i)^r - (\mu_i)^r] \tag{9}$$

where $(\mu_i)^r$ has been considered uniform in Ω_r . Hence, Euler's equations follow as:

1. Variating by displacements yields equilibrium equations involving partially uniformly distributed eigenstrains $(\mu_i)^r$. They are given from (5) for given distribution of Ω_r.

2. Approximating the problem in the sense of FEM with K, say, then the changes in the fields with respect to the subdomains can formally be written as:

$$\frac{1}{2}\frac{\partial K_{ik}}{\partial p_r}U_iU_k + \omega_r\frac{\partial \Omega_r}{\partial p_r} = 0 \tag{10}$$

   where p_r are internal parameters declaring the shape of the subdomain Ω_r. From (10) immediately follows that the Lagrangian multipliers have to be constant for each r, i.e. on each subdomain Ω_r all components of eigenstrain tensor remain uniform.

3. Partial differentiation of (8) by ω_r ensures that the measures of the subdomains are unchanges. Some recommendations on how to introduce the internal shape parameters could be found in [4], for example.

Numerical procedure for two subdomains

To show the ability of the above submitted procedure consider a simply supported beam with length 10 m, height 1 m, the bending stiffness EI = 1. The problem is solved as stretched plate, the external boundary of which is unmovable concerning the subdomains. Concentrated force at the middle of the span represents loading. Symmetric case is solved, i.e. shear eigenstrains disappear. Values at the lower boundary are prescribed (we simulate experiments) in 1/8, 1/4, 3/8, 3.5/8, and 1/2 of the span. The values of the deflection w are 0.092, 0.2, 0.333, 0.57, 0.72. The starting position of the subdomains is horizontal, and the upper subdomain is 7 m^2 and the lower 3 m^2. Starting position of the interface along common boundary of the subdomains leads to an error of 16.32% in the deflection at the middle of the span, the improved interface gives the error about 5%.
Since the extreme tensile damage can be expected at the middle of the span, the area of the lower subdomain is decreased to 1 m^2. Then the error for starting configuration is 18.72 of iterations of interfaces we get an acceptable value of 1.2%.

Conclusions

In some previous papers of the first author it has been shown that the coupled numerical and experimental (scale) modeling or the on site measurements can basically improve identification of numerical mechanical model. The only problem appeared the choice of subdomains. No receipt has been proposed so far. This paper tries to improve this lack of information using Inverse variational principles. Although simple example is presented here, the generalization to more subdomains is straightforward.
It is worth noting that for large extent of subdomains an extensive number of measurements is necessary. In former papers three or at most four subregions have been considered in applications to underground structures, particularly to assessment of tunnel face stability. The reason consists in the fact that (5) is created for 3 in 2D or 6 in 3D components of eigenstrains (or eigenstresses), it means 24 unknowns eigenparameters in 3D for four subdomains is necessary to determine in each iterative steps. From the point of view of numeric analysis this does not make any problem, but to feed (5) at least 25 measurements scattered enough in the original domain Ω, which can lead to insufficient set of data.

Acknowledgment: Financial support of GAČR, project number 103/06/1124, is appreciated.

References

[1] P. P. Procházka, J. Trčková (2000): Coupled modeling of concrete tunnel lining. In *P*roc. Our World in Concrete and Structures, Singapore, 2000, 125–132.

[2] P. P. Procházka, A. E. Yiakoumi (2006): Nonlinear transformation field analysis of inelastic composite structures. In *Proc. Conference on Composites/Nano Engineering*, Colorado, Univ. of New Orleans, CD, 2–8 July 2006.

[3] P. P. Procházka, J. Trčková: Assessment and control of tunnel structures based on coupled modeling. Submitted to *Géotechnique*.

[4] P. P. Procházka: Shape optimal design using Inverse Variational Principles. Submitted to *EABE*.

Onsager's Principle: A Handy Tool in Modelling of Evolving Microstructures

J. Svoboda[1*], **F. D. Fischer**[2]

[1]Institute of Physics of Materials, Academy of Sciences of the Czech Republic
Žižkova 22, CZ-616 62, Brno, Czech Republic
svobj@ipm.cz

[2]Institute of Mechanics, Montanuniversität Leoben
Franz-Josef-Strasse 18, A-8700 Leoben, Austria
mechanik@unileoben.ac.at

Summary: Onsager's thermodynamic extremal principle formulated in terms of discrete parameters represents a systematic way of derivation of evolution equations for the parameters characterizing the system. The Onsager's principle is presented and used for modelling of grain coarsening.

General instructions

The second law of thermodynamics admits all processes with positive entropy production (positive dissipation) and does not allow the determination of a distinct unambiguous evolution path of the system [1]. In 1931 L. Onsager [2] formulated an extremal principle, according to which the unambiguous path of the thermodynamic system near equilibrium corresponds to a constrained maximum of dissipation in any part of the system at any time. From the thermodynamic point of view Onsager's principle can be understood as a strong form of the second law of thermodynamics allowing the determination of the unambiguous evolution path of the system.

In 1991 Onsager's principle was formulated first in terms of discrete parameters characterizing the state of the system [3]. These parameters are destined to describe the system evolution in a natural way. The application of the principle provides a systematic way of derivation of the evolution equations for these parameters for a wide class of problems in the context of linear non-equilibrium thermodynamics [4].

Formulation of Onsager's principle in terms of discrete parameters

Let us limit to closed thermodynamic systems under constant temperature and pressure. In that case the total Gibbs energy G of the system is the characteristic potential. Furthermore, let us assume, that the state of the system can be described well by a set of discrete parameters $q_i(t), i = 1, ..., N$, at any time t and the total Gibbs energy of the systems can be expressed by means of the parameters: $G = G(q_1, ..., q_N)$. The parameters are assumed to be constrained by m relations of the type

$$\sum_{i=1}^{N} a_{ik}\left(q_1, ..., q_N\right)\dot{q}_i = 0, \quad k = 1, ..., m \tag{1}$$

The dot symbol is used for the time derivative.
We assume that the system evolves by diffusion and by migration of interfaces. Then the total dissipation in the system can be expressed by

$$Q = \sum_{k=1}^{n}\int_V \frac{RT\mathbf{j}_k^2}{c_k D_k}dV + \int_A \frac{v^2}{M}dA \tag{2}$$

The number of components in the system is denoted by n , R is the gas constant, T the absolute temperature, c_k is the concentration, $\boldsymbol{j}_k$ the diffusive flux and D_k the tracer diffusion coefficient of component k, v is the interface velocity and M the interface mobility. The volume of the system is denoted by V and the interface area by A.
Using the mass conservation laws, proper simplifications and assumptions on the geometry of the system, the linear relations

$$\boldsymbol{j}_k = \sum_{i=1}^{N} \boldsymbol{f}_{ik}\left(q_1, ..., q_N\right)\dot{q}_i, \quad k = 1, ..., n, \tag{3}$$

$$v = \sum_{i=1}^{N} h_i\left(q_1, ..., q_N\right)\dot{q}_i \tag{4}$$

can be obtained. This procedure together with the selection of parameters represents the key step in the development of the model. Insertion of (3) and (4) into (2) and performance of the integrals enables to express the total dissipation in the system as a positive definite quadratic form of the rates of parameters as

$$Q = \sum_{i=1}^{N}\sum_{j=1}^{N} U_{ij}\left(q_1, ..., q_N\right)\dot{q}_i\dot{q}_j \tag{5}$$

Onsager's thermodynamic extremal principle asserts that the evolution of the system corresponds to the maximum of Q constrained by $Q + \dot{G} = 0$ and (1). The necessary condition for the maximum reads

$$\frac{\partial}{\partial \dot{q}_i}\left[Q + \lambda\left(Q + \dot{G}\right) + \sum_{k=1}^{m}\beta_k\sum_{i=1}^{N} a_{ik}\dot{q}_i\right] = 0, i = 1, \ldots N \tag{6}$$

The quantities λ and β_k, $k = 1, \ldots m$, denote Lagrange multipliers. The mathematical treatment leads to resulting set of linear equations represented by

$$\sum_{j=1}^{N} U_{ij}\dot{q}_j + \sum_{k=1}^{m} a_{ik}\beta_k = -\frac{\partial G}{\partial q_i}, i = 1, \ldots N \tag{7}$$

and (1) for $\dot{q}_i$, $i = 1, \ldots N$, and β_k, $k = 1, \ldots m$.

Application of Onsager's principle to modelling of grain growth

The theoretical treatment of grain coarsening is possible only by accepting some model assumptions, which simplify the reality, however, still keep the important features of grain coarsening. One of such usual model assumptions is the approximation of each grain by a sphere of the same volume and the mean field approximation. Then the system of grains can be described by the radii R_k of individual grains representing the parameters of the system. The total Gibbs energy of the system is given by

$$G = \frac{1}{2} 4\pi\gamma \sum_{k=1}^{N} R_k^2 \tag{8}$$

the total dissipation in the system follows as

$$Q = \frac{1}{2} \frac{4\pi}{M} \sum_{k=1}^{N} R_k^2 \dot{R}_k^2 \tag{9}$$

The quantity γ is the Gibbs energy of the grain boundaries per unit area and M is the grain boundary mobility. The factor 0.5 in equations (1) and (2) takes into account that each grain boundary is common to two grains. The total volume of the grains in the system must be conserved and thus

$$\frac{4\pi}{3} \sum_{k=1}^{N} R_k^3 = \text{const.} \;\Rightarrow\; \sum_{k=1}^{N} R_k^2 \dot{R}_k = 0. \tag{10}$$

Using the formalism from the previous section final equations read

$$\dot{R}_k = 2\gamma M \left(\frac{1}{R_C} - \frac{1}{R_k} \right), \quad k = 1, ..., N \tag{11}$$

with $R_C = \sum_{i=1}^{N} R_i^2 \Big/ \sum_{i=1}^{N} R_i$ being a critical radius. The evolution equations (11) for R_k are equivalent to those derived first by Hillert [5] by means of heuristic considerations in 1965. More details can be found in [6].

References

[1] S.R. de Groot, P. Mazur (1984): *Non-equilibrium Thermodynamics*. Dover Publication, New York.

[2] L. Onsager (1931): Reciprocal relations in irreversible process. I. *Physical Review*, **37**, 405–426.

[3] J. Svoboda, I. Turek (1991): On diffusion-controlled evolution of closed solid state thermodynamic systems at constant temperature and pressure. *Philos. Mag. B*, **64**, 749–759.

[4] J. Svoboda, I. Turek, F. D. Fischer (2005): Application of the thermodynamic extremal principle to modeling of thermodynamic processes in material sciences. *Philosophical Magazine*, **85**, 3699–3707.

[5] M. Hillert (1965): On the theory of normal and abnormal grain growth. *Acta metallurgica*, **13**, 227–238.

[6] F. D. Fischer, J. Svoboda, P. Fratzl (2003): A thermodynamical approach to grain growth and coarsening. *Philosophical Magazine A*, **83**, 1075–1093.

Spongy Bone Mechanical Behavior under Quasi Static to Dynamic Loadings: Development of an Equivalent Physical Model

J. Halgrin*, F. Chaari, E. Markiewicz, P. Drazetic

Laboratory of Industrial and Human Automation Control, Mechanical Engineering and Computer Science, LAMIH UMR CNRS 8530, University of Valenciennes
Le Mont Houy, 59313 Valenciennes, Cedex 9, France
Julien.halgrin@univ-valenciennes.fr

Summary: In order to identify the spongy bone's mechanical behavior, we performed compression tests on cylindrical samples. Experimental results show an important dispersion and an unexpected inverse strain rate dependency. The origin of this dispersion is the combination of the architecture effect and the mechanical properties variation. In order to reduce these dispersion sources and to understand the inverse strain rate effect, we used a controlled constitutive material to build new equivalent samples with the spongy bone's architecture. These equivalent samples were subjected to compression tests with a large velocity range. However, we obtained a classical stain rate dependency usually observed for similar cellular materials.

Introduction

In the fields of crashworthiness, ballistic protections and other medical applications, the accurate material constitutive law of spongy bone is needed to carry out valid finite element analysis. Previous works [1, 2] show that spongy bone mechanical properties found in literature provide unsatisfying results. Spongy bone is a complex network of intersecting curved plates and tubes (trabeculae). The size and shape distribution of the trabeculae varies along the skull's thickness. The spaces in and around the trabeculae contain fluids and bone marrow. Moreover, different authors [3, 4] reported an important dispersion on the mechanical properties of the trabeculae. All these variations are usually explained by the inter individuality, by the osseous remodeling and by the extraction zone. That is why works on spongy bones are undertaken to better understand the global mechanical behavior and to identify a constitutive material law taking into account these variations.

Compression tests on spongy bone samples

Since it is restricting to perform tests on skull from human donors, we developed and validated our study on beef ribs. This study will be extended later to the skull characterization. Indeed, the skull and rib are both flat bones, which consist of two blades of cortical bone separated by a layer of spongy one. We isolated this layer and cored cylindrical samples. Compression tests were performed on these samples between two parallel plates, with a controlled loading velocity. Further information on the samples preparation and experimental conditions can be found in previous communications [5]. During the compression, we observe a strain localization and the section variation is not uniform. This is why we present the compression results in term of the force versus the upper plate displacement. Fig. 1 shows typical results obtained for five samples cut from the same rib. These curves can be divided into three stages: *(i)* Quasi linear compression of the network of trabeculae; *(ii)* Collapse of the trabeculae network; *(iii)* Complete compaction and acceleration of the fluid extrusion. These three stages are usually observed during the compression of other cellular materials (foams, honeycombs). For samples bored from the same rib, the stiffness seems to be constant but peak value and transitions strains vary significantly. These dispersions are generally attributed to the random architecture, to the localization of the strain and to the intrinsic constitutive material variation.

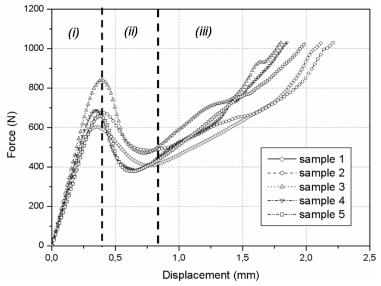

Figure 1: Compression force versus displacement for five samples cut in the same rib, and compressed at 5 mm/min.

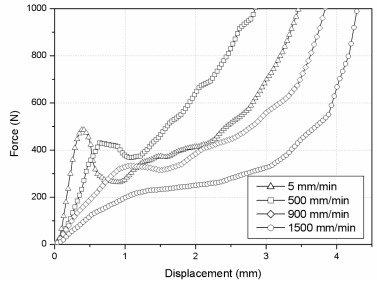

Figure 2: Compression force versus displacement for five samples cut in the same rib, and compressed at different loading velocities.

In order to characterize the strain rate effect on the mechanical properties of the spongy bone, samples cut in the same ribs are compressed at different velocities. As shown in Fig. 2, we obtain an unexpected strain rate dependency. When increasing the velocity of loading, the peak force value and the stiffness decrease. The geometrical continuity between the cortical and the spongy bone allow us to suppose that they have the same mechanical properties. Moreover Adharapurapu [6] showed that cortical bone has a classical visco plastic strain rate depen-

dency. So, the observed behavior can not be only explained by the mechanical properties of the constitutive material.

Compression tests provided us information on the structural behavior of the spongy bone but not on the trabeculae material properties. It is then fundamental to study the spongy bone's architecture effect in order to dissociate it from the mechanical properties of the constitutive material. We could then understand the observed strain rate dependency.

Physical model construction

The micro-architecture of each sample was acquired thanks to micro-computed tomography technique μCT. The resolution was high enough compared to trabeculae average size. The voxel size was of 70×70 μm and the distance between two consecutive slices was 200 μm. Thanks to the marching cube algorithm, we reconstructed the micro-architecture of some scanned samples. The obtained models were used to build the physical models by the rapid prototyping technique using a well-known constitutive material (ABS polymer). Both the ABS polymer and the trabeculae constitutive material have a similar strain rate dependency. We extracted a cube of $3 \times 3 \times 3$ mm in the center of the scanned sample and applied a scale factor of 10 in order to facilitate the strain observation. Thanks to this technique, we ensured that the equivalent models, with the same architecture are identical. Fig. 3 presents one example of equivalent model taken in the center of spongy bone sample.

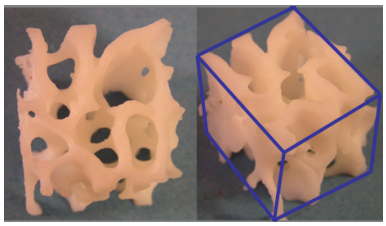

Figure 3: One equivalent cubic sample made of ABS polymer.

Compression tests on physical models

These models were subjected to compression tests between parallel plates. The loading velocity range was increased in order to compensate the scale factor effect on the strain rate. The obtained results presented in Fig. 4 confirm that the equivalent models are identical since two tests at the same velocity (500 mm/min) give the same response. When we varied the loading velocity, we obtained a classical strain rate dependency similar to that reported for cellular materials.

Discussion

An experimental study of spongy bone's mechanical behavior showed an important dispersion on results. We also obtained an unexpected strain rate dependency: by increasing the loading velocity, the stiffness and the peak force decreases. This is why we decided to build equivalent physical models, with a

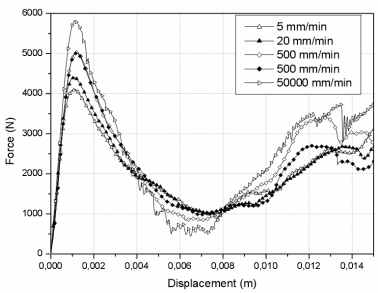

Figure 4: Compression force versus displacement for equivalent samples compressed at different loading velocities.

spongy bone's architecture and a controlled constitutive material. The compression tests on equivalent samples did not explain the particular behavior of the spongy bone. This results suggests that the strain rate effect in the spongy bone can not be explained only by its architecture. We are working on the investigation of the other possible parameters inducing this behavior. We will investigate the trabeculae/fluid interaction during the compression of equivalent samples.

Acknowledgment

The present research work accomplished in the common lab DRSC between the ONERA Lille and UVHC/LAMIH Valenciennes. It has been supported by the European Community, the French Ministry for Education, Research and Technology, the Nord-Pas de Calais Region and the National Center for Scientific Research. The authors gratefully acknowledge the support of these institutions.

References

[1] B. Van Rietbergen, H. Weinans, R. Huiskes and A. Odgaard (1995): A new method to determine trabecular bone elastic properties and loading using micromechanical finite-element models, *Journal of Biomechanics*, 28, 69–81.

[2] A. Al-Basharat, C. Zhou, H. King, Y. Tawfik, B. Khalil and A.I. King (1999): Intracranial Pressure in the Human Head due to Frontal Impact Based on a Finite Element Model, *Bioengineering Conference ASME*, **42**.

[3] C. H. Turner and D. B. Burr (1993): Basic biomechanical measurements of bone: A tutorial, *Bone*, **14**, 595–606.

[4] H. Follet (2002): Caractérisation Biomécanique et Modélisation 3D par Imagerie X et IRM haute résolution de l'os spongieux humain : Evaluation du risque fracturaire, *PHD Thesis, Institut national des sciences appliquées de Lyon.*

[5] S. Baivier, P. Drazetic and É Markiewicz (2005): Compression tests on spongy bone, *Second IASTED International Conference on Biomechanics*, Benidorm, Spain.

[6] R. R. Adharapurapu, F. Jiang, K. S. Vecchio (2006): Dynamic fracture of bovine bone, *Materials Science and Engineering C*, **26**, 1322–1332

Analytical Derivation of the Asymptotic Creep Behavior of Concrete by Multiscale Homogenization

Q.-V. Le[1,2*], F. Meftah[1], Q.-C. He[1], Y. Le Pape[2]

[1]LaM, Université de Marne-La-Vallée, 77420 Champs-sur-Marne, France
quoc-viet.le@univ-mlv.fr, fekri.meftah@univ-mlv.fr, qi-chang.he@univ-mlv.fr

[2]MMC, EDF R & D, Site des Renardières, 77818 Moret-sur-Loing, France
yann.le-pape@edf.fr

Summary: This work aims at investigating the influence of microscopic properties of concrete on its macroscopic creep behaviour. For this purpose, two solution strategies are proposed. The first one consists in determining semi-analytically the time evolution of the macroscopic creep compliance by relating the macroscopic retardation times to the microscopic properties. The second one limits the interest on constructing analytical asymptotes for the long term creep behaviour.

Concrete is a heterogeneous material which exhibits a viscoelastic behaviour under a long term applied load. The heterogeneous nature of the material is retrieved at different scales of observation. At each scale, the representative element volume can be seen as elastic and porous inclusions embedded in a viscoelastic matrix. A robust descript of the macroscopic behaviour of the material suggests therefore to use upscaling techniques to build the homogenised behaviour [1]. This breaks with the classical approaches in which macroscopic constitutive laws are constructed with several phenomenological parameters which are assumed, for instance, being able to describe the influence of the concrete mix on the creep behaviour. Indeed, homogenisation techniques incorporate naturally the microstructure associated with each concrete mix and then can make explicit its influence on the macroscopic behaviour.

Homogenisation of viscoelastic heterogeneous materials can be studied by using the correspondence principle which permits to extend elastic homogenization schemes to the viscoelastic case. The correspondence principle consists in using the Laplace-Carson transform in order to make the viscoelastic problem equivalent to an elastic one in the transform space [2]. The macroscopic viscoelastic properties (creep and relaxation functions) are therefore obtained in a straightforward manner but in the Laplace-Carson transform space. Thereafter, the difficulty consists in deriving theses properties in the time domain by inverting their Laplace-Carson transforms.

The inverse transformation requires prior to determine the macroscopic relaxation times which correspond to the roots of polynomials whose degree depends on both the number of the microscopic relaxation times and the number of homogenized phases. Therefore, determining these roots becomes rapidly infeasible, unless full numerical procedures are used which precludes assessing the influence of the microscopic properties on the macroscopic retardation spectrum.

In this contribution, interest is focused on two widely used elastic homogenisation schemes: the Mori-Tanaka scheme [3] and the Christensen and Lo generalized self consistent one [4]. Generalised Maxwell and Kelvin rheological models [5] are used for modelling the microscopic behaviour of the viscoelastic phase, i.e., the matrix as shown in figure 1. Then, a two steps procedure is proposed in order to derive long term analytical

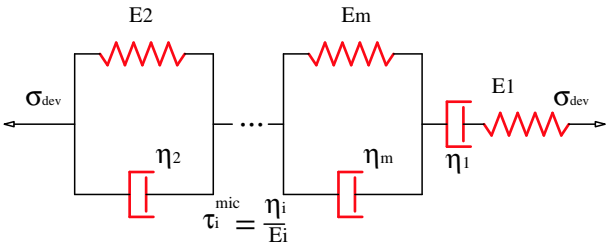

Figure 1: Generalised Kelvin model for the shear creep function of the matrix

and semi-analytical expressions for the macroscopic viscoelastic properties as shown in figure 2. In this procedure, it is shown

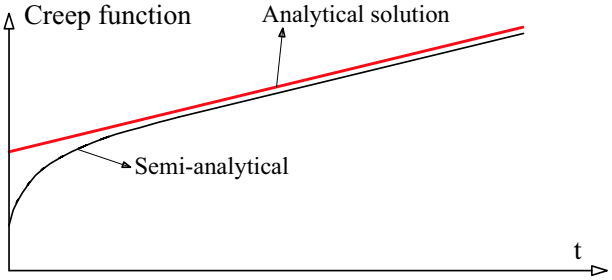

Figure 2: Asymptote of the effective creep function

that a part of the macroscopic retardation times τ^{hom}, for both creep and relaxation, coincides with the microscopic ones τ^{mic}:

$$\left\{\tau_k^{hom} : k = 1, \cdots, l\right\} = \begin{array}{l}\left\{\tau_i^{mic} : i = 1, \cdots, m\right\} \\ \bigcup \left\{\bar{\tau}_j^{hom} : j = 1, \cdots, \bar{l}\right\}\end{array} \quad (1)$$

The complementary part $\bar{\tau}^{hom}$ is then determined from the roots of polynomials with reduced order, which increases the number of the solutions to be analytically determined.

Furthermore, under some additional simplifying assumptions (constant Poisson ratio or constant bulk modulus of the matrix) the remaining part of the macroscopic retardation times presents as a family of sets of values, each set being bounded by two successive values of the microscopic retardation times:

$$\tau_i^{mic} < \left\{\bar{\tau}_k^{hom} : k = 1, \cdots, n\right\}_i < \tau_{i+1}^{mic} \quad (2)$$

This fact is very helpful when standard numerical procedures are used for roots determination. Using the generalised self-consistent scheme in the case of two phases composite ($n = 2$) , the inequality (2) can be represented by figure 3. In this case, it is shown that the spectrum presents as a continuous part necessarily bounded by two successive discrete retardation times of the discrete part of the microscopic spectrum.

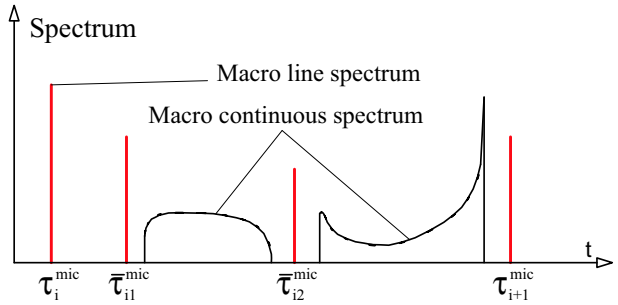

Figure 3: Spectrum of the effective creep function

This two steps procedure permits to separating the complexity generated by a large number n of phases from the one generated by a large number m of analogical units, when determining the macroscopic retardation times. Thus semi-analytic solutions can be determined for the macroscopic creep J_{hom} function, in the case of the Mori-Tanaka, writes:

$$J_{hom}(t) = L_0 + L_1 t + \sum_{i=2}^{m} L_i e^{-\frac{t}{\tau_i^{mic}}} + \sum_{j=1}^{m\times n} \bar{L}_j e^{-\frac{t}{\bar{\tau}_j^{hom}}} \quad (3)$$

where the $\bar{\tau}_j^{hom}$ can determined either analytically or numerically. The constant terms L_i and $\bar{L}_j$ depend on the microscopic properties of the material and the adopted homogenization scheme. In the case of a constant Poisson ratio, analytical solutions can be derived for problems with up to $m = 4$ analogical units and $n = 4$ inclusion phases, which in fact correspond to problems with a spectrum of up to $l = 20$ macroscopic retardation times.

Moreover, it is shown that situations with very close macroscopic retardation times $\bar{\tau}_j^{hom}$ may occur. In this case, the spectrum of the macroscopic viscoelastic functions may be reduced by replacing the population of close retardation times by an equivalent value, the average value for instance, and summing the corresponding amplitudes $\bar{L}_j$. This feature can be of great help when multi-scales homogenization is concerned, each upscaling generating new macroscopic retardation times that increase the size of the problem.

However, this approach reaches quickly its limit, namely when several homogenization scales are concerned together with a large number of phases. An alternative approach is therefore proposed from which asymptotes of the long term creep are determined at each homogenization scale. This approach does not need to compute the inverse of the Laplace-Carson transform but exploits some of its prosperities in order to construct asymptotes of the creep compliance in the time domain. This is clearly suggested by the affine part of equation (3). At each homogenization scale, the long term creep behaviour is related explicitly to the microscopic proprieties of all the previous scales by applying the initial and final theorem of Laplace transform.

The derived solutions are then coupled with a hydration model [1] in order to investigate the influence of the concrete mix on its creep behavior [6] as shown in figure 4.

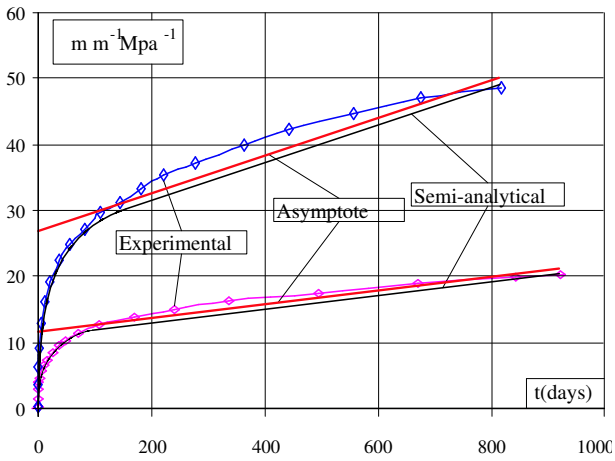

Figure 4: Experimental and analytical curves of the creep function of two concrete formulations

References

[1] O. Bernard, F. J. Ulm, E. Lemarchand (2003): A multiscal micromechanics-hydration model for the early-age elastic properties of cement-based materials. *Cement and Concrete Research*, **33**, 1293-1309.

[2] J. Mandel(1966): Mécanique des milieux continus. *Gauthier Villars*, Paris (in French).

[3] A. Zaoui(1997): Matériaux hétérogènes et composites. *Editions de l'école Polytechnique*, Paris (in French).

[4] R. M. Christensen, and K. H. Lo (1979): Solutions for effective shear properties in three-phases sphere and cylinder models. *Journal of the Mechanics and Physics of Solids*, **27**, 127-140.

[5] R. M. Christensen (1982): Theory of Viscoelasticity. *Dover Publications*, New York.

[6] L. Granger (1996): Comportement différé du béton dans les enceintes de confinement de centrales nucléaires, analyse et modélisation. In *Ouvrages d'art - OA21, 2-7208-2500 X*, LCPC, Paris (in French).

[7] S. Beurthey, and A. Zaoui (2000): Structural morphology and relaxation spectra of viscoelastic heterogeneous materials. *European Journal of Mechanics A: Solids*, **19**, 1-16.

The Analysis of Load Capacity Changes of RC Elements as the Result of Electrochemical Corrosion and Surface Active Substances

T. Krykowski[1*], **A. Zybura**[2]

[1]Silesian University of Technology, Department of Theory of Structures
st. Akademicka 5, 44-100 Gliwice, Poland
tomasz.krykowski@polsl.pl

[2]Silesian University of Technology, Department of Building Structures
st. Akademicka 5, 44-100 Gliwice, Poland
adam.zybura@polsl.pl

Summary: This work presents the influence of concrete structure damage and reinforcement corrosion process on the state of stress in concrete beams along with FEM application to the simulation of such types of process. The damage effects in concrete can be of mechanical and chemical type, however, the reinforcement corrosion consists of two types of process along with the interactions: electrochemical corrosion and surface active substances.

Introduction

Typical case of aggressive environment influence on the construction can led to the damage of both concrete and the rebar structure. The damage processes of concrete usually consist in the porosity increase, cracking and scratching. The reinforcement corrosion is initialized by electrode processes in local macrocell places that are mostly created in the neutralized concrete or chloride penetration places. As a result of electrochemical processes the active area of rebar is changed. The other type of reinforcement corrosion is connected with the adsorption action of ions and surface active particles that can be found in water solution (electrolyte) occurring in scratching and concrete pores. The adsorbed on the reinforcement surface ions penetrate through the defects deeper in the steel structure and activate the stress corrosion that is characterized by intercrystalline cracking. Intercrystalline corrosion seems to be particularly dangerous because it causes the change of the plastic properties into brittles in spite of the fact that in normal condition material shows high plasticity. The damages created as the result of corrosion processes can be treated as the material voids that cannot transfer the stresses.

Formulation of the model equation

We will treat concrete as the multicomponent composite (cf. [1]) that is consisting of concrete steel and migrating substances. It will be assumed that the composite macrocomponents: steel and concrete can be described by elastic-plastic constitutive relationships, cf. [2, 3]:

Concrete:

$$\boldsymbol{\sigma}_c = (1-D_c)\,\mathbf{C}_c : \boldsymbol{\varepsilon}_c^e = (1-D_c)\,\mathbf{C}_c^{ep} : \boldsymbol{\varepsilon}_c \quad (1)$$

$$\mathbf{C}_c^{ep} = \mathbf{C}_c - \frac{1}{H_c}\mathbf{C}_c : \frac{\partial g_c}{\partial \boldsymbol{\sigma}} \otimes \frac{\partial f_c}{\partial \boldsymbol{\sigma}} : \mathbf{C}_c \quad (2)$$

$$H_c = \frac{\partial f_c}{\partial \boldsymbol{\sigma}} : \mathbf{C}_c : \frac{\partial g_c}{\partial \boldsymbol{\sigma}} + h_c^v, \;\; \boldsymbol{\varepsilon}_c = \boldsymbol{\varepsilon}_c^e + \boldsymbol{\varepsilon}_c^p \quad (3)$$

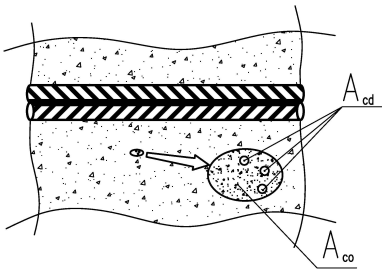

Figure 1: Degradation of pores structure in concrete.

Steel:

$$\boldsymbol{\sigma}_s = (1-D_s)\,\mathbf{C}_s : \boldsymbol{\varepsilon}_s^e = (1-D_c)\,\mathbf{C}_s^{ep} : \boldsymbol{\varepsilon}_s \quad (4)$$

$$\mathbf{C}_s^{ep} = \mathbf{C}_s - \frac{1}{H_s}\mathbf{C}_s : \frac{\partial f_s}{\partial \boldsymbol{\sigma}} \otimes \frac{\partial f_s}{\partial \boldsymbol{\sigma}} : \mathbf{C}_s \quad (5)$$

$$H_s = \frac{\partial f_s}{\partial \boldsymbol{\sigma}} : \mathbf{C}_s : \frac{\partial f_s}{\partial \boldsymbol{\sigma}} + h_s^v, \;\; \boldsymbol{\varepsilon}_s = \boldsymbol{\varepsilon}_s^e + \boldsymbol{\varepsilon}_s^p \quad (6)$$

In equations (1–4) $\mathbf{C}_c$, $\mathbf{C}_s$ are tensors of elasticity in concrete and steel, $\boldsymbol{\varepsilon}_c^e$, $\boldsymbol{\varepsilon}_s^e$ tensors of infinitesimal strains in concrete and steel, $\mathbf{C}_b^{ep}$, $\mathbf{C}_s^{ep}$ tensor of elastic-plastic material tangent module, f, g flow and plastic potential function, D_c global damage parameter caused by influence of aggressive media on structure of concrete, D_s global damage parameter of steel caused by electrochemical corrosion and surface active particles action.

Formulation of damage parameters evolution in concrete

It will be assumed that the damage mechanism associated with the influence of the aggressive substances on concrete is primary connected with the change of pores structure. Additionally we will assume cf. [4] that the concrete structure degradation parameter can be described by the use of the following formulas, cf. Fig. 1:

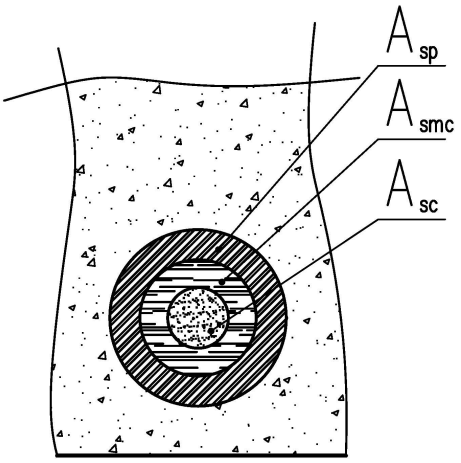

Figure 2: Degradation of rebar cross section area.

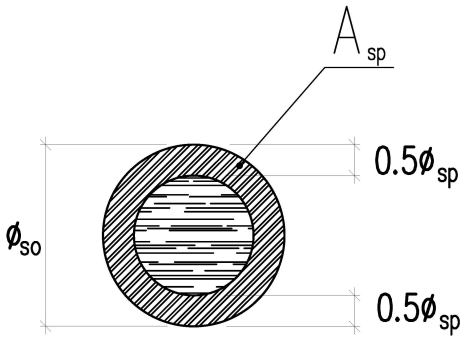

Figure 3: Change of rebar cross section diameter as a result of electrochemical corrosion.

$$D_c = \frac{A_{cd}}{A_{co}} \tag{7}$$

A_{cd} is the cross section area damaged as a result of aggressive substances action, A_{co} original undamaged cross section area.

Formulation of damage parameters evolution equation in steel

The scheme of rebar cross section area degradation cf. Fig. 2. It will be assumed that the steel global degradation parameter can be presented by using the following equation, cf. [5].

$$\begin{aligned} &D_s = 1-(1-D_{spo})(1-D_{scb}), \\ &D_{spo} = \tfrac{A_{sp}}{A_{so}},\ D_{scb} = \tfrac{A_{smc}}{A_{scb}},\ A_{scb} = A_{so} - A_{sp} \end{aligned} \tag{8}$$

where A_{sp} is the pit cross section area, A_{so} initial cross section of rebar, A_{smc} micro cracking cross section area, A_{scb} gross cross section area of the core.

Formulation of the degradation parameter D_{spo}: The degradation parameter D_{spo} evolution character is of electrochemical type and is described by the use of Faraday's law [6]:

$$A_{sp} = A_{so} - 0.25\pi(\phi_{so} - \phi_{sp})^2 \tag{9}$$

$$A_{so} = \frac{\pi\phi_{so}^2}{4}, \phi_{sp} = m\lambda i_{corr} t \tag{10}$$

where m type of corrosion dependent coefficient ($m = 2$ for the uniform corrosion), λ conversion coefficient [μ*A/cm*^{2}] $\rightarrow$ [*mm/year*], the size of this coefficient is λ=0.0115, i_{corr} density of corrosion electric current [μ*A/cm*^{2}].

Formulation of the degradation parameter D_{scb}: It will be assumed that the evolution equation describing the degradation parameter D_{scb} can be presented in the form of the following equations

$$\begin{aligned} \frac{dD_{scb}}{dt} &= K\left[\bar{\sigma}(t)\right]^v \qquad \bar{\sigma}(t) = \frac{N}{A_{so}-A_{smc}} \\ D_{scb}(t)|_{t=0} &= 0 \qquad D_{scb}(t)|_{t=t_{kr}} \cong 1 \\ \bar{\sigma}(t) = \frac{\sigma}{(1-D_{spo})(1-D_{scb})} &\qquad \sigma = \frac{\mathrm{N}}{A_{so}} \end{aligned} \tag{11}$$

Integrating the equation (11) the final form of the global degradation parameter of reinforcing steal in the form of the following equation will be obtained

$$\begin{aligned} D_{scb} &= 1 - \sqrt[v+1]{1-(1+v)B(w_0+4w_1+w_2)\cdot t} \\ w_0 &= A_{so}^{-2v} \\ w_1 &= (A_{so}-0.5A_{sp}(t))^{-2v}\cdot\pi\cdot(4\cdot \mathrm{A}_{so})^{-1} \\ w_2 &= (A_{so}-A_{sp}(t))^{-2v}\cdot\pi\cdot(4\cdot \mathrm{A}_{so})^{-1} \end{aligned} \tag{12}$$

In this equation K, v are material parameters. They can be designate experimentally by expressing the time of breaking down the steel specimen subjected to the influence of surface active substances.

Acknowledgement: This paper was created with the help of grant: FP6 Marie Curie Transfer of Knowledge MTKD-CT-2004-509775.

References

[1] . Krykowski (2006): *Computational model of corrosion damage in the reinforced concrete*. Archives of Civil Engineering, **2**, Warszawa, 319-337.

[2] . Jirásek, Z. P. Bažant (2002): *Inelastic analysis of structures.* John Wiley & Sons, LTD.

[3] . Hofstetter, H. A. Mang (1995): *Computational mechanics of reinforced concrete structures*. Friedr. Vieweg&Sohn Verlagsgesellschaft mbH, Braunschweig/Wiesbaden.

[4] . J. Ulm, J. M. Torrenti, F. Adenot (1999): *Chemoporoplasticity of calcium leaching in concrete.* Journal of Engineering Mechanics, ASCE, 1200-1211.

[5] . Zybura (1990): *Degradacja żelbetu w warunkach korozyjnych*. Zeszyty Naukowe Politechniki Slaskiej. Gliwice.

[6] . B. Roberts, C. Atkins, V. Hogg, C. Middleton (2000): *A proposed empirical corrosion model for reinforced concrete*. Proc. Instn. Civ. Engrs Structs&Bldgs, 140.

The Influence of Proton-Exchange-Membrane Thickness on Fuel Cell Efficiency

O. Mičan[1], **F. Maršík**[2]

[1]Faculty of Nuclear Science and Physical Engineering, Czech Technical University
Břehová 7, 115 19 Praha 1, Czech Republic
omican@gmail.com

[2]Mathematical Institute, Charles University
Ke Karlovu 3, 121 16 Praha 2, Czech Republic
marsik@it.cas.cz

Summary: We propose a simple diffusion model of a polymer-electrolyte-membrane fuel cell and perform its thermodynamic analysis. This model attempts to describe both transport processes in the membrane and electrochemical reactions at the electrodes with a single set of equations. By using linearization of the model equations and normal mode analysis, we derive an expression for characteristic thickness of the membrane. We also obtain an expression for the membrane efficiency and, as an example application, use it in an experimental design for the determination of membrane transport parameters.

A diffusion-type model of PEMFC involving electrochemical reaction and mass and charge transfer

Fuel cells represent a prospective, efficient, and clean alternative to traditional ways of generating electrical energy for automotive, portable and stationary applications. One of the most promising types of fuel cells are PEMFCs (Polymer-Electrolyte-Membrane or Proton-Exchange-Membrane Fuel Cells), since they are able to operate under ambient or near-ambient conditions, have simple design, and could be relatively inexpensive. A hydrogen-oxygen PEMFC produces electricity during electrochemical half-reactions that occur at its electrodes. The anode half-reaction reads

$$2\mathrm{H}_2 + 4\mathrm{H}_2\mathrm{O} \rightleftharpoons^{k_a^+}_{k_a^-} 4\mathrm{H}_3\mathrm{O}^+ + 4\mathrm{e}^- \tag{1}$$

while the cathode one reads

$$\mathrm{O}_2 + 4\mathrm{H}_3\mathrm{O}^+ + 4\mathrm{e}^- \rightleftharpoons^{k_c^+}_{k_c^-} 6\mathrm{H}_2\mathrm{O} \tag{2}$$

We proposed a simple diffusion model of a polymer-electrolyte-membrane fuel cell and performed its thermodynamic analysis. Our model takes into account transport of protons and water through the membrane as well as the electrochemical reaction (1), (2). The model has the following parameters: rate constants of the electrochemical reactions, diffusion coefficient of water in the membrane, proton conductivity of the membrane, and electro-osmotic drag coefficient of the membrane. The model output is comprised of water and protons concentration profiles.

Characteristic thickness of the membrane

Having assumed local electroneutrality within the cell and negligibility of the backward reaction rates in (1), (2), we linearized the model equations and performed normal mode analysis of the linearized model. As a result, we have obtained the following approximate relation between characteristic dimension of the membrane and its transport parameters:

$$L \approx \frac{2D_{H_2O} - 3D_\sigma}{20j} C_{H_2O} \pi^2 F \tag{3}$$

Here, L is the characteristic dimension (thickness) of the membrane, D_{H2O} is the diffusion coefficient of water, D_σ is the diffusion coefficient of protons, j is the current density, c_{H2O} is the concentration of water, π is the water production density, and F is the Faraday constant. The results calculated by using the values of transport coefficients from [1] are depicted in Fig. 1. The values around 200 μm for a highly hydrated membrane correspond with the usual thickness of common fuel cell membranes.

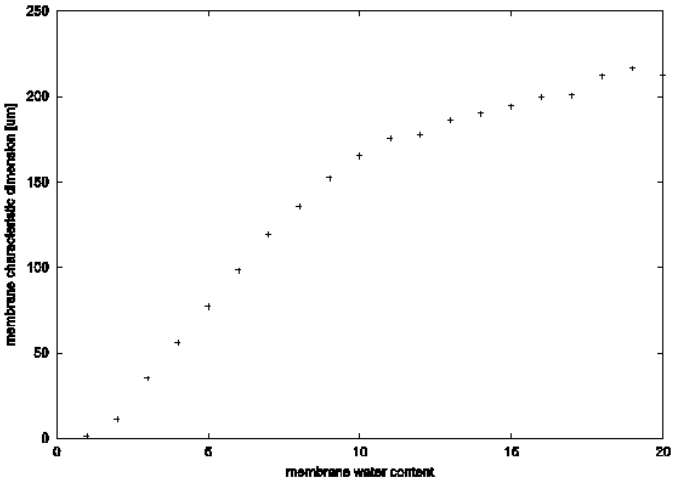

Figure 1: Characteristic dimension (thickness) L of a Nafion membrane as a function of the membrane water content λ at the temperature of 80 C and current density of 500 mA/cm^2.

Coupling and efficiency

A topic of significant interest from the irreversible-thermodynamic viewpoint is coupling between various

transport phenomena. In our model, we analyse coupling between electric current and water diffusion flux. Quantitatively, coupling is described by the so-called degree of coupling. It has been shown that there is a relation between maximum efficiency of conversion of energy of one process into energy of another process. For our PEMFC model, this relation takes the form

$$\eta_{max} = \left(\frac{1 - \sqrt{1 - q^2}}{q} \right)^2 \tag{4}$$

where η_{max} is the maximum efficiency and q is the degree of coupling. The results obtained from (4) using experimental data from various sources are in qualitative agreement with the empirical knowledge that the fuel cell membrane has to be well-hydrated in order to obtain reasonable performance. On the other hand, the figures obtained from (4) for some data sets were significantly lower than one would expect, which suggests possible application of the formula for checking validity of experimental data.

In-situ experimental determination of transport parameters

Another possible application of the relation (4) is in experimental determination of transport parameters of a working fuel cell. While the electric conductivity can be measured *in-situ* by using standard methods [2], the diffusion and electro-osmotic drag coefficients can be determined by measuring water flux through the cell as a response to known values of water concentration gradient and current density, cf. e. g. [3]. The problem is that transport parameters are functions of temperature and membrane water content [4]. This means that both of these quantities should be measured simultaneously with the measurement of transport parameters. By using the relation (4), membrane water content can be determined from the transport parameters and the cell voltage.

References

[1] H. P. L. H. Van Bussel, F. G. H. Koene, R. K. A. M. Mallant (1998): Dynamic model of solid polymer fuel cell water management. *Journal of Power Sources*, **71**, 218–222.

[2] K. S. Forland, T. Forland, S. K. Ratkje (1988): *Irreversible Thermodynamics. Theory And Applications*. Wiley, London.

[3] G. J. M. Janssen, M. L. J. Overvelde (2001): Water transport in the proton-exchange-membrane fuel cell: measurements of the effective drag coefficient. *Journal of Power Sources*, **101**, 117–125.

[4] A. Z. Weber, J., Newman (2004): Modeling Transport in Polymer-Electrolyte Fuel Cells. *Chem. Rev.*, **104**, 4679–4726.

Biomechanical Simulations of Corneal Refractive Surgery

E. Rizzi*, **S. Sangalli**

[1]Università di Bergamo, Facoltà di Ingegneria, Dipartimento di Progettazione e Tecnologie
viale G. Marconi 5, I-24044 Dalmine (BG), Italy
egidio.rizzi@unibg.it

Summary: This short paper reports some preliminary results on the biomechanical simulation of corneal refractive surgery techniques such as Radial Keratotomy (RK) and PhotoRefractive Keratectomy (PRK). These surgical techniques are used to reshape the human cornea and thus modify its refractive power as needed to resolve most common refractive disfunctions such as myopia, hyperopia and astigmatism.

Introduction

Refractive surgery of the cornea has become in recent years a diffuse technique to cope with most common refractive defects in human vision [1, 3, 6]. After the pioneering attempts of RK in the second half of 1900, the availability of excimer-based laser techniques such as PRK and flap-based LASIK (LAser in SItu Keratomileusis) have blown-up the number of patients that have been treated all over the world. The development and tuning of such techniques on the single, individual cornea, seems to have been approached mainly by an experience-gaining and trial-and-error approach. Despite the massive use of refractive surgery, an appropriate biomechanical model of the cornea under physiological conditions and under the effect of surgical treatments seems still to be lacking. Such an approach appears to be necessary for a correct tuning of the techniques on both a general and an individual basis. This would help in reducing the risk of complete or partial failure that are still connected to the implementation of these removal techniques (that weaken the cornea from a structural point of view).

This work attempts a biomechanical modelling of refractive surgery. Efforts in this direction have been already produced by different authors, mainly with respect to well-established RK, but also to PRK [7, 2, 9, 4, 5]. Analytical and numerical (FEM) approaches are employed to estimate the change in dioptric power of the myopic cornea following RK and PRK under the assumption of linear elastic behaviour. The following specific aspects as described in the sequel have been considered. A comprehensive account of the study is given in [8].

Membrane/flexure behaviour of the cornea based on Shells Theory

The basic equations of Shells Theory [10] are solved to analyze the stress/deformation response of the cornea in physiological conditions under internal IOP (IntraOcular Pressure). The pure membrane regime is investigated for a vanishing constraint at the limbus interface between cornea and sclera (rollers). Flexure behaviour is instead taken into account by assuming perfect built-in constraints at the limbus. Results are presented in terms of: i) the analytical solution with 8 terms of the hypergeometric series; ii) Geckeler approximate analytical solution I; iii) Hetény approximate analytical solution II. An average human cornea is considered as a constant thickness spherical elastic shell with medium radius R_m=7.35 mm, thickness s=0.59 mm, half opening apex-to-limbus angle θ_c=48°, Young's modulus E=1 MPa, Poisson's ratio ν=0.49, IOP p=15 mmHg=2 kPa. Output is obtained in terms of both stress resultants and deformation. Fig. 1 reports the vertical displacement of the shell η as a function of the anomaly angle θ from the apex. Notice that the truncated exact solution remains valid to represent the apical zone near θ=0°. These results have been compared to FEM simulations of an average physiological cornea with variable thickness, with order-of-magnitude agreement on both static and kinematic output.

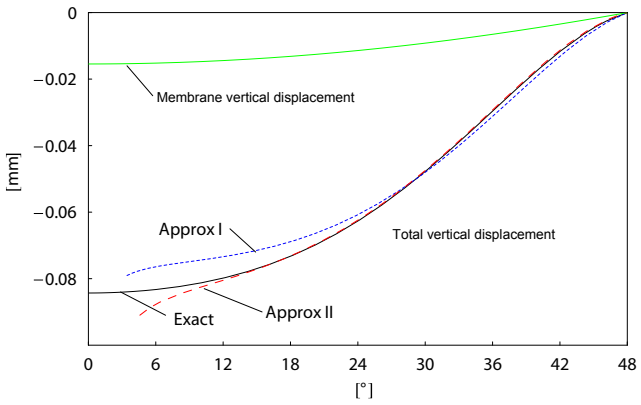

Figure 1: Vertical displacement of the corneal linear elastic shell under IOP according to Shells Theory.

FEM modelling of RK

A 3D model of revolution is assembled, with built-in conditions at the limbus. Four incisions are considered, by constraints removal, at 85% thickness depth of the cornea, preserved free optical zone of 4 mm diameter, length of 2.5 mm from that. Flattening of the central cornea and bulging of the peripheral regions are observed, trends in agreement with previous simulations [7, 4]. A FEM/CAD procedure has been developed to evaluate the local radii of curvature of the central cornea in pre- and post-operative conditions. This allows to evaluate the change in dioptric power of the cornea according to the formula

$$\Delta D = 337.5\ (1/R_f - 1/R_i)\ , \qquad (1)$$

where R_i and R_f are the estimated initial and final radii of curvature in mm [3]. Values of -3.85 D and -3.81 D have been evaluated along the incision meridians and at 45° between them.

FEM modelling of PRK

The physiological cornea is considered with both a Katsube-type [5], step-shaped constant thickness and a Munnerlyn-type variable thickness ablation profile [1]. The two main parameters in the latter PRK procedure are the maximum ablation depth h at the apex and the diameter d of the ablation zone. Parametric axisymmetric FEM analyses have been performed for various h and d. Figs. 2–3 resume the prediction of the degree of correction in diopters. Fig. 4 compares predictions that can be made in various ways, with reference to the so-called Munnerlyn's formula [1], $h = -\Delta D d^2/3$, that accounts just for the geometrical reshaping of the external surface of the cornea after laser ablation. This formula is normally employed in defining the input parameters h, d of the surgical PRK treatment for a given desired ΔD. Our results turn out under-corrective. However, it has to be noted that no attempts where made in the study towards a quantitative prediction, with ad-hoc calibration of the parameters (for example to the Young's modulus E is given the nominal value 1 MPa). On the other hand, the analysis shows the importance of considering not only the pure geometrical reshaping of the cornea but also the consequent change of the biomechanical response of the weakened cornea, which is reflected by the discrepancies between curves 1-2 and 3-4 in Fig. 4.

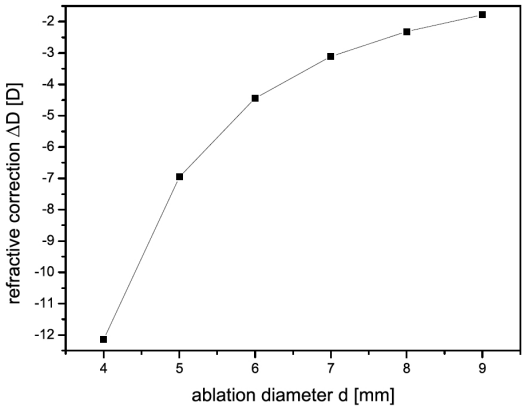

Figure 2: Degree of refractive correction ΔD after PRK as a function of ablation diameter d at constant maximum ablation depth (h=0.1 mm).

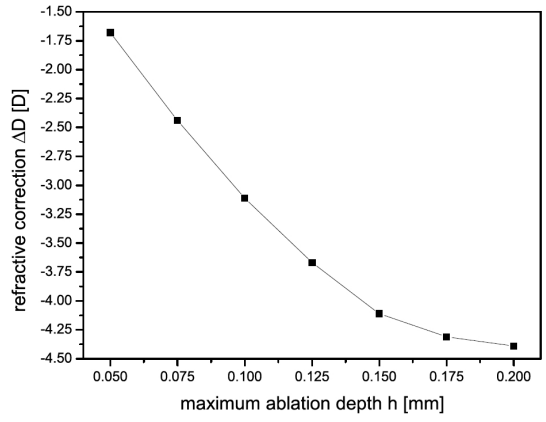

Figure 3: Degree of refractive correction ΔD after PRK as a function of maximum ablation depth h at constant ablation diameter (d=7 mm).

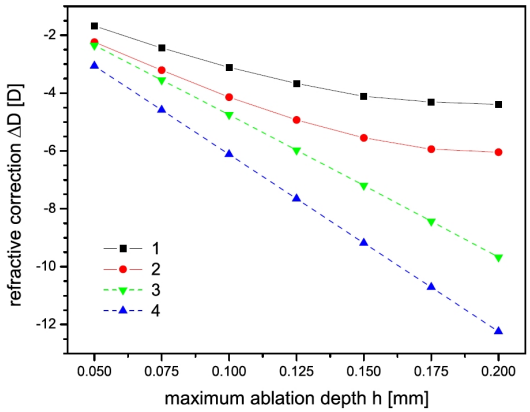

Figure 4: Idem as Fig. 3. Comparison of different estimates of pre- and post-operative shapes from: 1) deformed profiles; 2) same but through Munnerlyn's formula; 3) undeformed profiles; 4) pure Munnerlyn's formula on target ablation profile.

Conclusions

These preliminary results further support the need of a quantitative biomechanical modelling of refractive surgery, possibly even on an individual basis. This should complement the ophtalmologist's experience in defining the most appropriate treatment parameters and thus help in reducing the risk of failure.

References

[1] F. S. Brightbill (1999): *Corneal Surgery*. Mosby.

[2] M. R. Bryant, P. J. McDonnell (1996): Constitutive laws for biomechanical modeling of refractive surgery. *J. of Biomechanical Engineering*, **118**, 473–481.

[3] C. S. Foster, D. T. Azar, C. H. Dohlman (2004): *Smolin and Thoft's. The Cornea. Scientific Foundations and Clinical Practice*. 4th Ed., Lippincott Williams & Wilkins.

[4] F. A. Guarnieri (1999): Modelo biomecanico del ojo para diseño asistido por computadora de la cirugia refractiva. Tesis de Doctorado, Univ. Nacional del Litoral, Argentina.

[5] N. Katsube, R. Wang, E. Okuma, C. Roberts (2002): Biomechanical response of the cornea to phototherapeutic keratectomia when treated as a fluid-filled porous material. *J. of Refractive Surgery*, **18**, S593–S597.

[6] T. Kohnen, D. D. Koch (2005): *Cataract and Refractive Surgery*. Springer.

[7] P. M. Pinsky, D. V. Datye (1991): A microstructurally-based finite element model of the incised human cornea. *J. of Biomechanics*, **24**, 907–922.

[8] S. Sangalli (2005): Modellazione della biomeccanica corneale in chirurgia refrattiva. Tesi di Laurea, Univ. di Bergamo, Fac. di Ingegneria, Dalmine (BG), 260 pages.

[9] T. J. Shin, R. P. Vito, L. W. Johnson, B. E. McCarey (1997): The distribution of strain in the human cornea. *J. of Biomechanics*, **30**, 497–503.

[10] S. Timoshenko, S. Woinowsky-Krieger (1959): *Theory of Plates and Shells*. McGraw-Hill.

Measurement of Elastic Coefficients of Bovine Cortical Bone of General Shape by Ultrasonic Immersion Technique

T. Goldmann[1*], **H. Seiner**[2,3], **M. Landa**[3]

[1]CTU in Prague, Faculty of Mechanical Engineering, Department of Mechanics, Biomechanics and Mechatronics
Technická 4, 166 07 Prague 6, Czech Republic
Tomas.Goldmann@fs.cvut.cz

[2]CTU in Prague, Faculty of Nuclear Science and Physical Engineering, Department of Materials
Trojanova 13, 120 00 Prague 2, Czech Republic
hseiner@it.cas.cz

[3]Academy of Sciences of the Czech Republic, Institute of Thermomechanics
Dolejškova 5, 182 00 Prague 8, Czech Republic
ml@it.cas.cz

Summary: This work contributes to the methodology of an evaluation of elastic properties of cortical bones by ultrasonic wave inversion, whilst the bone is considered to be a linear elastic anisotropic continuum. Velocities of acoustic waves are used as an input data into inverse problem and they are experimentally detected by means of the ultrasonic based pulse-echo immersion technique. The geometry of bone specimens is also implicated into algorithm by the model of wave propagation through curvilinear anisotropic sample based on the simplified ray method.

Introduction

The aim of this study is contribution to the methodology of an evaluation of elastic properties of cortical bone by ultrasonic wave inversion, whilst the bone is considered to be a linear elastic anisotropic continuum. Velocities of acoustic waves are used as an input data into inverse problem and they are experimentally detected by means of the ultrasonic based pulse-echo immersion technique. This method was developed on composite structures such as plates and cylindrical shells. The geometry of bone specimens is also implicated into algorithm by the model of wave propagation through curvilinear anisotropic sample based on the simplified ray method, which is an original approach and its application to the experimental determination of the bovine femoral sample is the main subject of the interest of this work. The stability of resulting data from inverse algorithm is evaluated by the statistical method based on the Monte-Carlo simulation. The suggested approach has a potential for qualify of such measurements performed on fresh bones and also for improvement in-situ ultrasonic techniques.

Materials and methods

The main aim of this experiment is to deal with possibilities of the measurement of the matrix of elastic coefficients of the cortical bone by means of the dynamical, ultrasound based, mechanical tests. The methodology should be non-destructive; ultrasound based, appropriates for a rapid measurement and undemanding a sample preparation. The ultrasonic-pulsed through-transmission method with the specimen immersed in a liquid between two opposite trans-ducers has been chosen as a suitable technique.

Following experiments were performed on the dry bovine femur. Dry bovine bone was used instead of a wet bone [1] for the measurement, because of the independent determination of elastic properties separately, from the natural visco-elastic behavior of bones. The bone sample was slit into two parts along the bone axis in order to monitor just simple wave propagation through one face of the bone and each part was shape-measured on CNC milling machine. During the experiment, just one particular place in a middle part of the bone localized on a medial side of the bovine femur sample was examined.

The three different modes of the measurement, modes C, D and I, were performed. Modes C and D corresponded to the horizontal positioning of the bone between the transducer and the reflector where the wave propagation in an axial plane of the bone was observed. The bone geometry was not solved in these modes, the bone geometry was considered as planar in the surrounding of a measuring position. This mode was appropriate for evaluation of 6 out of 9 elastic coefficients ($c_{11}, c_{33}, c_{44}, c_{55}, c_{66}$ and c_{13}) of the orthotropic material symmetry. These elastic constants were evaluated from measured quasi-longitudinal and quasi-transverse wave velocities via the solution of an inverse problem of the Christoffel equation [2]. The mode I corresponded to the vertical configuration of the measurement. In this mode, the propagation of the planar wave was observed in the plane perpendicular to the long axis of the bone, so the bone curvature needs to be considered. This is resolved by means of Simplified Ray Method [3]. The technique [2] is based on a wavefront substitution by the closely localized energy flow (ray) in every geometrical point. The Christoffel's equation along rays and the ray behavior at a solid/liquid interface will be solved numerically afterwards. Rays in immersion are lines perpendicular to the wavefront - the planar wavefront is replaced by the set of respectively parallel rays. The anisotropy orientation is included in the model by the definition of the angle of anisotropy orientation in each point of the sample. The rays inside the sample are designed on the basis of Huygens axiom, thus each point of the cur-

rent wavefront is a new point source and those newly generated wavefronts are superimpose into new wave fronts. An example of a modeling of the complex interaction of a planar wave in an anisotropic curvilinear specimen is illustrated on Fig. 1. The Carbon Fibre Reinforced Plastic (CFRP) tube, the material having the transversely isotropic symmetry, is introduced on this figure as a model example.

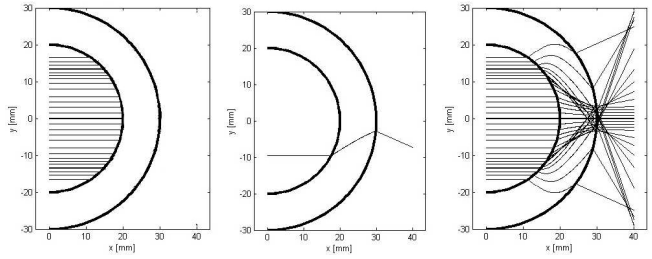

Figure 1: The interaction of planar wave with a strongly anisotropic tube. The selection of initial rays; the path of one ray; the complete interaction.

The mode I was used for the determination of coefficients c_{22} and c_{12}. The remaining coefficient c_{23} was determined by the simple contact pulse-transmission measurement.

To estimate the accuracy of the optimization procedure's results, no appropriate analytical approach is available. The only possible solution is, thus, the Monte Carlo simulation, based on running the whole optimization process several times with randomly distorted input data.

Results

The stability of elastic coefficients of the bovine bone sample resulting from an inverse problem optimization was evaluated by the simulation based on the Monte-Carlo statistical method [2]. Input parameters into this simulation were variations of specimen thickness, rotations of a sample (mode C,D) or a reflector (mode I), a temperature of the water bath and a density of the specimen. The Monte-Carlo simulation was repeated 30 times to generate a representative set of output data. The variability of this set is approximately expressed by the usual Gaussian statistic quantities, namely standard deviations. Obviously, the presented standard deviations cannot be treated absolutely, but they bring a valuable insight in how sensitive and stable the optimization procedure is for each particular coefficient. Final resultant coefficients c_{ij} in GPa can be expressed in the following form:

$$c_{ij} = \begin{pmatrix} c_{11} & c_{12} & c_{13} & 0 & 0 & 0 \\ c_{12} & c_{22} & c_{23} & 0 & 0 & 0 \\ c_{13} & c_{23} & c_{33} & 0 & 0 & 0 \\ 0 & 0 & 0 & c_{44} & 0 & 0 \\ 0 & 0 & 0 & 0 & c_{55} & 0 \\ 0 & 0 & 0 & 0 & 0 & c_{66} \end{pmatrix} = \begin{pmatrix} 27.4 \pm 1.6 & 9.1 \pm 3.5 & 8.3 \pm 5.3 & 0 & 0 & 0 \\ 9.1 \pm 3.5 & 30.3 \pm 2.8 & 8.5 & 0 & 0 & 0 \\ 8.3 \pm 5.3 & 8.5 & 34.1 \pm 1.7 & 0 & 0 & 0 \\ 0 & 0 & 0 & 9.3 \pm 0.9 & 0 & 0 \\ 0 & 0 & 0 & 0 & 7.0 \pm 0.4 & \\ 0 & 0 & 0 & 0 & 0 & 6.9 \pm 0.5 \end{pmatrix} \quad (1)$$

Particular coefficients of matrix (1) were evaluated from modes C, D and I (see Materials and Methods). The modes C and D were used for the determination of 6 elastic coefficients without considering the general geometry of bone specimen - without solving the ray model. The mode I served for the determination of 2 elastic coefficients. This mode corresponds to the vertical configuration of the measurement, so the wave propagation and the elastic constant evaluation of the bone specimen with the general geometry of a bone specimen must be resolved via the ray method.

The experimental procedure and the elastic constant evaluation of the mode I is subsequent. The input geometry of the bone specimen into the ray algorithm was obtained by the contact probe on milling machine. During the experiment, the bone sample was rotated into the vertical position, so the wave propagation in the plane perpendicular to the bone axis could be observed. Then, the ray algorithm is solved for a different positioning of the specimen until the ray model is tuned to the measured data. The Christoffel equation along thereby obtained rays and behavior of rays at the solid/specimen interface was numerically solved by means of the inverse problem.

The remaining coefficient was not possible to determine via immersion technique without additional specimen cutting. This coefficient was evaluated subsequently via simple pulse-echo contact technique.

Discussion and conclusion

The proposed methodology is usable for the measurement of all 9 elastic coefficients of compact bone, but specimen must be cut, which is at variance with request on non-destructivity of entire process. 8 coefficients can be measured non-destructively, but general specimen shape needs to be considered, which leads to application of ray method. The tuning of ray model to experiment and measurement of specimen shape is quite laborious. This immersion technique is very suitable for quick evaluation of 5 constants of long bone non-destructively without solution of ray model.

The resultant matrix of elastic coefficients (1) of the bovine dry femur evaluated in this work is in line with other data [2] and the original presumption, that the dry bone is known to be stiffer then the wet one was satisfied.

Acknowledgement: This work was supported by the Ministry of Education project No. MSM 6840770012, the Grant Agency of Sciences of the Czech Republic under project No. IBS2076919 and the Institutional project AVOZ2076919.

References

[1] M. Pithioux, P. Lasayques, P. Chabrand (2002): An alternative ultrasonic method for measuring the elastic properties of cortical bone. *Journal of Biomechanics*, **35**, 961–968.

[2] T. Goldmann (2006): *Propagation of Acoustic Waves in Composite Materials and Cortical Bone*. CTU in Prague, Prague.

[3] V. Cerveny (2001): *Seismic Ray Theory*. University Press, Cambridge.

Author Index